JOHANNES GUTENBERG UNIVERSITÄT MAINZ

JG|U

Finite magnetic-field Coupled-Cluster methods: Efficiency and Utilities

Dissertation
zur Erlangung des Grades
"Doktor der Naturwissenschaften"
im Promotionsfach Chemie

am Fachbereich Chemie, Pharmazie,
Geographie und Geowissenschaften
der Johannes Gutenberg-Universität Mainz

Marios Petros Kitsaras
geb. in Amarousio, Griechenland

Mainz, 2023

1. Gutachter/in: [redacted]
2. Gutachter/in: [redacted]
3. Gutachter/in: [redacted]

Tag der mündlichen Prüfung: 31.07.2023

For the completion of this thesis, I would like express my gratitude to various individuals. I am thankful to [redacted] for the opportunity to work in his group, and for his help and valuable insight in various challenges. I also like to warmly thank [redacted] for her supervision, her tutelage and the wonderful opportunity to work in this topic. Her mentorship has decisively shaped my academic identity and will guide my future development. I am truly indebted. I also appreciate the support, financial and academic, for taking part in international highly prestigious graduate schools, like the ESQC 2019 and the MRPSS 2021, as well as various conferences, where I was able to expand my knowledge in quantum chemistry, make new professional acquaintances and also new friends.

I would also like to express my gratitude to my colleagues and fellow students in the theoretical chemistry group in the Johannes Gutenberg Universität Mainz. Specifically, I want to thank [redacted], [redacted], and [redacted], whom I had the pleasure to supervise. I hope they learned as much from me as I was taught from them. I ought to give special thanks to [redacted] for extended debugging sessions. A grateful acknowledgment goes to [redacted], my office mate, that had to endure me and also live through numerous discussions and exchanges of ideas on our projects. Lastly, I want to express my heartfelt appreciation for [redacted], my dear colleague and friend. The current thesis would not have been possible without her deciphering skills. Being the other "Exote" in the group, made my life easier, more colourful and more musical in the professional and personal level. Thanks for being there in difficult times.

Moreover, I want to thank my friends outside work, those that were there when I started this new chapter of my life in Mainz, those that came along the way, and those that stayed until the finish. Thanks for being there for the journey. Living away from my home country makes me often feel detached and without roots. These friends made me at times retain a sense of belonging.

Lastly, my deepest appreciation goes to my parents [redacted] and [redacted]. I owe my accomplishments to their trust and support, as well as to the pressure they put on me, knowing how much I can really handle.

Contents

Chapter 1

Introduction

Using the concepts introduced by Kuhn in his book *The Structure of Scientific Revolutions*,[1] quantum mechanics emerged as a *normal science*[a] in 1925 following the work of Heisenberg and Schrödinger. Their contributions resolved the *crisis* at the start of the 20th century caused by the inability of the *paradigms* of classical mechanics to explain what today are called quantum phenomena. Very soon after, quantum chemistry emerged with the first quantum-mechanical description of the chemical bond by Heitler and London.[2] Since quantum chemistry today is an evolving *paradigm* almost one century old, it requires high amounts of specialised training to understand and to work with. Despite its longevity, modern quantum chemistry does not show many signs of a *crisis*. Its high interpretational and predictive value makes it useful to theoretical and experimental chemists alike, especially after the development and wide use of quantum-chemical programs.[3] Expressing a personal opinion, the model with which quantum mechanics describe reality is both beautiful and mysterious, making the quote attributed to Feynman "If you think you understand quantum mechanics, you don't understand quantum mechanics" an everlasting motivation to "keep digging". The "puzzles" of choice to solve in the boundaries of the *normal science* for this thesis are found in the quite new area of chemistry in strong magnetic fields.

The study of molecules in a magnetic field through theoretical means may have various motivations. Schmelcher et al.[4] mention various phenomena that may be encountered in a magnetic field, like the quantum Hall effect and the chaotic behaviour of highly excited atomic and molecular Rydberg states. The behaviour of nanostructures in strong magnetic fields attracts particular interest as well.[5,6] In recent decades, the study of linear, and more importantly, non-linear properties of small molecules in a magnetic field has emerged. This includes the calculation of magnetizabilities and NMR shieldings,[7,8] non-linear ring currents,[9] the behaviour of antiferromagnetic molecular wheels,[10] the magnetic circular dichroism[11,12] and closed-shell paramagnetism.[13] Such investigations were reinvigorated by the employment of London orbitals[14] for calculations in the presence of a magnetic field.[15] What drives the interest of quantum chemistry in the strong magnetic field regime using non-perturbative approaches[16] further is the discovery of magnetic fields on White Dwarfs (WD) strong enough to compete with the Coulomb interaction.[17] The study of chemistry in these celestial objects has reemerged in the last decade as an active field of interest.[13,18–23] Moreover, the interpretation of spectra from such strongly magnetic WDs (MWD) requires finite magnetic-field (ff) techniques for the assignment of absorption lines.[21,22] It has even been shown, that for MWDs, in which the magnetic-field strength is well under 100 MG = 10000 T, ff techniques are still necessary.[24]

White Dwarfs are stellar remnants.[25] When a star exhausts its hydrogen reserves to create energy through nuclear fusion and is below a critical mass, instead of becoming a neutron star or a black hole, it will eventually shed its outer layer creating a planetary nebula. The remaining core is the White Dwarf which is composed of different elements depending on the mass of the star and its ability to further fuse heavier nuclei. The vast majority of stars, including our sun, will eventually become WDs. They typically have a size similar to that of Earth but are as heavy as the sun. Their atmosphere

[a] *Normal science* is the regular research work, described as "puzzle solving", carried out while the foundation of the established scientific theory (*paradigm*) is not being put in question. Emerging anomalies during research that resist deciphering for a long time lead to a *crisis* of the *paradigm* that is resolved through a *paradigm* shift (scientific revolution).[1]

consists of H, He, and other heavier elements some of which may arise from planetary debris.[26–45] Since WDs no longer produce energy, they get cooler overtime by emitting radiation. Their typical effective temperatures are about 4000-150000 K. Because of their eventual low temperature, molecules may form. Indeed, H_2, CH, and C_2 have been observed on the atmospheres of WDs.[40,41,43] Moreover, current measurements have allowed the detection of a magnetic field stronger than 1 kG at about $20\% - 25\%$ of all WDs, with the strongest magnetic field reaching up to 100 kT.[46,47]

Studying the composition of the atmospheres of WDs is important for better understanding the stellar evolution and the evolution of the universe in general.[25,48–50] This is mainly done by analysing and interpreting their spectra and finding characteristic atomic and molecular absorption signatures. Numerous studies exist for the non-/weakly-magnetic WDs, since their spectra can be directly compared to experimental data from atomic and molecular spectroscopy.[51] However, this is impossible for the strongly MWDs, because magnetic fields of such magnitude are not reproducible on Earth for an experimental setting. To put the magnitude of the magnetic field of MWDs into perspective, Earth's field is about 10^{-5} T, a refrigerator magnet has a field of about 10^{-3} T, and an NMR uses fields at the order of 10 T. The strongest non-destructive field generated was 300 T[52] and the record for maximum indoor destructive field is around 1200 T.[53] In addition, converting these field strengths in atomic units of magnetic field, i.e., $1\ B_0 = 2.35051756758(71) \cdot 10^5$ T, brings the strongest of non-destructive magnetic fields to only $\sim 10^{-4}\ B_0$. MWDs in turn reach up to $\sim 0.4\ B_0$. There exist experimental settings that mimic the behaviour of atoms in strong magnetic fields,[19,54–56] but such settings are not flexible enough to serve as general model systems. It is thus clear that the lack in reference spectra for the study of MWD can only be bridged by theoretical predictions. Moreover, magnetic fields on Earth can usually be treated perturbatively within a quantum-chemical calculation, since the magnetic interaction is much weaker compared to the electron-electron, electron-nucleus and nucleus-nucleus Coulomb interactions dominant in a molecule. For fields close to $\sim 1\ B_0$ however, such a treatment is inappropriate as the magnetic and electrostatic interactions have to be treated on equal footing, necessitating the development and use of ff techniques. The behaviour of molecules in this so-called mixing regime proves to deviate significantly from the "standard" chemical intuition with various phenomena arising that have no field-free analogue,[4,16] like the perpendicular paramagnetic bonding[18] and other exotic molecular structures.[57]

The form of the Hamiltonian which takes the magnetic field interaction into consideration includes an imaginary term that describes the interaction of the magnetic field with the angular momentum (paramagnetic Zeeman term). The emergence of the angular momentum operator in first order dictates the use of complex algebra for the derivation of wavefunction solutions. Since existing quantum-chemical codes typically use real numbers, the need for complex algebra poses a serious incompatibility, resulting either in a non trivial and costly upgrading of existing program packages or the development of new ones. In addition, handling complex numbers requires twice as much memory and is typically three to four times slower than only handling real numbers.[58] The first studies for atoms and molecules in strong magnetic fields include calculations for the H[27,28,31] and He[35,59] atoms and the H_2^+ ion[60] and H_2 molecule.[61,62] The basics for the general study of atoms and molecules in magnetic fields were established by the work of Schmelcher et al.[4,16,63–65] These studies (including calculations for Li)[66] were based either on a self-consistent field (SCF) approach for the one-electron systems, or on a full-configuration interaction (FCI) approach. The latter, however, is applicable only to systems with a small number of electrons. The first quantum-chemical program to use London orbitals[14] that completely deal with the gauge-origin dependence of observables for approximate wavefunctions for calculations in the presence of magnetic field is the LONDON program package.[15,67] The next decade saw ff implementations in existing and new program packages like the QUEST[68] and TURBOMOLE[69,70] program packages with an emphasis on efficient integral calculation and current density-functional theory (DFT) methods,[71] BAGEL[72] and CHRONUS[73] on the treatment of relativistic effects, and numerical methods in HELFEM,[74] the MADNESS program package[75] to name a few. For the predictions and interpretation of spectra, however, an accuracy beyond that achieved by SCF methods (HF or DFT) is needed.[21,22] The QCUMBRE program package[76] that works in combination with LONDON,[67] BAGEL[72] or the ff implementation in CFOUR[77–79] can provide such a treatment.

QCUMBRE is able to handle various calculations in the presence of a magnetic field at the correlated level of theory.[76] The ff-CCSD, ff-CCSDT as well as ff-CCSD(T) methods were implemented for energy calculations of atoms and small molecules. The Equation of Motion (EOM)-CC implementation enables the prediction of excitation energies with high accuracy.[21,22,80] Transition properties at the EOM and linear response (LR) levels of theory are able to give information about absorption intensities.[81] Thus, the very basic tools for the simulation of spectra are present in QCUMBRE. Still, in many realistic applications, QCUMBRE was not able to provide an appropriate treatment. In order to extend the functionalities of QCUMBRE, a new interface to CFOUR was developed. This lifts the dependence on the LONDON program package for providing integrals over London orbitals and an SCF solutions. CFOUR provides a more efficient calculation of integrals over GIAOs and gives access to additional tools like symmetry exploitation, control of the SCF iteration, etc. Additionally, results at the CCSDT level of theory, despite being appropriate for the accurate simulation of spectra and the interpretation of MWD spectra without the help of input from experiment, are very costly and the applicability of (EOM-)CCSDT is restricted to very small systems.[80] Moreover, many tools that are necessary for the study of molecules or the general interpretation of a quantum-chemical calculation beyond a simple energy output were not available.

In this thesis, the aforementioned limitations are lifted through the development and implementation of new and existing tools and methods. These are implemented in the CFOUR and QCUMBRE program packages, alongside the development of a working interface between the two programs. The thesis focuses on two general topics. As foreshadowed in the title, the first focus point is the handling of the high cost of CC methods, which compared to conventional implementations is higher because of the use of complex algebra. The second is to improve on the utilities of the implemented ff methods beyond a simple energy calculation.

Before diving into the main topics of the thesis, a theoretical background is to be established in chap. 2. The chapter includes the behaviour of matter in the presence of an electromagnetic field and the derivation of the screened Born-Oppenheimer (BO) approximation that introduces necessary concepts for quantum chemistry. Next, the most prominent theories for approximate solutions to the electronic problem are presented. The calculation of analytic first-order derivatives to compute properties in these theories is addressed. Special care is taken to avoid assumptions for real-valued wavefunction solutions made in standard derivations.

The theoretical chapter is followed by a presentation of the programs used in this thesis, i.e., CFOUR and QCUMBRE, in chap. 3. The development of an interface between the two programs is addressed, which lifts the dependence on the LONDON program package and allows QCUMBRE to benefit from more efficient integral calculations as well as a more flexible implementation of ff-SCF.

The handling of the high cost of the ff-CC approach, which is the first focus point of the thesis, is mainly targeted through the use of approximations to the standard CC models in chap. 4. Firstly, iterative approximations, namely the CCn series of methods,[82–84] were implemented. The CC2 method extends the applicability of CC to larger systems with a scaling equal to that of MP2. CC3 offers an approximate treatment of triple excitations beyond CCSD that is vital for highly accurate results suitable for the assignment of spectra. Secondly, the non-iterative CCSD(T)(a) and EOM-CCSD(T)(a)* approaches[85] were used in ff calculations. Unlike the CCSD(T) gold standard,[86] these approaches offer a non-iterative handling of triple excitations not only for the ground state but also for excited states. These approximate methods are then used to study small- and medium-sized molecules in the presence of a magnetic field, testing their applicability by comparing them with the standard CC truncations.

In many cases, a bare energy calculation is not enough to study the complexity of the molecular electronic structure especially in the exotic mixing regime. Interpretational tools are specific concepts in quantum chemistry that hint either towards the quality of the calculation for a specific system (diagnostic tools) or towards the physics taking place. However, they do not necessarily provide an observable. The development and implementation of such tools that aid the analysis of quantum-chemical calculations are presented in chap. 5. The orbital picture is addressed by targeting the visualization of complex orbitals. Additionally, the spin multiplicity, which is calculated via the spin-squared expectation value, acts as a diagnostic tool[87–90] and it is an observable. These tools are then

used to shed more light on the examples of the previous chapter. In many cases, results directly derived from interpretational tools are only part of the intermediate analysis and they do not constitute an end goal of a study. For this reason, they are often not reported or mentioned in publications, but they contribute immensely to the understanding of a program output and in the processing of the results.

A milestone of this thesis is the implementation of symmetry through point-group theory in the presence of a magnetic field, which is presented in chap. 6. Symmetry contributes to both focus points of this thesis. It has interpretational value, giving information on the irreducible representation (IRREP) of the orbitals and wavefunction and it contributes to the calculation of properties, as vanishing expectation values can be identified a priori based on selection rules. Moreover, it gives significantly more control over the quantum-chemical calculation (e.g. by choosing the occupation of the reference state or the IRREP of an excited state) and results in significant savings regarding computational cost. Many calculations in this study would not have been feasible without the use of symmetry. It is also significant to point out that CFOUR and QCUMBRE are currently the only programs able to handle symmetry in the presence of a magnetic field. The merits of using symmetry, when present in the system, are exhibited by specific examples and applications.

The following chapter (chap. 7) introduces the development and implementation of a novel algorithm for geometry optimizations which is able to function in the presence of a magnetic field. The algorithm is based on numerical gradients as a first step, with minimal changes needed for an implementation based on analytic derivatives. Identifying the optimal geometry of a molecule is often the first step in a quantum-chemical study. It is vital for the study of molecules, as the electron structure is strongly dependent on the geometry. As such, this chapter serves the second focus point, i.e., the development of utilities. Here, the geometry optimization is used to reveal the influence of the magnetic field to the molecular structure, with applications on the methane CH_4 and water H_2O molecules.

The highlight of the thesis, presented in chap. 8, is the assignment of Mg lines in a MWD spectrum[24]. This study makes use of most tools developed and outlined in the previous chapters. It consist of an investigation of the ionization potentials of the metal atoms Na, Mg and Ca as a function of the magnetic-field strength in order to derive the most stable oxidation and electronic states in different magnetic fields. It further considers the electronic transitions of these atoms and the construction of B-λ curves that are directly used in the assignment of the observed spectrum. The achievements of the thesis are then summarized in chap. 9.

Chapter 2

Basic Theoretical Aspects

In this chapter, the theoretical aspects needed for the realization of the thesis are presented. The chapter is structured as follows.

The behaviour of matter in the presence of an electromagnetic field is addressed in sec. 2.1, where the quantum-mechanical formulation of the electric and magnetic interaction is recapitulated. The Schrödinger-Pauli equation for an electron in a magnetic field is derived. The screened Born-Oppenheimer approximation establishes the necessary quantum-chemical language and concepts for the study of molecules in the presence of a magnetic. The generalization of the electronic wavefunction and the effective electronic potential in ff methods is of particular importance. Standard theories for approximate solutions of the electronic problem in the wavefunction approach, i.e., HF, CI, MP, and CC, are presented in sec. 2.2-2.6. Properties calculation for these theories is discussed in sec. 2.7 using derivative theory and the Lagrangian approach is addressed.

The chapter finishes with the perturbative expansion of the CC approach in sec. 2.8. The expansion contributes to a deeper understanding of the success of the standard CC truncations, by estimating the accuracy at each truncation level, and it will be later used for the construction of approximations.

2.1 Magnetic-field interaction in the non-relativistic limit

In this section, the behaviour of a charged particle in an electromagnetic field will be reviewed. The electric $\boldsymbol{E}$ and the magnetic field $\boldsymbol{B}$ obey the four Maxwell equations[91–94]

$$\nabla \cdot \boldsymbol{E} = \frac{\rho}{\epsilon_0} \qquad \text{a charge distribution creates an electric field} \qquad (2.1.1)$$

$$\nabla \cdot \boldsymbol{B} = 0 \qquad \text{there are no magnetic monopoles} \qquad (2.1.2)$$

$$\nabla \times \boldsymbol{E} = -\frac{\partial \boldsymbol{B}}{\partial t} \qquad \text{a time-evolving magnetic field creates an electric field} \qquad (2.1.3)$$

$$\nabla \times \boldsymbol{B} = \mu_0 \left(\boldsymbol{j} + \epsilon_0 \frac{\partial \boldsymbol{E}}{\partial t} \right) \qquad \text{the electric current creates a magnetic field} \qquad (2.1.4)$$

These equation couple the electric and the magnetic field with each other, as well as with the charge density ρ and the current density $\boldsymbol{j}$. The constants ϵ_0 and μ_0 denote the vacuum permittivity and vacuum permeability, respectively.

Based on equations (2.1.2) and (2.1.3), a scalar potential ϕ and a vector potential $\boldsymbol{A}$ are introduced that generate $\boldsymbol{E}$ and $\boldsymbol{B}$

$$\boldsymbol{B} = \nabla \times \boldsymbol{A}$$

$$\boldsymbol{E} = -\nabla\phi - \frac{\partial \boldsymbol{A}}{\partial t}.$$

Using these potentials, the Maxwell equations (2.1.2) and (2.1.3) are automatically fulfilled

$$\nabla \cdot \boldsymbol{B} = \nabla \cdot \nabla \times \boldsymbol{A} = 0$$

$$\nabla \times \boldsymbol{E} = -\nabla \times \nabla\phi - \frac{\partial\left(\nabla \times \boldsymbol{A}\right)}{\partial t} = -\frac{\partial \boldsymbol{B}}{\partial t},$$

since the divergence of a curl and the curl of a gradient always vanish. This reduces the degrees of freedom from six (three coordinates for each vector field, $\boldsymbol{E}$ and $\boldsymbol{B}$) to four (three for the vector potential $\boldsymbol{A}$ and one for the scalar ϕ). Considering eq. (2.1.1) and (2.1.4) for the solutions to the Maxwell equations eliminates two additional degrees of freedom. The remaining two degrees of freedom can be freely chosen, meaning that $\boldsymbol{A}$ and ϕ are not uniquely defined. In other words, different $\boldsymbol{A}$ and ϕ, which are not physical observables, can give rise to the same $\boldsymbol{E}$ and $\boldsymbol{B}$. One can arbitrarily add the gradient of a scalar function to the vector potential, and simultaneously subtract the time derivative of said function from the scalar potential

$$\boldsymbol{A}' = \boldsymbol{A} + \nabla f \tag{2.1.5}$$

$$\phi' = \phi - \frac{\partial f}{\partial t}, \tag{2.1.6}$$

without affecting the observable fields

$$\begin{aligned}
\boldsymbol{B}' &= \nabla \times (\boldsymbol{A} + \nabla f) = \boldsymbol{B} + \overbrace{\nabla \times \nabla f}^{=0} = \boldsymbol{B} \\
\boldsymbol{E}' &= -\nabla\left(\phi - \frac{\partial f}{\partial t}\right) - \frac{\partial\left(\boldsymbol{A} + \nabla f\right)}{\partial t} = \boldsymbol{E} + \nabla\frac{\partial f}{\partial t} - \frac{\partial \nabla f}{\partial t} = \boldsymbol{E}.
\end{aligned}$$

This is mathematically defined as a gauge transformation. Using this freedom offered by equations (2.1.5) and (2.1.6), one is able to use a gauge suitable for the problem at hand, since the electric and the magnetic fields are gauge invariant. In this work, the Coulomb gauge will be used that requires the vector potential to have a vanishing divergence[91,92,94]

$$\nabla \cdot \mathbf{A} = \mathbf{0}. \tag{2.1.7}$$

The Coulomb gauge, however, does not completely fix the gauge freedom.

In the presence of the electromagnetic field, a charged particle with charge q and velocity $\boldsymbol{v}$ experiences the Lorentz force

$$\boldsymbol{F} = q\left(\boldsymbol{E} + \boldsymbol{v} \times \boldsymbol{B}\right),$$

leading to the following expression for the Lagrangian provided there is no further potential

$$L = \frac{m\boldsymbol{v}^2}{2} - q\left(\phi - \boldsymbol{v} \cdot \boldsymbol{A}\right).$$

In order to give a quantum-mechanical description, a Hamiltonian formulation to perform the first quantisation is preferred. The resulting Hamiltonian has the form

$$H = \frac{\boldsymbol{\pi}^2}{2m} + q\phi = \frac{\left(\boldsymbol{p} - q\boldsymbol{A}\right)^2}{2m} + q\phi.$$

Here, the kinetic momentum $\boldsymbol{\pi} = \boldsymbol{p} - q\boldsymbol{A}$ is introduced, which is different from the canonical conjugate momentum

$$\boldsymbol{p} = \frac{\partial L}{\partial \dot{\boldsymbol{r}}},$$

with $\dot{\boldsymbol{r}} = \boldsymbol{v}$ being the time derivative of the position. The first quantisation of the Hamiltonian

$$\begin{aligned}
\boldsymbol{p} &\to -i\hbar\nabla \\
\boldsymbol{r} &\to \hat{\boldsymbol{r}} \\
H &\to i\hbar\frac{\partial}{\partial t}
\end{aligned}$$

results in the time-dependent Schrödinger equation for a charged particle in an electromagnetic field is derived[94,95]

$$\hat{H}\Psi = i\hbar\frac{\partial \Psi}{\partial t} = \frac{1}{2m}\left(-i\hbar\nabla - q\boldsymbol{A}\right)^2\Psi + q\phi\Psi.$$

In order for the above expression for the Hamiltonian to correctly describe an electron in an electromagnetic field, the electron-spin interaction needs to be accounted for. The spin of elementary particles is a property with no classical mechanical analog and was not captured in the quantisation of the Hamiltonian. One way to include the interaction of the spin with the electromagnetic field is to replace the square of the kinetic momentum $\boldsymbol{\pi}^2$ with $(\boldsymbol{\sigma}\cdot\boldsymbol{\pi})^2$, where $\boldsymbol{\sigma}$ is a vector with its three components given by the Pauli matrices that describe spin

$$\begin{aligned}
(\boldsymbol{\sigma}\cdot\boldsymbol{\pi})^2\,\Psi &= \boldsymbol{\pi}^2\Psi + i\boldsymbol{\sigma}\cdot(\boldsymbol{\pi}\times\boldsymbol{\pi})\,\Psi \\
&= \boldsymbol{\pi}^2\Psi + i\boldsymbol{\sigma}\cdot\left[\overbrace{\boldsymbol{p}\times\boldsymbol{p}}^{=0} + q_e^2\overbrace{\boldsymbol{A}\times\boldsymbol{A}}^{=0} - q_e\boldsymbol{A}\times\boldsymbol{p} - q_e\boldsymbol{p}\times\boldsymbol{A}\right]\Psi \\
&= \boldsymbol{\pi}^2\Psi - q_e\hbar\boldsymbol{\sigma}\cdot[\boldsymbol{A}\times(\nabla\Psi) + \nabla\times(\boldsymbol{A}\Psi)] \\
&= \boldsymbol{\pi}^2\Psi - q_e\hbar\boldsymbol{\sigma}\cdot\left[\boldsymbol{A}\times(\nabla\Psi) + \overbrace{(\nabla\times\boldsymbol{A})}^{=\boldsymbol{B}}\Psi - \boldsymbol{A}\times(\nabla\Psi)\right] \\
&= \boldsymbol{\pi}^2\Psi - q_e\hbar\boldsymbol{B}\cdot\boldsymbol{\sigma}\Psi.
\end{aligned}$$

This then results in the Schrödinger-Pauli equation

$$i\hbar\frac{\partial\Psi}{\partial t} = \frac{1}{2m_e}\left(-i\hbar\nabla - q_e\boldsymbol{A}\right)^2\Psi - \frac{q_e}{m_e}\boldsymbol{B}\cdot\hat{\boldsymbol{s}}\Psi + q_e\phi\Psi. \tag{2.1.8}$$

Here, the charge q and mass m have been replaced by the electron charge $q_e = -e$, with e the elementary charge, and the electron mass m_e. The spin operator $\hat{\boldsymbol{s}} = \frac{\hbar}{2}\boldsymbol{\sigma}$ is introduced as well. Eq. (2.1.8) describes an electron in the presence of a magnetic field and is a two-component equation. Alternative to this ad hoc inclusion of the spin interaction, eq. (2.1.8) can be derived as the non-relativistic limit of the Dirac equation.[92]

Considering the action of the square of the kinetic momentum on the wavefunction gives rise to the following expression

$$\begin{aligned}
\boldsymbol{\pi}^2\Psi &= \left(-i\hbar\nabla - q\boldsymbol{A}\right)^2\Psi \\
&= -\hbar^2\nabla^2\Psi + iq\hbar\nabla\cdot(\boldsymbol{A}\Psi) + iq\hbar\boldsymbol{A}\cdot(\nabla\Psi) + q^2\boldsymbol{A}^2\Psi \\
&= -\hbar^2\nabla^2\Psi + iq\hbar\Psi\overbrace{\nabla\cdot\boldsymbol{A}}^{=0} + i2q\hbar\boldsymbol{A}\cdot(\nabla\Psi) + q^2\boldsymbol{A}^2\Psi \\
&= \left(\hat{\boldsymbol{p}}^2 - 2q\boldsymbol{A}\cdot\hat{\boldsymbol{p}} + q^2\boldsymbol{A}^2\right)\Psi,
\end{aligned}$$

where the Coulomb gauge from eq. (2.1.7) is used. This now brings eq. (2.1.8) in the form

$$\hat{H} = \frac{\hat{\boldsymbol{p}}^2}{2m_e} - \frac{q_e}{m_e}\boldsymbol{A}\cdot\hat{\boldsymbol{p}} - \frac{q_e}{m_e}\boldsymbol{B}\cdot\hat{\boldsymbol{s}} + \frac{q_e^2}{2m_e}\boldsymbol{A}^2 + q_e\phi.$$

This final form of the Hamiltonian includes terms in which the vector potential $\boldsymbol{A}$ appears in a linear fashion. The linear terms describe the paramagnetic contributions and consist of the orbital-Zeeman $-\frac{q_e}{m_e}\boldsymbol{A}\cdot\hat{\boldsymbol{p}}$ and the spin-Zeeman term $-\frac{q_e}{m_e}\boldsymbol{B}\cdot\hat{\boldsymbol{s}}$. The term, in which $\boldsymbol{A}$ appears quadratically $\frac{q_e^2}{2m_e}\boldsymbol{A}^2$, is the diamagnetic term. The paramagnetic terms can be either negative or positive depending on the spin state and angular momentum of the system, and favour anti-parallel orientation of the angular momentum/spin relative to the magnetic field. The diamagnetic term is always positive and dominates over the paramagnetic terms for sufficiently strong fields. It acts as a confining term in the plane perpendicular to the magnetic field.

Further assuming a homogeneous time-independent external magnetic field, $\boldsymbol{B} = \text{const.}$, allows the vector potential to be expressed as

$$\boldsymbol{A}_O(\boldsymbol{r}) = \frac{1}{2}\boldsymbol{B}\times(\boldsymbol{r} - \boldsymbol{r}_O). \tag{2.1.9}$$

As already noted, the freedom to describe the vector potential is not completely fixed by the Coulomb gauge, and the choice of the gauge origin O, where the vector potential vanishes, $\boldsymbol{A}_O(\boldsymbol{r}_O) = 0$, is arbitrary. A change of the gauge origin $O \to G$ results in the following transformation

$$\begin{aligned}\boldsymbol{A}_G(\boldsymbol{r}) &= \frac{1}{2}\boldsymbol{B} \times (\boldsymbol{r} - \boldsymbol{r}_G) \\ &= \frac{1}{2}\boldsymbol{B} \times (\boldsymbol{r} - \boldsymbol{r}_O + \boldsymbol{r}_O - \boldsymbol{r}_G) \\ &= \boldsymbol{A}_O(\boldsymbol{r}) - \boldsymbol{A}_O(\boldsymbol{r}_G), \end{aligned} \tag{2.1.10}$$

which can be expressed as adding the gradient of a scalar function

$$\boldsymbol{A}_G = \boldsymbol{A}_O \overbrace{-\nabla \boldsymbol{A}_O(\boldsymbol{r}_G) \cdot \boldsymbol{r}}^{+\nabla f},$$

as already shown in eq. (2.1.5). This gauge transformation regarding the gauge origin is important for the calculation of gauge-invariant expectation values in the case of approximate wavefunction and the use of London orbitals which will be discussed in sec. 2.1.2.

2.1.1 Born-Oppenheimer approximation in an external homogeneous magnetic field

The Hamiltonian that describes a molecule in an external homogeneous magnetic field is given as

$$\begin{aligned}\hat{H} = &\sum_A \left[\frac{\hat{\boldsymbol{p}}_A^2}{2M_A} - \frac{Z_A e}{2M_A}(\boldsymbol{B} \times \boldsymbol{r}_{OA}) \cdot \hat{\boldsymbol{p}}_A + \frac{Z_A^2 e^2}{8M_A}\left(\boldsymbol{B}^2 \boldsymbol{r}_{OA}^2 - |\boldsymbol{B} \cdot \boldsymbol{r}_{OA}|^2\right)\right] + \\ &\sum_i \left[\frac{\hat{\boldsymbol{p}}_i^2}{2m_e} + \frac{e}{2m_e}(\boldsymbol{B} \times \boldsymbol{r}_{Oi}) \cdot \hat{\boldsymbol{p}}_i + \frac{e}{m_e}\boldsymbol{B} \cdot \hat{\boldsymbol{s}}_i + \frac{e^2}{8m_e}\left(\boldsymbol{B}^2 \boldsymbol{r}_{Oi}^2 - |\boldsymbol{B} \cdot \boldsymbol{r}_{Oi}|^2\right)\right] + \\ &\frac{1}{2}\sum_{A \neq B} \frac{e^2}{4\pi\epsilon_0}\frac{Z_A Z_B}{|\boldsymbol{r}_{AB}|} + \frac{1}{2}\sum_{i \neq j} \frac{e^2}{4\pi\epsilon_0}\frac{1}{|\boldsymbol{r}_{ij}|} - \sum_{A,i} \frac{e^2}{4\pi\epsilon_0}\frac{Z_A}{|\boldsymbol{r}_{Ai}|}, \end{aligned} \tag{2.1.11}$$

where the indices A, B enumerate nuclei and i, j electrons.[4,63,64] Vectors $\boldsymbol{r}_{pq}$ signify the displacements $\boldsymbol{r}_q - \boldsymbol{r}_p$, symbols M_A the mass, and Z_A the atomic number of nucleus A. The vector potential $\boldsymbol{A}$ has been substituted using the expression in eq. (2.1.9). The nuclear-spin interaction with the magnetic field is neglected from the expression, since it is much weaker than the electron-spin interaction. The orbital-Zeeman terms (without the prefactor) can be rewritten as

$$[\boldsymbol{B} \times (\boldsymbol{r} - \boldsymbol{r}_O)] \cdot \hat{\boldsymbol{p}} = \boldsymbol{B} \cdot [(\boldsymbol{r} - \boldsymbol{r}_O) \times \hat{\boldsymbol{p}}] = \boldsymbol{B} \cdot \hat{\boldsymbol{l}}^O,$$

with $\hat{\boldsymbol{l}}^O$ as the angular-momentum operator with centre O as origin. The time-independent Schrödinger equation with the molecular Hamiltonian in (2.1.11) can ber rewritten in a compact manner as

$$\left(\hat{T}_\mathrm{N} + \hat{P}_\mathrm{N} + \hat{D}_\mathrm{N} + \hat{T}_\mathrm{e} + \hat{P}_\mathrm{e} + \hat{D}_\mathrm{e} + \hat{V}_\mathrm{NN} + \hat{V}_\mathrm{ee} + \hat{V}_\mathrm{Ne}\right)\Psi_\mathrm{mol} = E_\mathrm{mol}\Psi_\mathrm{mol}. \tag{2.1.12}$$

The individual terms are a shorthand notation for

$$\hat{T}_\mathrm{N} = \sum_A \frac{\hat{\boldsymbol{p}}_A^2}{2M_A} \qquad \text{nuclear kinetic energy}$$

$$\hat{P}_\mathrm{N} = -\sum_A \frac{Z_A e}{2M_A}\boldsymbol{B} \cdot \hat{\boldsymbol{l}}_A^O \qquad \text{nuclear paramagnetic term}$$

$$\hat{D}_\mathrm{N} = \sum_A \frac{Z_A^2 e^2}{8M_A}\left(\boldsymbol{B}^2 \boldsymbol{r}_{OA}^2 - |\boldsymbol{B} \cdot \boldsymbol{r}_{OA}|^2\right) \qquad \text{nuclear diamagnetic term}$$

$$\hat{T}_{\mathrm{e}} = \sum_i \frac{\hat{\boldsymbol{p}}_i^2}{2m_e} \qquad \text{electronic kinetic energy}$$

$$\hat{P}_{\mathrm{e}} = \sum_i \left(\frac{e}{2m_e} \boldsymbol{B} \cdot \hat{\boldsymbol{l}}_i^O + \frac{e}{m_e} \boldsymbol{B} \cdot \hat{\boldsymbol{s}}_i \right) \qquad \text{electronic paramagnetic term}$$

$$\hat{D}_{\mathrm{e}} = \sum_i \frac{e^2}{8m_e} \left(\boldsymbol{B}^2 \boldsymbol{r}_{Oi}^2 - |\boldsymbol{B} \cdot \boldsymbol{r}_{Oi}|^2 \right) \qquad \text{electronic diamagnetic term}$$

$$\hat{V}_{\mathrm{NN}} = \frac{1}{2} \sum_{A \neq B} \frac{e^2}{4\pi\epsilon_0} \frac{Z_A Z_B}{|\boldsymbol{r}_{AB}|} \qquad \text{nucleus-nucleus interaction}$$

$$\hat{V}_{\mathrm{ee}} = \frac{1}{2} \sum_{i \neq j} \frac{e^2}{4\pi\epsilon_0} \frac{1}{|\boldsymbol{r}_{ij}|} \qquad \text{electron-electron interaction}$$

$$\hat{V}_{\mathrm{Ne}} = -\sum_{A,i} \frac{e^2}{4\pi\epsilon_0} \frac{Z_A}{|\boldsymbol{r}_{Ai}|} \qquad \text{mixed electron-nucleus attraction}$$

Ψ_{mol} is the total molecular wavefunction and E_{mol} the total molecular energy.

Noting the nearly exact separation of the nuclear from the electronic degrees of freedom, the adiabatic separation as a basis to expand the wavefunction solution is used, similarly to the field-free case $\boldsymbol{B} = 0$,

$$\begin{aligned} \Psi_{\mathrm{mol}} &= \sum_n \Phi_{\mathrm{nuc}}^n \left(\{\boldsymbol{r}_A\} \right) \Psi_{\mathrm{el}}^n \left(\{\boldsymbol{r}_i\} ; \{\boldsymbol{r}_A\} \right) \\ &= \sum_n |\Phi_{\mathrm{nuc}}^n\rangle \, |\Psi_{\mathrm{el}}^n\rangle \, , \end{aligned} \tag{2.1.13}$$

with Φ_{nuc}^n the nuclear wavefunction corresponding to Ψ_{el}^n the electronic wavefunction with electronic quantum number n. The braket notation is introduced in a simplified manner

$$\langle \psi_1 | \, \hat{O} \, | \psi_2 \rangle = \int^S \psi_1^* \left(\tau \right) \hat{O} \psi_2 \left(\tau \right) \mathrm{d}\tau,$$

with S signifying the whole space, and τ all respective degrees of freedom of wavefunctions $\psi_{1,2} \left(\tau \right)$.

In this scheme, the electronic Hamiltonian is expressed as

$$\hat{H}_{\mathrm{el}} \left(\{\boldsymbol{r}_i\} ; \{\boldsymbol{r}_A\} \right) = \hat{T}_{\mathrm{e}} + \hat{P}_{\mathrm{e}} + \hat{D}_{\mathrm{e}} + \hat{V}_{\mathrm{ee}} + \hat{V}_{\mathrm{Ne}},$$

in which the nuclear coordinates $\{\boldsymbol{r}_A\}$ are treated as parameters (rather than as variables). The electronic Schrödinger equation is then

$$\hat{H}_{\mathrm{el}} \left(\{\boldsymbol{r}_i\} ; \{\boldsymbol{r}_A\} \right) \Psi_{\mathrm{el}}^n \left(\{\boldsymbol{r}_i\} ; \{\boldsymbol{r}_A\} \right) = E_{\mathrm{el}}^n \left(\{\boldsymbol{r}_A\} \right) \Psi_{\mathrm{el}}^n \left(\{\boldsymbol{r}_i\} ; \{\boldsymbol{r}_A\} \right), \tag{2.1.14}$$

where the energies $E_{\mathrm{el}}^n \left(\{\boldsymbol{r}_A\} \right)$ are functions of the nuclear coordinates. Returning to eq. (2.1.12) and substituting eq. (2.1.14) and (2.1.13), the total molecular Schrödinger equation is rewritten as

$$\left(\hat{T}_{\mathrm{N}} + \hat{P}_{\mathrm{N}} + \hat{D}_{\mathrm{N}} + \hat{H}_{\mathrm{el}} + \hat{V}_{\mathrm{NN}} \right) \sum_n \Phi_{\mathrm{nuc}}^n \Psi_{\mathrm{el}}^n = E_{\mathrm{mol}} \sum_n \Phi_{\mathrm{nuc}}^n \Psi_{\mathrm{el}}^n.$$

Projecting on an electronic eigenstate $\langle \Psi_{\mathrm{el}}^k |$ without integrating over the nuclear degrees of freedom, one derives the following expression

$$\begin{aligned} &\langle \Psi_{\mathrm{el}}^k | \left(\hat{T}_{\mathrm{N}} + \hat{P}_{\mathrm{N}} + \hat{D}_{\mathrm{N}} + \hat{H}_{\mathrm{el}} + \hat{V}_{\mathrm{NN}} \right) \sum_n |\Phi_{\mathrm{nuc}}^n\rangle \, |\Psi_{\mathrm{el}}^n\rangle = \\ &\langle \Psi_{\mathrm{el}}^k | \left(\hat{T}_{\mathrm{N}} + \hat{P}_{\mathrm{N}} + \hat{D}_{\mathrm{N}} \right) \sum_n |\Phi_{\mathrm{nuc}}^n\rangle \, |\Psi_{\mathrm{el}}^n\rangle + \langle \Psi_{\mathrm{el}}^k | \left(\hat{H}_{\mathrm{el}} + \hat{V}_{\mathrm{NN}} \right) \sum_n |\Phi_{\mathrm{nuc}}^n\rangle \, |\Psi_{\mathrm{el}}^n\rangle \, . \end{aligned} \tag{2.1.15}$$

The second term of the last expression can be further simplified

$$\begin{aligned}\langle\Psi^k_{\mathrm{el}}|\left(\hat{H}_{\mathrm{el}}+\hat{V}_{\mathrm{NN}}\right)\sum_n|\Phi^n_{\mathrm{nuc}}\rangle\,|\Psi^n_{\mathrm{el}}\rangle &= \sum_n\left(E^n_{\mathrm{el}}+V_{\mathrm{NN}}\right)|\Phi^n_{\mathrm{nuc}}\rangle\,\delta_{kn}\\ &= V^k_{\mathrm{el}}\,|\Phi^k_{\mathrm{nuc}}\rangle\,,\end{aligned} \tag{2.1.16}$$

with δ_{kn} the Kronecker delta and $V^k_{\mathrm{el}} = E^k_{\mathrm{el}} + V_{\mathrm{NN}}$ the effective electronic potential. Substituting (2.1.16) in (2.1.15) yields

$$\langle\Psi^k_{\mathrm{el}}|\left(\hat{T}_{\mathrm{N}}+\hat{P}_{\mathrm{N}}+\hat{D}_{\mathrm{N}}+V^k_{\mathrm{el}}\right)|\Psi^k_{\mathrm{el}}\rangle\,|\Phi^k_{\mathrm{nuc}}\rangle+\sum_{n\neq k}\langle\Psi^k_{\mathrm{el}}|\left(\hat{T}_{\mathrm{N}}+\hat{P}_{\mathrm{N}}+\hat{D}_{\mathrm{N}}\right)|\Psi^n_{\mathrm{el}}\rangle\,|\Phi^n_{\mathrm{nuc}}\rangle = E_{\mathrm{mol}}\,|\Phi^k_{\mathrm{nuc}}\rangle\,. \tag{2.1.17}$$

The standard Born-Oppenheimer (BO) approximation in the absence of a magnetic field completely neglects the action of the nuclear operators, collectively denoted by $\hat{O}_{\mathrm{N}}$, on the electronic parts of the wavefunction,

$$\begin{aligned}\hat{O}_{\mathrm{N}}\,|\Phi^n_{\mathrm{nuc}}\rangle\,|\Psi^n_{\mathrm{el}}\rangle &= |\Psi^n_{\mathrm{el}}\rangle\left(\hat{O}_{\mathrm{N}}\,|\Phi^n_{\mathrm{nuc}}\rangle\right)+|\Phi^{N,n}_{\mathrm{nuc}}\rangle\left(\hat{O}_{\mathrm{N}}\,|\Psi^n_{\mathrm{el}}\rangle\right)+\text{mixed terms}\\ &\approx |\Psi^n_{\mathrm{el}}\rangle\left(\hat{O}_{\mathrm{N}}\,|\Phi^n_{\mathrm{nuc}}\rangle\right)\end{aligned}$$

giving the BO energy from eq. (2.1.17)

$$\left(\hat{T}_{\mathrm{N}}+V^k_{\mathrm{el}}\right)|\Phi^k_{\mathrm{nuc}}\rangle = E^{\mathrm{BO}}_{\mathrm{mol}}\,|\Phi^k_{\mathrm{nuc}}\rangle\,. \tag{2.1.18}$$

The BO approximation, alternatively called the frozen-nuclei approximation, assumes that the movement of the electrons reacts instantaneously to the position of the nuclei, and that the nuclei only feel the effect of the electrons through the effective potential V^k_{el}. This approximation is justified by the big mass difference between the electrons and the nuclei. The modern paradigm of quantum chemistry has been build around the BO approximation and is so strongly associated to it, that many key concepts like the potential-energy curve, a geometry optimization, a vibrational analysis, etc. are based on it.

In eq. (2.1.18), the non-diagonal terms have been eliminated and the electronic degrees of freedom have been completely projected out, as they are part of the electronic problem eq. (2.1.14). Corrections beyond the BO approximation can be derived for via perturbation theory. Defining the perturbation

$$\hat{H}' = \hat{T}'_{\mathrm{N}},$$

with $\hat{O}'_{\mathrm{N}} = \hat{O}_{\mathrm{N}} - \langle\Phi^k_{\mathrm{nuc}}|\,\hat{O}_{\mathrm{N}}\,|\Phi^k_{\mathrm{nuc}}\rangle$, the first-order energy correction is then simply the expectation value of the zeroth-order wavefunction, typically called the diagonal BO correction

$$E^{(1)} = \Delta E^{\mathrm{BO}}_{\mathrm{diag}} = \langle\Phi^k_{\mathrm{nuc}}|\,\langle\Psi^k_{\mathrm{el}}|\,\hat{T}'_{\mathrm{N}}\,|\Psi^k_{\mathrm{el}}\rangle\,|\Phi^k_{\mathrm{nuc}}\rangle\,.$$

The off-diagonal terms are corrections of higher order

$$\Delta E^{\mathrm{BO}}_{\text{off-diag}} = \sum_{n\neq k}\langle\Phi^k_{\mathrm{nuc}}|\,\langle\Psi^k_{\mathrm{el}}|\,\hat{T}_{\mathrm{N}}\,|\Psi^n_{\mathrm{el}}\rangle\,|\Phi^n_{\mathrm{nuc}}\rangle\,.$$

As for finite-field calculations, the nuclear paramagnetic $\hat{P}_{\mathrm{N}}$ and diamagnetic $\hat{D}_{\mathrm{N}}$ terms are added to the perturbation

$$\hat{H}' = \hat{T}'_{\mathrm{N}} + \hat{P}_{\mathrm{N}} + \hat{D}_{\mathrm{N}}.$$

If they were included in the unperturbed BO energy eq. (2.1.18), they would handle the nuclei completely unscreened from the electrons with their bare nuclear charge $q_A = Z_A e$, which is a bad approximation for strong magnetic fields. Excluding the interaction of the nuclei with the magnetic field from the BO energy means that the nuclei are treated as completely screened, giving rise to the screened BO approximation.[63,64]

The screened-BO energy $E_{\mathrm{mol}}^{\mathrm{sBO}}$ is given by

$$\left(\hat{T}_{\mathrm{N}} + V_{\mathrm{el}}^{k}\right) |\Phi_{\mathrm{nuc}}^{k}\rangle = E_{\mathrm{mol}}^{\mathrm{sBO}} |\Phi_{\mathrm{nuc}}^{k}\rangle \,, \tag{2.1.19}$$

while the first-order correction takes the form

$$\begin{aligned}\Delta E_{\mathrm{diag}}^{\mathrm{sBO}} &= \langle\Phi_{\mathrm{nuc}}^{k}| \langle\Psi_{\mathrm{el}}^{k}| \left(\hat{T}_{\mathrm{N}}' + \hat{P}_{\mathrm{N}} + \hat{D}_{\mathrm{N}}\right) |\Psi_{\mathrm{el}}^{k}\rangle |\Phi_{\mathrm{nuc}}^{k}\rangle \\ &= \langle\Phi_{\mathrm{nuc}}^{k}| \langle\Psi_{\mathrm{el}}^{k}| \hat{T}_{\mathrm{N}}' |\Psi_{\mathrm{el}}^{k}\rangle |\Phi_{\mathrm{nuc}}^{k}\rangle + \langle\Phi_{\mathrm{nuc}}^{k}| \left(\hat{P}_{\mathrm{N}} + \hat{D}_{\mathrm{N}}\right) |\Phi_{\mathrm{nuc}}^{k}\rangle + \langle\Phi_{\mathrm{nuc}}^{k}| \langle\Psi_{\mathrm{el}}^{k}| \left(\hat{P}_{\mathrm{N}}' + \hat{D}_{\mathrm{N}}'\right) |\Psi_{\mathrm{el}}^{k}\rangle |\Phi_{\mathrm{nuc}}^{k}\rangle \,.\end{aligned} \tag{2.1.20}$$

It is shown that the second term in eq. (2.1.20) is the unscreed nuclear interaction, and the third term includes the electron screening.[63,64]

Considerations for methods in the presence of a magnetic field

The present work focuses on finding solutions to the electronic Schrödinger equation (2.1.14). In order to derive such solutions to the electronic problem in the presence of magnetic field, the centre of mass of the system is typically considered not to move. This offers some simplifications due to the absence of a Stark effect.[63,64] It is also important to note the emergence of the interaction of the magnetic field with the imaginary angular momentum operator in first order (orbital-Zeeman term) in the Hamiltonian. This means that for developing finite-magnetic field (ff) methods, complex algebra has to be employed. The needed complex solutions for the electronic problem, raise the complexity of the methods and their implementation as compared to field-free methods.[67,68,70,72,73,76–79] The cost of the calculations is also accompanied with a higher prefactor, as complex numbers need twice as much memory, and multiplications need 3 to 4 times more floating-point operations (flop).[58]

2.1.2 London orbitals

Methods that attempt to solve the many-electron problem often use different ansätze of one-electron wavefucntions.[96] A common basis to expand these one-electron functions is a linear combination of atomic orbitals (LCAO), meaning a set of atom-centered functions $\{\chi_{\mu}(\boldsymbol{r} - \boldsymbol{r}_A)\}$. This kind of basis set, however, is not flexible enough to approximate a wavefunction in the presence of a magnetic field, as explained in the following paragraphs.

The Hamiltonian inherits the gauge freedom of the vector potential introduced in eq. (2.1.5). This freedom is expressed as a unitary transformation

$$\hat{H}_{\mathrm{trans}} - i\frac{\partial}{\partial t} = \mathrm{e}^{-if} \left(\hat{H}_{\mathrm{orig}} - i\frac{\partial}{\partial t}\right) \mathrm{e}^{+if},$$

where $\hat{H}_{\mathrm{orig}}$ is the original Hamiltonian and $\hat{H}_{\mathrm{trans}}$ the gauge transformed Hamiltonian. In the exact case, the wavefunction needs to compensate for this unitary transformation with a phase oscillation

$$\Psi_{\mathrm{trans}} = \mathrm{e}^{-if}\Psi_{\mathrm{orig}}. \tag{2.1.21}$$

The Hamiltonian and the wavefunction thus become dependent on the choice of the gauge, while observables remain gauge unchanged/invariant

$$\langle\Psi_{\mathrm{trans}}| \hat{O}_{\mathrm{trans}} |\Psi_{\mathrm{trans}}\rangle = \langle\Psi_{\mathrm{orig}}| \hat{O}_{\mathrm{orig}} |\Psi_{\mathrm{orig}}\rangle \,.$$

Approximate wavefunctions spanned in the aforementioned basis, however, do not transform as in eq. (2.1.21). Energies and properties derived from such approximate wavefunctions are thus gauge-origin dependent, because the oscillatory behaviour is not properly modelled. The gauge-origin invariance is accounted for in the basis-set limit, but using bigger basis sets for the derivation of gauge-origin invariant results is not feasible, because the observed convergence is very slow.[91]

It is possible to systematically derive gauge-invariant results within the Coulomb gauge in the case of an external homogeneous magnetic field. Within the Coulomb gauge, the remaining gauge freedom

comprises the choice for the gauge origin eq. (2.1.10). In order to enforce gauge-origin invariance, London orbitals ω_μ are used, instead of the standard atomic orbitals[14,15,70,97–99]

$$\begin{aligned}\omega_\mu\left(\boldsymbol{r}-\boldsymbol{r}_A,\boldsymbol{B},\boldsymbol{r}_G\right) &= \mathrm{e}^{i[\boldsymbol{A}_A(\boldsymbol{r}_G)\cdot\boldsymbol{r}]}\chi_\mu\left(\boldsymbol{r}-\boldsymbol{r}_A\right)\\ &= \mathrm{e}^{\frac{i}{2}\boldsymbol{B}\times(\boldsymbol{r}_G-\boldsymbol{r}_A)\cdot\boldsymbol{r}}\chi_\mu\left(\boldsymbol{r}-\boldsymbol{r}_A\right).\end{aligned} \tag{2.1.22}$$

Using these orbitals, each function in the basis "locally changes" the gauge origin to the atomic centre, and gauge-origin invariant results can be obtained. Since London orbitals include the magnetic field and the gauge origin, they are alternatively called gauge-origin including atomic orbitals (GIAOs). Note that London orbitals simplify to the normal atomic orbitals in the limit of zero magnetic field

$$\omega_\mu\left(\boldsymbol{r}-\boldsymbol{r}_A,0,\boldsymbol{r}_G\right)=\chi_\mu\left(\boldsymbol{r}-\boldsymbol{r}_A\right), \tag{2.1.23}$$

but derivatives of London orbitals with respect to the magnetic field are non-zero even in the field-free case. London orbitals are thus not only used for finite-field calculations, but also for the calculation of magnetic properties as well.

2.2 Hartree-Fock theory

In order to describe the electronic problem in a physically sound manner, the wavefunction has to take into account the fermionic character of the electrons, which according to the Pauli principle means that the wavefunction is antisymmetric with respect to particle exchange

$$\hat{P}_{ij}\Psi(\mathbf{1},\ldots,\boldsymbol{i},\ldots,\boldsymbol{j},\ldots,\boldsymbol{N})=\Psi(\mathbf{1},\ldots,\boldsymbol{j},\ldots,\boldsymbol{i},\ldots,\boldsymbol{N})=-1\Psi(\mathbf{1},\ldots,\boldsymbol{i},\ldots,\boldsymbol{j},\ldots,\boldsymbol{N}),$$

where the exchange operator $\hat{P}_{ij}$ exchanges the coordinates of particles $\boldsymbol{i}$ and $\boldsymbol{j}$ in the wavefunction.[95,100] The simplest many-electron function to be antisymmetric is a Slater determinant

$$\begin{aligned}\Psi_{\mathrm{SD}} &= \frac{1}{\sqrt{N!}}\begin{vmatrix}\psi_1(\mathbf{1}) & \psi_2(\mathbf{1}) & \ldots & \psi_N(\mathbf{1})\\ \psi_1(\mathbf{2}) & \psi_2(\mathbf{2}) & & \\ \vdots & & \ddots & \\ \psi_1(\boldsymbol{N}) & & & \psi_N(\boldsymbol{N})\end{vmatrix}\\ &= \left|\psi_1\psi_2\ldots\psi_N\right\rangle.\end{aligned}$$

Here, $\psi_n(\boldsymbol{\tau})$ is a one-electron function, containing both spacial and spin coordinates $\boldsymbol{\tau}$, i.e., a spinorbital.

In Hartree-Fock (HF) theory,[101] a Slater determinant is used as a trial wavefunction for the electronic problem. The variational principle is then used, which states that any trial wavefunction Ψ' gives an energy higher than the ground-state energy of the system

$$E[\Psi']\geq E_0.$$

The "best" approximation to the exact ground-state energy E_0, given the degrees of freedom of the trial wavefunction, is obtained by varying the parameters of Ψ' in such a way that the energy $E[\Psi']$ is minimized. In HF theory, this translates to searching for critical points for the energy as a functional of the Slater deterniant

$$\begin{aligned}E[\Psi_{\mathrm{SD}}]=E_{\mathrm{HF}}&=\left\langle\Psi_{\mathrm{SD}}\right|\hat{H}\left|\Psi_{\mathrm{SD}}\right\rangle\\ &=\sum_i h_{ii}+\frac{1}{2}\sum_{ij}\left\langle\psi_i\psi_j\right|\left|\psi_i\psi_j\right\rangle,\end{aligned}$$

where h_{ii} are the diagonal elements of the one-electron Hamiltonian matrix $\left\langle\psi_i\right|\hat{h}\left|\psi_i\right\rangle$ with $\hat{h}$ including the one-electron terms of the electronic Hamiltonian, and $\left\langle\psi_i\psi_j\right|\left|\psi_i\psi_j\right\rangle$ the antisymmetrized two-electron interaction integrals $\left\langle\psi_i(\mathbf{1})\psi_j(\mathbf{2})\right|\hat{v}(\mathbf{1},\mathbf{2})\left|\psi_i(\mathbf{1})\psi_j(\mathbf{2})\right\rangle-\left\langle\psi_i(\mathbf{1})\psi_j(\mathbf{2})\right|\hat{v}(\mathbf{1},\mathbf{2})\left|\psi_j(\mathbf{1})\psi_i(\mathbf{2})\right\rangle$ with $\hat{v}(\mathbf{1},\mathbf{2})=\frac{e^2}{4\pi\epsilon_0}|\boldsymbol{r}_{12}|^{-1}$ the two-electron interaction operator. The summation i runs over all electrons.

To find a critical point for the HF energy, while simultaneously retaining the orthonormality of the spinorbitals, the method of Lagrange multipliers is used and the HF Lagrangian is introduced

$$L_{\mathrm{HF}} = E_{\mathrm{HF}} - \sum_{ij} \epsilon_{ij}(\langle\psi_i|\psi_j\rangle - \delta_{ij}),$$

with ϵ_{ij} as the Lagrange multipliers. Variations in the spinorbitals $\psi_i \to \psi_i + \delta\psi_i$ yield an expression for the first-order variation of the Lagrangian

$$\begin{aligned}\delta L_{\mathrm{HF}} &= \left(\langle\delta\psi_i|\, \hat{h}\, |\psi_i\rangle + \langle\delta\psi_i|\, \hat{J} - \hat{K}\, |\psi_i\rangle - \sum_j \epsilon_{ij} \langle\delta\psi_i|\psi_j\rangle \right) + \text{c.c.} \\ &= \left(\langle\delta\psi_i|\, \hat{F}\, |\psi_i\rangle - \sum_j \epsilon_{ij} \langle\delta\psi_i|\psi_j\rangle \right) + \text{c.c.},\end{aligned}$$

where c.c. stands for the complex conjugate of the terms in parentheses. The Coulomb and exchange operators have been introduced, the action of which results in

$$\langle\phi_1|\, \hat{J}\, |\phi_2\rangle = \sum_j \langle\phi_1(\mathbf{1})\psi_j(\mathbf{2})|\, \hat{v}(\mathbf{1},\mathbf{2})\, |\phi_2(\mathbf{1})\psi_j(\mathbf{2})\rangle$$

and

$$\langle\phi_1|\, \hat{K}\, |\phi_2\rangle = \sum_j \langle\phi_1(\mathbf{1})\psi_j(\mathbf{2})|\, \hat{v}(\mathbf{1},\mathbf{2})\, |\psi_j(\mathbf{1})\phi_2(\mathbf{2})\rangle\,,$$

respectively. The Fock operator in the last expression is $\hat{F} = \hat{h} + \hat{J} - \hat{K}$. Requiring the first-order variation to vanish $\delta L_{\mathrm{HF}} = 0$ in order to find a stationary point leads to the HF equations

$$\hat{F}\, |\psi_i\rangle = \sum_j \epsilon_{ij}\, |\psi_j\rangle\,,$$

which state that the Fock operator may only mix the occupied orbitals among themselves. Usually, the HF method produces more orbitals than electrons, and the unoccupied orbitals not present in the determinant do not contribute to the HF energy. They are for this reason also known as virtual orbitals ψ_a and they as well only mix among themselves under the Fock operator. Mathematically this is expressed as

$$\langle\psi_a|\, \hat{F}\, |\psi_i\rangle = 0,$$

which is equivalent to the Brillouin theorem.[101] The HF equations do not give a single orbital solution and their freedom can be further restricted by requiring the spinorbitals to be eigenfunctions of the Fock operator

$$\hat{F}\, |\psi_i\rangle = \epsilon_{ii}\, |\psi_i\rangle\,,$$

which results in the canonical HF equations and orbitals. Here the Lagrange multipliers ϵ_{ii} can be interpreted as orbital energies ϵ_i according to Koopmans' theorem.[101,102] Using canonical HF orbitals, the HF energy is given by

$$E_{\mathrm{HF}} = \sum_i \epsilon_i - \frac{1}{2} \langle\psi_i\psi_j|\, |\psi_i\psi_j\rangle\,.$$

A typical choice to express the spinorbitals is as a product of a spacial and a spin function. In the unrestricted HF approach (UHF), the spin part is a pure α or β spin function

$$\begin{aligned}\psi^{\alpha}(\boldsymbol{r},\boldsymbol{\sigma}) &= \phi^{\alpha}(\boldsymbol{r})\, |\alpha(\boldsymbol{\sigma})\rangle \\ \psi^{\beta}(\boldsymbol{r},\boldsymbol{\sigma}) &= \phi^{\beta}(\boldsymbol{r})\, |\beta(\boldsymbol{\sigma})\rangle\,,\end{aligned}$$

with $\boldsymbol{r}$ and $\boldsymbol{\sigma}$ the spacial and the spin coordinates respectively, and $\phi^\sigma(\boldsymbol{r})$ the orbital. The restricted HF approach (RHF) is a special case of UHF for closed-shell systems, where the orbital part of an α spinorbital is equal to the β for doubly-occupied orbitals.

$$\phi_i^\alpha = \phi_i^\beta = \phi_i^{\mathrm{RHF}}$$

The orbital part is then expressed in the LCAO ansatz, mentioned in sec. 2.1.2

$$\phi_i^\sigma = \sum_\mu c_{\mu i}^\sigma \omega_\mu, \tag{2.2.1}$$

where ω_μ are the functions of the basis sets chosen for the LCAO. As already discussed in subsec. 2.1.2, in the absence of a magnetic-field, these are atom-centered functions [eq. (2.1.23)]. In the case of a calculation in the presence of a magnetic field, or the calculation of derivatives involving the magnetic field, London orbitals [eq. (2.1.22)] have to be used. Substituting the LCAO ansatz in the canonical HF equations results in the Roothaan-Hall equations[101]

$$\mathbf{FC} = \mathbf{SC}\epsilon, \tag{2.2.2}$$

where $\mathbf{F}$ is the Fock matrix containing Fock elements $F_{\nu\mu} = \langle\omega_\nu|\,\hat{F}\,|\omega_\mu\rangle$, $\mathbf{S}$ the overlap matrix $S_{\nu\mu} = \langle\omega_\nu|\omega_\mu\rangle$, $\mathbf{C}$ the molecular orbital (MO) coefficient matrix, and ϵ the orbital energy vector.

The Fock matrix depends on the coefficient matrix $\mathbf{C}$ via the Coulomb $\mathbf{J}[\mathbf{C}]$ and exchange $\mathbf{K}[\mathbf{C}]$ operators, but $\mathbf{C}$ in turn is obtained by diagonalization of the Fock matrix. As a result, eq. (2.2.2) cannot be solved directly. A solution is provided by an iterative approach (see app B). Starting from an initial guess for $\mathbf{C}^0$, the Fock matrix $\mathbf{F}$ is created. It is then diagonalized to provide a new set of coefficients $\mathbf{C}'$ which in turn define a new Fock matrix. This procedure is repeated until convergence, making this iterative approach a self-consistent field method (SCF).

Returning to the HF energy and rewriting the expression in the form

$$E_{\mathrm{HF}} = \sum_i \langle\psi_i|\,\hat{h}\,|\psi_i\rangle + \frac{1}{2}\sum_i \langle\psi_i|\,\hat{J} - \hat{K}\,|\psi_i\rangle\,,$$

one can interpret the first term as the sum of all the one-electron energies of all electrons, and the second as the interaction of one electron with the mean field generated by all other electrons. For this reason HF is a mean-field theory, and it serves in many cases as a good approximation to the exact wavefunction. It neglects however the explicit dependence of the position of the electrons with respect to to each other which is a vital part of the physics of the system. This is the so-called dynamical electron correlation, and can be treated with post-HF methods. On the other hand, there are cases where a single Slater determinant reference is not a good approximation, as the exact wavefunction is dominated by more than one determinants (multi-configurational character). The neglected interaction at the HF level for system with a multi-configurational character is the so-called static electron correlation. Both static and dynamical electron correlations have to be taken into account in order to get chemically relevant results, with an error below 1 kcal/mol $\approx 10^{-3}$ E_{h} usually referred as chemical accuracy. Post-HF methods that aim to target electron correlation are presented in the next sections.

2.3 Second quantisation

In order to include electron correlation in the wavefunction and improve the approximated energy beyond the HF level, more than one Slater determinants need to be considered in the approximated wavefunction. Borrowing the notation and conventions of second quantisation[96,103] allows for an automatic inclusion of the Pauli principle in the resulting wavefunctions. A compact and handier notation thus arises.

In second quantisation, a Hilbert space is the space spanned by a set of orthonormal spinorbitals (e.g. the canonical HF orbitals)

$$\{\psi_i\} = \{\psi_1, \psi_2, \psi_3 \dots\}$$
$$\langle\psi_i|\psi_j\rangle = \delta_{ij}.$$

All possible Slater determinants with variable electron number formed in a given Hilbert space constitute the Fock space.

In second quantisation, the creation and annihilation operators, $\hat{a}_p^\dagger$ and $\hat{a}_p$ respectively, are introduced, which create or annihilate an electron in a spinorbital ψ_p

$$\begin{aligned}\hat{a}_p^\dagger \left|\psi_i\psi_j\psi_k\ldots\right\rangle &= \left|\psi_p\psi_i\psi_j\psi_k\ldots\right\rangle \\ \hat{a}_p \left|\psi_p\psi_i\psi_j\psi_k\ldots\right\rangle &= \left|\psi_i\psi_j\psi_k\ldots\right\rangle .\end{aligned}$$

An annihilation operator can be viewed as a creation operator acting on a bra state, and vice versa for the creation operator

$$\begin{aligned}\left\langle\psi_i\psi_j\psi_k\ldots\right| \hat{a}_p &= \left\langle\psi_p\psi_i\psi_j\psi_k\ldots\right| \\ \left\langle\psi_p\psi_i\psi_j\psi_k\ldots\right| \hat{a}_p^\dagger &= \left\langle\psi_i\psi_j\psi_k\ldots\right| .\end{aligned}$$

Any Slater determinant, and as such any element of the Fock space, can be represented as a string of creation operators acting on the vacuum state $|\text{vac}\rangle$, which is the state of zero particles.

$$\Psi_{\text{SD}} = \left|\psi_i\psi_j\psi_k\ldots\right\rangle = \hat{a}_i^\dagger\hat{a}_j^\dagger\hat{a}_k^\dagger\ldots\left|\text{vac}\right\rangle .$$

The action of a creation operator $\hat{a}_p^\dagger$ on a state, where orbital ψ_p is already occupied yields zero, which is different from the vacuum state. Similarly the action of an annihilator on an empty orbital gives also zero:

$$\begin{aligned}\hat{a}_p^\dagger \left|\psi_p\psi_i\psi_j\psi_k\ldots\right\rangle &= 0 \\ \hat{a}_p \left|\psi_i\psi_j\psi_k\ldots\right\rangle &= 0.\end{aligned}$$

The order of action of creation operators is important and follows the antisymmetry of the Slater determinant

$$\hat{a}_p^\dagger\hat{a}_q^\dagger \left|\psi_i\psi_j\psi_k\ldots\right\rangle = \left|\psi_p\psi_q\psi_i\psi_j\psi_k\ldots\right\rangle = -\left|\psi_q\psi_p\psi_i\psi_j\psi_k\ldots\right\rangle = -\hat{a}_q^\dagger\hat{a}_p^\dagger \left|\psi_i\psi_j\psi_k\ldots\right\rangle . \tag{2.3.1}$$

This is also true for the annihilation operators

$$\begin{aligned}\hat{a}_q\hat{a}_p \left|\psi_p\psi_q\psi_i\psi_j\psi_k\ldots\right\rangle &= \hat{a}_q \left|\psi_q\psi_i\psi_j\psi_k\ldots\right\rangle = \left|\psi_i\psi_j\psi_k\ldots\right\rangle \\ \hat{a}_p\hat{a}_q \left|\psi_p\psi_q\psi_i\psi_j\psi_k\ldots\right\rangle &= -\hat{a}_p \left|\psi_p\psi_i\psi_j\psi_k\ldots\right\rangle = -\left|\psi_i\psi_j\psi_k\ldots\right\rangle .\end{aligned} \tag{2.3.2}$$

Eq. (2.3.1) and (2.3.2) give rise to the following anticommutator relations

$$\begin{aligned}[\hat{a}_p^\dagger\hat{a}_q^\dagger]_+ &= \hat{a}_p^\dagger\hat{a}_q^\dagger + \hat{a}_q^\dagger\hat{a}_p^\dagger = 0 \\ [\hat{a}_p\hat{a}_q]_+ &= \hat{a}_p\hat{a}_q + \hat{a}_q\hat{a}_p = 0.\end{aligned} \tag{2.3.3}$$

As for the mixed anticommutator case

$$[\hat{a}_p^\dagger\hat{a}_q]_+ = [\hat{a}_q\hat{a}_p^\dagger]_+ = \hat{a}_p^\dagger\hat{a}_q + \hat{a}_q\hat{a}_p^\dagger,$$

its action always results to 0 unless $p = q$

$$[\hat{a}_p^\dagger\hat{a}_q]_+ = \delta_{pq}. \tag{2.3.4}$$

In second quantisation, one- and two-electron operators take the following form

$$\begin{aligned}\hat{O} &= \sum_{pq} o_{pq}\hat{a}_p^\dagger\hat{a}_q \\ \hat{G} &= \frac{1}{4}\sum_{pqrs} g_{pqrs}\hat{a}_p^\dagger\hat{a}_q^\dagger\hat{a}_s\hat{a}_r,\end{aligned}$$

where $o_{pq} = \langle p| \hat{o} |q\rangle$ are the matrix elements of the operator $\hat{O}$, and $g_{pqrs} = \langle pq| \hat{g} |rs\rangle - \langle pq| \hat{g} |sr\rangle$ are the antisymmetrized elements of the operator $\hat{G}$. The braket notation is simplified for spinorbitals $|\psi_p\rangle = |p\rangle$.

For the calculation of expectation values, a string of creation/annihilation operators $\hat{A}\hat{B}\dots$ can be conveniently brought in normal-ordered form or a normal product. In a normal product, all annihilation operators are on the right, and all creation operators are on the left. Annihilation and creation operators are characterized relative to a reference state. The vacuum state may act as a reference state. Alternatively, the Fermi state, can be used. The Fermi reference divides the system is the space of occupied and unoccupied orbitals and in our case is the HF determinant

$$|\Psi_{\mathrm{HF}}\rangle = |\Phi_0\rangle = |0\rangle\,.$$

A normal-ordered string is denoted as $N(\hat{A}\hat{B}\dots)$ relative to the vacuum and as $\{\hat{A}\hat{B}\dots\}$ for the Fermi vacuum. In the Fermi vacuum, the space of occupied orbitals $i, j, k, \dots$ is the hole space (h), while the space of the virtual orbitals $a, b, c, \dots$ is the particle space (p) and the creation operators and annihilation operators are called quasiparticle operators. Thus, quasiparticle creation operators are considered the creation operators of virtual orbitals $\hat{a}_a^\dagger$ and the annihilation operators of occupied orbitals $\hat{a}_i$, since the former create particles and the latter holes. Quasiparticle annihilation operators are the annihilation operators of virtual orbitals $\hat{a}_a$ and creation operators of occupied orbitals $\hat{a}_i^\dagger$, since the former annihilate particles and the latter holes. The simplification offered by a normal-ordered (quasi)particle operator string is that the vacuum state expectation value of a normal product is zero

$$\begin{aligned}\langle \mathrm{vac}|\, N(\hat{A}\hat{B}\dots)\,|\mathrm{vac}\rangle &= 0\\ \langle 0|\,\{\hat{A}\hat{B}\dots\}\,|0\rangle &= 0,\end{aligned}$$

unless the product is a constant.

Bringing a string of quasiparticle operators in a normal-ordered form is a straightforward procedure. First, the contraction between two operators is defined as

$$\overbracket{\hat{A}\hat{B}} = \hat{A}\hat{B} - \{\hat{A}\hat{B}\}.$$

The rules to calculate the contraction follow from the anticommutator relations eq. (2.3.3) and (2.3.4) and are summarized in the following equations for the Fermi vacuum

$$\begin{aligned}\overbracket{\hat{a}_p^\dagger \hat{a}_q^\dagger} &= 0\\ \overbracket{\hat{a}_p \hat{a}_q} &= 0\\ \overbracket{\hat{a}_p^\dagger \hat{a}_q} &= \delta_{pq\in i}\\ \overbracket{\hat{a}_p \hat{a}_q^\dagger} &= \delta_{pq\in a}.\end{aligned}$$

The normal-ordering of longer strings can be obtained using Wick's theorem[103]

$$\hat{A}\hat{B}\cdots = \{\hat{A}\hat{B}\dots\} + \sum_{\substack{\text{single}\\ \text{contractions}}} \{\overbracket{\hat{A}\hat{B}\dots\dots}\} + \sum_{\substack{\text{double}\\ \text{contractions}}} \{\overbracket{\hat{A}\hat{B}\dots\dots}\} + \dots$$

Lastly, the Hamiltonian operator is written as follows in normal-ordered form

$$\begin{aligned}\hat{H} &= E_{\mathrm{HF}} + \sum_{pq} f_{pq}\{\hat{a}_p^\dagger \hat{a}_q\} + \frac{1}{4}\sum_{pqrs}\langle pq|\,|rs\rangle\,\{\hat{a}_p^\dagger \hat{a}_q^\dagger \hat{a}_s \hat{a}_r\}\\ &= E_{\mathrm{HF}} + \hat{F}_N + \hat{V}_N\\ &= E_{\mathrm{HF}} + \hat{H}_N,\end{aligned}$$

where $\hat{F}_N$ is the normal-ordered Fock operator, $\hat{V}_N$ the normal-ordered two-electron interaction and $\hat{H}_N$ the total normal-ordered Hamiltonian.

2.4 Configuration Interaction Theory

In Configuration Interaction (CI) theory, the correlated wavefunction is given as a linear expansion of determinants starting from the HF reference in a straightforward manner[96]

$$\Psi_{\mathrm{CI}} = \hat{C}\,|0\rangle = \sum_I \hat{C}_I\,|0\rangle = \sum_I c_I \hat{\mu}_I\,|0\rangle = \sum_I c_I\,|\Phi_I\rangle \tag{2.4.1}$$

where $\hat{\mu}_I$ is the string of quasiparticle operators that creates the excited determinants $|\Phi_I\rangle$ from the reference determinant. In this notation, the index I hides further complexity by signifying the level of excitation or the collective excitation of a given level. $I = 1$, for example, stands for all single excitations $\hat{\mu}_1\,|0\rangle = |\Phi_1\rangle = \sum_{ia} |\Phi_i^a\rangle$, alternative written as $I = \mathrm{S}$. Specifying the exact excitation brings the previous notation to the form

$$\Psi_{\mathrm{CI}} = c_0\,|0\rangle + \sum_{ia} c_i^a \hat{a}_a^\dagger \hat{a}_i\,|0\rangle + \frac{1}{4}\sum_{ijab} c_{ij}^{ab} \hat{a}_a^\dagger \hat{a}_b^\dagger \hat{a}_j \hat{a}_i\,|0\rangle + \ldots,$$

where c_0 is the coefficient for the reference wavefunction, c_i^a for single excitations, c_{ij}^{ab} for double excitations, and so on. The CI coefficients c_I are found using the variational procedure, retaining the normalisation of the CI wavefunction. This is done by defining the CI Lagrangian

$$L_{\mathrm{CI}} = \langle\Psi_{\mathrm{CI}}|\,\hat{H}\,|\Psi_{\mathrm{CI}}\rangle - E_{\mathrm{CI}}\left(\langle\Psi_{\mathrm{CI}}|\Psi_{\mathrm{CI}}\rangle - 1\right),$$

where E_{CI} is the Lagrange multiplier. The bra state is the complex conjugate of the ket state, $\langle\Psi| = \langle 0|\,\hat{C}^\dagger$, since $\hat{H}$ is a Hermitian operator. Differentiating with respect to c_I and requiring the derivatives to be 0 leads to

$$\begin{aligned}
\frac{\partial}{\partial c_I} L_{\mathrm{CI}} &= 0 \\
\frac{\partial}{\partial c_I}\langle\Psi_{\mathrm{CI}}|\,\hat{H}\,|\Psi_{\mathrm{CI}}\rangle - E_{\mathrm{CI}}\frac{\partial}{\partial c_I}\langle\Psi_{\mathrm{CI}}|\Psi_{\mathrm{CI}}\rangle &= 0 \\
\langle\Psi_{\mathrm{CI}}|\,\hat{H}\,|\Phi_I\rangle &= E_{\mathrm{CI}}\langle\Psi_{\mathrm{CI}}|\Phi_I\rangle .
\end{aligned} \tag{2.4.2}$$

Here, the complex conjugate coefficients c_I^* were considered independent parameters during the differentiation. Since $\hat{H}$ is a Hermitian operator, eq. (2.4.2) can be rewritten as

$$\begin{aligned}
\langle\Phi_I|\,\hat{H}\,|\Psi_{\mathrm{CI}}\rangle &= E_{\mathrm{CI}}\langle\Phi_I|\Psi_{\mathrm{CI}}\rangle \\
\sum_J \langle\Phi_I|\,\hat{H}\,|\Phi_J\rangle\, c_J &= E_{\mathrm{CI}}\sum_J \langle\Phi_I|\Phi_J\rangle\, c_J \\
\sum_J H_{IJ} c_J &= E_{\mathrm{CI}} c_I \\
\mathbf{HC} &= E_{\mathrm{CI}}\mathbf{C}.
\end{aligned} \tag{2.4.3}$$

The elements $H_{IJ} = \langle\Phi_I|\,\hat{H}\,|\Phi_J\rangle$ of the Hamiltonian matrix $\mathbf{H}$ have been introduced and the matrix form in eq. (2.4.3) constitutes an eigenvalue problem. The Lagrange multiplier E_{CI} is in turn interpreted as the CI energy with different roots of the eigenvalue problem giving solution for different electronic states of the system. For the ground-state solution, the weight of the reference determinant c_0 can be used as diagnostic for the extent of static correlation in the system.

The linear expansion of CI naturally truncates at order n at which point all needed elements of the Fock space are included, where n is the number of electrons of the system. This constitutes the full CI (FCI) method which offers an exact solution for the problem for a given basis set. The scaling of the method is factorial with respect to the number of electrons. This makes the FCI approach applicable only for very small systems (small number of electrons and basis-set function). It is nonetheless commonly used as a benchmark to test approximate approaches.[96]

Truncating the CI expansion at a given excitation level is a common practice to get approximate results with a viable scaling. A common truncation schemes used is the CI singles doubles (CISD).

At this truncation level, around 95% of the total correlation of the ground state is recovered for a wavefunction dominated by the reference determinant, since double amplitudes have by far the largest contribution to the correlation and single amplitudes act as approximate orbital relaxation. Truncated CI energies, however, are not size-extensive. In addition, the correction to the correlation energy offered by including higher excitations beyond CISD is small at the individual excitation level. In other words, the convergence of the CI series beyond CISD towards the FCI limitis slow.[96,103] There exist approaches that remedy the shortcomings of CI with an equal scaling for the same truncation. Such approaches are the subject of sec. 2.6.

Another method that belongs to CI theory is the CI singles (CIS). The CIS method offers no inclusion of correlation because of the Brillouin theorem $\langle 0|\,\hat{H}\,|\Phi_i^a\rangle = \langle 0|\,\hat{F}\,|\Phi_i^a\rangle = \langle i|\,\hat{F}\,|a\rangle = 0$, and thus gives no correction to the ground-state energy. It is nevertheless used as an approximation for excited states beyond the HF ground state, alternatively known as the Tamm-Dancoff approximation.

2.5 Many-body perturbation theory

The many-body perturbation theory (MBPT) is another approach that aims to target (dynamical) correlation.[103] The Hamiltonian is divided in a zeroth-order unperturbed part $\hat{H}^0$ and in a perturbation W. Here, the Møller-Plesset (MP) partitioning[104] for canonical orbitals is chosen, where the unperturbed part is the reference HF energy plus the normal-ordered Fock operator, while the perturbation is the normal-ordered two-electron interaction

$$\begin{aligned}\hat{H}^0 &= E_{\mathrm{HF}} + \hat{F}_N \\ \hat{W} &= \hat{V}_N.\end{aligned} \tag{2.5.1}$$

In the case of orbitals different from the canonical HF case (in the restricted open-shell HF reference for example), the unperturbed Hamiltonian may have different definitions.[105–107] Semi-canonical orbitals may then be constructed. For such orbitals, the hole-hole and particle-particle blocks of the Fock matrix are diagonal, but the Brillouin condition is not fulfilled, meaning there are non-vanishing particle-hole and hole-particle contributions. The unperturbed Hamiltonian may then be defined to include only the diagonal elements of the Fock operator

$$\hat{H}^0 = E_{\mathrm{HF}} + \hat{F}_N^{\mathrm{diag}},$$

while the perturbation includes the off-diagonal Fock elements

$$\hat{W} = \hat{V}_N + \hat{F}_N^{\text{off-diag}}.$$

Unless stated otherwise, canonical HF orbitals are assumed in this thesis. Following perturbation theory and choosing the HF wavefunction as the zeroth-order wavefunction,

$$\Psi^{(0)} = \Psi_{\mathrm{HF}} = \Phi_0 = |0\rangle\,,$$

one expands the energy and the wavefunction in orders of perturbation.

$$\left(\hat{H}^0 + \hat{W}\right)\left(\Psi^{(0)} + \Psi^{(1)} + \dots\right) = \left(E^{(0)} + E^{(1)} + \dots\right)\left(\Psi^{(0)} + \Psi^{(1)} + \dots\right)$$

It is then shown that up to first order, there is no inclusion of correlation beyond the HF level

$$\begin{aligned}E^{(0)} &= \langle 0|\,\hat{H}^0\,|0\rangle = E_{\mathrm{HF}} \\ E^{(1)} &= \langle 0|\,\hat{W}\,|0\rangle = 0.\end{aligned}$$

In other words, the reference energy is contained in zeroth and first order

$$E_{\mathrm{ref}} = E^{(0)} + E^{(1)} = E_{\mathrm{HF}}.$$

In order to get a correction that accounts for correlation, the first-order wavefunction is needed. In general the wavefunction corrections are chosen as a linear combination of excited determinants

$$\Psi^{(n)} = \hat{T}^{(n)} |0\rangle ,$$

with $\hat{T}^{(n)} = \sum_I t_I^{(n)} \hat{\mu}_I$ as the MP amplitudes of order n. Thus, the first-order wavefunction is

$$\begin{aligned} \Psi^{(1)} &= \hat{T}^{(1)} |0\rangle \\ &= \sum_I t_I^{(1)} \hat{\mu}_I |0\rangle , \end{aligned}$$

and the amplitudes $t_I^{(1)}$ are given by

$$t_2^{(1)} = \frac{\langle \Phi_I | \hat{W} |0\rangle}{E_0^{(0)} - E_I^{(0)}}.$$

Here $E_I^{(0)}$ are the unperturbed-Hamiltonian expectation values of excited determinants

$$E_I^{(0)} = \langle \Phi_I | E_{\mathrm{HF}} + \hat{F}_N |\Phi_I\rangle = E_{\mathrm{HF}} + \Delta\epsilon_I,$$

with $\Delta\epsilon_I = \epsilon_a + \epsilon_b + \cdots - \epsilon_i - \epsilon_i - \ldots$ the orbital-energy difference between the reference determinant and determinant $|\Phi_I\rangle$. The first-order correction to the wavefunction, can only have corrections from doubly-excited determinants, since the elements $\langle \Phi_I | \hat{W} |0\rangle$ vanish unless Φ_I corresponds to a doubly excited determinant $I \neq 2$

$$t_2^{(1)} = t_{ij}^{ab(1)} = -\frac{\langle ab| \, |ij\rangle}{\Delta\epsilon_{ij}^{ab}}.$$

This explains the importance of double excitations and the reason they include most of the correlation at the CI level, since they contribute at first order in perturbation. The second-order correction to the energy is then given by

$$\begin{aligned} E^{(2)} &= \langle 0| \hat{W} |\Psi^{(1)}\rangle \\ &= -\frac{1}{4} \sum_{abij} \langle 0| \hat{V}_N |\Phi_{ij}^{ab}\rangle \frac{\langle ab| \, |ij\rangle}{\Delta\epsilon_{ij}^{ab}} \\ &= -\frac{1}{4} \sum_{abij} \frac{|\langle ab| \, |ij\rangle|^2}{\Delta\epsilon_{ij}^{ab}}. \end{aligned}$$

The total energy at the MP2 level of theory is given by

$$E_{\mathrm{MP2}} = E_{\mathrm{HF}} + E^{(2)}.$$

Energies in the MPn series, with n the cardinal number of the method that signifies the inclusion of energy corrections up to nth order, are size-extensive. The series though does not necessarily converge, due to intruder states close to the ground state.[108] MP2 nevertheless is a robust method which is often used to target electron correlation for medium to large system, when more precise methods are not applicable.

2.6 Coupled-Cluster theory

2.6.1 Ground-state energy

In Coupled-Cluster (CC) theory,[103,109] correlation is included in the wavefuction by an exponential expansion:

$$\Psi_{\mathrm{CC}} = e^{\hat{T}} |0\rangle = \left(1 + \hat{T} + \frac{1}{2}\hat{T}^2 + \frac{1}{6}\hat{T}^3 \ldots\right) |0\rangle = \left(\sum_{l=0} \frac{\hat{T}^l}{l!}\right) |0\rangle . \tag{2.6.1}$$

$\hat{T}$ is the cluster operator

$$\hat{T} = \hat{T}_1 + \hat{T}_2 + \ldots \hat{T}_n = \sum_{ia} t_i^a \hat{a}_a^\dagger \hat{a}_i + \frac{1}{4} \sum_{ijab} t_{ij}^{ab} \hat{a}_a^\dagger \hat{a}_b^\dagger \hat{a}_j \hat{a}_i + \cdots = \sum_I t_I \hat{\mu}_I,$$

where t_I are the cluster amplitudes. Substituting eq. (2.6.1) in the Schrödinger equation results in

$$\hat{H} e^{\hat{T}} |0\rangle = E_{\mathrm{CC}} e^{\hat{T}} |0\rangle . \tag{2.6.2}$$

Unlike HF and CI, the CC energy is not variational, but the wavefunction parameters, i.e., the cluster amplitudes are derived using the following approach. Starting from eq. (2.6.2) both sides are multiplied with $e^{-\hat{T}}$

$$\begin{aligned} e^{-\hat{T}} \hat{H} e^{\hat{T}} |0\rangle &= E_{\mathrm{CC}} \overbrace{e^{-\hat{T}} e^{\hat{T}}}^{=1} |0\rangle \\ \widetilde{H} |0\rangle &= E_{\mathrm{CC}} |0\rangle . \end{aligned}$$

Here, $\widetilde{H} = e^{-\hat{T}} \hat{H} e^{\hat{T}}$ is the similarity-transformed Hamiltonian. At this point the HF energy can be subtracted from both sides of the equation.

$$\begin{aligned} \widetilde{H} |0\rangle - E_{\mathrm{HF}} |0\rangle &= E_{\mathrm{CC}} |0\rangle - E_{\mathrm{HF}} |0\rangle \\ \widetilde{H}_N |0\rangle &= \Delta E_{\mathrm{CC}} |0\rangle , \end{aligned} \tag{2.6.3}$$

with $\widetilde{H}_N = e^{-\hat{T}} \hat{H}_N e^{\hat{T}}$ as the normal-ordered similarity-transformed Hamiltonian and $\Delta E_{\mathrm{CC}} = E_{\mathrm{CC}} - E_{\mathrm{HF}}$ as the correlation energy at the CC level of theory. The cluster amplitudes are derived by projecting eq. (2.6.3) on excited determinants

$$\langle \Phi_I | \widetilde{H}_N |0\rangle = 0,$$

which define the CC amplitude equations. The energy is derived by projection on the reference determinant

$$\langle 0 | \widetilde{H}_N |0\rangle = E_{\mathrm{CC}}.$$

Looking closer at the similarity-transformed Hamiltonian

$$\widetilde{H}_N = e^{-\hat{T}} \hat{H}_N e^{\hat{T}},$$

it can be expanded using the Baker–Campbell–Hausdorff (BCH) formula

$$\widetilde{H}_N = \hat{H}_N + [\hat{H}_N, \hat{T}] + \frac{1}{2!}[[\hat{H}_N, \hat{T}], \hat{T}] + \ldots \tag{2.6.4}$$

The commutators of the Hamiltonian with the cluster operator

$$[\hat{H}_N, \hat{T}] = \hat{H}_N \hat{T} - \hat{H}_N \hat{T}$$

result in an expression where only terms with at least one contraction between the operators survive, hereon deemed connected, while all terms with no contraction between the operators (disconnected) cancel out. For this reason, the above commutator is alternatively written as $(\hat{H}_N \hat{T})_{\mathrm{C}}$, where C indicates the connectedness. In the derivation of the working equation, diagrammatic techniques that utilized the antisymmetrized Goldstone diagrams are often used.[103,110] In these diagrams the connectedness is shown by a direct line connecting the vertices of the operators.

Because of the connectedness requirement, the similarity-transformed Hamiltonian eq. (2.6.4) naturally truncates at the fourth order

$$\widetilde{H}_N = \hat{H}_N + [\hat{H}_N, \hat{T}] + \frac{1}{2!}[[\hat{H}_N, \hat{T}], \hat{T}] + \frac{1}{3!}[[[\hat{H}_N, \hat{T}], \hat{T}], \hat{T}] + \frac{1}{4!}[[[[\hat{H}_N, \hat{T}], \hat{T}], \hat{T}], \hat{T}].$$

The fourth-order term

$$\frac{1}{4!}[[[[\hat{H}_N,\hat{T}],\hat{T}],\hat{T}],\hat{T}] = \frac{1}{4!}((((\hat{H}_N\hat{T})_{\mathrm{C}}\hat{T})_{\mathrm{C}}\hat{T})_{\mathrm{C}}\hat{T})_{\mathrm{C}} = \frac{1}{4!}(\hat{H}_N\hat{T}^4)_{\mathrm{C}}$$

is the highest-order term with connected contributions since the Hamiltonian has at most four quasi-particle operators from the two-electron interaction term. This natural truncation of the similarity-transformed Hamiltonian proves very handy for the derivation of the CC amplitude equations. As for the cluster operator $\hat{T}$, it also truncates naturally at the number of electrons n reproducing FCI results.

There exists an intrinsic connection between CC theory and MBPT.[103] The cluster amplitudes can be interpreted as a summation of the perturbation amplitudes until infinite order

$$\hat{T} = \sum_{l=0}^{\infty} \hat{T}^{(l)}. \tag{2.6.5}$$

Unlike MBPT though, the CC expansion is not truncated in a specific order of perturbation, but is truncated similarly to the CI truncations in a specific level of excitation. The most often used truncation is CCSD, $\hat{T} = \hat{T}_1 + \hat{T}_2$.

At this point, the CC and CI theory are to be compared. Both theories lead to the FCI exact solution, when the expansion is not truncated. For the same truncation, however, e.g. CCSD vs CISD, the following wavefunctions are to be compared

$$\Psi_{\mathrm{CISD}} = \left(\hat{C}_0 + \hat{C}_1 + \hat{C}_2\right)|0\rangle$$
$$\Psi_{\mathrm{CCSD}} = \left(1 + \hat{T}_1 + \hat{T}_2 + \frac{1}{2}\hat{T}_1^2 + \hat{T}_1\hat{T}_2 + \frac{1}{6}\hat{T}_1^3 + \frac{1}{2}\hat{T}_2^2 + \frac{1}{2}\hat{T}_2\hat{T}_1^2 + \frac{1}{24}\hat{T}_1^4 + \dots\right)|0\rangle\,.$$

The comparison shows, that Ψ_{CISD} only includes singly- and doubly- excited determinants, while Ψ_{CCSD} contains in principle all possible excited determinants (although only some of them contribute to the energy, and to the CC amplitude equation). More specifically, the CC wavefunction includes connected-cluster contributions with only one cluster operator (e.g. $\hat{T}_2$), and disconnected-cluster contributions that include products of cluster operators (e.g. $\hat{T}_1\hat{T}_2$). It can thus be deduced that the CC method for the same truncation includes correlation at a higher level, compared to the same CI truncation, while having a similar scaling.[103] CC results are also proven to be size-extensive.[103] More importantly, the corrections to the correlation energy offered by higher excitations beyond CCSD are much more significant at each level of excitation, meaning that the CC series converges to the FCI limit much faster as compared to the CI series. The CCSDT truncation gives errors of 1 mE_{h} relative to FCI for systems dominated by a single reference, while CISDT still has an error one order of magnitude larger. A significant reduction of error occurs at the CISDTQ level, because of the inclusion of the most important terms that account for the size-extensivity, which are though already included at the CCSD level. For this reason, the CC approach is nowadays preferred against CI, since it tackles most of the shortcomings of the latter.[103] Despite the advantages of CC theory, one major disadvantage is that the similarity-transformed Hamiltonian is no longer a Hermitian operator. Because of this, non-physical complex energies may arise. In the absence of a magnetic field, this is rarely the case, but for ff-methods this is an issue which needs to be monitored.[103,111,112]

2.6.2 The Equation-of-Motion CC approach

The non-linear problem of the CC equations gives a solution for the ground state of the system, but different solutions are not easily derived. In addition, it is not clear if higher-order roots are able to be interpreted as solution for the excited states as with the CI approach.[103,113] For this reason, in order to get information about excited states, a different approach is used, namely the equation-of-motion (EOM) CC approach.[103,114] Here, a CI-like linear excitation operator is applied on the CC wavefunction to obtain excited-state wavefunction of CC quality.

$$\Psi_{\mathrm{EOM}} = \hat{R}\Psi_{\mathrm{CC}} = \hat{R}e^{\hat{T}}\,|0\rangle\,, \tag{2.6.6}$$

with the EOM excitation operator

$$\hat{R} = \hat{R}_0 + \hat{R}_1 + \hat{R}_2 + \cdots = r_0 + \sum_{ia} r_i^a \hat{a}_a^\dagger \hat{a}_i + \frac{1}{4} \sum_{ijab} r_{ij}^{ab} \hat{a}_a^\dagger \hat{a}_b^\dagger \hat{a}_j \hat{a}_i + \cdots = \sum_I r_I \hat{\mu}_I.$$

Since both $\hat{T}$ and $\hat{R}$ are excitation operators, they commute

$$[\hat{T}, \hat{R}] = 0$$

and the exponential of $\hat{T}$ commutes as well

$$[e^{\hat{T}}, \hat{R}] = 0.$$

Eq. (2.6.6) is then inserted in the Schrödinger equation

$$\hat{H}\hat{R}e^{\hat{T}} |0\rangle = E_{\text{exc}} \hat{R} e^{\hat{T}} |0\rangle ,$$

the CC energy is subtracted

$$\begin{aligned} \hat{H}\hat{R}e^{\hat{T}} |0\rangle - E_{\text{CC}} \hat{R} e^{\hat{T}} |0\rangle &= E_{\text{exc}} \hat{R} e^{\hat{T}} |0\rangle - E_{\text{CC}} \hat{R} e^{\hat{T}} |0\rangle \\ \left(\hat{H} - E_{\text{HF}}\right) e^{\hat{T}} \hat{R} |0\rangle - e^{\hat{T}} \hat{R} \overbrace{\Delta E_{\text{CC}} |0\rangle}^{=\widetilde{H}_N |0\rangle} &= e^{\hat{T}} \Delta E_{\text{exc}} \hat{R} |0\rangle , \end{aligned}$$

and the expression is multiplied by $e^{-\hat{T}}$

$$\begin{aligned} \widetilde{H}_N \hat{R} |0\rangle - \hat{R} \widetilde{H}_N |0\rangle &= \Delta E_{\text{exc}} \hat{R} |0\rangle \\ (\widetilde{H}_N \hat{R})_{\text{C}} |0\rangle &= \Delta E_{\text{exc}} \hat{R} |0\rangle . \end{aligned}$$

The excitation energy $\Delta E_{\text{exc}} = E_{\text{exc}} - E_{\text{CC}}$ has been introduced. Projecting on excited determinants and explicitly writing the EOM operator

$$\begin{aligned} \sum_I \langle \Phi_J | (\widetilde{H}_N \hat{\mu}_I)_{\text{C}} |0\rangle \, r_I &= \Delta E_{\text{exc}} \sum_I r_I \langle \Phi_J | \hat{\mu}_I |0\rangle \\ \sum_I (\widetilde{H}_{JI})_{\text{C}} r_I &= \Delta E_{\text{exc}} r_J \\ \widetilde{\mathbf{H}}_{\text{C}} \mathbf{R} &= \Delta E_{\text{exc}} \mathbf{R}, \end{aligned}$$

gives rise to a CI like eigenvalue problem. Here $\widetilde{\mathbf{H}}_{\text{C}}$ is the connected part of the similarity-transformed Hamiltonian matrix, with elements $(\widetilde{H}_{JI})_{\text{C}} = \langle \Phi_J | (\widetilde{H}_N \hat{\mu}_I)_{\text{C}} |0\rangle$ and $\mathbf{R}$ the EOM vector. $\widetilde{\mathbf{H}}_{\text{C}}$ is also interpreted as the CC Jacobian matrix. Different solutions for the eigenvalue problem describe different excited states and excitation energies. The disconnected contribution in the similarity-transformed Hamiltonian matrix simply adds the CC correlation energy ΔE_{CC} to the eigenvalue. The disconnected contributions though are redundant as they have been solved with the CC amplitude equations. For this reason, the current form is preferred for the derivation of working equations.

Truncation of $\hat{R}$ is normally done at the same level as the truncation for the cluster operator $\hat{T}$. For example the EOM-CCSD approach has $\hat{R} = \hat{R}_0 + \hat{R}_1 + \hat{R}_2$ and $\hat{T} = \hat{T}_1 + \hat{T}_2$. Using the same level of truncation for the cluster and the EOM operator has the advantage that excitation energies are size-intensive, meaning that they are consistent at describing individual excitations on non-interacting fragments.[85] Additionally, calculating the EOM amplitude for the CC reference wavefunction $\hat{R}_0 = r_0$ is not needed for the computation of the excitation energy, since it is not coupled to the rest of the EOM parameters. This decoupling occurs because because the $\widetilde{H}_{J0}$ column vanishes as it constitutes the CC amplitude equations for the same truncation.

The EOM-CC approach is considered more advantageous for excited states compared to CI. The CI ansatz for excited states aims to target both the excitation energy compared to the reference

determinant and correlation with a single set of parameters (i.e., the CI coefficients). Because of this, results at the truncated CI level for excited states are of bad quality. The EOM-CC approach on the other hand, has already targeted a significant part of the correlation at the ground-state CC level with the cluster amplitudes, and the EOM vectors deal primarily with the excitation energy and differential correlation. At the EOM-CCSD level for excited states with primarily single-excitation character, this is indeed the case. However, excited states of predominant double-excitation character are described inadequately at the EOM-CCSD level, and the can only be described satisfactorily first at the EOM-CCSDT level.[103]

It has been silently assumed, that the EOM excitation vector $\hat{R}$ is spin-conserving, meaning despite working with spinorbitals, the total number of α- and β-spin orbitals is not changed by $\hat{R}$. This is a particular variant of the EOM-CC approach named Excitation-Energy EOM (EE-EOM). If instead one allows the quasiparticle operators to change the total spin, the Spin-Flip (SF) EOM variant is derived.[115] Further not restricting the $\hat{R}$ operator to conserve the number of particles one derives the Ionization-Potential (IP)[116] and Electron-Affinity (EA)[117] EOM variants, where one electron is removed or added, respectively. Using the CCSD truncation the IP-EOM-CCSD includes h and $2hp$ operators

$$\hat{R}^{\mathrm{IP}} = \sum_i r_i \hat{a}_i + \frac{1}{2} \sum_{ija} r_{ij}^a \hat{a}_a^\dagger \hat{a}_i \hat{a}_j,$$

while the EA-EOM CCSD includes p and $2ph$ terms

$$\hat{R}^{\mathrm{EA}} = \sum_a r^a \hat{a}_a^\dagger + \frac{1}{2} \sum_{abi} r_i^{ab} \hat{a}_b^\dagger \hat{a}_a^\dagger \hat{a}_i.$$

The non-Hermiticity of the similarity-transformed Hamiltonian poses an issue not only for the CC ground state, but for the EOM-CC approach as well. Computationally speaking, the left-side EOM-vectors are not the complex conjugate of the right-hand-side EOM vectors, and are needed for property calculations. In addition, non-physical complex energies arise for the field-free case in the vicinity of conical intersections and for calculations in the presence of a magnetic field.[111,112,118]

2.7 Properties as analytic derivatives

Properties are usually expressed through energy derivatives.[119] First-order properties like dipole moment, energy gradient, angular momentum, spin multiplicity, etc. are expressed as first derivatives of the energy, with respect to to a parameter ξ

$$A = \frac{\mathrm{d}E[\boldsymbol{c}]}{\mathrm{d}\xi},$$

where $\boldsymbol{c}$ are sets of parameters that define the wavefunction and A is the first-order property. Assuming the exact wavefunction Ψ, the above relationship is simplified to the time-independent Hellmann-Feynman theorem

$$\begin{aligned}
A &= \frac{\mathrm{d}}{\mathrm{d}\xi} \langle \Psi | \hat{H} | \Psi \rangle \\
&= \langle \Psi | \frac{\partial \hat{H}}{\partial \xi} | \Psi \rangle + E \left(\langle \frac{\partial \Psi}{\partial \xi} | \Psi \rangle + \langle \Psi | \frac{\partial \Psi}{\partial \xi} \rangle \right) \\
&= \langle \Psi | \frac{\partial \hat{H}}{\partial \xi} | \Psi \rangle + E \overbrace{\frac{\partial}{\partial \xi} \langle \Psi | \Psi \rangle}^{\partial 1/\partial \xi = 0} \\
A &= \langle \Psi | \frac{\partial \hat{H}}{\partial \xi} | \Psi \rangle .
\end{aligned}$$

For approximate wavefunctions, the energy derivative takes the following form

$$\frac{\mathrm{d}E[\boldsymbol{c}]}{\mathrm{d}\xi} = \frac{\partial E}{\partial \xi} + \frac{\partial E}{\partial \boldsymbol{c}} \frac{\partial \boldsymbol{c}}{\partial \xi},$$

following the chain rule for total derivatives. The first term $\frac{\partial E}{\partial \xi}$ is usually called the Hellmann-Feynman term, because it takes a form similar to the result of the Hellman-Feynman theorem $\langle \Psi_{\text{approx}}| \frac{\partial \hat{H}}{\partial \xi} |\Psi_{\text{approx}}\rangle$. The remaining terms require the computation of the perturbed wavefunction parameters $\frac{\partial \boldsymbol{c}}{\partial \xi}$. Variational wavefunctions though simplify to the Hellmann-Feynman theorem, because the derivatives of the energy with respect to the wavefunction parameters have been required to be 0, $\frac{\partial E}{\partial \boldsymbol{c}} = 0$. This greatly reduces the cost of the property calculation, since the perturbed wavefunction parameters do not have to be determined, but unfortunately, one rarely works with completely variational wavefunctions.

For non-variational wavefunctions an alternative Lagrangian formulation for the energy can be used in order to bypass the calculation of the perturbed wavefunction parameters

$$L[\boldsymbol{c}, \tilde{\boldsymbol{c}}] = E[\boldsymbol{c}] + \tilde{\boldsymbol{c}} \boldsymbol{f}(\boldsymbol{c}). \tag{2.7.1}$$

Here, $\tilde{\boldsymbol{c}}$ are the Lagrangian multipliers that correspond to the wavefunction parameters $\boldsymbol{c}$, and $\boldsymbol{f}(\boldsymbol{c}) = 0$ are the equations that determine the parameters themselves. The Lagrangian multipliers are then determined by requiring the derivatives of the Lagrangian with respect to the wavefunction parameters to vanish

$$\frac{\partial L}{\partial \boldsymbol{c}} = 0,$$

while the derivatives of the Lagrangian are zero when the wavefunction parameters have been determined

$$\frac{\partial L}{\partial \tilde{\boldsymbol{c}}} = \boldsymbol{f}(\boldsymbol{c}) = 0.$$

In his way, properties can be calculated as partial derivatives of the Lagrangian

$$A = \frac{\mathrm{d}L}{\mathrm{d}\xi} = \frac{\partial L}{\partial \xi},$$

since the terms that involve the perturbed wavefunction parameters and the perturbed Lagrange multipliers vanish.

This approach may seem unnecessary. Instead of simplifying the problem, the Lagrange multipliers are additional parameters that complicate the problem further, and moreover, they have to be determined instead of the perturbed wavefunction parameters. The Lagrange multipliers are though independent of the parameter ξ, meaning they have to be determined only once for each system. The perturbed wavefunction parameters, on the other hand, need to be determined for each different property.

2.7.1 CC ground-state properties

Following the Lagrangian approach eq. (2.7.1) for the calculations of properties, the CC Lagragian has the following form[120,121]

$$\begin{aligned} L_{\text{CC}} &= \langle 0| \widetilde{H}_N |0\rangle + \sum_J \lambda_J \langle \Phi_J| \widetilde{H}_N |0\rangle \\ &= \langle 0| \widetilde{H}_N |0\rangle + \sum_J \langle 0| \lambda_J \hat{\mu}_J^\dagger \widetilde{H}_N |0\rangle \\ &= \langle 0| \widetilde{H}_N |0\rangle + \langle 0| \hat{\Lambda} \widetilde{H}_N |0\rangle \\ &= \langle 0| (1 + \hat{\Lambda}) \widetilde{H}_N |0\rangle . \end{aligned} \tag{2.7.2}$$

The relaxation of the MO coefficients has been ignored in the formulation of this Lagrangian, as their contribution to the calculation of properties will be discussed later. Here the deexcitation operator

$$\hat{\Lambda} = \sum_{J \neq 0} \lambda_J \hat{\mu}_J^\dagger$$

is introduced that includes the Lagrange multipliers λ_J, also known as λ-amplitudes. The $\hat{\Lambda}$ operator is truncated at the same excitation level as cluster operator $\hat{T}$ in order to include all the CC amplitude equations required. Operator $\hat{\mu}_J^\dagger$ is the complex conjugate of $\hat{\mu}_J$ and creates the bra state $\langle\Phi_J|$ acting on $\langle 0|$.

Differentiation of the L_{CC} with respect to the Lagrange multipliers reproduces the CC amplitude equations

$$\begin{aligned}\frac{\partial L_{\mathrm{CC}}}{\partial \lambda_I} &= \frac{\partial}{\partial \lambda_I} \langle 0| (1+\hat{\Lambda}) \widetilde{H}_N |0\rangle \\ &= \frac{\partial}{\partial \lambda_I} \sum_J \langle 0| \lambda_J \hat{\mu}_J^\dagger \widetilde{H}_N |0\rangle \\ &= \langle 0| \hat{\mu}_I^\dagger \widetilde{H}_N |0\rangle \\ 0 &= \langle \Phi_I| \widetilde{H}_N |0\rangle ,\end{aligned} \tag{2.7.3}$$

while differentiation with respect to the cluster amplitudes

$$\begin{aligned}\frac{\partial L_{\mathrm{CC}}}{\partial t_I} &= \frac{\partial}{\partial t_I} \langle 0| (1+\hat{\Lambda}) \widetilde{H}_N |0\rangle \\ &= \langle 0| (1+\hat{\Lambda}) \frac{\partial \widetilde{H}_N}{\partial t_I} |0\rangle \\ &= \langle 0| (1+\hat{\Lambda}) [\widetilde{H}_N, \hat{\mu}_I] |0\rangle \\ 0 &= \langle 0| (1+\hat{\Lambda}) (\widetilde{H}_N, \hat{\mu}_I)_{\mathrm{C}} |0\rangle ,\end{aligned} \tag{2.7.4}$$

results in the λ-amplitude equations.

CC ground-state properties, or more specifically the correlation contribution to the property A_{CC}, can now be calculated by a Hellmann-Feynman like term

$$A_{\mathrm{CC}} = \langle \tilde{\Psi}_{\mathrm{CC}}| \frac{\partial \hat{H}_N}{\partial \xi} |\Psi_{\mathrm{CC}}\rangle ,$$

with

$$\langle \tilde{\Psi}_{\mathrm{CC}}| = \langle 0| (1+\hat{\Lambda}) e^{-\hat{T}} \tag{2.7.5}$$

the bra CC state not being the complex-conjugate of the ket state, as the similarity transformation of the Hamiltonian is a non-Hermitian parametrisation.

2.7.2 EOM-CC excited-state properties

In order to approach excited-state properties at the EOM-CC level of theory as analytic derivative, an expression for the energy is needed. In order to derive an expression for the EOM energy in an expectation-value type of form, the left-side EOM vectors are introduced

$$\hat{L} = \hat{L}_0 + \hat{L}_1 + \hat{L}_2 + \cdots = l_0 + \sum_{ia} l_a^i \hat{a}_i^\dagger \hat{a}_a + \frac{1}{4} \sum_{ijab} l_{ab}^{ij} \hat{a}_i^\dagger \hat{a}_j^\dagger \hat{a}_b \hat{a}_a + \cdots = \sum_I l_I \hat{\mu}_I^\dagger . \tag{2.7.6}$$

These are deexcitation operators. The left-side EOM vectors are required to solve the left-side eigenvalue problem

$$\mathbf{L}\widetilde{\mathbf{H}}_{\mathrm{C}} = \mathbf{L}\Delta E_{\mathrm{exc}},$$

which, as already mentioned, is not the complex-conjugate of the right-side eigenvalue problem because of the non-Hermiticity of the similarity-transformed Hamiltonian. The EOM vectors are additionally

normalised, thus fulfilling the biorthonormality condition

$$\begin{aligned}
\langle \tilde{\Psi}^m_{\mathrm{EOM}} | \Psi^n_{\mathrm{EOM}} \rangle &= \delta_{mn} \\
\langle 0 | \hat{L}^m \overbrace{e^{-\hat{T}} e^{\hat{T}}}^{=1} \hat{R}^n | 0 \rangle &= \\
\langle 0 | \hat{L}^m \hat{R}^n | 0 \rangle &= \\
\sum_I l_I^m r_I^n &= \delta_{mn},
\end{aligned}$$

with $\langle \tilde{\Psi}^m_{\mathrm{EOM}}| = \langle 0| \hat{L}^n e^{-\hat{T}}$, the bra EOM state, and m and n different eigenvalue solutions.

One may notice a special solution for the EOM vectors, namely the $\hat{R}^0 = \hat{1}$ that results in the ground-state solution. The left-side vector is then required to obey the following equation

$$\langle 0| \hat{L}^0 (\widetilde{H}_N, \hat{\mu}_I)_{\mathrm{C}} | 0 \rangle = 0,$$

which is another form of the λ-amplitude equations from eq (2.7.4). Thus $\hat{L}^0 = 1 + \hat{\Lambda}$ is the left-side solution for the ground state, and does obey the biorthonormality condition.

As for excited states, while r_0 is determined by the equation

$$r_0^n = \frac{\sum_I (\widetilde{H}_{0I})_{\mathrm{C}} r_I^n}{\Delta E^n_{\mathrm{exc}}},$$

and is needed for the calculations of properties, l_0^n needs to be set to zero for $n \neq 0$ in order for excited bra states to be orthogonal to the ground ket state. It is noteworthy to point out that r_0 is only needed to be considered in the EE-EOM variant. For all other EOM variants, there can be no overlap between the ground state and the excited state, and thus necessarily $r_0 = 0$. Even in EE-EOM, r_0 might be equal to zero, when the excited state belongs to a different irreducible representation or has a different spin-multiplicity compared to the reference CC state. In the absence of symmetry exploitation or when the calculation of spin-multiplicity has not been implemented, the emergence of numerical zeros for r_0 serves as an indication that the excited state has a different spatial or spin symmetry.

Expectation-value type properties

The following Lagrangian is defined for the calculation of properties at the EOM level of theory

$$L_{\mathrm{EOM}} = \langle 0| \hat{L} \widetilde{H}_N \hat{R} | 0 \rangle - E \left(\langle 0| \hat{L} \hat{R} | 0 \rangle - 1 \right), \tag{2.7.7}$$

which for now ignores the response of the cluster amplitudes.[121–126] Differentiation with respect to l_I results in the right-side EOM eigenvalue problem

$$\begin{aligned}
\frac{\partial L_{\mathrm{EOM}}}{\partial l_I} &= 0 \\
\langle 0| \hat{\mu}_I^\dagger \widetilde{H}_N \hat{R} | 0 \rangle - E r_I &= 0 \\
\langle 0| \hat{\mu}_I^\dagger \widetilde{H}_N \hat{R} | 0 \rangle &= E r_I
\end{aligned}$$

in its disconnected form. Similarly differentiation with respect to the r_I results in the left-side EOM equation

$$\begin{aligned}
\frac{\partial L_{\mathrm{EOM}}}{\partial r_I} &= 0 \\
\langle 0| \hat{L} \widetilde{H}_N \hat{\mu}_I | 0 \rangle - E l_I &= 0 \\
\langle 0| \hat{L} \widetilde{H}_N \hat{\mu}_I | 0 \rangle &= l_I E.
\end{aligned}$$

The introduced Lagrange multiplier E are the energy eigenvalues $E = \Delta E_{\mathrm{EOM}} = E_{\mathrm{exc}} - E_{\mathrm{HF}}$. Using this formulation, the CC and EOM-CC energy solution are interpreted as bivariational solutions of a non-Hermitian parametrisation of the Hamiltonian, similar to CI solutions.

Properties calculated using this Lagrangian are called EOM-expectation value properties, since they arise from the EOM expectation-value form

$$A_{\mathrm{EOM}} = \langle \tilde{\Psi}_{\mathrm{EOM}} | \frac{\partial \hat{H}_N}{\partial \xi} | \Psi_{\mathrm{EOM}} \rangle .$$

A_{EOM} is the correlation contribution to the property at the EOM-CC level of theory.

A similar formulation allows for the calculation of transition properties.

$$L^{mn}_{\mathrm{EOM}} = \langle 0 | \hat{L}^m \widetilde{H}_N \hat{R}^n | 0 \rangle - E_{mn} \langle 0 | \hat{L}^m \hat{R}^n | 0 \rangle , \tag{2.7.8}$$

with $m \neq n$ as the indices of the electronic states including the ground-state for $m, n = 0$. The Lagrange multipliers in this case vanish $E_{mn} = 0$. Regarding transition properties, only the correlation contribution survives

$$A^{mn}_{\mathrm{EOM}} = \langle \tilde{\Psi}^m_{\mathrm{EOM}} | \frac{\partial \hat{H}_N}{\partial \xi} | \Psi^n_{\mathrm{EOM}} \rangle ,$$

as there is no contribution from the HF reference. It is important to note, that in the exact case, the properties arising from transitions $n \to m$ and $m \to n$ form a complex-conjugate pair

$$\langle \Psi^m_{\mathrm{exact}} | \frac{\partial \hat{H}_N}{\partial \xi} | \Psi^n_{\mathrm{exact}} \rangle = \langle \Psi^n_{\mathrm{exact}} | \frac{\partial \hat{H}_N}{\partial \xi} | \Psi^m_{\mathrm{exact}} \rangle^*$$
$$A^{mn} = A^{nm*}.$$

This is, however, not the case for properties at the truncated EOM-CC level of theory $A^{mn}_{\mathrm{EOM}} \neq A^{nm}_{\mathrm{EOM}}{}^*$, which is a non-physical artifact of the non-Hermiticity. Fortunately, such transition properties are not physical observables themselves, but their absolute square normally has a physical interpretation $|A^{mn}_{\mathrm{EOM}}|^2$. For this reason, the absolute square is usually approximated as $|A^{mn}_{\mathrm{EOM}}|^2 \approx A^{mn}_{\mathrm{EOM}} \cdot A^{nm}_{\mathrm{EOM}}$ in the EOM-CC approach. Transition properties at this expectation-value level are not size-intensive.[103,122]

Eq. (2.7.7) and (2.7.8) can be combined to form the Lagrangian

$$L^{mn}_{\mathrm{EOM}} = \langle 0 | \hat{L}^m \widetilde{H}_N \hat{R}^n | 0 \rangle - E_{mn} \Big(\langle 0 | \hat{L}^m \hat{R}^n | 0 \rangle - \delta_{mn} \Big) ,$$

with $E_{mn} = \Delta E^m_{\mathrm{EOM}} \delta_{mn}$.

Response properties

The following Lagrangian

$$\begin{aligned} L_{\mathrm{resp}} &= L^{mm}_{\mathrm{EOM}} + \langle 0 | \hat{\mathscr{Z}} \widetilde{H}_N | 0 \rangle \\ &= \langle 0 | \hat{L}^m \widetilde{H}_N \hat{R}^m | 0 \rangle - \Delta E^m_{\mathrm{EOM}} \Big(\langle 0 | \hat{L}^m \hat{R}^m | 0 \rangle - 1 \Big) + \langle 0 | \hat{\mathscr{Z}} \widetilde{H}_N | 0 \rangle \end{aligned} \tag{2.7.9}$$

does take the response of the cluster amplitudes under consideration for single-state properties.[121–126] Here the deexcitation operator

$$\hat{\mathscr{Z}} = \sum_{J \neq 0} \zeta_J \hat{\mu}^\dagger_J$$

has been introduced, which is analogous to the $\hat{\Lambda}$ operator in eq. (2.7.2). This additional term is only needed for excited state $m \neq 0$, since the λ-amplitudes account for the response of the cluster amplitudes in the ground-state case. Differentiation with respect to r_I and l_I only affects the L^{mm}_{EOM}

term, and reproduces the same equations. Additional differentiation with respect to t_I gives working equations for the ζ-amplitudes

$$\frac{\partial L_{\text{resp}}}{\partial t_I} = 0$$
$$\langle 0| \hat{L}^m (\widetilde{H}_N \hat{\mu}_I)_{\text{C}} \hat{R}^m |0\rangle + \langle 0| \hat{\mathscr{Z}} (\widetilde{H}_N \hat{\mu}_I)_{\text{C}} |0\rangle = 0.$$

An alternative but totally equivalent Lagrangian formulation for the response of the cluster amplitudes for excited state, is to use the connected form of the EOM equations and independently add the reference energy

$$L'_{\text{resp}} = \langle 0| \hat{L}^m (\widetilde{H}_N \hat{R}^m)_{\text{C}} |0\rangle - \Delta E^m_{\text{exc}} \left(\langle 0| \hat{L}^m \hat{R}^m |0\rangle - 1 \right) + \langle 0| (1 + \hat{\mathscr{Z}}') \widetilde{H}_N |0\rangle . \tag{2.7.10}$$

This Lagrangian reproduces the excitation energy of the EOM state, instead of the correlation contribution. The exact form of the ζ'-amplitudes is different

$$\frac{\partial L'_{\text{resp}}}{\partial t_I} = 0$$
$$\langle 0| \hat{L}^m ((\widetilde{H}_N \hat{\mu}_I)_{\text{C}} \hat{R}^m)_{\text{C}} |0\rangle + \langle 0| (1 + \hat{\mathscr{Z}}') (\widetilde{H}_N \hat{\mu}_I)_{\text{C}} |0\rangle = 0, \tag{2.7.11}$$

but the two approaches in eq. (2.7.9) and (2.7.10) are equivalent, and give the same result. Using the disconnected approach the correlation contribution to the property is given by

$$\begin{aligned} A_{\text{resp}} &= \langle 0| \hat{L} \frac{\partial \widetilde{H}_N}{\partial \xi} \hat{R} |0\rangle + \langle 0| \hat{\mathscr{Z}} \frac{\partial \widetilde{H}_N}{\partial \xi} |0\rangle \\ &= \langle 0| \hat{L} (\frac{\partial \widetilde{H}_N}{\partial \xi} \hat{R})_{\text{C}} |0\rangle + \langle 0| \hat{L} \hat{R} \frac{\partial \widetilde{H}_N}{\partial \xi} |0\rangle + \langle 0| \hat{\mathscr{Z}} \frac{\partial \widetilde{H}_N}{\partial \xi} |0\rangle \\ &= \langle 0| \hat{L} (\frac{\partial \widetilde{H}_N}{\partial \xi} \hat{R})_{\text{C}} |0\rangle + \langle 0| \left(\hat{L} \hat{R} + \hat{\mathscr{Z}} \right) \frac{\partial \widetilde{H}_N}{\partial \xi} |0\rangle . \end{aligned} \tag{2.7.12}$$

The term $\langle 0| \hat{L} \hat{R} \frac{\partial \widetilde{H}_N}{\partial \xi} |0\rangle$ includes only the disconnected contributions. In the connected formulation, the disconnected contribution are completely absent

$$A_{\text{resp}} = \langle 0| \hat{L} (\frac{\partial \widetilde{H}_N}{\partial \xi} \hat{R})_{\text{C}} |0\rangle + \langle 0| (1 + \hat{\mathscr{Z}}') \frac{\partial \widetilde{H}_N}{\partial \xi} |0\rangle . \tag{2.7.13}$$

The correspondence between eq. (2.7.12) and (2.7.13) dictates that

$$\hat{L} \hat{R} + \hat{\mathscr{Z}} = 1 + \hat{\mathscr{Z}}'.$$

The working equations arising from $1 + \hat{\mathscr{Z}}'$ are slightly less complicated, as they involve fewer terms.

Lastly, the calculation of transition properties that includes the response of the cluster amplitudes and further takes under consideration the explicit interaction of the system with light is based on a time-dependent formulation of CC theory.[127–129] This approach gives frequency-dependent transition properties.[81,122,126] The resulting Lagrangian has the form

$$L^{mn}_{\text{resp}} = \langle 0| \hat{L}^m (\widetilde{H}_N \hat{R}^n)_{\text{C}} |0\rangle - \Delta E_{mn} \left(\langle 0| \hat{L}^m \hat{R}^m |0\rangle - \delta_{mn} \right) + \langle 0| \hat{\mathscr{Z}}' (\widetilde{H}_N - \omega \hat{T}) |0\rangle , \tag{2.7.14}$$

with ω as the frequency and $m \neq n$. The ζ'-amplitude equation in this case are given by

$$\frac{\partial L^{mn}_{\text{resp}}}{\partial t_I} = 0$$
$$\langle 0| \hat{L}^m ((\widetilde{H}_N \hat{\mu}_I)_{\text{C}} \hat{R}^n)_{\text{C}} |0\rangle + \langle 0| \hat{\mathscr{Z}}' (\widetilde{H}_N \hat{\mu}_I)_{\text{C}} |0\rangle = \omega_{mn} \zeta'_I, \tag{2.7.15}$$

which is an inhomogeneous set of linear equations.

2.7.3 Orbital relaxation

In order to fully derive analytic derivatives, the response of the parameters of the reference wavefunction, i.e., the MO coefficients $c_{\mu i}$ and the basis set, need to be considered.[119,121,130] The MO coefficients have indeed been derived as variational parameters for the HF energy, and their response need not be calculated for properties at the HF level, but they are not variational for the correlation energy at any level of theory (CI, MP, CC) discussed so far

$$\begin{aligned}\frac{\partial E_{\mathrm{HF}}}{\partial c_{\mu i}} &= 0\\ \frac{\partial \Delta E_{\mathrm{corr}}}{\partial c_{\mu i}} &\neq 0.\end{aligned}$$

For the calculation of certain properties the response of the basis set itself is to be calculated as well (geometrical derivatives, magnetic field).

The correlation energy can always be written with the help of the one- and two-body reduced density matrices, $\boldsymbol{\gamma}_N$ and $\boldsymbol{\Gamma}_N$

$$\Delta E_{\mathrm{corr}} = \sum_{pq} (\gamma_N)_{qp} f_{pq} + \frac{1}{4} \sum_{pqrs} (\Gamma_N)_{rspq} \langle pq| |rs\rangle . \tag{2.7.16}$$

The exact form of the one- and two-body reduced density matrices depends on the level of theory, but care should have been taken for them to include all the relaxation parameters discussed so far. For the different levels of theory the reduced body density matrices can be found in tab. 2.1.

Level of theory	Reduced density matrix
CI	$\langle 0\vert \hat{C}^\dagger \{\dots\} \hat{C} \vert 0\rangle$
CC ground-state	$\langle 0\vert (1+\hat{\Lambda}) e^{-\hat{T}} \{\dots\} e^{\hat{T}} \vert 0\rangle$
EOM-CC expectation value	$\langle 0\vert \hat{L} e^{-\hat{T}} \{\dots\} e^{\hat{T}} \hat{R} \vert 0\rangle$
EOM-CC response/LR-CC	$\langle 0\vert \hat{L} (e^{-\hat{T}} \{\dots\} e^{\hat{T}} \hat{R})_{\mathrm{C}} \vert 0\rangle + \langle 0\vert (1+\hat{\mathscr{Z}}') e^{-\hat{T}} \{\dots\} e^{\hat{T}} \vert 0\rangle$

Table 2.1: The general form of the reduced density matrices for CI, CC ground-state, EOM-CC expectation-value, and EOM-CC response/LR-CC properties. For $(\gamma_N)_{qp}$ the normal ordered quasiparticle operator string is $\{\dots\} = \{\hat{a}_p^\dagger \hat{a}_q\}$, when for $(\Gamma_N)_{rspq}$, $\{\dots\} = \{\hat{a}_p^\dagger \hat{a}_q^\dagger \hat{a}_s \hat{a}_r\}$.

For non-Hermitian theory it is advantageous to remove the imaginary contribution from the reduced density matrices. This is achieved by a symmetrization

$$\begin{aligned}\mathrm{Re}\,(\Delta E_{\mathrm{corr}}) &= \frac{1}{2} (\Delta E_{\mathrm{corr}} + \Delta E_{\mathrm{corr}}^*)\\ &= \frac{1}{2} \left(\sum_{pq} (\gamma_N)_{qp} f_{pq} + \sum_{qp} (\gamma_N)_{pq}^* f_{qp}^* + \frac{1}{4} \sum_{pqrs} (\Gamma_N)_{rspq} \langle pq| |rs\rangle + \frac{1}{4} \sum_{rspq} (\Gamma_N)_{pqrs}^* \langle rs| |pq\rangle^* \right)\\ &= \sum_{pq} \frac{1}{2} \left[(\gamma_N)_{qp} + (\gamma_N)_{pq}^* \right] f_{pq} + \frac{1}{4} \sum_{pqrs} \frac{1}{2} \left[(\Gamma_N)_{rspq} + (\Gamma_N)_{pqrs}^* \right] \langle pq| |rs\rangle\\ &= \sum_{pq} (\rho_N)_{qp} f_{pq} + \frac{1}{4} \sum_{pqrs} (P_N)_{rspq} \langle pq| |rs\rangle .\end{aligned}$$

The symmetrized reduced density matrices are introduced

$$\begin{aligned}(\rho_N)_{qp} &= \frac{1}{2} \left[(\gamma_N)_{qp} + (\gamma_N)_{pq}^* \right]\\ (P_N)_{rspq} &= \frac{1}{2} \left[(\Gamma_N)_{rspq} + (\Gamma_N)_{pqrs}^* \right],\end{aligned} \tag{2.7.17}$$

which are Hermitian. For a Hermitian theory like CI, the reduced density matrices coincide with the symmetrized reduced density matrices.

The canonical HF requirements together with the orthonormality requirement can be written as follows

$$f_{pq} - \delta_{pq}\epsilon_p = 0 \qquad \text{canonical HF orbitals} \tag{2.7.18}$$

$$f_{ia} = f_{ai} = 0 \qquad \text{Brillouin theorem} \tag{2.7.19}$$

$$S_{pq} - \delta_{pq} = 0 \qquad \text{orthonormal orbitals.} \tag{2.7.20}$$

Eq. (2.7.18) includes the Brillouin criterion [eq. (2.7.19)]. Both equations are in thus included qq. (2.7.18) when the indexes p and q are allowed in the occupied-virtual and virtual-occupied space. The orbital-relaxed Lagrangian is then

$$\begin{aligned} L_{\text{corr}}^{\text{rel}} &= \text{Re}\left(\Delta E_{\text{corr}}\right) - \sum_{ia}\left[\left(\rho_N\right)_{ai} f_{ia} + \left(\rho_N\right)_{ia} f_{ai}\right] \\ &\quad + \sum_{pq} z_{qp}\left(f_{pq} - \delta_{pq}\epsilon_p\right) + \sum_{pq} I_{qp}\left(S_{pq} - \delta_{pq}\right) \\ &= \sum_{ij}\Big[\left(\rho_N\right)_{ji} f_{ij} + z_{ji}\left(f_{ij} - \delta_{ij}\epsilon_i\right) + I_{ji}\left(S_{ij} - \delta_{ij}\right)\Big] + \\ &\quad \sum_{ab}\left[\left(\rho_N\right)_{ba} f_{ab} + z_{ba}\left(f_{ab} - \delta_{ab}\epsilon_a\right) + I_{ba}\left(S_{ab} - \delta_{ab}\right)\right] + \\ &\quad \sum_{ai}\left[z_{ia} f_{ai} + I_{ia} S_{ai} + z_{ai} f_{ia} + I_{ai} S_{ia}\right] + \\ &\quad \frac{1}{4}\sum_{pqrs}\left(P_N\right)_{rspq}\left\langle pq\right|\left|rs\right\rangle . \end{aligned} \tag{2.7.21}$$

Here the Lagrange multipliers z_{pq}, also called z-vector, ensure the canonical orbitals and the Brillouin theorem eq. (2.7.18) and (2.7.19), while the I_{pq} ensure orthonormality eq. (2.7.20). In the construction of the Lagrangian eq. (2.7.21), the occupied-virtual, and virtual-occupied blocks of the one-body (symmetrized) reduced density matrices have been eliminated from the energy, since in any case they had zero contribution because of the Brillouin theorem, and their full contribution is moved in the z-vector, which simplifies the final working equations. The multipliers are considered Hermitian, since one is working with a symmetrized Lagrangian. In addition, the occupied-occupied and virtual-virtual blocks of the z-vector are only needed if any kind of frozen-orbital approximation has been used. Otherwise these contributions are zero, because the correlation treatment is invariant to orbital rotation inside the occupied-occupied and virtual-virtual space.

The effect of any perturbation at parameters of the reference wavefunction can be expressed as a basis transformation from $\{\psi_p\}$ to $\{\psi_p^{'}\}$. Such transformation can be expressed as an orbital rotation

$$\left|\psi_p^{'}\right\rangle = \sum_q R_{pq}\left|\psi_q\right\rangle .$$

Thus a derivative with respect to the parameters of the reference wavefunction can be expressed as a derivative with respect to the rotation parameters R_{pq} starting from the unperturbed case $\mathbf{R} = \mathbb{1}$. The integral derivatives have the following form:

$$\begin{aligned} \frac{\partial}{\partial R_{rs}} S_{pq} &= \frac{\partial}{\partial R_{rs}} \sum_{tu} R_{pt}^{*} R_{qu}\left\langle\psi_t|\psi_u\right\rangle\Big|_{\mathbf{U}=\mathbb{1}} \\ &= \sum_t R_{pt}^{*}\delta_{rq}\left\langle\psi_t|\psi_s\right\rangle\Big|_{\mathbf{U}=\mathbb{1}} \\ &= \delta_{rq} S_{ps} = \delta_{rq}\delta_{ps} \end{aligned}$$

$$\begin{aligned}
\frac{\partial}{\partial R^*_{rs}} S_{pq} &= \frac{\partial}{\partial R^*_{rs}} \sum_{tu} R^*_{pt} R_{qu} \langle \psi_t | \psi_u \rangle \Big|_{\mathbf{U}=\mathbb{1}} \\
&= \sum_{u} \delta_{rp} R_{qu} \langle \psi_s | \psi_u \rangle \Big|_{\mathbf{U}=\mathbb{1}} \\
&= \delta_{rp} S_{sq} = \delta_{rp} \delta_{sq}
\end{aligned}$$

$$\begin{aligned}
\frac{\partial}{\partial R_{rs}} f_{pq} &= \frac{\partial}{\partial R_{rs}} \left(\langle p | \hat{h} | q \rangle + \sum_j \langle pj | | qj \rangle \right) \\
&= \frac{\partial}{\partial R_{rs}} \sum_{tu} R^*_{pt} R_{qu} \left(\langle t | \hat{h} | u \rangle + \sum_{vw} \sum_j R^*_{jv} R_{jw} \langle tv | | uw \rangle \right) \Big|_{\mathbf{U}=\mathbb{1}} \\
&= \sum_t R^*_{pt} \delta_{rq} \left(\langle t | \hat{h} | s \rangle + \sum_{vw} \sum_j R^*_{jv} R_{jw} \langle tv | | rw \rangle \right) \Big|_{\mathbf{U}=\mathbb{1}} + \\
&\quad \sum_{tu} R^*_{pt} R_{qu} \sum_v \sum_j R^*_{jv} \delta_{rj} \langle tv | | us \rangle \Big|_{\mathbf{U}=\mathbb{1}} \\
&= \delta_{rq} \left(\langle p | \hat{h} | s \rangle + \sum_j \langle pj | | sj \rangle \right) + \delta_{r \in \{i\}} \langle pr | | qs \rangle \\
&= \delta_{rq} f_{ps} + \delta_{r \in \{i\}} \langle pr | | qs \rangle
\end{aligned}$$

$$\begin{aligned}
\frac{\partial}{\partial R^*_{rs}} f_{pq} &= \frac{\partial}{\partial R^*_{rs}} \left(\langle p | \hat{h} | q \rangle + \sum_j \langle pj | | qj \rangle \right) \\
&= \frac{\partial}{\partial R^*_{rs}} \sum_{tu} R^*_{pt} R_{qu} \left(\langle t | \hat{h} | u \rangle + \sum_{vw} \sum_j R^*_{jv} R_{jw} \langle tv | | uw \rangle \right) \Big|_{\mathbf{U}=\mathbb{1}} \\
&= \sum_u \delta_{rp} R_{qu} \left(\langle s | \hat{h} | u \rangle + \sum_{vw} \sum_j R^*_{jv} R_{jw} \langle sv | | uw \rangle \right) \Big|_{\mathbf{U}=\mathbb{1}} + \\
&\quad \sum_{tu} R^*_{pt} R_{qu} \sum_w \sum_j R^*_{jv} \delta_{rj} R_{jw} \langle ts | | uw \rangle \Big|_{\mathbf{U}=\mathbb{1}} \\
&= \delta_{rp} \left(\langle s | \hat{h} | q \rangle + \sum_j \langle sj | | qj \rangle \right) + \delta_{r \in \{i\}} \langle ps | | qr \rangle \\
&= \delta_{rp} f_{sq} + \delta_{r \in \{i\}} \langle ps | | qr \rangle
\end{aligned}$$

$$\begin{aligned}
\frac{\partial}{\partial R_{rs}} \langle pq | | tu \rangle &= \frac{\partial}{\partial R_{rs}} \sum_{vwxy} R^*_{pv} R^*_{qw} R_{tx} R_{uy} \langle vw | | xy \rangle \Big|_{\mathbf{U}=\mathbb{1}} \\
&= \sum_{vwy} R^*_{pv} R^*_{qw} \delta_{rt} R_{uy} \langle vw | | sy \rangle + \sum_{vwx} R^*_{pv} R^*_{qw} R_{tx} \delta_{ru} \langle vw | | xs \rangle \Big|_{\mathbf{U}=\mathbb{1}} \\
&= \delta_{rt} \langle pq | | su \rangle + \delta_{ru} \langle pq | | ts \rangle
\end{aligned}$$

$$\begin{aligned}\frac{\partial}{\partial R^*_{rs}}\langle pq|\,|tu\rangle &= \frac{\partial}{\partial R^*_{rs}}\sum_{vwxy} R^*_{pv}R^*_{qw}R_{tx}R_{uy}\langle vw|\,|xy\rangle\Big|_{\mathbf{U}=\mathbb{1}} \\ &= \sum_{wxy}\delta_{rp}R^*_{qw}R_{tx}R_{uy}\langle sw|\,|xy\rangle + \sum_{vxy}R^*_{pv}\delta_{eq}R_{tx}R_{uy}\langle vs|\,|xy\rangle\Big|_{\mathbf{U}=\mathbb{1}} \\ &= \delta_{rp}\langle sq|\,|tu\rangle + \delta_{rq}\langle ps|\,|tu\rangle\end{aligned}$$

Continuing with the derivation, the Lagrangian is required to be stationary with respect to parameters of the reference wavefunction. Starting from the occupied-occupied block, equations

$$\begin{aligned}0 = \frac{\partial L^{\mathrm{rel}}_{\mathrm{corr}}}{\partial R_{kl}} =& \sum_i (\rho_N)_{ki} f_{il} + \sum_{ij}(\rho_N)_{ji}\langle ik|\,|jl\rangle + \sum_{ab}(\rho_N)_{ba}\langle ak|\,|bl\rangle \\ &+ \frac{1}{2}\sum_{pqs}(P_N)_{kspq}\langle pq|\,|ls\rangle \\ &+ \sum_p z_{kp}f_{pl} + \sum_{pq} z_{qp}\langle pk|\,|ql\rangle + I_{kl}\end{aligned} \tag{2.7.22}$$

and

$$\begin{aligned}0 = \frac{\partial L^{\mathrm{rel}}_{\mathrm{corr}}}{\partial R^*_{lk}} =& \sum_j (\rho_N)_{jl} f_{kj} + \sum_{ij}(\rho_N)_{ji}\langle ik|\,|jl\rangle + \sum_{ab}(\rho_N)_{ba}\langle ak|\,|bl\rangle \\ &+ \frac{1}{2}\sum_{qrs}(P_N)_{rslq}\langle kq|\,|rs\rangle \\ &+ \sum_q z_{ql}f_{kq} + \sum_{pq} z_{qp}\langle pk|\,|ql\rangle + I_{kl}\end{aligned} \tag{2.7.23}$$

are derived. Subtracting now eq. (2.7.23) from (2.7.22) results in

$$\begin{aligned}\frac{\partial L^{\mathrm{rel}}_{\mathrm{corr}}}{\partial R_{kl}} - \frac{\partial L^{\mathrm{rel}}_{\mathrm{corr}}}{\partial R^*_{lk}} =& 0 \\ =& \sum_i (\rho_N)_{ki} f_{il} - \sum_j (\rho_N)_{jl} f_{kj} + \\ & \frac{1}{2}\sum_{pqs}(P_N)_{kspq}\langle pq|\,|ls\rangle - \frac{1}{2}\sum_{qrs}(P_N)_{rslq}\langle kq|\,|rs\rangle + \\ & \sum_p z_{kp}f_{pl} - \sum_q z_{ql}f_{kq}.\end{aligned}$$

Exploiting the diagonal form of the Fock matrix

$$\begin{aligned}-z_{kl}(\epsilon_l - \epsilon_k) =& (\rho_N)_{kl}(\epsilon_l - \epsilon_k) + \\ & \frac{1}{2}\sum_{pqs}(P_N)_{kspq}\langle pq|\,|ls\rangle - \frac{1}{2}\sum_{qrs}(P_N)_{rslq}\langle kq|\,|rs\rangle\end{aligned} \tag{2.7.24}$$

results now in working equations for z_{kl}. Similarly for the virtual-virtual block

$$\begin{aligned}0 = \frac{\partial L^{\mathrm{rel}}_{\mathrm{corr}}}{\partial R_{cd}} =& \sum_a (\rho_N)_{ca} f_{ad} + \frac{1}{2}\sum_{pqs}(P_N)_{cspq}\langle pq|\,|ds\rangle \\ &+ \sum_p z_{cp}f_{pd} + I_{cd}\end{aligned} \tag{2.7.25}$$

and

$$\begin{aligned}0 = \frac{\partial L^{\mathrm{rel}}_{\mathrm{corr}}}{\partial R^*_{dc}} =& \sum_b (\rho_N)_{bd} f_{cb} + \frac{1}{2}\sum_{qrs}(P_N)_{rsdq}\langle cq|\,|rs\rangle \\ &+ \sum_q z_{qd}f_{cq} + I_{cd}\end{aligned} \tag{2.7.26}$$

are derived. Subtracting eq. (2.7.26) from (2.7.25) and using the diagonal Fock matrix results in the working equation for the virtual-virtual block

$$\begin{aligned} -z_{cd}\left(\epsilon_d-\epsilon_c\right) =& \left(\rho_N\right)_{cd}\left(\epsilon_d-\epsilon_c\right)+ \\ & \frac{1}{2}\sum_{pqs}\left(P_N\right)_{cspq}\langle pq|\,|ds\rangle-\frac{1}{2}\sum_{qrs}\left(P_N\right)_{rsdq}\langle cq|\,|rs\rangle\,. \end{aligned} \tag{2.7.27}$$

Eq. (2.7.24) and (2.7.27) have a solution for $k\neq l$ and $c\neq d$. Otherwise the left part of the equation vanishes. The diagonal elements of z_{pq} are thus assumed to be 0.

Further working with the occupied-virtual and virtual-occupied blocks, the following derivatives are defined

$$\begin{aligned} 0=\frac{\partial L_{\mathrm{corr}}^{\mathrm{rel}}}{\partial R_{kc}} =& \sum_i\left(\rho_N\right)_{ki}f_{ic}+\sum_{ij}\left(\rho_N\right)_{ji}\langle ik|\,|jc\rangle+\sum_{ab}\left(\rho_N\right)_{ba}\langle ak|\,|bc\rangle \\ &+\frac{1}{2}\sum_{pqs}\left(P_N\right)_{kspq}\langle pq|\,|cs\rangle \\ &+\sum_p z_{kp}f_{pc}+\sum_{pq}z_{qp}\langle pk|\,|qc\rangle+I_{kc} \end{aligned} \tag{2.7.28}$$

and

$$\begin{aligned} 0=\frac{\partial L_{\mathrm{corr}}^{\mathrm{rel}}}{\partial R_{ck}^*} =& \sum_b\left(\rho_N\right)_{bc}f_{kb}+\frac{1}{2}\sum_{qrs}\left(P_N\right)_{rscq}\langle kq|\,|rs\rangle \\ &+\sum_q z_{qc}f_{kq}+I_{kc}. \end{aligned} \tag{2.7.29}$$

Using a similar strategy as before, eq. (2.7.29) is subtracted from (2.7.28) to eliminate I_{kc}.

$$\begin{aligned} \frac{\partial L_{\mathrm{corr}}^{\mathrm{rel}}}{\partial R_{kc}}-\frac{\partial L_{\mathrm{corr}}^{\mathrm{rel}}}{\partial R_{ck}^*} =& 0 \\ =& \sum_i\left(\rho_N\right)_{ki}f_{ic}-\sum_b\left(\rho_N\right)_{bc}f_{kb}+\frac{1}{2}\sum_{pqs}\left(P_N\right)_{kspq}\langle pq|\,|cs\rangle-\frac{1}{2}\sum_{qrs}\left(P_N\right)_{rscq}\langle kq|\,|rs\rangle \\ &+\sum_{ij}\left(\rho_N\right)_{ji}\langle ik|\,|jc\rangle+\sum_{ab}\left(\rho_N\right)_{ba}\langle ak|\,|bc\rangle \\ &+\sum_p z_{kp}f_{pc}+\sum_{pq}z_{qp}\langle pk|\,|qc\rangle-\sum_q z_{qc}f_{kq}. \end{aligned}$$

Eliminating the terms that contain f_{ai} and f_{ia} contribution, the previous equation is rewritten

$$\begin{aligned} \sum_{bj}\left[z_{bj}\langle jk|\,|bc\rangle+z_{jb}\left(\delta_{jk}f_{bc}-\delta_{bc}f_{kj}+\langle bk|\,|jc\rangle\right)\right] =& \frac{1}{2}\sum_{qrs}\left(P_N\right)_{rscq}\langle kq|\,|rs\rangle-\frac{1}{2}\sum_{pqs}\left(P_N\right)_{kspq}\langle pq|\,|cs\rangle \\ &-\sum_{ij}\left[\left(\rho_N\right)_{ji}+z_{ji}\right]\langle ik|\,|jc\rangle \\ &-\sum_{ab}\left[\left(\rho_N\right)_{ba}+z_{ba}\right]\langle ak|\,|bc\rangle\,. \end{aligned}$$

Defining the right-hand side of the equation as X_{ck}, $A_{bjck}=\langle bc|\,|jk\rangle$, $B_{bjck}=\delta_{jk}f_{bc}-\delta_{bc}f_{kj}+\langle bk|\,|jc\rangle$ and exploiting the Hermiticity $z_{bj}=z_{jb}^*$, the equation is further simplified

$$\begin{aligned} \sum_{bj}\left(z_{jb}^*A_{bjck}^*+z_{jb}B_{bjck}\right)&=X_{ck} \\ \mathbf{z}^*\mathbf{A}^*+\mathbf{z}\mathbf{B}&=\mathbf{X}. \end{aligned} \tag{2.7.30}$$

Eq. (2.7.30) is a linear problem solvable for z_{ia}.

With the help of the z-vector, one-body orbital relaxed reduced density matrices are derived

$$\begin{aligned}(\rho_N)^{\text{rel}}_{ji} &= (\rho_N)_{ji} + z_{ji} \\ (\rho_N)^{\text{rel}}_{ba} &= (\rho_N)_{ba} + z_{ba} \\ (\rho_N)^{\text{rel}}_{ai} &= z_{ai} \\ (\rho_N)^{\text{rel}}_{ia} &= z_{ia}\end{aligned}$$

After deriving the z-vector, eq. (2.7.22), (2.7.25), and (2.7.28) can be used to derive the I_{pq} elements. It is apparent that orbital-relaxed properties necessarily require the two-body reduced densities, and as such, even one-body properties need the two-body reduced densities to be computed. The current derivation of orbital relaxation is general and as such can be used for any correlation method.

2.8 The perturbation expansion of CC theory

It has been stated that there exists an intrinsic correspondence between CC and MBPT theory,[103] meaning that the CC amplitudes can be viewed as infinite-order perturbation parameters [eq. (2.6.5)]. It is thus useful to look into the perturbation expansion of CC in order to gain a deeper understanding of the theory, and to help with the derivation of approximate CC methods.

Using the same MP partitioning[104] of the Hamiltonian as in eq. (2.5.1) and only considering the correlation part, one may expand the CC (ground-state) correlation energy, and the CC parameters in orders of the perturbation

$$\begin{aligned}\Delta E_{\text{CC}} &= \Delta E^{(0)}_{\text{CC}} + \Delta E^{(1)}_{\text{CC}} + L^{(2)}_{\text{CC}} + \dots \\ \hat{T} &= \hat{T}^{(0)} + \hat{T}^{(1)} + \hat{T}^{(2)} + \dots \qquad (2.8.1) \\ \hat{\Lambda} &= \hat{\Lambda}^{(0)} + \hat{\Lambda}^{(1)} + \hat{\Lambda}^{(2)} + \dots \qquad (2.8.2)\end{aligned}$$

Before deriving the perturbed CC parameters, the unperturbed Hamiltonian terms can be simplified for the canonical HF case. The BCH expansion for the Fock operator truncates at second order

$$\widetilde{F}_N = (\hat{F}_N e^{\hat{T}})_C = \hat{F}_N + (\hat{F}_N \hat{T})_{\text{C}} + \frac{1}{2}((\hat{F}_N \hat{T})_{\text{C}} \hat{T})_{\text{C}}. \qquad (2.8.3)$$

The action of single commutator on a determinant, however, results in the following expression

$$\begin{aligned}(\hat{F}_N \hat{T})_{\text{C}} |\Phi_J\rangle &= [\hat{F}_N, \hat{T}] |\Phi_J\rangle \\ &= \hat{F}_N \hat{T} |\Phi_J\rangle - \hat{T} \hat{F}_N |\Phi_J\rangle \\ &= \sum_I t_I \hat{F}_N |\Phi_{IJ}\rangle - \hat{T} \Delta\epsilon_J |\Phi_J\rangle \\ &= \sum_I t_I \Delta\epsilon_{IJ} |\Phi_{IJ}\rangle - \sum_I t_I \Delta\epsilon_J |\Phi_{IJ}\rangle \\ &= \sum_I t_I \Delta\Delta\epsilon_{IJ} \hat{\mu}_I |\Phi_J\rangle ,\end{aligned}$$

with $|\Phi_{IJ}\rangle = \hat{\mu}_I |\Phi_J\rangle$, if this is possible, and $\Delta\Delta\epsilon_{IJ} = \Delta\epsilon_{IJ} - \Delta\epsilon_J$. The latter simplifies to $\Delta\epsilon_I$, in the case $|\Phi_J\rangle = |0\rangle$. Since $[\hat{T}, \hat{\mu}_I] = 0$, eq. (2.8.3) truncates already after the first commutator for canonical HF orbitals

$$(\hat{F}_N e^{\hat{T}})_{\text{C}} = \hat{F}_N + (\hat{F}_N \hat{T})_{\text{C}}. \qquad (2.8.4)$$

For the expansion of the cluster- and λ-amplitudes from eq. (2.8.1) and (2.8.2), respectively, the variational conditions that demand the CC Lagrangian to have vanishing derivatives with respect

to the CC parameters, are required to be fulfilled order by order.[84] This corresponds to expanding eq. (2.7.3), and (2.7.4) in orders of the perturbation, and requiring them to vanish at every order. At zeroth order

$$\begin{aligned}\left(\frac{\partial L_{\mathrm{CC}}}{\partial t_I}\right)^{(0)} &= 0\\ \langle 0|\left(1+\hat{\Lambda}^{(0)}\right)(\hat{F}_N\hat{\mu}_I)_{\mathrm{C}}\,|0\rangle &= 0\\ \lambda_I^{(0)}\Delta\epsilon_I = 0 &\Rightarrow \lambda_I^{(0)} = 0\end{aligned}$$

and

$$\begin{aligned}\left(\frac{\partial L_{\mathrm{CC}}}{\partial \lambda_I}\right)^{(0)} &= 0\\ \langle 0|\,\hat{\mu}_I^\dagger(\hat{F}_N\hat{T}^{(0)})_{\mathrm{C}}\,|0\rangle &= 0\\ \Delta\epsilon_I t_I^{(0)} = 0 &\Rightarrow t_I^{(0)} = 0.\end{aligned}$$

Since the zeroth-order CC parameters are zero, the correlation energy at zeroth and first order are 0, consistent with the MP series.

$$\begin{aligned}\Delta E_{\mathrm{CC}}^{(0)} = L_{\mathrm{CC}}^{(0)} &= \langle 0|\,\hat{F}_N\,|0\rangle = 0\\ \Delta E_{\mathrm{CC}}^{(1)} = L_{\mathrm{CC}}^{(1)} &= \langle 0|\,\hat{V}_N\,|0\rangle = 0.\end{aligned}$$

The first-order equations

$$\begin{aligned}\left(\frac{\partial L_{\mathrm{CC}}}{\partial t_I}\right)^{(1)} &= 0\\ \langle 0|\,\hat{\Lambda}^{(1)}(\hat{F}_N\hat{\mu}_I)_{\mathrm{C}}\,|0\rangle + \langle 0|\,(\hat{V}_N\hat{\mu}_I)_{\mathrm{C}}\,|0\rangle &= 0\\ \lambda_I^{(1)}\Delta\epsilon_I &= -\langle 0|\,(\hat{V}_N\hat{\mu}_I)_{\mathrm{C}}\,|0\rangle\\ \lambda_I^{(1)} &= -\frac{\langle 0|\,(\hat{V}_N\hat{\mu}_I)_{\mathrm{C}}\,|0\rangle}{\Delta\epsilon_I}\end{aligned} \tag{2.8.5}$$

and

$$\begin{aligned}\left(\frac{\partial L_{\mathrm{CC}}}{\partial \lambda_I}\right)^{(1)} &= 0\\ \langle 0|\,\hat{\mu}_I^\dagger(\hat{F}_N\hat{T}^{(1)})_{\mathrm{C}}\,|0\rangle + \langle 0|\,\hat{\mu}_I^\dagger\hat{V}_N\,|0\rangle &= 0\\ \Delta\epsilon_I t_I^{(1)} &= -\langle 0|\,\hat{\mu}_I^\dagger\hat{V}_N\,|0\rangle\\ t_I^{(1)} &= -\frac{\langle 0|\,\hat{\mu}_I^\dagger\hat{V}_N\,|0\rangle}{\Delta\epsilon_I}\end{aligned} \tag{2.8.6}$$

survive only for double excitation $I = 2$. In this way, the first-order amplitudes at the MP2 level are recovered and the $\lambda^{(1)}$ amplitudes are their complex conjugate

$$t_{ij}^{ab(1)} = -\frac{\langle ab|\,|ij\rangle}{\Delta\epsilon_{ij}^{ab}} = -\frac{\langle ij|\,|ab\rangle^*}{\Delta\epsilon_{ij}^{ab}} = \lambda_{ab}^{ij(1)*}. \tag{2.8.7}$$

The first-order CC amplitudes contribute to the energy in second order, while the first-order Lagrange multipliers cancel out.

$$\begin{aligned}\Delta E_{\mathrm{CC}}^{(2)} = L_{\mathrm{CC}}^{(2)} &= \langle 0|\,(\hat{V}_N\hat{T}^{(1)})_{\mathrm{C}}\,|0\rangle + \langle 0|\,\hat{\Lambda}_2^{(1)}\hat{V}_N\,|0\rangle + \langle 0|\,\hat{\Lambda}_2^{(1)}(\hat{F}_N\hat{T}_2^{(1)})_{\mathrm{C}}\,|0\rangle\\ &= \langle 0|\,(\hat{V}_N\hat{T}_2^{(1)})_{\mathrm{C}}\,|0\rangle + \lambda_2^{(1)}\left(\langle 0|\,\hat{\mu}_2^\dagger\hat{V}_N\,|0\rangle + \langle 0|\,\hat{\mu}_2^\dagger(\hat{F}_N\hat{T}_2^{(1)})_{\mathrm{C}}\,|0\rangle\right)\\ &= \langle 0|\,(\hat{V}_N\hat{T}_2^{(1)})_{\mathrm{C}}\,|0\rangle + \lambda_2^{(1)}\overbrace{\left(\frac{\partial L_{\mathrm{CC}}}{\partial \lambda_2}\right)^{(1)}}^{=0} = -\frac{1}{4}\sum_{abij}\frac{|\,\langle ab|\,|ij\rangle\,|^2}{\Delta\epsilon_{ij}^{ab}}\end{aligned}$$

The trend observed in the perturbative expansion of the energy is well documented and states that the nth order corrections to the CC amplitudes and Lagrange multipliers determine the energy at order $2n+1$ and $2n+2$ respectively.[131] Thus the energy in third-order can be determined from $t_2^{(1)}$ and $\lambda_2^{(1)}$. It can be shown that

$$\Delta E_{\mathrm{CC}}^{(3)} = \langle 0| \hat{\Lambda}_2^{(1)} (\hat{V}_N \hat{T}_2^{(1)})_{\mathrm{C}} |0\rangle .$$

Going on to the second-order amplitude equations, the following equations are derived

$$\begin{aligned} \left(\frac{\partial L_{\mathrm{CC}}}{\partial t_I}\right)^{(2)} &= 0 \\ \langle 0| \hat{\Lambda}^{(2)} (\hat{F}_N \hat{\mu}_I)_{\mathrm{C}} |0\rangle &= -\langle 0| \hat{\Lambda}_2^{(1)} (\hat{V}_N \hat{\mu}_I)_{\mathrm{C}} |0\rangle - \overbrace{\langle 0| ((\hat{V}_N \hat{T}_2^{(1)})_{\mathrm{C}} \hat{\mu}_I)_{\mathrm{C}} |0\rangle}^{=0} \\ \lambda_I^{(2)} &= -\frac{\langle 0| \hat{\Lambda}_2^{(1)} (\hat{V}_N \hat{\mu}_I)_{\mathrm{C}} |0\rangle}{\Delta\epsilon_I} \end{aligned} \tag{2.8.8}$$

and

$$\begin{aligned} \left(\frac{\partial L_{\mathrm{CC}}}{\partial \lambda_I}\right)^{(2)} &= 0 \\ \langle 0| \hat{\mu}_I^\dagger (\hat{F}_N \hat{T}^{(2)})_{\mathrm{C}} |0\rangle &= -\langle 0| \hat{\mu}_I^\dagger (\hat{V}_N \hat{T}_2^{(1)})_{\mathrm{C}} |0\rangle \\ t_I^{(2)} &= -\frac{\langle 0| \hat{\mu}_I^\dagger (\hat{V}_N \hat{T}_2^{(1)})_{\mathrm{C}} |0\rangle}{\Delta\epsilon_I}. \end{aligned} \tag{2.8.9}$$

In eq. (2.8.8), there exist non-vanishing solutions for $I = 1, 2, 3, 4$ from the first term. As for the second term $\langle 0| ((\hat{V}_N \hat{T}_2^{(1)})_{\mathrm{C}} \hat{\mu}_I)_{\mathrm{C}} |0\rangle$, it involves a double excitation operator $\hat{T}_2^{(1)}$, that cannot be compensated from the $\hat{V}_N$ operator to allow further excitation from $\hat{\mu}_I$ and thus vanishes. As for the second-order CC amplitudes eq. (2.8.9) they contribute for $I = 1, 2, 3$ only because of the connectivity requirement. For singles, doubles, and triples the Lagrange multipliers at second order are the complex conjugates of the CC amplitudes

$$t_I^{(2)} = \lambda_I^{(2)*}, \ I = 1, 2, 3$$

but not for quadruples $I = 4$. Following the $2n+1$, and $2n+2$ rule, the CC second-order amplitudes contribute to the fourth- and fifth-order energy, $\Delta E_{\mathrm{CC}}^{(4)}$, and $\Delta E_{\mathrm{CC}}^{(5)}$, and the Lagrange multipliers to the fifth-order energy, $\Delta E_{\mathrm{CC}}^{(5)}$.

Summing up, double excitations first emerge in first order of perturbation for the wavefunction, and they alone contribute up to the third-order energy. Thus, CCD and CCSD include all the first-order wavefunction and third-order energy contributions. Single and triple excitations contribute to wavefunction parameters first in second order and they offer energy corrections up to fourth order. Quadruples also appear first as second-order wavefunction parameters, but they first contribute as fifth-order energy corrections. This makes CCSDT correct through second order for the wavefunction and fourth order for the energy.[103]

Considering EOM-CC theory in a perturbation expansion approach

For the EOM-CC approach, there exist various perturbation expansions, EOM-MBPT(n)/EOM-CCSD(n),[132] EOM(2)PT(n),[133] CC(m)PT(n)[134–138] to name a few. Unlike for the reference CC state, defining the correlation as perturbation in the EOM-CC approach is difficult, since the excited-state energies are the result of diagonalization of the Hamiltonian.[132] For this reason, distinguishing the contribution of ΔE_{EOM} to the (differential) correlation and non-correlated excitation energy is not possible. As a consequence, the expansion is dependent both on how the zeroth-order energy and wavefunction are to be defined, as well as the level of excitation to be considered.

For the purposes of estimating the accuracy of different truncations in the EOM-CC approach, the CIS method, which is equivalent to EOM-CCS for canonical HF orbitals, is considered as the

unperturbed system because it offers excited-state energies and wavefunctions with no inclusion of correlation.[85] A very rough division between differential correlation and non-correlated excitation is thus offered. The EOM amplitudes that include the zeroth-order corrections (non-correlated excitation) for the different EOM variants are presented in tab. 2.2.

EOM Variant	zeroth order	higher order
EE	r_i^a, l_a^i	r_0, r_{ij}^{ab}, l_{ab}^{ij}, etc
IP	r_i, l^i	r_{ij}^a, l_a^{ij}, etc.
EA	r^a, l_a	r_i^{ab}, l_{ab}^i, etc.

Table 2.2: The EOM amplitudes that include the zeroth order corrections for different EOM variants.

The failure of EOM-CCSD to describe excited states with predominant double-excitation character becomes now clearer. Predominantly doubly-excited states cannot be targeted at the CIS level, meaning that the leading double-excitation amplitudes, not only give minimal corrections to the differential correlation of these states, but they are poor correlation-free approximations for the excitation. Orbital relaxation needs to be included in order to have an adequate description of the excitation even if correlation is not accounted. This can be achieved by considering single- and triple-excitations at the EOM-CCSDT level of theory, thus deriving results with a similar accuracy to predominantly singly-excited states at the EOM-CCSD level of theory.[103]

Chapter 3

The CFOUR and QCUMBRE programs

In this chapter, the CFOUR[77–79] (sec. 3.1) and the QCUMBRE[76] (sec. 3.2) program packages are presented. A general overview over the programs is given together with a description of the newly implemented methods. Lastly, details on the interface from CFOUR to QCUMBRE for the execution of finite-field quantum-chemical calculation are presented in sec. 3.3.

3.1 CFOUR

Figure 3.1: CFOUR (Coupled-Cluster techniques for Computational Chemistry) logo.

The CFOUR program package[77,78] is used to provide the integrals over London orbitals needed for quantum-chemical calculations in the presence of a magnetic field and also the HF solution, i.e., the MO coefficients. As such, a CFOUR calculation reads in the specifications regarding the molecular system, that include the molecular geometry, the magnetic-field strength and orientation, the charge and the multiplicity of the ground state, the point group to be employed, etc. Moreover, it sets the type of calculation, for example a single-point calculation or a geometry optimization. For the latter, CFOUR provides the optimizer algorithm.

The CFOUR source code is written primarily in fortran (both fortran77 and fortran90) with some parts in C++. The structure of the program is rather complicated as it is a long-living program with a rich history of developments. The program package consists of different module packages. These are either function libraries that aim to keep a consistency between the different modules or the source code for executables. Each CFOUR executable performs a specific task needed for a quantum-chemical calculation. Moreover, some modules function as drivers that call the respective executables in the correct order to perform a specific type of calculation.

A basic implementation for the evaluation of integrals over GIAOs and for the ff-HF-SCF method had already been present in CFOUR. During course of this thesis, existing functionalities were expanded improving on the robustness of the implementation and the user-friendliness of the program. These developments were carried out within the following modules

- **joda**: This module is typically the first executable to be called by the driver module **run** and it is written in fortran77. It is responsible for reading the user-defined input and retrieving the specification for the calculation (molecular geometry, magnetic field, type of calculation, etc.). It is mainly responsible for creating archive interface files that regulate the communication between the different modules. Specifically, the tasks of this module in which modifications were needed

are the transformation between internal and Cartesian coordinates, the geometry-optimization algorithm (chap. 7), and the handling and recognition of symmetry (chap. 6).

- **mint**: The Mainz INTegral program[79] is a recently developed module. As such, it is written in fortran90 and makes use of object-oriented programming tools. It is tasked with the calculation of integrals over atomic orbitals and aims to replace the previous implementation. Modifications were carried out regarding the handling of complex Abelian groups via the double-coset decomposition (chap. 6).

- **vscf**: This module is responsible for providing a HF solution. It is mainly written in fortran77, but those parts of the code that deal with integrals provided by **mint** is newly developed in fortran90. Changes were realized here for specific issues of the ff-SCF-HF method, mainly regarding the direct inversion of the iterative subspace (DIIS)[139,140] extrapolation scheme for the complex case and for the implementation of the Maximum Overlap Matrix (MOM) approach (app. B).

3.2 QCUMBRE

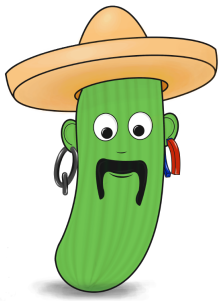

Figure 3.2: QCUMBRE (Quantum-Chemical Utility enabling Magnetic-field dependent investigations Benefiting from Rigorous Electron-correlation treatment) logo.

The QCUMBRE program[76] is written in C++ (logo in fig. 3.2). It is able to handle ff calculation at the post-HF level of theory and currently works with an interface to the LONDON program package.[67] and to CFOUR.[77,78] The latter interface was developed in this work.

Developments for QCUMBRE that are part of the current work include the implementation of new features for quantum-chemical calculations and the implementation of new data types that either exists alongside or replace the old ones to support the new features. The latter include:

- Various interpretational tools
  - → Mulliken population analysis (see sec. 5.1)
  - → Natural orbitals (see 5.1)
  - → Natural transition orbitals (see sec. 5.1)
  - → Angular-momentum expectation values (see app. A)
  - → Approximate spin multiplicity (see sec. 5.2)
    - ☐ Projected spin multiplicity [eq. (5.2.6)] at the MP2, CCSD, CCSDT, CC2, CC3 ground-state levels of theory
    - ☐ Approximate excited-state spin multiplicity [eq. (5.2.8)] at the CCSD, CCSDT, CC2, CC3, CISD levels of theory

- Two-electron properties (spin multiplicity, etc., see app. C)
  - → CCSD ground state

  - → CC2 ground state
  - → EE-EOM-CCSD excited states (expectation value and response)
  - → EE-EOM-CC2 excited states (expectation value and response)
  - → MP2
  - → CISD
  - → CIS
- Orbital-relaxed properties/analytic gradients (see app. C)
  - → CCSD ground state
  - → CC2 ground state
  - → EE-EOM-CCSD excited states
  - → EE-EOM-CC2 excited states
  - → MP2
  - → CISD
- CCn methods (see 4.1)
  - → CC2 ground-state energies and properties
  - → EE-EOM-CC2 excited-state energies and properties (expectation value and response)
  - → EE-EOM-CC2 transition properties (expectation value)
  - → CC3 ground-state energies
  - → EE-EOM-CC3 excited-state energies
  - → Alternative Davidson procedure for CCn methods
- EOM-CCSD(T)(a)* methods (see sec. 4.2)
  - → CCSD(T)(a) ground-state energy
  - → EE-, SF-, EA-, IP- EOM-CCSD(T)(a)* energies
- Multi-root Davidson procedure (see app. C)
- Exploitation of symmetry through point-group theory in ff calculations (see chap. 6)
- Visualization of complex orbitals through COrbit19 interface (see sec. 5.1)
- CFOUR interface
  - → Geometry optimization based on numerical gradients enabled at all levels of theory available in QCUMBRE (see chap. 7)

The new data types that were developed include:

- `basis`: Handles two-index matrices in the AO basis (overlap integrals, MO coefficients). Mainly used with the LONDON and COrbit19 interface. (see sec. 5.1)
- `basisS`: Handles two- and four- index matrices in the SAO basis (overlap, one-electron Hamiltonian, two-electron integrals, MO coefficients). Mainly used with the CFOUR interface. (see chap. 6)
- `groupS`: Handles tensors of constant rank in non-vanishing IRREP blocks. Aims to replace the `group` class. (see chap. 6)
- `completeS`: Handles tensors of variable rank in non-vanishing IRREP blocks. Aims to replace the `complete` class.

- `PointGroup`: Handles the point group of the system. (see chap. 6)

During this work, the QCUMBRE website was created (`https://www.qcumbre.org`). On the website, a manual and a list of keywords is available `https://www.qcumbre.org/manual/how-to-run-a-calculations`.

3.3 Developing a working interface

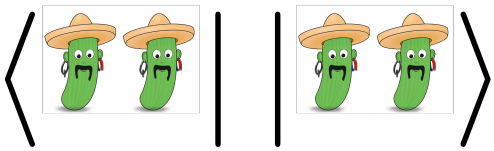

Figure 3.3: The QFOUR logo. Portmanteau from QCUMBRE and CFOUR used to describe a calculation using both programs by means of the developed interface. Copyright Simon Blaschke.

The interface from CFOUR to QCUMBRE for an ff post-HF calculation was developed in this work. It gives access to more elaborate and more efficient HF calculations and to previously unavailable information as CFOUR has more functionalities and is more efficient than the version of LONDON accessible. Moreover, it extends possibilities for developments (e.g., Cholesky decomposition) and the applicability and flexibility of QCUMBRE.

In order to develop the interface, the required data (including system and input specification, integrals over (London) orbitals, and the MO coefficients) needs to be transmitted from CFOUR to QCUMBRE. Developing a working interface between the two programs is in principle similar to the way the different programs in CFOUR communicate with each other, i.e., via interface files written on and read from the disk. CFOUR is, nonetheless, written mainly in fortran while QCUMBRE in C++, and some challenges emerge because of this.

3.3.1 Creating the necessary interaface data in CFOUR

Most of the interface files used inside CFOUR cannot in general be used by QCUMBRE because of two incompatibilities. First, the archive files (`JOBARC, OPTARC,` etc.) are written and read with specific functions of the CFOUR function libraries and are not readily available for reading by other programs. Integral and coefficient data also have a structure specific to the classes used in CFOUR. Duplicating or rewriting the same functionalities for the archive files in QCUMBRE is tedious and unnecessary because much of the information written in these files is not needed for a post-HF calculation. Regarding data files that include integrals and coefficients, they have a different structure in QCUMBRE than in CFOUR and as such raw-data files are preferred for such an interface. Second, files written in unformatted fortran files are typically written with logical records.[a] A file written in this way in fortran is practically unreadable by C++ based programs.

System and input specification data is written twice on disk when an interface to QCUMBRE is requested, unless the file containing such information is short and simple. The duplicate files contain only the data needed by QCUMBRE and are written as formatted data files. A complete list of those can be found in tab. 3.1.

The integrals and coefficient data constitutes the largest interface files. Because of the limitations described in the previous paragraph regarding the readability of the native CFOUR data files by QCUMBRE, this data is duplicated for the QCUMBRE interface. This raises the disk space needed for a calculation and it slows the CFOUR calculation since these I/O operations are doubled. This additional procedure is, however, not a bottleneck for a post-HF calculation.

[a] Writing with logical records means that every `write` command writes, along the data, a record of the size of the written data and of the action. Accordingly reading a file written with logical records means that every `read` command reads the logical record before reading the data. This kind of format for (input/output) I/O operations is only supported in fortran.

File name	Created in	Duplicate	Included information
`geometry_qcumbre`	**joda**	yes[a]	atom names, atom charges and Cartesian coordinates for each nucleus in the molecule
`syminfo`	**joda**, **mint**	no	point group and IRREP enumeration
`molinfo_qcumbre`	**joda**	yes	number of basis-set functions, number of electrons, nuclear repulsion
`bfield_qcumbre`	**joda**	yes	Cartesian coordinates of the magnetic-field vector
`spher_qcumbre`	**mint**	yes[b]	transformation table between Cartesian and spherical basis
`BASIS`	**joda**	no	basis-set definition
`active_irrep_comp_qcumbre`	**mint**	no[c]	subset of functions in a shell needed for the creation of non-redundant SAOs
`nocc_qcumbre`	**vscf**	yes	number of occupied orbitals per IRREP and information on restricted or unrestricted reference

[a] is not created for single-atom calculations
[b] only needed for calculations using a spherical basis set
[c] only created for QCUMBRE for calculation with complex Abelian point groups

Table 3.1: System and input specification data files used in the interface from CFOUR to QCUMBRE.

The one-electron integrals, the Fock matrix and the MO coefficient matrices are written as formatted files. The loss of efficiency for the formatting of the data is marginal because of the small size of these matrices which are only two-index quantities (N^2). A formatting of 22 decimal digits is chosen for the printing of double-precision numbers so as not to lose accuracy. The printing of the matrices is structured in symmetry blocks in the case of symmetry-adapted orbitals (SAO) (see chap. 6). In each block, the indices are associated with a single IRREP. For totally-symmetric matrices, at the start of each block, the IRREP of the left index is written in the first line the phrase "`symmetry block:`" The next line contains the number of functions associated with the IRREP after "`nbas:`". For symmetric matrices not associated with the totally symmetric IRREP Γ^1, the IRREP of the left and the right index is written after "`symmetry block:`", and the number of function associated with the left and the right IRREP after "`nbas:`". The elements of the matrix are then written, each one occupying one line with the following format

$$\texttt{[}i\texttt{,}j\texttt{]:(}\mathrm{Re}(c)\texttt{,}\mathrm{Im}(c)\texttt{)}$$

with i and j being the left and right index, $\mathrm{Re}(c)$ and $\mathrm{Im}(c)$ being the real and the imaginary part of the complex double-precision number c. In each block the enumeration of each index starts from 1. In **mint**, the functions that handle the writing of the interface files are the `print1ec_sym_qcumbre` and `print1eac_sym_qcumbre` subroutines and are used to print the one-electron integrals by `mint1e`. All one-electron integrals are written in the SAO basis. In `vscf`, the Fock matrix is printed in the SAO

File name	Created in	Included quantity
giao_overlap_qcumbre	**mint**	overlap integrals $\mathbf{S}$
giao_hamiltonian_qcumbre	**mint**	one-electron Hamiltonian integral matrix $\mathbf{h}$
giao_dipx_qcumbre[a]	**mint**	dipole-moment integrals in the x direction $\boldsymbol{\mu}_x$
giao_dipy_qcumbre[a]	**mint**	dipole-moment integrals in the y direction $\boldsymbol{\mu}_y$
giao_dipx1_qcumbre[b]	**mint**	dipole-moment integrals of the first component of the symmetry-adapted x direction $\boldsymbol{\mu}_x + i\boldsymbol{\mu}_y$
giao_dipx2_qcumbre[b]	**mint**	dipole-moment integrals of the second component of the symmetry-adapted x direction $\boldsymbol{\mu}_x - i\boldsymbol{\mu}_y$
giao_dipz_qcumbre	**mint**	dipole-moment integrals in the z direction $\boldsymbol{\mu}_z$
giao_angmomx_qcumbre[a]	**mint**	angular-momentum integrals in the x direction $\mathbf{L}_x$
giao_angmomy_qcumbre[a]	**mint**	angular-momentum integrals in the y direction $\mathbf{L}_y$
giao_angmomx1_qcumbre[b]	**mint**	angular-momentum integrals of the first component of the symmetry-adapted x direction $\mathbf{L}_x + i\mathbf{L}_y$
giao_angmomx2_qcumbre[b]	**mint**	angular-momentum integrals of the second component of the symmetry-adapted x direction $\mathbf{L}_x - i\mathbf{L}_y$
giao_angmomz_qcumbre	**mint**	angular-momentum integrals in the z direction $\mathbf{L}_z$
fock_qcumbre_a	**vscf**	α-spin block of the Fock matrix $\mathbf{F}^{\alpha}$
fock_qcumbre_b	**vscf**	β-spin block of the Fock matrix $\mathbf{F}^{\beta}$
MO_qcumbre	**vscf**	MO coefficients $\mathbf{C}$

[a] used in the case of real Abelian groups
[b] used in the case of complex Abelian groups

Table 3.2: Two-index matrices data files used in the interface from CFOUR to QCUMBRE.

File name	Present for point groups[a]	Included quantity
`giao_twoint_iiii_qcumbre`	all	two-electron integrals with all four indices i, j, k, l associated with the same IRREP
`giao_twoint_ijij_qcumbre`	$h \geq 2$	two-electron integrals with indices i, k associated with one IRREP and j, l associated with a different one
`giao_twoint_iijj_qcumbre`	$h \geq 2$	two-electron integrals with indices i, j associated with one IRREP and k, l associated with a different one
`giao_twoint_ijji_qcumbre`[b]	$h \geq 2$	two-electron integrals with indices i, l associated with one IRREP and j, k associated with a different one
`giao_twoint_ijkl_qcumbre`	$h > 2$	two-electron integrals with all four indices i, j, k, l associated with a different IRREPs

[a] h the order of the point group
[b] needed only for calculations in magnetic field because of the loss of the $(i\ j \mid k\ l) = (i\ j \mid l\ k)$ symmetry

Table 3.3: Four-index matrices data files used in the interface from CFOUR to QCUMBRE.

basis in different files for the α and the β block, using the `print1eac_sym_qcumbre` subroutine, and the MO coefficients are written in one file by the `printmat` member function of the `block_matrix` class. For the MO coefficients, the interface file is further structured in spin blocks above the symmetry blocks, with the α block starting with a line writing "`alpha`" and the β block with a line writing "`beta`". The β block is written only for an unrestricted reference. A list of the two-index matrices written in interface files can be found in tab. 3.2. The two-electron integrals are written in the interface files by the `vmol_int2e_qcumbre_bin` function of the `vmol` module called by `mint2e`.

The two-electron integrals are the most costly data of the interface. They are four-index quantities (N^4), and because of this, care is taken for the I/O operations to be as efficient as possible. They are written as unformatted files (`FORM='UNFORMATTED'`) without logical records (`ACCESS='STREAM'`) to avoid the transformation from binaries to strings both on writing and on reading and to avoid incompatibility problems. They use the Mulliken convention for the indices, they are not antisymmetrized and they are written in more than one files depending on the point group used.

$$(\omega_\mu \omega_\nu | \omega_\sigma \omega_\rho) = \langle \omega_\mu(\mathbf{1}) \omega_\sigma(\mathbf{2}) | \, \hat{v}(\mathbf{1},\mathbf{2}) \, | \omega_\nu \omega_\rho \rangle$$

Each `write` command writes four double-precision integer number μ, ν, σ, ρ corresponding to the four indices and two double-precision floats corresponding to the real and the imaginary part of the value of the integral. In the case of SAOs (see chap. 6), a universal enumeration of the indices starting from 1 is used, meaning there exists a common enumeration (which is still ordered according to the IRREPs with indices associated with the first IRREP coming before the second and so on), where each IRREP block does not have its own enumeration like in the two-index matrices interface files. The list of all possible interface files for the two-electron integrals can be found in tab. 3.3.

In order to activate the interface to QCUMBRE and to write the interface files on the disk, the `QCUMBRE_INT` keyword has to be set to `ON` in the CFOUR input file. The keyword can currently only be activated for an ff calculation `BFIELD=ON`. Additionally, for an automatic call of the QCUMBRE exe-

cutable ComplexEOM, the level of calculation can be set to a post-HF method CALC_LEVEL=CCSD and call for an external program CC_PROGRAM=EXTERNAL. If these requirements are fulfilled, the CFOUR driver **run** runs the shell command "ComplexEOM inputEOM". The inputEOM input file for QCUMBRE has to be independently prepared. For a geometry optimization, the additional METHOD=ENERONLY keyword option has to be asked, for the driver to use the numerical gradients algorithm. The optimizer reads the energy output of QCUMBRE via the iface interface file created by QCUMBRE. This includes the energy in a formatted format of double-precision float. The instructions to call QCUMBRE exist in the runqcumbre subroutine. If the QCUMBRE_INT keyword is set ON and an ff calculation BFIELD=ON is performed using the **vscf** program for the HF solution SCF_PROG=SCF, a minimal QCUMBRE run is performed by **vscf** in the print_mo_qcumbre subroutine. This minimal run only creates the MOL_ORB files needed for Corbit19. Depending on the shell environment, specific intel libraries need to be loaded together with the QCUMBRE call in runqcumbre (and print_mo_qcumbre) for it to function correctly. This is currently not regulated automatically and has to be adjusted before the compilation of the **run** (and **vscf**) programs.

3.3.2 Reading the interface data in QCUMBRE

In QCUMBRE, the Interface_cfour function is responsible for reading the interface files and for initialising many necessary global variables for the calculations. The files in tab. 3.1 are read in the start of Interface_cfour. The difference of IRREP enumeration between CFOUR and QCUMBRE also needs to be accounted for. The two-index tensors from tab. 3.2 are read. Specifically, MO_qcumbre is saved as as type 3 basisS instance and giao_overlap_qcumbre, giao_hamiltonian_qcumbre as type 1 basisS instances. If they are presents fock_qcumbre_a and fock_qcumbre_b are read as well as type 1 basisS instances. The Fock matrix is then transformed in the MO basis using the MO coefficients and saved in fS_pq groupS instances. This is handled by the groupS::contract_oneint member function.

The giao_twoint_****_qcumbre files from tab. 3.3 are read as a single type 2 basisS instance. The member function basisS::two_ao2mo_anti, performs the N^5 scaling transformation of the two-electron integrals from the SAO basis to the MO basis and creates the antisymmetrized two-electron integrals. The transformation takes place in individual IRREP blocks, in order to minimise the memory requirements which are in any attempt large. They are saved in IS_pqrs groupS instances. If not done in a previous step by CFOUR, the Fock matrix is constructed using the MO coefficients, the one-electron Hamiltonian matrix and the antisymmetrized two-electron integrals. It is then saved in fS_pq groupS instances. This is handled by the groupS::construct_fock member function.

The MO coefficients, the overlap and one-electron Hamiltonian integrals in the SAO basis, the Fock matrix and the two-electron integrals in the SAO basis are then written on disk in a basisS format as binaries, and are deleted from memory. If needed later in the program they can be read as basisS binaries instead of CFOUR interface files.

The two-index tensors needed for the calculations of properties from tab. 3.2 are read in the Prop1CCS and Prop1S functions, they are transformed in the MO basis and then used for the property calculation.

The interface is regulated by the user with the interface keyword in the interface topic of the input file. There is no default value for this keyword and the interface must always be given either from LONDON (interface=london) or CFOUR (interface=cfour).

Chapter 4

Approximate Coupled-Cluster Methods

This chapter focuses on approximations to the standard CC truncations as a means to lower the high cost of ff-CC. The two main approaches used are the CCn series and the EOM-CCSD(T)(a)* method. Both approximations are based on perturbation theory. The implementation strategies used here replicate existing approaches for implementation based on real numbers.

Sec. 4.1 focuses on the CCn series of methods, with n as the cardinal number. These methods are iterative and lower the overall scaling by one order of magnitude, relative to the corresponding parent methods. In this thesis, the CC2 and CC3 methods are used. The theoretical aspects of the series are presented first, followed by a description of the implementation in the QCUMBRE program. The CCn series is well established in the quantum-chemical literature and was first developed in 1995.[82–84]

Next, the non-iterative EOM-CCSD(T)(a)* approach is addressed in sec. 4.2. The method functions similar to the CCSD(T) gold standard, by offering correction on top of the CCSD energy. The method was developed in the last decade[85] and is able to target not only the reference CC state, but excited EOM-CC states as well.

Lastly, these approximate methods are used to study the electronic spectra of small molecules in sec. 4.3. The study focuses on the CH^+ and CH molecular systems, and also on the simple hydrocarbons CH_4 and C_2H_4. Moreover, the CC2 method is applied on the medium-sized pyrrole molecule. The methods are in each step compared to the results at the CCSD and CCSDT levels of theory.

4.1 The approximate CCn series

The standard CC truncations, i.e., CCSD and CCSDT, scale as M^6 and M^8, respectively, with M representing the size of the system. This scaling limits the applicability of the CC series significantly. The cost is further raised for ff-CC methods because of a larger prefactor dictated by the use of complex algebra. In order to extend the applicability of CC methods, approximations to the standard CC trunctation are derived that have a lower scaling compared to their parent method. Such an approach is offered by the CCn series.[82–84,141]

4.1.1 Theoretical aspects

The CCn methods offer inclusion of up to n level excitations and lower the scaling compared to the standard CC truncations using approximations based on perturbation theory. Additionally, their formulation is based on CC response theory in order to have access to excited-states energies and properties.

The two requirements of the CCn series are the following:

1. The singles amplitudes t_1 are treated as zeroth-order parameters, because they function as effective orbital relaxation.

2. The amplitude equations of excitation level n are approximated to the first non-vanishing order.

This means that the amplitude equations up to $n-1$ are identical between the standard CC truncation and CCn, and only the nth level excitations are approximated. Requirement 1 is ensured with the use of partially similarity transformed operators

$$\bar{O} = e^{-\hat{T}_1} \hat{O} e^{\hat{T}_1}.$$

Applying the recipe described so far, the CC singles approximate doubles (CC2) equations are derived.

$$\langle \Phi_1 | \left(\bar{H} e^{\hat{T}_2}\right)_{\mathrm{C}} | 0 \rangle = 0 \tag{4.1.1}$$

$$\langle \Phi_2 | \left(\bar{F}_N \hat{T}_2\right)_{\mathrm{C}} | 0 \rangle + \langle \Phi_2 | \bar{V}_N | 0 \rangle = 0. \tag{4.1.2}$$

The single-amplitude equations [eq. (4.1.1)] are identical to CCSD. Eq. (4.1.2) for the doubles on the other hand are an approximation to first order, similar to eq. (2.8.6), where $\hat{V}_N$ and $\hat{F}_N$ have been substituted with their partially similarity transformed version $\bar{V}_N$ and $\bar{F}_N$. As for the term involving the partially transformed Fock operator, it can be simplified to $\langle \Phi_2 | \left(\hat{F}_N \hat{T}_2\right)_{\mathrm{C}} | 0 \rangle$ for canonical HF orbitals. In this case, only single commutators of the Fock operator survive as shown in eq. (2.8.4). The double-amplitude equations can then be further simplified to

$$t_2 = -\frac{\langle \Phi_2 | \bar{V}_N | 0 \rangle}{\Delta\epsilon_2}. \tag{4.1.3}$$

The CC2 method scales as M^5, similar to MP2. Unlike MP2, CC2 includes contributions of higher order from the single amplitudes, and gives improved results[82]

Going on to the CC singles doubles approximate triples (CC3) method, the amplitude equations are the following.

$$\langle \Phi_1 | \left(\bar{H} e^{\hat{T}_2 + \hat{T}_3}\right)_{\mathrm{C}} | 0 \rangle = 0 \tag{4.1.4}$$

$$\langle \Phi_2 | \left(\bar{H} e^{\hat{T}_2 + \hat{T}_3}\right)_{\mathrm{C}} | 0 \rangle = 0 \tag{4.1.5}$$

$$\langle \Phi_3 | \left(\bar{F}_N, \hat{T}_3\right)_{\mathrm{C}} | 0 \rangle + \langle \Phi_3 | \left(\bar{V}_N, \hat{T}_2\right)_{\mathrm{C}} | 0 \rangle = 0 \tag{4.1.6}$$

Again in the CC3 case, eq. (4.1.4) and (4.1.5) are identical to CCSDT, and eq. (4.1.6) are the second-order correction from eq. (2.8.9), with the partially transformed $\bar{V}_N$ and $\bar{F}_N$. They can be further simplified for canonical HF orbitals as well

$$t_3 = -\frac{\langle \Phi_3 | \left(\bar{V}_N, \hat{T}_2\right)_{\mathrm{C}} | 0 \rangle}{\Delta\epsilon_3}. \tag{4.1.7}$$

CC3 is an approximation to CCSDT with a scaling of M^7. It offers an approximate inclusion of triples corrections of high quality, and is an invaluable tool since the scaling of CCSDT is very often forbidding.

The CCn series of methods fills the scaling ladder between the standard truncations. Thus, the following ordering of the methods regarding cost and accuracy is offered:

$$\begin{array}{ccccccccc} \mathrm{CC2} & < & \mathrm{CCSD} & < & \mathrm{CC3} & < & \mathrm{CCSDT} & \dots \\ M^5 & < & M^6 & < & M^7 & < & M^8 & \dots \end{array}$$

For the calculation of properties, Lagrangians are constructed that include eq. (4.1.1) and (4.1.2) for CC2

$$L_{\mathrm{CC2}} = \langle 0 | \left(\bar{H} e^{\hat{T}_2}\right)_{\mathrm{C}} | 0 \rangle + \langle 0 | \hat{\Lambda}_1 \left(\bar{H} e^{\hat{T}_2}\right)_{\mathrm{C}} | 0 \rangle + \langle 0 | \hat{\Lambda}_2 \left[\left(\bar{F}_N \hat{T}_2\right)_{\mathrm{C}} + \bar{V}_N\right] | 0 \rangle, \tag{4.1.8}$$

and eq. (4.1.4), (4.1.5) and (4.1.6) for CC3

$$L_{\mathrm{CC3}} = \langle 0 | \left(\bar{H} e^{\hat{T}_2 + \hat{T}_3}\right)_{\mathrm{C}} | 0 \rangle + \langle 0 | \left(\hat{\Lambda}_1 + \hat{\Lambda}_2\right) \left(\bar{H} e^{\hat{T}_2 + \hat{T}_3}\right)_{\mathrm{C}} | 0 \rangle + \langle 0 | \hat{\Lambda}_3 \left[\left(\bar{F}_N \hat{T}_3\right)_{\mathrm{C}} + \left(\bar{V}_N \hat{T}_2\right)_{\mathrm{C}}\right] | 0 \rangle. \tag{4.1.9}$$

It is important to note that the MP2 Lagrangian can be derived from eq. (4.1.8) by setting $t_1 = 0$

$$L_{\mathrm{MP2}} = \langle 0 | \left(\hat{H} e^{\hat{T}_2}\right)_{\mathrm{C}} | 0 \rangle + \langle 0 | \hat{\Lambda}_2 \left[\left(\hat{F}_N \hat{T}_2\right)_{\mathrm{C}} + \hat{V}_N\right] | 0 \rangle. \tag{4.1.10}$$

Solutions for eq. (4.1.10) are provided by eq. (2.8.7).

Derivation of EOM-CCn equations

An advantage of the CCn methods in contrast to other perturbative approaches is that they are readily generalized for excited states with the use of the EOM approach, as their derivation is based on CC response theory.[82,83,141]

One way to derive the EOM-eigenvalue problem is to define the CC Jacobian. In standard CC truncations, the Jacobian emerges in the differentiation of the Lagrangian. This is shown by recasting eq. (2.7.4) in a matrix form.

$$\frac{\partial L_{\mathrm{CC}}}{\partial \mathbf{T}} = (\mathbf{1} + \mathbf{\Lambda})\widetilde{\mathbf{H}}_{\mathrm{C}}.$$

The same strategy is applied to derive the EOM-CC2 and EOM-CC3 Jacobian matrices. Differentiation of eq. (4.1.8) and (4.1.9) with respect to t_I results in the following Jacobian matrices:

$$\widetilde{\mathbf{H}}_{\mathrm{C}}^{\mathrm{CC2}} = \begin{pmatrix} \langle\Phi_1|\left((\bar{H}\hat{\mu}_1)_{\mathrm{C}} e^{\hat{T}_2}\right)_{\mathrm{C}}|0\rangle & \langle\Phi_1|\left((\bar{H}e^{\hat{T}_2})_{\mathrm{C}}\hat{\mu}_2\right)_{\mathrm{C}}|0\rangle \\ \langle\Phi_2|\left[((\bar{F}_N\hat{\mu}_1)_{\mathrm{C}}\hat{T}_2)_{\mathrm{C}} + \bar{V}\hat{\mu}_1)_{\mathrm{C}}\right]|0\rangle & \langle\Phi_2|\left(\bar{F},\hat{\mu}_2\right)_{\mathrm{C}}|0\rangle \end{pmatrix}$$

which can be simplified for canonical HF orbitals

$$\widetilde{\mathbf{H}}_{\mathrm{C}}^{\mathrm{CC2}} = \begin{pmatrix} \langle\Phi_1|\left[(\bar{H}\hat{\mu}_1)_{\mathrm{C}} + ((\bar{H}\hat{\mu}_1)_{\mathrm{C}}\hat{T}_2)_{\mathrm{C}}\right]|0\rangle & \langle\Phi_1|\left(\bar{H}\hat{\mu}_2\right)_{\mathrm{C}}|0\rangle \\ \langle\Phi_2|\left(\bar{V}\hat{\mu}_1\right)_{\mathrm{C}}|0\rangle & \mathbb{1}\Delta\epsilon_2 \end{pmatrix},$$

and

$$\widetilde{\mathbf{H}}_{\mathrm{C}}^{\mathrm{CC3}} = \begin{pmatrix} \langle\Phi_1|\left((\bar{H}\hat{\mu}_1)_{\mathrm{C}} e^{\hat{T}_2+\hat{T}_3}\right)_{\mathrm{C}}|0\rangle & \langle\Phi_1|\left((\bar{H}e^{\hat{T}_2+\hat{T}_3})_{\mathrm{C}}\hat{\mu}_2\right)_{\mathrm{C}}|0\rangle & \langle\Phi_1|\left((\bar{H}e^{\hat{T}_2+\hat{T}_3})_{\mathrm{C}}\hat{\mu}_3\right)_{\mathrm{C}}|0\rangle \\ \langle\Phi_2|\left((\bar{H}\hat{\mu}_1)_{\mathrm{C}} e^{\hat{T}_2+\hat{T}_3}\right)_{\mathrm{C}}|0\rangle & \langle\Phi_2|\left((\bar{H}e^{\hat{T}_2+\hat{T}_3})_{\mathrm{C}}\hat{\mu}_2\right)_{\mathrm{C}}|0\rangle & \langle\Phi_2|\left((\bar{H}e^{\hat{T}_2+\hat{T}_3})_{\mathrm{C}}\hat{\mu}_3\right)_{\mathrm{C}}|0\rangle \\ \langle\Phi_3|\left[((\bar{F}_N\hat{\mu}_1)_{\mathrm{C}}\hat{T}_3)_{\mathrm{C}} + ((\bar{V}_N\hat{\mu}_1)_{\mathrm{C}}\hat{T}_2)_{\mathrm{C}}\right]|0\rangle & \langle\Phi_3|\left(\bar{V}_N,\hat{\mu}_2\right)_{\mathrm{C}}|0\rangle & \langle\Phi_3|\left(\bar{F}_N,\hat{\mu}_3\right)_{\mathrm{C}}|0\rangle \end{pmatrix}$$

further simplified for canonical HF orbitals

$$\widetilde{\mathbf{H}}_{\mathrm{C}}^{\mathrm{CC3}} = \begin{pmatrix} \langle\Phi_1|\left[(\bar{H}\hat{\mu}_1)_{\mathrm{C}} + ((\bar{H}\hat{\mu}_1)_{\mathrm{C}}\hat{T}_2)_{\mathrm{C}}\right]|0\rangle & \langle\Phi_1|\left(\bar{H}_1\hat{\mu}_2\right)_{\mathrm{C}}|0\rangle & \langle\Phi_1|\left(\hat{H}\hat{\mu}_3\right)_{\mathrm{C}}|0\rangle \\ \langle\Phi_2|\left[(\bar{H}\hat{\mu}_1)_{\mathrm{C}} + ((\bar{H}\hat{\mu}_1)_{\mathrm{C}}[\hat{T}_2+\hat{T}_3])_{\mathrm{C}}\right]|0\rangle & \langle\Phi_2|\left[(\bar{H}\hat{\mu}_2)_{\mathrm{C}} + ((\bar{H}\hat{T}_2)_{\mathrm{C}}\hat{\mu}_2)_{\mathrm{C}}\right]|0\rangle & \langle\Phi_2|\left(\bar{H}\hat{\mu}_3\right)_{\mathrm{C}}|0\rangle \\ \langle\Phi_3|\left((\bar{V}\hat{\mu}_1)_{\mathrm{C}}\hat{T}_2\right)_{\mathrm{C}}|0\rangle & \langle\Phi_3|\left(\bar{V}\hat{\mu}_2\right)_{\mathrm{C}}|0\rangle & \mathbb{1}\Delta\epsilon_3 \end{pmatrix}.$$

Because of the diagonal form of the doubles-doubles block in EOM-CC2 and triples-triples block in EOM-CC3, no excitation with a predominant double-excitation character can be derived at EOM-CC2 and a triple-excitation character at EOM-CC3, respectively. The latter case is of no practical interest, but the inability to target excited states with a predominant double-excitation character at the EOM-CC2 level may lead to unphysical results, as will be shown in sec. 4.3.

Finally, the response Lagrangians are introduced

$$\begin{aligned} L_{\mathrm{resp}}^{\mathrm{CC2}'} =& \mathbf{L}\widetilde{\mathbf{H}}_{\mathrm{C}}^{\mathrm{CC2}}\mathbf{R} + \Delta E_{\mathrm{exc}}\left(\mathbf{LR} - 1\right) + \langle 0|\left(\bar{H}e^{\hat{T}_2}\right)_{\mathrm{C}}|0\rangle \\ &+ \langle 0|\,\hat{\mathscr{Z}}_1'(\bar{H}e^{\hat{T}_2})_{\mathrm{C}}\,|0\rangle + \langle 0|\,\hat{\mathscr{Z}}_2'\left[(\bar{F}_N\hat{T}_2)_{\mathrm{C}} + \bar{V}_N\right]|0\rangle \end{aligned} \tag{4.1.11}$$

and

$$\begin{aligned} L_{\mathrm{resp}}^{\mathrm{CC3}'} =& \mathbf{L}\widetilde{\mathbf{H}}_{\mathrm{C}}^{\mathrm{CC3}}\mathbf{R} + \Delta E_{\mathrm{exc}}\left(\mathbf{LR} - 1\right) + \langle 0|\left(\bar{H}e^{\hat{T}_2+\hat{T}_3}\right)_{\mathrm{C}}|0\rangle \\ &+ \langle 0|\left(\hat{\mathscr{Z}}_1' + \hat{\mathscr{Z}}_2'\right)(\bar{H}e^{\hat{T}_2+\hat{T}_3})_{\mathrm{C}}\,|0\rangle + \langle 0|\,\hat{\mathscr{Z}}_3'\left[(\bar{F}_N\hat{T}_3)_{\mathrm{C}} + (\bar{V}_N\hat{T}_2)_{\mathrm{C}}\right]|0\rangle\,. \end{aligned} \tag{4.1.12}$$

Two-body properties for perturbative approaches

One- and two-body reduced density matrices can be constructed for MP2, CC2, CC3, EOM-CC2, and EOM-CC3, using the Lagrangians in eq. (4.1.10), (4.1.8), (4.1.9), (4.1.11), and (4.1.12) respectively, combined with the recipe given in tab. 2.1. Their explicit form is shown in app. C.

For these perturbative approaches, it can be deduced that the one-body density matrices include terms up to order n, since the Fock operator is defined as zeroth-order parameter according to the

MP partitioning, while the two-body density matrices include terms only up to order $n-1$, because the normal-ordered two-electron interaction operator constitutes the perturbation.[142] Thus, reduced-density matrices defined via the Lagrangians are only applicable for properties that involve derivatives of the Hamiltonian itself, i.e., dipole moments, geometric derivatives, etc.

$$\frac{\partial \hat{H}}{\partial \xi} = \frac{\partial \hat{h}}{\partial \xi} + \frac{\partial \hat{V}}{\partial \xi}$$

Special attention needs to be paid for properties that include the two-body density matrices and involve terms of the Hamiltonian added on top of it as a tool to define expectation values as energy derivatives.

$$\begin{aligned} \hat{H} &\rightarrow \hat{H} + \varepsilon \hat{O} \\ \frac{\partial(\hat{H} + \varepsilon \hat{O})}{\partial \varepsilon} &= \hat{O} \end{aligned} \tag{4.1.13}$$

Such a case is the spin-squared operator that is used for the calculation of the spin multiplicity and spin contamination in spin-unrestricted approaches. Spin properties are studied in detail in sec. 5.2. It is necessary to include contributions of order n to the two-body density matrices for calculations of properties of the form in eq. (4.1.13).

Two-body density matrices at the MP2 and CC2 levels of theory have been derived and are described in ref. [142]. For the MP2 approach, the MP3 two-body density matrices are used for calculation of spin-multiplicity, while for CC2, the modified two-body density matrix expressions are almost identical to CCSD without the $\hat{\Lambda}_2 \hat{T}_2 \hat{T}_2$ contributions. The same approach is to be used for CC3, EOM-CC2 and EOM-CC3, but these levels of theory have not been targeted in this work.

4.1.2 The implementation of CCn methods in QCUMBRE

Based on the presented theory of the CCn methods, CC2 and CC3 are implemented in QCUMBRE. Their implementation is based on existing strategies for programs that only utilise real numbers which were generalized to the complex plane. These strategies are described here.

For the implementation of CC methods, the working equations are factorised in such a way to transform the non-linear problem to a quasi-linear problem, and in order to keep the overall scaling limited. This factorisation for the CCn methods mostly coincides with the partially transformed operators. Thus the following intermediates are introduced

$$\begin{aligned} F_{1pq} &= \langle p | \, \bar{F} + \bar{V} \, | q \rangle \\ W_{1pqrs} &= \langle pq | \, \bar{F} + \bar{V} \, | rs \rangle - \langle pq | \, \bar{F} + \bar{V} \, | sr \rangle \end{aligned}$$

The exact blocks of the intermediates used in the code for different calculations are shown in tab. 4.1. The intermediates are saved in the `F_pq` and `W_pqrs groupS` instances and are calculated in `CCn_IntermediatesS`, `EOM_CCn_Intermediates` and `LR_CCn_Intermediates`.

CC2/CC3 ground-state energy

The CC2 and CC3 methods lower the scaling by one order of magnitude with respect to the standard CCSD and CCSDT truncations. Moreover, because of the simplification offered by the use of canonical HF orbitals eq. (4.1.3) and (4.1.7), the nth order amplitude equations are not needed in the linear solver. Due to this, the linear-solver algorithm has lower memory requirements. This is more clearly seen in the working equations for CC2 and CC3, where no $t_2 \leftarrow t_2$ contributions and no $t_3 \leftarrow t_3$ contributions exist, respectively.

The working CC amplitude equations for CC2 are

$$\begin{aligned} 0 &= F_{1ai} + \sum_{ck} F_{1kc} t_{ij}^{ac} + \frac{1}{2} \sum_{cdk} W_{1kacd} t_{ki}^{cd} - \frac{1}{2} \sum_{ckl} W_{1klci} t_{kl}^{ca} \\ t_{ij}^{ab} &= \frac{W_{1abij}}{\epsilon_i + \epsilon_j - \epsilon_a - \epsilon_b}. \end{aligned}$$

Intermediates	CC2 energy	EOM-CC2 energy	(EOM-)CC2 properties	CC3 energy	EOM-CC3 energy
F_{1ai}	✓	✓	✓	✓	✓
F_{1ia}	✓	✓	✓	✓	✓
F_{1ab}		✓[b]	✓[b]	✓	✓[b]
F_{1ij}		✓[b]	✓[b]	✓	✓[b]
W_{1abcd}				✓	✓
W_{1ijkl}				✓	✓
W_{1abij}	✓	✓	✓	✓	✓
W_{1ijab}[a]	✓	✓	✓	✓	✓
W_{1iabj}		✓[b]	✓[b]	✓	✓[b]
W_{1kaij}		✓	✓	✓	✓
W_{1abci}		✓	✓	✓	✓
W_{1ijka}	✓	✓	✓	✓	✓
W_{1ciab}	✓	✓	✓	✓	✓

[a] is not saved extra as $W_{1ijab} = \langle ij| \, |ab\rangle$
[b] include extra terms

Table 4.1: Intermediates needed for different CCn methods.

At the CC3 level, they are

$$
\begin{aligned}
0 =& F_{1ai} + \sum_{ck} F_{1kc} t_{ij}^{ac} + \frac{1}{2} \sum_{cdk} W_{1kacd} t_{ki}^{cd} - \frac{1}{2} \sum_{ckl} W_{1klci} t_{kl}^{ca} + \frac{1}{4} \sum_{deml} \langle lm| \, |de\rangle \, t_{ilm}^{ade} \\
0 =& W_{1abij} + P(ab) \sum_{d} F_{1bd} t_{ij}^{ad} - P(ij) \sum_{l} F_{1lj} t_{il}^{ab} + \frac{1}{2} \sum_{de} W_{1abde} t_{ij}^{de} \\
& \frac{1}{2} \sum_{lm} \left(W_{1lmij} + \frac{1}{2} \sum_{de} \langle lm| \, |de\rangle \, t_{ij}^{de} \right) t_{lm}^{ab} + P(ij)P(ab) \sum_{dl} \left(W_{1ladj} + \langle lm| \, |de\rangle \, t_{jm}^{be} \right) t_{il}^{db} \\
& - P(ij) \frac{1}{2} \sum_{delm} \langle lm| \, |de\rangle \, t_{li}^{de} t_{mj}^{ab} - P(ab) \frac{1}{2} \sum_{delm} \langle lm| \, |de\rangle \, t_{lm}^{da} t_{ij}^{eb} \\
& + \sum_{dl} F_{1ld} t_{ijl}^{abd} - P(ij) \frac{1}{2} \sum_{dlm} W_{1mljd} t_{iml}^{abd} + P(ab) \frac{1}{2} \sum_{del} W_{1bled} t_{ijl}^{aed} \\
t_{ijk}^{abc} =& \frac{P(ij/k)P(ab/c) \left(\sum_l W_{1lcji} t_{kl}^{ab} - \sum_d W_{1badk} t_{ij}^{cd} \right)}{\epsilon_i + \epsilon_j + \epsilon_k - \epsilon_a - \epsilon_b - + \epsilon_c}.
\end{aligned}
$$

The triple permutation operators have the following effect

$$P(pq/r) d_{pq\ldots} d'_{r\ldots} = d_{pq\ldots} d'_{r\ldots} - d_{rq\ldots} d'_{p\ldots} - d_{pr\ldots} d'_{q\ldots}.$$

The working equations are implemented in the `CCn_AmplitudesS`. The diagonal t_3 amplitudes are calculated in `t3_cc3S`.

The validation of the implementation was carried out for the field-free case by comparing results computed using the CFOUR program. For ff calculations, the CCSD and CCSDT functions respectively were modified to reproduce CC2 and CC3 results in order to verify ff-CC2 and ff-CC3.

EE-EOM-CC2/CC3 excited-state energy

For the calculation of EE-EOM-CCn excitation energies the working equations of the EOM eigenvalue equations are presented.

In the case EE-EOM-CC2, the eigenvalue problem has the form

$$\begin{aligned}
\Delta E_{\mathrm{exc}} r_i^a =& \sum_c \left(F_{1ac} - \frac{1}{2} \sum_{dkl} \langle kl| \, |cd\rangle \, t_{kl}^{ad} \right) r_i^c - \sum_k \left(F_{1ki} - \frac{1}{2} \sum_{cdl} \langle kl| \, |cd\rangle \, t_{li}^{cd} \right) r_k^a \\
& - \sum_{ck} \left(W_{1kaic} - \sum_{dl} \langle kl| \, |cd\rangle \, t_{li}^{da} \right) r_k^c + \sum_{kc} F_{1kc} r_{ik}^{ac} \\
& + \frac{1}{2} \sum_{cdk} W_{1akcd} r_{ik}^{cd} - \frac{1}{2} \sum_{ckl} W_{1klic} r_{kl}^{ac} \\
\Delta E_{\mathrm{exc}} r_{ij}^{ab} =& P(ab) \sum_c f_{bc} r_{ij}^{ac} - P(ij) \sum_k f_{kj} r_{ik}^{ab} \\
& - P(ab) \sum_k W_{1kbij} r_k^a + P(ij) \sum_c W_{1abcj} r_i^c .
\end{aligned}$$

The doubles equation can be rewritten as

$$r_{ij}^{ab} = \frac{-P(ab) \sum_k W_{1kbij} r_k^a + P(ij) \sum_c W_{1abcj} r_i^c}{\Delta E_{\mathrm{exc}} + \epsilon_i + \epsilon_j - \epsilon_a - \epsilon_b} .$$

The EE-EOM-CC3 equations are given by

$$\begin{aligned}
\Delta E_{\mathrm{exc}} r_i^a =& \sum_c \left(F_{1ac} - \frac{1}{2} \sum_{dkl} \langle kl| \, |cd\rangle \, t_{kl}^{ad} \right) r_i^c - \sum_k \left(F_{1ki} - \frac{1}{2} \sum_{cdl} \langle kl| \, |cd\rangle \, t_{li}^{cd} \right) r_k^a \\
& - \sum_{ck} \left(W_{1kaic} - \sum_{dl} \langle kl| \, |cd\rangle \, t_{li}^{da} \right) r_k^c + \sum_{kc} F_{1kc} r_{ik}^{ac} \\
& + \frac{1}{2} \sum_{cdk} W_{1akcd} r_{ik}^{cd} - \frac{1}{2} \sum_{ckl} W_{1klic} r_{kl}^{ac} + \frac{1}{4} \sum_{delm} \langle lm| \, |de\rangle \, r_{ilm}^{ade} \\
\Delta E_{\mathrm{exc}} r_{ij}^{ab} =& P(ij) \sum_d \left(W_{1abdj} - \sum_l F_{1ld} t_{lj}^{ab} + P(ab) \sum_{el} W_{1alde} t_{lj}^{eb} + \frac{1}{2} \sum_{lm} W_{1lmdj} t_{lm}^{ab} - \frac{1}{2} \sum_{elm} \langle lm| \, |de\rangle \, t_{lmj}^{aeb} \right) r_i^d \\
& - P(ab) \sum_l \left(W_{1lbij} - \sum_d F_{1ld} t_{ij}^{bd} + P(ij) \sum_{dm} W_{1lmid} t_{mj}^{db} + \frac{1}{2} \sum_{de} W_{1lbde} t_{ij}^{de} - \frac{1}{2} \sum_{dem} \langle lm| \, |de\rangle \, t_{mij}^{deb} \right) r_l^a \\
& + \sum_{dl} \left(P(ab) \sum_e W_{1alde} t_{lj}^{eb} - P(ij) \sum_m W_{1lmdi} t_{mj}^{ab} + \sum_{em} \langle lm| \, |de\rangle \, t_{mij}^{eab} \right) r_l^d \\
& + P(ab) \sum_d F_{1bd}^{\oplus} r_{ij}^{ad} - P(ij) \sum_l F_{1lj}^{\oplus} r_{il}^{ab} - P(ij) P(ab) \sum_{ld} W_{1ladj}^{\oplus} r_{il}^{bd} \\
& + \frac{1}{2} \sum_{lm} \left(W_{1lmij} + \frac{1}{2} \sum_{de} \langle lm| \, |de\rangle \, t_{ij}^{de} \right) r_{lm}^{ab} + \frac{1}{2} \sum_{de} \left(W_{1abde} + \frac{1}{2} \sum_{lm} \langle lm| \, |de\rangle \, t_{lm}^{ab} \right) r_{ij}^{de} \\
& + \frac{1}{2} P(ij) \sum_{delm} \langle lm| \, |de\rangle \, t_{mi}^{ab} r_{lj}^{de} - \frac{1}{2} P(ab) \sum_{delm} \langle lm| \, |de\rangle \, t_{ij}^{eb} r_{lm}^{da} \\
& + \sum_{dl} F_{1ld} r_{ijl}^{abd} + \frac{1}{2} P(ab) \sum_{del} W_{1blde} r_{ijl}^{ade} - \frac{1}{2} P(ij) \sum_{dlm} W_{1lmjd} r_{ilm}^{abd} \\
\Delta E_{\mathrm{exc}} r_{ijk}^{abc} =& P(ab/c) \sum_d f_{cd} r_{ijk}^{abd} - P(ij/k) \sum_l f_{lk} r_{ijl}^{abc} \\
& P(ij/k) \sum_d \left(P(bc/a) \sum_e W_{1bcde} r_k^e - P(abc) \sum_l W_{1bldk} r_l^c \right) t_{ij}^{ad} \\
& + P(ab/c) \sum_l \left(P(jk/i) \sum_m W_{1lmjk} r_m^c - P(ijk) \sum_d W_{1lcjd} r_k^d \right) t_{il}^{ab} \\
& P(ij/k) P(bc/a) \sum_d W_{1bcdk} r_{ij}^{ad} - P(ab/c) P(jk/i) \sum_l W_{1lcjk} r_{il}^{ab} .
\end{aligned}$$

Here, the following intermediates are introduced

$$\begin{aligned} F^{\oplus}_{1ab} =& F_{1ab} + \frac{1}{2}\sum_{ckl} \langle kl| \, |cb\rangle \, t^{ac}_{kl} \\ F^{\oplus}_{1ij} =& F_{ij} + \frac{1}{2}\sum_{cdk} \langle ki| \, |cd\rangle \, t^{cd}_{kj} \\ W^{\oplus}_{1iabj} =& W_{1iabj} + \sum_{dl} \langle li| \, |bd\rangle \, t^{ad}_{lj}. \end{aligned}$$

The triples equation can be rewritten as

$$r^{abc}_{ijk} = \frac{I^{abc}_{ijk}}{\Delta E_{\mathrm{exc}} + \epsilon_i + \epsilon_j + \epsilon_k - \epsilon_a - \epsilon_b - \epsilon_c},$$

with

$$\begin{aligned} I^{abc}_{ijk} =& P(ij/k)\sum_{d}\left(P(bc/a)\sum_{e} W_{1bcde} r^{e}_{k} - P(abc)\sum_{l} W_{1bldk} r^{c}_{l}\right) t^{ad}_{ij} \\ &+ P(ab/c)\sum_{l}\left(P(jk/i)\sum_{m} W_{1lmjk} r^{c}_{m} - P(ijk)\sum_{d} W_{1lcjd} r^{d}_{k}\right) t^{ab}_{il} \\ & P(ij/k)P(bc/a)\sum_{d} W_{1bcdk} r^{ad}_{ij} - P(ab/c)P(jk/i)\sum_{l} W_{1lcjk} r^{ab}_{il}. \end{aligned}$$

The full triple permutation operator is introduced as well

$$P(pqr) d_{p\ldots} d'_{q\ldots} d''_{r\ldots} = d_{p\ldots} d'_{q\ldots} d''_{r\ldots} + d_{q\ldots} d'_{r\ldots} d''_{p\ldots} + d_{r\ldots} d'_{p\ldots} d''_{q\ldots} - d_{r\ldots} d'_{q\ldots} d''_{p\ldots} - d_{q\ldots} d'_{p\ldots} d''_{r\ldots} - d_{p\ldots} d'_{r\ldots} d''_{q\ldots}$$

Similarly to the CC amplitude working equations for CC2 and CC3, the doubles at EOM-CC2 and the triples at EOM-CC3 equations show no $r_2 \leftarrow r_2$ and no $r_3 \leftarrow r_3$ mixing, respectively. This is exploited during the Davidson procedure with a few alterations in order to reduce the memory and flops needed.

The working equations are implemented in `ContractionsS_CCn` taking advantage of the diagonal form of the r_n amplitudes which in turn are calculated in `r2_cc2S` and `r3_cc3S`. In their non-diagonal form they are implemented in the `ContractionsS` function.

The validation of the implementation was carried out for the field-free case by comparing results computed using the CFOUR program. For ff calculations, the EE-EOM-CCSD and EE-EOM-CCSDT functions respectively were modified to reproduce EE-EOM-CC2 and EE-EOM-CC3 results in order to verify ff-EE-EOM-CC2 and ff-EE-EOM-CC3.

CC2 ground-state and EOM-CC2 properties

For ground-state CC2 and EOM-CC2 expectation-value properties, the left-hand side EOM eigenvalue problem is needed. This can be described by the following working equations

$$\begin{aligned} l^{i}_{a}\Delta E_{\mathrm{exc}} =& l_0 F_{1ia} + \sum_{d} F^{\oplus}_{1da} l^{i}_{d} - \sum_{l} F^{\oplus}_{1il} l^{l}_{a} + \sum_{dl} W^{\oplus}_{1idal} l^{l}_{d} \\ &- \frac{1}{2}\sum_{dlm} W_{1idlm} l^{lm}_{ad} + \frac{1}{2}\sum_{del} W_{1deal} l^{il}_{de} \\ l^{ij}_{ab}\Delta E_{\mathrm{exc}} =& l_0 \langle ij| \, |ab\rangle + P(ij)P(ab) F_{1jb} l^{i}_{a} \\ &- P(ab)\sum_{l} W_{1ijlb} l^{l}_{a} + P(ij)\sum_{d} W_{1djab} l^{i}_{d} \\ &+ P(ab)\sum_{d} f_{db} l^{ij}_{ad} - P(ij)\sum_{l} f_{jl} l^{il}_{ab} \end{aligned} \tag{4.1.14}$$

It is restated that $\Delta E_{\text{exc}} = 0$, $l_0 = 1$ and $l^{i\cdots}_{a\cdots} = \lambda^{i\cdots}_{a\cdots}$ for the ground state and $l_0 = 0$ for excited states. These working equations are implented in `ContractionsS_CCn`.

As for response properties at the EE-EOM-CC2 level of theory, the ζ' amplitudes are needed. These are derived from eq. (4.1.11) by differentiation with respect to the CC amplitudes

$$-\mathbf{L}\frac{\partial\widetilde{\mathbf{H}}^{\text{CC2}}_{\text{C}}}{\partial\mathbf{T}}\mathbf{R} - \langle 0|\,\frac{\partial(\bar{H}e^{\hat{T}_2})_{\text{C}}}{\partial\mathbf{T}}\,|0\rangle = \langle 0|\,\hat{\mathscr{Z}}'_1\frac{\partial(\bar{H}e^{\hat{T}_2})_{\text{C}}}{\partial\mathbf{T}}\,|0\rangle + \langle 0|\,\hat{\mathscr{Z}}'_2\frac{\partial\left[(\bar{F}_N\hat{T}_2)_{\text{C}} + \bar{V}_N\right]}{\partial\mathbf{T}}\,|0\rangle\,.$$

The right-hand side of the equation has the same form as the right-hand side of eq. (4.1.14) by replacing the l-amplitudes with the ζ'-amplitudes. It is implemented in `ContractionsZvecS`. The l_0 terms vanish from the right-hand side because there are no ζ'_0 amplitudes. The left-hand side constitutes the $\boldsymbol{\Xi}$ vector

$$\boldsymbol{\Xi} = \langle 0|\,\frac{\partial(\bar{H}e^{\hat{T}_2})_{\text{C}}}{\partial\mathbf{T}}\,|0\rangle + \mathbf{L}\frac{\partial\widetilde{\mathbf{H}}^{\text{CC2}}_{\text{C}}}{\partial\mathbf{T}}\mathbf{R}.$$

The working equations are the following

$$\begin{aligned}
\xi^i_a =& F_{1ia} + l_0\sum_{em} r^e_m\,\langle mi|\,|ea\rangle + \sum_{efm} l^m_e r^f_m W_{1eifa} - \sum_{emn} l^n_e r^e_m W_{1mina} + \sum_{efmn} l^m_e r^{ef}_{mn}\,\langle ni|\,|fa\rangle \\
&- \sum_e\left(\sum_m F_{1ma}r^e_m + \frac{1}{2}\sum_{fmn}\langle mn|\,|fa\rangle\,r^{fe}_{mn} - \sum_{fmn} W_{1emaf}r^f_m\right) l^i_e \\
&+ \sum_m\left(\sum_e F_{1ie}r^e_m + \frac{1}{2}\sum_{efn}\langle ni|\,|ef\rangle\,r^{ef}_{nm} - \sum_{efn} W_{1nime}r^e_n\right) l^m_a \\
&+ \sum_{em}\left(\frac{1}{2}\sum_{ln} W_{1minl}l^{nl}_{ea} + \frac{1}{2}\sum_{df} W_{1dfea}l^{mi}_{df} - \sum_{nd} W_{1mdna}l^{ni}_{ed} - \sum_{nd} W_{1diel}l^{ml}_{da}\right) r^e_m \\
\xi^{ij}_{ab} =& \langle ij|\,|ab\rangle + P(ij)P(ab)\sum_{ld} r^d_l l^i_a\,\langle lj|\,|db\rangle - P(ab)\sum_{ld} r^d_l l^l_a\,\langle ij|\,|db\rangle - P(ij)\sum_{ld} r^d_l l^i_d\,\langle lj|\,|ab\rangle
\end{aligned}$$

The first terms in both the singles and the doubles ξ-amplitudes arise from the CC reference energy. The calculation of the Ξ vector takes place in `ContractionsZetaS`.

The correctness of the implementation was tested against numerical gradients as described in previous paragraphs.

Alteration to the Davidson procedure

In the following paragraphs, alterations to the Davidson procedure are described that take advantage of the diagonal form of the nth EOM amplitudes equations and result in significant reduction of the computational cost needed for an EOM-CC2 or EOM-CC3 calculation. The presented strategy is an old idea already implemented also in other quantum-chemical program packages that only use real numbers for providing solutions to the EOM-CCn equations (in CFOUR[77,78] for example) and the implementation in QCUMBRE is a simple generalization to the complex plane.

The form of the r_n amplitudes for a EE-EOM-CCn method derived in the previous paragraphs is diagonal, meaning that there is no $r_n \leftarrow r_n$ mixing. The r_n amplitudes are thus readily available as long as the converged excitation energy is available (which is the case only with the converged amplitudes). This means that the linear-eigenvalue EOM problem can be reformulated in a non-linear manner including only up to $n-1$ EOM amplitudes. Such reformulation promises that during the diagonalization of the CCn Jacobian, which is done using a Davidson procedure, only the non-redundant excitation space needs to be considered I^-. The redundant excitation space I^+ can be generated on-the-fly when needed. For CC2, the redundant space includes doubles $I^+ = D$ and the non-redundant includes singles $I^- = S$. For CC3, the redundant space includes triples $I^+ = T$, while the non-redundant space includes singles and doubles $I^- = S, D$.

A Davidson procedure is used to derive a few of the eigenvalues and eigenvectors of a matrix too large to be fully diagonalized by standard algorithms. Instead, a space of base vectors is used starting from a guess vector. The full matrix is transformed to an effective matrix in the space of the base vectors, which can be diagonalized. These trial eigenvectors and eigenvalues give approximations to those of the full matrix. In turn they are used to extend the space of the base vectors to get better and better approximations until a convergence criterion is fulfilled. Such a Davidson procedure was introduced in 1975, and has been reformulated and presented in various reviews since then.[143–147]

Applied to the EOM (and CI) problem, the Jacobian matrix is to be diagonilised. The standard Davidson procedure is described in fig. 4.1. For reasons of simplification, the Einstein summation is used in the flowcharts and in the equations seen in this section. In step (0) a guess vector is chosen from a CIS calculation b_I^1. To build the effective Hamiltonian matrix, the σ_J^k vectors are constructed in step (1) and the effective Hamiltonian in step (2). The full Hamiltonian is never fully saved in memory. Instead, the σ_J^k vectors are saved in memory, so that in each iteration only one σ_J^k vector needs to be calculated. The effective Hamiltonian matrix $\bar{H}^{lm} = b_I^{l*} \widetilde{H}_{IJ} b_J^m$ is then diagonalized giving the trial eigenvalue-eigenvector pair λ^k, y_l^k in step (3). The eigenvector is transformed in the full basis as a linear combination of the base vectors to derive the current eigenvector approximation r_I^k in step (4). The convergence criterion is defined by the residual vector x_I^k in step (5). If convergence is not reached, a new direction t^{k+1} is calculated using a preconditioner D in step (6). This direction is orthogonalised using a Gram-Schmidt orthogonalisation against all previous base vectors in step (7) to give the new basis vector b_I^{k+1}.

Using the redundant and non-redundant space reformulation of the EE-EOM-CCn equations, the standard Davidson procedure cannot be used. Exact r_{I^+} contributions can only be calculated at the convergence limit when the exact excitation energy is available. Before convergence is reached, the calculated r_{I^+} in an iteration contain an error arising from the error of the non-converged excitation energy. This error is not implicitly corrected (unlike in the standard Davidson procedure) and needs to be explicitly eliminated by the algorithm.

The modified Davidson procedure is presented in fig. 4.2, where the altered steps of the algorithm are designated with bold boxes. They are the building of the $\sigma_J^k = \widetilde{H}_{JI} b_I^k$ vector (1a and 1b), the calculation of the new directions for the creation of the new base vector for each iteration t_I^{k+1} (6a and 6b), and the orthogonalization of the new direction with respect to all previous base vectors to create the new one b_I^{k+1}. During the first iteration, the I^+ space is ignored and the procedure continues similarly to the standard Davidson, since no guess for the eigenvalue is available. Starting from iteration $k = 2$, the first modified step is to generate $b_{I^+}^k$ from the eigenvalue of the previous iteration λ^{k-1} and the current lower excitation space $b_{I^-}^k$ (1a). The contributions of $b_{I^+}^k$ are incorporated in the creation of the $\sigma_{J^-}^k$ vector (1b), but explicit consideration of I^+ is otherwise purposefully absent from the algorithm. After the computation of the new direction $t_{I^-}^{k+1}$ (6a), instead of directly orthogonalising the new direction, the current eigenvector $r_{I^-}^k$ is skewed towards the new direction $t_{I^-}^{k+1}$ to create the new base vector $b_{I^-}^{k+1}$ (6b). This new base vector is kept unchanged and all previous $b_{I^-}^l$ are updated to be orthogonal to the new vector (7). The orthogonalisation of the $\sigma_{I^-}^l$ vectors must take place at the same time as the orthogonilisation of the of $b_{I^-}^l$ using the same coefficients, in order not to fully recompute all the elements of $\bar{H}^{lm}$ in each iteration, which would require regenerating all $b_{I^+}^l$. Having each new vector in the set of base vectors being closer to the exact eigenvector instead of just incorporating a new direction, drives the diagonalization of the effective Hamiltonian to yield eigenvector y_l^k with the largest contributions to the element arising from the most recent iteration. This is desired, because $\sigma_{J^-}^k$ from earlier iterations contain an error from the use of an unconverged excitation energy in the generation of $b_{I^+}^k$. Progressively smaller contributions of the eigenvector y_l^k to these inaccurate $\sigma_{J^-}^k$ vectors eliminates this error.

The rate-determining step in both the standard and the modified Davidson procedure is the creation of the $\sigma_{J^{(-)}}^k$ vectors, which scales as N^5 and N^7 for CC2 and CC3, respectively, and remains mostly unchanged in the QCUMBRE implementation. Handling vectors in the full excitation space in standard Davidson has a scaling of N^{2n}, with n being the cardinal number of the method, while only handling the non-redundant space I^- reduces this scaling to $N^{2(n-1)}$. For this reason, the additional steps and the more elaborate orthogonalisation scheme of the modified Davidson procedure do not slow

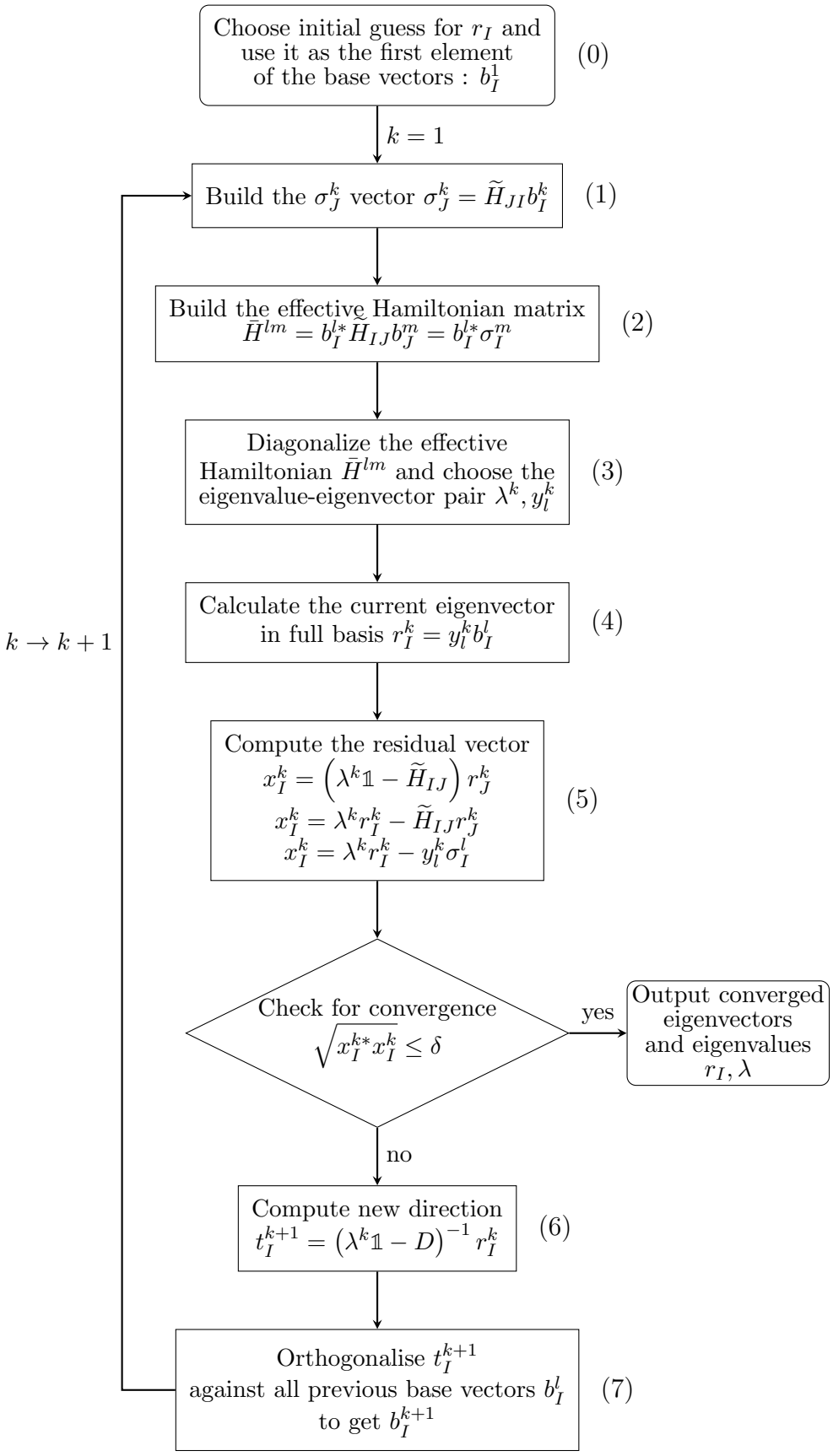

Figure 4.1: Standard Davidson procedure.

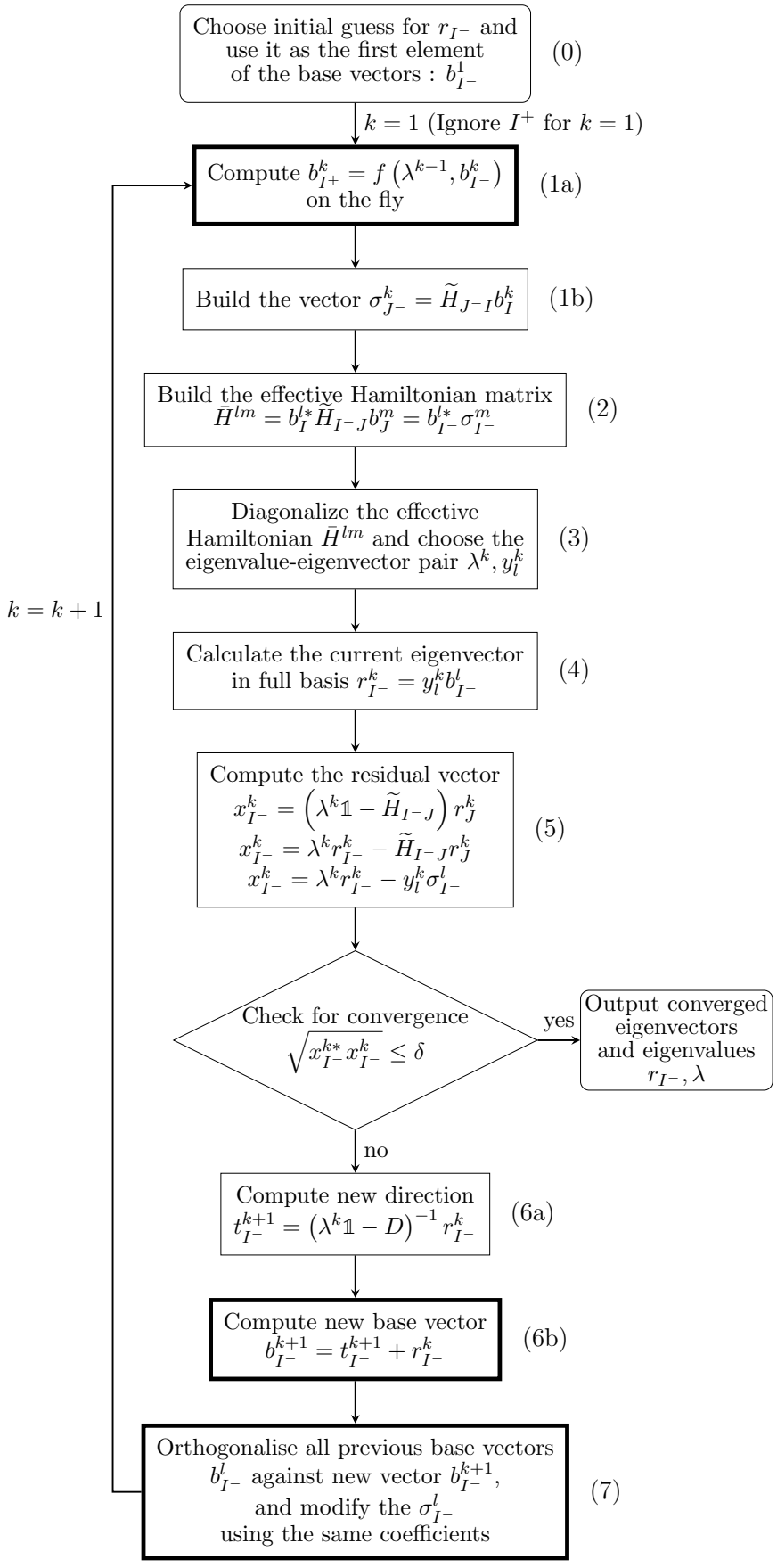

Figure 4.2: Modified Davidson procedure. The boxes in bold signify the altered steps.

the algorithm enough to lose efficiency compared to having to fully handle the additional redundant I^+ space. This means that only handling the non-redundant space results in savings in the timings and in the memory requirements, without changing the scaling of the procedure. Despite these gains, a slower convergence has been observed with the modified Davidson procedure, because of the way that the new direction is constructed. This means that usually more iterations are required to reach convergence, and especially for excited states that tend towards a strong multiconfigurational character, the modified Davidson may fail to converge. Slow convergence is also very often observed for calculations in the complex plane, which are a necessity for finite magnetic-field calculations. Therefore both the standard as well as the modified versions have been implemented in QCUMBRE for CCn method. The standard version is handled by the `DavidsonS` function and the modified version by `AltDavidsonS`. As already stated, this strategy for the alternative Davidson procedure for the calculation of energies and eigenvectors at the EOM-CCn levels of theory is an old idea, already implemented in existing quantum-chemical programs.

4.2 The EOM-CCSD(T)(a)* model

As already mentioned, CCSD includes most of the correlation for systems with a small amount of static correlation.[a] Chemical accuracy is achieved in many cases at the CCSDT level, which, however, is not applicable to a plethora of systems of interest. Finding approximation to CCSDT was an area of research very active in the early days of CC, until the CCSD(T) approach was formulated.[86,148–150] This model,[86] which today is considered the gold standard of quantum chemistry, is based on a CCSD calculation with its M^6 iterative scaling. Additionally, it includes perturbative triples corrections on top of the CCSD energy that scale non-iteratively as M^7. The success of CCSD(T), however, is limited to the ground-state energy. The CC3 method is indeed an approximate triples approach as well that is additionally able to target excited states through its EOM/LR-CC generalization, as the method was formulated in order to be compatible with CC response theory. The applicability of this method is restricted considerably by its iterative M^7 scaling. Many models that offer approximate triple correction in a non-iterative manner for excited states have been developed, but none so far has reached the success and the widespread acceptance in the scientific community of CCSD(T). In this work, the recently developed EOM-CCSD(T)(a)* approach of Matthews and Stanton[85] has been used. It offers a correction to the CC reference state at the CCSD(T)(a) level of theory, and also at the EOM-CCSD(T)(a)* level for EOM states.

4.2.1 Theoretical Aspects

The approach of approach Matthews and Stanton[85] starts from the CCSD similarity transformed Hamiltonian matrix

$$\widetilde{\mathbf{H}}^{\mathrm{CCSD}} = \begin{pmatrix} \widetilde{H}_{00} & \widetilde{H}_{0S} & \widetilde{H}_{0D} \\ 0 & \widetilde{H}_{SS} & \widetilde{H}_{SD} \\ 0 & \widetilde{H}_{DS} & \widetilde{H}_{DD} \end{pmatrix}$$

and tries to approximate the full CCSDT matrix

$$\widetilde{\mathbf{H}}^{\mathrm{CCSDT}} = \begin{pmatrix} \widetilde{H}_{00} & \widetilde{H}_{0S} & \widetilde{H}_{0D} & 0 \\ 0 & \widetilde{H}_{SS} & \widetilde{H}_{SD} & \widetilde{H}_{ST} \\ 0 & \widetilde{H}_{DS} & \widetilde{H}_{DD} & \widetilde{H}_{DT} \\ 0 & \widetilde{H}_{TS} & \widetilde{H}_{TD} & \widetilde{H}_{TT} \end{pmatrix}$$

by correcting $\widetilde{\mathbf{H}}_{\mathrm{C}}^{\mathrm{CCSD}}$ with second-order triples. Using eq. (2.8.9), and the converged t_1 and t_2 amplitudes, which is a common strategy for non-iterative approaches, the triple-excitation amplitudes are given by the following equation

$$t_3^{[2]} = -\frac{\langle \Phi_3 | \, (\hat{V}_N \hat{T}_2^{\mathrm{CCSD}})_{\mathrm{C}} \, |0\rangle}{\Delta\epsilon_3}. \tag{4.2.1}$$

[a] Different diagnostic tools, like the absolute value of the doubles cluster amplitudes, exist to estimate the multiconfigurational character

The brackets [ ] are used here instead of the parentheses ( ) to denote the use of the converged amplitudes cluster amplitudes at the CCSD level, i.e., $\hat{T}_I^{\mathrm{CCSD}}$. Adding the second-order corrections from the triple amplitudes to the singles and doubles amplitudes in lowest order, results in the following corrected amplitudes

$$\begin{aligned} t_1^{\mathrm{corr}} &= t_1^{\mathrm{CCSD}} - \frac{\langle \Phi_1 | \, (\hat{V}_N \hat{T}_3^{[2]})_{\mathrm{C}} \, | 0 \rangle}{\Delta\epsilon_1} \\ &= t_1^{\mathrm{CCSD}} + t_1^{\Delta} \\ t_2^{\mathrm{corr}} &= t_2^{\mathrm{CCSD}} - \frac{\langle \Phi_2 | \, ([\hat{F}_N + \hat{V}_N] \hat{T}_3^{[2]})_{\mathrm{C}} \, | 0 \rangle}{\Delta\epsilon_2} \\ &= t_2^{\mathrm{CCSD}} + t_2^{\Delta}. \end{aligned}$$

Unlike the expansion of the CC energy in orders of perturbation in sec. 2.8, where the Fock operator was not part of the perturbation, here, the Fock operator appears in the perturbative corrections because canonical HF or semi-canonical orbitals are assumed (see sec. 2.5).

This correction to the CCSD amplitudes has two consequences. First, a correction to the ground-state energy emerges

$$\begin{aligned} \Delta E_{\mathrm{CCSD}}^{\mathrm{corr}} &= \langle 0 | \, \widetilde{H}^{\mathrm{corr}} \, | 0 \rangle \\ &= \langle 0 | \, (\hat{F}_N \hat{T}_1^{\mathrm{corr}})_{\mathrm{C}} \, | 0 \rangle + \langle 0 | \, (\hat{V}_N [\hat{T}_2^{\mathrm{corr}} + \frac{1}{2} (\hat{T}_1^{\mathrm{corr}})^2)])_{\mathrm{C}} \, | 0 \rangle \\ &= \Delta E_{\mathrm{CCSD}} + \langle 0 | \, (\hat{F}_N \hat{T}_1^{\Delta})_{\mathrm{C}} \, | 0 \rangle + \langle 0 | \, (\hat{V}_N \hat{T}_2^{\Delta})_{\mathrm{C}} \, | 0 \rangle \\ &\quad + \frac{1}{2} \langle 0 | \, (\hat{V}_N (\hat{T}_1^{\Delta})^2)_{\mathrm{C}} \, | 0 \rangle + \langle 0 | \, ((\hat{V}_N \hat{T}_1^{\Delta})_{\mathrm{C}} \hat{T}_1^{\mathrm{CCSD}})_{\mathrm{C}} \, | 0 \rangle \, . \end{aligned}$$

Using the λ-amplitude corrections at first order for singles (that do not vanish for the non-canonical HF orbitals case) and doubles amplitudes from eq. (2.8.5) with the converged CC amplitudes, the energy correction can be written as

$$\begin{aligned} \Delta E_{\mathrm{CCSD}}^{\mathrm{corr}} - \Delta E_{\mathrm{CCSD}} &= \langle 0 | \, \frac{\hat{F}_N + (\hat{V}_N \hat{T}_1^{\mathrm{CCSD}})_{\mathrm{C}}}{-\Delta\epsilon_1} (\hat{V}_N \hat{T}_3^{[2]})_{\mathrm{C}} \, | 0 \rangle + \langle 0 | \, \frac{\hat{V}_N}{-\Delta\epsilon_2} ([\hat{F}_N + \hat{V}_N] \hat{T}_3^{[2]})_{\mathrm{C}} \, | 0 \rangle \\ &\quad + \frac{1}{2} \langle 0 | \, (\hat{V}_N (\hat{T}_1^{\Delta})^2)_{\mathrm{C}} \, | 0 \rangle \\ &= \langle 0 | \, \hat{\Lambda}_1^{[1]} (\hat{V}_N \hat{T}_3^{[2]})_{\mathrm{C}} \, | 0 \rangle + \langle 0 | \, \hat{\Lambda}_2^{[1]} ([\hat{F}_N + \hat{V}_N] \hat{T}_3^{[2]})_{\mathrm{C}} \, | 0 \rangle \\ &\quad + \frac{1}{2} \langle 0 | \, (\hat{V}_N (\hat{T}_1^{\Delta})^2)_{\mathrm{C}} \, | 0 \rangle \, . \end{aligned}$$

As stated in the original article,[85] this form of the correction has a similar form to the CCSD(T) correction

$$\Delta E_{\mathrm{CCSD(T)}} - \Delta E_{\mathrm{CCSD}} = \langle 0 | \, \hat{T}_1^{\dagger} (\hat{V}_N \hat{T}_3^{[2]})_{\mathrm{C}} \, | 0 \rangle + \langle 0 | \, \hat{T}_2^{\dagger} ([\hat{F}_N + \hat{V}_N] \hat{T}_3^{[2]})_{\mathrm{C}} \, | 0 \rangle \, ,$$

but resembles more closely the asymmetric correction aCCSD(T)[149,151,152]

$$\Delta E_{\mathrm{aCCSD(T)}} - \Delta E_{\mathrm{CCSD}} = \langle 0 | \, \hat{\Lambda}_1 (\hat{V}_N \hat{T}_3^{[2]})_{\mathrm{C}} \, | 0 \rangle + \langle 0 | \, \hat{\Lambda}_2 ([\hat{F}_N + \hat{V}_N] \hat{T}_3^{[2]})_{\mathrm{C}} \, | 0 \rangle \, ,$$

which uses the converged λ-amplitudes instead. For this reason the correction of Matthews and Stanton for the ground-state energy is named CCSD(T)(a). Second, the corrected Hamiltonian matrix $e^{-\hat{T}^{\mathrm{corr}}} \hat{H}_N e^{\hat{T}^{\mathrm{corr}}}$

$$\widetilde{\mathbf{H}}^{\mathrm{corr}} = \begin{pmatrix} \widetilde{H}_{00}^{\mathrm{corr}} & \widetilde{H}_{0S}^{\mathrm{corr}} & \widetilde{H}_{0D}^{\mathrm{corr}} & 0 \\ \mathbf{Z}_{S0} & \widetilde{H}_{SS}^{\mathrm{corr}} & \widetilde{H}_{SD}^{\mathrm{corr}} & \widetilde{H}_{ST}^{\mathrm{corr}} \\ \mathbf{Z}_{D0} & \widetilde{H}_{DS}^{\mathrm{corr}} & \widetilde{H}_{DD}^{\mathrm{corr}} & \widetilde{H}_{DT}^{\mathrm{corr}} \\ \mathbf{Z}_{T0} & \widetilde{H}_{TS}^{\mathrm{corr}} & \widetilde{H}_{TD}^{\mathrm{corr}} & \widetilde{H}_{TT}^{\mathrm{corr}} \end{pmatrix}$$

has non-zero $\mathbf{Z}_{X0}$ elements, with $X = S, D, T$. These elements do not vanish since the corrected cluster operator $\hat{T}^{\mathrm{corr}}$ does not coincide with the converged $\hat{T}$ of CCSDT. Moreover, they destroy

the size intensivity of the EOM energy and their calculation scales as M^8. To construct a non-iterative correction to EOM-CCSD, the $\mathbf{Z}_{X0}$ elements are removed, restoring the size intensivity and offering a more favourable scaling. In order to restrict the scaling to M^6, the $\langle\Phi_2|\left((\hat{V}_N\hat{T}_3^{[2]})_C\hat{\mu}_1\right)_C|0\rangle$ contributions from the DS block are removed as well. The following matrix is then derived

$$\widetilde{\mathbf{H}}^{\mathrm{CCSD(T)(a)}} = \begin{pmatrix} \widetilde{H}_{00}^{\mathrm{corr}} & \widetilde{H}_{0S}^{\mathrm{corr}} & \widetilde{H}_{0D}^{\mathrm{corr}} & 0 \\ 0 & \widetilde{H}_{SS}^{\mathrm{corr}} & \widetilde{H}_{SD}^{\mathrm{corr}} & \widetilde{H}_{ST}^{\mathrm{corr}} \\ 0 & \widetilde{H}_{DS}^{\mathrm{corr}'} & \widetilde{H}_{DD}^{\mathrm{corr}} & \widetilde{H}_{DT}^{\mathrm{corr}} \\ 0 & \widetilde{H}_{TS}^{\mathrm{corr}} & \widetilde{H}_{TD}^{\mathrm{corr}} & \widetilde{H}_{TT}^{\mathrm{corr}} \end{pmatrix}. \tag{4.2.2}$$

Finding the eigenvalues of the matrix in eq. (4.2.2) would result in an EOM-CCSD(T)(a) solution, which still scales iteratively higher than M^6. Further simplification is achieved by using the strategy of Stanton and Gauss[153] for the star (*) correction. A matrix $\mathbf{A}$ to be diagonalized is divided in subspaces P and Q. The P space is chosen in such a way that it is small enough to be feasible to diagonalize and large enough to contain the most important contributions to the eigenvalue problem. Q is the leftover space. Assuming the exact left $\mathbf{L}$ and right $\mathbf{R}$ eigenvectors are known, the following equations hold

$$\begin{aligned} \begin{pmatrix} A_{PP} & A_{PQ} \\ A_{QP} & A_{QQ} \end{pmatrix} \begin{pmatrix} R_P \\ R_Q \end{pmatrix} &= E \begin{pmatrix} R_P \\ R_Q \end{pmatrix} \\ \begin{pmatrix} L_P & L_Q \end{pmatrix} \begin{pmatrix} A_{PP} & A_{PQ} \\ A_{QP} & A_{QQ} \end{pmatrix} &= \begin{pmatrix} L_P & L_Q \end{pmatrix} E. \end{aligned} \tag{4.2.3}$$

From eq. (4.2.3) the solution in the complementary space is written as

$$R_Q = (E - A_{QQ})^{-1} A_{QP} R_P,$$

which yields an effective eigenvalue problem, which involves only the projected only on P space

$$(A_{PP} + A_{PQ}(E - A_{QQ})^{-1} A_{QP}) R_P = E R_P.$$

Lastly, projecting on the left eigenvector results in

$$L_P(A_{PP} + A_{PQ}(E - A_{QQ})^{-1} A_{QP}) R_P = E. \tag{4.2.4}$$

Substituting $\widetilde{\mathbf{H}}^{\mathrm{CCSD(T)(a)}}$ for $\mathbf{A}$ and regarding the P space to include all the excited determinants needed for the different variants of EOM-CCSD results in a zeroth-order approximation to the EOM-CCSD(T)(a) eigenvalue problem, named EOM-CCSD(T)(a)^0

$$\widetilde{\mathbf{H}}^{\mathrm{CCSD(T)(a)^0}} = \widetilde{\mathbf{H}}_{PP}^{\mathrm{CCSD(T)(a)}}.$$

Diagonalizing the $\widetilde{\mathbf{H}}^{\mathrm{CCSD(T)(a)^0}}$ matrix results in eigenvalues $\Delta E_{\mathrm{EOM-CCSD(T)(a)^0}} = E^{\langle 0\rangle}$, and eigenvectors $\mathbf{R}^{\{0\}} = R_P^{\{0\}}$ and $\mathbf{L}^{\{0\}} = L_P^{\{0\}}$

$$\begin{aligned} \widetilde{\mathbf{H}}^{\mathrm{CCSD(T)(a)^0}} \mathbf{R}^{\{0\}} &= \Delta E_{\mathrm{EOM-CCSD(T)(a)^0}} \mathbf{R}^{\{0\}} \\ \mathbf{L}^{\{0\}} \widetilde{\mathbf{H}}^{\mathrm{CCSD(T)(a)^0}} &= \mathbf{L}^{\{0\}} \Delta E_{\mathrm{EOM-CCSD(T)(a)^0}}. \end{aligned}$$

The exact eigenvectors are then expanded in correction terms

$$\begin{aligned} \mathbf{R} &= \mathbf{R}^{\{0\}} + \mathbf{R}^{\{1\}} + \mathbf{R}^{\{2\}} + \ldots \\ \mathbf{L} &= \mathbf{L}^{\{0\}} + \mathbf{L}^{\{1\}} + \mathbf{L}^{\{2\}} + \ldots \end{aligned} \tag{4.2.5}$$

The curly brackets are used here { } to signify the correction order to the eigenvalue problem, and are different from orders of MP perturbation theory, in which the Hamiltonian matrix is expanded

$$\widetilde{\mathbf{H}}^{\mathrm{CCSD(T)(a)}} = \widetilde{\mathbf{H}}^{(0)} + \widetilde{\mathbf{H}}^{(1)} + \widetilde{\mathbf{H}}^{(2)} + \ldots \tag{4.2.6}$$

Finally, the exact energy is expanded in correction terms of overall order

$$\Delta E_{\text{EOM-CCSD(T)(a)}} = E^{\langle 0\rangle} + E^{\langle 1\rangle} + E^{\langle 2\rangle} + \dots \tag{4.2.7}$$

with $\langle\ \rangle$.

Using the all the different expansions from eq. (4.2.5), (4.2.6) and (4.2.7) in the effective EOM expectation value eq. (4.2.4), results in the following corrections to the eigenvalue

$$\begin{aligned}
E^{\langle 0\rangle} =& \Delta E_{\text{EOM-CCSD(T)(a)}^0} \\
E^{\langle 1\rangle} =& 0 \\
E^{\langle 2\rangle} =& \langle 0|\, \hat{L}_P^{\{0\}} \widetilde{H}_{PQ}^{(1)} (E^{\langle 0\rangle} - \widetilde{H}_{QQ}^{(0)})^{-1} \widetilde{H}_{QP}^{(1)} \hat{R}_P^{\{0\}} \,|0\rangle \\
E^{\langle 3\rangle} =& \langle 0|\, \hat{L}_P^{\{0\}} \widetilde{H}_{PQ}^{(1)} (E^{\langle 0\rangle} - \widetilde{H}_{QQ}^{(0)})^{-1} \widetilde{H}_{QP}^{(2)} \hat{R}_P^{\{0\}} \,|0\rangle + \\
& \langle 0|\, \hat{L}_P^{\{0\}} \widetilde{H}_{PQ}^{(2)} (E^{\langle 0\rangle} - \widetilde{H}_{QQ}^{(0)})^{-1} \widetilde{H}_{QP}^{(1)} \hat{R}_P^{\{0\}} \,|0\rangle + \\
& \langle 0|\, \hat{L}_P^{\{0\}} \widetilde{H}_{PQ}^{(1)} (E^{\langle 0\rangle} - \widetilde{H}_{QQ}^{(0)})^{-1} \widetilde{H}_{QQ}^{(1)} (E^{\langle 0\rangle} - \widetilde{H}_{QQ}^{(0)})^{-1} \widetilde{H}_{QP}^{(1)} \hat{R}_P^{\{0\}} \,|0\rangle \,.
\end{aligned}$$

Corrections from higher orders of the eigenvectors to the energy $\hat{R}^{\{n\}}$, $\hat{L}^{\{n\}}$, contribute to $E^{\langle 4\rangle}$ and higher. Following the perturbation expansion of the EOM vectors made in subsec. 2.8, the lowest-order correction to the eigenvalue is in third order $E^{(3)}$ and includes contributions from $E^{\langle 2\rangle}$, and the first term of $E^{\langle 3\rangle}$

$$E^{(3)} = \langle 0|\, \hat{L}_P^{\{0\}} \widetilde{H}_{PQ}^{(1)} (E^{\langle 0\rangle} - \widetilde{H}_{QQ}^{(0)})^{-1} (\widetilde{H}_{QP}^{(1)} \hat{R}_2^{\{0\}} + \widetilde{H}_{QP}^{(2)} \hat{R}_1^{\{0\}}) \,|0\rangle \,.$$

$E^{(3)}$ constitutes the star correction, which can be written in a simpler manner as

$$E^{(3)} = \frac{\langle 0|\, \hat{L}_3^* \hat{R}_3^* \,|0\rangle}{\Delta E_{\text{EOM-CCSD(T)(a)}^0} - \Delta\epsilon_3}. \tag{4.2.8}$$

The EOM-CCSD(T)(a)* energy is given by

$$\Delta E_{\text{EOM-CCSD(T)(a)}^*} = \Delta E_{\text{EOM-CCSD(T)(a)}^0} + E^{(3)}.$$

4.2.2 The implementation of EOM-CCSD(T)(a)* method for the different EOM-CC variants in QCUMBRE

For the implementation of the EOM-CCSD(T)(a)* method for the different EOM variants, working equations for eq. (4.2.1) for the ground-state correction and the calculation of the CCSD(T)(a) energy are derived. Additional equations beyond the standard EOM-CCSD implementation for the EOM-CCSD(T)(a)^0 eigenvalue problem are required as well. These are found in the singles and doubles space from eq. (4.2.2). Lastly, the star(*) correction from eq. (4.2.8) needs to be implemented.

The working equations from eq. (4.2.1) are the following

$$t_{ijk}^{abc[2]} = \frac{-P(ij/k)P(ab/c)\sum_l \langle lc|\,|ij\rangle\, t_{kl}^{ab} - P(ij/k)P(ab/c)\sum_d \langle ab|\,|dk\rangle\, t_{ij}^{dc}}{\epsilon_i + \epsilon_j + \epsilon_k - \epsilon_a - \epsilon_b - \epsilon_c},$$

which scale as N^7. The $t_3^{[2]}$ amplitudes are then used to correct the singles amplitudes

$$t_i^{a^{\text{corr}}} = t_i^a + \frac{1}{4}\sum_{cdkl} \langle kl|\,|cd\rangle\, t_{ikl}^{acd[2]}$$

and the doubles amplitudes

$$t_{ij}^{ab^{\text{corr}}} = t_{ij}^{ab} + \frac{1}{2}P(ab)\sum_{cdk} \langle bk|\,|cd\rangle\, t_{ijk}^{acd[2]} - P(ij)\frac{1}{2}\sum_{ckl} \langle kl|\,|jc\rangle\, t_{ikl}^{abc[2]}.$$

These equations are handles by the `T_a_corr` function.

For the EOM-CCSD(T)(a)^0 eigenvalue problem, the EOM working equations are the same as for EOM-CCSD for all EOM variants. The corrected $t_1^{\rm corr}$ and $t_2^{\rm corr}$ amplitudes are used instead of the converged CCSD amplitudes, and the intermediates W_{pqrs} saved in `W_pqrs` have the following additional terms:

$$W_{abci} += \frac{1}{2}\sum_{emn} \langle mn| \, |ce\rangle \, t_{mni}^{abe[2]} \qquad\qquad W_{kaij} += -\frac{1}{2}\sum_{efm} \langle km| \, |ef\rangle \, t_{imj}^{efa[2]}$$

The calculation of the intermediates takes place once before the EOM-CC calculation in `EOMIntermediatesS`.

Lastly for the star(*) correction, the workings equations for the left and right amplitude corrections are the following for the EE and the SF variant

$$\begin{aligned}
l_{abc}^{ijk(*)} =& P(bc/a)P(jk/i) l_a^i \, \langle jk| \, |bc\rangle + P(bc/a)P(jk/i) l_{bc}^{jk} f_{ia} \\
&- P(ab/c)P(ij/k)\sum_l l_{ab}^{kl} \, \langle ij| \, |lc\rangle - P(ab/c)P(ij/k)\sum_d l_{dc}^{ij} \, \langle dk| \, |ab\rangle \\
r_{ijk}^{abc(*)} =& - P(ij/k)P(ab/c)\sum_l \langle lc| \, |ij\rangle \, r_{kl}^{ab} - P(ij/k)P(ab/c)\sum_d \langle ab| \, |dk\rangle \, r_{ij}^{dc} \\
&+ P(ij/k)P(ab/c)\sum_l \left(\sum_m \langle lm| \, |ij\rangle \, r_m^c + P(ij)\sum_d \langle lc| \, |di\rangle \, r_j^d \right) t_{kl}^{ab^{\rm corr}} \\
&- P(ij/k)P(ab/c)\sum_l \left(\sum_d \langle ab| \, |de\rangle \, r_k^e + P(ab)\sum_l \langle la| \, |di\rangle \, r_l^b \right) t_{ij}^{dc^{\rm corr}},
\end{aligned}$$

giving the following energy correction

$$E^{(3)} = \frac{1}{36}\sum_{abcijk} \frac{l_{abc}^{ijk(*)} \, r_{ijk}^{abc(*)}}{E^{\langle 0\rangle} + \epsilon_i + \epsilon_j + \epsilon_k - \epsilon_a - \epsilon_b - \epsilon_c}.$$

For IP, the vectors are given by

$$\begin{aligned}
l_{bc}^{jki(*)} =& P(jk/i) l^i \, \langle jk| \, |bc\rangle + P(bc)P(ij/k) l_b^{ji} f_{kc} \\
&- P(bc)P(jk/i)\sum_l l_b^{li} \, \langle jk| \, |lc\rangle + P(ij/k)\sum_d l_d^{ji} \, \langle dk| \, |bc\rangle \\
r_{jki}^{bc(*)} =& - P(ij/k)P(bc)\sum_l \langle lc| \, |jk\rangle \, r_{li}^b + P(ij/k)\sum_d \langle bc| \, |dk\rangle \, r_{ji}^d \\
&+ P(ij/k)\sum_{lm} \langle lm| \, |ij\rangle \, r_l t_{mk}^{bc^{\rm corr}} + P(jk/i)P(bc)\sum_{dl} \langle lb| \, |di\rangle \, r_l t_{jk}^{dc^{\rm corr}}
\end{aligned}$$

and the correction by

$$E^{(3)} = \frac{1}{12}\sum_{bcijk} \frac{l_{bc}^{jki(*)} \, r_{jki}^{bc(*)}}{E^{\langle 0\rangle} + \epsilon_i + \epsilon_j + \epsilon_k - \epsilon_b - \epsilon_c}.$$

For EA, the vectors are given by

$$\begin{aligned}
l_{bca}^{jk(*)} =& P(bc/a) l_a \, \langle jk| \, |bc\rangle + P(ab/c)P(jk) l_{ba}^j f_{kc} \\
&- P(ab/c)\sum_l l_{ba}^l \, \langle jk| \, |lc\rangle + P(bc/a)P(jk)\sum_d l_{da}^j \, \langle dk| \, |bc\rangle \\
r_{jk}^{bca(*)} =& - P(ab/c)\sum_l \langle lc| \, |jk\rangle \, r_l^{ba} + P(jk)P(bc/a)\sum_d \langle bc| \, |dk\rangle \, r_j^{da} \\
&+ P(ab/c)\sum_{de} \langle ab| \, |de\rangle \, r^d t_{jk}^{ec^{\rm corr}} - P(jk)P(bc/a)\sum_{dl} \langle la| \, |dj\rangle \, r^d t_{lk}^{bc^{\rm corr}},
\end{aligned}$$

giving the following energy correction

$$E^{(3)} = \frac{1}{12} \sum_{bcajk} \frac{l_{bca}^{jk^{(*)}} r_{jk}^{bca^{(*)}}}{E^{\langle 0 \rangle} + \epsilon_j + \epsilon_k - \epsilon_b - \epsilon_c - \epsilon_a}.$$

The star(*) correction is implemented in the `EOM_CCSD_star` function.

The implementation of the EOM-CCSD(T)(a)* method for different EOM variants was verified as follows. For the ground state and EE-EOM in the closed-shell field-free case, the implementation was checked against CFOUR. For open-shell systems, it was checked that the energy without the spin-Zeeman contribution is the same for a given system irrespective of the M_S quantum number. As the code in QCUMBRE for either RHF and UHF is equivalent, i.e., there exists no specific RHF implementation, the combination of the two tests yields a strong indication for the validity of the implementation. In the case of ff calculations, the imaginary part of the excitation energy was considered: If the imaginary part is non-zero, it should be smaller at the EOM-CCSD(T)(a)* level compared to EOM-CCSD. FCI results are Hermitian and exact thus having zero imaginary part for the energy eigenvalues. Approaching the FCI limit from the EOM-CCSD to the EOM-CCSD(T)(a)* level of theory is expected to partially correct this unphysical behaviour. Having excluded most errors in the implementation by validating the field-free case, possible errors that only affect the magnetic-field part within the ff calculations may only arise from a false or missing complex conjugation. The decrease of the imaginary part is a strong indication for the absence of such errors. The SF variant was checked to deliver the same energy (excluding the spin-Zeeman term) for different M_S components of the same state, starting from a closed-shell reference. Lastly the IP and EA variants were checked by excitations to and from continuum orbitals (that were generated as described in app. B) using the EE-EOM-CCSD(T)(a)* functions (excluding the spin-Zeeman term).

4.3 Molecular spectra

In this section, the CC2, CC3, and EOM-CCSD(T)(a)* methods are applied to small and medium-sized molecules. The results are then compared against the parent CCSD and CCSDT methods. Beyond the study of the electronic-excitation spectra of molecules in the presence of a magnetic field, the applications presented in the following paragraphs function first to test the accuracy of the implemented methods in the presence of a magnetic field and also to demonstrate their applicability to larger systems.

Studying the CH molecule could eventually contribute to the interpretation of MWD spectra. CH and C_2 have been observed in cool weakly magnetised WDs with a He dominated atmosphere, based on simple approximations for the molecular magnetic dichroism of these species.[40,41] Based on this motivation, the CH^+ cation was studied using the approximate CCn techniques and compared to CCSD, CCSDT, and FCI results from previous studies.[80] In addition, the open-shell CH molecule was targeted. CH is proven to be a challenging system and can act as a stress test for the implemented approximate methods.

Moreover the spectra of the small organic molecules CH_4 and $CH_2{=}CH_2$ were studied at relaxed geometries for specific orientations of the magnetic field (see chap. 7) at the CC2 and CCSD levels of theory. In this case, the performance of the CC2 approximation is put to the test, not only regarding the excitation energies, but also on the influence of the magnetic field on the geometry.

Lastly, the CC2 method was employed to study energetically low-lying electronic states of the heteroatomic pyrrole in the presence of a magnetic field. This way, the applicability of the method is exhibited for the study of medium-sized systems, that may prove too expensive for a study at the full CCSD level of theory.

4.3.1 The methylidinium cation CH^+

The methylidinium ion has been studied at the (EOM-)CCSD and CCSDT level in ref. [80], for varying magnetic-field strengths and angles ϕ with respect to the magnetic field. It was observed

that the CCSDT results are practically indistinguishable from those at the FCI level of theory. Following this study, the approximate ff-CCn methods were tested for this system, examining whether the (EOM-)CC3 method produces results of a quality comparable to CCSDT, and also to test the performance of (EOM-)CC2.

Results are shown in fig. 4.3 for a distance of 2.1275 a_0 between the atoms, which is the optimized CCSD/cc-pVDZ geometry for the ground state $^1\Sigma^+$ (purple) in the absence of magnetic field. This ground state, which is dominated by a single closed-shell configuration $1\sigma^2 2\sigma^2 3\sigma^2$, was chosen as the reference state for the EOM-CC approach. The first excited state is a degenerate $^1\Pi$ state (red and blue), described by a $1\sigma^2 2\sigma^2 3\sigma^1 1\pi^1$ configuration, and the second excited state is a degenerate $^1\Delta$ state (yellow), described by a $1\sigma^2 2\sigma^2 1\pi^2$ configuration. The $^1\Delta$ state has a predominant double-excitation character with respect to the $^1\Sigma^+$ reference, and as has been noted in ref. [80] is not well described at the CCSD level of theory. As further explained later in the subsection, the double-excitation character of this state, besides making the state unavailable at the EOM-CC2 level, influences the accuracy of other states when avoided crossings are encountered. The presence of the magnetic field reduces the linear symmetry of the molecule ($C_{\infty v}$) depending on the angle of the magnetic-field direction relative

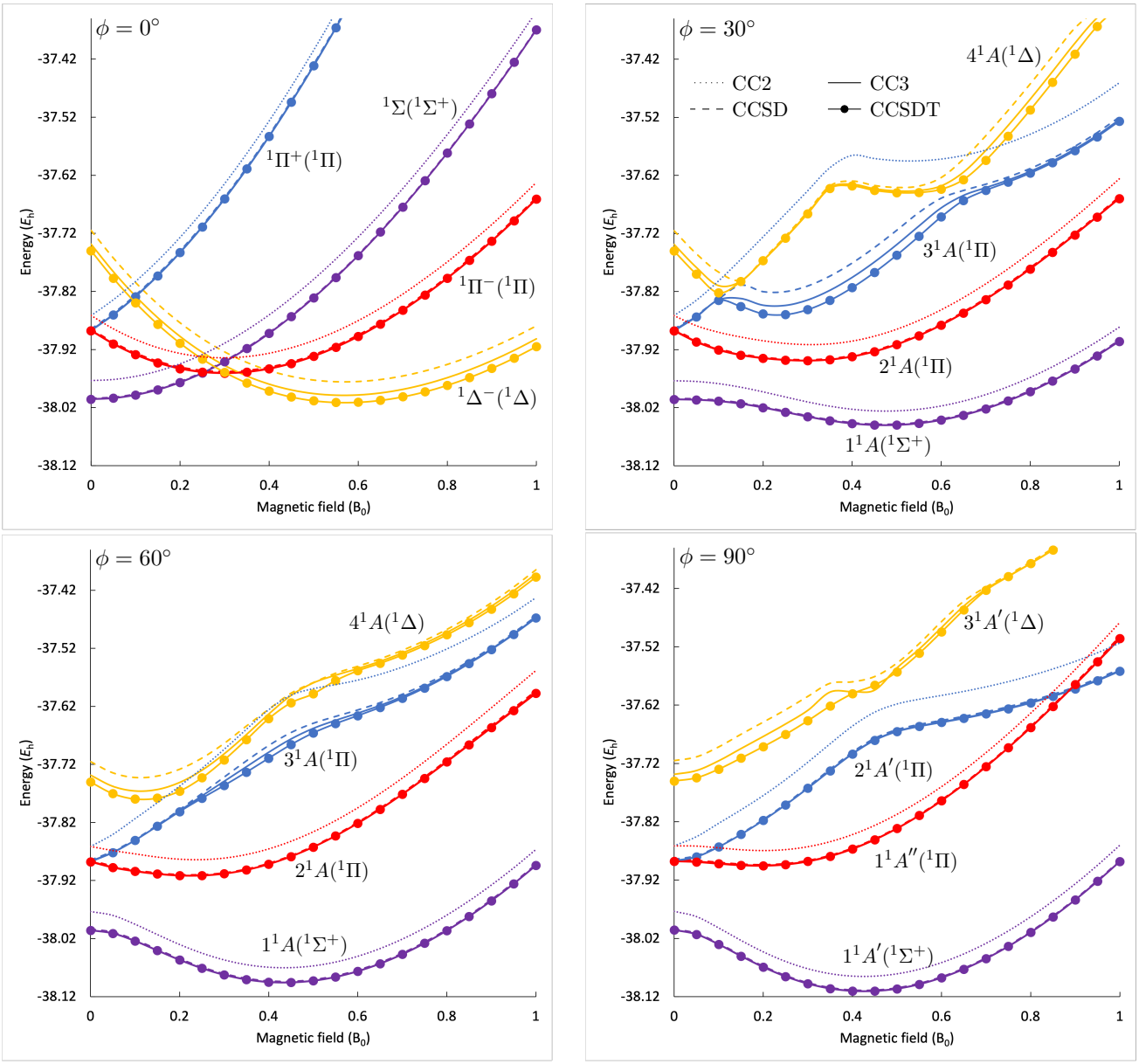

Figure 4.3: The low-lying singlet states of CH^+ as a function of the magnetic-field strengths for different direction of the molecule at the (EOM-)CC2 , CCSD, CC3 and CCSDT levels of theory with the contracted cc-pVDZ basis set.

to the molecular bond ϕ. In the parallel direction ($\phi = 0°$), the linearity is preserved resulting in C_∞, in the perpendicular direction $\phi = 90°$, a mirror plane passing through the molecular axis is preserved (C_s), while no symmetry elements exist for the skewed orientations $\phi = 30°, 60°$ (C_1). In all directions, the degeneracy of degenerate states is lifted. For the $^1\Delta$ state, only the energetically lower component was targeted.

For a parallel magnetic-field direction ($\phi = 0°$, C_∞) the total energies of the states are plotted in the upper left panel of fig. 4.3) as a function of the magnetic-field strength. The system remains highly symmetric. All involves states are associated to different IRREPs and as a results, no mixing between the targeted states takes place when they respond to the influence of the magnetic field. Π and Δ states split into their respective M_L components. This splitting is then trivially calculated as $\Delta E = |B||M_L|$. There is no spin-Zeeman contribution since all states are singlets ($M_S = 0$). The components with a negative M_L value are initially stabilised in weaker fields before the influence of the diamagnetic term dominates, in stronger fields. The $^1\Sigma$ ($M_L = 0$, purple curve) state only interacts diamagnetically with the magnetic field.

Total energy for angles 30° and 60° (C_1) are presented in the upper right and down left panel of fig. 4.3. All degeneracies are lifted in a non trivial manner and because of the lack of symmetry, avoided crossings arise. In the the perpendicular direction ($\phi = 90°$, C_sm down right panel), the degenerate states split into an A' and an A'' component, that do not mix and are allowed to cross. Unlike in the parallel direction, the paramagnetic (orbital-Zeeman) and diamagnetic interactions for the different states are not easily distinguished, and the allowed mixing results in closed-shell paramagnetism for the ground state in weaker fields.[13,154]

CC2 is not able to describe states with predominant double-excitation character. For this reason, CC2 results for the $^1\Delta$ state (yellow) are absent in the calculations. Regarding states with predominant single-excitation character, CC2 results for this system are higher in energy compared to results at the other levels of theory. The shift is nonetheless rather constant and does not influence the excitation energies nor the overall behaviour much. More specifically, for the parallel direction, the mean deviation from the CCSDT results for the excitation energies with a predominant single-excitation character is of the order of 10^{-2} E_h for CC2, 10^{-3} E_h for CCSD, and 10^{-4} E_h for CC3. For the $^1\Delta$ state, the mean error drops from $3.6 \cdot 10^{-2}$ E_h for CCSD by more than half to $1.2 \cdot 10^{-2}$ E_h for CC3.

In all non-parallel magnetic-field directions, the avoided crossings that arise between the original $^1\Delta$ state and the other states result in a transfer of the double-excitation character.[80] This is problematic, because firstly, a single state is not described with the same accuracy for every magnetic-field strength. Secondly, the field strength at which the (avoided) crossing is encountered is strongly method dependent. A transfer of the double-excitation character from the $4^1A(^1\Delta)$ state (yellow) to the $3^1A(^1\Pi)$ state (blue) is observed for the skewed magnetic-field orientations for magnetic fields at the range of 0.1 - 0.6 B_0. The transfer is most clearly seen at 30°, where the deviation relative to the CCSDT results changes abruptly from 10^{-2} E_h to 10^{-3}–10^{-4} E_h at the CCSD and CC3 levels of theory. CC2 proves to be particularly inappropriate for these cases. At 30°, the curve for the state arising from $^1\Pi$ (blue) is qualitatively different compared to the predictions at the other levels of theory. Due to the fact that the predominant double-excitation character cannot be described within CC2, the avoided crossing is simply not found. Instead, the curve follows the 4^1A state for field strengths greater than 0.1 B_0. Hence, for CC2, for resulting artificial state (blue dotted curve) is a nonphysical combination of two different (physical) states.

For the reference state (purple) and for the other component of the initial $^1\Pi$ state which is not involved in avoided crossings (red), the errors relative to CCSDT remain rather constant even for the skewed and perpendicular orientations. CC2 shows a maximum deviation of $3.6 \cdot 10^{-2}$ E_h relative to CCSDT, CCSD a maximum deviation of $4.3 \cdot 10^{-3}$ E_h, and finally CC3 a maximum error of $1.6 \cdot 10^{-3}$ E_h. In fact, the average deviation of CC3 is even one order of magnitude smaller than the maximum error, i.e., $5.7 \cdot 10^{-4}$ E_h, making the CC3 results practically indistinguishable from CCSDT.

For the more complicated 3^1A and 4^1A cases (blue and yellow, respectively), where a strong double-excitation character is present, the CCSD results have a larger error of about 10^{-2} E_h on average. This rather poor accuracy is improved by one order of magnitude at the CC3 level of theory. The error fluctuation for different magnetic-field strengths is also reduced by a large extent.

This study proves the CC2 method to be rather untrustworthy for systems where avoided crossings with predominantly doubly-excited states appear. In such cases, CC2 may yield non-physical results. On the other hand, using CC3 as an approximate triples correction seems to work well, even in cases where the state acquires a significant double-excitation character.

4.3.2 The CH radical

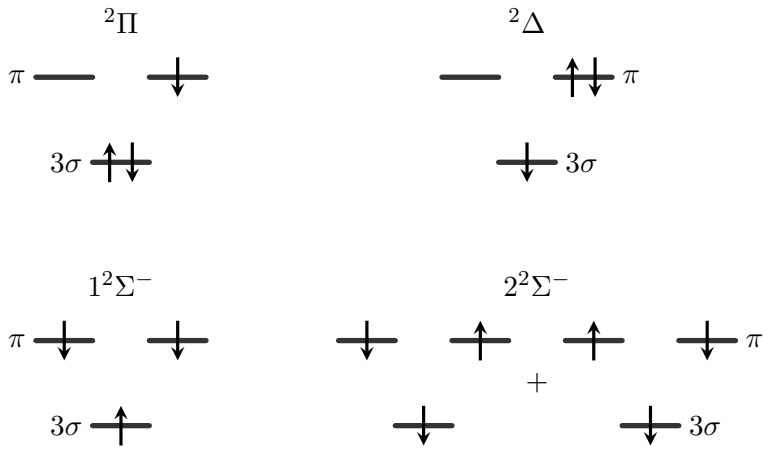

Figure 4.4: Electron configuration of the valence orbitals for the $^2\Pi$, $^2\Delta$, $1^2\Sigma^-$, and $2^2\Sigma^-$ states of the CH radical in the absence of magnetic field.

The CH radical was investigated in the presence of a magnetic field with two different approaches.

First, CH was studied at the (EOM-)CC2, CCSD, CC3 and CCSDT levels of theory using an uncontracted (unc) cc-pVDZ basis at a field-free optimized geometry at the CCSD level of 2.1431 Bohr interatomic distance.

The energy of the low-lying singlet states of the molecule is plotted as function of the magnetic-field strength for a parallel orientation of the magnetic field, as well as for skewed orientations of 30° and 60° angles relative to the molecular bond in fig. 4.5. In the absence of the magnetic field, the ground state of the molecule is a doubly degenerate $^2\Pi$ state (red and blue) with a predominant open-shell configuration $1\sigma^2 2\sigma^2 3\sigma^2 1\pi^1$. Choosing one of the components of this state as the reference state, introduces a bias to the subsequent EOM-CC calculation. This arises from the symmetry breaking, which treats the two Π components differently, one as a CC reference state and one as an excited EOM-CC state. As a result, the degeneracy of the two components is broken. The severity of this effect is quantified by the energy difference, which amounts to about $\sim 10^{-4}$ E_h at the CC2 and CCSD levels of theory, about $\sim 10^{-5}$ E_h for CC3, and about $\sim 10^{-6}$ E_h for CCSDT, showing that, as should be the case, the problem diminishes when going towards FCI. The degenerate excited $^2\Delta$ state (yellow and green) described by a $1\sigma^2 2\sigma^2 3\sigma^1 1\pi^2$ configuration was studied as well. For this state, one of the components (yellow) is characterised predominantly by a single excitation relative to the reference, while the other (green) is doubly excited and was studied only for the parallel direction of the magnetic-field. The doubly-excited component cannot be targeted at all at the EOM-CC2 level. The deviation from degeneracy is significantly larger for this state because of the double-excitation character of the second component. It amounts to about $\sim 10^{-2}$ E_h for CCSD and CC3, and for CCSDT to about $\sim 10^{-3}$ E_h. Lastly, two excited $^2\Sigma^-$ states were studied. The one lower in energy has a predominant $3\sigma^{\uparrow}1\pi^{-\downarrow}1\pi^{+\downarrow}$ configuration (purple) with a weight of about 0.51, while the second (pink) is a multiconfigurational state with predominant $\left(3\sigma^{\downarrow}1\pi^{-\downarrow}1\pi^{+\uparrow} + 3\sigma^{\downarrow}1\pi^{-\uparrow}1\pi^{+\downarrow}\right)$ configuration. Apart from the fact that due to the symmetry breaking in the reference, the configurations no longer have the same weight, one of the configurations is doubly excited with respect to the reference. Typically, EOM approaches are applicable to excited states with a multiconfigurational character, as long as the strongly contributing determinants are singly excited,[155] which is not the case here. The electron configuration of the valence orbitals for these four states is diagrammatically presented in fig. 4.4.

In the parallel direction, the reduction of symmetry is minimal, similar to the cationic case, and only minor mixing is observed between the states of the same symmetry (two $^2\Sigma$ states). No avoided crossings take place. The orbital-paramagnetic interaction of the states is described by their M_L quantum number. Unlike in the cationic case, the paramagnetic interaction includes the spin-Zeeman term with $M_S = -\frac{1}{2}$. For all states with $M_L \leq 0$, the paramagnetic influence results in a minimum in weaker fields, before the energy is raised by the diamagnetic term in second order. For $M_L = 1$, the spin-Zeeman and orbital-Zeeman term cancel each other, and the $^2\Pi^+$ state (blue curve) only reacts diamagnetically to the field. The $^2\Pi^-$ component (red), which is the lowest in energy state for fields up to 0.25 B_0, is chosen as the reference state for the calculations. The $^2\Delta^-$ state becomes lower in energy than the reference state for stronger fields. CC3 yields energies very close to CCSDT. CCSD results only show a significant deviation from CCSDT for the excited states with a significant double-excitation character, i.e., the two $^2\Sigma$ states (purple and pink) and the $^2\Delta^+$ state (green). For the predominant singly-excited states and the $1^2\Sigma$ state (purple), the CC2 results follow the CCSDT

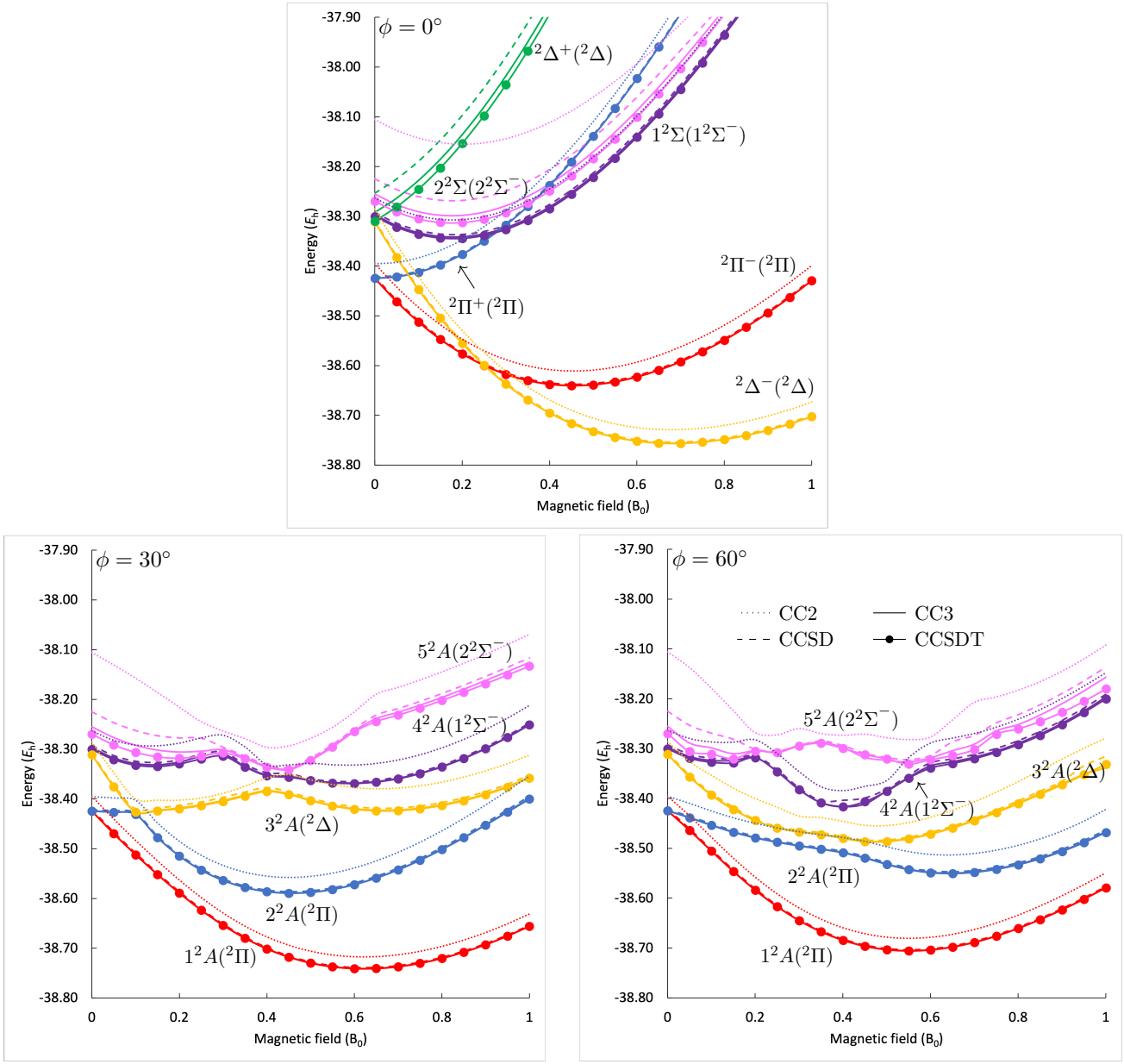

Figure 4.5: Low-lying singlet states of CH as a function of the magnetic-field strengths for a direction parallel (upper), with $\phi = 30°$ (lower left), $\phi = 60°$ (lower right) relative to the molecular bond obtained at the (EOM-)CC2, CCSD, CC3 and CCSDT levels of theory using the unc-cc-pVDZ basis set.

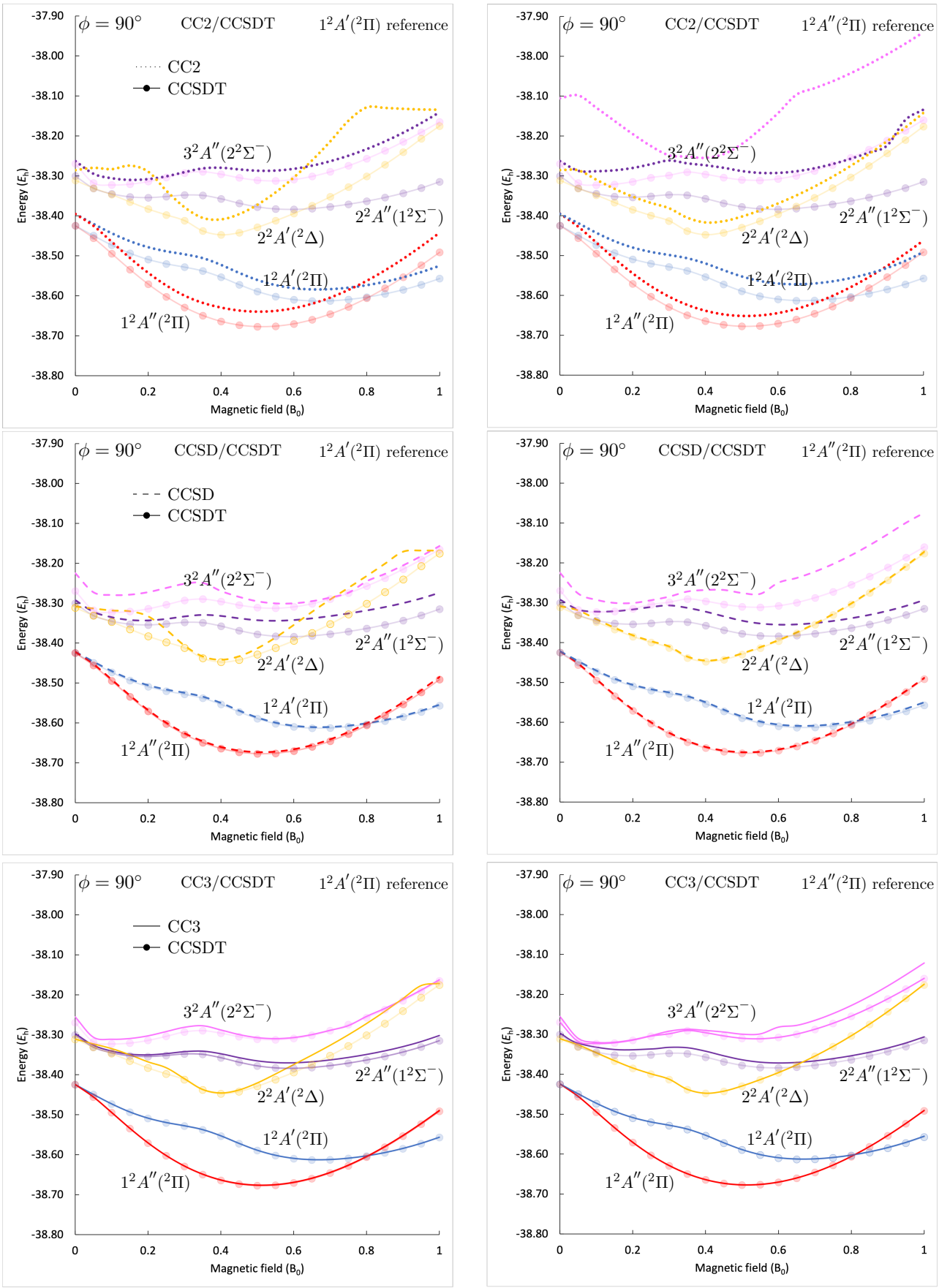

Figure 4.6: Comparison of CC2 (upper panel), CCSD (middle panel), and CC3 (lower panel) with CCSDT results (transparent curves) obtained using the unc-cc-pVDZ basis set for the low-lying states of the CH radical with different reference states: $1^2A'$ (blue) left column, $1^2A''$ (red) right column. The magnetic-field direction is perpendicular to the molecular bond.

curves in a parallel manner, albeit with a discrepancy of about $\sim 10^{-2} E_\mathrm{h}$. Calculating the excitation energies results in an error cancellation, that lowers the energy deviation by one order of magnitude, enabling at least a qualitatively correct prediction at the CC2 level. The $2^2\Sigma$ state (pink) shows a very large deviation of the CC2 energies from CCSDT of about 0.16 E_h in the field-free case due to the significant contribution from the doubly excited configuration with respect to the reference. For stronger magnetic fields, however, the double-excitation character becomes less important in the wavefunction, and the error at the CC2 level decreases accordingly.

As for the skewed directions in the lower panel of fig. 4.5, the 1^2A state (red) is chosen as reference state. Similar to the cationic case, the paramagnetic and the diamagnetic interactions are mixed. Only the spin-Zeeman interaction can be clearly recognized by the spin quantum number $M_S = -\frac{1}{2}$. Because the CC calculation is based on an unrestricted approach for the radical, spin contamination appears. Spin contamination at the CCSD and CC2 levels of theory is typically low for the reference states because of the inclusion of correlation together with the effective orbital relaxation of single t_1 excitations,[88,142] but EOM-CC states are much more sensitive to spin contamination of the UHF reference.[156] This is particularly prominent for the skewed orientations where strong mixing with the $M_S = -\frac{1}{2}$ component of a quartet states is observed for the $3^2A(^2\Delta)$, $4^2A(1^2\Sigma^-)$, and $5^2A(2^2\Sigma^-)$ states. The interfering state arises from the $^4\Sigma^-$ field-free state with a $3\sigma^1 1\pi^{-1} 1\pi^{+1}$ configuration, which appears energetically below the excited doublet states. The spin-expectation values for these states are shown in table 5.1 for different magnetic-field strengths.[b] These values not only help to assess the quality of the calculations but also contribute to the assignment of the states based on their multiplicity. Results at the CCSD and CC3 level exhibit the expected deviations from CCSDT, i.e., a deviation of about 10^{-3} E_h for CCSD and 10^{-4} E_h for CC3 in the case of a predominant single-excitation character, and of about 10^{-2} E_h in the case of double-excitation character. The CC2 method, still offers a crude qualitative description of the three lowest in energy states, but proves particularly problematic for the states arising from the $^2\Sigma^-$ states (purple and pink). The behaviour of the 4^2A (purple) and 5^2A (pink) states at the CC2 level is in many cases qualitatively different compared to the results from the more precise methods, especially for the state highest in energy (pink). For example, using CCSD, CC3, or CCSDT, the 5^2A state (pink) at the $\phi = 60°$ orientation is predicted to have a relatively constant energy for field strengths between B = 0 - 0.2 B_0. It is raised in energy until ~ 0.35 B_0 reaching a local maximum and exhibits a diamagnetic behaviour for $B > 0.6$ B_0. At these levels the state is also found in close energetical proximity to the 4^2A state (purple). At the CC2 level however, the 5^2A state (pink) is stabilised for B = 0 - 0.2 B_0, then remains relatively constant between $B = 0.25$ B_0 and $B = 0.6$ B_0, and then finally raises in energy for stronger magnetic fields, albeit with a different slope compared to the other levels of theory. It is also not found in close energetical proximity to the 4^2A state (purple), but instead exhibits two avoided crossings at $B = 0.25$ B_0 and $B = 0.6$ B_0.

The results for the magnetic-field orientation perpendicular to the bond are shown in fig. 4.6. In order to assess to what extent the choice of reference affects the results at the approximate levels of theory, both components of the field-free ground state $^2\Pi \rightarrow {}^2A', {}^2A''$ were tested as reference states. The symmetry and degeneracy breaking that arises from the choice of reference should become less important when approaching the FCI limit. In the left column, the results using the $^2A'$ (blue) components as a reference are shown, while in the right column, the $^2A''$ (red) component is targeted as a CC reference, which is lower in energy up to $B = 0.8$ B_0. For clarity, in every panel, the CCSDT results are compared against the results of one other method at a time, i.e., the CC2 results in the upper, the CCSD results in the middle, and the CC3 results in the lower panel. CC2 results prove to be rather sensitive to the choice of reference. Specifically, it is observed for the two components of the field-free ground state, i.e., the $1^2A'$ (blue) and $1^2A''$ (red) states, that they cross in different magnetic-field strengths based on the reference. The states cross at about 0.75 B_0 = 180 kT when using $1^2A'$ (blue) as reference and at about 0.9 B_0 = 210 kT when using $1^2A''$ (red) as reference. This amounts to about 0.15 B_0 = 35 kT difference. At all higher levels of theory, the two states cross at 0.8 B_0 consistently. The behaviour of the $2^2A'$ state (yellow) is also strongly reference dependent at the CC2 level of theory. Moreover, the $3^2A''$ (pink) state could not be targeted at the CC2 level

[b] For more details on the spin-expectation value as a diagnotstic and interpretational tool see sec. 5.2.

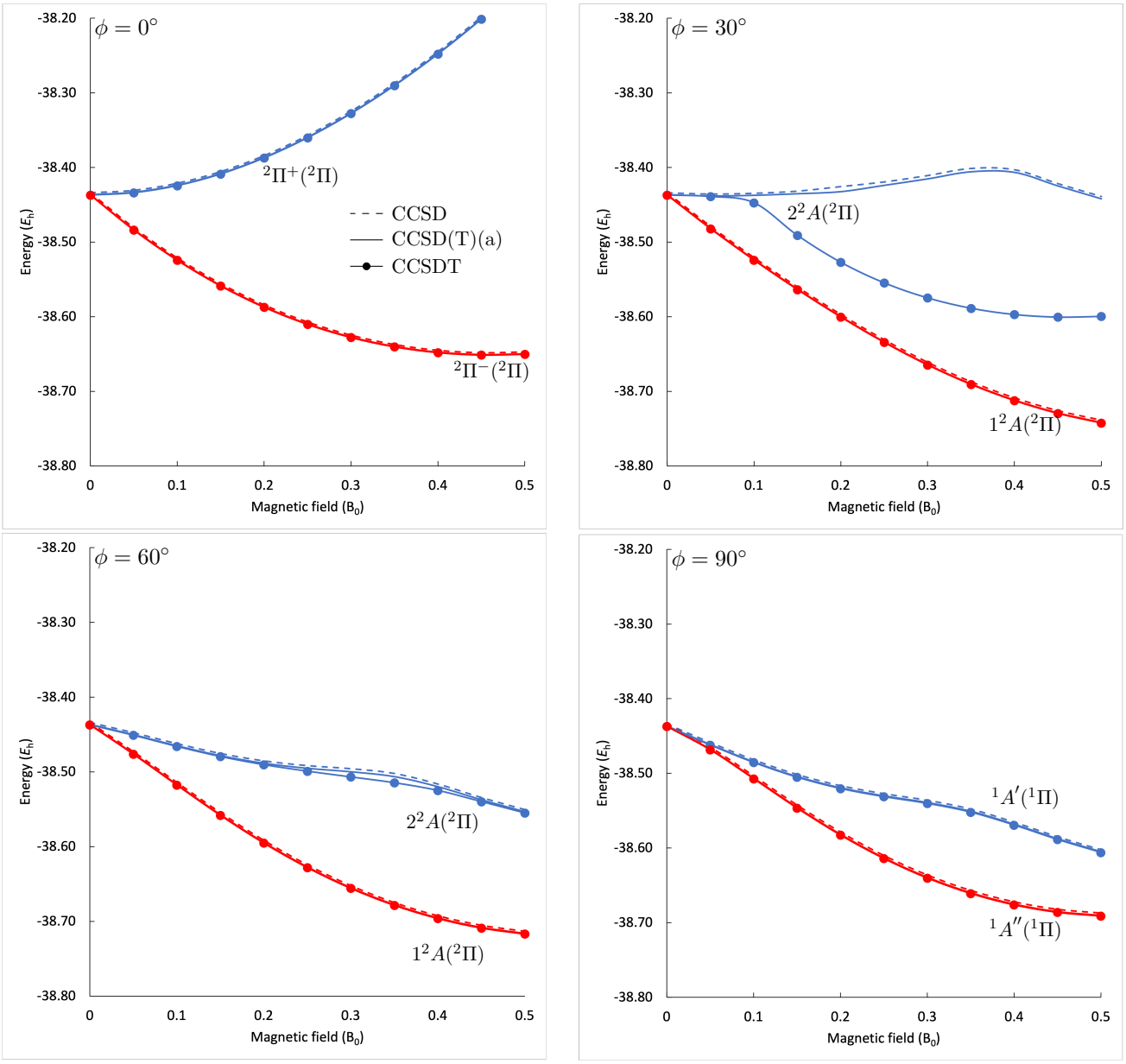

Figure 4.7: The two components of the $^2\Pi$ field-free ground state of CH in different magnetic-field orientations at the EA-EOM-CCSD and CCSD(T)(a)* levels of theory compared to EE-EOM-CCSDT results obtained using the unc-aug-cc-pCVDZ basis set.

when using the $^2A'$ (blue) reference. With both references, however, the $2^2A''$ (purple) state at CC2 shows a behaviour quite similar to that of the $3^2A''$ (pink) state at the CCSDT level. The CCSD approach performs equally well for the $1^2A'$ (blue) and $1^2A''$ (red) states, but the behaviour of the $2^2A'$ (yellow), $2^2A''$ (purple), and $3^2A''$ (pink) states changes for the two different references. At the CCSD level, the $1^2A''$ (red) reference is proven to be a better choice for the description of the $2^2A'$ state (yellow), shown by smaller energetic deviations relative to CCSDT and by lower spin contamination as evidenced in table 5.2, but a larger deviation and a stronger spin contamination is observed for the $3^2A''$ state (pink).[b] The energy deviation of the CC3 results relative to those at the CCSDT level is adequately small for both choices for the reference, with the $3^2A''$ state (pink) being described slightly better with the $1^2A'$ (blue) reference, and the $2^2A'$ state (yellow) with the $1^2A''$ (red) reference. This finding confirms that the CC3 method is a decent CCSDT substitute. The results at the CCSDT level do not change much for the different choices of the reference, as expected when going towards FCI. Even an approximate inclusion of triples correction at the CC3 level imitates this desired behaviour to a satisfactory extent.

The CH radical was further studied after this initial approach in the context of the Bachelor thesis of Lena Reimund,[157] which was completed under my supervision. Two strategies were used in an attempt to eliminate the symmetry-breaking bias. The first strategy uses the EA-EOM-CC approach starting from the closed-shell $^1\Sigma^+$ state of the cation. Using this reference the two components of the radical ground state $^2\Pi$ were targeted. The second strategy, on the other hand, employs the SF-EOM-CC approach starting from the $M_S = -\frac{3}{2}$ component of the quartet $^4\Sigma^-$ state mentioned in the previous paragraphs, which is the quartet state lowest in energy in the absence of magnetic field. Using the SF-EOM-CC approach all states studied so far are characterised by a predominant single-excitation character. The calculations were performed using an unc-aug-cc-pCVDZ basis set and an interatomic distance of 2.1410 a_0, which corresponds to the optimized geometry for the $^2\Pi$ state in the absence of field at the CCSD level of theory. The system was studied up to 0.5 B_0 at the EOM-CCSD level and, to account for approximate triples, at the EOM-CCSD(T)(a)* level. These results were compared to the EE-EOM-CCSDT results.[c]

The results obtained using the EA-EOM-CC approach for the two components of the field-free ground state of CH are shown in fig. 4.7. For magnetic-field orientations other than 30°, there is good agreement between the EA-EOM-CC and the (EE-)CCSDT results. Moreover, when approximate triples are considered within the EOM-CCSD(T)(a)* approach, the results are in most cases indistinguishable from those at the CCSDT level. In an orientation of 30° of the magnetic field relative to the molecular bond, the avoided crossing that is observed at 0.15 B_0 when using the EE-EOM-CC approach is completely absent from the EA-EOM-CC results. The excited state higher in energy that participates in this avoided crossing is the $3^2A(^2\Delta)$ state, which is doubly-excited with respect to the closed-shell reference of the cation. As a result, when using the EA-EOM-CC approach, this state is accompanied with a large positive error. This is a consequence of the insufficient accuracy for predominantly doubly-excited states at the EOM-CCSD level. Hence, the state in question is wrongly predicted to be energetically much higher than the other predominantly singly excited states. The avoided crossing is "missed", resulting in the observed unphysical behaviour of the EOM-EA curves. All states not arising from the degenerate ground $^2\Pi$ state in the absence of field were not targeted using the EA-EOM-CC approach because they are predominantly doubly-excited with respect to the reference to begin with. Evaluating the EA-EOM-CC approach for the study of the CH radical, it is concluded that, despite the absence of the symmetry-breaking bias, fewer states could be targeted compared to the EE-EOM-CC approach. Since the symmetry-breaking bias is manageable and quantifiable when using the EE-EOM-CC approach, the EA-EOM-CC approach is deemed less appropriate for this system.

Using the SF-EOM-CC approach allows in principle to target all states that were also studied using the EE-EOM-CC approach. In fig. 4.8, the energies of the states are plotted as a function of the magnetic-field strength at the SF-EOM-CCSD and SF-EOM-CCSD(T)(a)* levels of theory and they are compared to the EE-EOM-CCSDT results.[c] The $M_S = -\frac{1}{2}$ component of the state originating from the field-free $^4\Sigma^-$ state (thin purple curve) is shown in the results as well. Using the SF-EOM-CC approach both components of the $^2\Delta$ state can be targeted and studied in different orientations of the magnetic field. In the highly symmetric parallel case, it is found that the EOM-CCSD(T)(a)* results (continuous curves) are in very good agreement with and practically indistinguishable from the CCSDT results (continuous curves with points).

The results for the skewed and perpendicular magnetic-field orientations, however, reveal a complexity for the system that was not fully captured in the previous analysis solely based on EE-EOM-CC results. The three states lower in energy (red, blue, and yellow) as well as the quartet state (thin purple) are in good agreement using the different approaches, and the EOM-CCSD(T)(a)* results are again a very good approximation for the full inclusion of triples. The treatment of the other states, however, is less straightforward. In the presence of a magnetic field, the state that originates from the second component of the $^2\Delta$ state (green) is allowed to mix with the states originating from the $^2\Sigma^-$ states. This, together with the fact that the two components of this $^2\Delta$ state cannot be targeted consistently at the EE-EOM-CC level since one of the components has a predominant

[c]The EE-EOM-CCSDT results use the $^2\Pi^-$ state (red) in the parallel orientation, the 1^2A state (red) in the skewed orientations, and the $1^2A''$ state (red) in the perpendicular orientation as a reference.

double-excitation character with respect to the reference and hence the two components are not degenerate in the absence of field, has resulted in a false assignment at the EE-EOM-CC level. Namely, the state previously assigned to have originated from $1^2\Sigma^-$ (purple) rather corresponds to the second component of the $^2\Delta$ state. This is indicated in the areas labeled as 1 in fig. 4.9. In the perpendicular case (lower panel of fig. 4.9), the aforementioned coincidence is true for all non-zero magnetic-field strengths studied and is an indication in favour of the assignment based on the SF-EOM-CC results. Additional evidence of the required reassignment is the coincidence of the state that originates from the $1^2\Sigma^-$ state (purple) at the SF-EOM-CC levels with the state that originates from the $2^2\Sigma^-$ state (pink) at the EE-EOM-CCSDT level (areas 2). Again, in the perpendicular case, the behaviour of the two curves is indistinguishable up to $B = 0.25\ B_0$. For stronger fields, the curves diverge slightly, but follow the same qualitative trend. For the skewed orientations (upper and middle panel of fig. 4.9), both "coincidences" are observed for $B < 0.25\ B_0$ in the $\phi = 30°$ case and for $B < 0.20\ B_0$ in the $\phi = 60°$ case. For stronger fields in these two magnetic-field directions the curves diverge. The EE-EOM-CCSDT results show a stabilisation of both the 5^2A (purple) and the 6^2A (pink) states with

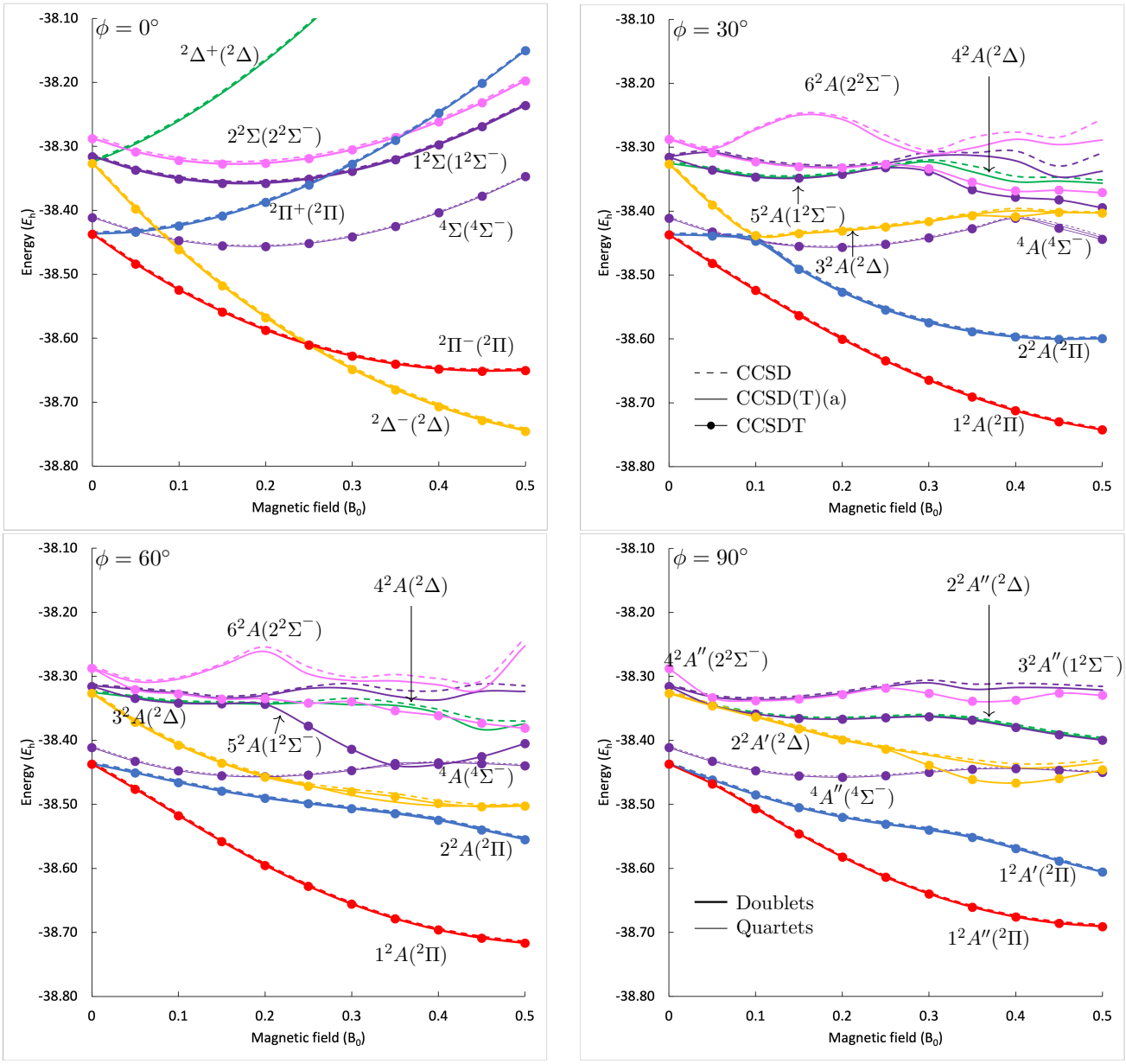

Figure 4.8: The low-lying doublet states and a quartet state of CH in different magnetic-field orientations at the SF-EOM-CCSD and CCSD(T)(a)* levels of theory compared to EE-EOM-CCSDT results obtained using the unc-aug-cc-pCVDZ basis set.

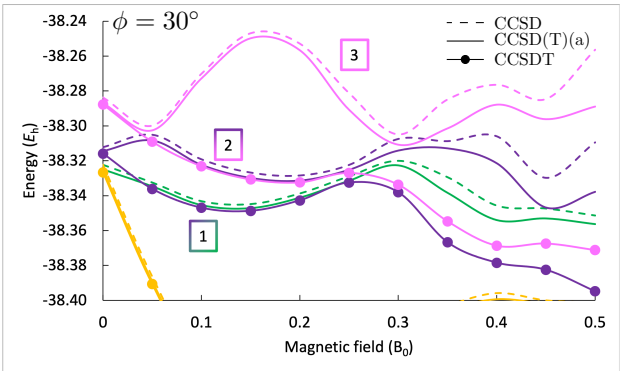

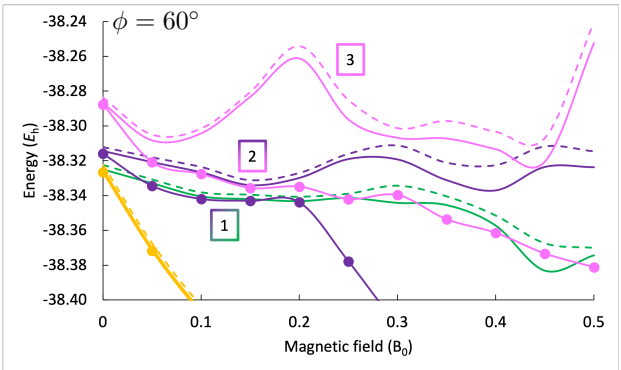

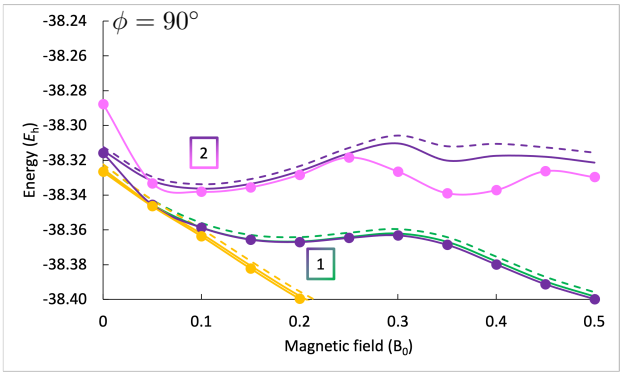

Figure 4.9: The higher excited states of CH for the skewed and perpendicular magnetic-field orientations at the SF-EOM-CCSD and CCSD(T)(a)* levels of theory compared to EE-EOM-CCSDT results obtained using the unc-aug-cc-pCVDZ basis set. A zoom of the plots from fig. 4.8

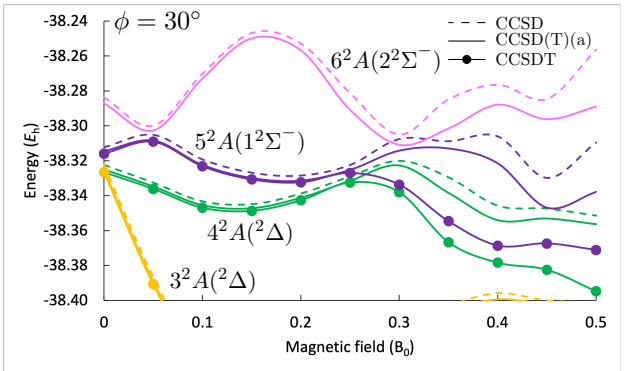

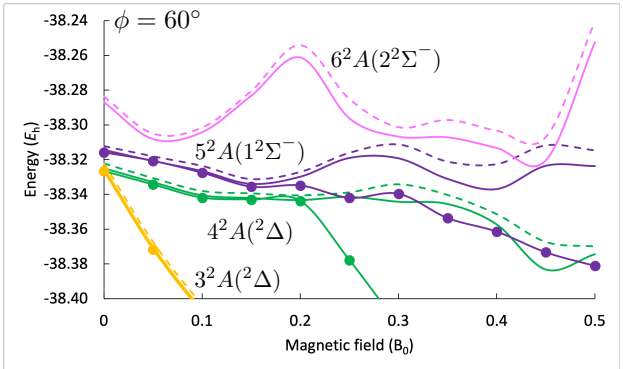

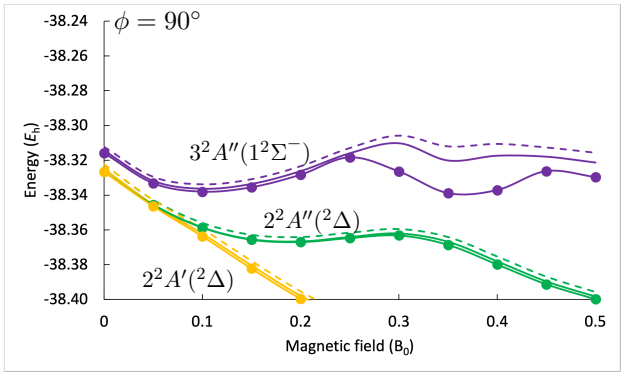

Figure 4.10: The higher excited states of CH for the skewed and perpendicular magnetic-field orientations at the SF-EOM-CCSD and CCSD(T)(a)* levels of theory with the corrected assignment of states at the EE-EOM-CCSDT level obtained using the unc-aug-cc-pCVDZ basis set. A zoom of the plots from fig. 4.8

increasing magnetic-field strength which hints at the existence of an avoided crossing. The divergence of the states at the SF- and EE-EOM-CC levels can be traced backed to a strong contribution from electron configurations that are singly excited when using the EE-EOM-CC approach but doubly excited when using the SF-EOM-CC approach. In these cases the SF-EOM-CC results are flawed because the avoided crossing is "missed". The SF-EOM-CC 6^2A state (pink) has a behaviour qualitatively different from the curves assigned to the same state at the EE-EOM-CCSDT level (areas 3). Specifically, the state exhibits a local maximum around 0.15 - 0.20 B_0 for the skewed orientations when using the SF-EOM-CC approach, instead of having an almost constant energy with increasing magnetic-field strength that is observed at the EE-EOM-CCSDT level. The behaviour of the SF-EOM-CC 6^2A state (pink) is qualitatively different from that of the EE-EOM-CCSDT 6^2A state even for magnetic-field strengths when the "coincidences" at areas 1 and 2 are not observed. The SF-EOM-CC $4^2A''$ state (pink) could not be targeted for the perpendicular orientation of the magnetic field. The outcome of this comparison between the SF- and EE-EOM-CC results is that the absence of a symmetry bias

and the good behaviour of the states in weaker fields when using the SF variant offer the correct characterisation and simplify the correct assignment of the states. The corrected assignment is presented in fig. 4.10. An assignment based only on the EE-EOM-CC results is more difficult because the error introduced by the symmetry bias is close to the energetic difference of the $^2\Delta$ and $^2\Sigma^-$ states. Additional complication stem from the existence of states with a strong double-excitation character that cannot be consistently targeted and other technical difficulties of the calculation [absence of good first guesses for predominant doubly-excited states in the Davidson procedure, high cost of multiroot Davidson (see app. C) at the CCSDT level, etc.]. It is importnat to note that, nonetheless, the full inclusion of triples at the EE-EOM-CCSDT level gives without a question the most trustworthy results for the total energy of the states. For the skewed and perpendicular orientations, where states are characterised based more on the energetical order rather than on the IRREP, the accuracy of the results is every case much more important than the correct assignment to a field-free limit.

It can be concluded that for the CH radical in the presence of a magnetic field an extensive study based on multiple approaches was needed. The results at the CCSDT level of theory are the only that give a qualitatively correct description of the system in arbitrary magnetic-field strength and orientation. Even these highly-accurate results required additional input to be correctly interpreted. Specifically, the states originating from the second component of the $^2\Delta$ state and the two $^2\Sigma$ states are proven notoriously difficult to target and, indeed, the SF approach was used to characterize our results consistently. Calculations at the CCSDT level of theory, however, are accompanied by many technical difficulties that arise from the high-cost of the calculation, the multiconfigurational character of the states, and the existence of strong double-excitation contributions. It is evident that this system cannot be targeted in a "black-box" manner. An adaptable multireference approach or an FCI study, which however comes with even higher computational cost, could shed more light on the behaviour of these higher-energy states.

4.3.3 Methane CH_4

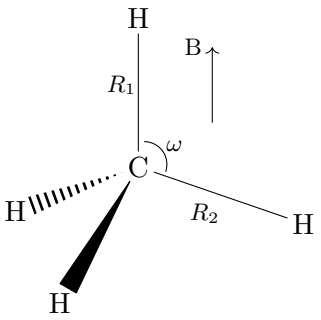

Figure 4.11: Methane with magnetic field directed parallel to a C-H bond. C_3 symmetry.

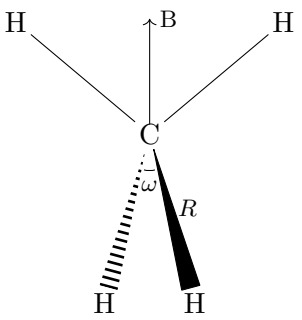

Figure 4.12: Methane with magnetic field directed parallel to the bisector of a H-C-H angle. S_4 symmetry.

In the absence of a magnetic field CH_4 has a tetrahedral symmetry T_d. Two magnetic-field orientations were studied, one with the magnetic field parallel to one of the C-H bonds, reducing the symmetry to C_3, and one with the magnetic field parallel to the bisector of a H-C-H angle resulting in an S_4 symmetry, see fig. 4.11 and 4.12 respectively. For these magnetic-field orientations, constrained geometry optimizations[d] were performed for the singlet state $^1A(^1A_1)$ lowest in energy. The system was studied for magnetic-field strengths up to 0.5 B_0 with a spacing of 0.05 B_0. For each point in the grid, singlet excited states were target with the EE-EOM-CC approach. Calculations were performed at the (EOM-)CC2 and CCSD levels of theory with an unc-cc-pVTZ basis.

In the C_3 case, the hydrogen that is located in the direction of the magnetic field is distinct from the other three. The geometry is characterized by the angle ω between the unique hydrogen and the three equivalent hydrogen, and the length of the two different kinds of C-H bonds, i.e., R_1 and R_2 as

[d]For more details see chap. 7.

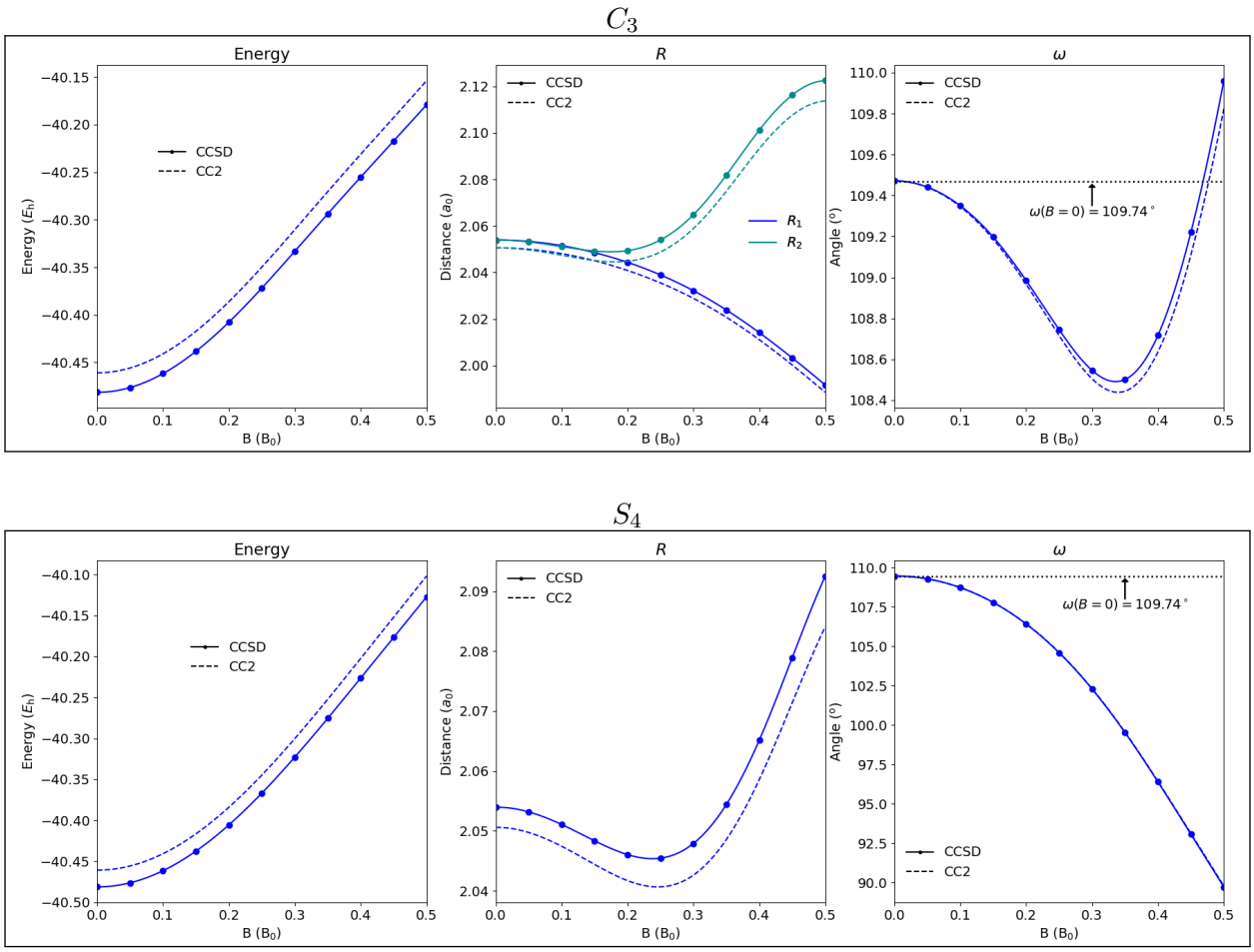

Figure 4.13: Energies in E_h (left), as well as bond lengths in a_0 (middle) and angles in degrees (right) for the energetically lowest singlet state of the methane molecule at the optimized geometry at the CCSD (full line) and CC2 (dashed line) levels of theory as a function of the magnetic-field strength for two different orientations of the magnetic field with respect to the molecule: upper panel B parallel to a C-H bond (C_3 symmetry), lower panel B parallel to the bisetrix of the H-C-H angle (S_4 symmetry).

seen in fig. 4.11. In the upper panel of fig. 4.13, the energy at the optimized geometry has been plotted, together with the change of the geometry parameters as functions of the magnetic-field strength for this orientation of the magnetic field. It is observed that the angle ω deviates only slightly, i.e., 1.4°, from the tetrahedral angle 109.74°. The fact that the angle reaches a minimum around 0.35 B_0 implies that there are two different mechanisms driving the geometric response to the magnetic field. For weaker fields, the three equivalent H nuclei come further apart from each other moving towards the fourth hydrogen, and the angle ω decreasing slightly by less than a degree. In stronger magnetic fields the diamagnetic influence confines the molecular geometry to the axis parallel to the field, bringing the equivalent hydrogens closer together, which counteracts the weaker-field behaviour. Looking at the bond lengths, one notices that R_1 and R_2 only start to deviate from each other significantly for magnetic-field strengths larger than 0.15 B_0. For weaker fields, the bonds slightly shorten by about 0.004 a_0. The bond length of the unique hydrogen R_1 keeps shortening up to 0.5 B_0 from 2.05 Bohr to 1.99 Bohr for both CCSD and CC2. On the other hand, R_2 elongates with stronger magnetic fields until about 2.12 a_0 at 0.5 B_0. Overall, the CC2 results for the geometry parameters reproduce the CCSD behaviour extremely well. Bond lengths are about 0.004 a_0 shorter when using CC2 compared to CCSD, while the angles deviate by only 0.1°.

The geometry-relaxed energy and the geometry parameters of methane in the S_4 configuration are presented in the lower panel of fig. 4.13. In this orientation of the field, all hydrogens remain equivalent as in the field-free case. The geometry is described by the C-H bond lengths and the angle between the H nuclei ω as seen in fig. 4.12. In this case, the influence of the magnetic field on the

geometry of the system is stronger, as the angle deviates more and more from tetrahedral when the magnetic-field strength increases. Eventually, it reaches about 90° at 0.5 B_0. This is a clear response to the diamagnetic influence, confining the system along the axis parallel to the magnetic field. The bond lengths are influenced by the diamagnetic term as well, shortening until about 0.25 B_0. For stronger magnetic fields, the proximity of the hydrogens caused by the decreasing H-C-H angle forces the bonds to elongate. In this case, the CC2 results for the geometry parameters are nearly identical to the CCSD results as well, i.e., bond lengths are shorter by only $\sim 0.004\ a_0$ and angles deviate at most by 0.06°.

The energy of the reference state for the C_3 case is slightly lower than for the S_4. Since no totally unconstrained geometry optimization has been performed at this point (the magnetic-field orientation was not varied during the optimization), and since not all highly symmetric orientations of the magnetic field (which are expected to be critical points) have been studied, it is not certain that this is the preferred orientation for this state. The two different responses are energetically very close and do not differ qualitatively regarding the energy of the system. The maximum energy difference between the C_3 and S_4 orientations is 52 mE_h at $B = 0.50\ B_0$.

Results for the first two excited $^1T_2$ states in a magnetic field are depicted in fig. 4.14. They are triply degenerate, and are described by a HOMO→LUMO and a HOMO→LUMO+1 transition, respectively. The orbitals of interest are visualized in fig. 5.4. In the C_3 direction, the T_2 IRREP splits into components A, E^1, and E^2, while in the S_4 direction T_2 splits into B, E^1, and E^2. Because of the different point groups used in the calculations of the molecule, the form of the degenerate orbitals differs drastically even for the $B = 0$ calculation. They do, however,have the same orbital energy

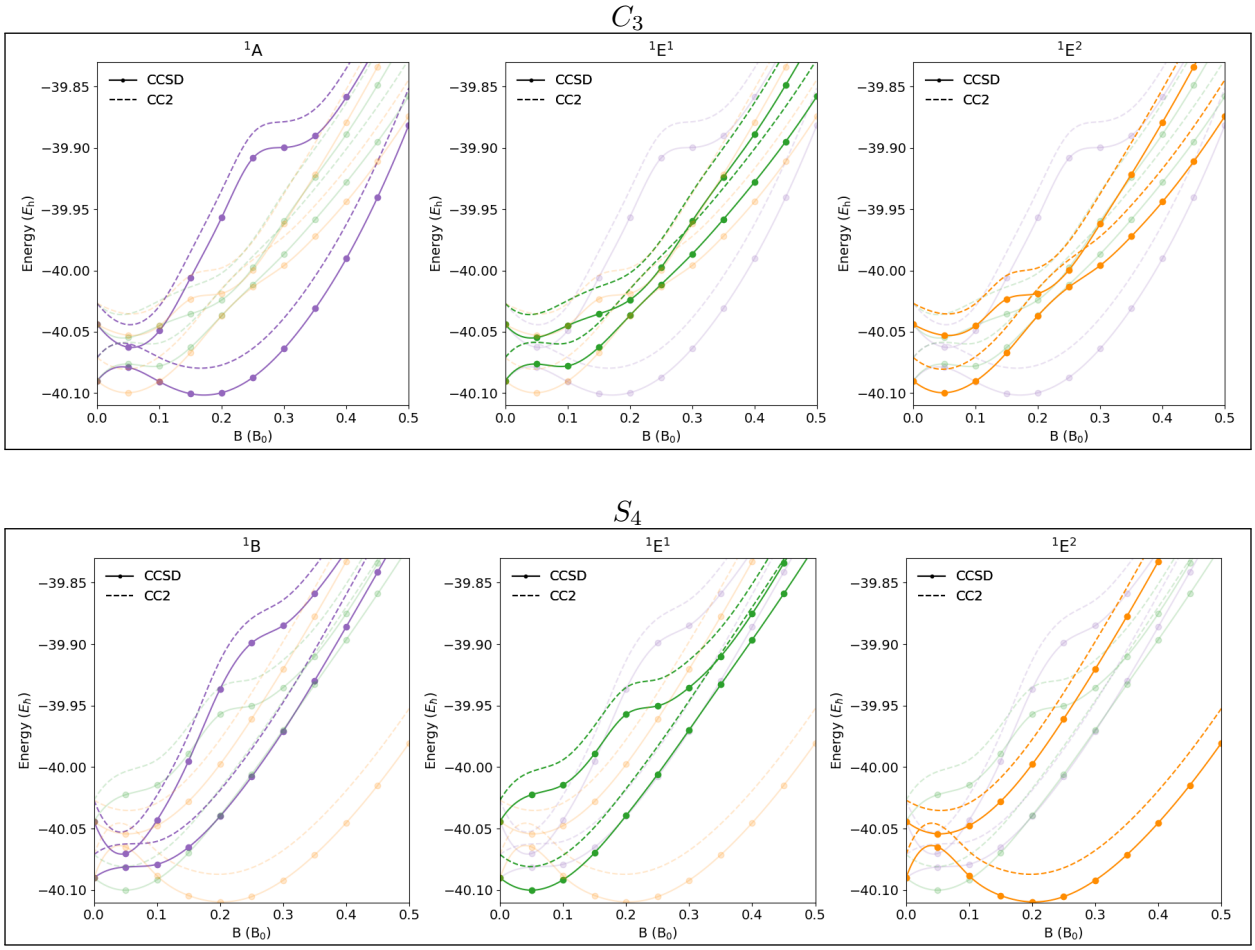

Figure 4.14: Change of the first two T_2 singlet degenerate states of methane in magnetic field at the EOM-CCSD (full line) and EOM-CC2 (dashed line) levels of theory. The magnetic field is oriented parallel to a C-H bond (C_3 symmetry) in the upper panel and parallel to the bisector of the H-C-H angle (S_4 symmetry) in the lower panel.

eigenvalue, which is physically consistent. In both magnetic-field orientations, the occupied orbitals only change slightly with increasing magnetic field, with one orbital having smaller contributions from C-center functions at field strength $B = 0.50\ B_0$. The response of the the virtual orbitals to increasing magnetic-field strength is more prominent. In the C_3 orientation they acquire a more diffuse character. In the S_4 direction instead they contract closer to the hydrogens and away from the central carbon. At $B = 0.50\ B_0$ field strength for this orientation one of the orbitals has acquired a diffuse character of d_{-2} shape. As for the excited states that arise, they are energetically very close, but, since they are associated with different IRREPs, they are allowed to cross. For clarity, the excited states are plotted in the fig. 4.14 according to their IRREP.

In the upper panel of fig. 4.14 total energies of the excited states at the ground state-optimized geometry for the C_3 configuration are presented. In the left panel, an avoided crossing between the ^1A states (purple) at 0.05 B_0 is observed and is further confirmed by an analysis of the EOM vectors. The ^1A state lower in energy crosses the $^1E^2$ state (right panel, orange) at 0.1 B_0 magnetic-field strengths and becomes the excited state lowest in energy for the range of magnetic-field strength studied here. Due to the avoided crossing, this ^1A state, despite arising from the first excited $^1T_2$ state, is more similar to the second $^1T_2$ state. An avoided crossing also takes place for the second ^1A state with an originally higher-lying state at around 0.25 B_0. The $^1E^1$ (green) and $^1E^2$ (orange) components also change in a rather complicated manner with avoided crossings among each other, and between other excited states. Despite the complicated behaviour of the excited states the overall trend of the states follows qualitatively the diamagnetic influence, i.e., the energy of the states rises with increasing magnetic-field strength.

The spectrum for the S_4 configuration in the lower panel of fig. 4.14 is equally complicated compared to the C_3 configuration. Multiple avoided crossings take place at 0.05 B_0 for the ^1B and $^1E^2$ states. The first $^1E^2$ excited state crosses the lower $^1E^1$ at 0.1 B_0 and becomes the excited state lowest in energy for stronger magnetic fields.

All excited states studied here have a predominant single-excitation character and do not acquire strong contributions from doubly-excited configurations in the magnetic-field strengths studied. Because of this, they are relatively well described both at the CC2 and CCSD levels of theory. Unlike the more complicated case of the CH^+ and CH studied in the previous sections, CC2 here does not exhibit a non-physical behaviour. The avoided crossings and observed trends are replicated qualitatively at the CC2 level with an overestimated total energy of about 0.02 E_h relative to CCSD. Because of the almost parallel shift, the resulting error cancellation yields quite smaller deviations for the excitation energies at the CC2 level compared to the CCSD results of about $10^{-3}\ E_\mathrm{h}$.

4.3.4 Ethylene CH_2=CH_2

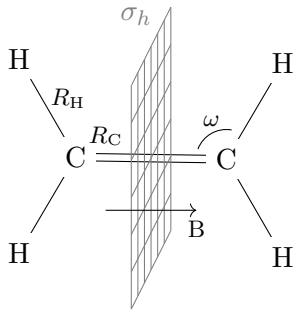

Figure 4.15: Ethylene in a magnetic field directed parallel to the C=C bond. C_{2h} symmetry. The mirror plane σ_h perpendicular to the magnetic field is depicted by the gray grid.

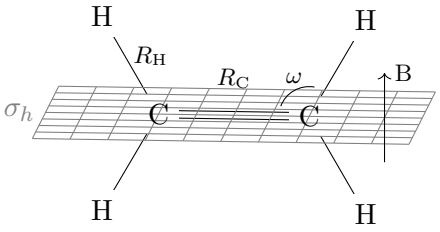

Figure 4.16: Ethylene in a magnetic field parallel to the molecular plane and directed perpendicular to the C=C bond. C_{2h} symmetry. The mirror plane σ_h perpendicular to the magnetic field is depicted by the gray grid.

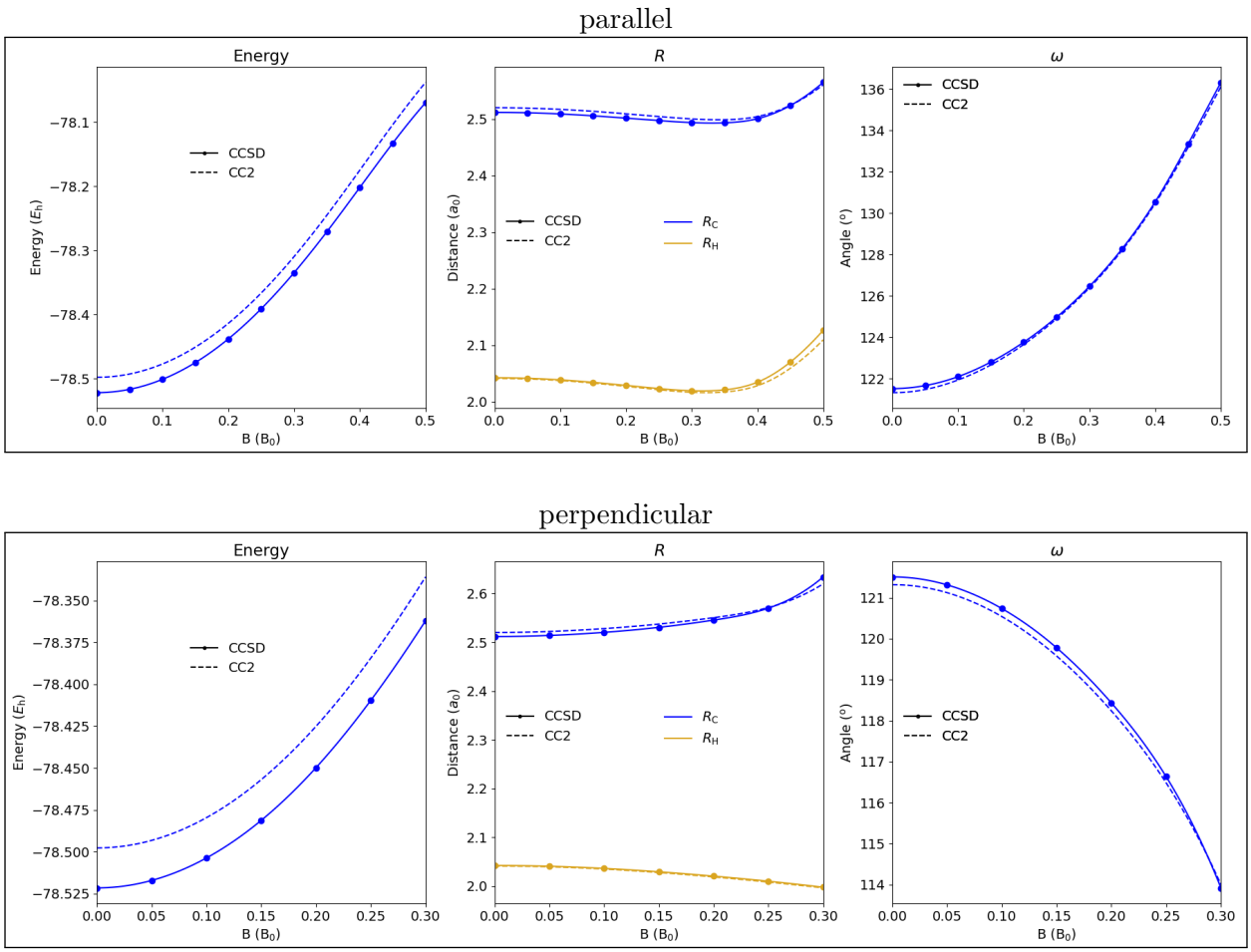

Figure 4.17: Energies in E_h (left), as well as bond lengths in a_0 (middle) and angles in degrees (right) for the energetically lowest singlet state of the ethylene molecule at the optimized geometry at the CCSD (full line) and CC2 (dashed line) levels of theory as a function of the magnetic-field strength for two different orientations of the magnetic field with respect to the molecule: upper panel B parallel to the C=C bond, lower panel B in-plane perpendicular to the C=C bond.

For the ethylene molecule CH_2=CH_2, two magnetic-field directions were studied. Ethylene in the absence of a magnetic field belongs to the D_{2h} symmetry group. A magnetic field parallel to the C=C bond reduces the symmetry to C_{2h} as shown in fig. 4.15. An in-plane magnetic field perpendicular to the C=C bond results in C_{2h} symmetry as well (fig. 4.16). The principal axes of rotation and the mirror planes (σ_h) in the two cases are, however, different. The mirror planes are depicted as a gray grid in the two figures. In both cases the H nuclei remain equivalent, as do the C nuclei, and the geometric parameters to be optimized are the C=C bond length R_C, the C-H bond length R_H and the C-C-H angle ω. Similar to the study of methane from the previous section, constrained geometry optimizations were performed for the singlet state $^1A_g(^1A_g)$ lowest in energy of ethylene for magnetic-field strengths up to 0.5 B_0 with a spacing of 0.05 B_0.[d] Singlet states were studied at the EE-EOM-CC level. All calculations were carried out at the (EOM-)CC2 and CCSD levels of theory using an unc-cc-pVTZ basis.

The results for the magnetic field parallel to the C=C bond are presented in the upper panel of fig. 4.17. The middle and the right column show the relaxation of the geometry responding to the magnetic field. The bond length R_C remains relatively constant between 0 and 0.35 B_0. As the C=C bond is parallel to the magnetic field, it is not directly affected by the diamagnetic influence. For magnetic fields stronger than 0.40 B_0 a lengthening of the C=C bond is observed. As for the C-H bond lengths, they shorten slightly from 0 to 0.35 B_0, responding to the diamagnetic influence. For stronger fields, the lengthening of the bonds can be attributed the widening of the angle. This widening is also directly attributed to the diamagnetic influence and, unlike the response of the bond

lengths, it has a monotonic trend.

In the lower panel of fig. 4.17, the results for the orientation of the magnetic field in the molecular plane and perpendicular to the C=C bond of the ethylene molecule are shown. Calculations are presented for magnetic-field strengths between 0 and 0.30 B_0. Both the CCSD as well as the CC2 results consistently predict a dissociation of the molecule for larger fields. The double-bond breaks and two linear CH_2 fragments are formed, CH_2=$CH_2 \rightarrow 2\ CH_2$, oriented parallel to the magnetic field. This dissociation occurs because of the stabilisation due to the orbital-Zeeman term for highly negative angular momenta for the fragments, i.e, $^2\Delta_g^-$ states with $M_L = -2$ of the linear fragments. In this calculation the spin-Zeeman term is not taken into consideration since the two fragments are forced by the calculation to have opposite spin. Certainly, the combination of the two open-shell fragments may results in M_S states lower in energy, but here, the $M_S = 0$ dissociation limit is targeted. For weaker magnetic fields where the molecule is bound, the response of the angle ω to the magnetic field is dictated by the diamagnetic influence. The C=C bond length is elongated in stronger magnetic fields, which indicates a weakening of the bond. The weakening of the bond is further indicated by the shape of the HOMO orbital (see right panel of fig. 5.5) that describes the π bond.[e] At $B = 0.3\ B_0$ it has already lost its bonding character. On the other hand, the C-H bonds shorten in stronger magnetic fields. This is consistent with the diamagnetic influence, and the response of the angle that gradually brings the CH_2 groups of the molecule closer to linearity and towards dissociation.

Results obtained at the CC2 and at the CCSD levels of theory agree very well with each other. As expected, the CC2 total energies are higher than the CCSD energies for different magnetic-field strengths and directions by a nearly constant shift of 0.025 E_h. Regarding the results for the geometry parameters, angles obtained at the CC2 level deviate on average by about 0.1° and bond lengths have a 0.006 Bohr absolute mean deviation relative to CCSD. R_H is consistently found to be shorter at the CC2 level relative to CCSD, while R_C is longer for magnetic-field strengths 0-0.45 B_0 in the parallel configuration and shorter for 0.5 B_0. In the perpendicular configuration of the magnetic field, R_C is also shorter when obtained at the CC2 level for 0.30 B_0.

In fig. 4.18, results on the singlet excited states obtained at the EOM-CC2 and EOM-CCSD levels of theory for the ethylene molecule are shown. The upper panel contains the results for the parallel direction of the magnetic field, while the lower one contains the results for the perpendicular orientation (fig. 4.15 and 4.16 respectively). The first two to three excited states of each IRREP have been calculated for the two different magnetic-field orientations investigated here. In both orientations the excited states are energetically close and have been plotted according to their IRREP. Reduction of symmetry from D_{2h} to one of the C_{2h} subgroups due to the presence of the magnetic field retains the g/u inversion parity, but allows the $A_{g/u}$ states to mix with one of the three $B_{ng/u}$ IRREPs of the same parity, while the other two $B_{ng/u}$ IRREPs may mix among each other. Further discussion will focus on the *ungerade* excited states, since transitions to these states from the ground reference state are dipole allowed. In the parallel case (upper panel in fig. 4.18), the first excited state is a ^1B_u state for all field strengths considered. The corresponding excitation from the A_g reference is a HOMO $\rightarrow$ LUMO transition. The orbitals involved are shown in fig. 5.5.[e] Analysis of the EOM excitation vectors and the orbital character show an avoided crossing at 0.10 B_0 of this state with another ^1B_u state, which is stabilized in the magnetic field. This is also easily seen in the change of the HOMO and LUMO orbitals in the magnetic field in the left panel of fig. 5.5. The HOMO orbital, which arises from the the field-free π-bonding orbital, mixes with a virtual orbital localized on the hydrogens. In the absence of magnetic field, this virtual orbital originally belongs to a different IRREP, but the magnetic field allows these orbitals to mix. In the in-plane perpendicular case (see lower panel in fig. 4.18) there are no obvious avoided crossings for the magnetic-field strengths studied here. The first excited state is a ^1B_u state as well, that arises from the same HOMO $\rightarrow$ LUMO transition as the parallel case. The change of the orbitals is shown in the right panel of fig. 5.5.

Comparing the total energies of the excited states, the overestimation at the EOM-CC2 level is about 0.02 E_h relative to EOM-CCSD. As was the case for the methane study of the previous section (4.3.3), the excited states do not acquire a significant double-excitation character for the magnetic-field strengths studied and the EOM-CC2 approach does not exhibit any unphyisical behaviour. The

[e]For more details on the molecular orbitals and orbital visualization see sec. 5.1

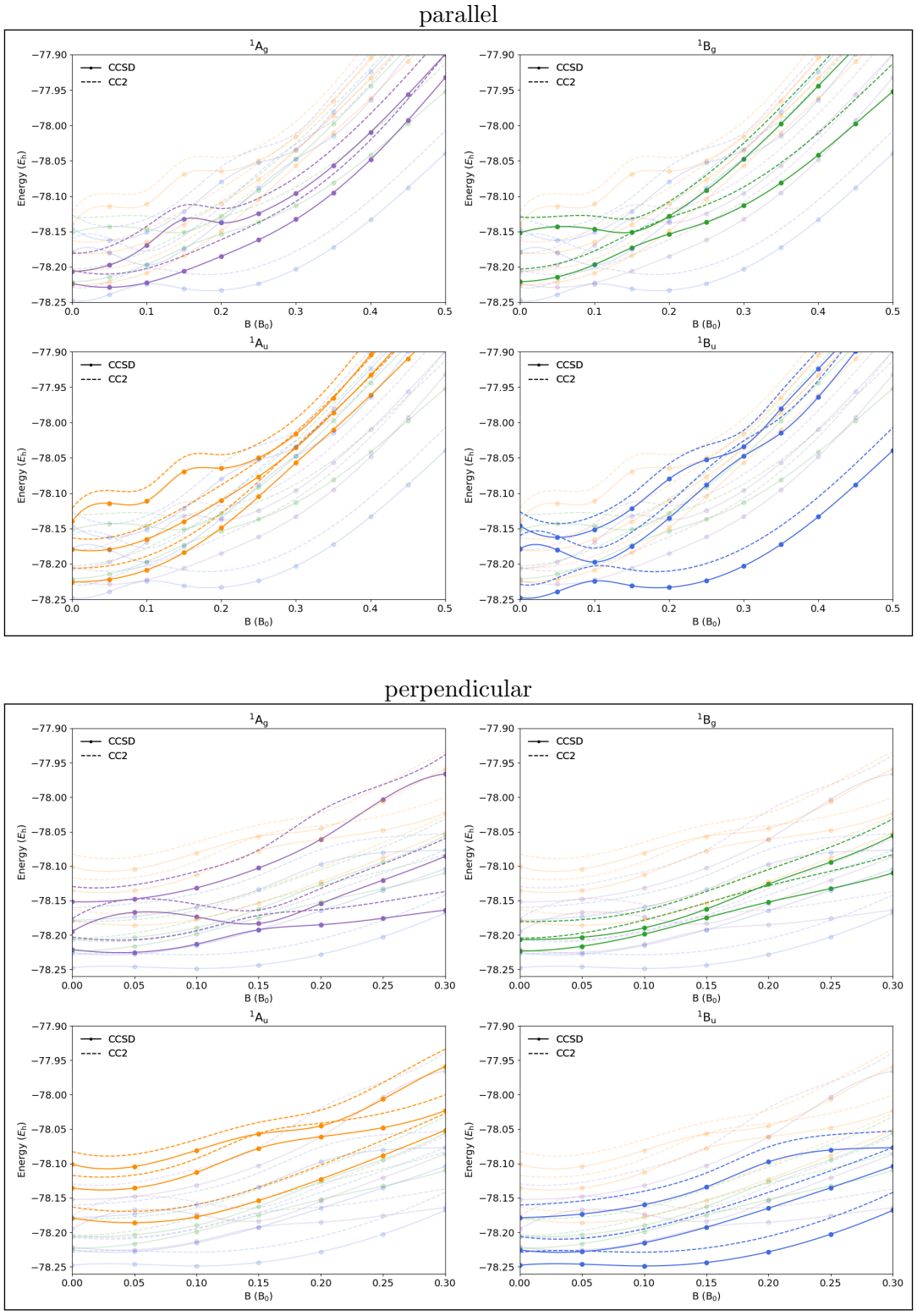

Figure 4.18: Change of the lowest in energy singlet excited states of ethylene as a function of the magnetic-field strength at the EOM-CCSD (full line) and EOM-CC2 (dashed line) levels of theory. Upper panel B parallel to the C=C bond, lower panel B in-plane perpendicular to the C=C bond.

deviation for the excitation energies drops by one order of magnitude compared to the total energies. Hence, for the excited states considered here, the CC2 method constitutes a reasonable alternative to CCSD.

4.3.5 Pyrrole in perpendicular magnetic field

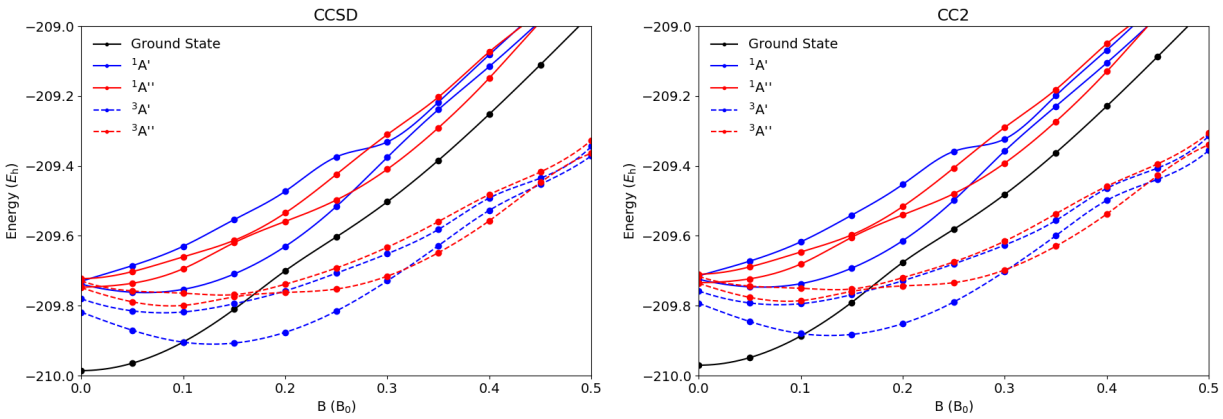

Figure 4.20: Total energies for the ground state, and excited states of pyrrole in a magnetic field perpendicular to the molecular plane calculated at the (EOM-)CCSD and (EOM-)CC2 level of theory. The $M_S = -1$ component of the triplet states is depicted.

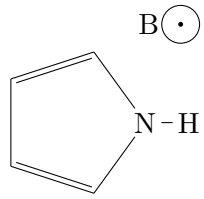

Figure 4.19: Pyrrole in magnetic field oriented perpendicular to the molecular plane.

Calculations on the pyrrole molecule have been carried out at the CC2 and CCSD levels of theory using the unc-cc-pVTZ basis set. The field-free CCSD optimized geometry was used for calculations in different magnetic-field strengths in a direction perpendicular to the molecular plane, as depicted in fig. 4.19. At the EOM-CC level, the first two singlet and triplet excited states of each IRREP were targeted. Using the EE-EOM-CC approach, it is possible to obtain states of different multiplicity with respect to the reference state with the same M_S value. In the pyrrole case, starting from the closed-shell reference state $^1A(^1A_1)$ both singlet ($S = 0$) and triplet ($S = 1, M_S = 0$) states can be targeted. In the non-relativistic limit and absence of magnetic field, the different M_S components of a state are degenerate. In the presence of magnetic field, however, the degeneracy is lifted by the spin-Zeeman term [see eq. (2.1.8)], which in our case is trivially accounted for ($P_e^{\text{spin}} = \frac{e}{m_e} B M_S$). Adding the spin-Zeeman contribution to the energy of a triplet $M_S = 0$ state obtained via an EE-EOM-CC approach enables the energy calculation of the other $M_S = \pm 1$ components of the same state without an SF-EOM-CC calculation. This way, the energy of the $M_S = -1$ component of the triplet states of pyrrole was calculated. In fig. 4.20, the results obtained at the CCSD and CC2 levels of theory are shown, and in tab. 4.2, a comparison of the results at the (EOM-)CC2 and the (EOM-)CCSD levels of theory is presented.

	$\overline{\Delta E}_{\text{tot}}$	$\Delta E_{\text{tot,max}}$	$\overline{\Delta E}_{\text{exc}}$	$\Delta E_{\text{exc,max}}$
Reference State	20.645	24.682	-	-
$1\ ^1A'$	14.3	17.9	−6.3	−12.5
$2\ ^1A'$	14.8	19.6	−5.8	−12.7
$1\ ^1A''$	17.0	23.5	−3.7	−4.9
$2\ ^1A''$	18.0	22.9	−2.6	−5.4
$1\ ^3A'$	24.1	28.6	3.4	10.1
$2\ ^3A'$	26.1	30.0	5.5	7.0
$1\ ^3A''$	17.4	24.5	−3.2	−4.7
$2\ ^3A''$	18.2	23.5	−2.4	−5.0

Table 4.2: The mean absolute error $\overline{\Delta E}_{\text{tot}}$ and the maximum absolute error $\Delta E_{\text{tot,max}}$ of the total (EOM-)CC2 energy relative to (EOM-)CCSD for magnetic-field strengths between 0.0 B_0 and 0.5 B_0, as well as the mean absolute error $\overline{\Delta E}_{\text{exc}}$ and the maximum absolute error $\Delta E_{\text{exc,max}}$ of the EOM-CC2 excitation energy relative to EOM-CCSD in mE_h for the pyrrole molecule in perpendicular magnetic field.

The results for the total energy are plotted in fig. 4.20 as a function of the magnetic-field strength. It is found that the closed-shell reference state (black) is not the ground state for all magnetic-field strengths examined. For magnetic-field strengths between 0.1 $B_0 < B < 0.3$ B_0, a $^3A'$ (dashed blue) is the ground state. At 0.3 B_0 and again at 0.45 B_0, this triplet state crosses with a $^3A''$ state (dashed red). In the absence of field, the $1^1A''$ and $1^3A''$ states (continuous and dashed red, respectively) are described by a HOMO $\rightarrow$ LUMO transition with respect to the reference state, while the $2^1A''$ and $2^3A''$ states (continuous and dashed red) by a HOMO $-$ 1 $\rightarrow$ LUMO transition. On the other hand, the $1^1A'$ and $1^3A'$ states (continuous and dashed blue, respectively) are predominantly described by a HOMO $\rightarrow$ LUMO + 3 transition, while the higher in energy excited states of the same IRREP, i.e., the $2^1A'$ and $2^3A'$ states, result from a HOMO $-$ 1 $\rightarrow$ LUMO + 3 transition. Avoided crossings occur between the $1^1A''$ and $2^1A''$ states (continuous red), and between the $1^3A''$ and $2^3A''$ states (dashed red) around 0.15 B_0. Additionally, an avoided crossing is observed for the $2^1A'$ state (continuous blue) around 0.25 B_0, which is confirmed by analysis of the EOM excitation vectors in these magnetic-field strengths.

Comparison between the CCSD and CC2 results shows that they are qualitatively equivalent. Looking at table 4.2, there are no errors larger than 30 mE_h for the total energies at the CC2 level compared to the CCSD results. The total energy is consistently overestimated for the examples investigated here. As observed for other systems so far, the deviation of the excitation energies is smaller by one order of magnitude compared to the deviation of the total energies. The exact sign of the deviation of the excitation energy depends on the character of the transition, which changes in different magnetic-field strengths. The maximum errors for the total energies and the excitation energies are in general close to the mean value, which means that even in difficult cases of abrupt character change in the excited state, the CC2 results are reliable. Note, however, that this is the case only because none of the excited states studied acquires a significant double-excitation character.

This study of pyrrole indicates the applicability of the CC2 method to medium-sized systems, and this is only a first approach at studying this system. A follow-up study that would include geometry-optimization calculations in the presence of magnetic field for the field-free ground state and the $1^3A'$ (dashed blue) and $1^3A''$ (dashed red) states would shed more light to the behaviour of this system, especially since these triplet states are found lower in energy that the field-free ground state for specific magnetic-field strengths.

Chapter 5

Miscellaneous Interpretational Tools

In the previous chapter, the analysis of the results for the CH_4 and C_2H_4 molecules and the CH radical went beyond the behaviour of the electronic energy as a function of the magnetic field. In the study of the CH_4 and C_2H_4 molecules, valence and virtual molecular orbitals were plotted that contributed to the characterisation of the electronic structure and the character of the excitation. In the case of the CH radical, the spin-expectation values of the excited states were calculated, that contributed to their characterisation and assignment.

Here, these two concepts will be demonstrated as interpretational and diagnostic tools. In sec. 5.1, the visualization of complex orbitals is addressed, that was realized by the development of the COrbit19 program. In sec. 5.2, the calculation of spin multiplicity through the expectation value of the spin-squared operator is derived. Its implementation in the QCUMBRE program package at different levels of theory and its use is presented as well.

5.1 The visualization of complex orbitals

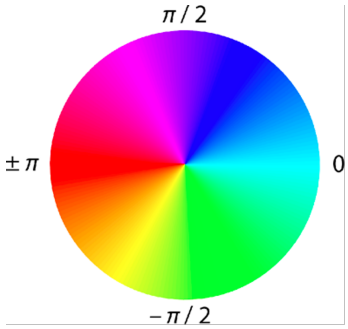

Figure 5.1: A colour-wheel assignment for the different phase values. Picture taken from ref. [158].

It is often stressed that molecular orbitals have a limited physical significance as they are not unique for the description of a wavefunction and they do not correspond directly to physical observables.[96,159,160] Their interpretation via the Koopmans' theorem regarding ionization potentials is also a very crude approximation.[102] Despite this, the molecular-orbital picture is central to the modern paradigm of chemistry and the understanding of the chemical bond. For example, there is active discussion about the bond order of certain compounds,[161–164] though in fact, the concept of the bond order itself is not uniquely defined in quantum mechanics (not being an observable).[165–167] Moreover, the visualization of orbitals is a common interpretational tool regarding the communication between theory and experiment,[168] and it may offer predictive results regarding chemical properties, like in the case of the Diels-Alder reaction.[169] There even exist attempts in the theoretical community to give physical meaning to orbitals by directly associating them with experimental observables.[159]

An orbital is a scalar function defined in the whole 3D space.

$$\phi(\boldsymbol{r}) = \phi(x, y, z)$$

Since 4D plots are not possible, different approaches for visualization exist. Most commonly, a surface S is plotted, to give an indication about the shape and size of the orbital. This can either be the the surface that encloses a specified proportion of the probability density that arises from the orbital

(boundary surface)

$$\int^{S} |\phi(x,y,z)|^2 \mathrm{d}x\mathrm{d}y\mathrm{d}z = c_{\text{prop}},$$

or the surface $x_S, y_S, z_S \in S$ where the orbital has a given absolute value c_{iso} (isosurface)

$$|\phi(x_S, y_S, z_S)| = c_{\text{iso}}.$$

The latter is used in this work because it is faster and simpler to calculate. In the case of real orbitals, the surface is given a different colour dependent on the sign of the orbital value. This idea is generalized for complex orbital using the phase θ of the orbital function. The phase arises from the polar form of complex numbers

$$z = \alpha + i\beta = re^{i\theta},$$

with $\theta = \arctan(\beta/\alpha)$, and where $r = |z| = \sqrt{\alpha^2 + \beta^2}$ is the absolute value of the complex number. Instead of a two-colour assignment for the sign, the surface is coloured based on the phase, with each phase value associated to a colour in a colour wheel (fig. 5.1).[158,170]

5.1.1 COrbit19

Figure 5.2: COrbit19 (Complex Orbital) logo.

Many programs offer orbital visualization,[171–173] and while most of them are applicable only to real orbitals, some of them deal with complex orbitals as well.[158,170] In this work, the COrbit19 (Complex Orbital) program (logo in fig. 5.2) was developed for the visualization of complex orbitals to be compatible with CFOUR[77,78] and QCUMBRE.[76] COrbit19 was developed to be native to a QCUMBRE calculation, and to offer a quick and flexible orbital visualization for ff calculations, when existing programs either have a different focus,[170] or were design with other quantum-chemical programs in mind.[158] Despite the limited functionalities of COrbit19, the simple implementation in the python program language, that hides many complexities under pre-developed and well-documented library packages, achieves a flexibility for the user to adjust the code to ones needs.

Calculation of molecular orbitals in the LCAO ansatz

For the visualization of complex orbitals, the COrbit19 program was developed in python3. It makes use of the numpy library for mathematical and numerical operations,[174] and the mayavi library for the visualization and creation of the plots.[175] The source code is available under `https://gitlab.com/mariospeterkits/corbit19`.

Orbitals are expressed in the LCAO ansatz [eq. (2.2.1)] using London orbitals [eq. (2.1.22)]. The magnetic-field independent part of the AOs χ_μ is a Gaussian function.

$$\begin{aligned}
&\text{LCAO} && \phi_i(x,y,z) = \sum_\mu c_{\mu i}\omega_\mu(x,y,z) \\
&\text{London orbital} && \omega_\mu(x,y,z) = e^{\frac{i}{2}[\boldsymbol{B}\times(\boldsymbol{r}_G-\boldsymbol{r}_A)]\cdot\boldsymbol{r}}\chi_\mu(x,y,z) \\
&\text{Contracted Gaussian} && \chi_\mu(x,y,z) = \sum_k d_{k\mu}g_k(x,y,z) \\
&\text{Primitive Gaussian} && g_k(x,y,z) = (x-x_A)^N (y-y_A)^L (z-z_A)^M e^{-a_k(\boldsymbol{r}-\boldsymbol{r}_A)^2}
\end{aligned} \tag{5.1.1}$$

with $\boldsymbol{r} = (x,y,z)$ the Cartesian coordinates, $c_{\mu i}$ the MO coefficients, $\boldsymbol{B}$ the magnetic field, $\boldsymbol{r}_G = (x_G, y_G, z_G)$ the coordinates of the gauge-origin, $\boldsymbol{r}_A = (x_A, y_A, z_A)$ the coordinates of atomic centre A,

$d_{k\mu}$ the contraction coefficients, N, L, and M the angular-momentum quantum numbers and a_k the exponents. The following program functions handle the orbitals

```
#LCAO
def MO_func(x , y , z , centre , atom_pos , Ang , Exp , Norm , MO_coeff , B , G):
    mo = 0.+0.j
    for ind in range(MO_coeff.shape[0]):
        mo += MO_coeff[ind] * LondonOrb(x , y , z , atom_pos[center[ind]][0] ,
            atom_pos[center[ind]][1] , atom_pos[center[ind]][2] , B , G , Exp[ind,:]
            , Norm[ind,:] , Ang[ind,0] , Ang[ind,1] , Ang[ind,2])
    return mo

#London orbital
def LondonOrb (x,y,z,x_0,y_0,z_0,B,G,a,C,M,L,K):
    GK = np.array([G[0]-x_0 ,G[1]-y_0,G[2]-z_0])
    cross=np.cross(B,GK)
    res = np.exp (1.j/2. *(x*cross[0] + y*cross[1] + z*cross[2]))*contrGauss(x , y ,
        z , x_0 , y_0 , z_0 , a , C, M ,L ,K)
    return res

#Contracted Gaussian
def contrGauss (x , y , z , x_0 , y_0 , z_0 , a , C, M ,L ,K):
    cg=0.+0.j
    for ind in range(C.shape[0]):
        cg += C[ind] * primGauss(x , y , z , x_0 , y_0 , z_0 , a[ind], M ,L, K)
    return cg

#Primitive Gaussian
def primGauss (x , y , z , x_0 , y_0 , z_0 , a, M , L , K):
    r2 = (x-x_0)**2 + (y - y_0)**2 + (z - z_0)**2
    g = (x-x_0)**M*(y-y_0)**L*(z-z_0)**K*np.exp(-a*r2)
    return g
```

As seen in the code, the outer most function `MO_func` is called, which in turn calls the other inner functions. The `x, y, z` variables receive the Cartesian coordinates, while all other variables are system specific and they are the constants of the function.

The COrbit19 program structure

The general COrbit19 structure is very simple, consisting only of the main *COrbit19.py* source code file, and the *COrbit19_fun.py* function library file. The program flow is the following

1. Start and check if an input is given. If no input was given, automatically print an input sample. Otherwise read the input.
2. Read the file containing the results from the calculation, typically named `MOL_ORB`.
3. Calculate the orbitals on a grid.
4. Draw the orbitals and the atoms in the molecule.
5. Visualize the results in a graphical-user interface (GUI) and hold.
6. End when all GUI windows are closed by the user.

The `MOL_ORB` file is created by QCUMBRE and contains all the data necessary for the orbital visualization. These include the MO coefficients, the magnetic field, the gauge origin, the atoms in the molecule and their coordinates and the definition of the basis set. Irrespective of the quantum-chemical calculation, the basis set and the MO coefficients are provided in the simplest form possible, meaning a Cartesian basis without the use of symmetry. This needs to be taken care of by the program that generates the `MOL_ORB` file.

A sample `MOL_ORB` file has the following form

```
bfield {
0.00000000e+00 0.00000000e+00 0.00000000e+00
}
gauge {
0.00000000e+00 0.00000000e+00 0.00000000e+00
}
geometry {
NE 10 0.00000000e+00 0.00000000e+00 0.00000000e+00
}
basis {
0 0 0 0 8.4e+00 2.0e+02 8.2e+00 3.7e+01 2.5e+00 1.0e+01  0.0e+00 8.2e+00 0.0e+00
    1.9e+00 0.0e+00  6.2e-01
0 0 0 0 0.0e+00 2.0e+02 0.0e+00 3.7e+01 0.0e+00 1.0e+01 -4.9e-01 8.2e+00 6.5e-01
    1.9e+00 4.93e-01 6.2e-01
0 1 0 0 2.1e+00 8.2e+00 1.3e+00 1.9e+00 2.1e-01 6.2e-01
0 0 1 0 2.1e+00 8.2e+00 1.3e+00 1.9e+00 2.1e-01 6.2e-01
0 0 0 1 2.1e+00 8.2e+00 1.3e+00 1.9e+00 2.1e-01 6.2e-01
}
orbitals {
mQ
[1,1] (-9.95014555e-01,0.00000000e+00)
[2,1] (-1.97766076e-02,0.00000000e+00)
..
mq
[1,1] (-9.95014555e-01,0.00000000e+00)
[2,1] (-1.97766076e-02,0.00000000e+00)
..
}
```

The data is ordered in categories. Each category starts with its name while the information is enclosed in curly brackets { }. The `bfield` category holds the three components of the magnetic-field vector $\boldsymbol{B}$ and `gauge` the vector of the gauge origin $\boldsymbol{r}_G$. Under `geometry` the information of the molecular scaffold is given. Each line is an atom entry with the name, the atomic number and the three Cartesian coordinates. The atoms are numbered according to the order they are given in `geometry`. The definition of the basis set is found under `basis`. Each row entry corresponds to a basis function. The first entry in a row is the index of the atom at which the function is centred. The following three integers are the N, L and M angular-momentum quantum numbers. The double-precision numbers that follow describe the contraction and are structured as contraction coefficients $d_{k\mu}$ and exponential coefficient a_k pair. In the last category `orbitals`, the MO coefficients $c_{\mu i}$ are given. Under `mQ`, the MO coefficients of α orbitals are found and under `mq` of β orbitals. In the brackets [ ], the indices $[\mu, i]$ are given, and in parentheses ( ) the real and the imaginary part in a double-precision format $(\alpha, \beta) = \alpha + i\beta$.

To give an overview of the functionalities of COrbit19 an input sample is given

```
#Sample Input for ComplexOrb
xmin =
xmax =
ymin =
ymax =
zmin =
zmax =
#Put the dimension of the box here
npoints_x =
npoints_y =
npoints_z =
#Put the resolution of the box here
cam_pos_x =
cam_pos_y =
cam_pos_z =
#Put the position of the camera here
Orb_file =
#put the file name containing the information of the molecule here
bscale =
#scaling factor for the magnetic field vector
```

```
orb_a_first=
orb_a_last=
orb_b_first=
orb_b_last=
#The first and the last orbital of each spin to be drawn should be put here.
    Numbering starts with index 1
orbital_mode=
#For printing orbitals set the orbital mode to on
draw_style =
#Put balls&sticks, balls, or sticks
```

In the input, all lines starting with a # are ignored. Keywords `xmin, xmax, ymin, ymax, zmin, zmax` define the dimension of the box where the molecular orbitals are calculated and `npoints_x, npoints_y, npoints_z` the number of points in each Cartesian direction, i.e., the resolution. Keywords `cam_pos_x, cam_pos_y, cam_pos_z` give the starting position of the viewing point with respect to the centre of mass of the molecule. This is an optional keyword and can be used for consistency when creating orbital images. Keyword `bscale` is also optional and is used to scale the vector representing the magnetic field in the created orbital plots. The `Orb_file` gives the name and the path of the file containing the results of the calculation (`MOL_ORB` file). The orbitals to be calculated and printed in a given run of the visualization program are given in `orb_a_first, orb_a_last, orb_b_first, orb_b_last`, where `orb_a` corresponds to α orbitals and `orb_b` to β orbitals. If `orbital_mode` is set to "on", the program runs normally, but if set to "off", it only draws the molecule. Lastly, the `draw_style` has options ball&sticks, balls and sticks. The program automatically draws bonds between atoms in vicinity, if their distance is shorter than the sum of their atomic radii. The exact radii used by the program do not correspond one to one to Van der Wals or other computed radii and they can be found in *atom_rad.py*.

Interface from QCUMBRE

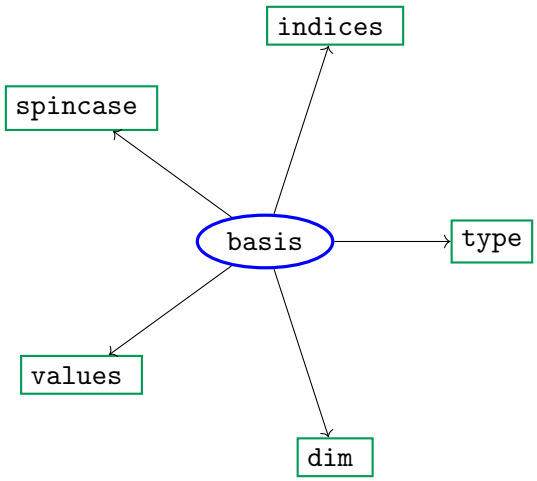

Figure 5.3: The `basis` class and its member variables.

As already described in the previous paragraphs, the COrbit19 interface files require the MO coefficients in a Cartesian AO basis. This means an explicit transformation from the SAO basis back to the AO basis is required and additionally a back transformation from the spherical basis to the Cartesian basis.

In QCUMBRE, an object class that is designed to handle tensors in the AO basis exists. This is the `basis` class. Unlike the `group` and `complete` classes, the `basis` is not to be completely substituted by the `basisS` class, since it serves different functionalities.[a] It comes in two types determined by `type`. Type 1 is similar to the type 1 of `basisS`, handling two-index tensors in the AO basis that do not have a spin case (e.g., overlap integrals in the AO basis) and type 2 is similar to the type 3 of

[a] For more details see chap. 6

basisS, handling two-index tensors in the AO basis with spin-differentiation (e.g., MO coefficients). Beyond the use of the basis class for the COrbit19 interface, the class was developed for the LONDON interface that does not exploit symmetry and for the Mulliken analysis that needs a function basis centred on atoms (i.e., the AO basis). In fig. 5.3 the member variables of the class are shown.

Transformation from a type 3 basisS instance to a type 2 basis instance for the MO coefficients takes place in the basisS::desymmetrize_MO function. This functions uses the SAO to AO transformation matrix that is created with the help of the PointGroup::Projection functions. An inverse transformation is currently not needed in the program and has not been implemented.

In the case of a calculation with spherical basis with the CFOUR interface, the transformation from the spherical basis to the Cartesian basis is needed for the MO coefficients. This is handled by the basis::trans_shp2cart function. The needed transformation matrix is provided by the CFOUR interface.

As a default QCUMBRE always creates a MOL_ORB file after reading the LONDON (if all the necessary information is available) or CFOUR interface and before starting the post-HF calculation. The creation of the interface file takes place in the print_orbitals function. An additional keyword (corbit19=on in the interface topic) is created for QCUMBRE to perform a minimal run only for the creation of the MOL_ORB file. If requested, the costly reading of the two-electron integrals from the interface files (and their transformation from the SAO basis to the MO basis and its subsequent antisymmetrization for the CFOUR interface) from the interface is skipped. The MOL_ORB file is created and the program stops.

5.1.2 Applications on the study of small molecules

Here, the valence molecular and lowest in energy virtual orbitals of the methane and ethylene molecules from the previous study (subsec. 4.3.3 and 4.3.4) are depicted.

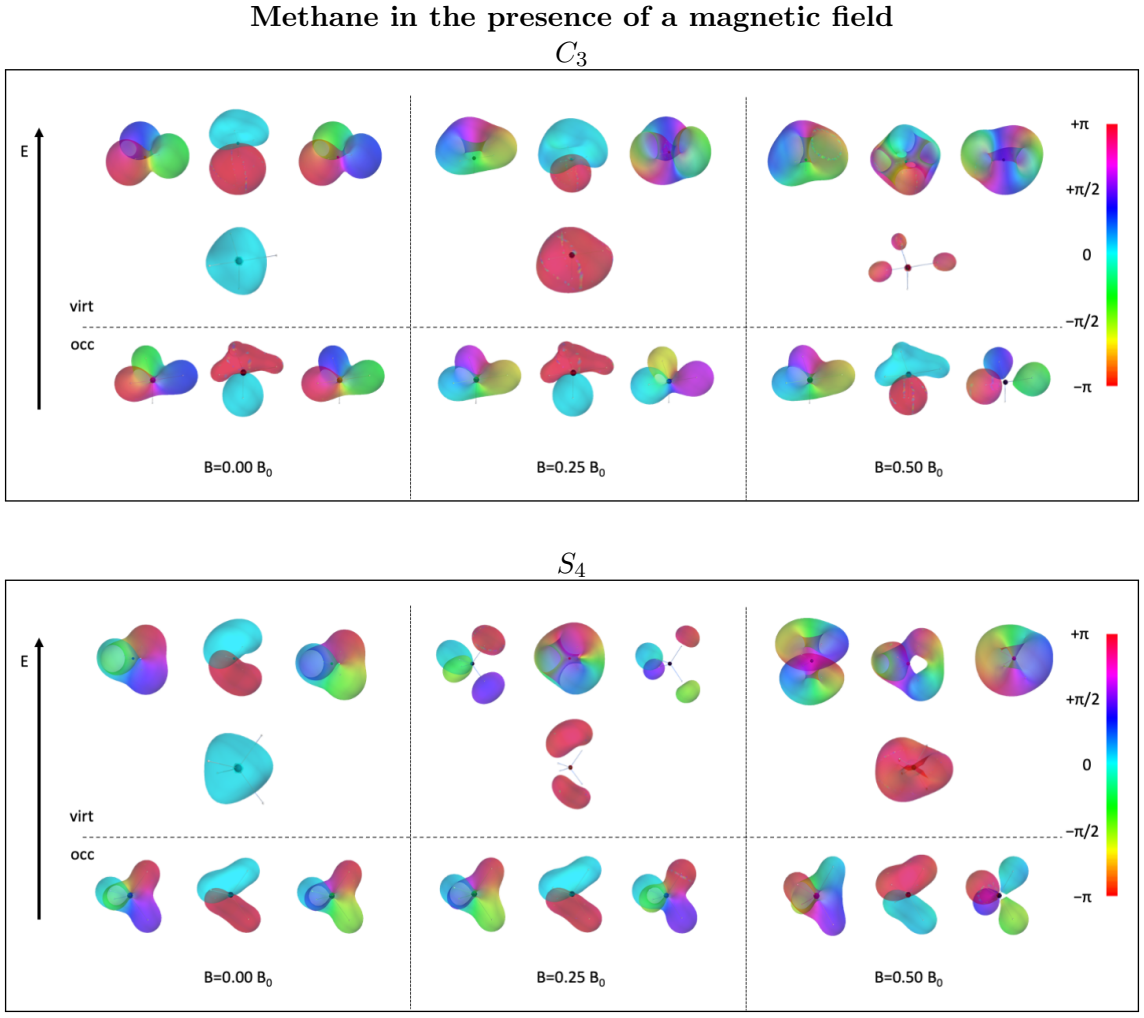

Figure 5.4: Depiction of the HOMO (t_2), LUMO (a_1), and LUMO+1 (t_2) orbitals of methane and their development in the presence of a magnetic field. The magnetic field is oriented parallel to a C-H bond (C_3 symmetry) in the upper panel and parallel to the bisector of the H-C-H angle (S_4 symmetry) in the lower panel. Orbitals have been plotted for an absolute isosurface value of 0.1 $a_0^{-3/2}$ and the phase of the complex value is colour-coded according to the scales on the right. The degeneracy of the orbitals holds only in the absence of the magnetic field. In the middle and right column the relative position of the orbitals on the energy axis is strongly simplified to improve readability.

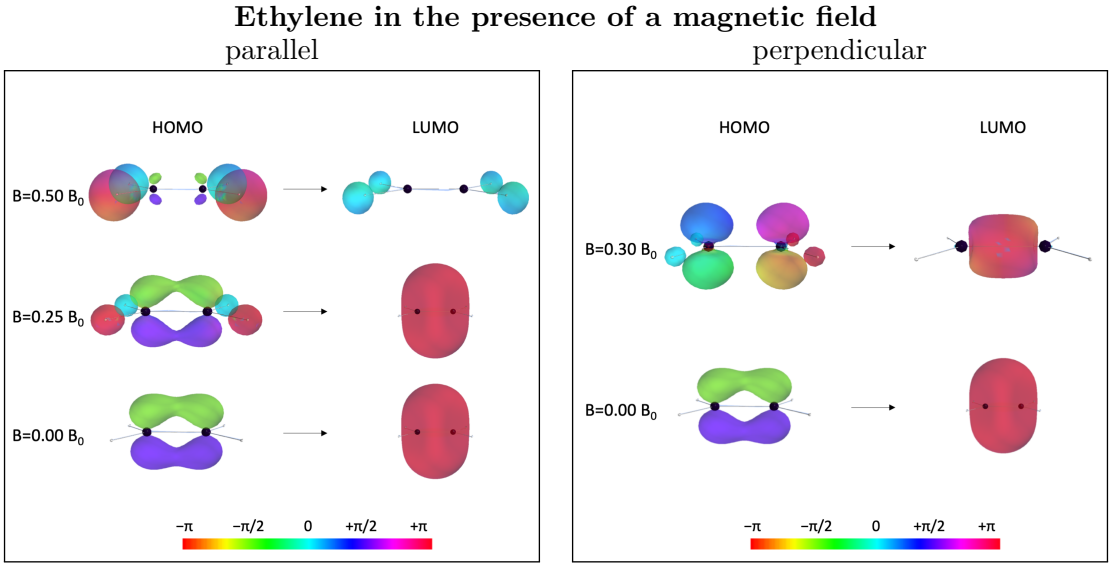

Figure 5.5: Depiction of the HOMO (b_{2u}) and LUMO (a_g) orbitals of ethylene for different magnetic field strengths. Left panel B parallel to the C=C bond, right panel B in-plane perpendicular to the C=C bond. Orbitals have been plotted for an absolute isosurface value of 0.1 $a_0^{-3/2}$ The phase of the complex value is colour-coded according to the scales on the bottom.

5.2 Spin multiplicity

5.2.1 Theory and implementation

An important property targeted in this work, that requires the two-body density matrices, is the spin multiplicity. The latter is calculated via the expectation value of the spin-squared operator $\hat{\boldsymbol{S}}^2$, with $\hat{\boldsymbol{S}} = \sum_i \hat{\boldsymbol{s}}^i$. Exact wavefunctions at the non-relativistic limit, are eigenfunctions of the spin-squared operator, and one of the individual components of $\hat{\boldsymbol{S}}$, usually chosen as the $\hat{S}_z$.

$$\hat{\boldsymbol{S}}^2 \left|\Psi_{S,M_S}\right\rangle = \hbar^2 S(S+1) \left|\Psi_{S,M_S}\right\rangle \tag{5.2.1}$$

$$\hat{S}_z \left|\Psi_{S,M_S}\right\rangle = \hbar M_S \left|\Psi_{S,M_S}\right\rangle \tag{5.2.2}$$

The spin multiplicity is given as $2S + 1$.

The knowledge of the spin multiplicity for an approximate wavefunction is important for different reasons. Wavefunctions based on an unrestricted reference $|\Psi^{\text{unr}}\rangle$ are eigenvalues of $\hat{S}_z$ eq. (5.2.2) (since spinorbitals are spin pure) but are not eigenfunctions of $\hat{\boldsymbol{S}}^2$ eq. (5.2.1).[87–90] This non-physical behaviour of the wavefunction is attributed to the failure of the mean-field approximation at the HF level of theory to correctly describe the system, and is connected to the presence of static correlation.[90] The deviation of the eigenvalue of $\hat{\boldsymbol{S}}^2$ from the expected exact value is called spin contamination and is quantified as

$$\langle \hat{\boldsymbol{S}}^2 \rangle - S_{\text{exact}}(S_{\text{exact}} + 1).$$

Spin contamination is typically lowered at the correlated level as compared to the reference because of the inclusion of correlation.[88–90] It is also important to be monitored for non-iterative corrections, since such methods are sensitive to the contamination of the reference.[156]

Another case where the spin multiplicity needs to be monitored is when excited states are targeted. The M_S quantum number of the excited states can be controlled by the choice of the EOM-variant. For EE-EOM, $\Delta M_S = 0$, with $\Delta M_S = 0$ being the difference of M_S between the ground state and the excited one. For SF-EOM ΔM_S can be chosen between $+1$ when exciting a β to an α spinorbital, or -1 when exciting an α to a β. For IP-EOM, $\Delta M_S = +1/2$ when removing an electron from a β spinorbital, and $\Delta M_S = -1/2$ when removing from an α. Lastly for EA-EOM, $\Delta M_S = +1/2$ results when an electon in an β spinorbital is attached, while $\Delta M_S = -1/2$ to a β. Despite this control over M_S at the EOM level, states with different S number (but the same M_S number) may be accessed, because an S state has possible M_S values in the range $[-S, -S+1, \ldots S-1, S]$. As an example, both singlets ($S = 0$) and triplets ($S = 1$) can result at the EE-EOM level starting from a closed-shell reference, since both multiplicities have an $M_S = 0$ component. In addition, excited states are much more sensitive to the spin contamination of the reference compared to the ground states even at the correlated level (beyond CIS).[156,176,177]

To practically calculate the multiplicity, the total spin-squared operator $\hat{\boldsymbol{S}}^2 = \hat{S}^2$ can be expressed through the following sum:

$$\hat{S}^2 = \hat{S}_- \hat{S}_+ + \hat{S}_z^2 + \hbar \hat{S}_z$$

where $\hat{S}_\pm$ are the spin-ladder operators

$$\hat{S}_\pm = \hat{S}_x \pm \mathrm{i}\hat{S}_y.$$

In second quantisation these operators have the following form:

$$\begin{aligned}
\hat{S}_+ &= \sum_{r,\bar{s}} S_{+_{r\bar{s}}} \hat{a}_r^\dagger \hat{a}_{\bar{s}} \\
\hat{S}_- &= \sum_{\bar{p},q} S_{-_{\bar{p}q}} \hat{a}_{\bar{p}}^\dagger \hat{a}_q \\
\hat{S}_z &= \frac{\hbar}{2} \sum_q \hat{a}_q^\dagger \hat{a}_q - \frac{\hbar}{2} \sum_{\bar{p}} \hat{a}_{\bar{p}}^\dagger \hat{a}_{\bar{p}} \\
&= \frac{\hbar}{2} \hat{n}_\alpha - \frac{\hbar}{2} \hat{n}_\beta = \frac{\hbar}{2} \Delta \hat{n}
\end{aligned}$$

The indices used in this derivation differentiate between spinorbitals with α spin that use no bar, while indices with bar denote spinorbitals with β spin

$$|p\rangle = |\phi_p\rangle\,|\alpha\rangle$$
$$|\bar{p}\rangle = |\phi_{\bar{p}}\rangle\,|\beta\rangle\,.$$

The electron-number operators for α and β spin are $\hat{n}_\alpha$ and $\hat{n}_\beta$ respectively, and $\Delta\hat{n} = \hat{n}_\alpha - \hat{n}_\beta$ is their difference. The $S_\pm$ elements of the ladder operators are their one-electron expectation values and they are derived as follows.

$$\hat{s}_+\,|p\rangle = |\phi_p\rangle\,\hat{s}_+\,|\alpha\rangle = 0$$
$$\hat{s}_-\,|\bar{p}\rangle = |\phi_{\bar{p}}\rangle\,\hat{s}_-\,|\beta\rangle = 0$$

$$\hat{s}_+\,|\bar{p}\rangle = |\phi_{\bar{p}}\rangle\,\hat{s}_+\,|\beta\rangle = |\phi_{\bar{p}}\rangle\,\hbar\sqrt{(s-m_s)(s+m_s+1)}\,|\alpha\rangle = |\phi_{\bar{p}}\rangle\,\hbar\sqrt{\left(\frac{1}{2}+\frac{1}{2}\right)\left(\frac{1}{2}-\frac{1}{2}+1\right)}\,|\alpha\rangle = \hbar\,|\phi_{\bar{p}}\rangle\,|\alpha\rangle$$
$$\hat{s}_-\,|p\rangle = |\phi_p\rangle\,\hat{s}_-\,|\alpha\rangle = |\phi_p\rangle\,\hbar\sqrt{(s+m_s)(s-m_s+1)}\,|\beta\rangle = |\phi_p\rangle\,\hbar\sqrt{\left(\frac{1}{2}+\frac{1}{2}\right)\left(\frac{1}{2}-\frac{1}{2}+1\right)}\,|\beta\rangle = \hbar\,|\phi_p\rangle\,|\beta\rangle$$

Symbols $s = \frac{1}{2}$ and $m_s = \pm\frac{1}{2}$ denote the one-electron spin quantum numbers. The one-electron spin-ladder operators $\hat{s}_\pm$ act only on the spin part. The bar on the orbital part signifies only the original spin function that the orbital part accompanies. The elements thus have the following expression.

$$\langle\phi_{\bar{q}}|\,\langle\beta|\,\hat{s}_+\,|\phi_{\bar{p}}\rangle\,|\beta\rangle = \hbar\,\langle\phi_{\bar{q}}|\phi_{\bar{p}}\rangle\,\overbrace{\langle\beta|\alpha\rangle}^{=0}$$
$$\langle\phi_q|\,\langle\alpha|\,\hat{s}_+\,|\phi_{\bar{p}}\rangle\,|\beta\rangle = \hbar\,\langle\phi_q|\phi_{\bar{p}}\rangle\,\overbrace{\langle\alpha|\alpha\rangle}^{=1} = S_{+_{q\bar{p}}}$$
$$\langle\phi_q|\,\langle\alpha|\,\hat{s}_-\,|\phi_p\rangle\,|\alpha\rangle = \hbar\,\langle\phi_q|\phi_p\rangle\,\overbrace{\langle\alpha|\beta\rangle}^{=0}$$
$$\langle\phi_{\bar{q}}|\,\langle\beta|\,\hat{s}_-\,|\phi_p\rangle\,|\alpha\rangle = \hbar\,\langle\phi_{\bar{q}}|\phi_p\rangle\,\overbrace{\langle\beta|\beta\rangle}^{=1} = S_{-_{\bar{q}p}}$$

From these expressions, it is apparent that the elements are the orbital-overlap integrals between ϕ_p and $\phi_{\bar{q}}$ (originating from different spin) multiplied by $\hbar$. In the case of a restricted reference, the overlaps are simply given by $\delta_{p\bar{q}}\hbar$, because the orbital part of spinorbitals is the same between α and β. These elements are complex conjugate of each other.

$$S^*_{+_{q\bar{p}}} = \hbar\,\langle q|\bar{p}\rangle^* = \hbar\,\langle q^*|\bar{p}^*\rangle = \hbar\,\langle\bar{p}|q\rangle = S_{-_{\bar{p}q}}.$$

The norm of these elements is also defined:

$$|S_{q\bar{p}}|^2 = S_{+_{q\bar{p}}}S_{-_{\bar{p}q}}.$$

Following Wick's Theorem, the operators can be written in a normal-ordered form :

$$\hat{S}_z = \frac{\hbar}{2}\{\Delta\hat{n}\} + \frac{\hbar}{2}\Delta n \tag{5.2.3}$$
$$\hat{S}_z^2 = \frac{\hbar^2}{4}\{\Delta\hat{n}\}^2 + \frac{\hbar^2}{2}\{\Delta\hat{n}\}\Delta n + \frac{\hbar^2}{4}\Delta n^2$$

Δn is the electron difference of the reference wavefunction. $\{\Delta\hat{n}\}$ is a normal-order operator whose expectation value gives the excess of electrons between the reference and the correlated wavefunction.

The latter is given by $2\Delta M_S$. The $\hat{S}_-\hat{S}_+$ term can be expressed as:

$$\begin{aligned}
\hat{S}_-\hat{S}_+ &= \sum_{\bar{p},q,r,\bar{s}} S_{-_{\bar{p}q}} S_{+_{r\bar{s}}} \hat{a}^\dagger_{\bar{p}} \hat{a}_q \hat{a}^\dagger_r \hat{a}_{\bar{s}} \\
&= \sum_{\bar{p},q,r,\bar{s}} S_{-_{\bar{p}q}} S_{+_{r\bar{s}}} \{\hat{a}^\dagger_{\bar{p}} \hat{a}_q \hat{a}^\dagger_r \hat{a}_{\bar{s}}\} + \sum_{\bar{p},q,r,\bar{s}} S_{-_{\bar{p}q}} S_{+_{r\bar{s}}} \{\hat{a}^\dagger_{\bar{p}} \hat{a}_{\bar{s}}\} \hat{a}_q \hat{a}^\dagger_r \\
&\quad + \sum_{\bar{p},q,r,\bar{s}} S_{-_{\bar{p}q}} S_{+_{r\bar{s}}} \{\hat{a}_q \hat{a}^\dagger_r\} \hat{a}^\dagger_{\bar{p}} \hat{a}_{\bar{s}} + \sum_{\bar{p},q,r,\bar{s}} S_{-_{\bar{p}q}} S_{+_{r\bar{s}}} \hat{a}^\dagger_{\bar{p}} \hat{a}_q \hat{a}^\dagger_r \hat{a}_{\bar{s}} \\
&= - \sum_{\bar{p},q,r,\bar{s}} S_{-_{\bar{p}q}} S_{+_{r\bar{s}}} \{\hat{a}^\dagger_{\bar{p}} \hat{a}^\dagger_r \hat{a}_q \hat{a}_{\bar{s}}\} + \sum_{\bar{p},q,r,\bar{s}} S_{-_{\bar{p}q}} S_{+_{r\bar{s}}} \{\hat{a}^\dagger_{\bar{p}} \hat{a}_{\bar{s}}\} \delta_{qr\in a} \\
&\quad - \sum_{\bar{p},q,r,\bar{s}} S_{-_{\bar{p}q}} S_{+_{r\bar{s}}} \{\hat{a}^\dagger_r \hat{a}_q\} \delta_{\bar{p}\bar{s}\in\bar{i}} + \sum_{\bar{p},q,r,\bar{s}} S_{-_{\bar{p}q}} S_{+_{r\bar{s}}} \delta_{qr\in a} \delta_{\bar{p}\bar{s}\in\bar{i}} \\
&= - \sum_{\bar{p},q,r,\bar{s}} S_{-_{\bar{p}q}} S_{+_{r\bar{s}}} \{\hat{a}^\dagger_{\bar{p}} \hat{a}^\dagger_r \hat{a}_q \hat{a}_{\bar{s}}\} + \sum_{\bar{p},\bar{s},a} S_{-_{\bar{p}a}} S_{+_{a\bar{s}}} \{\hat{a}^\dagger_{\bar{p}} \hat{a}_{\bar{s}}\} \\
&\quad - \sum_{\bar{i},q,r} S_{-_{\bar{i}q}} S_{+_{r\bar{i}}} \{\hat{a}^\dagger_r \hat{a}_q\} + \sum_{\bar{i},a} S_{-_{\bar{i}a}} S_{+_{a\bar{i}}}.
\end{aligned}$$

The full spin-squared operator is then given by

$$\hat{S}^2 = \hat{C}_2 + \hat{\beta}_+ + \hat{\alpha}_- + \frac{\hbar^2}{2}\{\Delta\hat{n}\}\Big(\frac{\{\Delta\hat{n}\}}{2} + \Delta n + 1\Big) + \frac{\hbar^2}{2}\Delta n\Big(\frac{\Delta n}{2} + 1\Big) + \sum_{\bar{i},a} |S_{a\bar{i}}|^2,$$

with

$$\begin{aligned}
\hat{C}_2 &= - \sum_{\bar{p},q,r,\bar{s}} S_{-_{\bar{p}q}} S_{+_{r\bar{s}}} \{\hat{a}^\dagger_{\bar{p}} \hat{a}^\dagger_r \hat{a}_q \hat{a}_{\bar{s}}\} && \text{Two-body contributions} \\
\hat{\beta}_+ &= + \sum_{\bar{p},\bar{s},a} S_{-_{\bar{p}a}} S_{+_{a\bar{s}}} \{\hat{a}^\dagger_{\bar{p}} \hat{a}_{\bar{s}}\} && \text{One-body } \beta \text{ contributions} \\
\hat{\alpha}_- &= - \sum_{\bar{i},q,r} S_{-_{\bar{i}q}} S_{+_{r\bar{i}}} \{\hat{a}^\dagger_r \hat{a}_q\} && \text{One-body } \alpha \text{ contributions}
\end{aligned}$$

The operator is thus divided in a normal-ordered part

$$\hat{S}^2_N = \hat{C}_2 + \hat{\beta}_+ + \hat{\alpha}_- + \frac{\hbar^2}{2}\{\Delta\hat{n}\}\Big(\frac{\{\Delta\hat{n}\}}{2} + \Delta n + 1\Big) \tag{5.2.4}$$

and the reference contribution

$$\hat{S}^2_{\text{ref}} = \frac{\hbar^2}{2}\Delta n\Big(\frac{\Delta n}{2} + 1\Big) + \sum_{\bar{i},a} |S_{a\bar{i}}|^2. \tag{5.2.5}$$

In order to express the spin-squared expectation value as a derivative of a Lagrangian the spin-squared operator is added to the Hamiltonian linearly

$$\hat{H} \to \hat{H} + \xi\hat{S}^2.$$

The expectation value explicitly assumes the orbitals to remain unchanged, meaning the expectation value must not include orbital relaxation. The derivative of the Lagrangian with respect to ξ then gives the expectation value

$$\frac{\partial L}{\partial \xi} = \langle \hat{S}^2 \rangle .$$

Since the spin-squared operator was introduced to the Hamiltonian, and it does involve the two-body density matrices, care should be taken when constructing the two-body reduced densities in the case of perturbative methods[142] as noted in sec. 4.1.1.

The two-body density matrices are not readily available at the CC and EOM-CC level of theory together with the calculation of the energy as they require the left-side eigenfuctions. In addition, the calculation of the two-body density matrices may scale higher than M^4. For these reasons approximations to the spin-squared expectation value exist. For CC and MP2, the projected spin-squared value is given by

$$S^2_{\text{proj}} = \langle 0| \hat{S}^2 |\Psi_{\text{CC/MP2}}\rangle . \tag{5.2.6}$$

This projected variant is readily available with the calculation of the energy and the correlation contribution is given by

$$S^2_{N\text{proj}} = -\sum_{\bar{j},a,i,\bar{b}} S_{-_{\bar{j}a}} S_{+_{i\bar{b}}} (t^{a\bar{b}}_{i\bar{j}} + t^a_i t^{\bar{b}}_{\bar{j}}) + \sum_{\bar{j},\bar{b},a} S_{-_{\bar{j}a}} S_{+_{a\bar{b}}} t^{\bar{b}}_{\bar{j}} - \sum_{\bar{j},a,i} S_{-_{\bar{j}a}} S_{+_{i\bar{j}}} t^a_i \tag{5.2.7}$$

at CC. For MP2, $t_1 = 0$ and t_2 are substituted by $t_2^{(1)}$. S^2_{proj} is a good indication for $\langle \hat{S}^2 \rangle$, but gives misleading results for a restricted open-shell (RO) reference. In this case the reference wavefunction $|\Phi_{\text{RO}}\rangle$ fulfils both eq. (5.2.2) and (5.2.1), but this is not the case at the correlated level. Still the projected variant gives no spin contamination because of the Hermiticity of $\hat{S}^2$

$$\langle \Phi_{\text{RO}}| \hat{S}^2 |\Psi_{\text{CC}}\rangle = \langle \hat{S}^2 \Phi_{\text{RO}} | \Psi_{\text{CC}}\rangle = \hbar^2 S(S+1) \langle \Phi_{\text{RO}} | \Psi_{\text{CC}}\rangle = \hbar^2 S(S+1).$$

Monitoring the multiplicity of an EOM state before or during the diagonalization procedure would give the possibility of choosing the multplicity. This is important especially at the closed-shell reference case, where the wavefunctions are exact eigenfunctions of eq. (5.2.2) and (5.2.1), and no mixing occurs between singlets and triplets. In the case of real spinrobitals, choosing or monitoring the multiplicity is simple compared to the complex case because of the emergence of a symmetry, or an antisymmetry of the EOM amplitudes. This symmetry, however, is not present in the case of complex orbitals. In order to inexpensively monitor the multiplicity in such cases, the multiplicity of the CIS guess states can be chosen before starting the diagonalization procedure. Since the calculation of the CIS two-body density matrices scales only as M^4, this is viable strategy. Extending this idea to monitoring the EOM states during the diagonalization procedure the following approximations are made. Since ket states are good eigenfunction, the exact bra states are not needed, just an approximation. $\hat{R}^\dagger$ can be used as an approximation

$$\langle 0| \hat{L} e^{-\hat{T}} \approx \langle 0| \hat{R}^\dagger e^{-\hat{T}}.$$

This then gives the following expression for the eigenvalue

$$\hbar^2 S_{\text{EOM}}(S_{\text{EOM}}+1) = \frac{\langle 0| \hat{R}^\dagger e^{-\hat{T}} \hat{S}^2 e^{\hat{T}} \hat{R} |0\rangle}{\langle 0| \hat{R}^\dagger \hat{R} |0\rangle}.$$

Because the CC amplitudes do not change the multiplicity of the reference state, the higher-order terms of the BCH expansion do not contribute. In other words $\hat{S}^2$ and $\hat{T}$ commute, $[\hat{S}^2, \hat{T}] = 0$, for a closed-shell restricted reference. The equation can then be simplified to

$$\hbar^2 S_{\text{EOM}}(S_{\text{EOM}}+1) = \frac{\langle 0| \hat{R}^\dagger \hat{S}^2 \hat{R} |0\rangle}{\langle 0| \hat{R}^\dagger \hat{R} |0\rangle}.$$

A last simplification can be made by using only the single-excitation amplitudes of the EOM-vector, since the different excitation spaces have to be consistent at every level of excitation regarding the multiplicity of the state

$$\hbar^2 S_{\text{EOM}}(S_{\text{EOM}}+1) = \frac{\langle 0| \hat{R}_1^\dagger \hat{S}^2 \hat{R}_1 |0\rangle}{\langle 0| \hat{R}_1^\dagger \hat{R}_1 |0\rangle}. \tag{5.2.8}$$

This novel strategy reduces the cost of calculating the multiplicity of an EOM state, assuming both the EOM and the CC state are exact eigenfunctions of $\hat{S}^2$, to that of a CIS expectation-value calculation as the form of eq. (5.2.8) is the same as the equation for CIS. This allows the multiplicity to be monitored during the diagonalization procedure, and also to be readily available with the calculation of the energy. It is important to note, that this is a new approach for monitoring the multiplicity of

EOM-CC states during the diagonalization procedure, and was needed to be developed because the strategies used for the field-free cases are not applicable for complex wavefunctions.

The calculation of the spin-expectation value for the reference wavefunction [eq. (5.2.5)], the spin-expectation value using the projected approximation at the MP and CC levels of theory [eq. (5.2.7)], the full contributions to the spin-expectation value at the correlated level [eq. (5.2.4)] and the approximation for exact eigenfunctions at the EOM-CC level [eq. (5.2.8)] were implemented in the QCUMBRE program package.

5.2.2 Calculations of the spin-multiplicity of open-shell systems

Here, the spin-squared expectation values at the EOM-CCSD level of theory that helped with the analysis of the excited states of the CH radical from subsec. 4.3.2 are presented.

	30°			60°		
B (B_0)	$3^2A(^2\Delta)$	$4^2A(1^2\Sigma^-)$	$5^2A(2^2\Sigma^-)$	$3^2A(^2\Delta)$	$4^2A(1^2\Sigma^-)$	$5^2A(2^2\Sigma^-)$
0.00	0.7501	0.7646	**0.8691**	0.7501	0.7646	**0.8691**
0.05	0.7502	0.7636	**0.8686**	0.7522	0.7620	**0.8095**
0.10	**1.9200**	0.7602	**0.8640**	0.7733	0.7566	**0.8639**
0.15	**0.9872**	0.7556	**0.8555**	**0.9330**	0.7526	**0.8652**
0.20	**0.9271**	0.7521	**0.8485**	**1.3097**	0.7507	0.7521
0.25	**0.9348**	0.7507	**0.6612**	**0.8298**	0.7518	0.7521
0.30	**0.9700**	0.7282	**0.8285**	0.7818	0.7529	**1.5662**
0.35	**1.0510**	0.7483	**0.9342**	0.7655	**0.8669**	**0.8321**
0.40	**1.4328**	0.7911	**0.8163**	0.7570	**0.9331**	**0.8362**
0.45	0.7742	**0.9901**	**0.8223**	0.7535	**1.7397**	**1.4159**
0.50	0.7539	**1.1484**	**0.8480**	0.7523	**0.8164**	0.7724
0.55	0.7539	**0.8279**	**0.8335**	0.7517	0.7732	0.7611
0.60	0.7544	0.7908	**0.8059**	0.7513	0.7692	0.7663
0.65	0.7552	0.7779	0.7756	0.7510	0.7639	**0.9674**
0.70	0.7561	0.7716	**0.8158**	0.7510	0.7636	**1.5374**
0.75	0.7573	0.7680	**0.8147**	0.7528	0.7637	**2.0505**
0.80	0.7587	0.7658	0.7670	0.7612	0.7629	**1.4875**
0.85	0.7603	0.7645	0.7706	0.7975	0.7605	**1.2271**
0.90	0.7622	0.7639	0.7794	**0.9726**	0.7570	**1.0844**
0.95	0.7642	0.7636	0.7975	**1.7584**	0.7540	**0.9928**
1.00	0.7659	0.7632	**0.8423**	**1.6027**	0.7540	**0.9235**

Table 5.1: Spin-expectation value as a function of the magnetic field in $\hbar^2$ for the $3^2A(^2\Delta)$, $4^2A(1^2\Sigma^-)$ and $5^2A(2^2\Sigma^-)$ states at the EOM-CCSD level for a field direction of 30° and 60° relative to the molecular bond. The values that deviate from the exact 0.75 $\hbar^2$ value by more than 0.1 $\hbar^2$ are marked as bold.

	$1^2A'$ reference			$1^2A''$ reference		
B (B_0)	$2^2A'(^2\Delta)$	$2^2A''(1^2\Sigma^-)$	$3^2A''(2^2\Sigma^-)$	$2^2A'(^2\Delta)$	$2^2A''(1^2\Sigma^-)$	$3^2A''(2^2\Sigma^-)$
0.00	0.7501	0.7646	**0.8691**	0.7501	0.7646	**0.8691**
0.05	0.7512	0.7561	**0.9326**	0.7512	0.7544	**0.9414**
0.10	0.7515	0.7624	**0.9002**	0.7509	0.7583	**0.9284**
0.15	0.7531	0.7682	**0.8739**	0.7507	0.7697	**0.9126**
0.20	0.7540	0.7731	**0.8581**	0.7506	0.7985	**0.8862**
0.25	0.7507	0.7792		0.7505	**0.8537**	**0.8628**
0.30	0.7504	0.7917	**1.2948**	0.7504	**1.0744**	**1.7902**
0.35	0.7503	**0.8248**	**1.3567**	0.7504	**1.7037**	**0.9337**
0.40	0.7511	**0.8774**	**1.2784**	0.7503	**1.3278**	**1.0240**
0.45	0.7522	**0.9288**	**0.8933**	0.7502	**0.9914**	**1.3300**
0.50	0.7538	**0.9764**	**0.8917**	0.7502	**0.9686**	**1.8151**
0.55	0.7570	**1.0205**	**0.9105**	0.7502	**0.9898**	**2.2553**
0.60	0.7648	**1.0601**	**0.9623**	0.7503	**1.0168**	**1.6122**
0.65	0.7823	**1.0918**	**1.0946**	0.7503	**1.0455**	**1.4078**
0.70	**0.8080**	**1.1127**	**1.4019**	0.7504	**1.0744**	**1.3328**
0.75	**0.8317**	**1.1229**	**1.9381**	0.7504	**1.1013**	**1.3058**
0.80	**0.8518**	**1.1237**	**1.9134**	0.7505	**1.1225**	**1.3022**
0.85	**0.8693**	**1.1162**	**1.5534**	0.7507	**1.1352**	**1.3129**
0.90	**0.8384**	**1.1012**	**1.3568**	0.7509	**1.1380**	**1.3282**
0.95	0.7521	**1.0796**	**1.2521**	0.7512	**1.1312**	**1.2897**
1.00	0.7507	**1.0521**	**1.2051**	0.7517	**1.1161**	**1.0668**

Table 5.2: Spin-expectation value as a function of the magnetic field in $\hbar^2$ for the $2^2A'(^2\Delta)$, $2^2A''(1^2\Sigma^-)$ and $3^2A(2^2\Sigma^-)$ states at the EOM-CCSD level for a perpendicular field direction relative to the molecular bond. The values that deviate from the exact 0.75 $\hbar^2$ value by more then 0.1 $\hbar^2$ are marked as bold.

Chapter 6

Exploitation of Molecular Symmetry in a Magnetic Field

Most large molecules, like polymers, biological systems, etc., are not symmetric. Still, a large fraction of molecular systems of interest that can be and that are studied by means of quantum-chemical calculations exhibit various degrees of symmetry. Even non-symmetric molecules can be studied under the lens of deviation from a symmetric model system. The exploitation of symmetry, when possible, can drastically lower the cost of a quantum-chemical calculation and an analysis based on symmetry may offer insight on the physics behind the chemical phenomena studied, and may also lead to qualitative predictions like the derivation of selection rules for transitions, or the existence of a Jahn-Teller effect.[178–183]

In the presence of a magnetic field, symmetry is in most cases reduced, due to the introduced anisotropy. The use of symmetry, as will be shown, results nonetheless in significant changes when it is possible to be exploited. Moreover, the kind of symmetry that molecular systems in a magnetic field exhibit in combination with the need for complex algebra differentiates the strategies used compared to the field-free case. These intricacies will be addressed in the following sections.

6.1 Group theory and molecular symmetry

The study of symmetry is mathematically formulated in group theory.[181,183] In this section, the basics of group theory will be briefly recapitulated, and its employment in this thesis will be presented.

A mathematical group is a collection of elements $\mathscr{G}$ that together with a binary operation $\circ$ possess the following properties[181]

1. The collection is closed under the operation: If $x, y \in \mathscr{G}$, then $z = x \circ y$ is also in the collection $z \in \mathscr{G}$.

2. The elements have associativity with respect to the binary operation: $(x \circ y) \circ z = x \circ (y \circ z)$.

3. There exists a neutral element $E \in \mathscr{G}$, such that $x \circ E = E \circ x = x$. This is the identity element (Einheit).

4. For each element x, there exists an inverse element x^{-1}, such that $x \circ x^{-1} = x^{-1} \circ x = E$.

In addition, if the commutative property is true for a given group

$$x \circ y = y \circ x,$$

the group is said to be Abelian.

The collection of symmetry operations regarding an object in space forms a group. Here, the binary operation is the multiplication, under which the symmetry operations act successively, with the right-most operation on the expression acting first. The results of multiplying two symmetry operations is another symmetry operation (first property of a group). For molecules, all the symmetry

operations leave at least one point in space unchanged (the centre of mass) and are thus called point groups. For infinite crystals, there exist symmetry operations that move all points and are called space groups.[181] The possible symmetry operations in a point group are the following:

- The identity $\hat{E}$ which is the neutral element and exists in all point groups.
- The proper rotation $\hat{C}_n^m = \overbrace{\hat{C}_n\hat{C}_n\hat{C}_n\dots}^{m \text{ times}}$ over an axis. Numbers m, n define the rotational angle $\theta = \frac{2m\pi}{n}$. If m is absent, $m = 1$ is assumed.
- The inversion $\hat{i}$ with respect to a point.
- The reflection $\hat{\sigma}$ with respect to a plane. The reflection can be written as $\hat{\sigma} = \hat{C}_2\hat{i}$, with $\hat{C}_2$ being defined by the axis perpendicular to the reflection plane, and $\hat{i}$ defined by the point of intersection between the rotational axis and the reflection plane.
- The improper rotation $\hat{S}_n^m = \overbrace{\hat{S}_n\hat{S}_n\hat{S}_n\dots}^{m \text{ times}}$ over an axis and a plane. For m even $\hat{S}_n^m = \hat{C}_n^m$, while for m odd $\hat{S}_n^m = \hat{\sigma}\hat{C}_n^m$, with $\hat{\sigma}$ being defined on a plane perpendicular to the rotation axis.

Assuming a function of space $f(\boldsymbol{r})$, the action of a symmetry operation $\hat{G}$ on $f(\boldsymbol{r})$ is expressed as

$$\hat{G}f(\boldsymbol{r}) = f(\hat{G}^{-1}\boldsymbol{r}). \tag{6.1.1}$$

Matrix representations

In a system that exhibits symmetry, a set of (non-symmetric) functions $\{f_i(\boldsymbol{r})\}$ transforms among themselves under a symmetry operation $\hat{G}$

$$\hat{G}\left(f_1(\boldsymbol{r}), f_2(\boldsymbol{r}), f_3(\boldsymbol{r})\dots\right) = \left(f_1(\boldsymbol{r}), f_2(\boldsymbol{r}), f_3(\boldsymbol{r})\dots\right)\mathbf{D}(G). \tag{6.1.2}$$

The matrix $\mathbf{D}(G)$ is a square matrix with the transformation coefficients resulting from operating with $\hat{G}$ on the function

$$\hat{G}f_i = \sum_j D_{ij}(G)f_j.$$

The set of matrices $\mathrm{D} = \{\mathbf{D}(G)\}$ for all elements G belonging to a group $\mathscr{G}$ is the matrix representation of the group. The matrices follow the same rules regarding multiplication as the symmetry elements.

If a matrix representation can be brought in a block diagonal form under non-equivalent unitary transformations

$$\begin{pmatrix} \boldsymbol{\Gamma}^\alpha(G) & 0 & \dots \\ 0 & \boldsymbol{\Gamma}^\beta(G) & \\ \vdots & & \ddots \end{pmatrix},$$

for every G, it is called reducible. $\boldsymbol{\Gamma}^\alpha(G)$, $\boldsymbol{\Gamma}^\beta(G)$, etc. are matrices corresponding to symmetry element G that have resulted from the aforementioned transformation. Any representation that cannot be

Notation	Use
G	Symmetry element
$\hat{G}$	Symmetry operation
$\mathscr{G}$	Group
$\mathbf{D}(G)$	The matrix corresponding to symmetry element G
D	Matrix representation consisting of all matrices $\mathbf{D}(G)$
Γ^α	IRREP with index α
$\boldsymbol{\Gamma}^\alpha(G)$	The matrix corresponding to symmetry element G of IRREP Γ^α

Table 6.1: A collection of the different notations used.

brought into this form for at least one symmetry element is an irreducible representation (IRREP) $\Gamma^\alpha = \{\mathbf{\Gamma}^\alpha(G)\}$. The dimensions of matrices of the IRREP are $n^\alpha \times n^\alpha$ with n^α the order of the IRREP. Functions that transform as IRREP Γ^α of a point group under symmetry operations are called symmetric and form the basis functions of the IRREP. IRREPs of Abelian groups are necessarily one-dimensional.

In order to ease the readability of the abstract mathematical expressions used in group theory, the symbols are summarized and explained in tab. 6.1.

Two operations are defined for the matrix representations, the direct sum $\oplus$ as

$$\Gamma^\alpha \oplus \Gamma^\beta = \mathrm{D}^{\alpha\oplus\beta},$$

where

$$\mathbf{D}^{\alpha\oplus\beta}(G) = \begin{pmatrix} \mathbf{\Gamma}^\alpha(G) & 0 \\ 0 & \mathbf{\Gamma}^\beta(G) \end{pmatrix}$$

for every G, and the direct product $\otimes$ as

$$\Gamma^\alpha \otimes \Gamma^\beta = \mathrm{D}^{\alpha\otimes\beta},$$

where $\mathrm{D}^{\alpha\otimes\beta}$ is reducible in the general case. If F_i^α and F_j^β are the basis functions of Γ^α and Γ^β, respectively, the basis functions of $\mathrm{D}^{\alpha\otimes\beta}$ are all the possible products

$$F_p^{\alpha\otimes\beta} = F_i^\alpha F_j^\beta,$$

and the elements of the matrices are given by

$$D_{pq}^{\alpha\otimes\beta}(G) = \Gamma_{ik}^\alpha(G)\Gamma_{jl}^\beta(G),$$

with index p corresponding to the combination i, j and q to k, l. A reducible representation can always be reduced to a direct sum of IRREPs

$$\mathrm{D} = c^\alpha\Gamma^\alpha \oplus c^\beta\Gamma^\beta \oplus \ldots,$$

with c^α, c^β the degeneracy of the IRREPs in D. For every point group, a special IRREP exists, namely the totally-symmetric IRREP Γ^1. Γ^1 is one-dimensional and the matrices for all symmetry operations equal to 1 ($\Gamma_{11}^1(G) = 1$ for every G). Additionally, in the case of complex Abelian groups, there exist pairs of complex conjugate IRREPs Γ^α and $\Gamma^{\alpha*}$, so that the elements of the matrices of $\Gamma^{\alpha*}$ are the complex conjugate of Γ^α

$$\Gamma^\alpha = (\Gamma^{\alpha*})^*.$$

The direct product of complex conjugate IRREPs always includes the totally symmetric IRREP

$$\Gamma^\alpha \otimes \Gamma^{\alpha*} = \Gamma^1 \oplus \ldots$$

For the irreducible representations, the great orthogonality theorem holds

$$\sum_G \Gamma_{ij}^{\alpha*}(G)\Gamma_{kl}^\beta(G) = \frac{g}{n^\alpha}\delta_{\alpha\beta}\delta_{ik}\delta_{jl},$$

with g as the order of the group $\mathscr{G}$, given by the sum over squares of the dimensions n^α of all IRREPs

$$g = \sum_\alpha (n^\alpha)^2.$$

The order of the group is also given by the number of elements. The great orthogonality theorem relates the matrix elements among the different symmetry elements and IRREPs. It results in many useful relations, like the vanishing integral rule which will be introduced in the following paragraphs.

Characters of the matrix representations

To achieve a more compact handling of the IRREPs, instead of working with the matrices themselves, the characters χ_G^α can be used instead, with

$$\chi_G^\alpha = \sum_i^{n^\alpha} D_{ii}^\alpha(G).$$

The characters of each point group can be found in character tables,[184] together with the symmetry elements and the IRREPs. Additionally, polynomials of the Cartesian coordinates are associated with IRREPs, for which they can act as basis functions. With the use of characters, the great orthogonality theorem simplifies to

$$\sum_G \chi_G^\alpha \chi_G^\beta = g\delta_{\alpha\beta}.$$

Projectors

The projector $\hat{\mathscr{P}}^\alpha$ acting on a random representation D gives the degeneracy of IRREP α

$$\hat{\mathscr{P}}^\alpha \mathrm{D} = c^\alpha.$$

The projector is idempotent

$$\hat{\mathscr{P}}^\alpha \hat{\mathscr{P}}^\alpha = \hat{\mathscr{P}}^\alpha$$

and takes the following form

$$\hat{\mathscr{P}}^\alpha = \frac{n^\alpha}{g} \sum_G \chi_G^{\alpha *} \hat{G}. \tag{6.1.3}$$

Symmetry-adapted functions

Starting from a set of non-symmetric basis functions $\{f_i(\boldsymbol{r})\}$, symmetry-adapted functions can be constructed by applying the projection operators

$$\hat{\mathscr{P}}^\alpha f_i = F_i^\alpha. \tag{6.1.4}$$

Symmetry-adapted functions can act as basis functions for a given IRREP. For IRREPS with $n^\alpha > 1$, it is necessary to act with the projector on different f_i in order to derive the complete set of basis functions, which is a "trial and error" procedure. Symmetry-adapted functions of Abelian groups reproduce the character of the IRREP upon action of the symmetry element

$$\hat{G} F_i^\alpha = \chi_G^\alpha F_i^\alpha. \tag{6.1.5}$$

The rule of vanishing integrals

One of the most important advantages of working with symmetry-adapted functions, instead of non-symmetric functions, is that integrals over the whole space involving symmetric functions vanish in certain cases and hence do not need to be explicitly calculated. More specifically, an integral of the form

$$I = \int^S \hat{O}^{\alpha'} F^\alpha \hat{O}^{\beta'} F^\beta \ldots \mathrm{d}\boldsymbol{r},$$

with operators $\hat{O}^{\alpha'}$ and $\hat{O}^{\beta'}$ associated with the respective IRREPs, may be non-zero only if the direct product of the IRREPs associated with the involved functions and operators contains the totally-symmetric IRREP

$$\Gamma^{\alpha'} \otimes \Gamma^\alpha \otimes \Gamma^{\beta'} \otimes \Gamma^\beta \otimes \ldots \neq \Gamma^1 \oplus \cdots \Rightarrow I = 0. \tag{6.1.6}$$

This rule of vanishing integrals follows from the great orthogonality theorem.

Cosets and double cosets

Cosets and double cosets provide disjoint partitionings of the group elements.[144,182,183,185–187] For a subgroup $\mathscr{H}$ of $\mathscr{G}$

$$\mathscr{H} \subset \mathscr{G},$$

a symmetry element $G \in \mathscr{G}$ defines the left coset as

$$G\mathscr{H} = \{GH_1, GH_2, \dots\},$$

with $GH_i = G \circ H_i$ a shorter notation for the binary operation. Similarly the right coset is defined

$$\mathscr{H}G = \{H_1G, H_2G, \dots\}.$$

In the case that $\mathscr{H} = \mathscr{G}$, all left and right cosets reproduce the original group $\mathscr{G}$ with its elements rearranged (rearrangement theorem). This property can be used in a given sum over all elements of a group[a]

$$\sum_G \dots G = \sum_G \dots GU. \tag{6.1.7}$$

Here, G is replaced by GU (or UG), where U is an element of $\mathscr{G}$. The notation $\dots G$ signifies any possible expression that contains the symmetry element G in any form (matrix, operation, character, etc.). In a coset, each element occurs only once. Cosets arising from different elements of $\mathscr{G} \ni F, G$, namely $F\mathscr{H}$ and $G\mathscr{H}$, are either distinct, having no common elements, or identical, having all elements in common.

Going one step further, double cosets are defined as

$$\mathscr{F}G\mathscr{H} = \{F_1GH_1, F_1GH_2, \dots, F_2GH_1, \dots\},$$

with $\mathscr{F}, \mathscr{H} \subset \mathscr{G}$. In a given double coset, each element G occurs λ_G times, with λ_G being the number of common elements of subgroups $\mathscr{F}$ and $G\mathscr{H}G^{-1}$

$$\lambda_G = |\mathscr{F} \cap G\mathscr{H}G^{-1}|.$$

For Abelian groups, this degeneracy number is independent of G

$$\lambda_G = |\mathscr{F} \cap \mathscr{H}|,$$

since the elements commute. Because double cosets are either distinct or identical as well, one may choose a random element from each distinct double coset R, to represent it. These so-called double-coset representatives (DCRs) are normally chosen as the first element R from each distinct double coset and are associated with a degeneracy number λ_R. Using the DCRs, a given sum over all elements may be replaced by a double-coset decomposition (DCD).

$$\sum_G^{\mathscr{G}} \dots G = \sum_F^{\mathscr{F}} \sum_R^{\text{DCRs}} \sum_H^{\mathscr{H}} \frac{1}{\lambda_R} \dots FRH \tag{6.1.8}$$

In the above substitution, the elements G are generated by all the distinct double cosets $\mathscr{F}R\mathscr{H}$ λ_R times. In order to gain any simplification from this decomposition, the subgroups $\mathscr{F}$ and $\mathscr{H}$ are chosen in such a way that the action of their elements leaves the expression invariant

$$\dots FRH = \dots R.$$

In this case, these elements can be neglected and the sum over all elements is reduced to a sum over DCRs, thus avoiding redundant or equivalent calculations. To achieve this goal, F may be substituted by F^{-1}, which does not affect the overall result since $\mathscr{F}$ is a group (group property no. 4).

[a] In the sum over elements of a group, the elements themselves are used as indices as a more compact notation. $\sum_i \dots G_i = \sum_G \dots G$.

Specifics of molecular symmetry

As stated at the beginning of this section, many molecules of interest exhibit symmetry which can be mathematically described by point groups. For a given molecule, consisting of nuclei $A, B, C, \ldots$, there exist symmetry-equivalent nuclei that transform into each other under symmetry operations. A given symmetry element G transforms nucleus A to $G(A)$

$$GA = G(A).$$

Choosing one of the equivalent nuclei A, there exist a subset of symmetry elements $\{U\}$ that leave this nucleus invariant $U(A) = A$. This subset, forms a group $\mathscr{U} = \{U\}$, making it a subgroup of the molecular point group $\mathscr{G} \supset \mathscr{U}$. $\mathscr{U}$ is then called the stabiliser of A, $\mathscr{U}_A$.[144,183,186,187] All symmetry equivalent nuclei of the same type as A may be found by the distinct left cosets of $\mathscr{U}$ in $\mathscr{G}$, namely $G\mathscr{U}$. The number of the distinct left cosets is the number of equivalent nuclei A. This number is given by the orders of groups $\mathscr{U}$ and $\mathscr{G}$, u and g respectively, as the index of the stabilizer g/u.

The symmetry elements of the magnetic field

The magnetic field introduces an anisotropy to the system that usually lowers the molecular symmetry. The reduction of symmetry is dependent on the orientation of the magnetic field relative to the molecule.

The magnetic field is a pseudovector, and as such it remains invariant under inversion. This has no effect for the identity and for proper rotations, but changes the action of reflection and improper rotation. This different behaviour for the action of the the possible symmetry operations on a pseudovector is summarized by the following relations

$$\begin{aligned} \hat{i}\boldsymbol{p} &= \boldsymbol{p} \\ \hat{\sigma}\boldsymbol{p} &= \hat{C}_2\boldsymbol{p} \\ \hat{S}_n\boldsymbol{p} &= \hat{C}_n\hat{C}_2\boldsymbol{p}. \end{aligned}$$

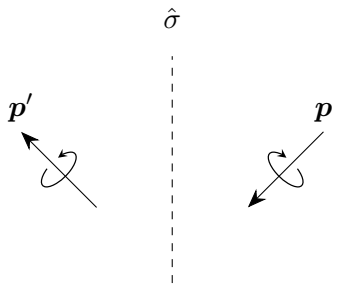

Figure 6.1: The action of a reflection $\hat{\sigma}$ on a pseudovector $\boldsymbol{p}$.

The action of the reflection on a pseudovector is visualized in fig. 6.1. Symmetry elements of the magnetic field are hence the proper and improper rotations parallel to the magnetic field, as well as inversions, and reflections perpendicular to the magnetic field.

Because of the behaviour of the magnetic field under symmetry operations, only specific groups can describe the symmetry of a molecule in the presence of a magnetic field. It can be shown that such point groups are necessarily Abelian.[188]

It is important to note that the magnetic field interaction does not depend on the direction of the magnetic field for a given axis relative to the molecule. This is best seen in fig. 6.2. The two different directions result in two systems described by different wavefunctions. Still, the energies of the systems are nonetheless the same in either direction. This equivalence may result in counter-intuitive situations where nuclei are not strictly symmetry equivalent, but still experience the same chemical environment. Examples of the latter will be encountered in chap. 7.

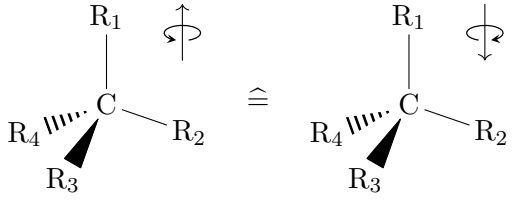

Figure 6.2: Depiction a molecule in two different directions of the magnetic field along the same axis.

6.2 Employment of molecular symmetry in quantum-chemical calculations

The symmetry of the molecule is reflected in the electronic Hamiltonian and as such, the electronic wavefunction solution must transform as an IRREP of the molecular point group. Moreover, canonical HF orbitals are symmetric functions themselves.[178–183,b] The symmetric form of the wavefunctions allows the exploitation of symmetry in quantum-chemical calculations. This is achieved by avoiding redundant calculations that are symmetry equivalent, and by the use of the vanishing-integral rule thus avoiding the calculation of trivial zeros. The observed savings are at least $1/g$ or better, with g, the order of the point group of the molecule. The use of symmetry often makes the resulting computer code more complicated and difficult to read, which is a price readily paid for efficiency.

Symmetry can also be exploited in the study of molecular vibrations or the geometry optimization of a molecule. The exploitation of symmetry in geometry optimization is achieved by restricting the optimization steps to displacements that are associated with the totally symmetric IRREP only, so that the symmetry of the molecule is retained during the geometry optimization, thus decreasing the degrees of freedom of the optimization. Such a procedure makes sense because displacements associated to IRREPs different than the totally-symmetric one have a vanishing gradient resulting from the vanishing-integral rule.[181,186,c]

For the exploitation of symmetry, Abelian groups are very convenient to use because of the one-dimensional IRREPs and the commutative property. As such, even molecules with higher symmetry are often studied in an Abelian subgroup. Most quantum-chemical programs make use of real Abelian point groups, meaning D_{2h} and its subgroups, and their handling is well documented in the literature.[144,179,180,183,186,189] For molecules in a magnetic field, complex algebra needs to be used. More importantly, the symmetry that molecules exhibit in the presence of a magnetic field is often described by complex Abelian point groups, with real Abelian subgroups of lower order. For this reason, it is important for ff methods that not only real Abelian groups but also complex Abelian groups are used to yield significant reduction in the computational cost. As such, the theoretical background for the handling of symmetry were extended to the case of complex Abelian groups in this thesis.

In the following paragraphs, the implementation of symmetry in the CFOUR and QCUMBRE program packages is discussed. In CFOUR, developments include the symmetry recognition of a molecule in the presence of a magnetic field and the symmetry exploitation in the calculation of integrals over atomic orbitals in the case of complex Abelian point groups. In QCUMBRE, the symmetry of the wavefunction and the orbitals are used to take advantage of the vanishing-integral rule.

6.2.1 Implementation of symmetry in CFOUR

Symmetry handling in a magnetic field

The symmetry handling in CFOUR has been realized throughout the different module programs. The symmetry recognition, i.e., identifying the point group of the molecule takes place in **joda**. The main function that controls the symmetry recognition is the `symmetry` subroutine.

In the `symmetry` subroutine, the symmetry recognition starts after the reorientation of the molecule. The reorientation is done by diagonalizing the inertia tensor

$$I_{ij} = \sum_{A}^{N_\mathrm{N}} m_A \left(|\vec{x}_A|^2 \delta_{ij} - x_{A_i} x_{A_j} \right),$$

and choosing the smallest eigenvalue to coincide with the z-axis. Here, m_A is the mass of the nucleus A, $\vec{x}_A = (x_{A_1}, x_{A_2}, x_{A_3}) = (x_{Ax}, x_{Ay}, x_{Az})$ its Cartesian coordinates, indices i, j run from 1 to 3 representing x, y, and z, respectively, and N_N is the number of nuclei in the molecule. In case of

[b] A symmetric wavefunction may result from non-symmetric orbital functions, for example localized orbital may be non-symmetric.

[c] For more details see chap. 7.

a double degeneracy the unique eigenvalue is chosen for the z-axis. This ensures that the principal rotation axis is the z-axis, which is handy for the recognition algorithm. The recognition of the point group starts by checking the degeneracy of the inertia tensor. No degeneracy corresponds to real Abelian groups (D_{2h} and subgroups), double degeneracy to complex Abelian with pairs of complex conjugate IRREPs (C_n, C_{nh} with $n > 2$ and S_n with even $n > 2$) or non-Abelian groups with at most two-dimensional IRRERs (D_n, D_{nh}, C_{nv} with $n > 2$ and D_{nd} with $n > 1$), and triple degeneracy to cubic or higher groups (I, I_h, T, T_d, T_h, O, O_h). The algorithm then determines the group by operating on the coordinates of the nuclei in the molecule with symmetry operations and comparing the result with the original set of coordinates to determine whether they are symmetry elements. CFOUR can recognize all the aforementioned point groups up to $n = 24$. In the case of linear molecules, the inertia tensor has two degenerate vanishing eigenvalues. This is used by the algorithm to recognize such systems. The point groups describing linear molecules are of infinite order and are either non-Abelian ($D_{\infty h}$, $C_{\infty v}$) or complex Abelian ($C_{\infty h}$, C_∞). Atoms belong to the group of full rotation, $SO(3)$, which is also an infinite non-Abelian point group, but $SO(3)$ cannot be recognized by the algorithm, recognizing it instead as I_h. The full point group is saved as a string in `FPGRP`. Based on the results, the largest real Abelian group is saved in `BPGRP`, which is either the full point group or a subgroup, and then the computational point group `PGRP` which is either the same as `BPGRP` or a user-defined subgroup. The use of symmetry is regulated by the keyword `SYMMETRY=ON` or `SYMMETRY=OFF`, and a specific computational point group is defined with keyword `SUBGROUP`. The use of no symmetry (`SYMMETRY=OFF`) is equivalent to using the C_1 point group `SUBGROUP=C1`, which is the group containing only the identity.

The symmetry recognition in the presence of a magnetic field was newly implemented during this thesis, based on the existing algorithm. The magnetic-field vector is handled as an additional entry to the nuclear coordinates of the molecule at the end of the `Q` array, where the coordinates of the nuclei are saved. As already mentioned, the molecule and the magnetic field are always reoriented so that the magnetic field is parallel to the z-axis. This ensures that the z-axis is the principal rotation axis, since only rotations parallel to the magnetic field can be symmetry elements. In the case that a magnetic field is present, reorientations based on the inertia tensor are skipped. The symmetry operations on the nuclear coordinates and on the magnetic-field vector are carried out through matrix multiplications. The matrices used regrading a spacial vector (not a pseudovector) are

$$\begin{aligned}
\hat{i} &= \begin{pmatrix} -1 & 0 & 0 \\ 0 & -1 & 0 \\ 0 & 0 & -1 \end{pmatrix} && \text{Inversion with respect to the Cartesian origin} \\
\hat{\sigma}(k) &= \hat{C}_2(k)\hat{i} && \text{Reflection on the } ij \text{ plane with } k \text{ the perpendicular direction} \\
\hat{S}_n^m(k) &= \hat{\sigma}(k)\hat{C}_n^m(k),\ m \text{ odd} && \text{Improper rotation over axis } k
\end{aligned} \tag{6.2.1}$$

The rotation matrix $\hat{C}_n^m(k)$ can be derived from the general case of a $\hat{C}(\theta, \hat{u})$ rotation around unit vector $\hat{u} = (u_x, u_y, u_z)$ by angle θ, which is given by

$$\hat{C}(\theta, \hat{u}) = \begin{pmatrix} \cos\theta + u_x^2(1-\cos\theta) & u_x u_y(1-\cos\theta) - u_z\sin\theta & u_x u_z(1-\cos\theta) + u_y\sin\theta \\ u_y u_x(1-\cos\theta) + u_z\sin\theta & \cos\theta + u_y^2(1-\cos\theta) & u_y u_z(1-\cos\theta) - u_x\sin\theta \\ u_z u_x(1-\cos\theta) - u_y\sin\theta & u_z u_y(1-\cos\theta) + u_x\sin\theta & \cos\theta + u_z^2(1-\cos\theta) \end{pmatrix}.$$

Since the magnetic field is an axial vector (pseudovector), additional matrices are required:

$$\begin{aligned}
\hat{i} &= \begin{pmatrix} 1 & 0 & 0 \\ 0 & 1 & 0 \\ 0 & 0 & 1 \end{pmatrix} = \hat{E} && \text{Pseudovector inversion with respect to the Cartesian origin} \\
\hat{\sigma}(k) &= \hat{C}_2(k) && \text{Pseudovector reflection on the } ij \text{ plane with } k \text{ the perpendicular direction} \\
\hat{S}_n^m(k) &= \hat{C}_2(k)\hat{C}_n^m(k) && \text{Pseudovector improper rotation over axis } k
\end{aligned}$$

The rotation matrices are the same as for polar (true) vectors. The point group of a molecule in the presence of magnetic field is determined by the exact same recognition algorithm as in the field-free

case, rather than as a special case different from the recognition in the absence of field. The latter variant is described in ref. [188]. In practice, both approaches are equivalent.

Point groups describing molecules in a magnetic field are necessarily Abelian, but may be complex. For ff calculations that are invoked by setting `BFIELD=ON`, the possibility to use complex Abelian groups as the computational group is activated with the keyword `SYMMETRY=COMPLEX`. `SYMMETRY=ON` (default) only allows for real Abelian computational groups. The maximum order of a computational point group is restricted to 8. This way, C_n with n = 3-8, C_{nh} with $n = 3, 4$, and S_n with $n = 4, 6, 8$ have been implemented in CFOUR as possible computational point groups. Complex point groups can be used for the field-free case as well, but since the resulting wavefunction will necessarily be complex, the `BFIELD=ON` keyword has to be set. `SYMMETRY=COMPLEX` works for single-point calculations and for geometry optimizations, but has so far not been implemented for a vibrational analysis. User-defined complex Abelian groups can also be given in the `SUBGROUP` keyword.

Double-coset decomposition in the calculation of integrals over atomic orbitals

The atomic-orbital (AO) basis set is a set of non-symmetric functions that transform among themselves under the symmetry elements of the molecular point group as seen in eq. (6.1.2). In many approaches including the one used in this thesis, the AOs are pretransformed to symmetry-adapted orbitals (SAOs) using the projections in eq. (6.1.4). Since orbitals resulting from the canonical HF equations are expected to be symmetric functions, it is more convenient to approach them as a combination of symmetric functions, which restricts the linear expansion to SAOs associated with the same IRREP, rather than as a combination of non-symmetric AOs (which does not restrict the expansion). This transformation that would lead to the exploitation of the vanishing-integral rule, is bothersome and non-unique. In addition, it does not ensure that symmetry-equivalent calculations of integrals are avoided.

The approach used in this thesis for the exploitation of symmetry during the calculation of integrals over AOs makes use of the DCD.[144,183,186] The original formulation of this approach targets both Abelian and non-Abelian groups, but it is most suitable for the implementation in the case D_{2h} and subgroups. In the following paragraphs, the simplifications used in the original papers for real Abelian groups are reexamined in order to construct new working equations for the use of DCD in the case of complex Abelian groups.

In the DCD method, avoiding symmetry-equivalent calculations of integrals is ensured by first dividing the molecule into a non-redundant and a redundant part, where the latter can be generated by the action of symmetry operations onto the former. For the construction of SAOs, projections are then limited to the non-redundant part. Secondly, SAOs are not explicitly calculated. Instead, integrals over SAOs are calculated directly with implicitly generated SAOs.

Here, an SAO is denoted by F^{α}_{kA} and is associated with index k, IRREP Γ^{α}, and nuclei equivalent to A. It is assumed to be generated by the action of a projector on the AO function $f_{k'A}$, associated with index k' and non-redundant nucleus A.

$$F^{\alpha}_{kA} = \hat{\mathscr{P}}^{\alpha} f_{k'A} = \frac{1}{g} \sum_{G} \chi^{\alpha *}_{G} \hat{G} f_{k'A}. \tag{6.2.2}$$

The action of a symmetry operation on the AO

$$\hat{G} f_{k'A} = \sum_{\bar{k}'} C^{A}_{k'\bar{k}'}(G) f_{\bar{k}'G(A)} \tag{6.2.3}$$

generates a linear combination of functions of the same type as $f_{k'A}$ (same angular-momentum number, exponents, contraction coefficients, etc.) centred on nucleus $G(A)$ of the same type as A. Eq. (6.2.2) then becomes

$$F^{\alpha}_{kA} = \frac{1}{g} \sum_{G\bar{k}'} \chi^{\alpha *}_{G} C^{A}_{k'\bar{k}'}(G) f_{\bar{k}'G(A)}.$$

The DCD eq. (6.1.8) also gives an alternative form of eq. (6.2.2)

$$F^{\alpha}_{kA} = \frac{1}{g\lambda_R} \sum_{URV} \chi^{\alpha *}_{U^{-1}RV} \hat{U}^{-1} \hat{R} \hat{V} f_{k'A}.^{\mathrm{d}} \tag{6.2.4}$$

As already explained, choosing the subgroups of the DCD in eq. (6.2.4) should be carefully done in order to exploit some simplifications. Here, the choice should ensure that only non-redundant calculations of integrals over AOs are performed for the construction of SAO integrals. This will become apparent when the DCD is inserted in the expression for the integrals in the following paragraphs.

For the case of one-electron integrals, the DCD is derived as follows. Assuming a one-electron integral

$$\langle F^{\alpha}_{kA} | \, \hat{O} \, | F^{\beta}_{lB} \rangle \, ,$$

with an operator $\hat{O}$, one first substitutes the bra with the help of eq. (6.2.2) and additionally inserts an identity GG^{-1} in the ket

$$\begin{aligned} &\langle \frac{1}{g} \sum_{G} \chi^{\alpha *}_{G} \hat{G} f_{k'A} | \, \hat{O} \, | \hat{G} \hat{G}^{-1} F^{\beta}_{lB} \rangle = \\ &\frac{1}{g} \sum_{G} \chi^{\alpha}_{G} \chi^{\beta}_{G^{-1}} \langle \hat{G} f_{k'A} | \, \hat{O} \, | \hat{G} F^{\beta}_{lB} \rangle = \\ &\frac{1}{g} \sum_{G} \chi^{\alpha}_{G} \chi^{\beta *}_{G} \langle \hat{G} f_{k'A} | \, \hat{O} \, | \hat{G} F^{\beta}_{lB} \rangle \, . \end{aligned}$$

Here, the first step has made use of eq. (6.1.5) for the inverse of an element G^{-1} and the second step is based on the unitarity of the symmetry elements, $\chi^{\beta}_{G^{-1}} = \chi^{\beta *}_{G}$. Now the ket function is substituted by the DCD from eq. (6.2.4) choosing $\mathscr{U}$ as the stabilizer of A and $\mathscr{V}$ as the stabilizer of B.

$$\begin{aligned} &\frac{1}{g} \sum_{G} \chi^{\alpha}_{G} \chi^{\beta *}_{G} \langle \hat{G} f_{k'A} | \, \hat{O} \, | \hat{G} \frac{1}{g\lambda_R} \sum_{URV} \chi^{\beta *}_{U^{-1}RV} \hat{U}^{-1} \hat{R} \hat{V} f_{l'B} \rangle = \\ &\frac{1}{g^2 \lambda_R} \sum_{G} \sum_{URV} \chi^{\alpha}_{G} \chi^{\beta *}_{G} \chi^{\beta *}_{U^{-1}RV} \langle \hat{G} f_{k'A} | \, \hat{O} \, | \hat{G} \hat{U}^{-1} \hat{R} \hat{V} f_{l'B} \rangle \end{aligned}$$

The rearrangement theorem eq. (6.1.7) is then used to replace G with GU, and the property of the characters $\chi^{\alpha}_{WX} = \chi^{\alpha}_{W} \chi^{\alpha}_{X}$ is used for further simplification

$$\begin{aligned} &\frac{1}{g^2 \lambda_R} \sum_{G} \sum_{URV} \chi^{\alpha}_{GU} \chi^{\beta *}_{GU} \chi^{\beta *}_{U^{-1}RV} \langle \hat{G} \hat{U} f_{k'A} | \, \hat{O} \, | \hat{G} \hat{U} \hat{U}^{-1} \hat{R} \hat{V} f_{l'B} \rangle = \\ &\frac{1}{g^2 \lambda_R} \sum_{G} \sum_{URV} \chi^{\alpha}_{G} \chi^{\alpha}_{U} \chi^{\beta *}_{G} \chi^{\beta *}_{RV} \langle \hat{G} \hat{U} f_{k'A} | \, \hat{O} \, | \hat{G} \hat{R} \hat{V} f_{l'B} \rangle \, . \end{aligned}$$

Since $\mathscr{U}$ has been chosen as the stabilizer of A and $\mathscr{V}$ of B the following equations are true

$$\hat{U} f_{k'A} = \sum_{\bar{k}'} C^{A}_{k'\bar{k}'}(U) f_{\bar{k}'A} \tag{6.2.5}$$

$$\hat{R}\hat{V} f_{l'B} = \hat{R} \sum_{\bar{l}'} C^{B}_{l'\bar{l}'}(V) f_{\bar{l}'B} = \sum_{\bar{l}'} C^{B}_{l'\bar{l}'}(RV) f_{\bar{l}'R(B)}. \tag{6.2.6}$$

Eq. (6.2.5) and (6.2.6) are then substituted into the previous expression

$$\frac{1}{g^2 \lambda_R} \sum_{G} \sum_{URV} \sum_{\bar{k}'\bar{l}'} \chi^{\alpha}_{G} \chi^{\beta *}_{G} \chi^{\alpha}_{U} C^{A}_{k'\bar{k}'}(U)^{*} \chi^{\beta *}_{RV} C^{B}_{l'\bar{l}'}(RV) \langle \hat{G} f_{\bar{k}'A} | \, \hat{O} \, | \hat{G} f_{\bar{l}'R(B)} \rangle \, .$$

[d] The index of a character χ^{α}_{G} receives one symmetry element G. If more symmetry elements are given, e.g., $\chi^{\alpha}_{URV\ldots}$, the index $URV\ldots$ is to be understood as the symmetry element G that results from the multiplication of the given elements $G = URV\ldots$

Introducing the following factorisation

$$\begin{aligned}\Lambda^{\alpha A}_{k'\bar{k}'} &= \frac{1}{g}\sum_U \chi^{\alpha *}_U C^A_{k'\bar{k}'}(U) = \Lambda^{\alpha A}_{k'\bar{k}'}(E)\\ \Lambda^{\alpha A}_{k'\bar{k}'}(G) &= \frac{1}{g}\sum_U \chi^{\alpha *}_{GU} C^A_{k'\bar{k}'}(GU),\end{aligned} \tag{6.2.7}$$

one may rewrite the previous expression

$$\frac{1}{\lambda_R}\sum_G\sum_R\sum_{\bar{k}'\bar{l}'} \chi^{\alpha}_G \chi^{\beta *}_G \Lambda^{\alpha A *}_{k'\bar{k}'}\Lambda^{\beta B}_{l'\bar{l}'}(R)\left\langle \hat{G} f_{\bar{k}' A}\right| \hat{O}\left|\hat{G} f_{\bar{l}' R(B)}\right\rangle .$$

Lastly, the symmetry operation $\hat{G}$ acts on the operator $\hat{O}$

$$\frac{1}{\lambda_R}\sum_G\sum_R\sum_{\bar{k}'\bar{l}'} \chi^{\alpha}_G \chi^{\beta *}_G \Lambda^{\alpha A *}_{k'\bar{k}'}\Lambda^{\beta B}_{l'\bar{l}'}(R)\left\langle f_{\bar{k}' A}\right| \hat{G}^{-1}\hat{O}\hat{G}\left|f_{\bar{l}' R(B)}\right\rangle . \tag{6.2.8}$$

In the case of totally-symmetric operators $\hat{G}^{-1}\hat{O}\hat{G} = \hat{G}^{-1}\hat{O}\hat{G} = \hat{O}$, eq. (6.2.8) becomes:

$$\frac{1}{\lambda_R}\sum_G\left[\chi^{\alpha}_G \chi^{\beta *}_G\right]\sum_{\bar{k}'}\Lambda^{\alpha A *}_{k'\bar{k}'}\sum_{\bar{l}'}\sum_R \Lambda^{\beta B}_{l'\bar{l}'}(R)\left\langle f_{\bar{k}' A}\right| \hat{O}\left|f_{\bar{l}' R(B)}\right\rangle = \left\langle F^{\alpha}_{kA}\right| \hat{O}\left|F^{\beta}_{lB}\right\rangle . \tag{6.2.9}$$

In eq. (6.2.9) the vanishing-integral rule arises by the sum over G as a consequence of the great orthogonality theorem. The sum can be replaced by $I_{\alpha\beta} = \sum_G\left[\chi^{\alpha}_G\chi^{\beta *}_G\right]$, which is either g or 0. One-electron Hamiltonian and overlap operators are totally symmetric operators.

In the case of non-symmetric operators (e.g., the dipole moment or the angular-momentum operators), one needs to express the total operator as a linear combination of projected operators:

$$\hat{O} = \sum_\gamma \hat{O}^\gamma . \tag{6.2.10}$$

where the projected operator $\hat{O}^\gamma$ is a symmetric operator associated to IRREP γ

$$\hat{O}^\gamma = \hat{\mathscr{P}}^\gamma \hat{O} = \frac{1}{g}\sum_C \chi^{\gamma *}_C \hat{C}\hat{O}. \tag{6.2.11}$$

As for the transformation of symmetric operators associated with an IRREP different than Γ^1, the transformation with respect to operation $\hat{G}$ is

$$\hat{G}\hat{O}^\gamma\hat{G}^{-1} = \hat{O}^\gamma \chi^\gamma_G \tag{6.2.12}$$

Eq. (6.2.10) and (6.2.12) are used in eq. (6.2.8)

$$\begin{aligned}&\frac{1}{\lambda_R}\sum_G\sum_R\sum_{\bar{k}'\bar{l}'}\sum_\gamma \chi^{\alpha}_G \chi^{\beta *}_G \Lambda^{\alpha A *}_{k'\bar{k}'}\Lambda^{\beta B}_{l'\bar{l}'}(R)\left\langle f_{\bar{k}' A}\right| \hat{G}^{-1}\hat{O}^\gamma\hat{G}\left|f_{\bar{l}' R(B)}\right\rangle =\\ &\frac{1}{\lambda_R}\sum_\gamma\sum_G\left[\chi^{\alpha}_G \chi^{\gamma *}_G \chi^{\beta *}_G\right]\sum_{\bar{k}'}\Lambda^{\alpha A *}_{k'\bar{k}'}\sum_R\sum_{\bar{l}'}\Lambda^{\beta B}_{l'\bar{l}'}(R)\left\langle f_{\bar{k}' A}\right| \hat{O}^\gamma\left|f_{\bar{l}' R(B)}\right\rangle .\end{aligned} \tag{6.2.13}$$

The selection rule for the vanishing integrals arises again from the sum $I_{\alpha\gamma\beta} = \sum_G\left[\chi^{\alpha}_G\chi^{\gamma *}_G\chi^{\beta *}_G\right]$. Non-symmetric operators $\hat{O}$ like the dipole moment or the angular momentum integrals that are defined via the basis of Cartesian coordinates or the basis of rotations, can be expressed as $\hat{O}_i$, where i is the

for A, B atomic centres of the non-redundant part of the molecule **do**
  Find stabilisers $\mathscr{F}$ and $\mathscr{H}$ for atomic centres A and B
  Get the DCRs
  for R in DCRs **do**
    for $\bar{k}'$, $\bar{l}'$ indices of AOs **do**
      Calculate the AO integral $\langle f_{\bar{k}'A}|\,\hat{O}\,|f_{\bar{l}'R(B)}\rangle$
      for α, β in IRREPs **do**
        for k', l' the necessary subset of AOs indices with non-zero contributions **do**
          Weight the integral by $\frac{g}{\lambda_R}\Lambda^{\alpha A*}_{k'\bar{k}'}\Lambda^{\beta B}_{l'\bar{l}'}(R)$
          Add its contribution to the $\langle F^{\alpha}_{kA}|\,\hat{O}\,|F^{\beta}_{lB}\rangle$ matrix element
        end for
      end for
    end for
  end for
end for

Figure 6.3: The algorithm for the calculation of totally symmetric one-electron integrals using the DCD in eq. 6.2.8.

Cartesian direction (x, y, z). The projection of such an operator in eq. (6.2.11) can be written as follows:

$$\begin{aligned}\hat{e}^{\gamma}_{i} &= \frac{1}{g}\sum_{X}\chi^{\gamma *}_{X}\cdot\hat{X}\hat{O}_{i}\\ &= \frac{1}{g}\sum_{X}\chi^{\gamma *}_{X}\sum_{j}c^{O}_{ij}(X)\hat{O}_{j}\\ &= \sum_{j}L^{\gamma O}_{ij}\hat{O}_{j},\end{aligned} \tag{6.2.14}$$

with

$$L^{\gamma O}_{ij} = \frac{1}{g}\sum_{X}\chi^{\gamma *}_{X}c^{O}_{ij}(X).$$

Replacing eq. (6.2.14) in eq. (6.2.13), the final expression is derived:

$$\sum_{\gamma}\frac{I_{\alpha\gamma\beta}}{\lambda_R}\sum_{\bar{k}'}\Lambda^{\alpha A*}_{k'\bar{k}'}\sum_{j}L^{\gamma O}_{ij}\sum_{\bar{l}'}\sum_{R}\Lambda^{\beta B}_{l'\bar{l}'}(R)\,\langle f_{\bar{k}'A}|\,\hat{O}_{j}\,|f_{\bar{l}'R(B)}\rangle = \langle F^{\alpha}_{kA}|\,\hat{O}\,|F^{\beta}_{lB}\rangle\,. \tag{6.2.15}$$

In eq. (6.2.9) and (6.2.15), a careful choice of the stabilizer subgroups for the DCD limits the sum over all elements to a sum over DCRs. This makes sure that centre A is kept constant while only non-redundant pairs $AR(B)$ are generated by operation R. This is due to the left coset $R\mathscr{V}$ generating the non-equivalent redundant centres of type B with respect to the $AR(B)$ combination.

In the implementation of the DCD for the calculation of integrals over SAOs, the slow steps of calculating the integrals over AOs, i.e., $\langle f_{\bar{k}'A}|\,\hat{O}_{(j)}\,|f_{\bar{l}'R(B)}\rangle$, are performed within the loop over DCRs R. The computed AO integral is weighted by the corresponding prefactors and added to all the SAO matrix elements, i.e, $\langle F^{\alpha}_{kA}|\,\hat{O}\,|F^{\beta}_{lB}\rangle$ to which it contributes. The algorithm for the totally-symmetric case is depicted in fig. 6.3. All factors in front of the integrals are computed in advance.

An analogous derivation can be done for the two-electron integrals, which are expressed as

$$(F^{\alpha}_{kA}F^{\beta}_{lB}|F^{\gamma}_{mC}F^{\delta}_{nD}) = \langle F^{\alpha}_{kA}(\mathbf{1})F^{\gamma}_{mC}(\mathbf{2})|\,\hat{v}(\mathbf{1},\mathbf{2})\,|F^{\delta}_{lB}(\mathbf{1})F^{\delta}_{nD}(\mathbf{2})\rangle\,,$$

in Mulliken notation, which is used by the program. First, the functions in the bra F^{α}_{kA} and F^{γ}_{mC} are

substituted by eq. (6.2.2)

$$(\frac{1}{g}\sum_{G}\chi_{G}^{\alpha*}\hat{G}f_{k'A}F_{lB}^{\beta}|\frac{1}{g}\sum_{H}\chi_{H}^{\gamma*}\hat{H}f_{m'C}F_{nD}^{\delta}) = \frac{1}{g^2}\sum_{GH}\chi_{G}^{\alpha}\chi_{H}^{\gamma}(\hat{G}f_{k'A}F_{lB}^{\beta}|\hat{H}f_{m'C}F_{nD}^{\delta}).$$

Next, identities $\hat{G}\hat{G}^{-1}$ and $\hat{H}\hat{H}^{-1}$ are added in the ket functions:

$$\frac{1}{g^2}\sum_{GH}\chi_{G}^{\alpha}\chi_{H}^{\gamma}(\hat{G}f_{k'A}\hat{G}\hat{G}^{-1}F_{lB}^{\beta}|\hat{H}f_{m'C}\hat{H}\hat{H}^{-1}F_{nD}^{\delta}) = \frac{1}{g^2}\sum_{GH}\chi_{G}^{\alpha}\chi_{G}^{\beta*}\chi_{H}^{\gamma}\chi_{H}^{\delta*}(\hat{G}f_{k'A}\hat{G}F_{lB}^{\beta}|\hat{H}f_{m'C}\hat{H}F_{nD}^{\delta}).$$

The next step involves the DCD form of the projection from eq. (6.2.4). In this case $\mathscr{U}R\mathscr{V}$ is used for the left side of the integral and $\mathscr{W}S\mathscr{X}$ for the right side, with $\mathscr{U}$, $\mathscr{V}$, $\mathscr{W}$, $\mathscr{X}$ as the stabilizers of A, B, C, D respectively

$$\frac{1}{g^2}\sum_{GH}\chi_{G}^{\alpha}\chi_{G}^{\beta*}\chi_{H}^{\gamma}\chi_{H}^{\delta*}(\hat{G}f_{k'A}\hat{G}\frac{1}{g\lambda_R}\sum_{URV}\chi_{U^{-1}RV}^{\beta*}\hat{U}^{-1}\hat{R}\hat{V}f_{l'B}|\hat{H}f_{m'C}\hat{H}\frac{1}{g\lambda_S}\sum_{WSX}\chi_{W^{-1}SX}^{\delta*}\hat{W}^{-1}\hat{S}\hat{X}f_{n'D}) = \frac{1}{g^4\lambda_R\lambda_S}\sum_{GH}\sum_{URV}\sum_{WSX}\chi_{G}^{\alpha}\chi_{G}^{\beta*}\chi_{U^{-1}RV}^{\beta*}\chi_{H}^{\gamma}\chi_{H}^{\delta*}\chi_{W^{-1}SX}^{\delta*}(\hat{G}f_{k'A}\hat{G}\hat{U}^{-1}\hat{R}\hat{V}f_{l'B}|\hat{H}f_{m'C}\hat{H}\hat{W}^{-1}\hat{S}\hat{X}f_{n'D}).$$

Using the rearrangement theorem, G is replaced by GU and H is replaced by HW

$$\frac{1}{g^4\lambda_R\lambda_S}\sum_{GH}\sum_{URV}\sum_{WSX}\chi_{GU}^{\alpha}\chi_{G}^{\beta*}\chi_{RV}^{\beta*}\chi_{HW}^{\gamma}\chi_{H}^{\delta*}\chi_{SX}^{\delta*}(\hat{G}\hat{U}f_{k'A}\hat{G}\hat{R}\hat{V}f_{l'B}|\hat{H}\hat{W}f_{m'C}\hat{H}\hat{S}\hat{X}f_{n'D}).$$

Lastly, H is replaced by GH

$$\frac{1}{g^4\lambda_R\lambda_S}\sum_{GH}\sum_{URV}\sum_{WSX}\chi_{GU}^{\alpha}\chi_{G}^{\beta*}\chi_{RV}^{\beta*}\chi_{GHW}^{\gamma}\chi_{GH}^{\delta*}\chi_{SX}^{\delta*}(\hat{G}\hat{U}f_{k'A}\hat{G}\hat{R}\hat{V}f_{l'B}|\hat{G}\hat{H}\hat{W}f_{m'C}\hat{G}\hat{H}\hat{S}\hat{X}f_{n'D}) = \frac{1}{g^4\lambda_R\lambda_S}\sum_{GH}\sum_{URV}\sum_{WSX}\chi_{GU}^{\alpha}\chi_{G}^{\beta*}\chi_{RV}^{\beta*}\chi_{GHW}^{\gamma}\chi_{GH}^{\delta*}\chi_{SX}^{\delta*}\hat{G}(\hat{U}f_{k'A}\hat{R}\hat{V}f_{l'B}|\hat{H}\hat{W}f_{m'C}\hat{H}\hat{S}\hat{X}f_{n'D}).$$

At this point, it is important to note that the integral is invariant to any symmetry operation as a whole, as it is a scalar

$$\hat{G}(\hat{U}f_{k'A}\hat{R}\hat{V}f_{l'B}|\hat{H}\hat{W}f_{m'C}\hat{H}\hat{S}\hat{X}f_{n'D}) = (\hat{U}f_{k'A}\hat{R}\hat{V}f_{l'B}|\hat{H}\hat{W}f_{m'C}\hat{H}\hat{S}\hat{X}f_{n'D}).$$

The symmetry operations then act on the non-symmetric functions using the factorisation of eq. (6.2.7)

$$\frac{1}{g^4\lambda_R\lambda_S}\sum_{GH}\sum_{URV}\sum_{WSX}\chi_{GU}^{\alpha}\chi_{G}^{\beta*}\chi_{RV}^{\beta*}\chi_{GHW}^{\gamma}\chi_{GH}^{\delta*}\chi_{SX}^{\delta*}(\hat{U}f_{k'A}\hat{R}\hat{V}f_{l'B}|\hat{H}\hat{W}f_{m'C}\hat{H}\hat{S}\hat{X}f_{n'D}) = \frac{1}{\lambda_R\lambda_S}\sum_{GH}\sum_{RS}\sum_{\bar{k}'\bar{l}'\bar{m}'\bar{n}'}\chi_{G}^{\alpha}\chi_{G}^{\beta*}\chi_{G}^{\gamma}\chi_{G}^{\delta*}\chi_{H}^{\gamma}\chi_{H}^{\delta*}\Lambda_{k'\bar{k}'}^{\alpha A*}\Lambda_{l'\bar{l}'}^{\beta B}(R)\Lambda_{m'\bar{m}'}^{\gamma C*}\Lambda_{n'\bar{n}'}^{\delta D}(S)(f_{\bar{k}'A}f_{\bar{l}'R(B)}|\hat{H}f_{\bar{m}'C}\hat{H}f_{\bar{n}'S(D)}).$$

The summation over G may be replaced by the selection rule $\sum_G \chi^{\alpha}(G)\chi^{\beta}(G)^*\chi^{\gamma}(G)\chi^{\delta}(G)^* = I_{\alpha\beta\gamma\delta}$ simplifying the expression slightly

$$\frac{I_{\alpha\beta\gamma\delta}}{\lambda_R\lambda_S}\sum_{H}\sum_{RS}\sum_{\bar{k}'\bar{l}'\bar{m}'\bar{n}'}\chi_{H}^{\gamma}\chi_{H}^{\delta*}\Lambda_{k'\bar{k}'}^{\alpha A*}\Lambda_{l'\bar{l}'}^{\beta B}(R)\Lambda_{m'\bar{m}'}^{\gamma C*}\Lambda_{n'\bar{n}'}^{\delta D}(S)(f_{\bar{k}'A}f_{\bar{l}'R(B)}|\hat{H}f_{\bar{m}'C}\hat{H}f_{\bar{n}'S(D)}).$$

The derivation though is still not complete since the summation over H introduces redundancies. To get rid of the summation H is replaced by the DCD using the subgroups $\mathscr{M} = \mathscr{U} \cap \mathscr{V}$ which leaves the charge distribution $AR(B)$ unchanged and $\mathscr{N} = \mathscr{W} \cap \mathscr{X}$ which leaves the charge distribution $CS(D)$ unchanged

$$\frac{I_{\alpha\beta\gamma\delta}}{\lambda_R\lambda_S\lambda_T}\sum_{MTN}\sum_{RS}\sum_{\bar{k}'\bar{l}'\bar{m}'\bar{n}'}\chi^{\gamma}_{MTN}\chi^{\delta*}_{MTN}\Lambda^{\alpha A*}_{k'\bar{k}'}\Lambda^{\beta B}_{l'\bar{l}'}(R)\Lambda^{\gamma C*}_{m'\bar{m}'}\Lambda^{\delta D}_{n'\bar{n}'}(S)(f_{\bar{k}'A}f_{\bar{l}'R(B)}|\hat{M}\hat{T}\hat{N}f_{\bar{m}'C}\hat{M}\hat{T}\hat{N}f_{\bar{n}'S(D)}).$$

Application of the symmetry operations $\hat{T}\hat{N}$ results in

$$\frac{I_{\alpha\beta\gamma\delta}}{\lambda_R\lambda_S\lambda_T}\sum_{MTN}\sum_{RS}\sum_{\bar{k}'\bar{l}'\bar{m}'\bar{n}'}\chi^{\gamma}_{MN}\chi^{\delta*}_{MN}\Lambda^{\alpha A*}_{k'\bar{k}'}\Lambda^{\beta B}_{l'\bar{l}'}(R)\Lambda^{\gamma C*}_{m'\bar{m}'}(T)\Lambda^{\delta D}_{n'\bar{n}'}(TS)(f_{\bar{k}'A}f_{\bar{l}'R(B)}|\hat{M}f_{\bar{m}'T(C)}\hat{M}f_{\bar{n}'TS(D)}).$$

Next, the operation $\hat{M}^{-1}$ may act on the integral and leave it unchanged as a scalar

$$\frac{I_{\alpha\beta\gamma\delta}}{\lambda_R\lambda_S\lambda_T}\sum_{MTN}\sum_{RS}\sum_{\bar{k}'\bar{l}'\bar{m}'\bar{n}'}\chi^{\gamma}_{MN}\chi^{\delta*}_{MN}\Lambda^{\alpha A*}_{k'\bar{k}'}\Lambda^{\beta B}_{l'\bar{l}'}(R)\Lambda^{\gamma C*}_{m'\bar{m}'}(T)\Lambda^{\delta D}_{n'\bar{n}'}(TS)(\hat{M}^{-1}f_{\bar{k}'A}\hat{M}^{-1}f_{\bar{l}'R(B)}|f_{\bar{m}'T(C)}f_{\bar{n}'TS(D)})$$

but since $\hat{M}^{-1}$ leaves the $AR(B)$ invariant as a symmetry operation of the stabiliser, the equation simplifies to

$$\frac{I_{\alpha\beta\gamma\delta}}{\lambda_R\lambda_S\lambda_T}\sum_{MTN}\sum_{RS}\sum_{\bar{k}'\bar{l}'\bar{m}'\bar{n}'}\chi^{\gamma}_{MN}\chi^{\delta*}_{MN}\Lambda^{\alpha A*}_{k'\bar{k}'}\Lambda^{\beta B}_{l'\bar{l}'}(R)\Lambda^{\gamma C*}_{m'\bar{m}'}(T)\Lambda^{\delta D}_{n'\bar{n}'}(TS)(f_{\bar{k}'A}f_{\bar{l}'R(B)}|f_{\bar{m}'T(C)}f_{\bar{n}'TS(D)}).$$

Because of how $\mathscr{M}$ and $\mathscr{N}$ were defined and according to the selection rules, summation over M and N leads to λ_R and λ_S respectively

$$\sum_M \chi^{\gamma}_M\chi^{\delta*}_M = \lambda_R,$$
$$\sum_N \chi^{\gamma}_N\chi^{\delta*}_N = \lambda_S,$$

leading to a further simplification

$$\begin{aligned}\frac{I_{\alpha\beta\gamma\delta}}{\lambda_T}\sum_{\bar{k}'\bar{l}'\bar{m}'\bar{n}'}\Lambda^{\alpha A*}_{k'\bar{k}'}\sum_R\Lambda^{\beta B}_{l'\bar{l}'}(R)\sum_T\Lambda^{\gamma C*}_{m'\bar{m}'}(T)\sum_S\Lambda^{\delta D}_{n'\bar{n}'}(TS)(f_{\bar{k}'A}f_{\bar{l}'R(B)}|f_{\bar{m}'T(C)}f_{\bar{n}'TS(D)})\\ = (F^{\alpha}_{kA}F^{\beta}_{lB}|F^{\gamma}_{mC}F^{\delta}_{nD}).\end{aligned} \tag{6.2.16}$$

For the two-electron interaction integral case, summations over R, S, and T generate all unique quadruples of centres. Eq. (6.2.16) can be implemented by calculating once integrals over the AOs $(f_{\bar{k}'A}f_{\bar{l}'R(B)}|f_{\bar{m}'T(C)}f_{\bar{n}'TS(D)})$ and then adding the contributions to the corresponding SAO integrals, i.e., $(F^{\alpha}_{kA}F^{\beta}_{lB}|F^{\gamma}_{mC}F^{\delta}_{nD})$, similar to the one-electron integral case.

Symbols	Use
$\mathscr{G}$, G, H	Full point group and elements of the full point group
$\mathscr{U}$, $\mathscr{V}$, $\mathscr{W}$, $\mathscr{X}$, $\mathscr{M}$, $\mathscr{N}$	Stabilisers, subgroups of $\mathscr{G}$
U, V, W, X, M, N	Elements of the subgroups of $\mathscr{G}$
R, S, T	Double-coset representatives
k', l', m', ...	Indices of AOs corresponding to k, l, m, ... indices of the SAOs
$\bar{k}'$, $\bar{l}'$, $\bar{m}'$, ...	Indices of AOs used to express the linear combination resulting from the symmetry operation onto k', l', m', ... AOs
α, β, ...	Indices of IRREPs
i, j	Indices for the Cartesian directions

Table 6.2: A collection of the symbols used for the DCD.

In order to aid the readability of the dense expressions for the DCD, the notation used is summarized in tab. 6.2.

The implementation of DCD for complex Abelian groups has been carried out in the **mint** program. Eqs. (6.2.9), (6.2.15), (6.2.16) are used for the calculation of the integrals needed in quantum-chemical computations using complex Abelian groups. The algorithm handling D_{2h} and its subgroups has not been altered in order not to influence its efficiency. It was only used as a model to construct a separate routine to handle the complex group case.

The first step to implement the DCD is to implicitly generate the SAO basis from the AO basis and to calculate the $\Lambda^{\alpha A}_{k'\bar{k}'}(G)$ prefactors. This takes place in the `get_basis` subroutine. The point group and the non-redundant part of the molecule as described in sec. 6.1 have been determined in **joda** and are given to **mint** via interface files together with the basis functions at each atomic centre.

The basis functions are ordered in shells. Each shell has information on primitive functions eq. (5.1.1) of the same total angular-momentum number $L_{\text{tot}} = N + L + M$ with which the contracted functions of the the basis set are constructed. The algorithm then constructs all the N, L, M combinations corresponding to L_{tot} which are all the Cartesian polynomials of order L_{tot} and are $\frac{(L_{\text{tot}}+1)(L_{\text{tot}}+2)}{2}$ in number. These are used directly in the case of a Cartesian basis, or are reduced in number to $2L_{\text{tot}} + 1$ for a spherical basis. The transformation from Cartesian polynomial functions

$$P_{NLM} = x^N y^L z^M$$

to real spherical harmonic functions[96]

$$S_{L_{\text{tot}}M_{L_{\text{tot}}}} = \sum_{NLM} p_{L_{\text{tot}}M_{L_{\text{tot}}}}(N, L, M) P_{NLM} \tag{6.2.17}$$

is done in the `spherical` module using the Herglotzian definition implemented by Jürgen Gauss,[79,190] which automatically generates the transformation matrices $p_{L_{\text{tot}}M_{L_{\text{tot}}}}$ for arbitrarily high L_{tot}.

The SAO set is then implicitly generated, by determining the matrix representation of the functions in a given shell. In other words, the number of unique symmetric functions associated with an IRREP arising from the functions in a shell is to be calculated. First, the matrix representation of the nuclei A of the shell is calculated as the direct sum of those IRREPs of the molecular point group that are totally symmetric with respect to the stabiliser of A

$$\mathrm{D}_A = \sum_i \Gamma^i \;\forall\; \Gamma^i \leftarrow \Gamma^1(\mathscr{U}_A).$$

Then the matrix representation of the functions in the shell is calculated, as if the functions were centred in the Cartesian origin. For an individual polynomial P_{NLM}, the matrix representation is the direct product of the IRREPs of the consisting linear Cartesian functions

$$\mathrm{D}_{P_{NLM}} = \prod^N \Gamma_x \otimes \prod^L \Gamma_y \otimes \prod^M \Gamma_z.$$

For a Cartesian basis, the representation of the origin-centered functions is the direct sum of all polynomial combinations in a shell (with L_{tot} the total angular-momentum number of the shell).

$$\mathrm{D}^{\text{cart}}_{L_{\text{tot}}} = \sum_{\{L_{\text{tot}}\}} \mathrm{D}_{P_{NLM}}$$

For a spherical basis, the representation can be derived from the Cartesian basis, by subtracting the representations of all the lower-order polynomials of the same parity

$$\mathrm{D}^{\text{spher}}_{L_{\text{tot}}} = \mathrm{D}^{\text{cart}}_{L_{\text{tot}}} \ominus \sum_{K=1}^{L_{\text{tot}}/2} \mathrm{D}^{\text{cart}}_{(L_{\text{tot}}-2K)}.$$

Shells with $L_{\text{tot}} = 0$ are associated with the totally-symmetric IRREP Γ^1. The representation of the functions in the shell is finally the direct product of the representation of the origin-centered function with the representation of the atomic centres

$$\mathrm{D}_{\text{shell}} = \mathrm{D}^{\text{cart/spher}}_{L_{\text{tot}}} \otimes \mathrm{D}_A.$$

For the creation of the $\Lambda^{\alpha A}_{k'\bar{k}'}(G)$, the linear combination of the action of the symmetry operation on a basis function eq. (6.2.3) needs to be determined. The symmetry operation can be seen as an independent action on the function followed by the action on the centre. Based on this, it is sufficient for the determination of the $C^{A}_{k'\bar{k}'}(G)$ coefficients to look at the function as if it were centred on the Cartesian origin. For a Cartesian polynomial, the result of a symmetry operation on the linear Cartesian functions is determined by the action of the operation matrices on true vectors as was presented in eq. (6.2.1). As such, polynomial multiplication algorithms are used to calculate the action of the symmetry operation to the whole polynomial

$$\begin{aligned}\hat{G}P_{NLM} &= (\hat{G}x)^N(\hat{G}y)^L(\hat{G}z)^M \\ &= (a_x x + b_x y + c_x z)^N (a_y x + b_y y + c_y z)^L (a_z x + b_z y + c_z z)^M \\ &= \sum_{\bar{N}\bar{L}\bar{M}} C^{NLM}_{\bar{N}\bar{L}\bar{M}}(G) P_{\bar{N}\bar{L}\bar{M}}.\end{aligned} \tag{6.2.18}$$

The $C^{NLM}_{\bar{N}\bar{L}\bar{M}}(G)$ coefficients are then used to create $C^{A}_{k'\bar{k}'}(G)$. This is handled by the `rot_polynom_cart` member function of the `pointgroup` class in the `sym_info` module. Real spherical harmonics are handled in a different way. The real spherical harmonic functions S_{lm} are characterized by l and m, the total angular-momentum and its projection on the z-axis, respectively. They are defined as

$$\begin{aligned}S_{l0} &= c_{l0} Y_{l0} \\ S_{l|m|} &= c_{l|m|}\mathrm{Re}(Y_{l|m|}) \\ S_{l-|m|} &= c_{l-|m|}\mathrm{Im}(Y_{l|m|})\end{aligned}$$

with a prefactor c_{lm} and Y_{lm} the complex spherical harmonic

$$Y_{l\pm|m|} = r^l c'_{l\pm|m|} P_l^{\pm|m|}(\cos\theta)\exp(i \pm |m|\phi).$$

Here r, θ, ϕ are the spherical coordinates and P_l^m the associated Legendre polynomials. The real spherical harmonics can then be separated in a that part involves only r and θ named $F_{lm}(r,\theta)$, and another involving ϕ

$$\begin{aligned}S_{l|m|} &= F_{l|m|}(r,\theta)\cos(|m|\phi) \\ S_{l-|m|} &= F_{l|m|}(r,\theta)\sin(|m|\phi).\end{aligned}$$

In Cartesian form, the real spherical harmonics are expressed as polynomials

$$S_{lm}(r,\theta,\phi) = K_{lm} P_{lm}(x,y,z), \tag{6.2.19}$$

Eq. (6.2.17) and (6.2.19) are equivalent. This expression helps with determining the action of symmetry operations on the spherical harmonic. The action of an inversion depends only on the l number

$$\hat{i}S_{lm} = (-1)^l S_{lm}.$$

The action of $\hat{C}_2(k)$ rotation and $\hat{\sigma}(k)$ reflections is determined from one of the individual components of $P_{lm}(x,y,z)$, since all of them yield the same result if they are symmetry elements, and always results in an eigenvalue of ± 1. Rotations of arbitrary angle only need to be determined for the z-axis. Since such rotations only affect the angle ϕ of the spherical coordinates, only $S_{l|m|}$ and $S_{l-|m|}$ are involved with no further mixing between different $|m|$ values. The S_{l0} functions are invariant to such rotations. Using eq. (6.1.1) the action of a rotation by angle ω over the z-axis $\hat{C}(\omega)(z)$ is equivalent to substituting ϕ with $\phi - \omega$ in the function

$$\begin{aligned}S_{l|m|}(\phi-\omega) &= F_{l|m|}\cos(|m|\phi - |m|\omega) \\ &= F_{l|m|}\left[\cos(|m|\phi)\cos(|m|\omega) + \sin(|m|\phi)\sin(|m|\omega)\right] \\ &= S_{l|m|}\cos(m\omega) + S_{l-m}\sin(m\omega)\end{aligned}$$

$$\begin{aligned}S_{l-|m|}(\phi-\omega) &= F_{l|m|}\sin(|m|\phi - |m|\omega) \\ &= F_{l|m|}\left[\sin(|m|\phi)\cos(|m|\omega) - \cos(|m|\phi)\sin(|m|\omega)\right] \\ &= S_{l-|m|}\cos(|m|\omega) - S_{l|m|}\sin(|m|\omega).\end{aligned} \tag{6.2.20}$$

For these rotations, special care should be taken, so that the pair of polynomials $P_{l\pm|m|}(x,y,z)$ in $S_{l\pm|m|}$ have the same prefactor $K_{l|m|} = K_{l\pm-|m|}$. In other words, the real spherical harmonics pair with the same absolute value for m, $S_{l\pm|m|}$, must have the same norm. In this is taken care of in the construction of the transformation matrix from Cartesian to spherical in the `spherical` module, by considering $S_{l|m|}$ and $S_{l-|m|}$ together. Improper rotations are constructed by combining the proper rotation and the reflection. This way, the $C^A_{k'\bar{k}'}(G)$ are calculated by the `rot_polynom_spher` member function of the `pointgroup` class in the `sym_info` module.

For the generation of all the unique SAOs in a shell, projections on a subset of the functions in the shell is needed. This subset is to be determined by the following procedure. If $\{f^{\text{shell}}_{k'}\}$ the functions in the shell, then projections take place as

$$F^\alpha_k = \hat{\mathscr{P}}^\alpha f^{\text{shell}}_{k'} = \sum_m c^\alpha_{k'\bar{k}'} f^{\text{shell}}_{\bar{k}'},$$

starting from $k' = 1$. If $f^{\text{shell}}_{l'}$ with $l' > k'$ appears in F^α_k, then it is excluded from the projection. Such a projection would not result in an independent function because

$$F^\alpha_l = \hat{\mathscr{P}}^\alpha f^{\text{shell}}_{l'} = e^{i\vartheta} F^\alpha_k,$$

with $e^{i\vartheta}$ being a phase factor. It would thus be a non-unique projection. For a spherical basis this procedure always works. For a Cartesian basis, an additional criterion is needed. If $f^{\text{shell}}_{k'}$ is associated with polynomial P_{NLM}, then the function $f^{\text{shell}}_{l'}$ associated with polynomial P_{LNM} is only excluded from projection if the prefactors on $f^{\text{shell}}_{k'}$ and $f^{\text{shell}}_{l'}$ have the same absolute value

$$|c^\alpha_{k'k'}| = |c^\alpha_{k'l'}|.$$

Otherwise, $f^{\text{shell}}_{l'}$ must be included in later projections to get a complete set of symmetry adapted functions. This procedure occurs in the algorithm together with the creation of the $\Lambda^{\alpha A}_{k'\bar{k}'}(E) = \Lambda^{\alpha A}_{k'\bar{k}'}$ prefactors. The rest of $\Lambda^{\alpha A}_{k'\bar{k}'}(G)$ are calculated after $\Lambda^{\alpha A}_{k'\bar{k}'}$ has be determined to be non-zero and unique. All these prefactors are saved in the `rfact_c(`α`, `k'`, `$\bar{k}'$`, `G`)` member of the `shell` class in the `aoint` module. Restating the symbols used, indices k' correspond to the subset of functions in a shell that create all the unique k SAO functions, and $\bar{k}'$ are all the functions in the shell that contribute to the linear combination creating the SAOs.

The $L^{\gamma O}_{ij}$ prefactors are calculated in a similar way to $\Lambda^{\alpha A}_{k'\bar{k}'}(G)$. They involve only linear Cartesian functions for the dipole moments or linear Cartesian rotation for the angular momentum integrals. They are saved in `prx`, `pry` and `prBx`, `prBy` members of the `pointgroup` class. In this case, it is known that projection only on one of the x, y components (in the algorithm the x) is enough to get all the components of the dipole integral and the angular-momentum integral matrices.

The calculation of the one- and two-electron integrals takes place in `mint1e` and `mint2e`, respectively. The functions that handle the calculation can be found in the modules `aoint1e` and `aoint2e` as members of the `int1e` and `int2e` classes. The algorithm loops first over shells to create shell pairs or shell quadruples. For a given shell pair/quadruple combination, the procedure loops over the double-coset representatives R, T, S. Integrals are calculated over primitive (London) Gaussian functions which are then contracted (and transformed to the spherical basis if requested) to create $\langle f_{\bar{k}'A}| \hat{O} |f_{\bar{l}'R(B)}\rangle$ or $(f_{\bar{k}'A} f_{\bar{l}'R(B)}|f_{\bar{m}'T(C)} f_{\bar{n}'TS(D)})$. The calculated integrals over AOs are then passed to the `distributec_sym_c` member subroutines that add their contribution to the SAO integrals matrices, multiplied by the corresponding $\Lambda^{\alpha A}_{k'\bar{k}'}(G)$ and $L^{\gamma O}_{ij}$ prefactors.

6.2.2 Implementation of symmetry in QCUMBRE

The implementation of symmetry in QCUMBRE takes advantage of the vanishing-integrals rule. Its main purpose is to lower the computational demands by avoiding the explicit calculation of trivial zero-matrix entries. This is achieved by saving the matrices in non-vanishing IRREP blocks and by creating rules for the matrix multiplications between the IRREP blocks of the matrices.

To realize this goal, QCUMBRE needs to be able to recognize the symmetry of the molecular system and of the orbitals. In which way the symmetry recognition takes places depends on the program that

provides the SCF solution. For a calculation using the LONDON interface, the symmetry recognition needs to take place in QCUMBRE, since LONDON does not exploit symmetry. Despite this, the canonical HF orbitals are expected to be symmetric as stated earlier.[e] Using the CFOUR interface the symmetry information is transferred from CFOUR to QCUMBRE via the interface data files.

The implementation of symmetry in QCUMBRE attempts to address the issue of the raised complexity in the resulting code. This has been achieved by hiding most of the complexity in the innermost functions of QCUMBRE and in the code of the member functions of the different classes. Using this strategy, the structure of the program and the existing code does need to change drastically and, more importantly, further development has to deal with the symmetry exploitation only implicitly. To this end, the `Symmetry` function library has been developed that includes functions that handle symmetry operations. The `PoinGroup` object class was also developed that handles point-group theory. The classes `basisS`, `groupS` and `completeS` have been implemented to handle the tensors needed for the calculations in the non-vanishing IRREP block format. The most important member function of the `groupS` and `completeS` classes is the `contract` routine that handles the matrix multiplication. This function needs to be as efficient as possible in order to have significant gains from the symmetry exploitation, since it handles the bottleneck operations of a calculations and it is widely used in the program.

The implementation of symmetry in QCUMBRE closely follows ref. [184]. Most of the functionalities of QCUMBRE currently exploit symmetry through point-group theory and the non-vanishing integral rule. In the following sections the most important features of this implementation are presented.

The symmetry of correlated wavefunctions

Before presenting the symmetry implementation in QCUMBRE, the symmetry of the wavefunction at the correlated level and the handling of symmetry in second quantisation are addressed. Each creation/annihilation operator $\hat{a}_p^\dagger, \hat{a}_q$ is associated with an orbital, which as already mentioned transforms as a basis function of an IRREP.

If Γ_Φ is the IRREP of a Slater determinant Φ and Γ_r are the IRREPs of the orbitals of the wavefunction, then

$$\Gamma_\Phi = \prod_r \Gamma_r.$$

A creator operator $\hat{a}_p^\dagger$ is associated with an orbital of IRREP Γ_p. Then the IRREP of the determinant $\Phi_p = p^\dagger |\Phi\rangle$ is

$$\Gamma_{\Phi_p} = \prod_r \Gamma_r \otimes \Gamma_p = \Gamma_\Phi \otimes \Gamma_p$$

and for this reason, a creation operator is associated with IRREP Γ_p. In contrast, when an annihilation operator $\hat{a}_q$ that is associated with an orbital of IRREP Γ_q operates on the determinant $\Phi_q = q |\Phi\rangle$, the IRREP Γ_{Φ_q} is

$$\Gamma_{\Phi_q} = \prod_{r\neq q} \Gamma_r = \prod_{r\neq q} \Gamma_r \otimes \Gamma_q \otimes \Gamma_q^* = \prod_r \Gamma_r \otimes \Gamma_q^* = \Gamma_\Phi \otimes \Gamma_q^*.$$

The annihilation operator is thus associated with IRREP Γ_q^*.

A correlated wavefunction is expanded in a linear or exponential manner as a sum of single-determinant functions, weighted by the amplitudes. The resulting wavefunction has to be symmetric.

[e] The symmetry recognition in the case of degenerate orbitals (molecular symmetry described by non-Abelian point groups) will fail almost always when using the LONDON program. Any linear combination of degenerate orbitals among themselves is a solution to the canonical HF problem. Since Abelian subgroups are used in this type of calculations and given the infinite allowed linear combinations, it is difficult to recognize the symmetry of such orbitals, if this is not regulated at the SCF level. This is not to say that the orbitals are not symmetric with respect to the full non-Abelian point group. However, reconstructing the exact matrix representation of such orbitals given that there exist infinite equivalent matrix representations that are related to one another by equivalent unitary transformations (see sec. 6.1) is feasibly impossible. Symmetry cannot be exploited in the case of non-Abelian full point groups when using the LONDON interface.

Since the sum of functions that transform with different IRREPs is not necessarily a symmetric function, the non-zero amplitudes that appear in second quantisation (density matrices $\gamma_{\mathrm{N}pq}$, CC amplitudes t_I, EOM vectors r_I, etc.) have to be associated with a single IRREP. The indices of the amplitudes are accompanied by a quasiparticle operator each, and as such are associated with an IRREP as well. Because of the requirement that the amplitudes as a whole have the same IRREP, there are many entries in the amplitude matrices that are trivially zero following the vanishing-integral selection rule eq. (6.1.6). An operator in second quantisation appears as

$$\hat{O} = \frac{1}{n!} \sum_{pq\ldots rs\ldots} o^{pq\ldots}_{rs\ldots} \hat{a}^\dagger_p \hat{a}^\dagger_q \ldots \hat{a}_s \hat{a}_r,$$

with the amplitudes $o^{pq\ldots}_{rs\ldots}$. The IRREP of the amplitude is thus given by

$$\Gamma_p \otimes \Gamma_q \otimes \ldots \otimes (\Gamma_r)^* \otimes (\Gamma_s)^* \otimes \ldots = \Gamma_o.$$

The amplitude entries are not trivial zeros if

$$\Gamma_o = \Gamma_{\hat{O}},$$

with $\Gamma_{\hat{O}}$ as the single collective IRREP of the operator.

The CC wavefunction eq. (2.6.1) with IRREP Γ_{CC} must be associated with the same IRREP as the HF wavefunction Γ_{HF}, since both describe the same state.[189,191] Since

$$\Gamma_{\hat{T}} \otimes \Gamma_{\mathrm{HF}} = \Gamma_{\mathrm{CC}},$$

the IRREP of the cluster operator $\Gamma_{\hat{T}}$, has to be the totally-symmetric IRREP

$$\Gamma_{\hat{T}} = \Gamma^1.$$

The bra CC state eq. (2.7.5) also retains the IRREP of the ground state and as such

$$\Gamma_{\hat{\Lambda}} = \Gamma^1.$$

The same is true for the amplitudes of all correlation methods that handle the ground state (MBPT, CI).

The EOM wavefunction eq. (2.6.6) is associated with the IRREP of the excited state Γ_{exc}, which may be different than Γ_{CC}. The IRREP of the EOM vector $\Gamma_{\hat{R}}$, must be such that

$$\Gamma_{\mathrm{exc}} = \Gamma_{\hat{R}} \otimes \Gamma_{\mathrm{HF}}.$$

In other words, $\Gamma_{\hat{R}}$ is the IRREP of the excitation. The left-side EOM vector eq. (2.7.6) must accordingly have the IRREP of the deexcitation which is the complex conjugate of the excitation.

$$\Gamma_{\hat{L}} = \Gamma^*_{\hat{R}},$$

The same argumentation holds for the CI amplitudes eq. (2.4.1) that describe excited states, meaning that $\Gamma_{\hat{C}}$ is the IRREP of the excitation.

The IRREP of the Lagrange multipliers in the deexcitation operator $\hat{\mathscr{Z}}'$ in eq. (2.7.10) and (2.7.14) $\Gamma_{\hat{\mathscr{Z}}'}$ depends on the transition it describes. The amplitudes are found by eq. (2.7.11) and (2.7.15). Using the vanishing-integral rule

$$\begin{aligned} \Gamma_{\hat{L}^m} \otimes \Gamma_{\hat{\mu}_I} \otimes \Gamma_{\hat{R}^n} &= \Gamma^1 \\ \Gamma_{\hat{L}^m} \otimes \Gamma_{\hat{R}^n} &= \Gamma^*_{\hat{\mu}_I} \end{aligned} \tag{6.2.21}$$

and

$$\begin{aligned} \Gamma_{\hat{\mathscr{Z}}'} \otimes \Gamma_{\hat{\mu}_I} &= \Gamma^1 \\ \Gamma_{\hat{\mathscr{Z}}'} &= \Gamma^*_{\hat{\mu}_I}. \end{aligned} \tag{6.2.22}$$

Equating the left parts of eq. (6.2.21) and (6.2.22)

$$\Gamma_{\hat{\mathscr{Z}}'} = \Gamma_{\hat{L}^m} \otimes \Gamma_{\hat{R}^n},$$

with $\Gamma_{\hat{L}^m} \otimes \Gamma_{\hat{R}^n}$ being the IRREP of transition $m \leftarrow n$. It thus follows that for single-state properties $\Gamma_{\hat{\mathscr{Z}}'} = \Gamma^1$.

Lastly for the IRREPs of the density matrices, single-state properties have totally-symmetric density matrices. The transition-density matrices on the other hand, reflect the IRREP of the transition.

The `Symmetry` functions library

The functions `rotation`, `reflection`, `inversion` and `improper_rotation` operate on $\mathbb{R}^3$ vectors or pseudovectors the respective symmetry operations exactly as described in subsec. 6.2.1. The function `symmetry_check` checks if the molecular system belongs to a specific point group.

Functions `reflect_orb`, `rotate2_orb`, `invert_orb`, `rotate_orb` and `improper_rotate_orb` perform symmetry operations on a molecular orbital, meaning in a vector of MO coefficients in an non-symmatric atomic orbital basis (AO and not SAO). These functions are used mainly with the LONDON interface for the symmetry recognition of the (canonical) orbitals. Since LONDON does not handle a spherical AO basis, the operations are carried through using the strategy described by eq. (6.2.18). The function `assign_symmetry` checks whether the orbital solution provided belongs to a certain point group, and if this is the case, assigns IRREPs to each orbital.

Function `Symmetry`() has the necessary information to be called by the main program and finds the point group of the molecular system, the IRRREPs of the molecular orbitals, saves the information to global variables, and prints the results for the LONDON interface. The symmetry recognition for the LONDON interface is controlled by the `symmetry` keyword with option `on`/`off` or the name of the point group. The instruction `on` enforces an automatic search for a point group of order smaller than 8, while `off` assigns the point group C_1. If instead, a point group is passed to the `symmetry` keyword, the program checks that the system has the given symmetry before assigning it. If the check is not passed, no symmetry is used. The keywords `symmetry-thresh` and `orb-thresh` control the symmetry-identification threshold of the molecular system and the orbitals respectively.

The necessary global variables in the case of a calculation using the CFOUR interface are initialised by the function `Symmetry_cfour`. No symmetry recognition takes place, as all necassary information are passed through interface files.

The `PointGroup` class

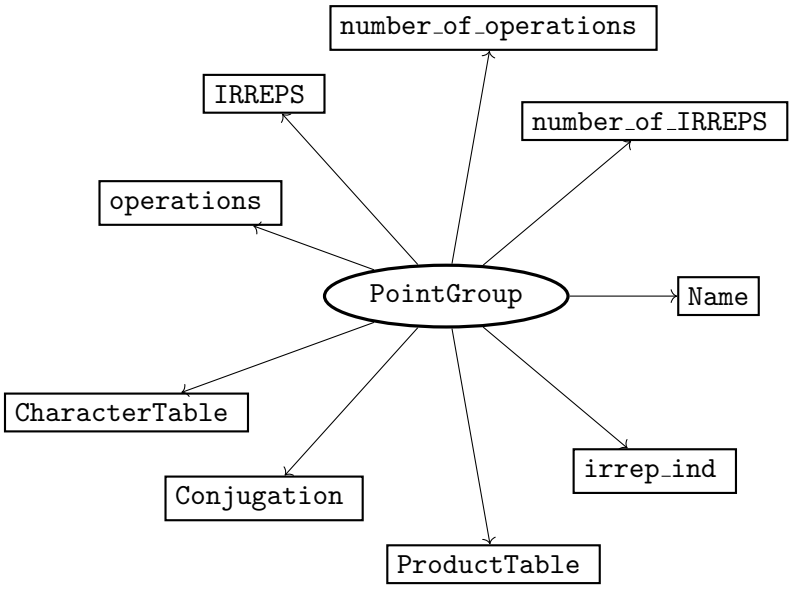

Figure 6.4: The `PointGroup` class and its member variables.

The `PointGroup` class handles point-group information. This class has the following member variables

- `Name`: name of the point group
- `number_of_IRREPS`: number of IRREPs in the group
- `number_of_operations`: number of operations in the group
- `IRREPS`: names of the IRREPs

- `operations`: names of the symmetry operations
- `CharacterTable`: the entries of the character table
- `ProductTable`: the entries of the product table
- `Conjugation`: the entries of the conjugation table
- `irrep_ind`: the IRREP combinations of a given rank whose direct product results in a given IRREP

which are depicted in fig. 6.4. The supported point groups are C_1, C_i, C_s, D_2, C_{2v}, D_{2h}, C_n, C_{nh}, $S_{(2n)}$ for n = 2-10. The QCUMBRE implementation is flexible enough to handle the groups, even if the principal rotation axis of the group is not the z-axis but either the x- of the y-axis.

The direct product operation is handled by the `PointGroup::DirectProduct` and `PointGroup::DirectProduct_ind` member function. They use the entries of the `ProductTable` and `Conjugation` variables, after they have been initialised.

The initialisation of the `irrep_ind` member is handled by the `PointGroup::calc_num_block` member function, after the level of theory of the calculation has been read from the input. This member variable is important for the correct packing of the tensors in symmetry blocks, as it contains all non-vanishing IRREP combinations for a block of an nth dimensional tensor of a given IRREP. There are h^{n-1} non-vanishing IRREP combinations, with h being the order of the group, and their calculations scales as h^n. It is more efficient to hold these in memory and not recalculate them every time needed, because keeping this information in memory proves more efficient than continuously reproducing it.

The member functions `PointGroup::operate` and `PointGroup::operate_orb` act as wrappers to the respective functions that handle symmetry operations on vectors and orbitals from the `Symmetry` library.

The `PointGroup::Projection` member functions handles the projection eq. (6.1.3). It is used for the reconstruction of the transformation from the SAO basis to the AO basis for a calculation using the CFOUR interface and is needed for the Mulliken population analysis and for the generation of the interface data files for the orbital visualization with COrbit19. It uses eq. (6.2.20), or (6.2.18) for a spherical or Cartesian basis set, respectively.

Updates to the `flex` object class

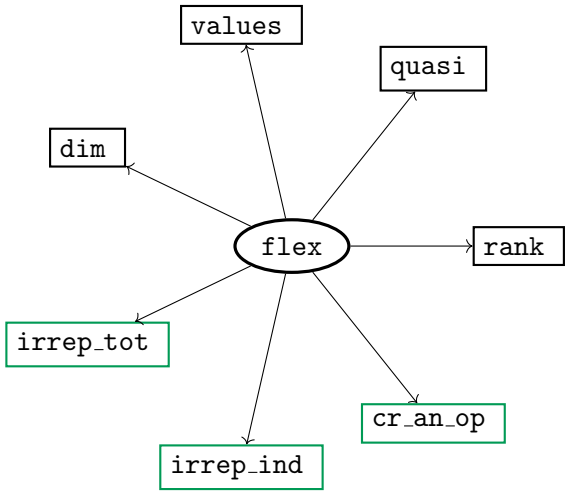

Figure 6.5: The `flex` class and its members. New member variables in green boxes.

The `flex` object class in QCUMBRE was originally designed to hold the values of a tensor in the MO basis in `values`. The tensor saved in a flex belongs to a specific quasiparticle combination and spin block, which information is held in `quasi` and, along with its rank and size of each dimension in `rank` and `dim`. In the symmetry-block structure each flex holds a specific IRREP block, meaning

the IRREP of each dimension of the tensor is constant in the flex. The additional member variables are the `irrep_tot`, that holds the IRREP of the tensor, `irrep_ind` that holds the IRREP of each dimension/index and the `cr_an_op` that contains the characterisation of each index as a creator or annihilator. If the value of `irrep_tot` is set to -1, it means that it does not contain an IRREP block, but the values of tensor in a non-symmetric packed form, and is used as legacy for the `group` and `complete` classes. The members of the `flex` class are shown in fig. 6.5.

The `groupS` and `completeS` object classes

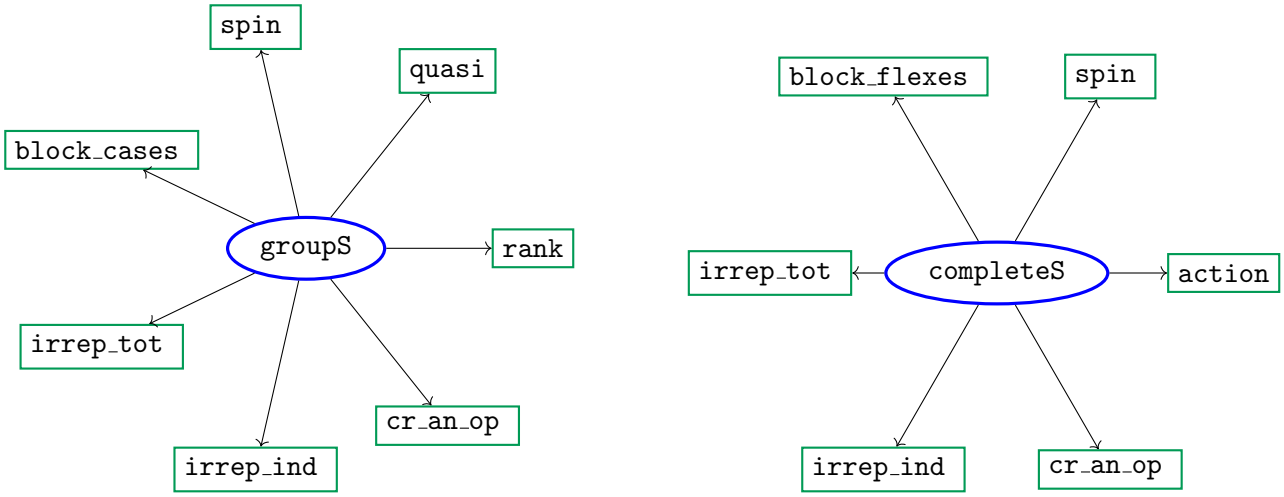

Figure 6.6: The new `groupS` and `completeS` classes and their member variables.

The `group` and `complete` classes serve as collections of `flex` instances, and order tensors in different spin cases. In `group`, the tensors corresponding to a given quantity have constant rank (like the two-electron integrals), while in `complete`, tensors of variable rank are contained (like the CC amplitudes). For the consideration of symmetry and for packing the tensors in non-vanishing blocks, an additional ordering layer is added below the spin cases which are blocks with a constant IRREP combination for the indices as described in the `flex` class. The newly implemented object classes `groupS` and `completeS` serve this purpose while retaining the ideas and functionalities for the non-symmetric classes. The member variables of the classes are depicted in fig. 6.6

		rs			
	o	AA	AB	BA	BB
pq	AA	1	×	×	2
	AB	×	3	4	×
	BA	×	5	6	×
	BB	7	×	×	8

Table 6.3: Block enumeration and empty blocks for tensor o^{pq}_{rs} in an order 2 point group with IRREPs A and B.

The member variables `block_cases` and `block_flexes` of `groupS` and `completeS` respectively contain the flex instances. In both cases, the first level layer distinguishes the spin cases which is saved in `spin` and the second the non-vanishing IRREP blocks saved in `irrep_ind`. The number of non-vanishing blocks is h^{n-1} and the exact non-vanishing combinations are found in the `PointGroup::irrep_ind` variable. The IRREP blocks are ordered in ascending order, with the IRREP of the last index being the fast one. The number of the IRREP blocks saved in an instance is further decreased by completely ignoring these blocks that would have size equal to 0. An example of this IRREP block structure for a totally-symmetric tensor o^{pq}_{rs} in a point group of order 2 with IRREPs A and B can be seen in tab. 6.3. The green cells denote enumerated blocks of non-vanishing IRREP combinations, while the boxes with a red × denote blocks that contain trivial zeros that are not saved.

The member `action` of `completeS` is absent from `groupS`. This variable holds the information of whether the operator that corresponds to a `completeS` instance is an excitation operator ("right") or deexcitation ("left") and is needed for the correct assignment of values in the `cr_an_op` member.

For compatibility and testing reasons, symmetric `groupS` and `completeS` instances can be transformed in non-symmetric `group` and `completeS` instances using the `spit` member functions, and the

other way around with the `absorb` functions. Thus, the non-symmetric classes are not rendered completely obsolete.

The `basisS` class

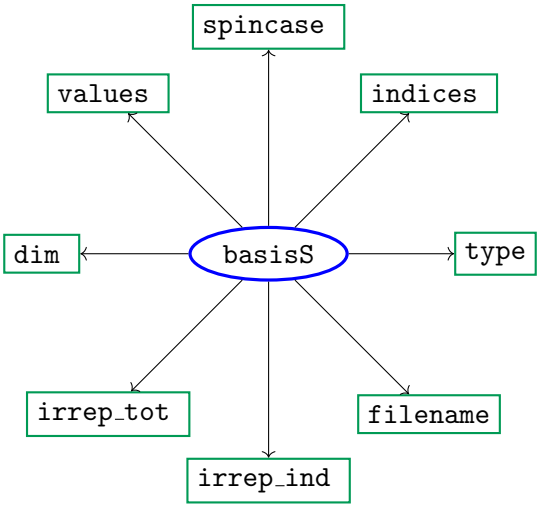

Figure 6.7: The `basisS` class and its member variables.

The `basisS` object class handles tensors in the SAO basis and is mainly used for the CFOUR interface. Its members can be seen in fig. 6.7. It comes in three types saved in `type`. Type 1 is purposed to handle one-electron integrals in the SAO basis, e.g., the one-electron Hamiltonian or the overlap matrix or more general two-index matrices with no spin differentiation. Type 2 handles two-electron integrals in the SAO basis, e.g., the two-electron integrals or more generally four-index matrices with no spin differentiation. Lastly, type 3 handles the MO coefficients, or more generally two-index matrices with two spin cases.

The binary IRREP block search algorithm

For many cases the number of blocks grows unfavourably with the order of the group, namely h^{n-1}. This is not a problem in itself, because despite the large number of blocks the program saves memory by not dealing with trivial-zero matrix entries. The large number of blocks may, however, cause problem when a specific block (meaning a specific IRREP combinations) needs to be accessed. Using a naive linear-search algorithm raises the cost high enough, so that for higher-order groups, there were no gains in computation time or the calculation was slower compared to cases where symmetry has not been exploited. To tackle this, a binary-search algorithm has been implemented.

A binary search requires some kind of numerical assignment for each block and the blocks to be saved in ascending order according to the numerical assignment. This numerical assignment $\#m$ is defined by the following equation

$$\#m = \sum_{\mathrm{i}=1}^{n} \#\Gamma_i \cdot h^{i-1}, \tag{6.2.23}$$

with i counting the index of the tensor starting from the fastest one (rightmost) and $\#\Gamma_i$ being the enumeration of the IRREP of the ith index with $\#\Gamma^1 = 0$. The ordering described in the previous sections coincides with the ordering according to this number assignment.

The binary-search algorithm accepts an IRREP combinations and returns the position of the block with said combination or -1 if this is not found. The asked combination is first assigned a number according to eq. (6.2.23) $\#m_{inp}$. The following recursive procedure then takes place:

1. Check if the first block is assigned with $\#m_{inp}$. If yes, return the position of the first block.

2. Check if $\#m_{inp}$ is lower than the number assigned to the first block. If yes, return -1.

3. Check if the last block is assigned with $\#m_{inp}$. If yes, return the position of the last block.

4. Check if $\#m_{inp}$ is larger than the number assigned to the last block. If yes, return -1.

5. Check if the middle block is assigned with $\#m_{inp}$. If yes, return the position of the middle block.

6. Check if $\#m_{inp}$ is larger than the number assigned to the middle block. If yes, limit the search between the block after the middle and before the last one and go to the first step. Otherwise, limit the search between the block after the first and before the middle one and go to the first step.

The binary-search algorithm is implemented in the `bin_block_search` recursive function. It scales logarithmic with the number of elements

$$\sim \log(h^{n-1}) = (n-1)\log(h) \sim \log(h) < h,$$

which means it scales in every case better than linearly with the order of the point group.

The new `contract` routine

An important function used very frequently in the program is the `contract` function of the `complete` and `group` classes. It is the function that deals with matrix multiplication of the kind

$$W_{pq\ldots rs\ldots} \mathrel{+}= f \sum_{tu\ldots} K_{pq\ldots tu\ldots} L_{tu\ldots rs\ldots}, \tag{6.2.24}$$

that is a key feature the structure of the QCUMBRE program. Its efficiency is central for the efficiency of the whole program. In the contraction the indices $pq\ldots$ and $rs\ldots$ are the target indices while $tu\ldots$ are the summation indices, $W_{pq\ldots rs\ldots}$ is the matrix that the result of the contraction is added to, f is a factor, and $K_{pq\ldots tu\ldots}$ and $L_{tu\ldots rs\ldots}$ are the tensors that take part in the contraction.

For the new instance classes the `contract` member function was developed is such a way to consider the IRREP block structure. The intention is that the new routine should lower the number of flops, in comparison to the previous implementation. At the same time, the input and output should not deviate from the previous routine so that the whole program does not need to be rewritten.

Calling the member function has the following syntax

$$out.\texttt{contract}(\ spincase\ ,\ factor\ ,\ in1\ ,\ indices1\ ,\ in2\ ,\ indices2\ ).$$

In this syntax *spincase* contains the spin case of the calling instance *out* that the results of the contraction is to be added to. The latter represents $W_{pq\ldots rs\ldots}$ of eq. (6.2.24). The input *factor* represents the factor f. Inputs $in1$ and $in2$ take the places of $K_{pq\ldots tu\ldots}$ and $L_{tu\ldots rs\ldots}$ respectively and $indices1$ and $indices2$ represent the indices $pq\ldots tu\ldots$ and $tu\ldots rs\ldots$ of $in1$ and $in2$. The common indices are the summation indices and the rest are the target indices. The algorithm of the new routine is the following:

1. Choose the correct spin case of *out* based on *spincase*.

2. Choose the correct spin case of $in1$ based on *indices1*.

3. Choose the correct spin case of $in2$ based on *indices2*.

4. Save the addresses of the `flex` instances belonging to the IRREP blocks of $in1$. If the indices of $in1$ need to be reordered, create new `flex` instances, copy the entries of the original `flex` instances and reorder them accordingly.

5. Save the addresses of the `flex` instances belonging to the IRREP blocks of $in2$. If the indices of $in2$ need to be reordered create new `flex` instances, copy the entries of the original `flex` instances and reorder them accordingly.

6. Compare the IRREPs of the target indices from $in1$ $(pq\dots)$ between $in1$ and out. For each block of out save the addresses of the contributing blocks from $in1$.

7. Compare the IRREPs of the target indices from $in2$ $(rs\dots)$ between $in2$ and out. For each block of out save the addresses of the contributing blocks from $in2$.

8. Create `flex` instances that will save the results of the multiplication.

9. Compare the IRREPS of the summation indices $(tu\dots)$ between the saved addresses of $in1$ and $in2$ for each IRREP block of out and perform the matrix multiplication.

10. Add the results of the matrix multiplication to out by reordering the indices of the resulting tensor of the previous step weighted by $factor$.

Steps 6, 7 and 9 are specific to the new `contract` algorithm needed for considering the IRREP block structure of the tensors.

W_{abij}		t_{ik}^{ae}		$\langle kb\vert\vert ej\rangle$	
block	indices	block	indices	block	indices
	$a\ b\ i\ j$		$a\ e\ i\ k$		$k\ b\ e\ j$
1	AAAA	1	AAAA	1	AAAA
2	AABB	2	AABB	2	AABB
3	ABAB	3	ABAB	3	ABAB
4	ABBA	4	ABBA	4	ABBA
5	BAAB	5	BAAB	5	BAAB
6	BABA	6	BABA	6	BABA
7	BBAA	7	BBAA	7	BBAA
8	BBBB	8	BBBB	8	BBBB
		$t_{ik}^{ae} \rightarrow t_{aiek}$		$\langle kb\vert\vert ej\rangle \rightarrow I_{ekbj}$	
	$a\ b\ i\ j$		$a\ i\ e\ k$		$e\ k\ b\ j$
1	AAAA	1	AAAA	1	AAAA
2	AABB	2	ABAB	2	BAAB
3	ABAB	3	AABB	3	AABB
4	ABBA	4	ABBA	4	BABA
5	BAAB	5	BAAB	5	ABAB
6	BABA	6	BBAA	6	BBAA
7	BBAA	7	BABA	7	ABBA
8	BBBB	8	BBBB	8	BBBB

Table 6.4: Symmetry-block structure of the quantities in the example before and after reordering the indices.

An example is given for clarification. The contraction

$$W_{abij} \mathrel{+}= \sum_{ek} t_{ik}^{ae} \langle kb\vert\vert ej\rangle$$

in the case of a point group with IRREPs A and B is handled as follows. All involved quantities (the t_2 amplitudes, the two-electron integrals $\langle kb\vert\vert ej\rangle$ and the intermediate W_{abij}) are four-index tensors are have the block structure described in tab. 6.3. In tab. 6.4, the block enumeration and the IRREP combinations of the indices are listed. The influence of the swap-reordering steps is also made clear for the IRREP combinations in the lower part of the table. Furthermore, the indices are colour coded: Green indices indicate the target indices from t_{ik}^{ae}, blue indices are the target indices from $\langle kb\vert\vert ej\rangle$ and the underlined indices are the summation indices. The index-reordering steps are chosen in such a way, that the summation indices are the last indices of $in1$ and the first indices of $in2$. In this way, efficient LAPACK/BLAS matrix-multiplication functions can be used for the contraction.

W_{abij}	Contributing blocks of t_{aiek}	IRREPs of target indices
1	1,3	AA
2	2,4	AB
3	1,3	AA
4	2,4	AB
5	5,7	BA
6	6,8	BB
7	5,7	BA
9	6,8	BB

Table 6.5: Collection of contributing blocks of t_2 for each block of W_{abij}.

W_{abij}	Contributing blocks of I_{ekbj}	IRREPs of the target indices
1	1,6	AA
2	2,5	AB
3	3,8	BB
4	4,7	BA
5	2,5	AB
6	1,6	AA
7	4,7	BA
8	3,8	BB

Table 6.6: Collection of contributing blocks of I_{ekbj} for each block of W_{abij}.

W_{abij}	t_{aiek}	I_{ekbj}	symmetry block combination to be multiplied $(in1)$ - $(in2)$	IRREPs of summation indices
1	1,3	1,6	1 - 1	AA
			3 - 6	BB
2	2,4	2,5	2 - 5	AB
			4 - 2	BA
3	1,3	3,8	1 - 3	AA
			3 - 8	BB
4	2,4	4,7	2 - 7	AB
			4 - 4	BA
5	5,7	2,5	5 - 5	AB
			7 - 2	BA
6	6,8	1,6	6 - 1	AA
			8 - 6	BB
7	5,7	4,7	5 - 7	AB
			7 - 4	BA
8	6,8	3,8	6 - 3	AA
			8 - 8	BB

Table 6.7: Choosing the correct IRREP block combination to be multiplied for each block of W_{abij}.

After the reordering steps, the algorithm determines the symmetry-block combination to be passed in the for the matrix-multiplication function.

In step 6, the algorithm compares the IRREPs of the target indices of t_2 (green indices) for each block of W_{abij} and saves the addresses of the `flex` instances for each block. The results is shown in tab. 6.5. Step 7 works analogously comparing the IRREPs of the target indices from I_{ekbj} (blue indices) for each block of W_{abij}. The procedure described, is further presented in tab. 6.6. These two steps act as a preselection of the IRREP block from t_2 and I_{ekbj}.

In the aftermath of steps 6 and 7, the program knows which blocks of $in1$ and $in2$ contribute to specific blocks of out. The algorithm then decides which combinations of the contributing blocks need to be multiplied. This is done by comparing the IRREPs of the summation indices, and performing the multiplications for these combinations that have the same IRREPs as described in step 9. The combinations that contribute for each block can be seen in tab. 6.7.

The scaling of the `contract` routine is investigated next by calculating the number of operations in a worst-case scenario. Such a scenario would mean that all tensors have to be reordered (conjugation is ignored). The order of the point group is h, the number of possible values of an index is N_i and is assumed to be the same for every IRREP for simplification, r_k is the rank of the tensor k, and s is the number of the summation indices. The scaling of the most expensive steps follows can be see in tab. 6.8

step 4	# of blocks × # of elements in each block	$h^{r_{in1}-1}N_i^{r_{in1}}$
step 5	# of blocks × # of elements in each block	$h^{r_{in2}-1}N_i^{r_{in2}}$
step 6	# of blocks of out × # of blocks of $in1$	$h^{r_{out}-1}h^{r_{in1}-1}$
step 7	# of blocks of out × # of blocks of $in2$	$h^{r_{out}-1}h^{r_{in2}-1}$
step 9	# of blocks of out × # of elements saved from 6 × # of elements saved from 7 + # of multiplications ($h^{r_{out}-1}h$) × the cost of each multiplications	$h^{r_{out}-1}h^2 + h^{r_{out}}N_i^{r_{out}+s}$
step 10	# of blocks × # of elements in each block	$h^{r_{out}-1}N_i^{r_{out}}$

Table 6.8: The scaling of the most expensive steps in the new `contract` routine.

Comparing the scaling of symmetry exploitation to no use of symmetry and assuming an equal distributions of the indices in each IRREP ($N_i \approx N/h$, with N the abstract size of the system), the following can be concluded. Steps 4, 5, 10 have a lower scaling

$$h^{r-1}N_i^r = h^{r-1}\left(\frac{N}{h}\right)^r = h^{r-1-r}N^r = h^{-1}N^r.$$

The original scaling with no symmetry exploitation is N^r. There is a gain of $1/h$. The second part of step 9 is also more efficient

$$h^r N_i^{r+s} = h^r\left(\frac{N}{h}\right)^{r+s} = h^{r-r-s}N^{r+s} = h^{-s}N^{r+s}$$

against an original scaling of N^{r+s} for the matrix multiplication. A gain of $1/(h^s)$ is observed. For no summation indices $s = 0$ there is still a gain of $1/h$ because the number of multiplications is lowered to h^{r-1}.

Steps 6, 7 and the first part of step 9 give additional cost to the algorithm. They are independent of N, and only depend on the order of the point group. Testing the implementation has shown that significant gains can be achieved up to $h = 8$. Beyond that the number of IRREP blocks becomes too high, the assumption of equal distribution is more strongly violated, and no significant gains or even loss of efficiency was observed for the systems investigated.

6.3 Examples of symmetry exploitation

The newly implemented code for symmetry exploitation in CFOUR and QCUMBRE is here applied to specific examples. First, the reduction in computation time is studied. Calculations on small molecules are performed a) without the use of symmetry, b) with the use of real Abelian groups, and c) with complex Abelian groups. A study of the $B(OH)_3$ molecule follows. The molecule belongs to complex Abelian group even in the absence of magnetic field. This peculiarity poses some issues at the CC and EOM-CC levels of theory that are addressed in subsec. 6.3.2.

6.3.1 Effective reduction of computational time

The reduction of the computational time needed for ff quantum-chemical calculations achieved when using complex Abelian groups is addressed. The computational time of a single-point energy calculation at the CCSD level of theory is measured for four different molecules in the presence of a magnetic field. In order to have comparable results, the calculations for each molecule were performed using a single node on the computer cluster of the theoretical chemistry in the University of Mainz.[192] No parallelisation was used, and care had been taken so that the calculation in question was the only calculation running on the node each time.

Molecule		Magnetic field (PG)	Largest real Abelian PG
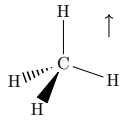	Methane	parallel to a C-H bond (C_3)	C_1
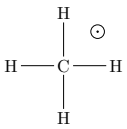	Planar methane	perpendicular to the plane (C_{4h})	C_{2h}
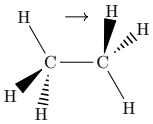	Ethane	parallel to the C-C bond (S_6)	C_i
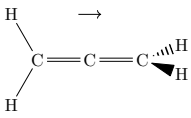	Allene	parallel to the C-C-C axis (S_4)	C_2

Table 6.9: The molecules used for the study of the cost reduction when exploiting symmetry through point-group theory.

The systems studied were chosen so that they belong to a complex Abelian point group (PG), whose largest real Abelian subgroup is either smaller or the C_1 group. Three calculations were performed for each molecule: a calculations without the exploitation of symmetry, a calculation exploiting only the real Abelian subgroup and a calculations exploiting the full complex Abelian group. The molecules studied are found in tab. 6.3.1.

The second system is methane in a planar geometry, which is a critical geometry but not a local minimum, meaning the gradients along a distortion away from the planar geometry are zero, but the Hessian eigenvalue is negative. This geometry is only used for the purpose of studying symmetry exploitation. The geometries of the molecules used are the field-free optimized geometries at the SCF level of theory with the corresponding basis set.

Results for the timings measurements for the studied systems are presented in tab. 6.10-6.13. The timings for the different processes required for a full CCSD calculation are shown. These include the

calculation of integrals over (S)AOs, the SCF procedure, a transformation of the integrals from the (S)AO basis to the MO basis, and the CCSD iterations until convergence. The difference between the sum of these processes and the total time required includes all other processes in the column "Rest" (I/O operations for the interface, allocation of memory, etc.). In order to better determine the observed scaling and the reduction of computational cost, the ratio time needed with no symmetry exploitation (C_1) over time needed with symmetry has been calculated and is compared to the order of the group h in the last columns. It should be noted that some ratios could not be calculated for the smaller systems, because the timing output in QCUMBRE does not print digits beyond the decimal point. For processes that only lasted a fraction of a second, the output only gives 0 s for the duration, which does not give any valuable information in the calculation of ratios. Moreover, the calculation for the allene and the correlation calculation for the ethane molecules using a cc-pVQZ(cart) basis set, were not feasible because of memory requirements. This already shows the merits of symmetry exploitation.

The ratio of the individual processes is expressed in powers of the point group in order to assess the reduction of the cost. First looking at the calculation of integrals, which corresponds to the implementation of the DCD, the use of complex and real groups is compared. The DCD for real point groups is based on an existing implementation in CFOUR, while the implementation for complex point groups is new and was described in subsec. 6.2.1. The ratio calculated for the different systems using real groups is $h^{0.9}$ on average. This drops to $h^{0.6}$ for complex groups. The difference amounts to the emergence of loops in the DCD from eq. (6.2.3). In the case of real point groups, eq. (6.2.3) simplifies to a phase prefactor (± 1). For complex point groups, the sum runs in principle over more than one index, and more specifically, it runs over at most two indices in the case of a spherical basis set [eq. (6.2.20)], or more in the case of a Cartesian basis [eq. (6.2.18).] As such, the average ratios for a spherical and a Cartesian basis differ significantly, and are $h^{0.7}$ and $h^{0.5}$, respectively. The reduction of cost for the SCF procedure exhibits an average ratio of $h^{1.6}$ and the AO to MO transformation $h^{1.5}$, with no difference between the use of real or complex point groups. Lastly for the CCSD calculation, a ratio of $h^{1.3}$ is observed for real point groups. For complex point groups, the ratio is $h^{1.1}$, which is significantly smaller. This difference, however, is not inherent to the use of complex groups, as the implementation in QCUMBRE does not differentiate between real and complex point groups. It is due to the overhead that is accompanied with the use of high-order point groups for small systems. The observed ratio for CCSD increases to $h^{1.2}$ for the complex point groups when the results using the cc-pVDZ basis set are not considered in the calculation of the average. Regarding the total duration of a total CCSD calculation, the observed reduction is $h^{1.2}$, confirming the very crude prediction of a gain greater than h.

Additionally, it is important to note that the reduction observed in the duration of a CCSD calculation is greater for larger systems (larger number of electrons and basis functions). As already explained in subsec. 6.2.2, the cost of symmetry exploitation is mostly dependent on the order of the point group h and on the type of the calculation, but not on the size of the system. For this reason, this cost is more negligible in larger systems and the observed reduction greater.

Basis set[a]	Comp. PG	Time[b]/s						Ratio (C_1/Comp. PG)					h
		Integrals	SCF	AO to MO	CCSD	Rest	Total	Integrals	SCF	AO to MO	CCSD	Total	
cc-pVDZ(cart)	C_1	0.75	0.10	1	2	2	6	1.0	1.0	1.0	1.0	1.0	1
	C_3	0.34	0.02	0	1	3	4	2.2	5.0		2.0	1.5	3
cc-pVDZ(sph)	C_1	0.74	0.09	1	2	2	6	1.0	1.0	1.0	1.0	1.0	1
	C_3	0.33	0.03	0	1	3	4	2.2	3.0		2.0	1.5	3
cc-pVTZ(cart)	C_1	17.69	5.25	54	78	13	168	1.0	1.0	1.0	1.0	1.0	1
	C_3	8.09	0.74	10	16	4	39	2.2	7.1	5.4	4.9	4.3	3
cc-pVTZ(sph)	C_1	14.93	3.42	28	52	9	107	1.0	1.0	1.0	1.0	1.0	1
	C_3	6.11	0.48	5	12	4	28	2.4	7.1	5.6	4.3	3.8	3
cc-pVQZ(cart)	C_1	439.80	120.89	2327	1255	232	4375	1.0	1.0	1.0	1.0	1.0	1
	C_3	199.79	17.75	309	333	86	946	2.2	6.8	7.5	3.8	4.6	3
cc-pVQZ(sph)	C_1	317.43	58.04	750	657	114	1896	1.0	1.0	1.0	1.0	1.0	1
	C_3	119.86	8.83	140	169	43	481	2.6	6.6	5.4	3.9	3.9	3

[a] sph stands for the use of a spherical basis, while cart for a Cartesian basis set.

[b] Only CFOUR timings have an accuracy beyond seconds in the second decimal point.

Table 6.10: Timing measurements for a full CCSD calculation using different basis sets and computational point groups for the methane in a tetrahedral geometry.

Basis set[a]	Comp. PG	Time[b]/s						Ratio (C_1/Comp. PG)					h
		Integrals	SCF	AO to MO	CCSD	Rest	Total	Integrals	SCF	AO to MO	CCSD	Total	
cc-pVDZ(cart)	C_1	0.75	0.26	0	2	3	6	1.0	1.0		1.0	1.0	1
	C_{2h}	0.36	0.02	0	1	3	4	2.1	13.0		2.0	1.5	4
	C_{4h}	0.34	0.01	0	2	3	5	2.2	26.0		1.0	1.2	8
cc-pVDZ(sph)	C_1	0.74	0.08	1	2	2	6	1.0	1.0	1.0	1.0	1.0	1
	C_{2h}	0.36	0.02	0	1	3	4	2.1	4.0		2.0	1.5	4
	C_{4h}	0.33	0.01	0	2	3	5	2.2	8.0		1.0	1.2	8
cc-pVTZ(cart)	C_1	17.61	5.50	54	86	12	175	1.0	1.0	1.0	1.0	1.0	1
	C_{2h}	6.88	0.60	6	14	7	34	2.6	9.2	9.0	6.1	5.1	4
	C_{4h}	6.78	0.16	2	13	5	27	2.6	34.4	27.0	6.6	6.5	8
cc-pVTZ(sph)	C_1	14.63	3.41	29	57	9	113	1.0	1.0	1.0	1.0	1.0	1
	C_{2h}	5.98	0.37	4	9	5	24	2.4	9.2	7.3	6.3	4.7	4
	C_{4h}	5.15	0.10	1	10	5	21	2.8	34.1	29.0	5.7	5.4	8
cc-pVQZ(cart)	C_1	439.65	120.96	2316	1380	229	4486	1.0	1.0	1.0	1.0	1.0	1
	C_{2h}	161.69	13.10	224	237	82	718	2.7	9.2	10.3	5.8	6.2	4
	C_{4h}	122.20	3.58	72	209	40	447	3.6	33.8	32.2	6.6	10.0	8
cc-pVQZ(sph)	C_1	317.84	58.48	742	721	114	1953	1.0	1.0	1.0	1.0	1.0	1
	C_{2h}	125.32	6.02	103	120	40	394	2.5	9.7	7.2	6.0	5.0	4
	C_{4h}	76.86	1.72	29	91	21	220	4.1	34.0	25.6	7.9	8.9	8

[a] sph stands for the use of a spherical basis, while cart for a Cartesian basis set.

[b] Only CFOUR timings have an accuracy beyond seconds in the second decimal point.

Table 6.11: Timing measurements for a full CCSD calculation using different basis sets and computational point groups for the methane in a planar geometry.

Basis set[a]	Comp. PG	Time[b]/s						Ratio (C_1/Comp. PG)					h
		Integrals	SCF	AO to MO	CCSD	Rest	Total	Integrals	SCF	AO to MO	CCSD	Total	
cc-pVDZ(cart)	C_1	6.66	0.85	6	38	3	55	1.0	1.0	1.0	1.0	1.0	1
	C_i	3.39	0.27	3	11	3	21	2.0	3.1	2.0	3.5	2.6	2
	S_6	2.81	0.04	0	6	3	12	2.4	21.3		6.3	4.6	6
cc-pVDZ(sph)	C_1	6.54	0.68	5	33	4	49	1.0	1.0	1.0	1.0	1.0	1
	C_i	3.33	0.22	2	10	3	19	2.0	3.1	2.5	3.3	2.6	2
	S_6	2.51	0.04	0	5	3	11	2.6	17.0		6.6	4.5	6
cc-pVTZ(cart)	C_1	154.01	40.81	415	1179	83	1872	1.0	1.0	1.0	1.0	1.0	1
	C_i	70.80	13.06	158	428	51	721	2.2	3.1	2.6	2.8	2.6	2
	S_6	103.92	1.80	38	110	17	271	1.5	22.7	10.9	10.7	6.9	6
cc-pVTZ(sph)	C_1	127.73	26.75	258	832	54	1298	1.0	1.0	1.0	1.0	1.0	1
	C_i	57.06	8.72	101	294	33	494	2.2	3.1	2.6	2.8	2.6	2
	S_6	56.25	1.26	24	76	13	171	2.3	21.2	10.8	10.9	7.6	6
cc-pVQZ(cart)	C_1	4151.88	1009.82					1.0	1.0				1
	C_i	1628.65	321.78	9318	7549	1023	19840	2.5	3.1				2
	S_6	2814.98	43.73	1119	2295	351	6624	1.5	23.1				6
cc-pVQZ(sph)	C_1	3216.76	467.70	9860	9391	869	23804	1.0	1.0	1.0	1.0	1.0	1
	C_i	1117.32	141.56	2641	3470	444	7814	2.9	3.3	3.7	2.7	3.0	2
	S_6	880.79	20.08	615	1054	171	2741	3.7	23.3	16.0	8.9	8.7	6

[a] sph stands for the use of a spherical basis, while cart for a Cartesian basis set.

[b] Only CFOUR timings have an accuracy beyond seconds in the second decimal point.

Table 6.12: Timing measurements for a full CCSD calculation using different basis sets and computational point groups for the ethane molecule.

Basis set[a]	Comp. PG	Time[b]/s						Ratio (C_1/Comp. PG)					h
		Integrals	SCF	AO to MO	CCSD	Rest	Total	Integrals	SCF	AO to MO	CCSD	Total	
cc-pVDZ(cart)	C_1	8.56	1.32	10	72	5	97	1.0	1.0	1.0	1.0	1.0	1
	C_2	5.15	0.45	4	22	3	35	1.7	2.9	2.5	3.3	2.8	2
	S_4	2.94	0.12	1	9	5	18	2.9	11.0	10.0	8.0	5.4	4
cc-pVDZ(sph)	C_1	8.31	1.10	7	64	12	92	1.0	1.0	1.0	1.0	1.0	1
	C_2	4.97	0.37	3	18	5	31	1.7	3.0	2.3	3.6	3.0	2
	S_4	2.80	0.10	1	9	3	16	3.0	11.0	7.0	7.1	5.8	4
cc-pVTZ(cart)	C_1	191.37	53.55	571	2066	82	2964	1.0	1.0	1.0	1.0	1.0	1
	C_2	111.44	17.39	201	712	50	1092	1.7	3.1	2.8	2.9	2.7	2
	S_4	58.15	4.88	82	264	27	436	3.3	11.0	7.0	7.8	6.8	4
cc-pVTZ(sph)	C_1	159.74	32.98	304	1377	52	1926	1.0	1.0	1.0	1.0	1.0	1
	C_2	94.61	10.70	108	471	31	715	1.7	3.1	2.8	2.9	2.7	2
	S_4	45.49	2.97	47	176	18	289	3.5	11.1	6.5	7.8	6.7	4
cc-pVQZ(cart)	C_1												1
	C_2	2428.96	355.07	5096	84956	954	93790						2
	S_4	1177.49	101.73	2261	38156	470	42166						6
cc-pVQZ(sph)	C_1	3498.31	486.19	7855	13279	725	25843	1.0	1.0	1.0	1.0	1.0	1
	C_2	1915.18	156.52	2340	4856	418	9686	1.8	3.1	3.4	2.7	2.7	2
	S_4	823.13	41.82	908	2006	205	3984	4.3	11.6	8.7	6.6	6.5	4

[a] sph stands for the use of a spherical basis, while cart for a Cartesian basis set.

[b] Only CFOUR timings have an accuracy beyond seconds in the second decimal point.

Table 6.13: Timing measurements for a full CCSD calculation using different basis sets and computational point groups for the allene molecule.

6.3.2 Boric acid $B(OH)_3$

In order to further investigate and present the usefulness of the exploitation of complex Abelian groups, the $B(OH)_3$ molecule was studied within the EOM-CC and CI approach. Moreover, this study functions as an analysis of the unphysical complex energies which are an artifact of the non-Hermiticity of the CC formulation. The $B(OH)_3$ molecule is an example of a peculiar case that has the symmetry of a complex Abelian group C_{3h} even in the absence of a magnetic field.

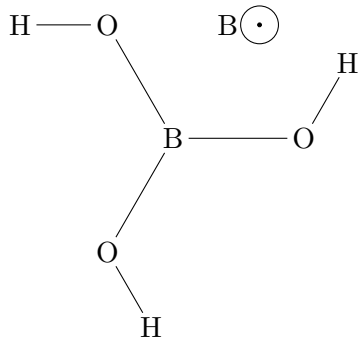

Figure 6.8: Boric acid in a magnetic field perpendicular to the molecular axis. C_{3h} symmetry.

It is known for molecules whose symmetry is described by a complex Abelian point group even in the absence of a magnetic field that orbitals and electronic states belonging to the pair of complex conjugate IRREPs are accidentally degenerate. Such accidentally degenerate wavefunctions or orbitals are necessarily complex themselves. This accidental degeneracy, however, allows the orbitals and the wavefunctions describing such states to form real-valued linear combinations that no longer transform as the IRREPs of the point group, but as the IRREPs of a real subgroup. As such, accidental degeneracy can be used to approach systems of this type using real numbers,[183] as in most cases, the cost of dealing with complex algebra is not compensated by the cost reduction of a higher-order point group.

Hermitian approaches like (F)CI theory always result in real energy eigenvalues. At the truncated EOM-CC level, however, complex energy eigenvalues may occur, and specifically for the accidentally degenerate states described in the previous paragraph, the diagonalization results in complex-conjugate energy eigenvalue pairs. This means that the energy eigenvalues of these states are not mathematically degenerate, but instead have the same real part (physical degeneracy) but an opposite non-vanishing imaginary part.[111,112] This absence of a mathematical degeneracy forbids the formation of real-valued linear combinations for the wavefunction solutions. As such, quantum-chemical programs that only utilize real numbers are not able to converge to these states at all at the EOM-CC level of theory.

The $B(OH)_3$ molecule (fig. 6.8) has such a symmetry. Its symmetry is described by the C_{3h} point group, which is a complex Abelian group. The point group has two pairs of complex conjugate IRREPs, the E_1'/E_2' and E_1''/E_2''. A magnetic field oriented perpendicular to the plane of the molecule, does not reduce the symmetry of the system. Here, the $B(OH)_3$ molecule was studied at the CISD, CCSD, CCSD(T)(a)* and CC3 levels of theory for the highly symmetric perpendicular magnetic-field orientation for field strengths up to 1.0 B_0 using a 0.05 B_0 step. The unc-aug-cc-pVDZ basis set was employed. The field-free optimized CCSD geometry (2.6018 a_0 B-O distance, 1.8181 a_0 O-H distance, 68.23° B-O-H angle) obtained with the same basis set was used for the ff calculations .

It is also noteworthy to comment on the computational cost of the methods used. CCSD and CISD are comparable regarding their cost. On the other hand, the cost of the non-iterative CCSD(T)(a) method versus the iterative CC3 is vastly different despite that the cost of both methods scales as N^7. In the QCUMBRE implementation, a CCSD(T)(a) calculation needs about 0.5 TB memory and about 1.5 days until completion. Using multiple cores on the cluster,[192] the calculations at the CCSD(T)(a)* level for all different magnetic-field strengths were completed after 3-4 days. A CC3 calculation, however, currently needs 2 TB memory and about 4 days until completion. Since only two cores with the needed memory capacity were available, the calculations at this level for the different magnetic-field strengths were completed in the span of more than a month. Moreover, these calculations would obviously not be feasible without the exploitation of symmetry, as the memory requirements would be about 6 times higher and would exceed the currently available capacity.

In fig. 6.9, the total energy of the field-free ground state $^1A'$ is plotted as a function of the magnetic field. Being a closed-shell state, there is no contribution from the spin-Zeeman term, and the energetical response of the state to the magnetic field mostly arises from the diamagnetic term. The total energy is for this reason monotonically increasing with stronger magnetic fields. In the absence of field, the ground state energies using different CC variants are completely real, but in the presence of field, they acquire a small imaginary part that is plotted on the right panel of the

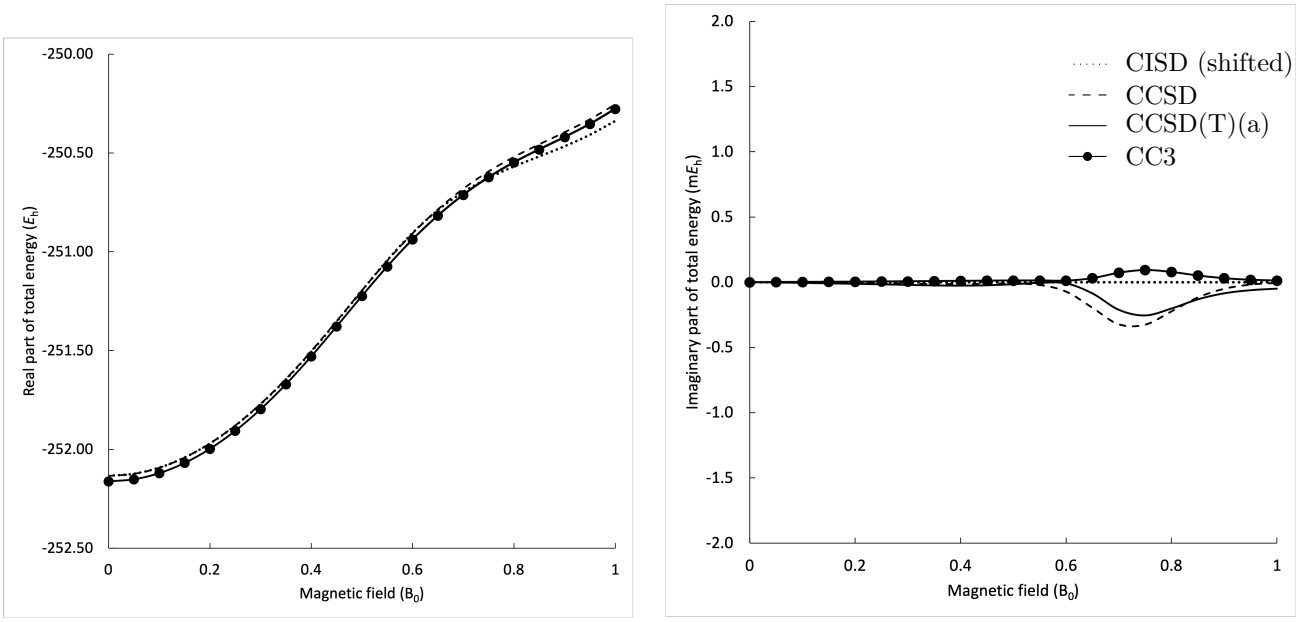

Figure 6.9: Total energy of the reference $^1A'$ state of $B(OH)_3$ as a function of the magnetic field (left panel) and the imaginary part of the energy at the CISD, CCSD, CCSD(T)(a) and CC3 levels of theory. The CISD energy shown is shifted so that it coincides with the CCSD energy at $B = 0$ B_0.

figure. The imaginary part is of the order of 10^{-5} E_h, except for magnetic-field strengths between $0.65\ B_0 < B < 0.8\ B_0$, where it is of the order of 10^{-4} E_h at the CCSD and CCSD(T)(a) levels. In the "problematic" region, the CCSD(T)(a) energies have a smaller imaginary part up to $B = 0.8\ B_0$. The reduction of the imaginary part of the energy is, however, only marginal at $6 \cdot 10^{-5}/E_\mathrm{h}$ on average. For field strengths stronger than $0.85\ B_0$, however, the CCSD(T)(a) triple corrections do not reduce the imaginary contributions, but increase them slightly. Lastly, the imaginary part of the CC3 energies never exceeds 10^{-4} E_h for this state, offering a clear improvement over CCSD. It can be deduced that the imaginary contribution do indeed vanish when approaching the FCI limit,[112] but the trend is not necessarily monotonic, and the way approximate triples are included plays a role. In addition, the CISD energy is plotted in the figure to compare the non-Hermitian approaches to a Hermitian one. In order to eliminate the discrepancy of the CISD results due to unequal inclusion of correlation, the CISD energies shown are shifted so that they coincide with CCSD in the absence of the field. This comparison shows no direct correlation of the imaginary contributions in the "problematic" region with an increased deviation from CISD.

The first excited states of each IRREP were studied at the CISD, EOM-CCSD, EOM-CCSD(T)(a)* and EOM-CC3 levels of theory. In the upper panel of fig 6.10, the results for $^1A'$ and $^1A''$ (purple and dark blue, respectively) are shown. These states have completely real energies in the field-free case. In the middle panel, the behaviour of the states of $^1E'_1$ and $^1E'_2$ symmetry (blue and red, respectively), and in the lower panel the states of $^1E''_1$ and $^1E''_2$ symmetry (yellow and green, respectively) is plotted as a function of the magnetic field. As already mentioned, these E' and E'' pairs of excited states are physically accidentally degenerate in the absence of field and at the EOM-CC level, they are found as complex conjugate pairs. As such, they are can only be targeted utilising complex algebra. In the absence of the magnetic field, the imaginary part amounts to 10^{-5} E_h using the different EOM-CC approaches, which is very small. The $^1E''_1$ and $^1E''_2$ (yellow and green) states are characterised strongly by the HOMO→LUMO transition and are found as the first excited states.

In the left column of fig. 6.10, the excitation energies are plotted as a function of the magnetic field strength. Similarly to the ground state, the excitation energies at the CISD level are shifted so that they coincide with the CCSD results for $B = 0$ B_0, to eliminate the unequal inclusion of correlation in the comparison of the methods. The response of the states to the magnetic field is mostly accounted for by the diamagnetic term, with the total energy being raised monotonically for an increasing magnetic-field strength. The field-free accidentally degenerate states show a completely

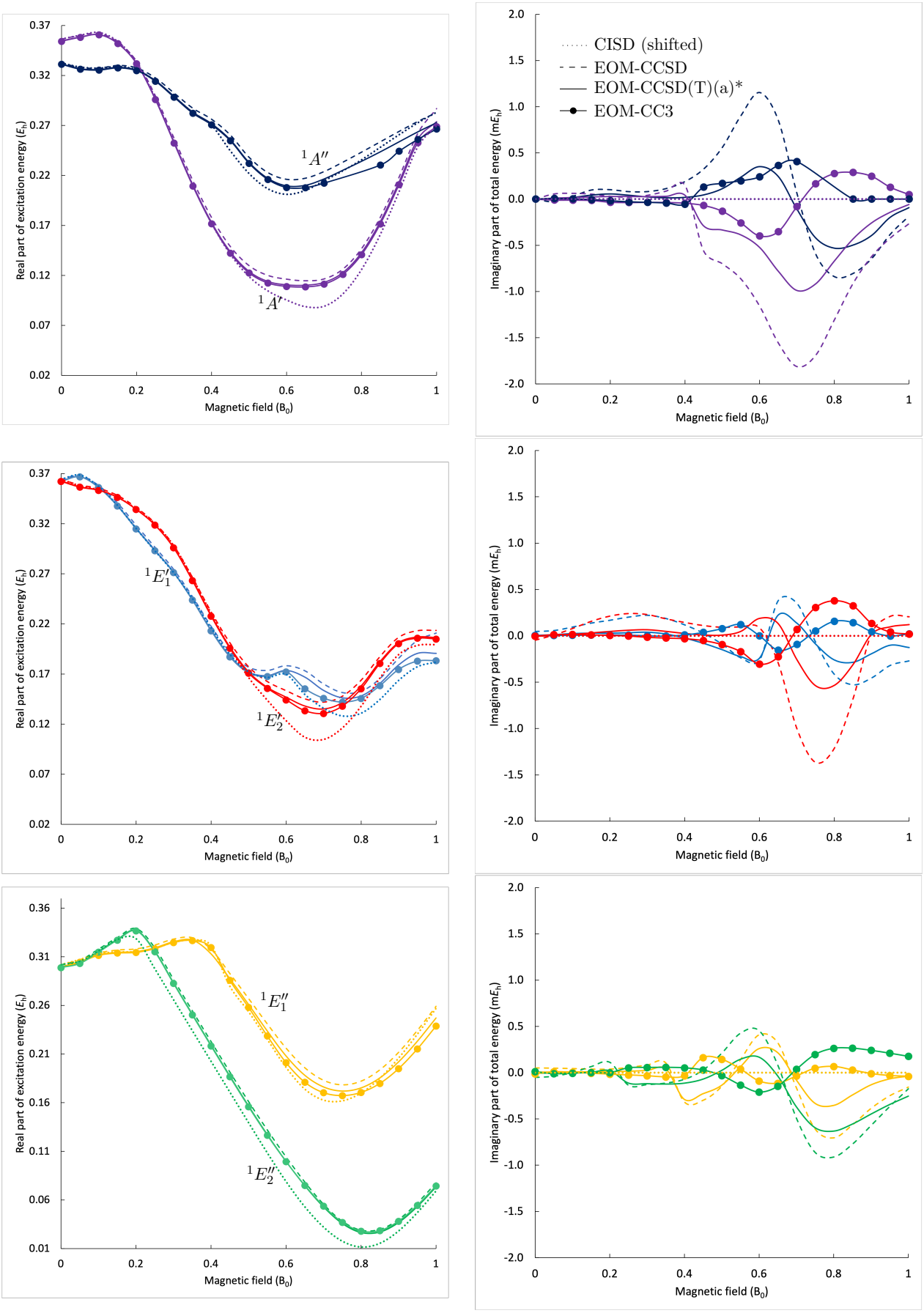

Figure 6.10: Excitation energy of the first singlet excited states for each IRREP of $B(OH)_3$ as a function of the magnetic field (left column) and imaginary part of the total energy (right column) at the CISD, EOM-CCSD, EOM-CCSD(T)(a)* and EOM-CC3 levels of theory. The CISD excitation energies have been shifted in order to coincide with CCSD at $B = 0$ B_0.

different behaviour in the magnetic field. First, looking at the excited state lower in energy in the lower panel of fig. 6.10, for both the $^1E''_1$ state (yellow) and $^1E''_2$ state (green), the excitation energy is higher in weaker fields compared to the field-free case. It then decreases to a minimum around $B = 0.8\ B_0$. The $^1E''_2$ state (green) tends to be lower in energy than the other singlet states for the magnetic-field strengths studied. The excitation energies of the $^1E'_1$ (light blue) and $^1E'_2$ (red) states in the middle panel decrease until about $B = 0.5\ B_0$. The $^1E'_2$ (red) state reaches a minimum of the excitation energy around $B = 0.7\ B_0$, which is also indicated by large deviations of the CISD from the EOM-CC results. The $^1E'_2$ (light blue) state acquires some important contributions from double excitations around $B = 0.6\ B_0$, also shown as a larger deviation between EOM-CCSD, and the approximate triples EOM-CCSD(T)(a)* and EOM-CC3 results. Lastly, the excitation energies of the $^1A'$ (purple) and $^1A''$ (dark blue) states in the upper panel are initially relatively constant for weaker fields. The $^1A'$ (purple) excitation energy reaches a low plateau between $B = 0.55\ B_0$ and $B = 0.75\ B_0$ when using the EOM-CC approach. At the CISD level on the other hand, a minimum at $B = 0.7\ B_0$ is observed. The $^1A''$ (dark blue) excitation energy is found higher relative to the $^1A'$ state (purple). Because of the slow convergence of the EOM-CC3 method when using the alternative Davidson scheme (see subsec. 4.1.2), the $^1A''$ (dark blue) state could not be converged for $B = 0.75\ B_0$ and $B = 0.80\ B_0$, where double-excitation character is also somewhat significant.[f]

Looking at the imaginary part of the energy at the EOM-CC levels of theory in the right column of fig. 6.10, it is observed that all excited states acquire an imaginary part in a magnetic field, which does not exceed $10^{-3}\ E_\mathrm{h}$. It is, nonetheless, more pronounced compared to the ground state. Larger imaginary contributions are expected for excited EOM-CC states compared to reference CC states.[112] An increased imaginary contribution is observed between $0.65\ B_0$ and $0.8\ B_0$ for all excited state. Inclusion of perturbative triples via the EOM-CCSD(T)(a)* method in this case consistently reduces the imaginary part of the states relative to EOM-CCSD by approximately half. The imaginary part of EOM-CC3 method follows slightly different trends compared to EOM-CCSD and EOM-CCSD(T)(a)*, since unlike EOM-CCSD(T)(a)*, the method is not based on an CCSD/EOM-CCSD(T)(a)^0 solution. The average imaginary contributions are $3.4 \cdot 10^{-4}\ E_\mathrm{h}$ at EOM-CCSD, $1.7 \cdot 10^{-4}\ E_\mathrm{h}$ at EOM-CCSD(T)(a)* and $0.9 \cdot 10^{-4}\ E_\mathrm{h}$ at EOM-CC3. Hence, including higher-order excitations beyond CCSD even approximately, brings the results closer to FCI which would necessarily yield real energies.[112] The non-Hermiticity error is addressed better at the EOM-CC3 level compared to EOM-CCSD(T)(a)*.

Imaginary contributions to the energy do indeed hint at a failure of the CC approach due to the non-Hermiticity of the theory,[112] but their extent cannot be used directly as a diagnostic tool. A physical interpretation of the imaginary part does not exist yet, and more importantly, a large imaginary part does not necessarily suggest that the physical real part of the energy is of bad quality. Attempting to find such a correlation between the extent of the imaginary part and the quality of the real part of the energy, the EOM-CC approaches are compared against the shifted excitation energies at the CISD level of theory which is a Hermitian approach. The shift of the CISD excitation energies, as described in the previous paragraph, is rather large and almost constant at $\sim 0.11\ E_\mathrm{h}$. This can be traced back to the insufficient inclusion of correlation especially for the excited state. In order to be able to compare the CISD results for the excited states with the EOM-CC results, the energy shift is used to eliminate the deviation arising from this unequal treatment. No direct correlation is observed between the deviation of the shifted CISD energies from the EOM-CC energies and the extent of the calculated imaginary part. The overall trend at the EOM-CC levels is the same as at the CISD level of theory, and any fluctuation of the deviation beyond the constant shift is not correlated to the extent of the imaginary part. On the contrary, a more significant effect regarding the accuracy of the methods is the extent of the double-excitation character. The $^1E'_1$ state (blue curve, middle panel) acquires a notable double-excitation character for $B > 0.6\ B_0$, and as such, the EOM-CC3 results, which have been shown to capture the double-excitation character better than the other approaches, are the most accurate for this region. The EOM-CCSD(T)(a)* approach is not designed for such cases and does not correct the EOM-CCSD energies as well. Despite the emergence of a non-physical imaginary part in the energy, the calculated real parts of the energies do not show any signs of bad quality beyond the truncated character of the exponential at CC and linear at EOM-CC expansion. As such they are

[f] A calculation using the standard Davidson method exceeds the currently available computational capacity.

still deemed as valid and good approximations. The magnitude of the imaginary part could not even be directly related to the accuracy of the results. Moreover, systematically increasing the quality of the results lowers its extent.

This study shows that the implementation of complex Abelian point groups and the use of complex algebra in quantum-chemical calculations is important beyond the study of the behaviour of molecules in the presence of a magnetic field. $B(OH)_3$ cannot be targeted thoroughly at the CC and EOM-CC level using only real numbers even in the field-free case. Moreover, the use of symmetry is decisive both for the overall cost of the calculations and the interpretational value. The findings of this investigation serve as an evaluation of the imaginary artifacts in the complex CC energy that arise from the non-Hermiticity of the ansatz.

Chapter 7

Geometry Optimization in a Magnetic Field

Two important questions that very often quantum chemistry is tasked to answer is what is the exact structure of a molecular system, what is the relative stability of the molecule with respect to other compounds. The molecular geometry gives insight about the chemistry of the compound regarding its shape, it gives results that can be readily compared with experiment and also offers a common language for the communication between experimentalists and theoreticians. Calculation of the relative stability between compounds can be done only when the molecular structures of all the compounds involved are known. The molecular structure is understood as the minimum of the effective electronic potential V_{el} within the Born-Oppenheimer approximation, which was generalized as the screened BO approximation [eq. (2.1.19)] for calculations in the presence of a magnetic field.[91,193]

A total geometry optimization in a magnetic field corresponds not only to the optimization of the molecular structure, but also the optimization of the relative orientation of the molecule to the magnetic field. Unlike other optimization strategies in the presence of a magnetic field in the literature,[57,69,97,99] the algorithm in this thesis can additionally rigorously perform constrained geometry optimizations. Regarding the magnetic-field parameters, a constrained geometry optimization would mean that the orientation of the molecule relative to the field remains constant during the optimization steps. A special case of such a geometry optimization is that the magnetic field coincides with a symmetry element of the molecule. Lastly, the newly developed algorithm functions in a way equivalent to optimizations in the absence of a magnetic field as it uses internal instead of Cartesian coordinates which is not the case for existing approaches. This makes it consistent with the established approach for the field-free case in the quantum-chemical community and its use simple and user-friendly.

In this chapter, the details of the geometry optimization algorithm. First, the theoretical aspects, and more specifically, the development of an algorithm able to function in the presence of a magnetic field are introduced. The implementation of the newly developed algorithm in CFOUR together with the handling of the magnetic field is presented next. In the last part of this chapter, the geometry optimization algorithm is used for the study of the molecular fragments of H_2O and CH_4 and their relative stability in the presence of a magnetic field.

7.1 Theoretical aspects

In order to understand the specific issues present in optmizing the geometry in a magnetic field, the theoretical background of geometry-optimization algorithms is addressed.

For a molecule of N_{N} nuclei, the total nuclear degrees of freedom, on which V_{el} depends, are $3N_{\mathrm{N}}$. These are usually divided in 3 translational degrees of freedom, which describe the movement of the centre of mass of the molecule in the 3D space, N_{rot} rotational degrees of freedom that describe the orientation of the molecule, and the $3N_{\mathrm{N}}-3-N_{\mathrm{rot}}$ internal degrees of freedom. The rotational degrees of freedom are 2 for linear and 3 for non-linear molecules. Since the effective electronic potential is invariant to translations and rotations in the absence of a field, most studies of molecular structure get rid of these degrees of freedom one way or another, so that they work only with the internal

ones.[194–197]

In order to find the molecular structure in the absence of a magnetic field, optimization algorithms are used to find the minimum of V_{el}. This is needed as, even if an analytic form for V_{el} were available, the optimization is a non-trivial multidimensional problem. The optimization is restricted to the internal degrees of freedom, since translation and rotational degrees of freedom are energy invariant. The optimization strategies fall under the general category of Newton-Raphson (NR) optimizations that require the calculation of geometric gradients and Hessians. Because the exact calculation of Hessian matrices is very expensive, quasi Newton-Raphson algorithms are employed that approximate the Hessian, and also impose certain characteristics on it (positive eigenvalues, etc.) that help with convergence.[193] For specific studies, not only totally unconstrained geometry optimizations, but optimizations with constraints may also be performed.[193] E.g., the optimization of the ethane molecule for given relative orientations of the methyl groups can be used to study the barrier of the rotation about the C-C bond.

In the presence of a magnetic field, V_{el} is not only dependent on the internal degrees of freedom, but also on the relative orientation of the molecule with respect to the magnetic field for a given magnetic-field strength. Translational invariance holds in the presence of the magnetic field as well, and it is additionally ensured for approximate wavefunctions via the use of London orbitals as explained in subsec. 2.1.2. In order to avoid the calculation of derivatives with respect to the magnetic field, the dependence of the energy regarding the relative orientation can be targeted via rotations of the molecule. More specifically, two rotational degrees of freedom for non-linear molecules and one for linear molecules are no longer energy invariant. Rotations around any axis parallel to the magnetic field do not change the system.[57,97,99]

The $3N_{\mathrm{N}}$ Cartesian coordinates of the nuclei in a molecule include all $3N_{\mathrm{N}}$ degrees of freedom. Working with Cartesian coordinates in the absence of magnetic field requires special handling to get rid of the translation and rotational degrees of freedom, which is done with projections.[194,196,198] Geometrical constraints (constant interatomic distance, constant angle between three nuclei, etc.) are non-linear in Cartesian coordinates and are very bothersome to be introduced and to be fulfilled.[194–197] When internal coordinates are used instead, the translational and the rotational degrees of freedom are absent from the problem, and geometric constraints are more naturally introduced since the coordinates can be chosen in such a way that the constraints are linear. The problem of internal coordinates in the presence of a magnetic field is that the two (or one) rotational degrees of freedom that are needed for the relative orientation to the magnetic field need to be reintroduced.

7.1.1 From Cartesian to internal coordinates

Internal coordinates, unlike Cartesian coordinates, are not defined with respect to an origin, but use relative quantities instead (interatomic distances, angles, etc.) reducing the degrees of freedom to be defined. In order to fully define the position of a nucleus in a molecule, one needs three coordinates for each atom. In the current work, the internal coordinate system used describes the position $\vec{r}_A$ for nucleus A in the form

$$\vec{r}_A = (r_{A_1}, r_{A_2}, r_{A_3}) = (d_B, \theta_C, \varphi_D), \tag{7.1.1}$$

where d_B is the distance of nuclei A and B, $d_B = |\boldsymbol{r}_{AB}|$, θ_C the angle $\widehat{ABC}$, and φ_D the dihedral angle of planes ABC and BCD. These are given in analytic form as functions of the Cartesian coordinates

$$\begin{aligned} d_B &= |\vec{x}_B - \vec{x}_A| \\ \theta_C &= \arccos \frac{(\vec{x}_C - \vec{x}_B)}{|\vec{x}_C - \vec{x}_B|} \cdot \frac{(\vec{x}_A - \vec{x}_B)}{|\vec{x}_A - \vec{x}_B|} \\ \varphi_D &= \arccos \left[\frac{(\vec{x}_B - \vec{x}_A) \times (\vec{x}_C - \vec{x}_B)}{|\vec{x}_B - \vec{x}_A|\,|\vec{x}_C - \vec{x}_B| \sin\theta_C} \cdot \frac{(\vec{x}_C - \vec{x}_B) \times (\vec{x}_D - \vec{x}_C)}{|\vec{x}_C - \vec{x}_B|\,|\vec{x}_D - \vec{x}_C| \sin\theta_D} \right], \end{aligned} \tag{7.1.2}$$

with

$$\theta_D = \arccos \frac{(\vec{x}_D - \vec{x}_C)}{|\vec{x}_D - \vec{x}_C|} \cdot \frac{(\vec{x}_B - \vec{x}_C)}{|\vec{x}_B - \vec{x}_C|}.$$

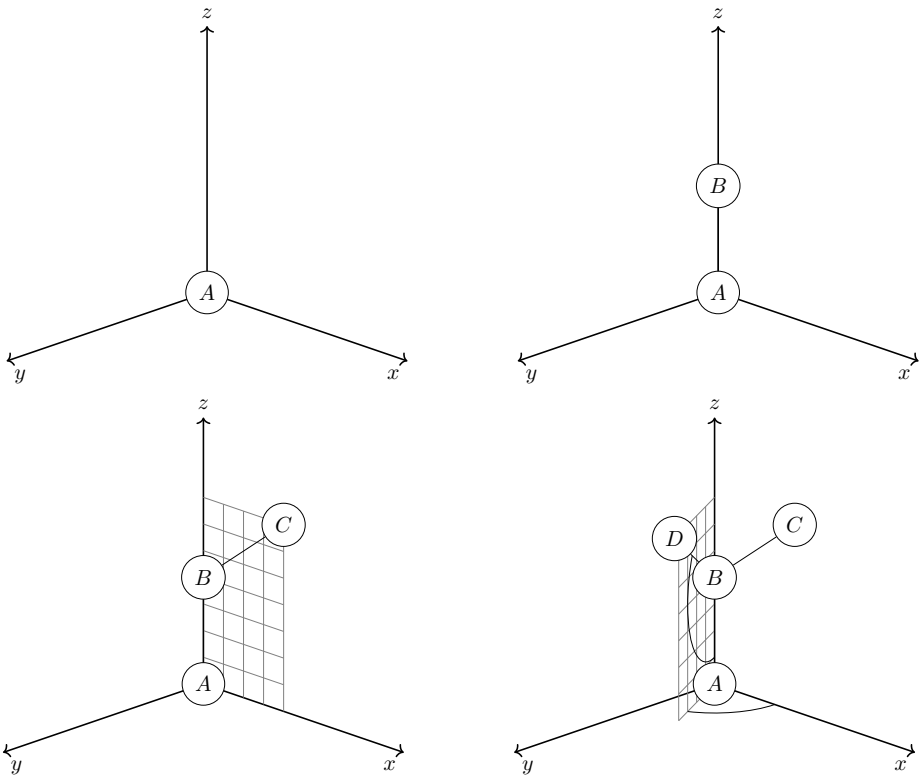

Figure 7.1: Positioning of the first four nuclei A, B, C, and D from internal coordinates to Cartesian.

Cartesian coordinates are of the form

$$\vec{x}_A = (x_{A_1}, x_{A_2}, x_{A_3}) = (x_{Ax}, x_{Ay}, x_{Az})\,.$$

The above equations describe the transformation from the Cartesian $\boldsymbol{x} = \{\vec{x}_A\}$ to the internal $\boldsymbol{r} = \{\vec{r}_A\}$ coordinate system. The arrow notation used indicates three-vectors.

The 6 (or 5 for linear molecules) invariant degrees of freedom are set in the definition of the internal coordinates for the position of the first 3 nuclei.[199] The first nucleus A is put in the Cartesian origin and needs no internal coordinates. The second nucleus B is put on the z axis and only needs d_A. The third C needs d_B and θ_B to be defined and is put in the zx plane. This convention[77] eliminates the translational and rotational degrees of freedom. The positioning of the first 4 nuclei A, B, C, and D is shown in fig. 7.1. Most commonly, the molecule is repositioned, so that the centre of mass coincides with the Cartesian origin, and is reoriented so that the z-axis is either the axis with the smallest moment of inertia, or the non-degenerate one in symmetric molecules.[a] Working with internal coordinates is also rendered more flexible by the use of dummy atoms that contribute only to the definition of the molecular geometry and do not take part in the quantum-chemical calculation.

The definition of the molecular geometry takes place typically in internal coordinates while the quantum-chemical calculation takes place in Cartesian coordinates. For this reason, algorithms for the transformation between the two coordinates systems have been developed.[199] For a geometry optimization in internal coordinates though, a transformation of the gradients is also needed since both analytic and numerical gradients are calculated in Cartesian coordinates. This transformation takes the form

$$\mathrm{d}\boldsymbol{x} = \mathbf{B}^\intercal \mathbf{G}^{-1} \mathrm{d}\boldsymbol{r}$$

for infinitesimal displacements. The Wilson B-matrix $\mathbf{B}$ is here introduced as the matrix of the partial derivatives of the internal coordinates with respect to Cartesian coordinates[194]

$$B_{A_i B_j} = \frac{\partial r_{A_i}}{\partial x_{B_j}}.$$

[a] Special reorientations may take place in order for symmetry elements to coincide with the z-axis as described in chap. 6.

Analytic forms for the elements of the Wilson B-matrix are derived by differentiation of eq. (7.1.2). The non-zero Wilson B-Matrix entries for nucleus A are at most $4 \cdot 3 = 12$, since internal coordinates depend on at most 4 nuclei. Matrix $\mathbf{G}$ is given as

$$\mathbf{G} = \mathbf{B}\mathbf{B}^{\intercal}.$$

7.1.2 Handling the magnetic-field orientation through rotations

Since rotations are no longer free in the presence of a magnetic field, the molecule is repositioned so that the centre of mass coincides with the Cartesian origin but no reorientations take place. Instead, the magnetic field is "turned-on" after the repositioning. The magnetic-field orientation is typically chosen to be the z-direction. This is particularly handy regarding the handling of symmetry, since symmetry elements (except inversions) surviving the anisotropy of the magnetic field are defined parallel (rotations) or perpendicular (reflections) to the magnetic field.

In order to offer more control for the relative orientation of the molecule with respect to the magnetic field, a rotation of the molecule defined as part of the molecular geometry takes place after the field is "turned-on". This rotation is expressed as an exponential-map vector $\vec{v}_{\text{rot}}$,[200] which defines a rotation around the axis

$$\hat{e}_{\text{rot}} = \frac{\vec{v}_{\text{rot}}}{|\vec{v}_{\text{rot}}|}$$

for an angle

$$\theta_{\text{rot}} = |\vec{v}_{\text{rot}}|.$$

The exponential map is more appropriate for the needs of a geometry optimization in a magnetic field compared to the more commonly used Euler angles because it exhibits less singularities, and is more readily related to the rotation quaternion (which will be introduced in the next paragraph). In addition, the exponential map has the correct number of degrees of freedom i.e., three, to describe the rotations. It can be chosen perpendicular to the magnetic field $\boldsymbol{B} = \vec{B}$,

$$\vec{B} \perp \vec{v}_{\text{rot}},$$

to activate only the two (or one for linear molecules) non-invariant rotational degrees of freedom.

7.1.3 Introducing rotations to the Wilson B-matrix

In order to handle rotations in a geometry optimization, the exponential map $\vec{v}_{\text{rot}}$ is taken under consideration together with the set of internal coordinates. Thus, the Wilson B-matrix entries for the rotation are needed[200]

$$B_{\vec{v}_{\text{rot}} B_j} = \frac{\partial \vec{v}_{\text{rot}}}{\partial x_{B_j}}.$$

The elements of $B_{\vec{v}_{\text{rot}} B_j}$ are found by means of the rotation quaternion $\vec{\vec{q}}_{\text{rot}}$, which is a four-vector

$$\vec{\vec{q}} = (q_0, \vec{q}) = (q_0, q_1, q_2, q_3)\,.$$

The rotation quaternion is defined as

$$\vec{\vec{q}}_{\text{rot}} = \left(\cos\frac{\theta_{\text{rot}}}{2}, \hat{e}_{\text{rot}} \cdot \hat{e}_x \sin\frac{\theta_{\text{rot}}}{2}, \hat{e}_{\text{rot}} \cdot \hat{e}_y \sin\frac{\theta_{\text{rot}}}{2}, \hat{e}_{\text{rot}} \cdot \hat{e}_z \sin\frac{\theta_{\text{rot}}}{2} \right) \tag{7.1.3}$$

The action of a rotation defined by the quaternion $\hat{C}(\vec{\vec{q}}_{\text{rot}})$ on a Cartesian vector is expressed as pure quaternion $\vec{\vec{x}} = (0, \vec{x})$ takes the following form in quaternion algebra

$$\hat{C}(\vec{\vec{q}}_{\text{rot}}) = \vec{\vec{q}}_{\text{rot}}\, \vec{\vec{x}}\, \vec{\vec{q}}^{\,c}_{\text{rot}},$$

with $\vec{\vec{q}}^{\,c} = (q_0, -\vec{q})$ the conjugate quaternion.

If $\boldsymbol{y} = \{\vec{y}_A\}$ are the Cartesian coordinates before the rotation and $\boldsymbol{x} = \{\vec{x}_A\}$ the coordinates after the rotation, then $\vec{\tilde{q}}_{\text{rot}}$ is the eigenvector with the lowest eigenvalue λ of the symmetric matrix

$$\mathbf{F} = \begin{pmatrix} R_{11}+R_{22}+R_{33} & R_{23}-R_{32} & R_{31}-R_{13} & R_{12}-R_{12} \\ R_{23}-R_{32} & R_{11}-R_{22}-R_{33} & R_{12}+R_{21} & R_{13}+R_{31} \\ R_{31}-R_{13} & R_{12}+R_{21} & -R_{11}+R_{22}-R_{33} & R_{23}+R_{32} \\ R_{12}-R_{12} & R_{13}+R_{31} & R_{23}+R_{32} & -R_{11}-R_{22}+R_{33}, \end{pmatrix}$$

with

$$R_{ij} = \sum_A x_{A_i} y_{A_j},$$

derived from the calculation of the root-mean-square deviation (RMSD).[200,201] Using now the formula for the gradient of an eigenvector, the derivatives of the rotation quaternion with respect to the Cartesian coordinates are

$$\frac{\partial\, \vec{\tilde{q}}_{\text{rot}}}{\partial x_{B_j}} = (\lambda \mathbb{1} - \mathbf{F})^{-1} \frac{\partial \mathbf{F}}{\partial x_{B_j}} \vec{\tilde{q}}_{\text{rot}}.$$

In order to derive the derivatives of the exponential map, $\vec{v}_{\text{rot}}$ is written as a function of the quaternion

$$v_{\text{rot}_i} = 2 q_{\text{rot}_i} \left(\frac{\arccos q_{\text{rot}_0}}{\sqrt{1 - q_{\text{rot}_0}^2}} \right).$$

The Wilson B-matrix entries are then found using the chain rule

$$B_{v_{\text{rot}_i} B_j} = \sum_{k=0}^{3} \frac{\partial v_{\text{rot}_i}}{\partial q_{\text{rot}_k}} \frac{\partial q_{\text{rot}_k}}{\partial x_{B_j}}.$$

The derivatives of the exponential map with respect to the quaternion are given by

$$\begin{aligned} \frac{\partial v_{\text{rot}_i}}{\partial q_{\text{rot}_k}} &= \left(\frac{\arccos q_{\text{rot}_0}}{\sqrt{1 - q_{\text{rot}_0}^2}} \right) \delta_{ik}, \;\; k = 1,2,3 \\ \frac{\partial v_{\text{rot}_i}}{\partial q_{\text{rot}_0}} &= 2 q_{\text{rot}_i} \left(\frac{q_{\text{rot}_0} \arccos q_{\text{rot}_0}}{\left(1 - q_{\text{rot}_0}^2\right)^{3/2}} - \frac{1}{1 - q_{\text{rot}_0}^2} \right). \end{aligned} \tag{7.1.4}$$

For small rotations, the quaternion approaches a scalar $\vec{\tilde{q}}_{\text{rot}} \approx q_{\text{rot}_0}$ and since it is normalised $q_{\text{rot}_0} \to 1$. In this region eq. (7.1.4) becomes ill-defined. The derivatives are then found by a Taylor expansion around $q_{\text{rot}_0} = 1$

$$\begin{aligned} \frac{\partial v_{\text{rot}_i}}{\partial q_{\text{rot}_k}} &= \left[2 - \frac{2}{3} \left(q_{\text{rot}_0} - 1 \right) \right] \delta_{ik}, \;\; k = 1,2,3 \\ \frac{\partial v_{\text{rot}_i}}{\partial q_{\text{rot}_0}} &= -\frac{2}{3} q_{\text{rot}_i}. \end{aligned}$$

7.2 Implementation in CFOUR

Having derived the necessary theory for the construction of a geometry optimization algorithm able to function in the presence of a magnetic field, its implementation in CFOUR is introduced. Before addressing the algorithm itself, details on the handling of the magnetic field in the program and the user-interface, which were improved in this thesis, have to be presented.

7.2.1 Handling of the magnetic field

Initially, CFOUR handled the magnetic field as a vector input. Such an input was only able to function together with Cartesian coordinates for the molecular structure, which input, however, is not designed to work for a geometry optimization. As such, a magnetic-field input able to function in combination with an internal coordinates input for the nuclei in the molecule was to be enabled.

The molecular geometry in Cartesian coordinates is read by the subroutine `getxyz` in **joda** in CFOUR and their use is activated by the keyword `COORDINATES=CARTESIAN`. Internal coordinates are handled in **joda** as well. The reading of the internal-coordinates input takes place in the `fetchz` subroutine. Taking the form of eq. (7.1.1) for internal coordinates, the indices of the nuclei B, C and D that describe the connectivity are saved in the array `NCON`, while the variable names associated with the values of d_B, θ_C and φ_D in `VARNAM`, and the values themselves in `R`. The internal coordinates are then translated to Cartesian coordinates in the `gmetry` subroutine according to the conventions described in subsec. 7.1.1. Irrespective of the input of the molecular geometry (Cartesian or internal coordinates), the position of the nuclei in the molecule are saved in the array `Q` and the atomic symbols in `ZSYM` in the **joda** module. The molecule is then repositioned so that the centre of mass coincides with the Cartesian origin and is reoriented in a convenient way (see subsec. 6.2.1) in the `symmetry` subroutine. All program variables that handle the molecular geometry are stored in common blocks `COORD` and `CBCHAR`.

To activate an ff calculation, the keyword `BFIELD=ON` must be set. For the previously implemented Cartesian-coordinate input, the magnetic field is given as a vector in Cartesian coordinates under the additional argument `%bfield`[b] and is read by the `get_bfield` subroutine. The `get_bfield` subroutine is called in the `symmetry` subroutine and the magnetic field is saved as an array named `bfield`.

A Cartesian-coordinate input, however, is often difficult to generate, and, especially for small to medium sized molecules, internal coordinates are preferred in many cases. In order to make the input more user-friendly and the recognition of the magnetic field more flexible, the option for an internal-coordinate input for an ff calculation was developed during this thesis along with improved logistics for the magnetic-field handling. Two kinds of magnetic-field inputs are implemented that work with internal coordinates: the dummy-atom input, and the vector/rotation input.

Dummy-atom input

In the dummy-atom input for the magnetic field, a special dummy atom `BFLD` is introduced. Dummy atoms are entries in the internal-coordinate input whose primary function is to introduce constraints in a geometry optimization. Their use alters the form of the Wilson B-matrix (see subsec. 7.1.1). Dummy atoms have no mass and do not take any other part in a quantum-chemical calculation. In CFOUR, dummy atoms are understood as entries with the atomic symbol `X`.[c] Dummy atoms acquire Cartesian coordinates in the `gmetry` subroutine as described in the previous paragraph.

For an ff calculation, the assignment of the magnetic field using the dummy-atom input takes place in `get_bfield`. The special dummy atom for the magnetic field is only allowed after the third entry to the internal coordinate input. If the subroutine finds a `BFLD` entry, it defines the magnetic field as

$$\vec{B} = \vec{x}_{\texttt{BFLD}} - \vec{x}_B.$$

Here, $\vec{x}_{\texttt{BFLD}}$ are the Cartesian coordinates of the `BFLD` dummy atom as translated from the internal coordinates $\vec{r}_{\texttt{BFLD}} = (d_B, \theta_C, \varphi_D)$ from eq. (7.1.1). The vector $\vec{x}_B$ contains the coordinates of the centre B in the first component of the internal coordinate for `BFLD`, d_B. This way, the strength of the magnetic field equals the value of the first component of the internal coordinate, directly given in the input by the user

$$|\vec{B}| = |\vec{x}_{\texttt{BFLD}} - \vec{x}_B| = d_B,$$

and the direction is dictated by θ_C and φ_D. The magnetic field is then saved in `bfield`.

[b] Alternative forms: `%Bfield`, `%BFIELD`

[c] Dummy atoms are not to be confused with ghost atoms that are indeed part of the quantum-chemical calculation acting as centres for basis functions.

Vector/rotation input

The definition of the magnetic field in the vector/rotation input is more similar to the Cartesian input that was already available before the developments in this thesis. If no `BFLD` dummy atom is given, a vector/rotation input is assumed and the `get_bfield` subroutine assigns the magnetic field under the `%bfield`[b] additional argument to `bfield`, after the repositioning of the molecule to the centre of mass while the `symmetry` subroutine is instructed to ignore any kind of automatic reorientation of the molecule. This kind of input requires careful consideration of the conventions for the internal to Cartesian transformation described in subsec. 7.1.1. It is possible to specify any kind of magnetic field via this input, but an additional flexibility is given through a user-defined rotation: In the case that the option `ROTATION=ON` is set, the user may define a manual rotation of the molecule while leaving the magnetic field unaffected. The `get_rot` subroutine reads a rotation angle under the `%rot_angle`[d] keyword in degrees, and a rotation axis under the `%rot_axis`[e] keyword as three double precision numbers separated by a comma "," for the three Cartesian coordinates. The `get_expmap` subroutine then constructs the exponential map vector. It first normalises the rotation axis vector, constructing the unit vector $\hat{e}_{\text{rot}}$, and redefines the rotation angle so that $0 \leq \theta_{\text{rot}} < 2\pi$, thus avoiding some redundancies in their definition. It then calculates the exponential map vector as

$$\vec{v}_{\text{rot}} = \theta_{\text{rot}} \hat{e}_{\text{rot}}$$

and the rotation quaternion via eq. (7.1.3). A rotation matrix $\mathbf{C}$ is build in `rotmq`

$$\mathbf{C} = \begin{pmatrix} q_0^2 + q_1^2 - q_2^2 - q_3^2 & 2q_1q_2 - 2q_0q_3 & 2q_1q_3 + 2q_0q_2 \\ 2q_1q_2 + 2q_0q_3 & q_0^2 - q_1^2 + q_2^2 - q_3^2 & 2q_2q_3 - 2q_0q_1 \\ 2q_1q_3 - 2q_0q_2 & 2q_2q_3 + 2q_0q_1 & q_0^2 - q_1^2 - q_2^2 + q_3^2 \end{pmatrix}$$

which is used to rotate the molecule. All variables that concern the rotation exist in the common block `ROTAT`. The program does not check whether the rotation axis is perpendicular to the magnetic field. Care is to be taken by the user that this is the case, as the component of the rotation parallel to the magnetic field leaves the system invariant. Having the rotation perpendicular to the magnetic field is easiest realized by defining the magnetic field in the z-axis, and the rotation axis in the xy plane.

The `symmetry` subroutine performs a final reorientation of the whole molecule together with the magnetic field, so that the magnetic field is parallel to the z-axis, before starting with the symmetry recognition.

7.2.2 Geometry optimization in magnetic field

A geometry optimization algorithm following a (quasi) Newton-Raphson method is described in fig. 7.2. The geometry optimization finds a local minimum of the effective electronic potential $V_{\text{el}}(\boldsymbol{r}_{\text{opt}})$, at which point the gradient is zero

$$\boldsymbol{\nabla} V_{\text{el}}(\boldsymbol{r}_{\text{opt}}) = \begin{pmatrix} \frac{\partial}{\partial r_1} \\ \frac{\partial}{\partial r_2} \\ \vdots \\ \frac{\partial}{\partial r_n} \end{pmatrix} V_{\text{el}}(\boldsymbol{r}_{\text{opt}}) = \boldsymbol{g}_{\text{opt}} = 0$$

and the Hessian

$$\nabla^2 V_{\text{el}}(\boldsymbol{r}_{\text{opt}}) = \begin{pmatrix} \frac{\partial^2}{\partial r_1 \partial r_1} & \frac{\partial^2}{\partial r_1 \partial r_2} & \cdots & \frac{\partial^2}{\partial r_1 \partial r_n} \\ \frac{\partial^2}{\partial r_2 \partial r_1} & \frac{\partial^2}{\partial r_2 \partial r_2} & & \\ \vdots & & \ddots & \\ \frac{\partial^2}{\partial r_n \partial r_1} & & & \frac{\partial^2}{\partial r_n \partial r_n} \end{pmatrix} V_{\text{el}}(\boldsymbol{r}_{\text{opt}}) = \mathbf{H}_{\text{opt}}$$

[d] Alternative form: `%ROT_ANGLE`
[e] Alternative form: `%ROT_AXIS`

only has positive eigenvalues. A global minimum cannot be guaranteed by such a procedure. For this reason, the search for the molecular structure has to be be accompanied by a chemical intuition.

The algorithm is handled mostly in **joda**, but, because of the multi-step character of such a calculation, many other CFOUR modules contribute. The driver module `run` plays for this reason an essential role, as it is responsible for calling the individual modules. For any single-point energy calculation beyond the ff-HF level of theory, the QCUMBRE interface is also involved in this algorithm, which is described in chap. 3. Changes for a geometry optimization in the presence of a magnetic field were required for the calculation of the gradient step $\boldsymbol{g}^{[k]}$, which for an ff calculation is currently only implemented for numerical geometric gradients, and for the approximate calculation of the Hessian $\mathbf{H}^{[k]}$ using the Broyden-Fletcher-Goldfarb-Shanno (BFGS) update.[202]

As already explained in subsec. 7.1.1, the calculation of gradients takes place in Cartesian coordinates. For the transformation of Cartesian coordinates to internal coordinates, which the geometry optimization algorithm in CFOUR uses, the Wilson B-matrix is calculated in the `buildb` subroutine. To have a correct transformation in the presence of a magnetic field, the rotational degrees of freedom have to be taken into consideration using the rotation quaternion and the exponential map. The construction of the analytic derivatives of the exponential map with respect to the Cartesian coordinates for the entries to the Wilson-B matrix is implemented as follows: The rotated $\boldsymbol{x}$ and the reference $\boldsymbol{y}$ frameworks needed for the construction of the R_{ij} elements are calculated in the `symmetry` subroutine and saved in the `JOBARC` archive file under the `XMAT` and `YMAT` labels. The rotational quaternion is also saved in `JOBARC` under the label `QUART` in the `get_expmap` subroutine. The symmetric $\mathbf{F}$ matrix is calculated in `make_frotmat`. The matrix is then diagonalized for the calculation of $(\lambda\mathbb{1} - \mathbf{F})^{-1}$ in the `make_lambdaif` subroutine. At this point, the algorithm checks that the eigenvector with the lowest eigenvalue corresponds to the rotational quaternion and stops (`call errex`) if this is not the case. The derivatives $\frac{\partial \mathbf{F}}{\partial x_i}$ are calculated in `make_diffij`, while the derivative of the quaternion are calculated in `make_diffquart`. Finally, the Wilson-B matrix entries are calculated by `make_dif_v` called by `buildb`.

The BFGS update for the approximate Hessian needs an initial Hessian to be defined. The initial Hessian has a diagonal form and in the present implementation, according to the suggestion of Wang and Song,[200] a value of 0.05 is used for the entries corresponding to the rotations.

For the calculation of numerical gradients, (symmetry-adapted) displacements are generated by the **symcor** program. For each displaced geometry, a single-point energy calculation takes place, and the numerical gradient is calculated via energy differences. For a geometry optimization, only that block of the gradient and the Hessian is needed that is associated with totally-symmetric displacements, since the optimization is constrained leave the symmetry of the molecule unchanged. Because of this, symmetry-adapted displacements to be used in a geometry optimization can be calculated in **symcor** even for complex Abelian groups (despite the fact that the program has been written explicitly excluding such groups), because only the totally-symmetric displacements are needed.

The parameters to be optimized in CFOUR are given in the input. As such, the user must be careful when asking for an optimization, and care should be taken that the optimization requested is indeed an unconstrained and not overdefined optimization in a given point group. For an optimization in a magnetic field, the generated warning messages do not necessarily cover all ill-defined inputs. In a constrained optimization, only the parameters of the internal coordinates requested to be optimized are updated in the step that involves the calculation of the new geometry (fig 7.2). In order to activate the rotational degrees of freedom needed for an optimization in a magnetic field, the `ROTATION=OPT` keyword option must be used, and the additional options `%VX*`, `%VY*`, and `%VZ*` define which of the components of the exponential map are to be used as parameters in the optimization. In the case that the rotations are to remain constrained parameters, the `ROTATION=ON` keyword option should be used, for the correct transformation from Cartesian to internal coordinates.

A general remark on the geometry optimization in magnetic field is that the algorithm may fail to converge to a true minimum regarding the rotational degrees of freedom. This happens because the gradient of the rotations may be small for example in the case of weaker fields or in systems with small differences between the magnetisabilies in different directions, as will be shown in sec. 7.3. Strategies to recognize such cases and to tackle this failure achieving a true minimum are currently

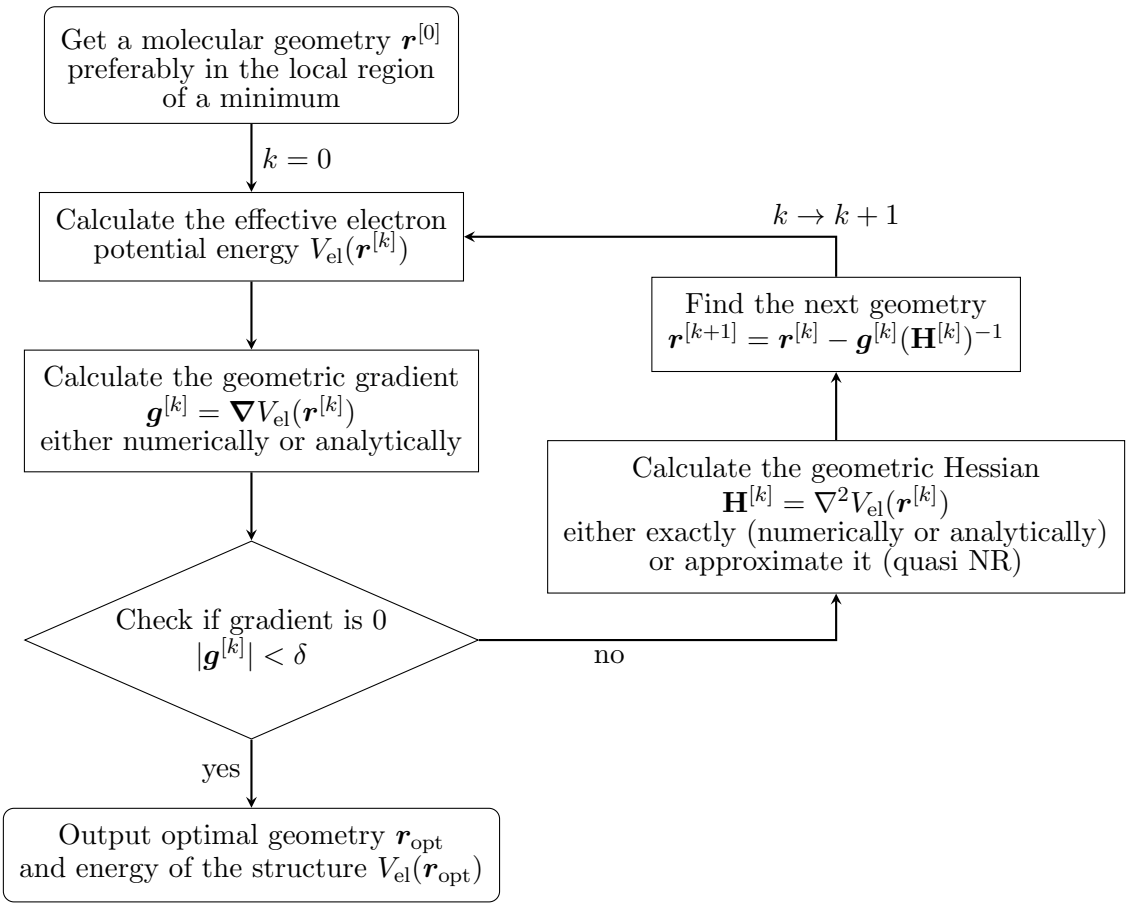

Figure 7.2: A geometry optimization algorithm following the (quasi) Newton-Raphson method.

under development.

7.3 Molecular fragments

Finally in this chapter, the water H_2O and methane CH_4 molecules were studied in the presence of a magnetic field. The goal of this study is to find the electronic ground state and the ground-state geometry of these molecules for different magnetic-field strengths, as well as to determine how the molecule is oriented relative to the magnetic field. To achieve this, the lowest energy states of different multiplicities were studied in the presence of a magnetic field. Totally unconstrained geometry optimizations (internal + rotational degrees of freedom) were performed, accompanied by rotationally constrained optimizations for highly symmetric orientations of the magnetic field. The systems were investigated for field strengths up to 0.5 B_0 with a step size of 0.05 B_0. For these magnetic-field strengths, no paramagnetic bonding is expected[f] and for this reason, starting geometries were chosen based on chemical intuition. Note, however, that studies that deal with stronger magnetic fields employ different strategies for generating starting geometries, as the chemical intuition is less applicable in those cases.[57] Nonetheless, even up to $B = 0.5\ B_0$, the molecules are not necessarily bound. As seen in previous sections for the ethylene molecule, the stabilisation of an electronic state of the linear fragment results in a dissociation, and in the case of pyrrole, different open-shell electron configurations become more stable than the closed-shell configuration because of the spin-Zeeman interaction. In the absence of double bonds, the stabilisation of states of higher multiplicity may result in bond breaking. In order to examine possible similar situations for H_2O and CH_4, the fragments of these molecules removing one H atom at a time needed to be studied as well. The calculations were performed at the CCSD level using an unc-aug-cc-pVTZ basis set.

[f] H_2 exhibits paramagnetic bonding for $B > 0.5\ B_0$.[18]

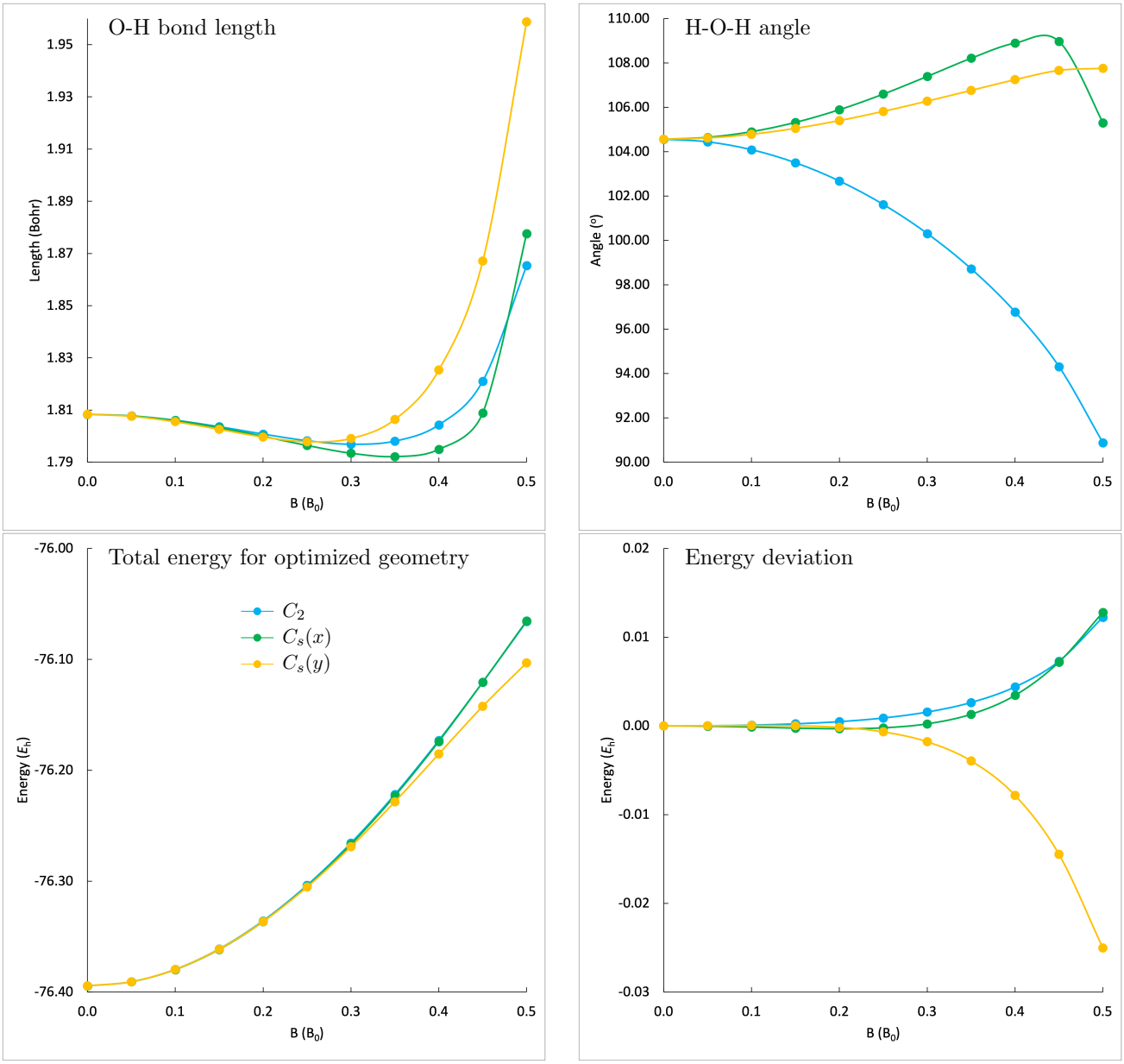

Figure 7.3: Geometry optimization results for water for the three highly-symmetric orientations (C_2 blue, $C_s(x)$ green, $C_s(y)$ yellow). O-H bond length in the upper left panel, H-O-H angle in the upper right panel, total energy for the optimized geometry in the lower left panel, energy deviation from the mean of the three orientation (see text) in the lower right panel.

7.3.1 Fragments of water

For the water, the following fragmentation path was studied

$$\overset{(1)}{\mathrm{H_2O}} \rightarrow \overset{(2)}{\mathrm{OH}} + \mathrm{H} \rightarrow \overset{(3)}{\mathrm{O}} + 2\mathrm{H}.$$

H_2O

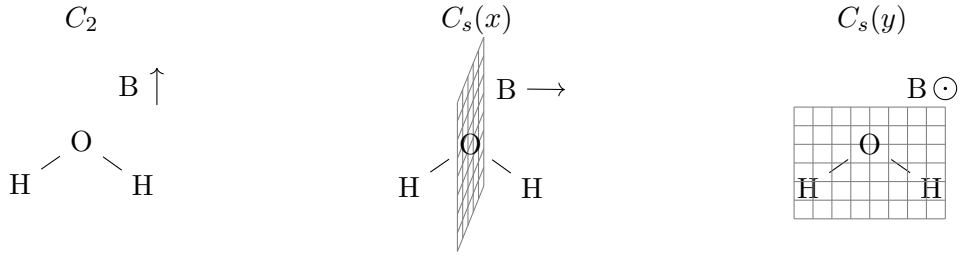

Figure 7.4: Highly-symmetric orientations of the water molecule in a magnetic field. The mirror planes that are perpendicular to the magnetic field in the $C_s(x)$ (middle) and $C_s(y)$ (right) orientations are depicted by the gray grids.

The water molecule [fragment (1)] has a C_{2v} symmetry in the absence of a magnetic field. For most orientations of the magnetic field, the symmetry is reduced to C_1, i.e., no symmetry element is retained. Three highly-symmetric orientations of the molecule exist, as seen in fig. 7.4. In each one of these highly-symmetric orientations, only one of the field-free symmetry elements of C_{2v} is retained. In the C_2 orientation (left), the C_2 rotation is retained, while in $C_s(x)$ and $C_s(y)$, the σ mirror plane perpendicular to the molecular plane (middle) and the mirror plane coinciding with the molecular plane (right) are retained, respectively. The field-free ground state of water $^1A_1$ was studied. For this system, the lowest states of higher multiplicity are not bound.

The internal degrees of freedom that characterise the water molecule are the H-O-H angle and the two O-H bond lengths. For the field-free case, and the C_2 and $C_s(x)$ orientations the O-H bonds are symmetry equivalent. In the $C_s(y)$ case, the O-H bond lengths are not restricted by the $\sigma(y)$ symmetry element to be equivalent, but during the geometry optimization, they were found to have the same value even when using starting geometries with different O-H bond lengths. This happens because the two hydrogens experience the same chemical environment despite the absence of symmetry operations that would make the nuclei symmetry equivalent. The reason for this equivalence is that the energy of the system is not dependent on the direction of the magnetic field for a given orientation along an axis, as was mentioned in sec. 6.1. The O-H bond length and the H-O-H angle as a function of the magnetic field for the three highly symmetric orientations can be found in the upper panels of fig. 7.3.

In the lower right panel of fig. 7.3, the total energy for the optimized geometry is plotted as a function of the magnetic-field strength. Because the differences in the total energies among the different orientations are not large enough to be visible in the plot, for every point in the grid of magnetic fields, the mean of the three orientations is calculated

$$\frac{E_{C_2}(B) + E_{C_s(x)}(B) + E_{C_s(y)}(B)}{3} = \overline{E}(B).$$

It is then subtracted from the energy of each different orientation $E_X(B)$.[g] The deviation from the mean is then given by

$$\Delta E_X(B) = E_X(B) - \overline{E}(B).$$

This energy deviation is plotted in the lower right panel of fig. 7.3. It is concluded based on these results that the preferred orientation of the molecule relative to the magnetic field changes for different magnetic-field strengths. For a magnetic field of up to 0.2 B_0, the $C_s(x)$ (green) is found to be the orientation lowest in energy. However, the energy differences are of the order of 10^{-4} E_h, which is very small corresponding to about 0.3 kJ/mol. Experience by further calculations with different basis sets has shown that the energetic ordering of the different orientations may change depending on the basis set used. In addition, these qualitative results may be dependent on the method with which electron correlation is considered as well. There is no indication, however, that the order of magnitude of this small energetic difference changes, and it seems that it is a physical characteristic of the system. Despite the inability of our approach to predict the preferred orientation in this case, the fact that

[g]The subscript X in this notation denotes the orientation $X = C_2, C_s(x), C_s(y)$.

B (B_0)	Starting geometry	Unconstrained result	Cumulative prediction[a]
0.00	-	-	-
0.05	B in molecular plane[b]	B in molecular plane[c]	$C_s(x)$
0.10	B in molecular plane[b]	B in molecular plane[c]	$C_s(x)$
0.15	B in molecular plane[b]	B in molecular plane[c]	$C_s(x)$
0.20	B in molecular plane[b]	approximately $C_s(x)$	$C_s(x)$
0.25	B in skewed orientation[d]	$C_s(y)$	$C_s(y)$
0.30	B in skewed orientation[d]	$C_s(y)$	$C_s(y)$
0.35	B in skewed orientation[d]	approximately $C_s(y)$	$C_s(y)$
0.40	B in skewed orientation[d]	dissociated to (2)	dissociated to (2)
0.45	B in skewed orientation[d]	dissociated to (2)	dissociated to (2)
0.50	B in skewed orientation[d]	dissociated to (2)	dissociated to (2)

[a] A cumulative prediction results from comparison of the results from the unconstrained geometry optimization and from the rotationally constrained geometry optimizations as explained in the text.

[b] Different starting orientations of the magnetic field in the molecular plane were tested.

[c] The geometry optimization converges to a magnetic field direction that is in the molecular plane, but does not coincide with the C_2 nor with the $C_s(x)$ orientation.

[d] Different starting orientations of the magnetic field that are neither perpendicular to the molecular plane $C_s(y)$ nor within the molecular plane were tested.

Table 7.1: Results from the unconstrained geometry optimizations and cumulative predictions obtained by comparison of the results from the unconstrained and rotationally constrained geometry optimizations.

the energetical difference of the two orientations is so small is in important finding for the system. For magnetic fields stronger than 0.25 B_0, the $C_s(y)$ (yellow) orientation is predicted to be the most stable. The energy differences are slightly larger, reaching $\Delta E[C_s(y)] = -0.025\ E_\mathrm{h}$ for $B = 0.5\ B_0$.

Since the field-free chemical intuition cannot to be trusted in ff calculations for stronger fields, totally unconstrained optimizations, starting from different orientations of the magnetic field, but still using starting geometries that approximate the field-free optimized geometry were performed. The starting geometries that resulted in physically sound and (mostly) reproducible predictions from this approach are shown in table 7.1. Comparison of the unconstrained results with the rotationally constrained results allows for a cumulative prediction shown in the last column. The cumulative result corresponds to the geometry lowest in energy dound by either of the two approaches, i.e., rotationally constrained or unconstrained. It is observed that for magnetic fields up to 0.2 B_0, the in-plane orientation of the magnetic field has to be used as starting geometry. Otherwise, the geometry optimization does not converge at all. Even when the in-plane orientation is used as a starting point, the optimizer does not converge to the orientation lowest in energy. The reason for this failure of the optimizer is that the gradients of the rotational degrees of freedom are very small, since the corresponding energy difference is small as well, giving rise to a very flat potential-energy surface. The optimizer (handling all degrees of freedom as potentially equally contributing to the optimization) yields very small steps in these directions, never reaching the minimum. This behaviour is not corrected by using stricter convergence criteria for the optimizer. The issue arises from the fact that degrees of freedom whose gradients have values in very different orders of magnitudes are handled on equal footing. As an example, the gradients at starting geometries of water for $B = 0.10\ B_0$ are of the order of $10^{-2} E_\mathrm{h}/a_0$ and $10^{-2} E_\mathrm{h}$/rad for bond lengths and angles, respectively, while only $10^{-4} E_\mathrm{h}$/rad for the rotations relative to the magnetic field. As mentioned in subsec. 7.2.2, ideas on how to tackle such cases are under development. Optimizations in a stronger magnetic field are less sensitive to the starting orientation of the magnetic field, as the energy surface becomes less flat. The $C_s(y)$ orientation is predicted to be the lowest in energy for $0.25 \leq B \leq 0.35\ B_0$. For even stronger fields, the unconstrained results suggest that the molecule becomes unbound, dissociating to fragment (2) which has a lower energy than the $C_s(y)$ orientation of H_2O.

OH

Figure 7.5: Highly-symmetric orientations of the hydroxyl radical OH in a magnetic field.

The hydroxyl radical in the field-free case, has an open-shell $^2\Pi$ ground state, mainly described

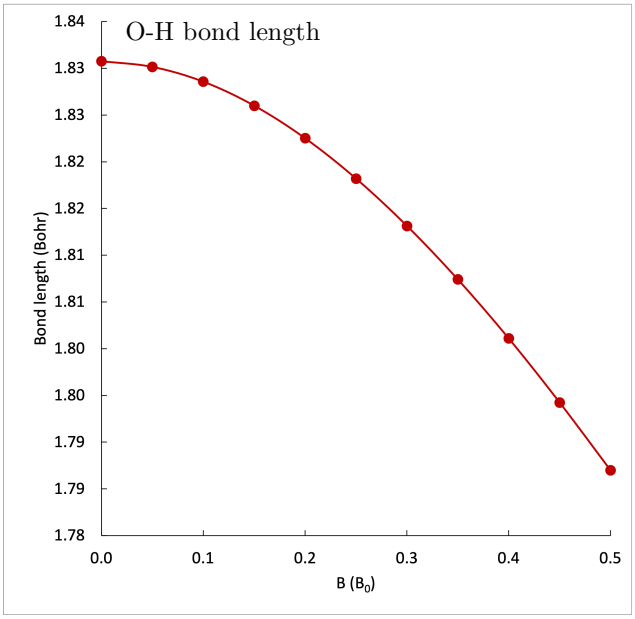

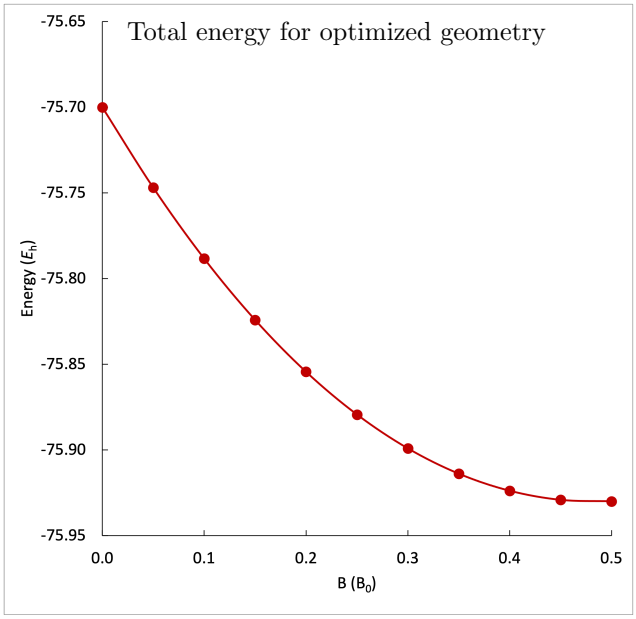

Figure 7.6: Geometry optimization results for the OH radical. The orientation of the magnetic field is consistently predicted parallel to the O-H bond resulting in a C_∞ symmetry. The depicted doublet state is characterised by the $^2\Pi^-$ term.

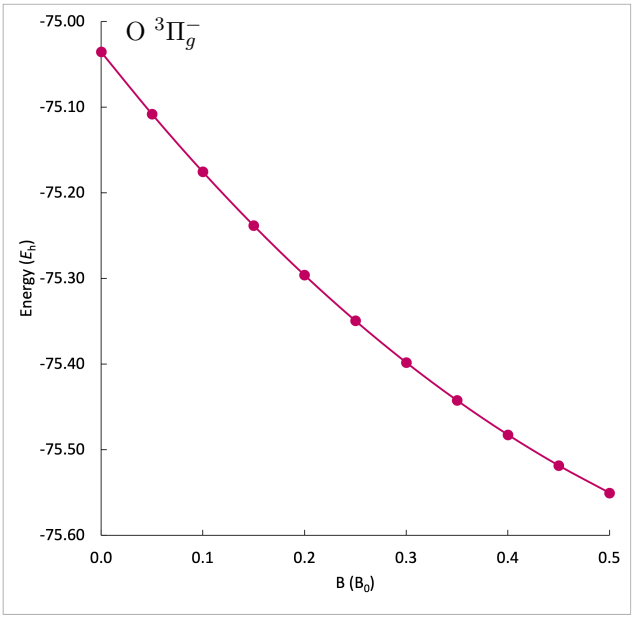

Figure 7.7: The $^3\Pi_g^-$ state, $M_S = -1$ component of the O atom.

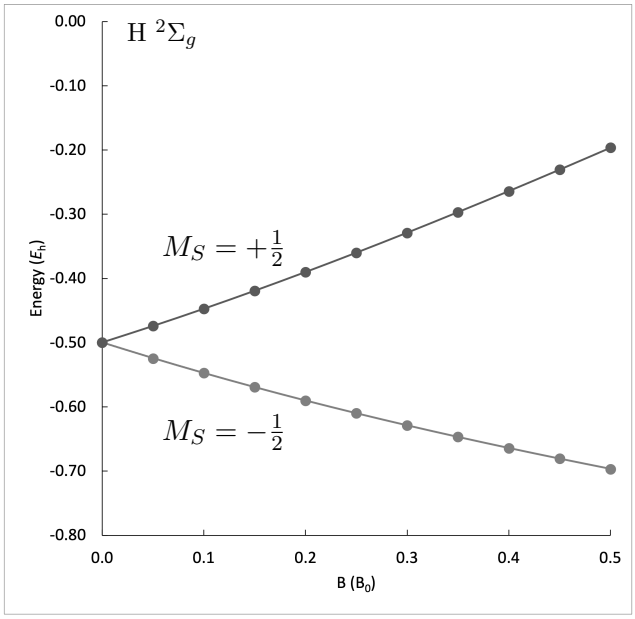

Figure 7.8: The $M_S = -\frac{1}{2}$ and $M_S = +\frac{1}{2}$ components of the $^2\Sigma_g$ state of the H atom.

by a $1\sigma^2 2\sigma^2 3\sigma^2 1\pi^3$ electron configuration. In the presence of a magnetic field, an orientation of the field perpendicular to the O-H bond reduces the symmetry to C_s. An orientation parallel to the O-H bond, on the other hand, reduces the symmetry to C_∞. These two highly-symmetric orientations are depicted in fig. 7.5. The field-free doublet ground state was studied in a magnetic field using the totally unconstrained geometry optimization at different field strengths. The quartet state of OH lowest in energy, which would be stabilised significantly in a magnetic field because of the spin-Zeeman term, was studied as well. In the absence of a magnetic field, this quartet state is not bound, as the unpairing of the electrons in the 3σ bonding orbital breaks the O-H bond. In the presence of a magnetic field, no paramagnetic bond formation was observed either. As such these results are not plotted, but are

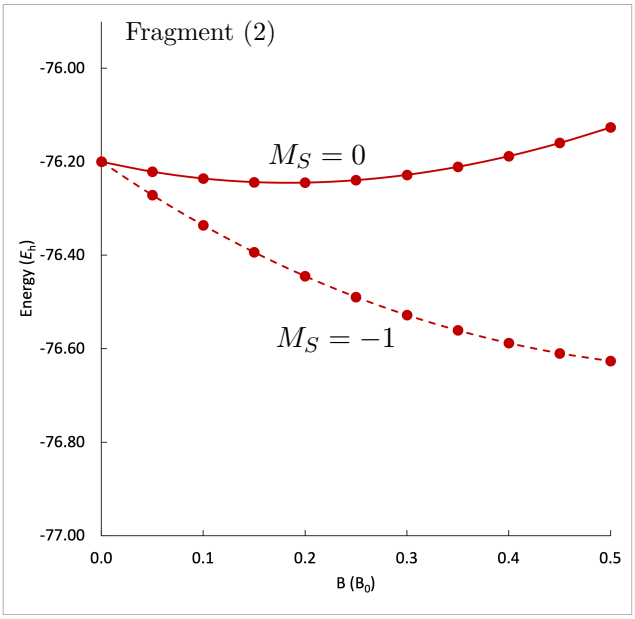

Figure 7.9: The $M_S = 0, -1$ components of water fragment (2).

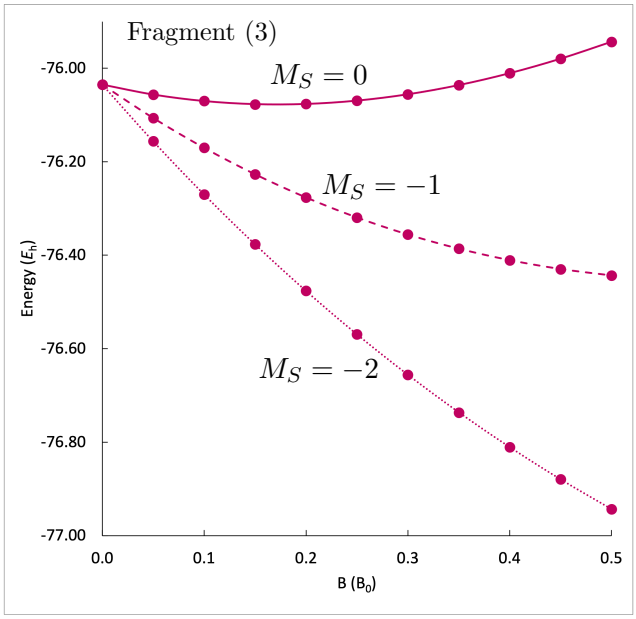

Figure 7.10: The $M_S = 0, -1, -2$ components of water fragment (3).

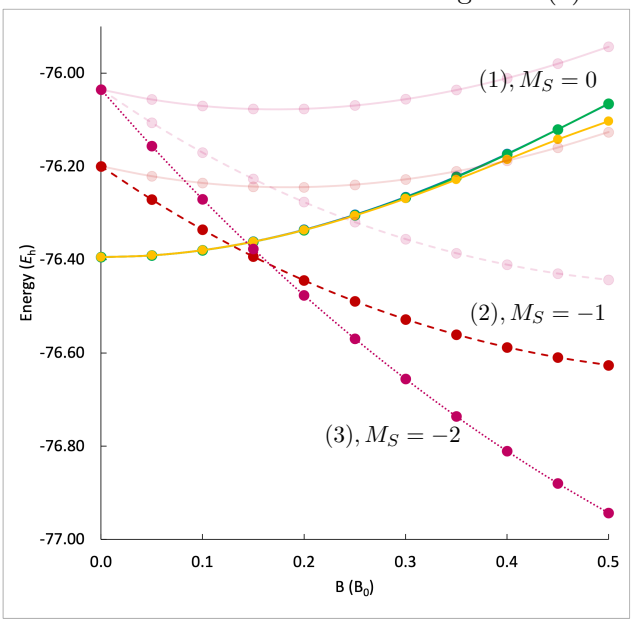

Figure 7.11: The $M_S = 0, -1, -2$ components of the water fragments (1), (2) and (3) as continuous, dashed and dotted lines, respectively. The M_S components higher in energy for a given fragment are plotted using low opacity.

nonetheless included through the study of the atomised fragments.

The results of the unconstrained optimization consistently find the parallel orientation to be lower in energy. This happens because of the stabilisation of the $M_L = -1$ component of the $^2\Pi$ state, i.e., $^2\Pi^-$, due to the orbital-Zeeman term. The length of the O-H bond as well as the total energy for the optimized geometry are plotted in fig. 7.6 as a function of the magnetic-field strength.

O and H

Lastly for water, the atomised fragments were studied in the presence of a magnetic field. Atoms are described by the $C_{\infty h}$ point group under the influence of a magnetic field.

The field-free ground state of the oxygen atom is ^3P_g. In the magnetic field, the $M_L = -1$ component of the field-free ground state, i.e., the $^3\Pi_g^-$ state, was studied. The total electronic energy as a function of the magnetic-field strength is plotted in fig. 7.7.

In addition, the $M_S = -\frac{1}{2}$ and $M_S = +\frac{1}{2}$ components of the ground state of the H atom, $^2\Sigma_g$, are plotted in fig. 7.8.[h]

Fragments

In order to be able to make predictions about the relative stability of the fragments for the dissociation path of water, the total energies of the fragments need to be calculated. Fragment (1) coincides with the energy plot in the lower left panel of fig. 7.3. For fragment (2), different M_S combinations are used to form the total $M_S = 0$ and $M_S = -1$ components of interest which are shown in fig. 7.9. Similarly for fragment (3), the $M_S = 0, -1, -2$ components are calculated and are shown in fig. 7.10. In fig. 7.11, the energies of all the fragments are shown.

Based on these results, one can conclude that for magnetic fields weaker than 0.15 B_0 the water molecule is bound and exhibits a $C_s(x)$ orientation relative to the magnetic field. For magnetic-field strengths around 0.15 B_0, water is dissociated to fragment (2), and for stronger fields, water is completely atomised. It can be noted that the prediction for dissociation of the water molecule from the unconstrained geometry optimization for $B \geq 0.4\ B_0$ is confirmed by the crossing of the yellow line with the red continuous line of low opacity fig. 7.11.

7.3.2 Fragments of methane

Dissociating one H atom from methane at a time gives rise to the following dissociation path

$$\overset{(1)}{\mathrm{CH_4}} \rightarrow \overset{(2)}{\mathrm{CH_3}} + \mathrm{H} \rightarrow \overset{(3)}{\mathrm{CH_2}} + 2\mathrm{H} \rightarrow \overset{(4)}{\mathrm{CH}} + 3\mathrm{H} \rightarrow \overset{(5)}{\mathrm{C}} + 4\mathrm{H}$$

$\mathbf{CH_4}$

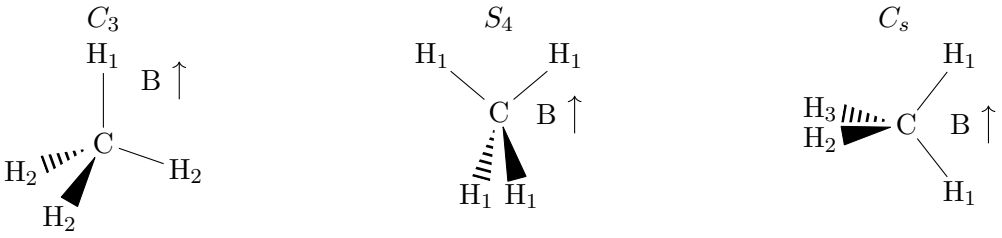

Figure 7.12: Highly-symmetric orientations of the methane molecule in a magnetic field. The subscripts denote equivalent and non-equivalent H nuclei.

The methane molecule was studied in subsec. 4.3.3 for the geometry of the field-free singlet ground state in the presence of a magnetic field in two highly-symmetric orientations and for the excited states

[h]Since the hydrogen atom only has one electron, no inclusion of correlation is needed, and the calculations were carried out at the HF level of theory.

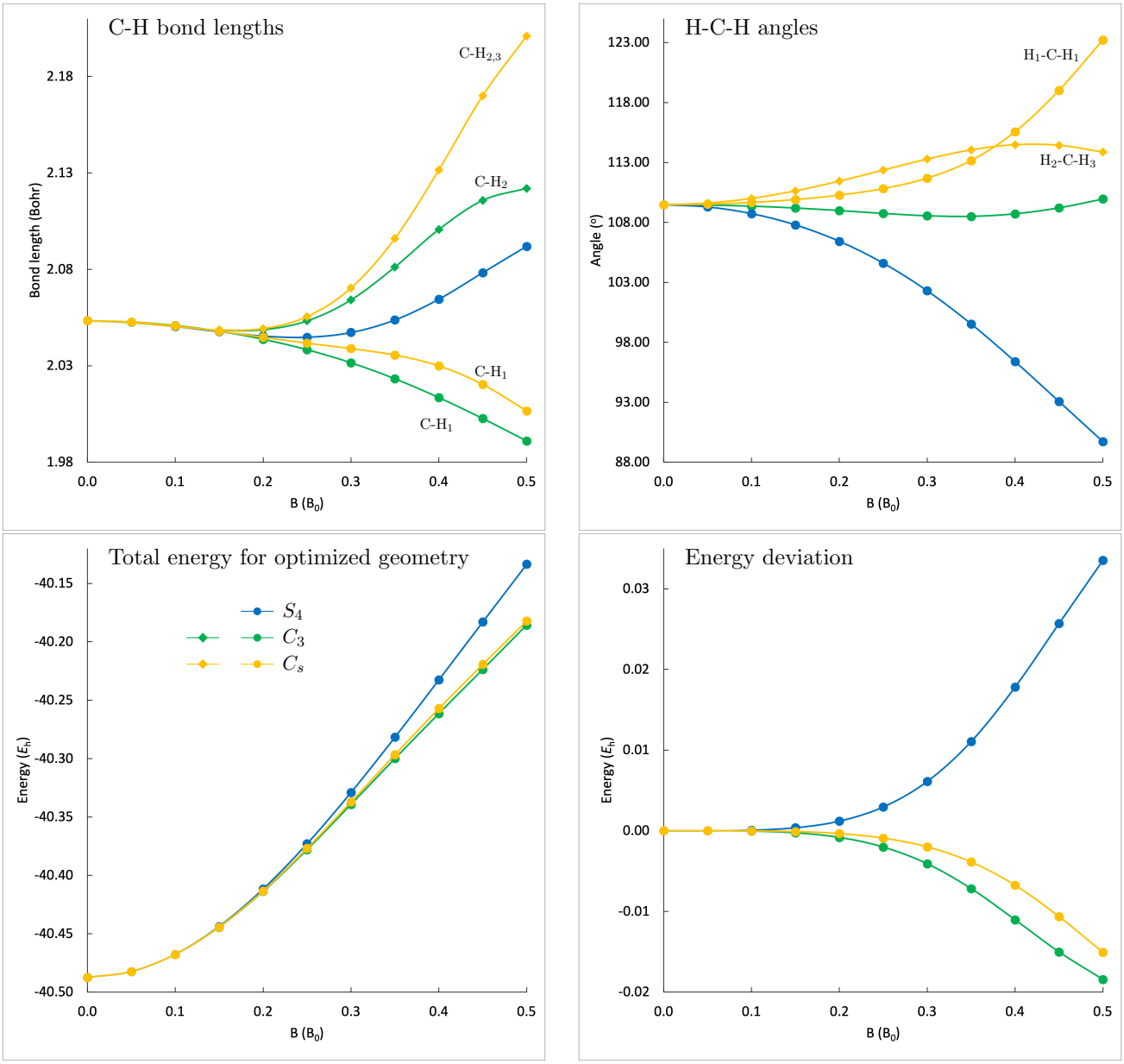

Figure 7.13: Geometry optimization results for methane for the three highly-symmetric orientations (C_3 green, S_4 blue, C_s yellow). C-H bond lengths in the upper left panel, H-C-H angles in the upper right panel, total energy for the optimized geometry in the lower left panel, energy deviation from the mean of the three orientation (see text) in the lower right panel. Different shapes have been used for the non-equivalent bond lengths or angles.

of the same multiplicity. Here, the molecule was studied for all three highly symmetric magnetic field orientations shown in fig. 7.12. A magnetic field parallel to a C-H bond results in a C_3 orientation (left), with three equivalent bonds C-H_2, one unique C-H_1 and a H_1-C-H_2 angle defining the internal degrees of freedom. A magnetic field parallel to the bisector results in an S_4 orientation (middle), with four equivalent bond lengths and the H_1-C-H_1 angle bisected by the field defining the molecular geometry. Lastly, a magnetic field perpendicular to the plane spanned by two H nuclei and the C nucleus results in C_s symmetry (right). This is the least symmetric orientation with the C-H_1 out-of-plane bonds being equivalent, and the two C-H bonds, C-H_2 and C-H_3, coinciding with the mirror plane being. The angles needed to define the molecular geometry are the H_1-C-H_1 angle, the H_2-C-b' and H_3-C-b' angles, with C-b' being the inverse ray of the bisector of the H_1-C-H_1 angle.

The closed-shell ground state of methane was studied in a magnetic field. As the valence orbitals are responsible for the bond formation, unpairing the electrons in these orbitals results in bond breaking. For this reason, low-lying states of higher spin-multiplicity have at least one H atom unbound from the

rest of the molecule. Additionally no paramagnetic bond formation is observed for up to $B = 0.5\ B_0$. The results from the geometry optimizations can be seen in fig. 7.13. In the upper panels, the C-H bond lengths (left) and the angles H-C-H angles (right) are plotted as a function of the magnetic field for the three highly-symmetric orientations. The results for the C_3 and S_4 (green and blue, respectively) orientation are similar to those in subsec. 4.3.3.

For the C_s orientation (yellow), the C-H_2 and C-H_3 bond lengths coincide despite being formally non symmetry equivalent. The same holds for the H_2-C-b' and H_3-C-b' angles. This coincidence is explained by the same chemical environment of the nuclei, similar to the $C_s(y)$ orientation of the water molecule. For this reason, C-H_2 and C-H_3 bonds are plotted as one named C-$H_{2,3}$ in the upper left panel and the H_2-C-H_3 angle is plotted instead of the two individual angles in the upper right panel. The C-H_1 bonds decreases in length monotonically with increasing magnetic field. The C-$H_{2,3}$ bonds on the other hand, follow the C-H_1 bonds for $B < 0.2\ B_0$, reaching a minimum in length, but are then elongated for stronger magnetic fields. While a shortening of the bonds in magnetic field is generally expected as a response to the diamagnetic influence, the results have to be judged together with the consideration of the H-C-H angles. The H_1-C-H_1 angle that describes the H nuclei that do not coincide with the mirror plane is being widened towards 180° with increasing magnetic-field strength, responding to the diamagnetic influence. The preference for the system to adopt an orientation as parallel as possible to the magnetic field in this constrained geometry optimization tends to create a linear CH_2 section in the molecule parallel to the magnetic field, that also shortens the C-H_1 bonds as seen earlier. As the H_2 and H_3 nuclei are constrained in the plane perpendicular to the magnetic field, they cannot be displaced out of it to minimise their contribution to the diamagnetic interaction. The H_2-C-H_3 angle is widened as well with increasing magnetic-field strength reaching a flat maximum around $0.4/B_0$ at about 114°. The response of the C-$H_{2,3}$ bonds is a reaction to the shortening of the C-H_1 bonds and the geometric strain against the tetrahedral shape, resulting in the elongation and destabilisation of the bonds that lye in the mirror plane.

Total energies results from optimzations are found to be energetically very close for the three magnetic field orientations. Hence, similarly to the plots for water, the deviation from the mean value ΔE_X, with $X = S_4, C_3, C_s$ is plotted as well in the lower right panel. The results indicate that the C_3 orientation is consistently lower in energy, predicting it to be the preferred orientation. The S_4 (blue) orientation is highest in energy from the three, and the C_s orientation (yellow) is energetically very close to the C_3 orientation (green). The general trend of the energy is dictated by the diamagnetic interaction. The prediction for the C_3 orientation (green) as the preferred orientation is however not definitive, because the energy differences are very small, especially for weaker fields ($\Delta E_X < 10^{-3}\ E_\mathrm{h}$ for $B < 0.2\ B_0$). Because of the resulting flat potential-energy surface, the current algorithm for finding the optimal geometry via an unconstrained approach would be problematic, as was the case for water. For this reason, only the rotationally constrained approach has been employed

CH_3

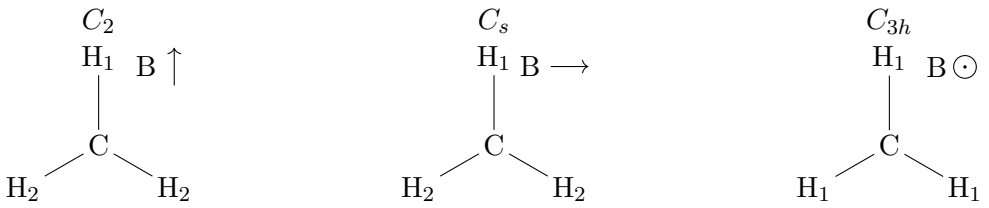

Figure 7.14: Highly-symmetric orientations of the methyl radical in a magnetic field. The subscripts denote equivalent and non-equivalent H nuclei.

The methyl radical CH_3 in the absence of a magnetic field is planar and belongs to the D_{3h} point group. Its ground state is an ${}^2A_2''$ with a singly occupied p orbital perpendicular to the plane of the molecule. The lowest lying quartet state is not bound in the absence of a magnetic field, as electrons in a bonding orbital become unpaired. No paramagnetic bonding is found for $B \leq 0.5\ B_0$. In the presence of the magnetic field, three highly symmetric orientations exist, as shown in fig. 7.14. A magnetic

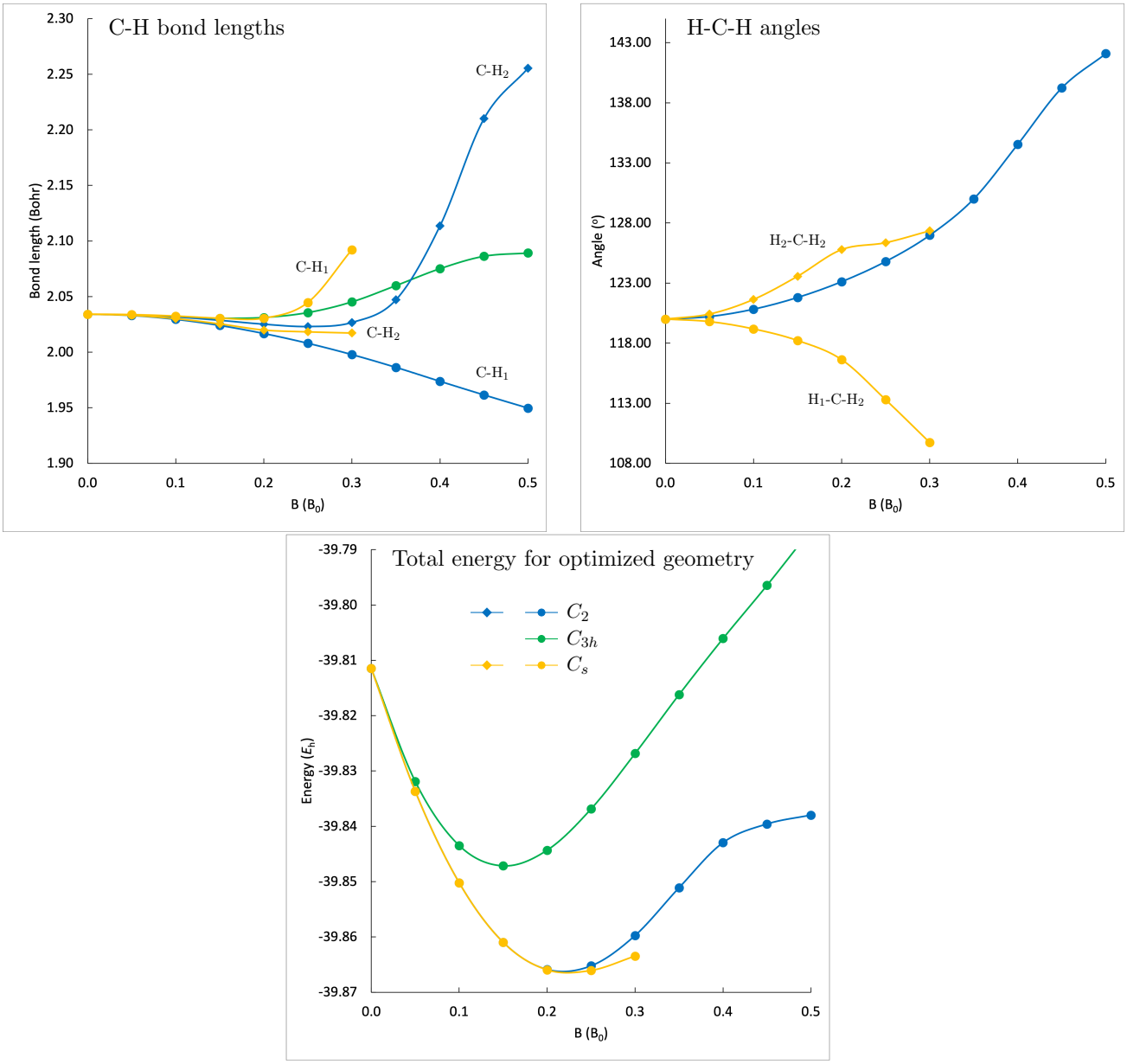

Figure 7.15: Geometry optimization results for the CH_3 radical for the three highly-symmetric orientations (C_2 blue, C_s yellow, C_{3h} green). C-H bond lengths in the upper left panel, H-C-H angles in the upper right panel, total energy for the optimized geometry in the lower panel.

field parallel to one C-H bond results in a C_2 symmetry (left), described by the C-H_1 and C-H_2 bond lengths, and the H_1-C-H_2 angle. The C_s orientation results from a magnetic field perpendicular to one C-H bond in such a way that the one σ mirror plane is retained (middle). The internal degrees of freedom are the C-H_1 and C-H_2 bond lengths and the H_1-C-H_2 and H_2-C-H_2 angles. Two angles are required, since the molecule is symmetry allowed to deviate from planarity and the angles do not need to add up to 360°. Lastly, a magnetic field perpendicular to the molecular plane results in a C_{3h} point group (right). Here, the C-H bonds remain equivalent and only the C-H bond lengths are the internal degrees of freedom.

The results for the three highly symmetric orientations are shown in fig. 7.15. The out-of-plane C_{3h} orientation is consistently found to be higher in energy, while the two in-plane orientations are very close energetically. For B$<$ 0.15 B_0, the C_2 orientation (blue) is slightly lower in energy, while the C_s orientation (yellow) is preferred for magnetic field stronger than 0.15 B_0. The energetic difference of the two orientation only becomes larger than 10^{-5} E_h for $B \geq 0.25$ B_0. Looking at C_s orientation more closely, the molecule is planar for up to 0.2 B_0. For stronger fields, there is a deviation from the

planar geometry, which is quantified by

$$d = 360 - 2 \cdot \omega[\mathrm{H_1\text{-}C\text{-}H_2}] - \omega[\mathrm{H_1\text{-}C\text{-}H_2}],$$

as in the totally planar case $d = 0$.[i] This deviation reaches up to 13° for B= 0.30 B_0. Even stronger fields dissociate the molecule for this orientation. Hence the molecule is predicted to be unbound for a magnetic field stronger than 0.30 B_0.

The unconstrained geometry optimization approach was tested for this system as well. For magnetic fields up to 0.2 B_0, the energetic difference between out-of-plane orientations and in-plane orientations of the molecule are of the order of 10^{-2} E_h. As stated previously, however, the difference for the different in-plane orientations is much smaller at the order of 10^{-5} E_h. Because of this, the unconstrained approach is able to easily converge to an in-plane orientation for these magnetic fields, as the gradients of such rotations are at the same order as the gradients of the geometric parameters, but it is not able to converge to the C_s or C_2 orientations as the potential-energy surface in those directions is very flat. This case serves both as a crash test for the unconstrained geometry optimization and to explore the physical insight that can be offered by it. For magnetic fields between 0.25 B_0 and 0.3 B_0, the unconstrained geometry optimization converges to the C_s orientation where the molecule deviates from planarity. For even stronger fields, $B > 0.3$ B_0, the molecules dissociates. These results are in agreement with the results from the constrained approach.

CH_2

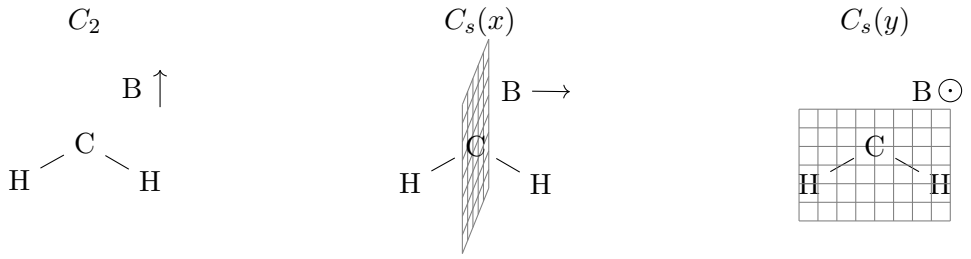

Figure 7.16: Highly-symmetric orientations of the CH_2 molecular fragment in a magnetic field. The mirror planes that are perpendicular to the magnetic field in the $C_s(x)$ (middle) and $C_s(y)$ (right) orientations are depicted by the gray grids.

The next fragment studied here is the methylene CH_2 molecule. It has two low-lying states of singlet and triplet multiplicity, both of which have a bent C_{2v} geometry in the absence of field. The $^3B_2$ is the ground state and the $^1A_1$ is the lowest singlet state, which is predicted to be 0.017422 E_h = 0.47 eV higher than the ground state at the CCSD level of theory. The ground state has strong contributions from the ^3P_g [He]$2s^2 2p^2$ state of the C atom, while the singlet has contributions mostly from the low-lying ^1D_g [He]$2s^2 2p^2$ state of C. Both states can be conceptualised as Jahn-Teller deformations of the lowest degenerate $^3\Pi_g$ and $^1\Delta_g$ states of the linear configuration. Similarly to the water molecule which has the same symmetry, the three highly-symmetric magnetic-field orientations are shown in fig. 7.16.

Results from the constrained optimizations are found in fig. 7.17. The dashed curves signify the results for the triplet state and continuous curves for the excited singlet state.

Regarding the energy, the three different orientations for the excited singlet state show a radically different behaviour in the magnetic field . For the field strengths studied here, the energy difference is large enough to decisively predict the $C_s(x)$ orientation (blue continuous line) as the preferred one. This orientation is particularly interesting because the magnetic field enforces a linear geometry for fields stronger than 0.35 B_0. This occurs because of the stabilisation offered by the orbital-Zeeman term interacting with the total angular momentum of the $^1\Delta_g^-$ state with $M_L = -2$. The C-H bonds shorten monotonically with increasing magnetic-field strength for this orientation. While for the

[i] The sum of the three angles in a plane that result from three rays of a common origin adds up to a full rotation 360°.

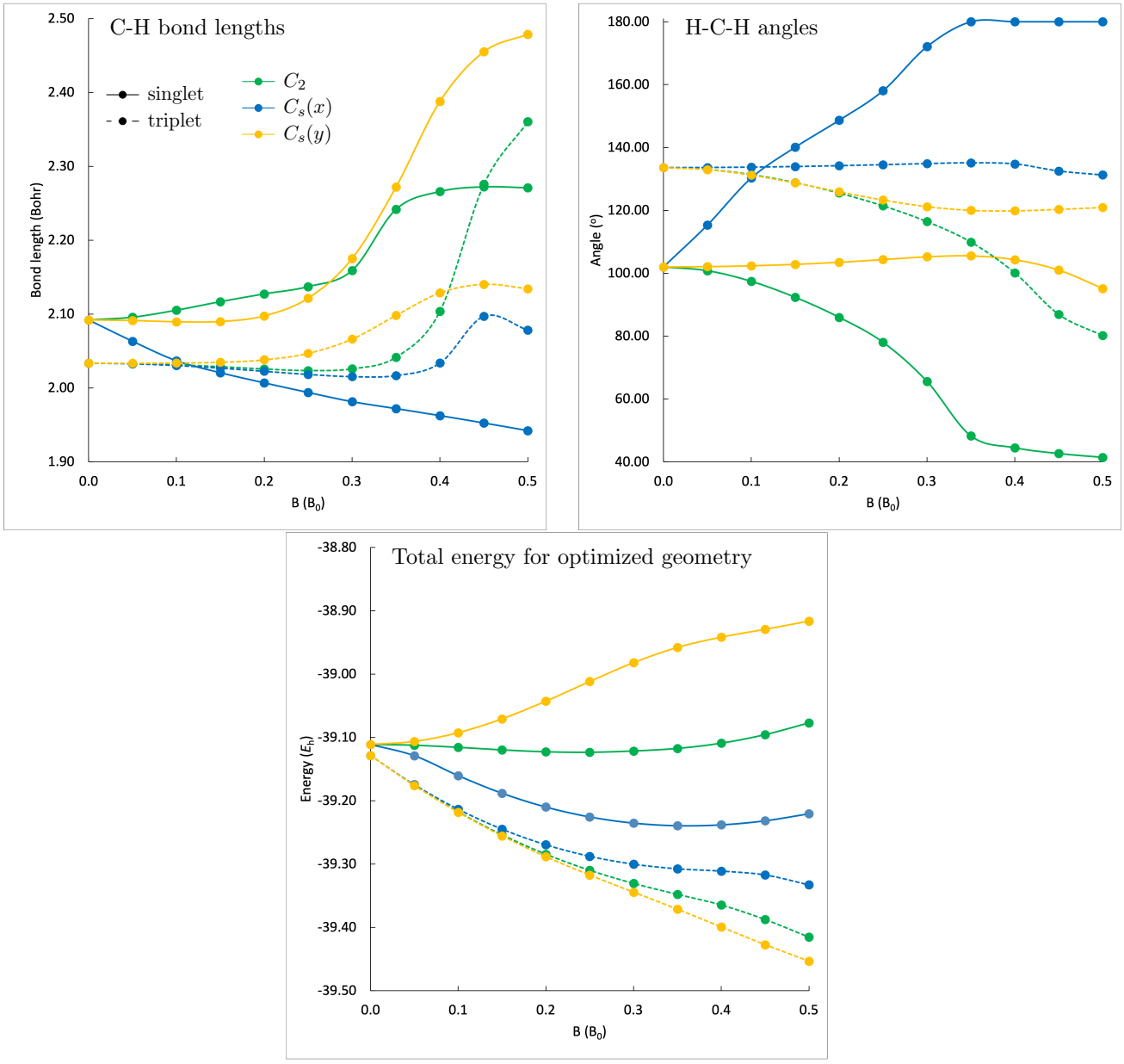

Figure 7.17: Geometry optimization results for methylene CH_2 for the three highly-symmetric orientations (C_2 green, $C_s(x)$ blue, $C_s(y)$ yellow). The dashed lines depict the ground state arising from the field-free $^3B_2$ state and the continuous lines the low-lying singlet state arising from the field-free $^1A_1$ state.

preferred $C_s(x)$/parallel orientation, the orbital-Zeeman dominates over the diamagnetic interaction resulting in a stabilisation of the state in field, the C_2 orientation has a relative constant energy with increasing magnetic field. In the $C_s(y)$ orientation, the reaction of the molecule to the field arises mostly from the diamagnetic term. For the C_2 orientation (continuous green), the H-C-H angle is found to be smaller with increasing magnetic-field strength. This decrease is a results of the molecule minimising the diamagnetic interaction. The angle reaches a plateau of about 40° for $B > 0.35\ B_0$, which cannot be further restricted because of the close proximity of the H nuclei. The C-H bonds are lengthened slightly until $B = 0.30\ B_0$. The small H-C-H angle results in an abrupt lengthening of the C-H bond at around 2.28 a_0 for stronger fields. In the $C_s(y)$ orientation (continuous yellow), the H-C-H angle remains relatively constant when increasing the magnetic field, as no significant minimisation of the diamagnetic interaction may result in this orientation. The C-H bonds are also relatively constant for $B < 0.2\ B_0$ and are predicted to be equal, due to the same chemical environment despite being formally non-symmetry equivalent . For stronger fields, the bonds are lengthened up to 2.5 a_0 for

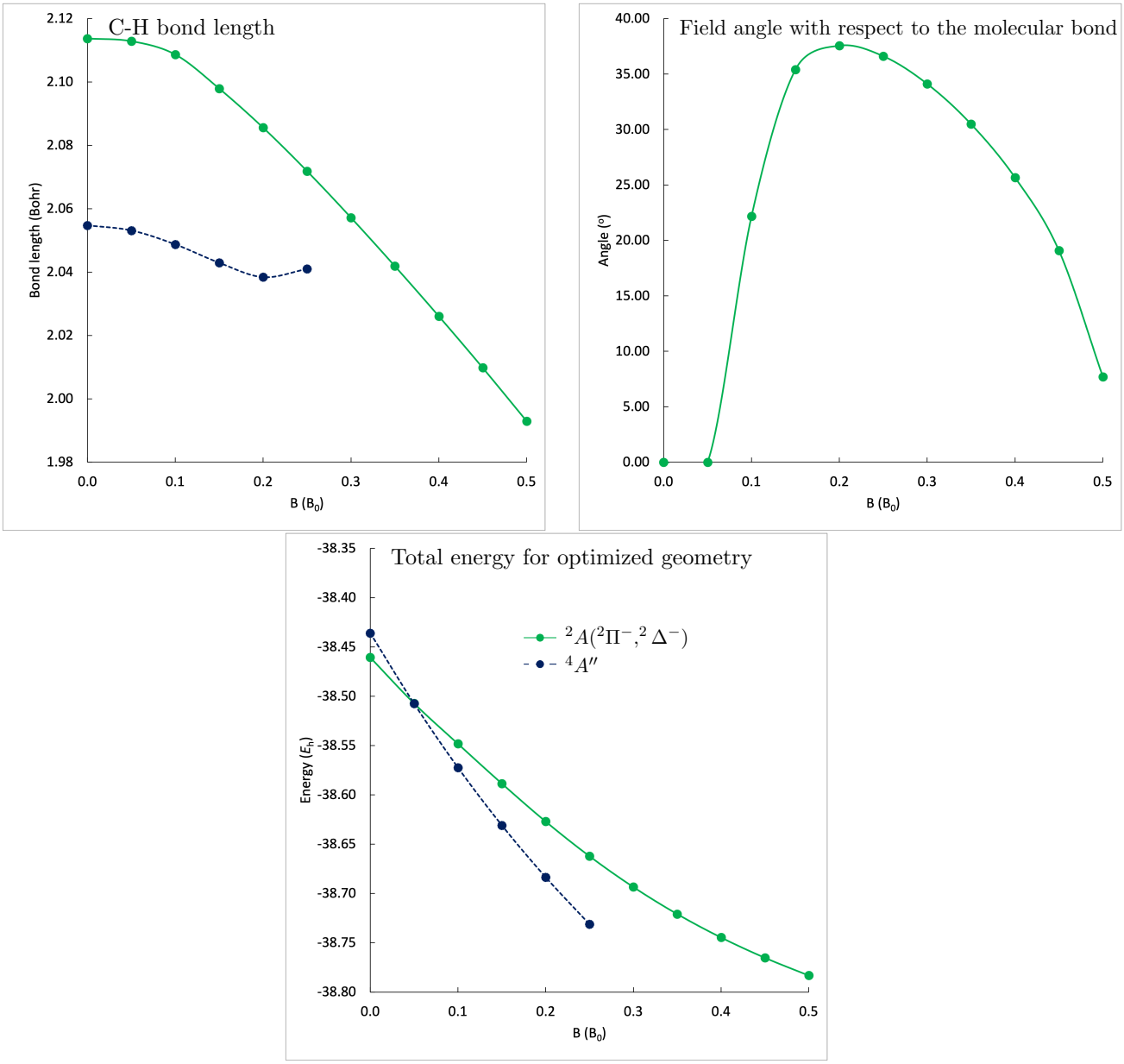

Figure 7.18: Geometry optimization results for the CH radical for the lowest doublet state (green) arising from the field-free $^2\Pi$ and $^4A''$ (blue) state arising from the $^4\Sigma^-$ state.

$B = 0.5\ B_0$, signifying a weakening with increasing magnetic-field strength.

As for the triplet ground state, its energetic behaviour is dominated by the spin-Zeeman interaction. It is significantly stabilised in the presence of magnetic field and the energy differences between the different orientations are not as large as for the singlet state. They are nonetheless more pronounced than in other cases observed so far. The out-of-plane $C_s(y)$ orientation (dashed yellow) is predicted to be the preferred orientation. The C-H bond lengths for this orientation are found to coincide despite not being symmetry equivalent. They are found constant in length at about 2.05 a_0 for up to 0.25 B_0. For stronger fields they are lengthened with increasing magnetic-field strength at about 2.10 a_0. The H-C-H angle is monotonically shortened with increasing magnetic-field strength reaching 120° at $B = 0.50\ B_0$ starting from 133° in the field-free case. The $C_s(x)$ orientation is highest in energy and the C_2 orientation is predicted energetically to lie energetically between the other two orientations. Similarly to the excited singlet case for the same orientation, the H-C-H angle decreases with increasing magnetic-field strength in the C_2 case (dashed green). The C-H bond is relatively constant in length with increasing magnetic-field strength up to $B = 0.35\ B_0$, but abruptly lengthens for stronger magnetic fields reaching 2.36 a_0 at $B = 0.5\ B_0$ because of the closer proximity

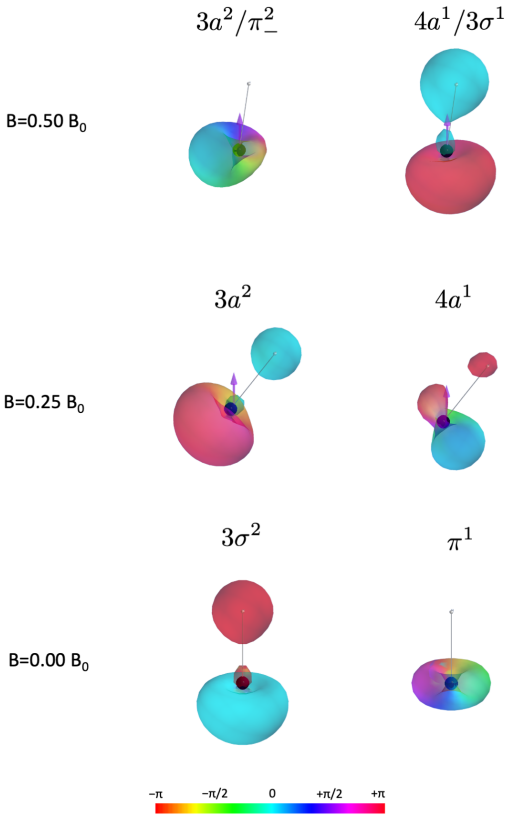

Figure 7.19: The HOMO singly occupied and HOMO−1 doubly occupied orbitals of CH in the absence of field, and at $B = 0.25\ B_0$ and $B = 0.50\ B_0$ at the optimized geometry and preferred magnetic field orientation.

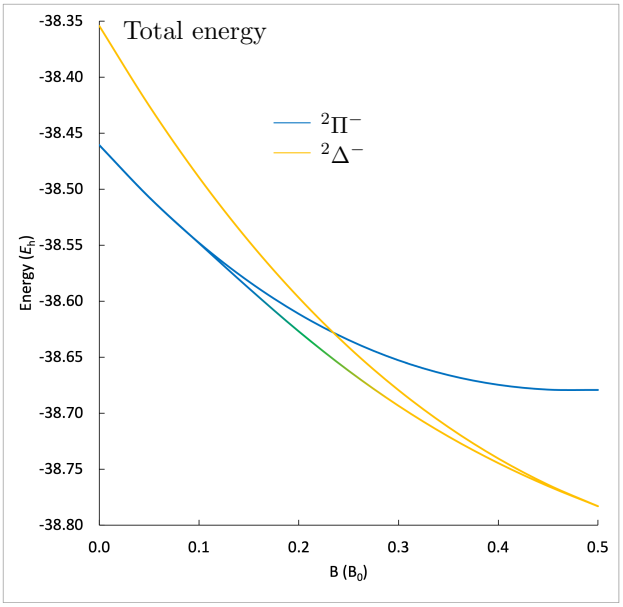

Figure 7.20: Geometry optimization results for the $^2\Pi^-$ (blue) and $^2\Delta^-$ (yellow) states of the CH radical for a parallel magnetic field orientation, overlayed with the unconstrained geometry optimization results for the lowest in energy doublet state (blue-green-yellow gradient).

of the H nuclei. Lastly, for the $C_s(x)$ orientation (dashed blue), the H-C-H angle remains relatively constant with increasing magnetic-field strength. The C-H bond is shortened slightly until 0.35 B_0. It is lengthened until a maximum of 2.10 a_0 at 0.45 B_0 for stronger fields, and then shortens for $B = 0.50\ B_0$.

The unconstrained geometry optimizations replicate the findings of the constrained approaches for the singlet state up to 0.30 B_0 and for the ground triple state up to 0.35 B_0. In the case of the excited singlet state, the molecule is linear for $B > 0.30\ B_0$. This linearity removes one rotational degree of freedom giving a singularity in the unconstrained geometry optimization procedure, which slows the convergence of the algorithm. For this reason no convergence was achieved for the excited singlet state for magnetic fields stronger than 0.30 B_0 when using the uncontrained geometry optimization. However, the constrained optimization is unproblematic. In the case of the triplet state on the other hand, the unconstrained approach predicts the dissociation of the molecular fragment for fields stronger than 0.35 B_0. The dissociated molecule is predicted more stable than the bound molecule predicted by the constrained geometry optimization for $B > 0.35\ B_0$.

CH

The geometry optimization of the doublet state lowest in energy, i.e., the field-free $^2\Pi$ state, and quartet state, i.e., the field-free $^4\Sigma^-$ state are studied here. As mentioned in subsec. 4.3.2, the ground state has a predominant $1\sigma^2 2\sigma^2 3\sigma^2 1\pi^1$ electron configuration, while the quartet state lowest in energy

is described by the $1\sigma^2 2\sigma^2 3\sigma^1 1\pi^2$ electron configuration. For both states, the unconstrained approach was used, and the results are shown in fig. 7.18.

Regarding the doublet state, the molecule is not oriented in neither of the extreme parallel or perpendicular orientation, which is surprising. It is oriented under a field-dependent angle, which is plotted in the upper right panel. In a parallel orientation of the molecule relative to the magnetic field, the $M_L = -1$ and $M_L = -2$ components of the (field-free ground) $^2\Pi$ state and the low-lying $^2\Delta$ state, respectively are the components lower in energy. They have maximum stabilisation from the orbital-Zeeman term and they cross around B= 0.25 B_0, as seen in the constrained optimization results in fig. 7.20. Despite this maximum interaction with the orbital-Zeeman term, the mixing between these two states that is only allowed in a skewed field orientation stabilises the lower state more than the orbital-Zeeman term, resulting in the observed skewed preferred orientation. The state in the skewed orientation is thus more similar to the $^2\Pi^-$ state for weaker field and more similar to $^2\Delta-$ for stronger fields. This can be also seen in fig. 7.19, where the HOMO (singly occupied) and the HOMO−1 (doubly occupied) orbitals are plotted in different magnetic-field strengths in the optimized geometry and preferred orientation. At $B = 0.0\ B_0$, the 3σ orbital is doubly occupied, and the π_- orbital is singly occupied, with a p_- character on the C atom. In the case of $B = 0.25\ B_0$, which is near the maximum of the preferred angle of the molecule relative to the magnetic field at about 35° (upper right panel of fig. 7.18), both orbitals belong to the same IRREP as there are no symmetry elements. The $3a$ orbital is doubly occupied and is characterised as mostly of σ character, while the $4a$ orbital is singly occupied with predominant p_z character[j] based on the carbon with some admixtures of σ character. Lastly, at $B = 0.50\ B_0$, the stabilisation offered by the mixing of the $M_L = -1$ and $M_L = -2$ pure states is smaller. The systems benefits more from the stabilisation of the orbital-Zeeman term of the $^2\Delta^-$ state and the molecule aligns mostly parallel with the magnetic field. The $3a$ orbital is again doubly excited, but at this magnetic-field strength it has a dominant p_- character on the C atom, while the $4a$ orbital is singly occupied with a σ character. As the orientation of the magnetic field relative to the molecule for the doublet state is not one of the extreme orientation, the unconstrained approach has to be used. Nonetheless, for B= 0.05 B_0, the resulting energy differences for the different orientations are very small, and the unconstrained geometry optimization does not converge, as seen also in other cases so far. The geometry parallel to the magnetic field should be close to the true minimum. The geometry optimization of the parallel orientation is thus used for this magnetic-field strength in the plot in fig. 7.18. The unconstrained approach converges for stronger magnetic fields because of larger energy differences between the different orientations. The C-H bond is shortened with increasing magnetic-field strength.

As for the quartet state, the results decisively show the perpendicular orientation to be preferred for all field strengths considered. Arising from the $^4\Sigma^-$ state in the absence of field, it is characterised as $^4A''$. The C-H bond length is relatively constant in different magnetic-field strengths with a minimum for $B = 0.2\ B_0$ at around 2.04 a_0. Because of the lower M_S value, the $M_S = -\frac{3}{2}$ component becomes the ground state for B> 0.05 B_0. The dissociation of the molecule is predicted for fields stronger than 0.25 B_0.

C

The atomic C states, i.e., the ^3P_g ([He]$2s^2 2p^2$) and the ^5S_u ([He]$2s^1 2p^3$) transform to $^3\Pi_g^-$ and $^5\Sigma_u$ in the presence of a magnetic field, respectively, and their energy is plotted as function of the magnetic-field strength in fig. 7.21. The $^3\Pi_g$ is the ground state for up to 0.3 B_0. For stronger fields, the spin-Zeeman interactions stabilises the system more than the orbital-Zeeman interaction and the $^5\Sigma_u$ becomes the ground state.

Fragments

Having calculated all the individual molecular fragments, the dissociation scheme is studied as a whole and the energies of all the fragments are plotted as a function of the magnetic-field strength in fig. 7.22. Different M_S components for the different fragments are calculated. Specifically, fragment (1) consists

[j] z is considered the direction of the magnetic field.

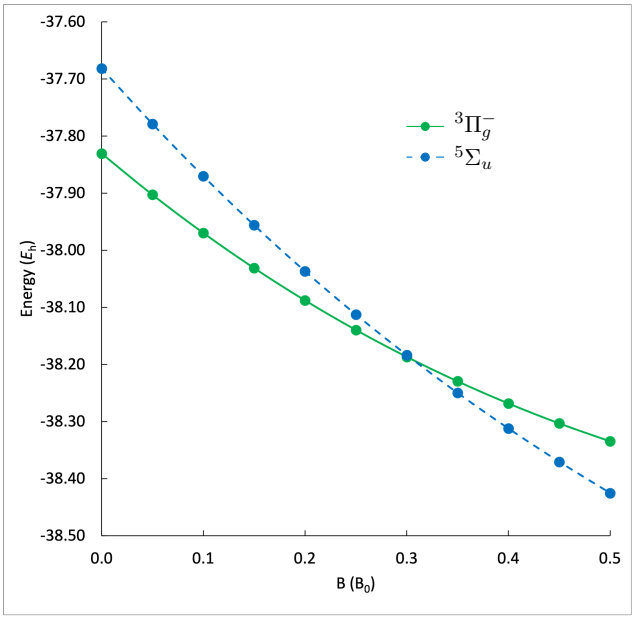

Figure 7.21: The $^3\Pi_g^-(^3P_g)$ ground state (continuous green) and $^5\Sigma_u(^5S_u)$ low-lying state (dashed blue) of C as a function of the magnetic-field strength.

of a closed-shell molecule only having an $M_S = 0$ (green continuous line). Fragment (2) (dark blue) has the CH_3 radical and a H atom that can be combine to give an $M_S = 0$ (low opacity continuous), and $M_S = -1$ (long dashed blue). Following the dissociation, fragment (3) consists of two H atoms and methylene. The triplet state (purple) of CH_2 can be combined with the H atoms to form $M_S = 0, -1, -2$, while the singlet state (light blue) only forms $M_S = 0, -1$. Fragment (4) with the CH radical and three H atoms forms $M_S = 0, -1, -2$ with the doublet state (yellow) and $M_S = 0, -1, -2, -3$ with the quartet (orange). Lastly, the atomised fragment forms $M_S = 0, -1, -2, -3$ from the triplet atomic state (red) and the four H atoms and $M_S = 0, -1, -2, -3, -4, -5$ from the quintet atomic state (magenta).

Methane is found bound up to about 0.15 B_0. Fragment (2) dominates for a small magnetic field-strength window around 0.17 B_0. The molecule then further fragments to (3) around 0.20 B_0. For stronger fields, the molecule is found completely atomised. Further evolution is also observed for the atomised fragment (5) at 0.3 B_0, where the quintet state becomes the ground state.

It has been shown that for stronger field around 0.6 B_0, a CH_4 bound species is formed due to paramagnetic bonding, with a "fan"-like structure.[57] Such structures that are completely outside the chemical intuition are outside the scope of this study.

Generally comparing the study of water and methane in the presence of a magnetic field up to 0.5 B_0, it is found that both molecules fragment around 0.15 B_0 and are eventually completely atomised around 0.2 B_0. The atomization is a direct result of the spin-Zeeman interaction that favours open-shell states, and such, the electron pairing that results in bond formation becomes less favoured. Paramagnetic bond formation, which is compatible with highly open-shell cases, occurs for magnetic fields stronger than 0.6 B_0, which is however not that relevant for the study of the atmospheres of MWDs, as the observed magnetic fields reach up to only 0.4 B_0.

It is also quite important to note that finding the preferred orientation and the optimal geometry of the molecule in the presence of a magnetic field is non trivial at all. Especially for closed-shell systems, where there is no significant paramagnetic interaction, and for molecules that are relatively spherical, the energy differences of different orientations of the molecule may be very small. In such cases, the present black-box unconstrained approach fails to converge. The small energetical difference, however, also suggest, that the relative orientation is not as chemically relevant and the optimization of the internal coordinates, which is much more important, is mostly unaffected. Improvements to this unconstrained algorithm that would take these small differences under consideration are under development. In addition, the starting geometry and orientation of the molecule relative to the

magnetic field affect the convergence of the optimization significantly in most cases, and since the chemical intuition cannot be trusted, other approaches or more extensive studies are needed for the search of molecules on MWDs.

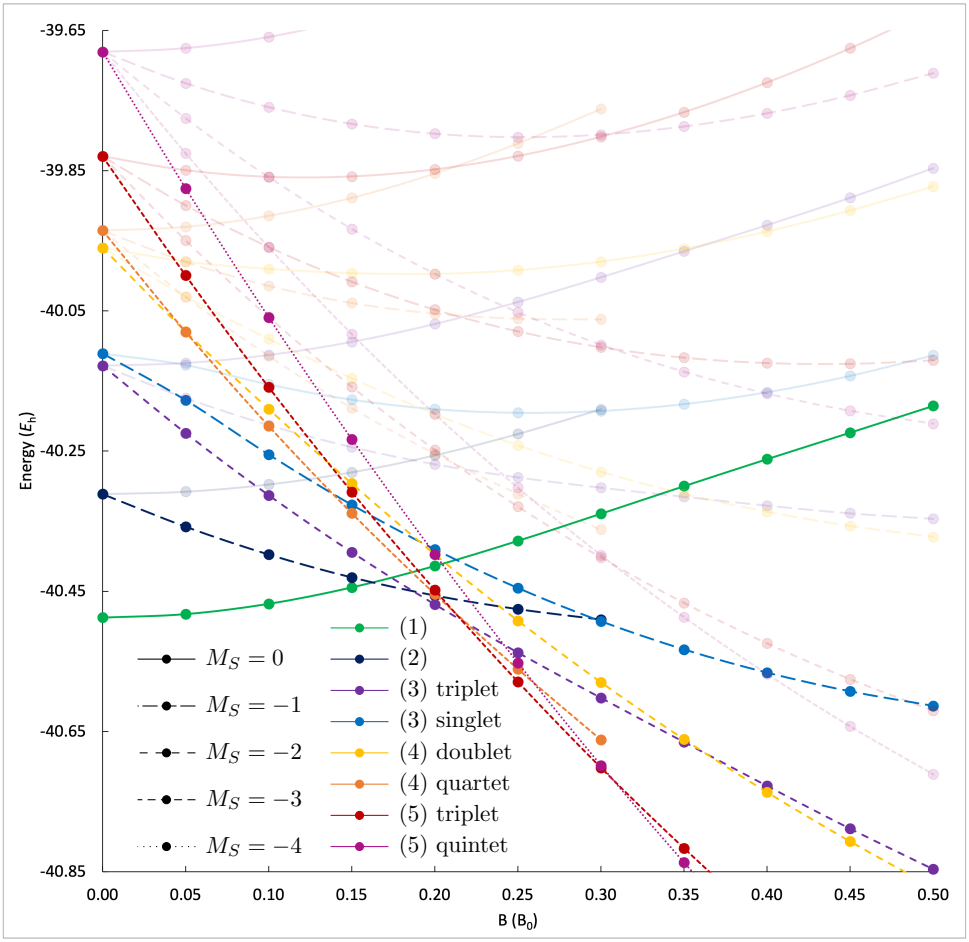

Figure 7.22: The lowest in energy M_S components of fragments methane (1) (green), (2) (dark blue),(3) (triplet purple, singlet light blue), (4) (doublet yellow, quartet orange) and (5) (triplet red, quintet magenta) in non-transparent lines. The higher in energy components are depicted with low opacity. The M_S components are depicted as: $M_S = 0$ continuous line, $M_S = -1$ long dashed line, $M_S = -2$ dashed line, $M_S = -3$ narrow dashed line, $M_S = -4$ dotted line.

Chapter 8

Studying the Spectra of a Magnetic White Dwarf

Having presented the newly implemented and newly developed methods realized in this thesis, the focus of this last chapter turns to the study of the spectra of strongly magnetic white dwarfs. This is done via highly-accurate quantum-chemical calculations for the alkali metal Na, as well as the alkali earths Mg and Ca. In order to acquire a general picture on the oxidation state and the electronic state that is most stable for each atom in the presence of a magnetic field, the ionization potential (IP) was studied at the EOM-CCSD and EOM-CCSD(T)(a)* levels of theory using augmented core-valence correlation-consistent basis sets aug-cc-pCVQZ. Moreover, specific electronic excitations of Mg and Ca were studied at the EOM-CCSD, EOM-CCSD(T)(a)*, EOM-CC3, and at the EOM-CCSDT levels of theory using basis sets of up to 5Z quality. Uncontracted basis sets were used to provide the sufficient flexibility to described the deformation caused by the magnetic field. The study of the excitations of the Mg atom together with existing results for the Na atom,[80] enabled the interpretation of a MWD spectrum by the assignment of lines to electronic excitations of Na and Mg.

8.1 Ionization potentials

Before studying the excitation spectra of metal atoms, it is important to identify the most stable state in the presence of magnetic field. The multiplicity of the electronic state as well as the oxidation state are taken under consideration by studying the IPs as a function of the magnetic-field strength. The IPs of the atoms in the first and second row of the periodic table have been studied in ref. [203]. Here, the IPs of Na, Mg, and Ca from the third and fourth rows are investigated.

For the calculation of ionization potentials in the presence of a magnetic field, the energy of the free electron has to be considered. Unlike in the field-free case, the free-electron energy is quantized regarding the cyclotron movement perpendicular to the magnetic field and is given by the Landau levels

$$E^{\text{Landau}}_{n,m_l,m_s} = \left(n + \frac{1}{2}m_l + m_s + \frac{1}{2}|m_l| + \frac{1}{2}\right)\frac{e}{m_e}\hbar|\boldsymbol{B}| + \frac{\langle \hat{p}^2_{\text{par}}\rangle}{2m_e}.$$

Here, the quantum number $n = 0, 1, 2, \ldots$ is the radial quantum number of the electron and describes the radial motion in the cyclotron, $m_l = 0, \pm1, \pm2, \ldots$ is the magnetic angular-momentum quantum number and $m_s = \pm\frac{1}{2}$ is the magnetic spin quantum number. The last term is the non-quantized kinetic energy arising from the movement of the electron parallel to the magnetic field and involves the momentum component of this movement $\hat{p}_{\text{par}}$. The terms $\frac{1}{2}m_l + m_s$ are interpreted as the orbital- and spin-Zeeman contributions, and $\frac{1}{2}|m_l| + \frac{1}{2}$ as the diamagnetic and zero-point energy contributions. Additionally, it is noted that for the case of negative m_l values, the paramagnetic and diamagnetic influences cancel each other out, giving an infinite degeneracy.[26,203]

When studying the IPs in the presence of a magnetic field, the non-quantized kinetic energy is ignored, and the emitted electron is assumed to occupy the radial motion lowest in energy, i.e., $n = 0$. The angular movement of the electron is however preserved giving the energy of the emitted electron

as

$$E^{\mathrm{em}}_{m_l,m_s} = \left(\frac{1}{2}m_l + m_s + \frac{1}{2}|m_l| + \frac{1}{2}\right)\frac{e}{m_e}\hbar|\boldsymbol{B}|,$$

with m_l and m_s the quantum numbers of the electron in the atomic structure.[26,203] The IP is then calculated as

$$\Delta_{\mathrm{IP}} = E(\text{cation}) + E^{\mathrm{em}}_{m_l,m_s} - E(\text{neutral atom}).$$

8.1.1 Na

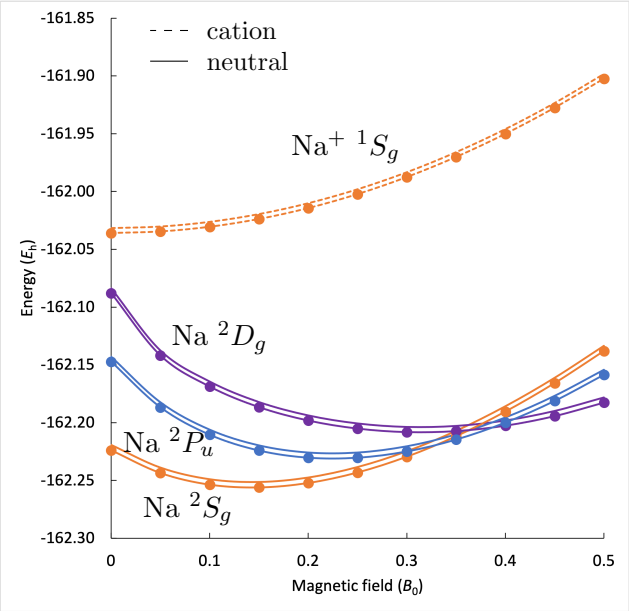

Figure 8.1: The lowest-lying states of Na, and Na^+ calculated at the (EOM)-CCSD and (EOM)-CCSD(T)(a)* levels of theory with the unc-aug-cc-pCVQZ basis set.

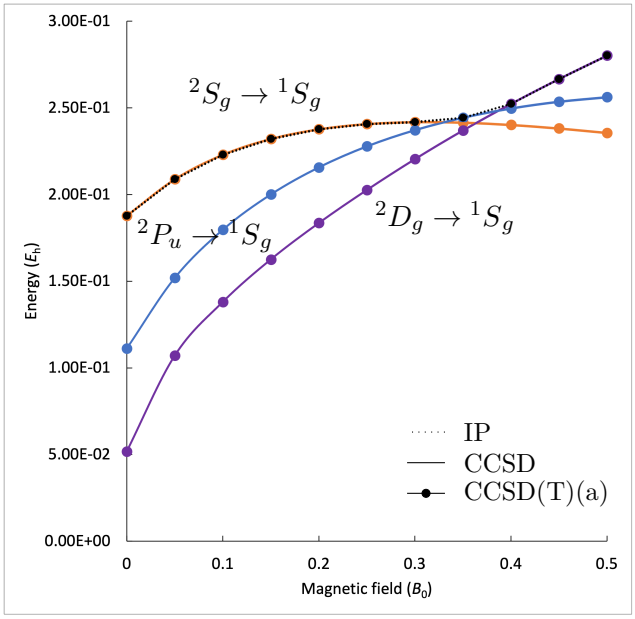

Figure 8.2: The ionization energies for different transitions of Na calculated at the (EOM)-CCSD and (EOM)-CCSD(T)(a)* levels of theory with the unc-aug-cc-pCVQZ basis set. The ionization potential is depicted as a black curve.

The IP of Na was studied as follows. The ^1S_g state of the Na^+ cation was used for its closed-shell configuration as the reference state in the calculation. On top of the reference state, EA-EOM-CC ($\Delta M_S = -\frac{1}{2}$) calculations were performed at the CCSD and CCSD(T)(a)* levels of theory. The IP was studied for magnetic-field strengths up to 0.5 B_0 using a 0.05 B_0 step. The results are shown in figs. 8.1 and 8.2.

In fig. 8.1 the total energies of the neutral and cationic states are plotted. The closed-shell ^1S_g state of Na^+ is characterized by a noble-gas electron configuration [Ne] and is shown as a dashed orange curve in fig. 8.1. The low-lying doublet states of the neutral atom, that were targeted via the EA-EOM-CC approach, are shown as continuous lines and are the ^2S_g ([Ne]$3s^1$) in orange colour, which is the ground state in the absence of field, and the excited ^2P_u ([Ne]$3p^1$) and ^2D_g ([Ne]$3d^1$) states in blue and purple colour, respectively. The $M_S = -\frac{1}{2}$ component of the doublet states was targeted, along with the lowest M_L component of the degenerate states. This means the $M_L = -1$ state of ^2P_u that transforms to $^2\Pi_u^-$ in the presence of a magnetic field, and the $M_L = -2$ component of ^2D_g that transforms to $^2\Delta_g^-$. S states transform to Σ states in the presence of magnetic field. Following the spin-Zeeman terms, the doublet states are stabilised in magnetic field while the closed-shell cationic state is consistently destabilised by the diamagnetic influence. Accordingly, the states with negative M_L values are stabilised more against the $^2\Sigma_g$ state that arises from the field-free ^2S_g state. As a result, around 0.3 B_0, the $^2\Pi_u^-$ state becomes more stable than the $^2\Sigma_g$ state. The $^2\Delta_g^-$ states becomes the ground state of the atom for a slightly stronger field around 0.35 B_0. The behaviour of the Na atom shows some similarities to Li studied in ref. [203]. In the Li case, the $^2\Pi_u^-$ state that arises from

the ${}^2P_u$ ($1s^2 2p^1$) field-free state becomes the ground state for magnetic fields stronger than 0.17 B_0 as it is found to be lower in energy than the ${}^2\Sigma_g$ state (field-free ${}^2S_g$ state with predominant configuration $1s^2 2s^1$). This change of the ground state takes place in stronger fields for Na. In the Li case, there exist no ${}^2D_g$ state because of the absence of d orbitals in the second shell, which however, is important for the behaviour of Na in the magnetic field.

The ionization energies are shown in fig. 8.2 as a function of the magnetic field. The transitions ${}^2S_g \to {}^1S_g$, ${}^2P_u \to {}^1S_g$, and ${}^2D_g \to {}^1S_g$ have been calculated. In all of these cases, the spin of the emitted electron is $m_s = -\frac{1}{2}$ and the magnetic quantum number is zero or negative $m_l \leq 0$. The Landau energy thus vanishes $E^{\mathrm{em}}_{m_l \leq 0, -\frac{1}{2}} = 0$. The IP that corresponds to the ground state of the neutral system is depicted as a black thin curve in fig. 8.2 and the transitions that contribute to the IP are summarized in tab. 8.1. There is an ascending trend with increasing magnetic-field strength as long as the paramagnetic terms dominate, since the target singlet state is destabilised, while the doublet states are stabilised.

B	Transition	$E^{\mathrm{em}}_{m_l, m_s}$
$B < 0.3\ B_0$	${}^2S_g(M_S = -\frac{1}{2}) \to {}^1S_g$	$E^{\mathrm{em}}_{0,-\frac{1}{2}} = 0$
$0.3\ B_0 < B < 0.4\ B_0$	${}^2P_u(M_S = -\frac{1}{2}) \to {}^1S_g$	$E^{\mathrm{em}}_{-1,-\frac{1}{2}} = 0$
$B > 0.4\ B_0$	${}^2D_g(M_S = -\frac{1}{2}) \to {}^1S_g$	$E^{\mathrm{em}}_{-2,-\frac{1}{2}} = 0$

Table 8.1: Transitions for the IP of the Na atom in different magnetic fields and the energy of the emitted electron.

Regarding the energy calculations, the CCSD(T)(a)* results have a visible relative parallel shift with respect to CCSD, by an average deviation of $-4 \cdot 10^{-3}\ E_{\mathrm{h}}$. The calculated IP at $B = 0$ at the EOM-CCSD and at the EOM-CCSD(T)(a)* level is 0.187551 E_{h} = 5.10353 eV and 0.187883 E_{h} = 5.11256 eV, respectively, being in good agreement to the experimental value 5.13907696 eV±0.00000025 eV.[51] The difference between the CCSD and CCSD(T)(a)* results is not visible in fig. 8.2, as the deviations are one order of magnitude lower than for the energies, $3 \cdot 10^{-4}\ E_{\mathrm{h}}$ by average.

8.1.2 Mg

The low-lying states of Mg and Mg^+ are shown in fig. 8.3 and were studied using the IP-EOM-CC approach. The ground state of Mg in the absence of field, i.e., the ${}^1S_g$ state (continuous orange) has a closed-shell configuration ([Ne]$3s^2$) and was chosen as reference state for the CCSD and CCSD(T)(a) calculations. The cationic ${}^2S_g$ state (dashed orange) with configuration [Ne]$3s^1$ was targeted via IP-EOM-CC ($\Delta M_S = -\frac{1}{2}$). Additionally, the low-lying atomic state ${}^3P_u$ (continuous blue) was studied at the CCSD and CCSD(T)(a) levels as a reference state as well, choosing the $M_L = -1$ component with configuration [Ne]$3s^1 3p^1_-$. Accordingly, the ${}^2P_u$ ($M_L = -1$) state (dashed blue) with configuration [Ne]$3p^1_-$ was targeted via IP-EOM-CC ($\Delta M_S = +\frac{1}{2}$). In this way, the cationic states are targeted as predominant single-excitation EOM states. The following ionization energies were studied as a function of the magnetic field: ${}^1S_g \to {}^2S_g + e(0, +\frac{1}{2})$ (orange), ${}^1S_g \to {}^2P_u + e(0, +\frac{1}{2})$ (yellow), ${}^3P_u \to {}^2S_g + e(-1, -\frac{1}{2})$ (purple) and ${}^3P_u \to {}^2P_u + e(0, -\frac{1}{2})$, and are shown in fig. 8.4. The last terms in the IP reactions correspond to the emitted electron as $e(m_l, m_s)$, and its energies are $E^{\mathrm{em}}_{0,+\frac{1}{2}} = \frac{e}{m_e}\hbar|\boldsymbol{B}|$ for the first two transitions and $E^{\mathrm{em}}_{m_l \leq 0, -\frac{1}{2}} = 0$ for the latter two. The IP based on the ground state of the neutral atom in each magnetic-field strength is depicted as a thin black curve. The exact IP transitions can be found in tab. 8.2.

The ${}^1S_g$ atomic state (continuous orange) is the only closed-shell state studied here. It transforms to ${}^1\Sigma_g$ in the magnetic field and is consistently destabilised by the diamagnetic influence in increasing magnetic-field strength. The ${}^3P_u$ (${}^3\Pi_u^-$ in field) state is stabilised both by the spin- and orbital- Zeeman term ($M_S = -1$ and $M_L = -1$ respectively) and becomes the ground state of the system around $B = 0.06\ B_0$. The cationic states are also affected primarily by the spin-Zeeman term ($M_S = -\frac{1}{2}$). They have a stabilising trend with ascending magnetic-field strength. The excited ${}^2P_u$ (${}^2\Pi_u^-$ in field) state (dashed blue) is stabilised even more because of the orbital-Zeeman term ($M_L = -1$). It becomes lower in energy than the ${}^2\Sigma_g$ (dashed orange) state around $B = 0.5\ B_0$. The cationic states are also

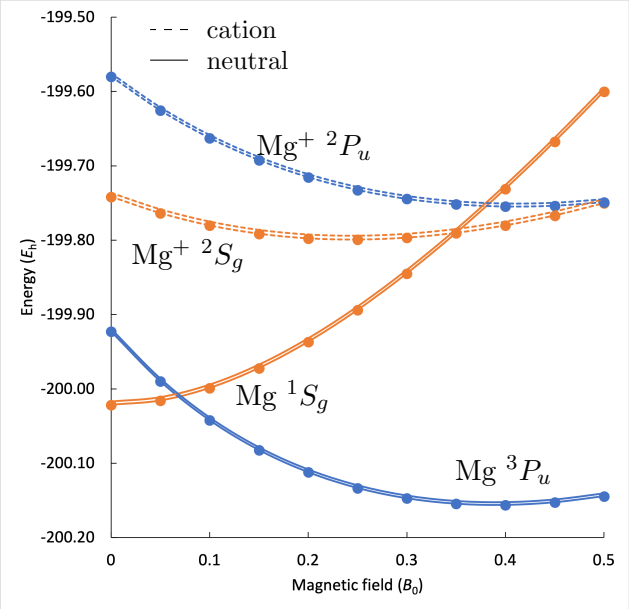

Figure 8.3: The lowest-lying states of Mg , and Mg^+ calculated at the (EOM)-CCSD and (EOM)-CCSD(T)(a)* levels of theory with the unc-aug-cc-pCVQZ basis set.

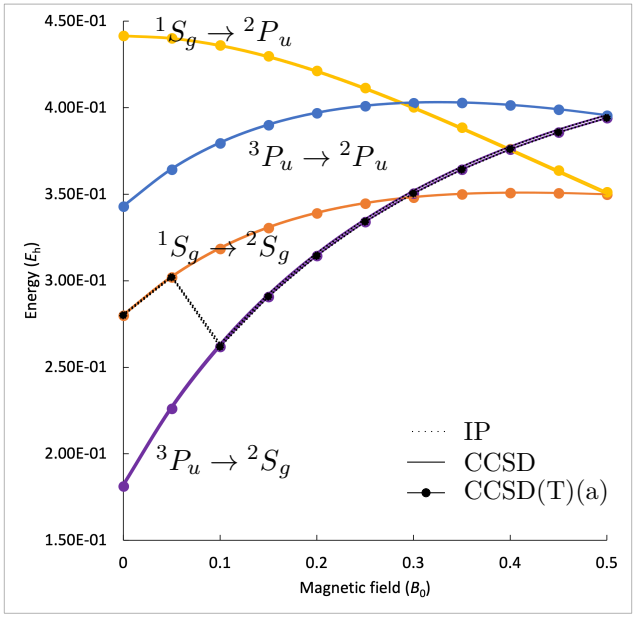

Figure 8.4: The ionization energies for different transitions of Mg calculated at the (EOM)-CCSD and (EOM)-CCSD(T)(a)* levels of theory with the unc-aug-cc-pCVQZ basis set. The ionization potential is depicted as a black curve.

B	Transition	$E^{\text{em}}_{m_l,m_s}$
$B < 0.06\ B_0$	$^1S_g \rightarrow {}^2S_g(M_S = -\frac{1}{2})$	$E^{\text{em}}_{0,+\frac{1}{2}} = \frac{e}{m_e}\hbar\lvert\boldsymbol{B}\rvert$
	$^1S_g \rightarrow {}^2S_g(M_S = +\frac{1}{2})$	$E^{\text{em}}_{0,-\frac{1}{2}} = 0$
$B > 0.06\ B_0$	$^3P_u(M_S = -1) \rightarrow {}^2S_g(M_S = -\frac{1}{2})$	$E^{\text{em}}_{-1,-\frac{1}{2}} = 0$

Table 8.2: Transitions for the IP of the Mg atom in different magnetic fields and the energy of the emitted electron. For $B < 0.06\ B_0$, emitting either the α or the β electron results in the same IP.

found to be more stable than the closed-shell atomic $^1\Sigma_g$ state (continuous orange) for magnetic fields stronger than 0.35 B_0 for the $^2\Sigma_g$ (dashed orange) and 0.4 B_0 for the $^2\Pi_u^-$ (dashed blue).

The IPs starting from the closed-shell $^1\Sigma_g$ state (orange and yellow lines in fig. 8.4) involve the non-zero Landau energy of the emitted electron. This ionization energy is degenerate to the $^1S_g \rightarrow {}^2S_g(M_S = +\frac{1}{2})$ transition, where the emitted electron is of β spin and the final cationic state has an $M_S = +\frac{1}{2}$. The yellow curve that describes the $^1S_g \rightarrow {}^2P_u$ transition has a descending trend for larger magnetic-field strengths. The ionization energies starting from the $^3\Pi_u^-$ state (purple and blue) have an ascending trend for larger magnetic fields. The Landau energy here is zero and the observed trend is attributed to the stronger stabilisation of the starting state relative to the target states.

In the field-free case, the IP is found at 0.280690 E_h = 7.63797 eV at the CCSD and at 0.279981 E_h = 7.61867 eV at the CCSD(T)(a)* level of theory. Compared to the experimental value 7.646236 eV ± 0.000004 eV,[51] the agreement is satisfactory. The deviation of the CCSD from the CCSD(T)(a)* results is more or less constant in the magnetic field. It amounts to about 10^{-3} E_h for the total energies, and about 10^{-4} E_h for the IPs.

8.1.3 Ca

The Ca atom belongs to the same group as Mg and Be. It is expected to have a similar behaviour regarding the lowest cationic and neutral states. For this reason, it was studied using the same strategy as Mg and the results are shown in in fig. 8.5. The ground state ^1S_g (orange curve) with configuration [Ar]$4s^2$ was targeted as reference state, and the cationic ^2S_g state [Ar]$4s^1$ (dashed orange) via the IP-EOM-CC approach ($\Delta M_S = -\frac{1}{2}$). On top, the atomic ^3P_u (blue curve) state with configuration

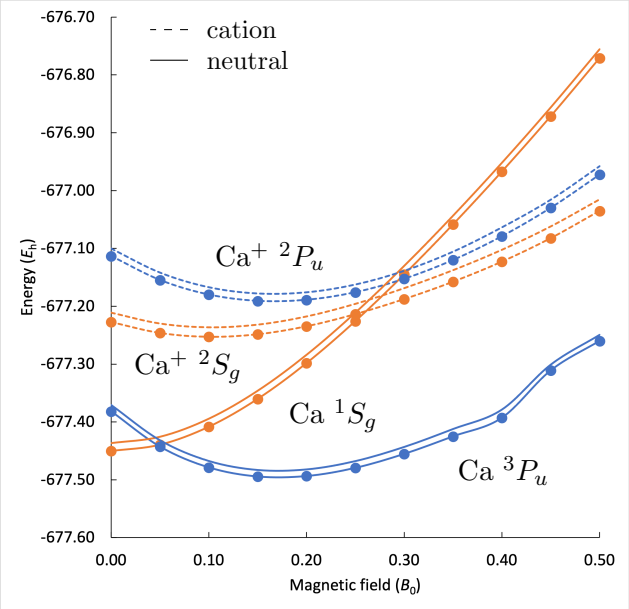

Figure 8.5: The lowest-lying states of Ca, and Ca^+ calculated at the (EOM)-CCSD and (EOM)-CCSD(T)(a)* levels of theory with unc-aug-cc-pCVQZ basis set.

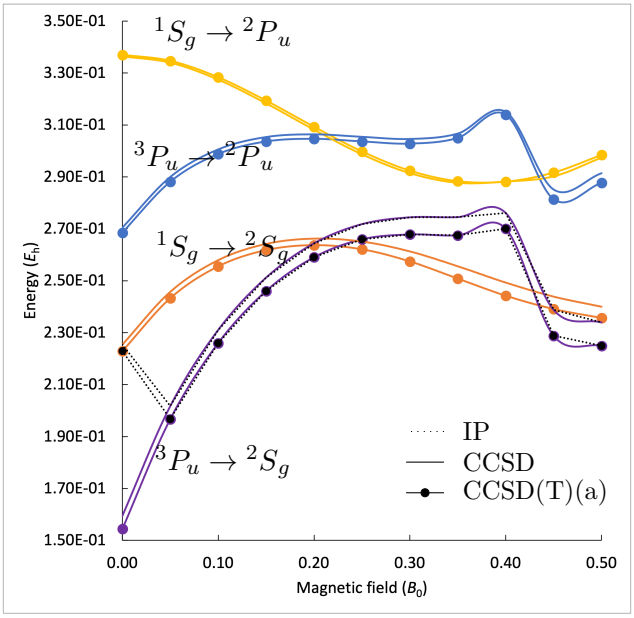

Figure 8.6: The ionization energies for different transitions of Ca calculated at the (EOM)-CCSD and (EOM)-CCSD(T)(a)* levels of theory with the unc-aug-cc-pCVQZ basis set. The ionization potential is depicted as a black curve.

$[\mathrm{Ar}]4s^14p^1$ was used as reference to target the cationic ^2P_u state $[\mathrm{Ar}]4p^1$ (dashed blue) via the IP-EOM-CC approach ($\Delta M_S = +\frac{1}{2}$). The calculated ionization energies correspond to the same transitions as studied for Mg and are shown in fig. 8.6. A black thin line depicts the IP and the contributing transitions are summarized in tab. 8.3 based on the ground state of the neutral atom.

B	Transition	$E^{\mathrm{em}}_{m_l,m_s}$
$B < 0.05\ B_0$	$^1S_g \rightarrow {}^2S_g(M_S = -\frac{1}{2})$	$E^{\mathrm{em}}_{0,+\frac{1}{2}} = \frac{e}{m_e}\hbar\lvert\boldsymbol{B}\rvert$
	$^1S_g \rightarrow {}^2S_g(M_S = +\frac{1}{2})$	$E^{\mathrm{em}}_{0,-\frac{1}{2}} = 0$
$B > 0.05\ B_0$	$^3P_u(M_S = -1) \rightarrow {}^2S_g(M_S = -\frac{1}{2})$	$E^{\mathrm{em}}_{-1,-\frac{1}{2}} = 0$

Table 8.3: Transitions for the IP of the Ca atom in different magnetic fields and the energy of the emitted electron. For $B < 0.05\ B_0$, emitting either the α or the β electron results in the same IP.

The behaviour of the atomic states is similar to those of Mg for weaker field. The $^3\Pi_u^-$ state (continuous blue) becomes the ground state at around $B = 0.05\ B_0$, a weaker field, compared to the lighter Mg. Considering the Be results from ref. [203] as well, it can be said that the change of the ground state occurs more or less for the same strength of the magnetic field, without an obvious trend. In addition for Ca, the $^3\Pi_u^-$ state shows a discontinuity hinting at an avoided crossing at around $B = 0.4\ B_0$. Indeed, this feature seems to be independent of the method used, as it is present in additional preliminary calculations, where the state was targeted via SF-EOM-CC starting from $^1\Sigma_g$. The behaviour is attributed to an acquired multiconfigurational character of the state, as a strong mixing with the configuration $[\mathrm{Ar}]4d^1_{-1}4p^1_0$ is observed in field. This configuration contributes to the excited ^3F_u and ^3D_u states in the absence of field, but due to the symmetry reduction, the $^3\Pi_u^-$ components of these states are allowed to mix. Nonetheless, the SF-EOM-CC approach does not offer an improvement and targeting the $^3\Pi_u^-$ state as a reference CCSD or CCSD(T)(a) rather than at the SF-EOM-CC level is deemed more favourable. In order, however, to acquire more trustworthy results for the behaviour of this state, all three mixing states should be targeted. This is however not feasible with the current approach because of the strong double-excitation contributions, the size of the system and the need for triple inclusion at the CCSDT level. A double EA (DEA)-EOM-CC or a

multireference approach would be better suited for this system. The cationic $^2\Pi_u^-$ state is, nonetheless, unaffected by this "strange" behaviour of the reference state. As for the $^1\Sigma_g$ state (continuous orange), it is being destabilised in the presence of field, and becomes higher in energy than the cationic states around 0.25-0.3 B_0. Regarding the cationic states (dashed orange and blue), they are affected by the diamagnetic influence more compared to Mg^+ due to the increased size of the Ca atom. This is shown by the destabilisation of the states for magnetic fields stronger than 0.15 B_0. Unlike in the Mg^+ case, the $^2\Pi_u^-$ state (dashed blue) is not found lower in energy than the $^2\Sigma_g$ state (dashed orange) in the magnetic-field range studied here.

The ionization energies as functions of the magnetic field are shown in fig. 8.6. The behaviour is similar to the lighter Mg, with a qualitative difference arising from the feature of the $^3\Pi_u^-$ state for $B \geq 0.4$ B_0. Between 0.15 and 0.4 B_0, the ionization energies with $^3\Pi_u^-$ as the initial state are relatively constant in ascending magnetic field. The ionization energies starting from $^1\Sigma_g$ both are found to decrease in energy when increasing the magnetic-field strength for a field stronger than 0.15 B_0. It is also important to note, that relativistic effects (both scalar and spin-orbit coupling) are expected to be significant for Ca compared to the lighter elements, which were, however, not considered in this study.

In the field free case, the IP calculated at the CCSD(T)(a)* level has a value of 0.222936 E_h = 6.06640 eV, in good agreement with the experimental 6.11315547 eV ± 0.00000025 eV.[51] The inclusion of triples is more important for this system. This is indicated by the large deviation of the CCSD(T)(a)* results compared to CCSD, which is found to be at the order of 10^{-2} E_h for the energies, dropping to 10^{-3} E_h for the IPs. This deviation is one order of magnitude larger than for the metals of the previous row.

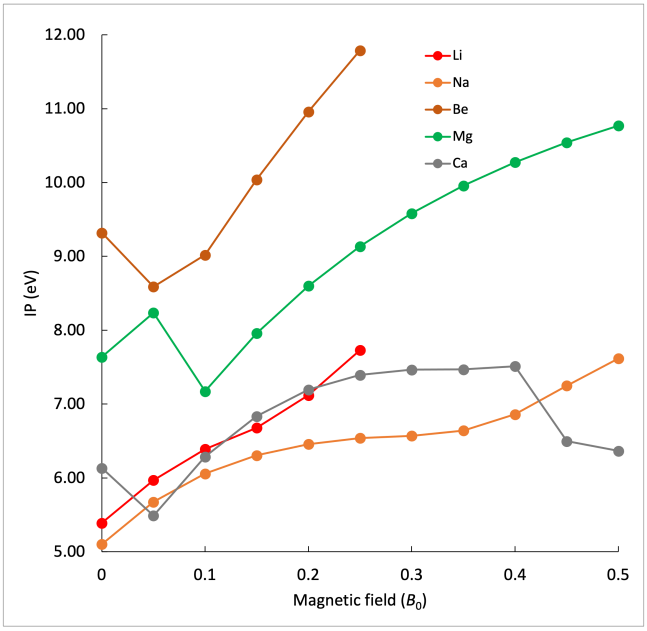

Figure 8.7: The IPs of Li,[203] Be,[203] Na, Mg and Ca at the CCSD level of theory.

To achieve a deeper understanding of the physics taking place regarding the ionization potentials of the studied atoms, the findings in this study are compared to those of ref. [203] for the Li and Be atom in more detail. The IPs are plotted as a function of the magnetic-field strength in fig. 8.7. As previously mentioned, the comparison between Li and Na shows that the change of the Na ground state takes place in stronger fields compared to Li, and moreover, the 3d orbitals, which are much higher in energy for Li, play an important role. Comparison of the Be with Mg and Ca, shows that the qualitative behaviour of Be is mostly similar to the behaviour of Mg and Ca. The change of the ground state occurs more or less at the same magnetic-field strength around 0.05 B_0. For this reason, the low-lying triplet state of the alkali earths may be important in the study of MWD even in weaker magnetic fields. In addition, the study of Ca shows that for this system, the multiconfigurational character of the triplet state lowest in energy in stronger fields leads to a qualitative different behaviour that needs

further investigation. In ref. [203], it is reported that the IPs of the atoms studied show a near linear dependence to the magnetic-field strength. This is because the driving mechanism behind the response is the paramagnetic term. This is however not the case for the larger atoms. The increased size of the atoms in the third and fourth row of the periodic table makes the diamagnetic response of the cation relative to that of the neutral atom an important contribution to the IPs. The curves shown in fig. 8.7 for the heavier atoms deviate significantly from linearity. A general trend of the IPs being raised in energy with increasing magnetic-field strength is confirmed. Both Na and Mg are about 1.5 times more difficult to ionize in $B = 0.5\ B_0$ compared to $B = 0\ B_0$. The trend however is not universal, as for the Ca atom in stronger magnetic fields, the IP is found relative constant for fields stronger than $0.3\ B_0$. Not taking the abrupt decrease of the IP for magnetic fields stronger than $B = 0.45\ B_0$ under consideration since its physicality is not certain, Ca is more difficult to ionize by about 1 eV for $B = 0.4\ B_0$ compared to the field-free case.

In this study, the IPs for the Na, Mg and Ca give valuable insight on the relative stability of the cationic against the neutral states of the atoms and how this changes in the presence of a magnetic field. Moreover, the relative stability of different states of the neutral atoms play an important role in the study of the atmospheres of MWDs. Here the ground state for the aforementioned atoms has been investigated for different magnetic-field strengths.

8.2 Electronic excitations

As already pointed out, the assignment of spectra from MWDs cannot be done based on experimental data, because magnetic fields similar to those in the atmospheres of WDs are not reproducible on Earth. Results from theoretical predictions have to be used instead. Despite the relative simplicity of studying atomic spectra in the field-free and weak field cases, the behaviour of electronic excitations in such magnetic fields significantly deviates from a simple consideration of a Zeeman splitting and becomes chaotic because of the competing influences of the diamagnetic and paramagnetic terms.[22,59] Moreover, the direct assignment of spectra based on theoretical predictions demands the very high quality of the later. In the absence of FCI results, CC methods are employed, and more specifically, an accuracy beyond that of CCSD is demanded.[80]

An existing study for the electronic states of Na at the CCSDT level may contribute to the interpretation of MWD spectra.[80] The study of atoms is expanded in this thesis with calculations for the alkali earths Mg at the CCSD(T)(a), CC3 and CCSDT, and Ca at the CCSD(T)(a) and CC3 levels of theory. The motivation behind the study of these atoms is a collaboration with Dr. Hollands from the University of Sheffield for the interpretation of a spectrum from a WD which was believed to be magnetic. Indeed, Na and Mg absorption peaks were identified and assigned for the first time in a strongly MWD, while the assignment of Ca turned out likely but less certain. This assignment would have been impossible without ff quantum-chemical methods.[24]

8.2.1 Mg

For Mg, the ${}^3P_u([\mathrm{Ne}]3s^1 3p^1) \rightarrow {}^3S_g([\mathrm{Ne}]3s^1 4s^1)$ transition was deemed important for the assignment of spectra. It is recognized as an intense peak in the field-free case and has been used for the assignment of Mg in weakly magnetic WDs.[204] In addition, intense absorption near the position expected for this peak was observed in the WD spectrum in question with a shift of 50 Å. For these reasons, the components of the ${}^3P_u$ state together with the ${}^3S_g$ were calculated at the CC and EOM-CC levels. The triplet state lowest in energy, namely the $M_L = -1$ component of the ${}^3P_u$ state, was used as the reference state for the subsequent EOM-CC calculations. The transition was studied for a magnetic field up to $0.2\ B_0$, using a dense grid of $0.004\ B_0$ up to $B = 0.04\ B_0$, following with a sparser grid of $0.02\ B_0$. Additionally, the ${}^3P_u([\mathrm{Ne}]3s^1 3p^1) \rightarrow {}^3D_g([\mathrm{Ne}]3s^1 3d^1)$ transition was studied as well. The transition was studied up to $0.04\ B_0$ using the denser grid. Only the $M_L = -2$ and $M_L = 0$ components of the ${}^3D_g$ state were studied up to $0.2\ B_0$. The $M_L = -2$ component appears to cross with the $M_L = +1$ component of the ${}^3P_u$ state at about $0.06\ B_0$. The $M_L = 0$ component on the other hand belongs to the same IRREP in the magnetic field as the ${}^3S_g$ state (${}^3\Sigma_g$) and as a result, the

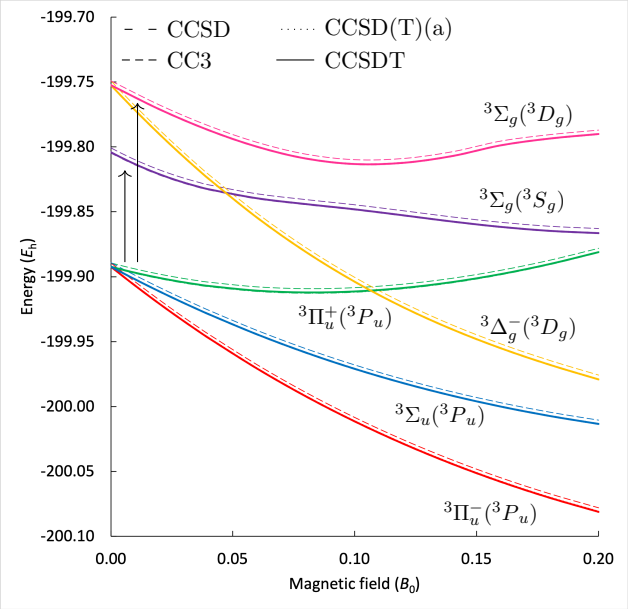

Figure 8.8: Low-lying triplet states of Mg calculated at the EOM-CCSD, EOM-CCSD(T)(a)*, EOM-CC3, and EOM-CCSDT levels of theory with unc-aug-cc-pCVTZ basis set.

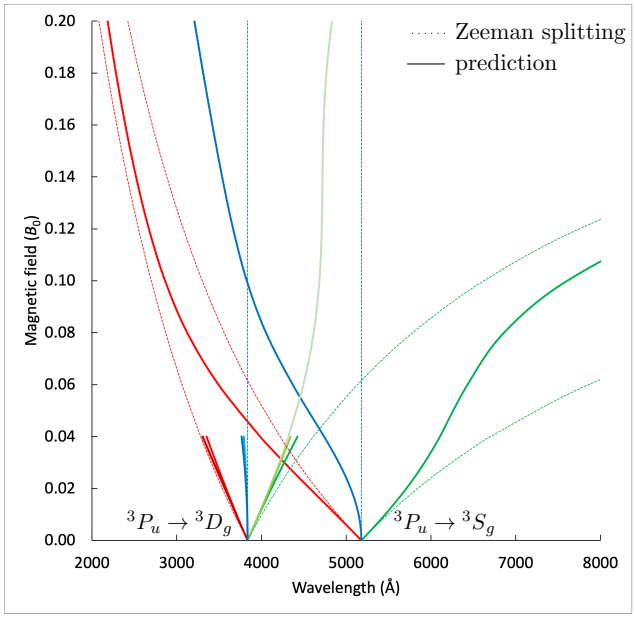

Figure 8.9: The extrapolated B-λ curves for the $^3P_u \rightarrow {}^3S_g$ and $^3P_u \rightarrow {}^3D_g$ transitions of Mg. The $\Delta M_L = 0$ components are shown in blue, the $\Delta M_L = +1$ in red and the $\Delta M_L = -1$ in green. The $^3P_u \rightarrow {}^3S_g$ transition and one component of the $^3P_u \rightarrow {}^3D_g$ have been studied up to 0.20 B_0, while the rest of the transitions has been studied only up to 0.04 B_0.

states mix leading to an avoided crossing. The basis sets used for the study were unc-aug-cc-pCVXZ, X =T, Q, 5. The results for the total energy at various levels of theory are shown in fig. 8.8

Based on the results for the total energies, an extrapolation scheme as described in ref. [80] was used to derive accurate B-λ curves

$$\Delta E_{\text{exc}}^{\text{corrected}} = \Delta E_{\text{exc}} + \Delta E_{\text{basis}} + \Delta E_{\text{triples}} \, .$$

These B-λ curves are shown in fig. 8.9. For the extrapolation, the CCSD/unc-aug-cc-pV5Z results were used for the excitation energies ΔE_{exc} and the unc-aug-cc-pCVQZ and unc-aug-cc-pCV5Z basis sets for the basis-set extrapolation ΔE_{basis}. Higher-order correlation was accounted for via triples corrections $\Delta E_{\text{triples}}$ at the CCSD(T)(a)*/unc-aug-cc-pCVQZ and CC3/unc-aug-cc-pCVQZ levels of theory giving rise to two series of predictions. Lastly, an offset correction relative to the NIST spin-averaged reference[51] is added. The agreement between the two predictions is good enough not to be visible in the scale of the plot. The selection rule $\Delta M_L = 0, \pm 1$ (0 blue, +1 red, −1 green) was used to construct visible transitions. In the figure, the results of a simple orbital-Zeeman perturbative correction were plotted as well (dotted curves), to show the importance of quantum-chemical calculations for the assignment of spectra.

As seen in fig. 8.8, the results at the CCSD level (long dashed curves) are found slightly higher in energy compared to the more accurate results, while the results that approximately account for triple excitations (CCSD(T)(a)* and CC3) are practically identical to the CCSDT results and cannot be distinguished in the plot. The calculated deviation of the approximate triples relative to the full triple inclusion is at the order of 10^{-5} E_{h}. Based on this minuscule deviation for smaller basis sets, it is deemed more useful to use approximate triple corrections with larger basis sets, rather than exact inclusion of triples with the unc-aug-cc-pCVTZ basis, as the difference between the full triples and approximate triples is not expected to change significantly with larger basis sets. Exact triples would not be feasible beyond that basis-set size for this system.

Looking at the $^3P_u([\text{Ne}]3s^1 3p^1) \rightarrow {}^3S_g([\text{Ne}]3s^1 4s^1)$ transition (5179.60 Å)[51] in fig. 8.9, the calcu-

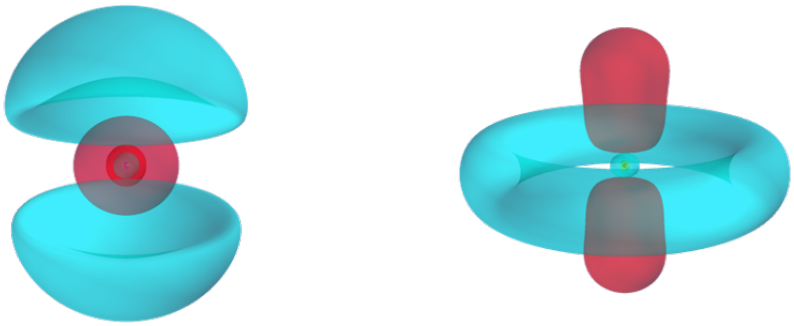

Figure 8.10: The $4\sigma_g(4s)$ (left, strongly polarized) and the $5\sigma_g(3d_0)$ (right) orbitals of Mg at 0.1 B_0.

lated offset relative to the experimental values is found at most 18 Å in the extrapolated schemes. This small offset correction justifies the use of the theoretical predictions for the interpretation of spectra. The most interesting feature in the presence of magnetic field is the deviation of the middle component ($\Delta M_L = 0$, blue) relative to the orbital-Zeeman picture, which predicts it unchanged in all field strengths. This deviation is attributed to a strong polarisation of the $4s$ orbital. The latter becomes apparent by the Mulliken population analysis of the $^3\Sigma_g(^3S_g)$ state by showing strong contributions from d_0 functions. Additionally, the analysis of the EOM-vectors for this state and the avoided crossing of with the $^3\Sigma_g(^3D_g)$ state around 0.1 B_0 further indicate this polarisation. The orbitals involved, $4\sigma_g(4s)$ and $5\sigma_g(3d_0)$ are visualized in fig. 8.10. In comparison to the case of sodium,[80,81] the phenomenon here is much more prominent even in weaker magnetic fields, because the sodium $3s$ orbital is less diffuse, and its polarization is more gradual. Based on these results, it can be deduced that $np \rightarrow (n+1)s$ transitions will have a strong deviation of the middle component because of the difference in the polarisation of different shells, while the deviation of $ns \rightarrow np$ transitions is much less significant.[24,205]

The $^3P_u([\mathrm{Ne}]3s^13p^1) \rightarrow {}^3D_g([\mathrm{Ne}]3s^13d^1)$ transition in the left part of the plot in fig. 8.9 exhibits a much larger offset correction of 350 Å relative to the spin-averaged experimental values (3836.39 Å).[51] This large deviation is attributed to the basis set, which is developed to best describe the field-free ground state of the atom ($^1S_g([\mathrm{Ne}]3s^2)$), and describes the excited $^3D_g([\mathrm{Ne}]3s^13d^1)$ state with $L = 2$ less accurately. Nonetheless, the allowed transitions were studied and plotted up to $B = 0.04$ B_0. Each ΔM_L transition is triply degenerate when only the orbital-Zeeman splitting is considered. The $^3\Pi_u^- \rightarrow {}^3\Delta_g^-$ component was studied up to $B = 0.2$ B_0. The middle component ($\Delta M_L = 0$ blue) splits in one non-degenerate ($^3\Sigma_u^- \rightarrow {}^3\Sigma_g^-$) and one doubly degenerate ($^3\Pi_u^- \rightarrow {}^3\Pi_g^-$ and $^3\Pi_u^+ \rightarrow {}^3\Pi_g^+$) transition when considering both the paramagnetic and diamagnetic terms. The other components exhibit no degeneracy in the ff calculation (for the $\Delta M_L = -1$ green-shaded curves for example, all transition $^3\Pi_u^+ \rightarrow {}^3\Sigma_g$, $^3\Sigma_u \rightarrow {}^3\Pi_g^-$ and $^3\Pi_u^- \rightarrow {}^3\Delta_g^-$ are qualitatively different). The deviation from the orbital-Zeeman splitting is smaller for this transition relative to the $^3P_u \rightarrow {}^3S_g$ transition, but still non-trivial. Most important for the assignment of spectra is that the green curves arising from $^3P_u \rightarrow {}^3D_g$ transition cross the red ones arising from the $^3P_u \rightarrow {}^3S_g$ transition, as this might make the identification of a $\Delta M_L = +1$ component in the spectrum difficult.

The transition-dipole moments were also calculated at the expectation-value EOM-CCSD level of theory to give an indication on the relative intensity of the peaks and its behaviour as a function of the magnetic field strength. The absolute square of the transition moments is needed for the calculation of the oscillator strength $f = \frac{2}{3}|\boldsymbol{\mu}_{fi}|^2 (E_f - E_i)$, which directly expresses the absorption/emission probability. For the three components of the $^3P_u \rightarrow {}^3S_g$ transition, $|\boldsymbol{\mu}_{fi}|^2$ is calculated at 2.3 a.u.. The $\Delta M_L = \pm 1$ components of this transition become less intense with stronger magnetic field, with a practical zero transition probability for fields stronger than 0.16 B_0. The $|\boldsymbol{\mu}_{fi}|^2$ value of the $\Delta M_L = 0$ component on the other hand increases up to 0.12 B_0 and remains relatively constant at $|\boldsymbol{\mu}_{fi}|^2 = 5.6$ a.u. for stronger fields. As for the $^3P_u \rightarrow {}^3D_g$ transition, each component has a significantly different intensity. The $|\boldsymbol{\mu}_{fi}|^2$ values nonetheless remain relative constant in the magnetic fields studied. The most intense is the $|M_L| = 1 \rightarrow |M_L| = 2$ transition with $|\boldsymbol{\mu}_{fi}|^2 = 6.5$ a.u.,

followed by the $|M_L| = 1 \rightarrow |M_L| = 1$ and $|M_L| = 0 \rightarrow |M_L| = 1$ transition ($|\boldsymbol{\mu}_{fi}|^2 = 3.2$ a.u.). The $|M_L| = 1 \rightarrow |M_L| = 0$ transition is the least intense with $|\boldsymbol{\mu}_{fi}|^2 = 1.1$ a.u.

The calculations presented here contributed to the assignment of Mg in the spectrum of a magnetised WD,[24] which would have not been possible without ff quantum-chemical calculations. The assignment is presented in sec. 8.3.

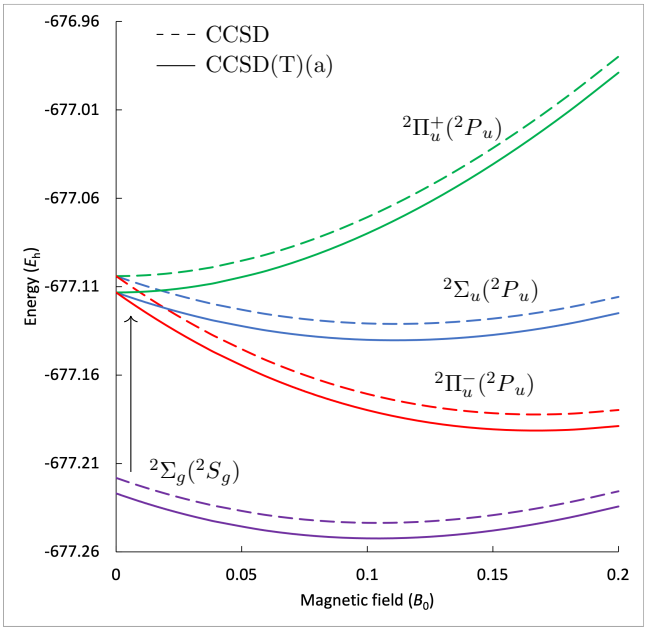

Figure 8.11: The ^2S_g and ^2P_u states of the Ca^+ cation calculated at the EA-EOM-CCSD and EE-EOM-CCSD(T)(a)* levels of theory with the unc-aug-cc-pCVQZ basis set.

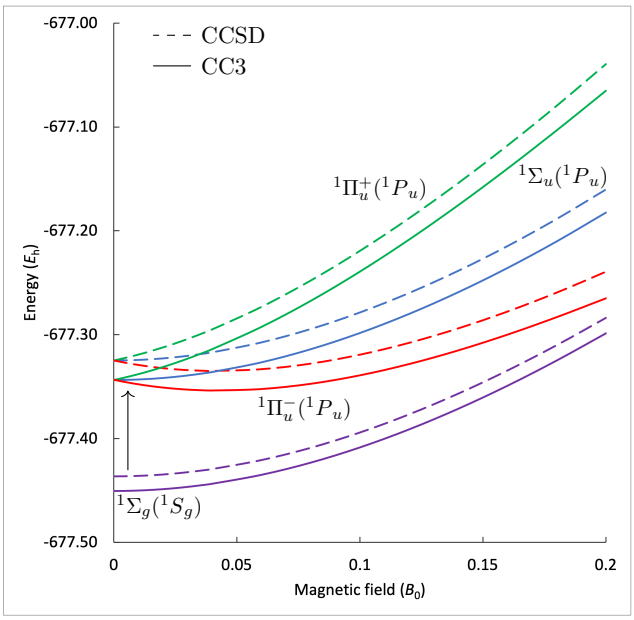

Figure 8.12: Low-lying singlet states of Ca calculated at the EE-EOM-CCSD and EE-EOM-CC3 levels with unc-aug-cc-pCVQZ basis set.

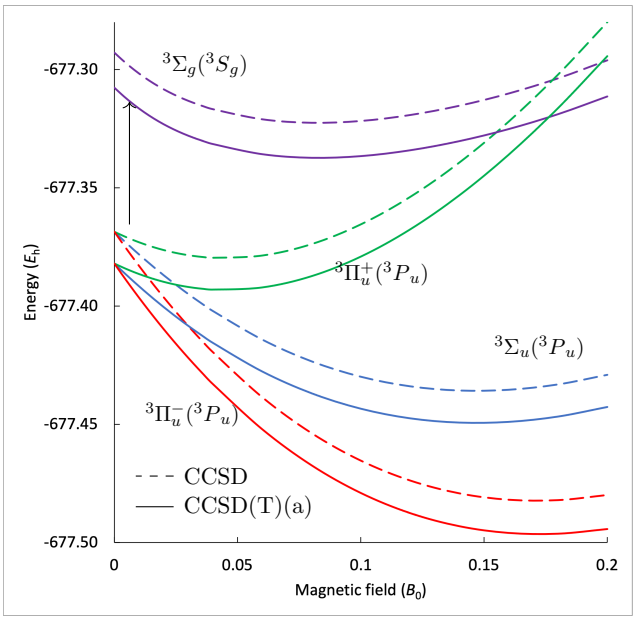

Figure 8.13: Low-lying triplet states of Ca calculated at the SF-EOM-CCSDand SF-EOM-CCSD(T)(a)* levels with unc-aug-cc-pCVQZ basis set.

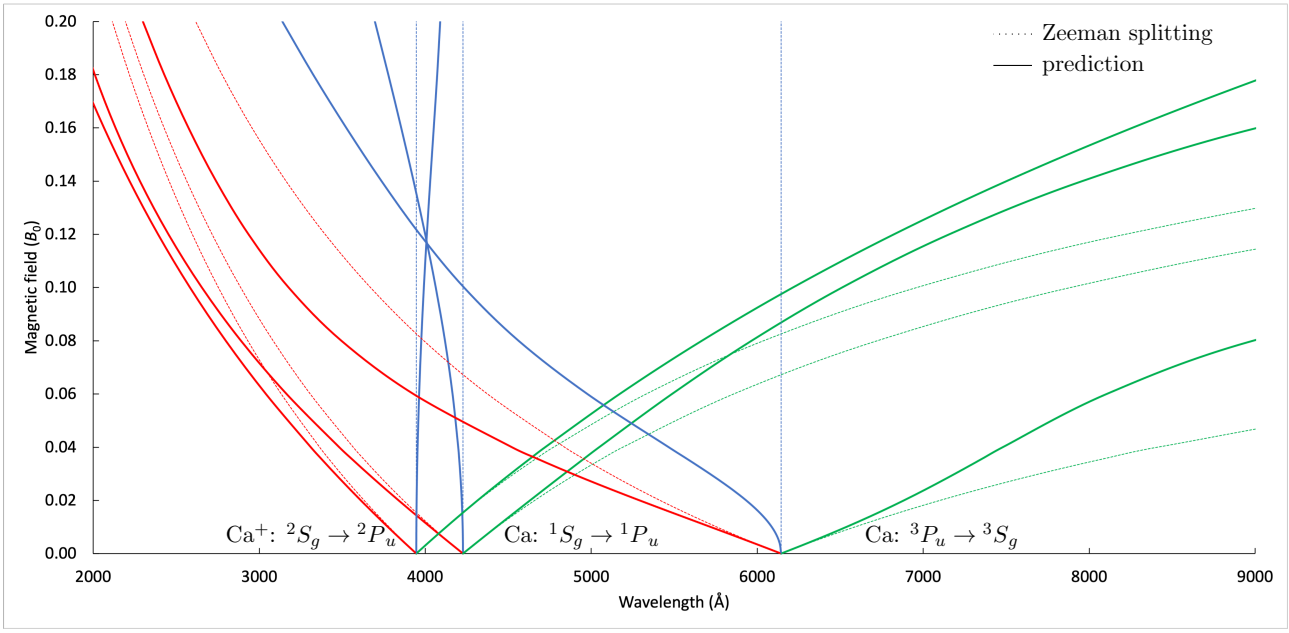

Figure 8.14: The extrapolated B-λ curves for the $^2S_g \rightarrow {}^2P_u$ transition of Ca^+ and the $^1S_g \rightarrow {}^1P_u$ and $^3P_u \rightarrow {}^3S_g$ transitions of Ca. The dotted lines are the results of a simple orbital-Zeeman splitting. The $\Delta M_L = 0$ components are shown in blue, the $\Delta M_L = +1$ in red and the $\Delta M_L = -1$ in green.

8.2.2 Ca

For the Ca atom, basis sets of unc-aug-cc-pCVXZ quality were generated for $X = \mathrm{T}, \mathrm{Q}, 5$. Up to $X = \mathrm{T}$ the standard procedure is used. For $X = 5$, the cc-pCV5Z was used as starting point and diffuse functions were added. Diffuse s and p functions were generated by using the existing most diffuse functions of the same angular-momentum number and extrapolating the next even-tempered function. For higher angular-momentum functions the existing most diffuse exponents were divided by 1.5 to generate the diffuse function.

The transitions that were targeted were $^2S_g([\mathrm{Ar}]4\mathrm{s}^1) \rightarrow {}^2P_u([\mathrm{Ar}]4\mathrm{p}^1)$ for the cation Ca^+ with an experimental spin-averaged value of 3946.31 Å, $^1S_g([\mathrm{Ar}]4\mathrm{s}^2) \rightarrow {}^1P_u([\mathrm{Ar}]4\mathrm{s}^1 4\mathrm{p}^1)$ for the neutral atom with an experimental spin-averaged value of 4227.92 Å and $^3P_u([\mathrm{Ar}]4s^1 4p^1) \rightarrow {}^3S_g([\mathrm{Ar}]4s^1 5s^1)$ with an experimental spin-averaged value of 6143.86 Å.[51] These are characteristic absorption signatures for Ca with high intensity, which are used for the identification of Ca in WD spectra.[204] In addition, absorption peaks in the vicinity of these transitions were observed in aforementioned WD spectrum, although in a rather noisy part of it.

For the transitions of the cation Ca^+ ($^2S_g \rightarrow {}^2P_u$), the reference excitation energies for the extrapolation scheme ΔE_{exc} were calculated at the EA-EOM-CCSD level using the unc-aug-cc-pCV5Z basis starting from the closed-shell ground state of Ca^{2+} $^1S_g([\mathrm{Ar}])$. The basis-set extrapolation $\Delta E_{\mathrm{basis}}$ was performed using the unc-aug-cc-pCV5Z and unc-aug-cc-pCVQZ basis sets. Triple corrections were calculated at the EE-EOM-CCSD(T)(a)* level. For the triple corrections $\Delta E_{\mathrm{triples}}$, a different EOM-approach was used. Results with approximate triples were generated at the EE-EOM-CCSD(T)(a)* level of theory using the $M_L = 0$ component of the excited $^2D_g([\mathrm{Ar}]3\mathrm{d}^1_0)$ state of Ca^+ as reference state, because this state was accessible at the SCF level. In this approach, both initial (^2S_g) and final (^2P_u) states were calculated as EE-EOM-CC states. The EA-EOM-CCSD/unc-aug-cc-pCVQZ and EE-EOM-CCSD(T)(a)*/unc-aug-cc-pCVQZ results are shown in fig. 8.11. In the calculations, the $^2D_g([\mathrm{Ar}]4\mathrm{d}^1)$ state was found to lie energetically between the field-free ground ^2S_g and excited ^2P_u states, which is confirmed by experimental results.[51]

As for the transitions of the neutral atom Ca, the components of the ^1P_u were targeted using an EE-EOM-CC approach starting from the field-free ground state reference ^1S_g. For the extrapolation, the basis-set correction was calculated using the unc-aug-cc-pCVQZ and unc-aug-cc-pCV5Z basis sets at the EOM-CCSD level, and the triples correction was obtained at the EOM-CC3/unc-

aug-cc-pCVQZ level. Total energy of the singlet states as a function of the magnetic field strength at the EE-EOM-CCSD and EOM-CC3 level with the unc-auc-cc-pCVQZ can be found in fig. 8.12. The triplet states were targeted via the SF-EOM-CC approach using the same reference. The excited $^3D_g([Ar]4s^13d^1)$ state is energetically very close to the triplet state lowest in energy, ^3P_u. For this reason, the components of the $^3D_g([Ar]4s^13d^1)$ state were monitored during the calculation. Specifically, it was monitored whether the $M_L = 0$ component interferes with the final state of the transition ^3S_g as they belong to the same IRREP Σ_g in the field. As mentioned out in subsec. 8.1.3, the components of the ^3P_u state exhibit contributions from doubly-excited [Ar]$3d^13p$ configurations with respect to the reference in the presence of a magnetic field. For this reason, the inclusion of triple excitations is of particular importance in order to correctly describe the multiconfigurational character and to (approximately) account for a mild double-excitation character. Results for the triplet states at the SF-EOM-CCSD/unc-aug-cc-pCVQZ and SF-EOM-CCSD(T)(a)*/unc-aug-cc-pCVQZ levels of theory are shown in fig. 8.13. For the extrapolation, the SF-EOM-CCSD(T)(a)* results were used, using the unc-aug-cc-pCV5Z basis and unc-aug-cc-pCVQZ basis sets for the basis-set correction. Since triple excitations are already included, no further triples corrections are needed.

The extrapolated B-λ curves are shown in fig. 8.14. The offset corrections for the transitions studied are moderately small, justifying the use of the extrapolated data for predictions, with the $^2S_g \rightarrow {}^2P_u$transition of Ca^+ (3946.31 Å) at around 57 Å, around 30 Å for the atomic $^1S_g \rightarrow {}^1P_u$ transition (4227.92 Å) and around 10 Å for the $^3P_u \rightarrow {}^3S_g$ transition (6143.86 Å). The middle component of the transition of the cation shows a weak shift to longer wavelengths in the presence of the magnetic field. For the neutral singlet case on the other hand, the middle component is shifted towards shorter wavelengths with a larger absolute deviation compared to the cation. In both cases, the deviation is attributed to the diamagnetic term. The first is an $ns^1 \rightarrow np^1$ transition and as the s starting orbital is spherical, while the involved p_0 final orbital is oriented parallel to the magnetic field, the initial state is raised in energy slightly more than the final one, explaining the red shift. On the other hand in the case of the $ns^2 \rightarrow ns^1np^1$ transition, the diamagnetic interaction of the s orbital is present in both the initial and the final state. The final state is however more diffuse because of its open-shell character, thus the interaction through the diamagnetic term raises the energy more compared to the initial state, explaining the blue shift. Both $S_g \rightarrow P_u$ transitions though are $ns \rightarrow np$ transitions, and the effect is not so prominent, especially compared to the deviation of the middle component of the $^3P_u \rightarrow {}^3S_g$ transition. Being an $np \rightarrow (n+1)s$ transition, the stronger polarisation of the $(n+1)s$ orbital relative to np leads to a large shift of the middle component in the presence of the magnetic field as previously observed for the Mg $^3P_u \rightarrow {}^3S_g$ transition. Additionally, comparing the Ca and the Mg deviation for the respective excitation, the deviation is larger for Ca. The larger deviation is explained by the bigger size of the Ca atom. The difference is, nonetheless, in the same order of magnitude regarding energy differences.

The Ca and Ca^+ transitions were also considered in the study of Hollands et al.,[24] but the assignment was not conclusive. Further investigation is needed. Challenges specific to Ca have to be addressed. These include the fact that the states of Ca exhibit a slight multiconfigurational character which results in larger triple corrections compared to Na and Mg. Unfortunately, the extra shell of Ca relative to the atoms studied so far renders full CCSDT calculations not feasible for this system. It is also noteworthy to point out that the scalar-relativistic effects are more important for Ca compared to the atoms of the previous rows. Their contributions were so far only taken into consideration via the offset corrections. Hence, the field-response of scalar relativistic effects is not included in the current study, which might make a significant contributions to quantitative results especially for stronger fields. Spin-orbit effects should also be considered as they are expected to be more important for heavier elements.

8.3 The spectrum of the SDSS J114333.48+661531.83 white dwarf

[a]The physicist notation is used for the ionization states, in which roman numerals are used starting from the neutral atom as one, i.e., M I corresponds to M^0, M II corresponds to M^+, M III corresponds to M^{+2}, and so on.

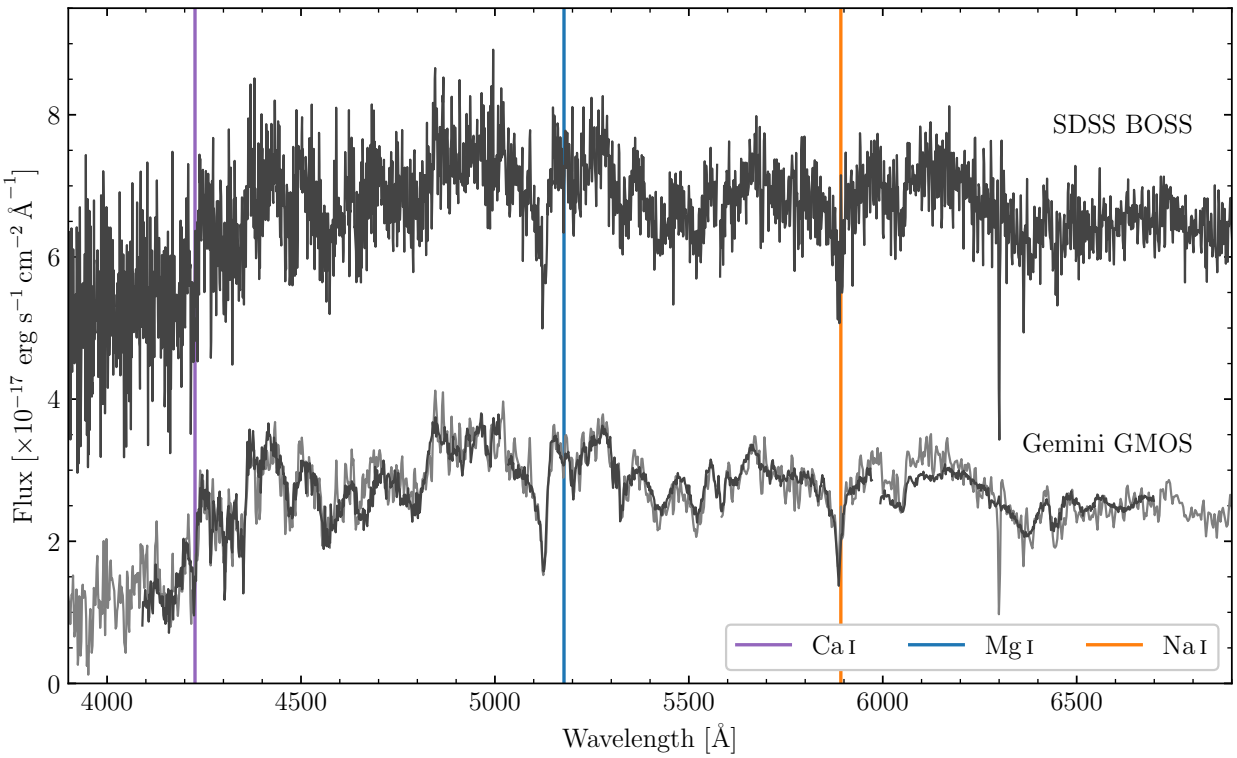

Figure 8.15: SDSS BOSS and Gemini GMOS spectra of SDSS J114333.48+661531.83 (G=20.1 mag). The SDSS spectrum is shifted upwards by 4×10^{-17} erg s^{-1} cm^{-2} Å^{-1}.[24,a]

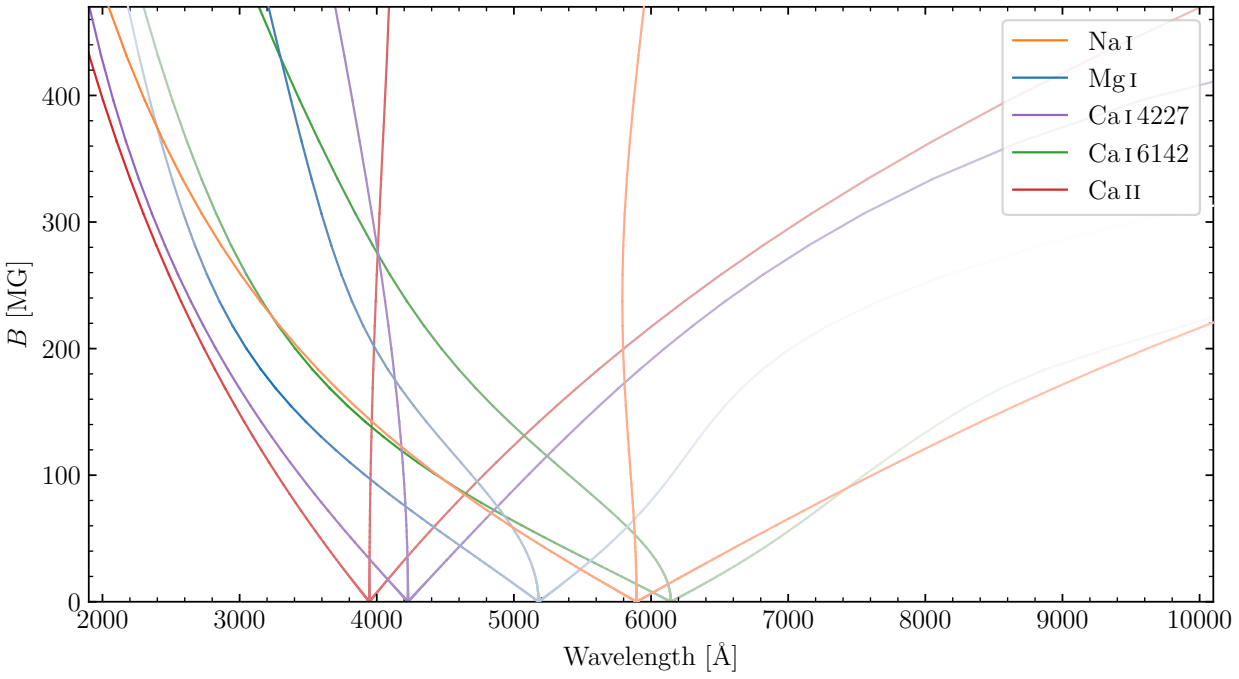

Figure 8.16: Calculated transition wavelengths as a function of field strength. The line opacities are scaled to the oscillator strengths.[24,a]

In this last section, the assignment of the spectrum from the SDSS J114333.48+661531.83 WD is presented. The celestial object can be found above the constellation of Ursa Major in the night sky (see fig. 8.20). It is nonetheless invisible to the naked eye. The spectrum of this WD observed with two different spectrographs can be seen in fig. 8.15. The field-free position of the Na $^2S_g \rightarrow {}^2P_u$,

Mg ${}^3P_u \rightarrow {}^3S_g$, and Ca Na ${}^1S_g \rightarrow {}^1P_u$ absorptions are shown as orange, blue, and purple lines, respectively. Two prominent features of the spectrum closely agree with the Na and Mg lines, however with a drastically different shift. The shift is about 5 Å for the orange line and about 50 Å for the blue. Because of this difference, the shift cannot be attributed to a Doppler effect due to the relative movement of the celestial object with respect to the spectograph. The shift for the blue line is also unexpectedly large to be attributed to a Doppler effect. For this reason, the presence of a magnetic field altering the exact location of the absorption of Mg and Na is investigated. As for Ca, the field-free transition is in an area of the spectrum with multiple absorption peaks, making the assignment difficult.

The extrapolated B-λ curves from the Na,[81] Mg, and Ca[205] studies gave rise to the plot in fig. 8.16. The opacities are scaled to the oscillator strength to give an indication on the intensity of the peaks. Zooming in on the middle components of the Na, Mg and Ca absorptions (see fig. 8.17), it is observed that, while there is a turnover for the Na transition, making both strong and weak strengths of the magnetic field compatible with the observed spectrum, this is not the case for Mg, thus setting the relevant magnetic-field strength range.

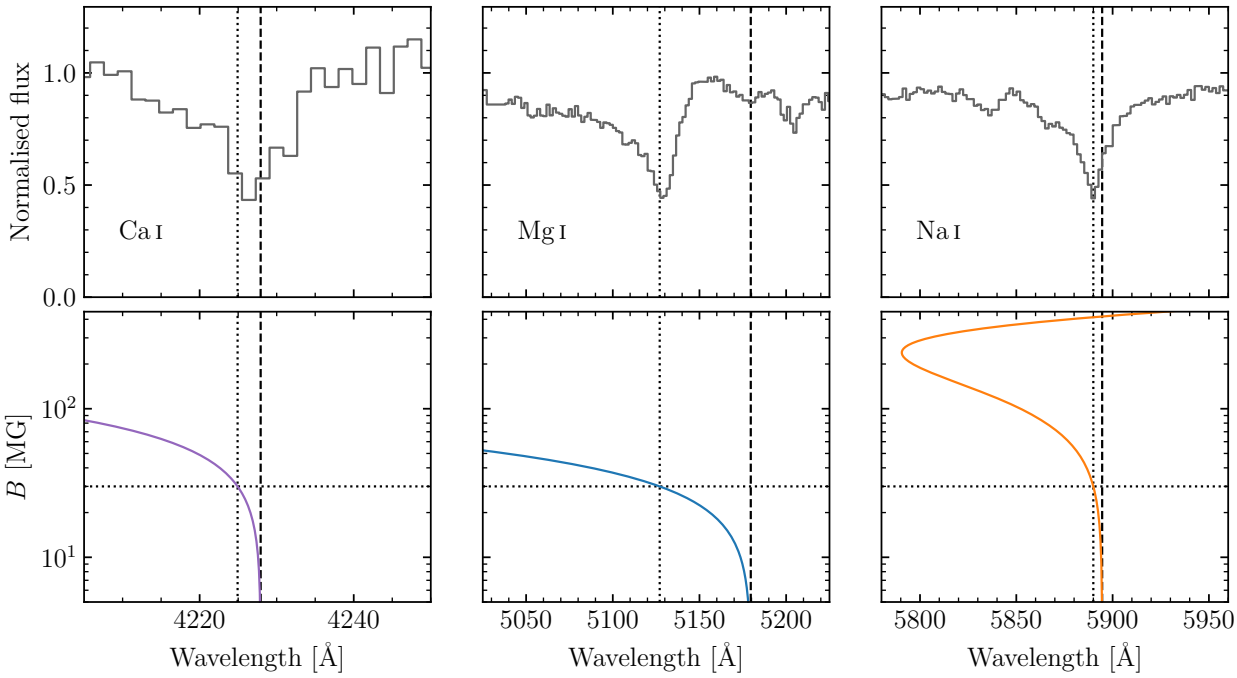

Figure 8.17: Top row: Spectral regions covering the suspected middle components of Ca, Mg, and Na. Bottom row: B-λ curves for the corresponding middle components as a function of field strength. In all panels the black dashed lines indicate the field-free vacuum wavelengths for each line, whereas the dotted lines indicate the wavelengths expected for a 30 MG field.[24,a]

Finally, combining the generated B-λ curves with the observed spectrum, a good agreement for the middle components (about 5100 Å for Mg and about 5900 Å for Na) as well as for the $\Delta M_L = \pm 1$ components (about 4800 Å and 5500 Å for Mg, about 5400 Å and 6400 Å for Na) of the transitions is found for $B = 30$ MG as seen in fig. 8.18 An offset dipole model is used to simulate the magnetic-field structure of the white dwarf. The offset dipole model is a very simple toy-model of the magnetic-field structure of the WD, which nonetheless is accurate enough for the needs of the assignment and is computationally efficient. This gives rise to the simulated absorption spectrum seen in fig. 8.19. A very good agreement of the simulated spectrum for the Na transitions shape is observed. The asymmetric feature of the middle component of Mg is attributed to neutral broadening.[24] Many of the features of the observed spectrum are still not accounted for, and the assignment of absorption peaks to Ca is unsure. Further investigation is therefore needed. Still, the assignment of the heavier elements Na and Mg to a MWD is a significant milestone, which would have been impossible without

ff quantum-chemical calculations.[24]

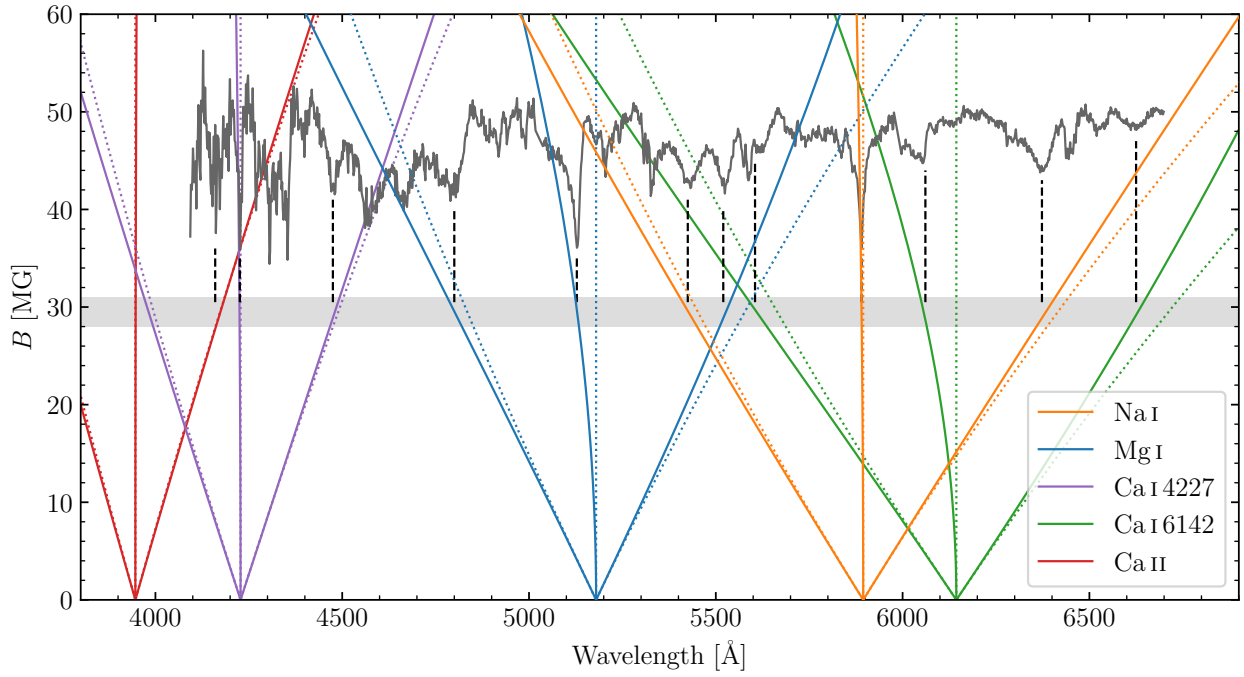

Figure 8.18: Line identification diagram for SDSS J114333.48+661531.83. Extrapolated results are shown by continuous curves, while the predictions of simple Zeeman splitting is indicated by dotted lines.[24,a]

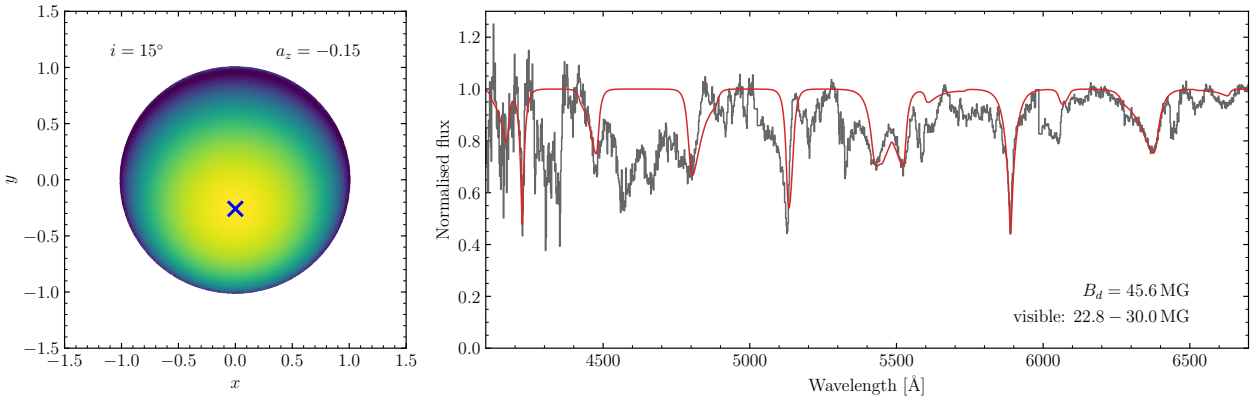

Figure 8.19: Left: Visualization of the field structure of SDSS J114333.48+661531.83 modeled with an offset-dipole. Right: The simulated absorption spectrum of SDSS J114333.48+661531.83 (red) using data from our finite-field coupled cluster calculations.[24]

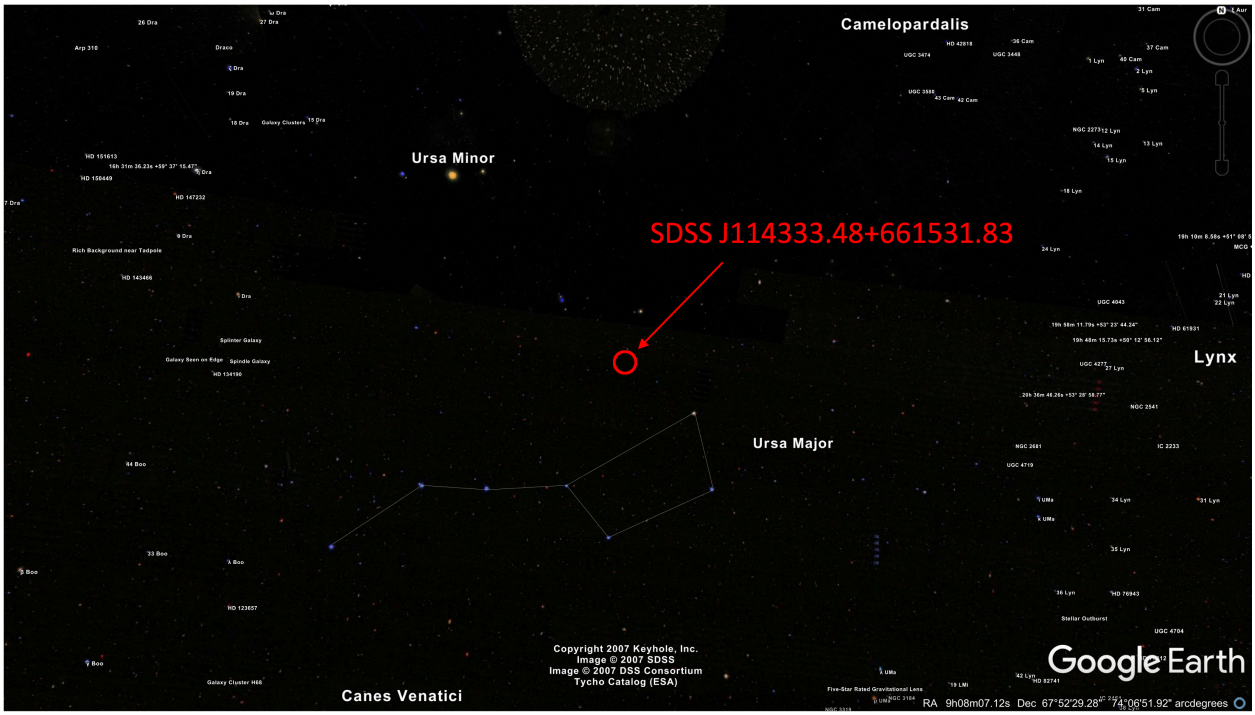

Figure 8.20: Position of the SDSS J114333.48+661531.83 WD in the night sky.

Chapter 9

Summary and Outlook

Objectives and results

The work in this thesis is a contribution to the field of finite magnetic-field methods in quantum chemistry. It mainly focuses on wavefunction methods and includes developments ranging from the calculation of integrals to correlated post-HF methods with an emphasis on Coupled-Cluster and Equation-of-Motion Coupled-Cluster theory. The two main motifs behind the present thesis are the efficiency and the utilities of ff-CC methods. The developments associated to the first motif aim to reduce the high cost of the CC methods when using complex algebra. They thus offer more affordable approaches when targeting larger molecular systems in the presence of a magnetic field and when demanding highly accurate results appropriate for the simulation and interpretation of spectra from magnetic white dwarfs in the absence of an experimental input. Contributions connected to the second motif concern the development of the necessary tools for controlling and interpreting quantum-chemical calculations, especially for targeting the complex electronic structure of atoms and molecules in the mixing regime. The thesis also presents exemplary applications that demonstrate the realization of these objectives as well as outline the potential of the newly implemented ff methods.

Under the objective of handling the high cost of ff-CC methods, the following strategies were used.

- The approximate CCn series and the EOM-CCSD(T)(a)* triples correction were generalized as ff methods and they were implemented in the QCUMBRE program. The CCn methods were developed in past decades and have been tested in the quantum-chemical literature for the study of ground and excited states. Specifically for investigations in the presence of a magnetic field, in this thesis, ff-CC2 is used to target medium-sized systems and ff-CC3 to obtain results with an accuracy beyond ff-CCSD required for the assignment of electronic excitations at a cost lower than ff-CCSDT by one order of magnitude. The relatively newly developed EOM-CCSD(T)(a)* approach was also implemented in an ff version and used for approximate non-iterative triples corrections.

  Using these methods, the CH^+ cation and CH radical were studied in the presence of a magnetic field, and the results were compared to those from the standard CCSD and CCSDT truncations. The findings for CH^+ show that CC2 may lead to unphysical results when excited states with a predominant double-excitation character relative to the reference are present since this method is unable to account for them. This is particular problematic when the double-excitation character changes in different magnetic-field strengths and travels among different states. The results also establish CC3 as a very good approximation to CCSDT for excited states with a predominant single-excitation character, and a significant improvement compared to CCSD results in the presence of a strong double-excitation character. The CH radical study served as a crash test for the methods, as the system itself was revealed to be highly demanding and complicated. The complications arise due to the multiconfigurational character of the involved states which changes in different magnetic-field strengths. None of the methods used to tackle this system were proven appropriate for the whole magnetic-field range studied. Nonetheless, the CH study confirmed and reinforced the findings for the CC2 and CC3 methods from the CH^+ cation. In addition, the SF-EOM variants were found more appropriate for the description of the CH radical

in weaker fields and for a qualitative understanding of the system, while the EE-EOM-CCSDT approach gave more trustworthy results for fields in the vicinity of 0.5 B_0 strength.

The response of the geometric parameters of CH_4 and $CH_2{=}CH_2$ for constrained orientations of the magnetic field was studied at the CC2 and CCSD levels of theory. Here, in contrast to the case of CH^+ and CH, CC2 is proven to be an adequate approximation to CCSD. A subsequent EOM-CC study at the optimized geometry was carried out at the same levels of theory. Because of the absence of a predominant doubly-excited character in the studied states, the deviation of the CC2 results from CCSD is approximately constant in the magnetic fields studied and all physical trends could be reproduced.

Lastly, the pyrrole molecule was studied for a magnetic field perpendicular to the molecular plane using the field-free optimized geometry. The closed-shell state, which is the ground state in the absence of a magnetic field, was targeted at the CC2 and CCSD levels of theory. The low-lying singlet and triplet excited states were studied using the EOM-CC approach. The pyrrole study was an application of the CC2 method on a medium-sized system in the presence of a magnetic field followed by a comparison to CCSD. CC2 results reproduce the CCSD behaviour here as well.

- The exploitation of symmetry using point-group theory was implemented in the QCUMBRE program package and essential developments regarding the handling of symmetry were carried out in the CFOUR program. While symmetry exploitation in general is a widely-used approach to lower the computational cost without making any approximation, symmetry implementations only use real Abelian point groups in most cases. In the presence of a magnetic field, the symmetry of the molecules studied is very often described by complex Abelian groups. This fact in combination with the need for complex wavefunctions makes the use of complex Abelian groups more profitable compared to the field-free case. As such, the double-coset decomposition for the calculation of integrals over SAOs in the case of complex Abelian groups was developed in this thesis and implemented in CFOUR. Additionally, the block structure and the use of the vanishing-integral rule were implemented in QCUMBRE for both real and complex Abelian groups in order to reduce the cost of ff calculations at the correlated level of theory. The implementation was designed to suite the needs and the existing structure of QCUMBRE.

  The observed rise in efficiency was demonstrated through the calculation of small molecular systems (methane, planar methane, ethane, and allene) in the presence of a magnetic field at the CCSD level of theory. The duration of the different processes was compared among calculation with no exploitation of symmetry, the use of only real Abelian point groups, and the use of complex Abelian point groups.

  Lastly, in order to further investigate the merits of using complex Abelian point groups, the low-lying singlet electronic states of the $B(OH)_3$. Specifically, the $E'_{1,2}$ and $E''_{1,2}$ excitations cannot be targeted at the EOM-CC level of theory without the use of complex algebra even in the absence of a magnetic field and the symmetry exploitation significantly aids such a calculation. The study also served as an investigation on the extent of the non-physicality of the complex energy artifacts of the CC methods, which are present even in the absence of a magnetic field for this system and arise from the non-Hermiticity of the CC formulation. The system was studied at the CISD, CCSD, CCSD(T)(a)*, and CC3 levels of theory. The imaginary part of the energies is typically reduced when triple corrections are included and the overall behaviour is judged mostly physical despite the complex energy eigenvalues.

To achieve a rigorous and appropriate analysis in a quantum-chemical study of atoms and molecules in the presence of a magnetic field, the following tools were developed and implemented.

- Various interpretational tools were implemented with special focus on the visualization of orbitals and the calculation of the spin multiplicity.

  → The visualization of complex-valued orbitals was realized by the development of the COrbit19 visualization program. Despite the existence of other visualization programs that are

able to handle complex-valued orbitals, they are limited in number and they often have a different focus, or are incompatible with CFOUR and QCUMBRE. The COrbit19 program is an addition to the limited number of visualization programs suitable for complex-valued orbitals and is designed to exactly fulfil the needs of studying the chemistry in the mixing regime. The visualization of the valence and low-lying virtual orbitals of the CH_4 and CH_2=CH_2 molecules using COrbit19 contributed to the analysis of the electronic structure of these molecules in the presence of a magnetic field.

→ The calculation of the spin multiplicity via the expectation value of the spin-squared operator contributes not only to the characterisation of the calculated states (singlet, doublet, triplet, etc.), but also serves as a diagnostic tool for spin-unrestricted calculations estimating the quality of the results through the extent of spin-contamination. Here, a novel implementation was developed for a low-cost calculation of the multiplicity of EOM-CC states when using a closed-shell reference, in order to correctly target states of a specific spin-multiplicity during an EOM-CC calculation. Existing approaches used by other quantum-chemical programs are not suitable for complex-valued wavefunctions. The study of the CH radical benefited significantly through the calculated spin-multiplicity and spin-contamination at the EOM-CCSD level of theory as well.

- The implementation of symmetry contributed to the flexibility and control over a quantum-chemical calculation. This is achieved by giving control to the user to choose the occupation of the reference determinant at the SCF level during a calculation with the CFOUR program. Additionally, excited states can also now be targeted based on their IRREP in a QCUMBRE calculation. Both options massively accelerated and simplified the quantum-chemical analysis of the electronic wavefunctions and it is important to note that CFOUR and QCUMBRE are currently the only programs able to handle symmetry using both real and complex Abelian point groups for quantum-chemical calculations in the presence of a magnetic field.

- The development of a geometry-optimization algorithm based on internal coordinates able to function in the presence of a magnetic field was necessary, as such an algorithm was missing for the study of molecules in the presence of magnetic fields. The newly developed algorithm is able not only to perform totally unconstrained optimizations, but also to introduce constraints regarding the internal and rotational degrees of freedom. The latter are of importance in the presence of a magnetic field as they describe the relative orientation of the molecule to the magnetic field. The optimization algorithms used by other programs in the case of ff quantum-chemical calculations are not as rigorous and they are unable to introduce constraints easily in a user-friendly way. The algorithm was implemented in the existing optimizer in CFOUR and, as such, is as intuitive as in the field-free case. Through the interface to QCUMBRE, geometry optimization at the correlated level are available for ff methods as well.

  This geometry-optimization algorithm was used to study the H_2O and CH_4 molecules in a magnetic field. Specifically, the stability of the molecules and their fragments, as well as their geometry relaxation and the preferred orientation relative to the magnetic field for different magnetic field strengths were studied at the CCSD level of theory. This led to an extended investigation that firstly tested the applicability of the geometry optimization algorithm and secondly gave valuable insight on the ground state and ground-state geometry of these molecules under the extreme conditions of the atmospheres of magnetic white dwarfs.

The realization of these objectives lead to the successful assignment of Na and Mg lines in a magnetic white-dwarf spectrum. This was achieved by studying the ionization potentials and electronic excitations of the metal atoms Na, Mg, and Ca in different magnetic-field strengths. The ionization potentials offer a picture on the oxidation and electronic state of the atoms in the presence of a magnetic field, while the electronic excitation can directly be used to simulate a spectrum. Specifically in this thesis, the Na, Mg and Ca atoms were studied at the CCSD and CCSD(T)(a)* levels for the evolution of the IPs in the presence of a magnetic field, using different EOM variants, namely IP, EA, and SF. Despite the relative simplicity of the atomic compared to the molecular electronic structure, the

behaviour of the different atomic and cationic states in a magnetic field is not trivial. Especially for the larger Ca atom, triple corrections play a more important role, and the low-lying states acquire multiconfigurational character. This arises because of the symmetry reduction in the presence of a magnetic field. In addition, electronic excitations of Mg, Ca and Ca^+ were targeted using large basis sets and approximate triples corrections at the CCSD(T)(a)* and CC3 levels of theory. These results in combination with an extrapolation scheme lead to the generation B-λ curves that are typically used for the analysis of spectra from magnetic white dwarfs. The assignment of Na and Mg in a strongly MWD spectrum would not have been possible without the use of the ff quantum-chemical toolkit.

Outlook

The investigations presented in this work assert and reveal existing and future challenges. The development of a "chemical intuition" for the mixing regime of the magnetic field is still in very early stages, despite active investigation for over a decade. Moreover, a generalization of theories and methodologies to the complex plane and to a non-perturbative inclusion of the magnetic field is seldom trivial and requires significant investment in theory development and implementation.

As has been highlighted throughout the present thesis, the chemistry in the mixing regime is drastically different compared to the chemistry on Earth. Studying it only using a theoretical approach in the absence of experimental data is akin to blindly looking for a switch in an unknown dark room. Scientific investigations can only go forth using our familiar chemistry as a starting point, despite knowing that it is in most cases inappropriate. Given the limited understanding of this exotic chemistry, searching for molecular species in the atmospheres of white dwarfs, as well as investigating their stability and geometry relies on serendipity, similar to the historical discovery of drugs "by chance". Numerous exploratory computational projects searching for exotic molecules in the mixing regime raise the chances for a serendipitous discovery. Such projects would likely be based on low-cost approaches (DFT, MP2, MCSCF, etc.) together with a robust geometry-optimization algorithm to test for exotic molecular species. Such species might later be confirmed and studied further using more accurate approaches (FCI, MRCI, CC, etc.). The contributions in this thesis indeed make such searches easier by the development of a geometry-optimization algorithm applicable in the presence of a magnetic field that is based on internal coordinates. Internal coordinates are more appropriate for chemical problems and familiar to computational chemists. Additionally, the applicability of highly-accurate ff-CC methods is extended by the developments in this thesis. Relying on the serendipitous discovery is currently a viable first-line approach, but there is room for improvement regarding its efficiency. In parallel, attempts should be made to light a match in the dark room by expanding our understanding of the mixing regime. This will conceivably involve the study of known bound species in the presence of a strong magnetic field in more detail, thus expanding on the "chemical intuition" in these extreme conditions. The development of various interpretational tools certainly contributes to this goal. The study of chemistry in the mixing regime could then go on using such an expanded understanding, similar to a screening protocol in modern drug discovery, by enabling the generation of better informed guesses.

The prediction of the paramagnetic bonding[18] has fascinated scientists in the field. The paramagnetic interaction is observed using theoretical approaches in field strengths dominating on magnetic white dwarfs. Nevertheless, systems bound in the chemical sense as a result of paramagnetic bonding have only been predicted for stronger fields.[a] One of the goals of investigating the mixing regime is to find species that would exhibit such a bonding situation in weaker magnetic fields as it would open the way for their experimental detection. Ideally, the prediction and discovery of a model paramagnetically-bound system in magnetic-field strengths reproducible on Earth would allow a more careful study by means beyond the theoretical approach.

It is further important to note that until today no molecule has indeed been detected in a strongly magnetic white dwarf, despite strong indications for their existence. Even molecular species that have been theoretically predicted have not been experimentally confirmed. This lack of proof is likely attributed at least partly if not fully to the lack of simulated molecular electronic spectra. The relative

[a] Paramagnetic bonding for the triplet state of H_2 and for the fan-like structure of CH_4[57] takes place for magnetic fields stronger than 0.6 B_0.

simplicity of atoms compared to molecules has enabled an accurate simulation of atomic spectra through the generation of B-λ curves. For molecules, however, the complexity arising from their electronic and nuclear structure introduces many more variables to the problem at hand, making such a simulation immensely more complex. First steps have been attempted for tackling rovibrational and electronic spectra of molecules in strong magnetic fields,[206–208] but a full prediction that could be used directly by astronomers is still lacking. Simulated electronic spectra would indeed be very valuable for comparison with astronomical observations and for the subsequent assignment of spectral lines and magnetic-field strength. The corresponding simulations are difficult not only in the presence of a magnetic field but in the field-free case as well. The state-of-the-art methods available for the field-free case (ab-initio MD, QM-MM, Franck-Condon coefficients, etc.) require specialized training and are not readily applicable to a wide range of problems. Two additional obstacles still exist for ff methods: The first obstacle is the increased complexity of the electronic structure as compared to the field-free case. The existing ff-methodology toolkit, even with the contributions from the present thesis, still cannot solve the electronic problem in the presence of a magnetic field in a black-box manner in most cases. The "simple" case of the CH radical targeted in this thesis is such an example. The development of ff-multireference techniques to consistently capture the static correlation in such systems would be an important step. The inclusion of dynamical correlation for multireference methods poses an even more general challenge. Efficiency, simplicity, rigorous-error control and high accuracy are desired properties of a computational protocol. Nonetheless, no existing quantum-chemical method possesses all four properties. Addressing this challenge at least partially is much wanted, especially in the study of the mixing regime. Conceptualising ff-methods that couple the electronic transitions to the nuclear motion beyond the ultrafast scope poses the second challenge. The Franck-Condon principle[209] for example is formulated to target this vibronic problem in the absence of a magnetic field. In the presence of a magnetic field, however, rotational invariance dictates that the rotational motion needs to be included in this treatment. Moreover, it would be of importance to consider the atmospheric models used by astrophysicists in the simulation of electronic spectra.

The developments in ff-CC theory carried out in this thesis were readily applied to study the spectra of magnetic white dwarfs and the mixing regime in general. This is however not the only application, and there exist numerous uses of ff quantum-chemical techniques in less exotic situations, like the study of magnetic circular dichroism.[11,12] It has also been suggested that phenomena taking place in strong magnetic fields may be relevant for specific systems in the weaker magnetic-field regime, including the magnetic properties of nanostructures, the behaviour of highly excited Rydberg states, quantum dots, etc.[4–6,19] Exploring these systems may not only aid the study of the chemistry in the mixing regime, which is relevant to the thematic of the presence thesis, as they could be used as analogues in less exotic conditions. This kind of exploration directly contributes to the challenges of Earth-bound chemistry.

Progress in the field of ff quantum chemistry for the study of the mixing regime has until now relied on the generalization of existing quantum-chemical tools to the complex plane and the non-pertubative treatment of the magnetic field. Future research could also benefit by expanding the methodology to strategies that do not necessarily originate from field-free quantum chemistry. The "puzzles" to "solve" are in many cases either drastically different from those of conventional quantum chemistry or unique to the complexities of the magnetic-field. For this reason, it is vital that new independent ideas to address these challenges are produced and tested in order to bridge the gap arising from the absence of an easily controllable and flexible model system for the mixing regime.

Appendix A

Further interpretational tools

This appendix includes the theory of further interpretational tools implemented in this thesis, that only helped indirectly to the analysis of the results.

The one- and two-body reduced density matrices [eq. (2.7.16)] are used to calculate the contribution of correlation to properties. More generally, the density matrices ρ_{qp} and P_{rspq} can be introduced that include contributions from the reference HF as well. Their derivation follows Wick's theorem and the density matrices have reference contributions depending on the particle-hole combination. Most importantly for the one-body density, the HF contribution comes in the diagonal of the hole-hole block for canonical orbitals.

Properties that require the two-body density matrix are less often required compared to the one-body properties. Still their significance is not to be underestimated, as the two-body densities are required for the orbital relaxation seen in subsec. 2.7.3. In addition, magnetisabilites, geometric gradients, and other properties that not only affect the Hamiltonian, but affect the (London) orbitals of the basis set, require the two-body densities.

$$\rho_{qp} = (\rho_N)_{qp} + \delta_{pq\in i}$$

A property can then be then be calculated by

$$A = \sum_{pq} \rho_{qp}\chi_{pq} + \frac{1}{4}\sum_{pqrs} P_{rspq}\chi_{pqrs},$$

with χ_{pq} and χ_{pqrs}, the integrals related to property A.

The density matrices presented so far have been derived in the molecular orbital basis. For certain applications, it is sometimes handier to transform them in the basis of the atomic orbitals

$$d_{\nu\mu} = \sum_{pq} c_{\nu q}\rho_{qp}c^*_{\mu p}$$
$$D_{\rho\sigma\mu\nu} = \sum_{pqrs} c_{\rho r}c_{\sigma s}P_{rspq}c^*_{\mu p}c^*_{\nu q}.$$

The density matrices do not only function as a mathematical tool for the calculation of properties as energy derivatives. They offer hindsight on the characteristics of the wavefunction and thus on the physics of the underlying system as well.

A.1 Mulliken population analysis

It is apparent that the number of the electrons can be derived from the one-electron density

$$\sum_{pq} S_{pq}\rho_{qp} = \sum_{pp} \rho_{pp} = \sum_{\mu\nu} S_{\mu\nu}d_{\nu\mu} = N_{\text{el}}. \tag{A.1.1}$$

Associating a subset of the basis functions $\{\omega_\mu\}$ with a certain characteristic $\mathscr{F}$ ($\kappa \in \mathscr{F}$), one can identify an effective number of electrons with said characteristic

$$N_{\mathscr{F}} = \sum_{\kappa\in\mathscr{F}} \sum_{\nu} S_{\kappa\nu} d_{\nu\kappa}. \tag{A.1.2}$$

In eq. (A.1.2) the index κ runs in a subset of the basis set, while ν runs over all basis functions.

This population analysis named after Mulliken[210] can be used to appoint effective charges on atoms. For atom X, the subset of functions centred on X can be used in eq. (A.1.2) to derive the effective number of electrons N_X based on X and the atomic charge is given by

$$q_X = Z_X - N_X.$$

Using a similar tactic the number of electrons associated with type s, p, d, etc. functions, or even the number of α, or β orbitals on a certain atom or type of function can be calculated.

It is important to note that the effective electron numbers and the effective atomic charges from the Mulliken population analysis are not observables, and are rather a partitioning of the electron number N_{el} which is. Because of this, results from this analysis are rather sensitive to the basis set used, and give more information about the characteristics of the wavefunction and not about the physics of the system. For example, when calculating the number of electrons of a specific high angular momentum number function on a certain atom, negative effective electron numbers may appear. This describes then the polarisation of functions of lower angular momentum number, rather than the number of electrons with that type of character. For this reason, conclusions from Mulliken population analysis have to be carefully judged and taken with a "grain of salt".

A.2 Natural orbitals

At the HF level, the only contribution to the one-body density matrix is the reference contribution

$$\rho_{pq}^{\text{HF}} = \delta_{pq\in i}.$$

This makes the matrix diagonal in the hole-hole space with vanishing contributions from the particle space, following the definition of canonical orbitals. For correlated methods, the density matrix can also be brought in a diagonal form

$$\boldsymbol{\rho}\boldsymbol{g}^\iota = \lambda^\iota \boldsymbol{g}^\iota.$$

The eigenvectors $\boldsymbol{g}^\iota$, with elements $g_{p\iota}$ are associated with the eigenvalues λ^ι, and are assumed orthonormal. The eigenvalues can be interpreted as occupation numbers and are normally ordered in ascending order. The eigenvalues are in the range

$$0 \leq \lambda^\iota \leq 1.$$

These eigenvectors can be interpreted as a transformation of the basis to a set of orbitals where the one-electron density is diagonal. These new orbitals $|\psi_p^{\text{nat}}\rangle$ are the natural orbitals[211]

$$|\psi_p^{\text{nat}}\rangle = \sum_q g_{qp} \, |\psi_q\rangle \, .$$

In the basis of natural orbitals, one-body properties can be calculated with the help of the occupation number in a diagonal form

$$\begin{aligned} A &= \sum_{pq} \rho_{qp} \chi_{pq} \\ &= \sum_{pq} \sum_{\iota} \rho_{qp} g_{p\iota} g_{\iota q}^* \chi_{pq} \\ &= \sum_{pq} \sum_{\iota} \overbrace{g_{\iota q}^* \rho_{qp} g_{p\iota}}^{\lambda^\iota} \overbrace{g_{\iota q}^* \chi_{pq} g_{p\iota}}^{\chi_{\iota\iota}} \\ &= \sum_{\iota} \lambda^\iota \chi_{\iota\iota}. \end{aligned}$$

There exist many uses of natural orbitals for the construction of approximations, but in this work, they are used as an indication of the correlation of the system. Following from eq. (A.1.1), the sum of the occupation numbers reproduces the electron number

$$\sum_{\iota} \lambda^{\iota} = N_{\mathrm{el}}.$$

One can divide the space of natural orbital space in a mostly occupied space $\iota = [1, N_{\mathrm{el}}]$, and a mostly virtual space $\iota = [N_{\mathrm{el}} + 1, N_{\mathrm{bas}}]$, where N_{bas}, the number of the basis functions. The amount of electrons in the mostly virtual space gives an indication about the correlation of the system, as well as the shape of the orbitals that mostly contribute to it. Lastly, comparing the natural orbitals of the ground state with those of excited states gives an indication about the transition, and the occupation picture of the excited state.

A.3 Natural transition orbitals

Studying the character of an excited state at the CI and EOM-CC levels of theory is based on the excitation vector, i.e. the CI-amplitudes vector or the EOM-amplitudes vector, respectively, as a first approach. A straightforwards characterisation with regard to the level of excitation with respect to the reference state, for example, can be done by comparing the collective absolute values of the amplitudes at difference levels of excitation, thus characterising a state as predominantly singly, doubly, etc. excited. Additionally, examining the orbitals involved in the strongly contributing CI/EOM amplitudes gives further information about the qualitative character of the excited state and its orbital picture, possibly revealing or confirming an avoided crossing.[212] CI/EOM amplitudes though are strongly dependent on the choice of basis set and the reference solution, and they may even be non-unique in the case of degeneracy. It is difficult, for example, to assess the multiconfigurational character of an excited state solely based on the excitation amplitudes. The presence of multiple excitations contributing with similar amplitudes does not necessarily correlate to a multiconfiguration character, but may arise from an effective orbital relaxation or from the mere size of the system.[159] To study the orbital picture of excited states beyond this simple analysis of the excitation vectors, different approaches exists.[159,213–215] One readily used is the density difference

$$\Delta_{qp} = \rho^{f}_{qp} - \rho^{i}_{qp},$$

with the superscripts f and i denoting the final and the initial state respectively. A similar idea was presented in the previous paragraph for comparison of the natural orbitals of different states.

A different approach is to use the transition density matrices

$$\rho^{fi}_{qp} = \langle \Psi^{f} | \, \hat{a}^{\dagger}_{p} \hat{a}_{q} \, | \Psi^{i} \rangle \, .$$

For Hermitian approaches like CI, the transition density matrices are indeed Hermitian

$$\rho^{fi}_{qp} = \rho^{if*}_{pq},$$

but this is not the case for the EOM-CC approaches, where the deexcitation transition matrix is approximated as

$$\rho^{if}_{pq} \approx \rho^{fi*}_{qp}.$$

Using the one-body transition density which accounts for single excitations, a first approximation of the final state from the initial state can be derived from predominant one-electron transitions

$$|\Psi^{f}\rangle = \sum_{pq} \rho^{fi}_{qp} \hat{a}^{\dagger}_{q} \hat{a}_{p} \, |\Psi^{i}\rangle + \text{higher excitations}.$$

The natural transition orbitals are derived by a singular value decomposition of the one-body reduced density matrix

$$\boldsymbol{\rho}^{fi} = \mathbf{V} \boldsymbol{\Sigma} \mathbf{U}^{\dagger}.$$

The matrix $\mathbf{U}$ represents the orbitals from which the electrons are excited and diagonalizes the matrix

$$H_{pq} = \sum_r \rho_{rp}^{fi} \rho_{rq}^{fi*}$$
$$\mathbf{H}\mathbf{u}^\iota = \lambda^\iota \mathbf{u}^\iota,$$

while $\mathbf{V}$ represents the orbitals to which the electrons are excited and diagonalizes the matrix

$$P_{pq} = \sum_p \rho_{pr}^{fi*} \rho_{qr}^{fi}$$
$$\mathbf{P}\mathbf{v}^\iota = \lambda^\iota \mathbf{v}^\iota$$

The matrix $\mathbf{\Sigma}$ is diagonal and collects the square roots of the eigenvalues λ^ι. These values, of which usually only a few survive, are interpreted as the weights of the natural transition orbitals contributing to the excitation. The sum of the eigenvalues can be used to judge the amount of single excitation character.

Similar to the natural orbitals, the natural transition orbitals offer a picture for the excitation that is more invariant to the the choice of basis set and the reference solution, compared to simply considering the excitation vector.

A.4 Angular momentum

One of the most chemically relevant property of a molecule is the dipole moment, associated with the operator $\hat{\boldsymbol{\mu}} = (\hat{\mu}_x, \hat{\mu}_y, \hat{\mu}_z)$, since it gives important information about the polarity of the system. Transition properties are also derived using the dipole moment operator, since in the dipole approximation, the transition probability is associated to the transition dipole moment. Both dipole and transition dipole moments are directly comparable to experiments. In this work, the expectation value of the angular momentum operator is also of importance.

The angular momentum of a system may give information about the magnetisability of the system, since the angular-moment operator is involved in the magnetic field interaction (orbital Zeeman term). Most importantly though, the angular momentum is important for the study of atoms in magnetic fields, and for linear molecules in a magnetic field parallel to the molecular axis. For these two cases the magnetic quantum number, which is the angular momentum projection on the axis of the magnetic field (typically the z-axis) remains a good quantum number

$$\hat{L}_z \left|\Psi_{M_L}\right\rangle = \hbar M_L \left|\Psi_{M_L}\right\rangle .$$

$\hat{L}_z = \sum_i \hat{l}_z^i$ is the z component of the total angular momentum operator $\hat{\boldsymbol{L}} = (\hat{L}_x, \hat{L}_y, \hat{L}_z)$, and $|\Psi_{M_L}\rangle$ is a wavefunction with M_L the total magnetic quantum number.

The M_L quantum number characterizes the spectroscopic term of the state, with Σ for $M_L = 0$, Π for $M_L = \pm 1$, Δ for $M_L = \pm 2$, Γ for $M_L = \pm 3$, etc. M_L also gives rise to selection rules. Allowed transition may only change the M_L quantum number by one or not at all, $\Delta M_L = 0, \pm 1$.

It is thus important to be able to derive the M_L of a state from its wavefunction in order to characterize it. This can be achieved by calculating L_z as a property, because even in the simplest case of an expectation value (without any inclusion of wavefunction parameters relaxation), this reproduces M_L

$$L_z = \langle \tilde{\Psi}_{M_L} | \hat{L}_z | \Psi_{M_L} \rangle = \langle \tilde{\Psi}_{M_L} | \hbar M_L | \Psi_{M_L} \rangle = \hbar M_L.$$

Special attention should be given for calculations in the absence of magnetic field regarding pure M_L states. Depending on the system, degenerate states of different M_L may exist. The degeneracy allows states of different M_L quantum number to mix. In order to derive pure M_L states in the absence of field, symmetry consideration must be made. Alternatively the use of a very weak field ($B = 10^{-7}\ B_0$), forces the calculation to derive pure M_L states, without affecting the energy.

Appendix B

Specifics of ff-HF: details on the implementation in CFOUR

In this appendix, some details on the SCF implementation in the CFOUR program are addressed. These include the consideration of the spin-Zeeman contribution for open-shell systems, when this is not included in the one-electron Hamiltonian integrals, an issue on the DIIS procedure when complex wavefunctions are used, and the implementation of the MOM scheme.

The HF procedure takes place in the **vscf** program. It reads the integrals over SAOs created by **mint** and other system specification given in the input through interface files created by **joda** and performs the SCF algorithm described in fig. B.1 to give the HF solution.[101] In short, the SCF algorithm needs a transformation matrix in order to solve the Roothaan-Hall equation (2.2.2) as an eigenvalue problem. Here, the symmetric orthogonalisation is used that needs the transformation matrix $\mathbf{S}^{-1/2}$. The aufbau principle dictates that after the MO coefficients and the orbital energies have been determined in every iteration, the orbitals with the lowest energy eigenvalue will be used as occupied to define the Fermi vacuum. In case that a certain occupation is defined in the input, meaning that the number of occupied orbitals associated with a specific IRREP is set with the system specification, those orbitals lowest in energy with a specific IRREP will be chosen to define the occupied space. Lastly, for the generation of the Fock matrix of the next iteration, some kind of acceleration scheme is used. These include either damping procedures,[216] but in **vscf** the DIIS procedure is used that extrapolates the Fock matrix based on the errors of the previous iterations.[139,140]

Regarding the creation of the $\mathbf{S}^{-1/2}$ there exist one (user-defined) parameter introduced for numerical stability, which is the linear dependency. The linear-dependency tolerance t checks that the eigenvalues of the overlap matrix $\mathbf{S}_D$ are non-zero

$$|S_{D_{ii}}| > t$$

for the creation of the inverse matrix $\mathbf{S}_D^{-1/2}$. If the eigenvalues are below the tolerance, their inverse is set to 0 to avoid numerical infinities that slow the SCF convergence. This is particularly important for calculation in the presence of a magnetic-field, where large uncontracted basis-sets are typically used, that may introduce many linear dependencies. This can be exploited for the creation of continuum orbitals for the verification of EA and IP methods. Dublicating a basis function in the AO set is guaranteed to create a linear dependency. The 0 entries will thus results in a continuum orbital in the HF solution.

B.1 Inclusion of the spin-Zeeman contribution

Specifics to the ff-HF and its implementation in the **vscf** have to do with the aufbau principle for the open-shell case and with the calculation of the HF energy, both of which have to do with the one-electron Hamiltonian integrals. Specifically, these integrals do not include the spin-Zeeman interaction. Instead, the electrons in the non-relativistic limit are assumed to automatically align themselves parallel or antiparallel to the magnetic-field, and thus the quantised m_S spin-eigenstates are defined

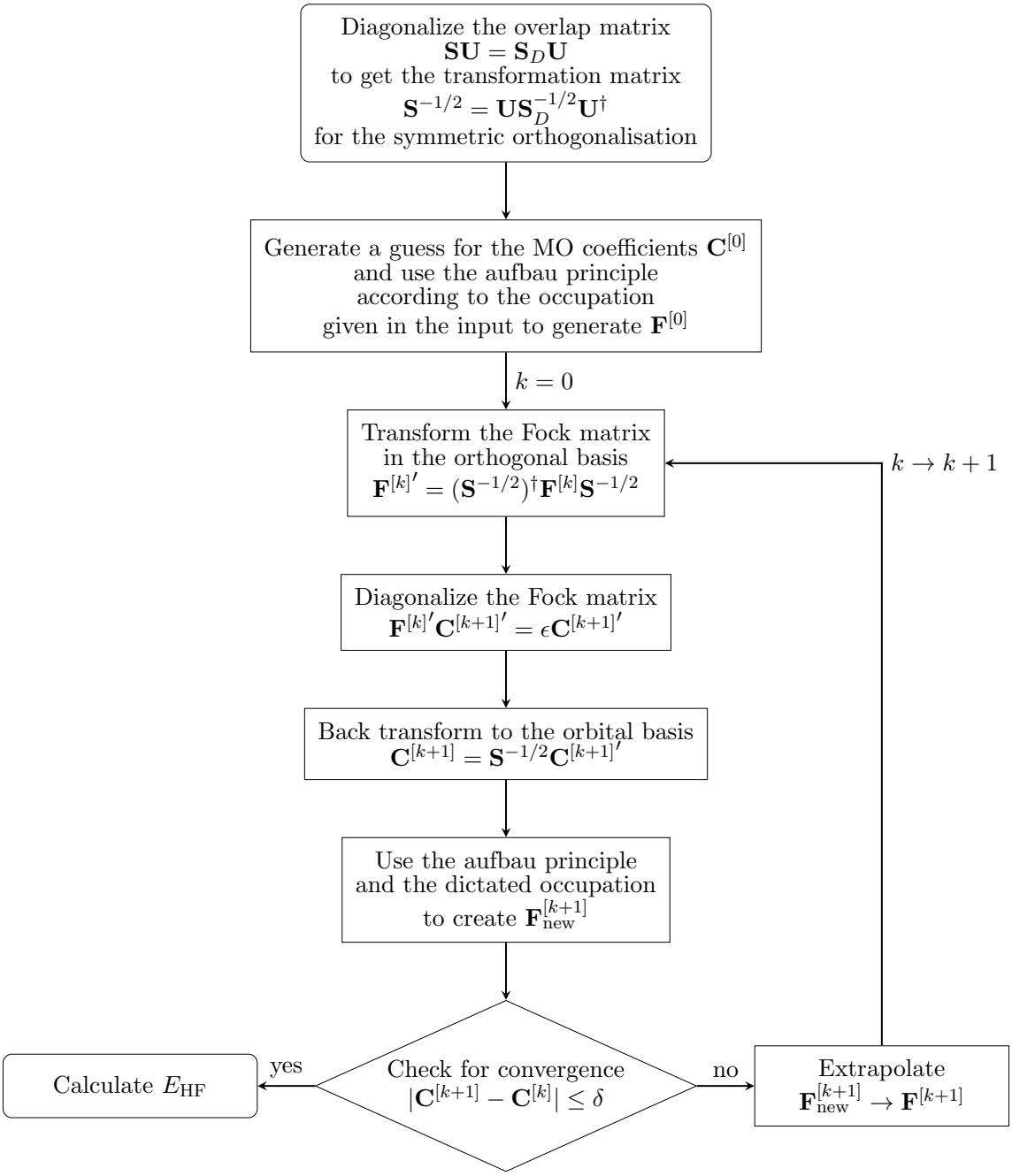

Figure B.1: The SCF algorithm

by the magnetic-field vector. The spin-Zeeman interaction, is thus trivial to calculate on top of any quantum-chemical calculation

$$\hat{P}_{\mathrm{e}}^{\mathrm{spin}} = \frac{e}{m_e}|\boldsymbol{B}|\hat{S}_z = \frac{e\hbar}{2m_e}|\boldsymbol{B}|\left(\Delta n + \{\Delta\hat{n}\}\right).$$

The $\hat{S}_z$ operator has been written in normal-ordered form with the help of eq. (5.2.3). The contribution of the spin-Zeeman term is totally absent in the CFOUR implementation and the resulting E_{HF} energies do not include it either. Attention stills needs to be given to the aufbau principle. Since the derived orbital energies in each eigenvalue do not include the spin-Zeeman term, they unphysically give a degeneracy between the M_S states for open-shell system. This needs to be taken under consideration in the implementation, and (unless given as an occupation), the maximum negative M_S state for a given multiplicity is constructed during the aufbau principle explicitly, in contrast to a field-free calculation where the maximum positive M_S state is the default.

B.2 DIIS for complex wavefunctions

The direct inversion of the iterative space is an extrapolation scheme used in general as convergence acceleration to linear and quasi-linear iterative solvers.[139,140] It aims to give a better updated solution vector in each iteration, by taking under consideration, not only the error of the current iteration, but also that of the previous as well.

Assume $\boldsymbol{p}^i$ the trial vector in iteration i and the $\boldsymbol{e}^i$ the error vector associated with the trial vector in the iteration. In the DIIS method, the extrapolated vector arises as a linear combination of all previous vectors

$$\sum_j c_j \boldsymbol{p}^j = \boldsymbol{p}.$$

The coefficients c_j are required to be normal

$$\sum_j c_j = 1$$

and to approximate the error vector of the extrapolated trial vector to zero in a least-squares sense

$$\sum_j c_j \boldsymbol{e}^j = 0.$$

This leads to the following linear-equation system

$$\begin{pmatrix} 0 & -1 & -1 & \dots & -1 \\ -1 & B_{11} & B_{12} & & \\ -1 & B_{21} & B_{22} & & \\ \vdots & & & \ddots & \\ -1 & & & & B_{ii} \end{pmatrix} \begin{pmatrix} \lambda \\ c_1 \\ c_2 \\ \vdots \\ c_i \end{pmatrix} = \begin{pmatrix} -1 \\ 0 \\ 0 \\ \vdots \\ 0 \end{pmatrix}. \tag{B.2.1}$$

The λ Lagrange multipliers are introduced to fulfil the normalisation condition that is taken care by the first line and column of the matrix. The $B_{jk} = \boldsymbol{e}^{j*} \cdot \boldsymbol{e}^k$, are the elements of the error matrix according to an inner product operation between the error vectors. For the ith iteration an $(i+1)^2$ linear system needs to be solved for the extrapolation. In practice only m pairs of error and trial vectors are saved from previous iteration, making the linear system at most $(m+1)^2$. In case the error matrix $\mathbf{B}$ becomes ill-defined, lines and columns corresponding to the oldest iterations are removed from it, until eq. (B.2.1) is numerically solvable.

For the SCF-HF case, the trial vector are the Fock matrices of each iteration $\mathbf{F}_{\mathrm{new}}^{[i]}$ and the error vector is defined as

$$\boldsymbol{e^i} = \mathbf{F}_{\mathrm{new}}^{[i]}\mathbf{d}^{[i]}\mathbf{S} - \mathbf{S}\mathbf{d}^{[i]}\mathbf{F}_{\mathrm{new}}^{[i]},$$

where $\mathbf{d}^{[i]}$ is the one-body density matrix in the AO basis of the iteration (see app. A). The norm of an error vector may act as a convergence criterion along with the MO coefficients difference described in fig. B.1. In the real case, the extrapolated Fock matrix

$$\mathbf{F}^{[k+1]} = \sum_{j=k-m}^{k+1} c_j \mathbf{F}^{[j]}$$

is always symmetric (real case Hermitian) as a linear combination of symmetric matrices. In the complex case though, because the coefficients c_j are allowed to be complex, the extrapolated matrix as a linear combination of Hermitian matrices is not necessarily Hermitian. This is an issue that needs to be taken care in the algorithm. The non-Hermitian Fock-matrix, despite being non-physical, poses no real problem to the SCF algorithm. Real HF energies and orbital eigenvalues are still ensured by the rest of the steps in the SCF procedure.

The DIIS scheme is handled in the `dodiis` module in **vscf**, and has been adapted for the complex ff-HF solution.

B.3 The MOM scheme

The maximum overlap method acts as an alternative to the aufbau principle for an SCF calculation. It aims at targeting excited states at the SCF level of theory.[217] This is especially useful for ff calculations, where a more controllable SCF procedure is needed because of the complicated relative energetic reordering of electronic states in the presence of field.[218] Having a greater control and being able to have excited states as reference also enables better targeting strategies for multi-configurational states through the EOM variants.

In contrast to the aufbau principle, the occupation of the next iteration is not based on the energetical ordering of the orbital eigenvalues. Instead the new occupied orbitals are chosen as those orbitals that overlap the most with the orbitals of the previous iteration. To achieve this, the orbital overlap matrix is defined

$$\mathbf{O} = \mathbf{C}^{[k]}\mathbf{S}\mathbf{C}^{[k+1]}.$$

Thus, the element O_{ij} describes the overlap between the ith old orbital with the jth new orbital. The projection of a new orbital to the set of old occupied orbitals is then defined as

$$p_j = \sum_{i}^{n_e} O_{ij},$$

where the summation runs over the set of the old occupied orbitals. The new occupied orbitals are chosen as those j orbitals with the largest p_j values.

A variation of the MOM procedure exists, where instead of using the orbitals of the previous iteration for the old orbitals $\mathbf{C}^{[k]}$, the starting orbitals are used instead $\mathbf{C}^{[0]}$. This is the initial MOM (IMOM) variant.

In the CFOUR implementatio of (I)MOM, a MOM calculation takes place after a standard SCF solution. It is activated by the `MOM=ON` for MOM or `MOM=INIT` for IMOM keyword in the input. After converging to the standard SCF solution using the aufbau principle, a new occupation is given to the program via the input. This new occupation for the (old) converged orbitals actes as the first guess for the (I)MOM calculation and the SCF procudure is restarted, using (I)MOM instead of the aufbau principle.

The new occupation for the (I)MOM calculation is give in the input after the `%momguess`[a] additional option. The lines after the keyword define the number of occupied orbitals per IRREP (similar to the `OCCUPATION` keyword). The first line defines the occupation of the α orbitals, and the next line the occupation of the β orbitals in a UHF calculation. The next lines give the indices of the orbitals to be occupied. Each new line refers to a different IRREP. Again the α-orbital occupation precedes the β-orbital. An example input is given:

[a] Alternative forms: `%MOMguess`, `%MOMGUESS`

```
%MOMguess
3 2 2 1 #Occupation of alpha orbitals
4 2 2 1 #Occupation of beta orbitals (only for UHF)
1 2 4   #Occupy the following alpha orbitals from IRREP 1: 1, 2, 4
1 2     #Occupy the following alpha orbitals from IRREP 2: 1, 2
1 2     #Occupy the following alpha orbitals from IRREP 3: 1, 2
1       #Occupy the following alpha orbitals from IRREP 4: 1
1 2 3 4 #Occupy the following beta orbitals from IRREP 1: 1, 2, 3, 4 (Only for UHF)
1 2     #Occupy the following beta orbitals from IRREP 2: 1, 2 (Only for UHF)
1 2     #Occupy the following beta orbitals from IRREP 3: 1, 2 (Only for UHF)
1       #Occupy the following beta orbitals from IRREP 4: 1 (Only for UHF)
```

This input defines a singly excited determinant given for the (I)MOM calculation, where an electron is excited from the 3rd α orbital to the 4th. The purple text after the # symbols explains each line, and must be absent from a real input.

The (I)MOM implementation exists in the `mom_info` module in **vscf**.

Appendix C

QCUMBRE: further details on the implementation

Here, some additional details on the development of QCUMBRE are presented. The explicit form of the one- and two-electron integrals, the implementation of the orbital-relaxation of properties, and also the implementation of a multi-root Davidson procedure for the solution to the EOM-CC problem are presented.

C.1 One- and two-body reduced density matrices

For the calculation of properties, the one- and two-body reduced density matrices are needed. One-body density matrices were already implemented in QCUMBRE at the EE-, SF-, EA- and IP-EOM-CCSD levels of theory. Despite this, for reasons of consistency, EE-EOM-CCSD one-body reduced density matrices were implemented anew.

For ground-state properties, the form of the one- and two-body reduced densities can be seen in fig. C.1, C.2 and C.5 at the MP2, CC2 and CCSD levels of theory. The contributions have been divided to those arising solely from the reference with no Lagrange multipliers (fig. C.1), and those that include the λ-amplitudes (fig. C.2 and C.5).

$$\langle 0|\,(1+\hat{\Lambda})e^{-\hat{T}}\{\dots\}e^{\hat{T}}\,|0\rangle = \langle 0|\,e^{-\hat{T}}\{\dots\}e^{\hat{T}}\,|0\rangle + \langle 0|\,\hat{\Lambda}e^{-\hat{T}}\{\dots\}e^{\hat{T}}\,|0\rangle$$

For excited-state EE-EOM properties at the expectation-value level, the contributions are divided as follows:

$$\begin{aligned}\langle 0|\,\hat{L}^n e^{-\hat{T}}\{\dots\}e^{\hat{T}}\hat{R}^m\,|0\rangle = \langle 0|\,\hat{L}^n(e^{-\hat{T}}\{\dots\}e^{\hat{T}}\hat{R}^m)_{\mathrm{C}}\,|0\rangle + \langle 0|\,(\hat{L}^n\hat{R}^m - \delta_{nm} - \hat{L}^n r_0^m)e^{-\hat{T}}\{\dots\}e^{\hat{T}}\,|0\rangle \\ + r_0^m\,\langle 0|\,\hat{L}^n e^{-\hat{T}}\{\dots\}e^{\hat{T}}\,|0\rangle + \delta_{nm}\,\langle 0|\,e^{-\hat{T}}\{\dots\}e^{\hat{T}}\,|0\rangle\,.\end{aligned}$$

The contributions arising from the first term are connected and can be seen at fig. C.3 and C.7 for EE-EOM-CC2 and EE-EOM-CCSD. The second term includes only disconnected contributions (fig. C.4 and C.6). It excludes all the contributions that involve r_0, which are identical in form with the contributions in fig. C.2 and C.5 and the contributions that arise from the reference state (fig. C.1). In QCUMBRE, the functions that calculate the third and the fourth term are recycled using the same functions used for the ground-state properties.

Similarly to the expectation-value level, the (linear-)response reduced density matrices are divided as well:

$$\langle 0|\,\hat{L}^n(e^{-\hat{T}}\{\dots\}e^{\hat{T}}\hat{R}^m)_{\mathrm{C}}\,|0\rangle + \langle 0|\,\hat{\mathscr{Z}}'(\omega_{nm})e^{-\hat{T}}\{\dots\}e^{\hat{T}}\,|0\rangle + \delta_{nm}\,\langle 0|\,e^{-\hat{T}}\{\dots\}e^{\hat{T}}\,|0\rangle\,.$$

The connected contributions of the first term are identical between the expectation-value and the response approach and are calculated by the functions described in fig. C.3 and C.7 for EE-EOM-CC2 and EE-EOM-CCSD. LR-transition properties are not completely debugged at the CC2 level of theory. No disconnected contriubtions are included nor contributions that involve r_0. The second

$$(\gamma_N)_{ia} += t_i^a$$

$$(\Gamma_N)_{ijab} += t_{ij}^{ab} + P(ab) t_i^a t_j^b$$

Figure C.1: Reference contributions to the one- and two-body reduced density matrices for properties at the MP2, CC2 and CCSD levels of theory $\langle 0| e^{-\hat{T}} \{ \dots \} e^{\hat{T}} |0\rangle$. Red-coloured terms are the only terms that contribute at the MP2 level of theory.

$$(\gamma_N)_{ab} += \sum_m t_m^b \lambda_a^m + \frac{1}{2} \sum_{emn} t_{mn}^{be} \lambda_{ae}^{mn}$$

$$(\gamma_N)_{ij} += -\sum_e t_i^e \lambda_q^j - \frac{1}{2} \sum_{efm} t_{mi}^{ef} \lambda_{ef}^{mj}$$

$$(\gamma_N)_{ai} += \lambda_a^i$$

$$(\gamma_N)_{ia} += -\sum_{em} t_m^a \left(t_i^e \lambda_e^m + \frac{1}{2} \sum_{fn} t_{in}^{ef} \lambda_{ef}^{mn} \right) + \sum_{em} t_{mi}^{ea} \lambda_e^m + \frac{1}{2} \sum_{efmn} t_i^e t_{mn}^{af} \lambda_{cf}^{mn}$$

Figure C.2: Contributions to the one-body reduced density matrices for properties from the $\langle 0| \hat{\Lambda} e^{-\hat{T}} \{ \hat{a}_p^\dagger \hat{a}_q \} e^{\hat{T}} |0\rangle$ term at the MP2, CC2 and CCSD levels of theory. Red-coloured terms are the only terms that contribute at the MP2 level of theory.

$$(\gamma_N)_{ab} += \sum_m r_m^b l_a^m + \frac{1}{2} \sum_{emn} r_{mn}^{be} l_a^{mn} e$$

$$(\gamma_N)_{ij} += -\sum_e r_i^e l_q^j - \frac{1}{2} \sum_{efm} r_{mi}^{ef} l_{ef}^{mj}$$

$$(\gamma_N)_{ia} += -\sum_{em} \left(l_e^m t_i^e + \frac{1}{2} \sum_{fn} l_{ef}^{mn} t_{in}^{ef} \right) r_m^a - \sum_{em} \left(l_e^m r_i^e + \frac{1}{2} \sum_{fn} l_{ef}^{mn} r_{in}^{ef} \right) t_m^a - \frac{1}{2} \sum_{efmn} l_{ef}^{mn} t_{mn}^{ea} r_i^f - \frac{1}{2} \sum_{efmn} l_{ef}^{mn} r_{mn}^{ea} t_i^f$$

Figure C.3: Connected contributions to the one-body density matrices for excited state properties $\langle 0| \hat{L} (e^{-\hat{T}} \{ \hat{a}_p^\dagger \hat{a}_q \} e^{\hat{T}} \hat{R})_C |0\rangle$ at the EE-EOM-CC2 and EE-EOM-CCSD levels of theory.

$$(\gamma_N)_{ab} += \sum_{emn} r_m^e l_{ea}^{mn} t_m^b$$

$$(\gamma_N)_{ij} += -\sum_{efm} r_m^e l_{ef}^{mj} t_i^f$$

$$(\gamma_N)_{ai} += \sum_{em} r_m^e l_{ea}^{mi}$$

$$(\gamma_N)_{ia} += \sum_{efmn} r_m^e l_{ef}^{mn} \left(t_{ni}^{fa} - t_i^f t_n^a \right)$$

Figure C.4: Disconnected contributions to the one-body density matrices for excited-state properties not including the reference and r_0, $\langle 0| \left(\hat{L} \hat{R} - \hat{L} r_0 - 1 \right) e^{-\hat{T}} \{ \hat{a}_p^\dagger \hat{a}_q \} e^{\hat{T}} |0\rangle$, at the EE-EOM-CC2 and EE-EOM-CCSD levels of theory.

$$
\begin{aligned}
(\Gamma_N)_{abcd} +&= \frac{1}{2}\sum_{lm} \lambda_{ab}^{lm}\left(t_{lm}^{cd} + P(cd)t_l^c t_m^d\right)\\
(\Gamma_N)_{ijkl} +&= \frac{1}{2}\sum_{de} \lambda_{de}^{kl}\left(t_{ij}^{de} + P(ij)t_i^d t_j^e\right)\\
(\Gamma_N)_{abij} +&= \lambda_{ab}^{ij}\\
(\Gamma_N)_{ijab} +&= \frac{1}{4}\sum_{mn}\left(t_{mn}^{ab} + P(ab)t_m^a t_n^b\right)\sum_{ef}\left(t_{ij}^{ef} + P(ij)t_i^e t_j^f\right)\lambda_{ef}^{mn}\\
&\quad - \frac{1}{2}P(ab)P(ij)\sum_{em}\left(t_{mi}^{ae} + 2t_m^a t_i^e\right)\left(2t_j^b\lambda_e^m + \sum_{fn} t_{jn}^{bf}\lambda_{ef}^{mn}\right) + 3P(ij)P(ab)\sum_{me} t_j^b t_i^e t_m^a \lambda_e^m\\
&\quad - P(ab)\sum_{e}\left(t_{ij}^{eb} + P(ij)t_i^e t_j^b\right)\sum_{m}\left(t_m^a\lambda_e^m + \frac{1}{2}\sum_{fn} t_{mn}^{af}\lambda_{ef}^{mn}\right)\\
&\quad - P(ij)\sum_{m}\left(t_{mj}^{ab} + P(ab)t_m^a t_j^b\right)\sum_{e}\left(t_i^e\lambda_e^m + \frac{1}{2}\sum_{fn} t_{in}^{ef}\lambda_{ef}^{mn}\right)\\
(\Gamma_N)_{iabj} +&= t_i^b\lambda_a^j + \sum_{ld}\left(t_{li}^{db} - t_i^d t_l^b\right)\lambda_{da}^{lj}\\
(\Gamma_N)_{kaij} +&= -\sum_{d} t_k^d \lambda_{da}^{ij}\\
(\Gamma_N)_{abci} +&= \sum_{l} t_l^c \lambda_{ab}^{li}\\
(\Gamma_N)_{ijka} +&= -\sum_{d}\left(t_{ij}^{da} + P(ij)t_i^d t_j^a\right)\lambda_k^d - \frac{1}{2}P(ij)\sum_{del} t_j^a t_{il}^{de}\lambda_{de}^{kl} - P(ij)\sum_{del} t_i^d t_{jl}^{ae}\lambda_{de}^{kl}\\
&\quad + \frac{1}{2}\sum_{del}\left(t_{ij}^{de} + P(ij)t_i^d t_j^e\right)t_l^a\lambda_{de}^{kl}\\
(\Gamma_N)_{ciab} +&= \sum_{l}\left(t_{li}^{ab} + P(ab)t_l^a t_i^b\right)\lambda_c^l + \frac{1}{2}P(ab)\sum_{dlm} t_i^b t_{lm}^{da}\lambda_{dc}^{lm} + P(ab)\sum_{dlm} t_l^a t_{im}^{bd}\lambda_{cd}^{lm}\\
&\quad - \frac{1}{2}\sum_{dlm}\left(t_{lm}^{ab} + P(ab)t_l^a t_m^b\right)t_i^d\lambda_{cd}^{lm}
\end{aligned}
$$

Figure C.5: Contributions to the two-body reduced density matrices for properties from the $\langle 0|\,\hat{\Lambda}e^{-\hat{T}}\{\hat{a}_p^\dagger\hat{a}_q^\dagger\hat{a}_s\hat{a}_r\}e^{\hat{T}}\,|0\rangle$ term. At MP2, only red-coloured terms contribute. At CC2, blue- and red- coloured terms contribute. At CCSD, purple-, blue- and red-coloured terms contribute.

$$
\begin{aligned}
(\Gamma_N)_{ijab} +&= P(ab)P(ij)\sum_{em} r_m^e l_{ef}^{mn}\left(t_{in}^{af} - t_i^f t_n^a\right)t_j^b\\
&\quad + P(ij)\sum_{efmn} r_n^e l_{ef}^{nm} t_j^f t_{im}^{ab}\\
&\quad - P(ab)\sum_{efmn} r_m^e l_{ef}^{mn} t_n^a t_{ij}^{eb}\\
(\Gamma_N)_{iabj} +&= \sum_{em} r_m^e l_{ea}^{mj} t_i^b
\end{aligned}
\qquad
\begin{aligned}
(\Gamma_N)_{ijka} +&= -\sum_{efm} r_m^e l_{ef}^{mk}\left(t_{ij}^{fa} + P(ij)t_i^f t_j^a\right)\\
(\Gamma_N)_{ciab} +&= \sum_{emn} r_m^e l_{ec}^{mn}\left(t_{ni}^{ab} + P(ab)t_n^a t_i^b\right)
\end{aligned}
$$

Figure C.6: Disconnected contributions to the two-body density matrices for excited-state properties not including the reference and r_0, $\langle 0|\left(\hat{L}\hat{R} - \hat{L}r_0 - 1\right)e^{-\hat{T}}\{\hat{a}_p^\dagger\hat{a}_q^\dagger\hat{a}_s\hat{a}_r\}\}e^{\hat{T}}\,|0\rangle$, at the EE-EOM-CC2 and EE-EOM-CCSD levels of theory. At CC2, blue- coloured terms contribute. At CCSD, purple- and blue-coloured terms contribute.

$$
\begin{aligned}
(\Gamma_N)_{abcd} +&= \frac{1}{2}\sum_{lm} l_{ab}^{lm} r_{lm}^{cd} + \sum_{lm} l_{ab}^{lm}\left(r_l^c t_m^d + t_l^c r_m^d\right)\\
(\Gamma_N)_{ijkl} +&= \frac{1}{2}\sum_{de} l_{de}^{kl} r_{ij}^{de} + \sum_{de} l_{de}^{kl}\left(r_i^d t_j^e + t_i^d r_j^e\right)\\
(\Gamma_N)_{ijab} +&= P(ab)P(ij)\left[\sum_{em} l_e^m\left(r_{im}^{ae} - r_m^a t_i^e - t_m^a r_i^e\right) + \frac{1}{2}\sum_{efmn} l_{ef}^{mn}\left(r_{mn}^{ae} t_i^f + t_{mn}^{ae} r_i^f - r_{mi}^{ef} t_n^a - t_{mi}^{ef} r_n^a\right)\right] t_j^b\\
&\quad + P(ab)P(ij)\left[\sum_{em} l_e^m\left(t_{im}^{ae} - t_m^a t_i^e\right) + \frac{1}{2}\sum_{efmn} l_{ef}^{mn}\left(t_{mn}^{ae} t_i^f - t_{mi}^{ef} t_n^a\right)\right] r_j^b\\
&\quad + P(ij)\sum_{me}\left(l_e^m r_j^e + \frac{1}{2}\sum_{fn} l_{ef}^{mn} r_{nj}^{ef}\right) t_{im}^{ab} + P(ij)\sum_{me}\left(l_e^m t_j^e + \frac{1}{2}\sum_{fn} l_{ef}^{mn} t_{nj}^{ef}\right) r_{im}^{ab}\\
&\quad - P(ab)\sum_{me}\left(l_e^m r_m^a + \frac{1}{2}\sum_{fn} l_{ef}^{mn} r_{mn}^{af}\right) t_{ij}^{eb} - P(ab)\sum_{me}\left(l_e^m t_m^a + \frac{1}{2}\sum_{fn} l_{ef}^{mn} t_{mn}^{af}\right) r_{ij}^{eb}\\
&\quad + \frac{1}{4}\sum_{efmn} l_{ef}^{mn}\left(r_{ij}^{ef} + 2 r_i^e t_j^f + 2 t_i^e r_j^f\right)\left(t_{mn}^{ab} + P(ab) t_m^a t_n^b\right)\\
&\quad + \frac{1}{4}\sum_{efmn} l_{ef}^{mn}\left(t_{ij}^{ef} + P(ij) t_i^e t_j^f\right)\left(r_{mn}^{ab} + 2 r_m^a t_n^b + 2 t_m^a r_n^b\right)\\
&\quad + P(ab)P(ij) l_{ef}^{mn} r_{mi}^{ea}\left(t_{jn}^{bf} - t_j^f t_n^b\right) - P(ab)P(ij) l_{ef}^{mn} t_{mi}^{ea}\left(r_j^f t_n^b + t_j^f r_n^b\right)\\
(\Gamma_N)_{iabj} +&= r_i^b l_a^j + \sum_{em} r_{mi}^{eb} l_{ae}^{jm} - \sum_{em}\left(r_m^b t_i^e + t_m^b r_i^e\right) l_{ae}^{jm}\\
(\Gamma_N)_{kaij} +&= -\sum_{d} r_k^d l_{da}^{ij}\\
(\Gamma_N)_{abci} +&= \sum_{l} r_l^c l_{ab}^{li}\\
(\Gamma_N)_{ijka} +&= -P(ij)\sum_{e}\left(r_i^e l_e^k + \frac{1}{2}\sum_{fm} r_{mi}^{fe} l_{fe}^{mk}\right) t_j^a - P(ij)\sum_{e}\left(t_i^e l_e^k + \frac{1}{2}\sum_{fm} t_{mi}^{fe} l_{fe}^{mk}\right) r_j^a\\
&\quad - P(ij)\sum_{efm} l_{fe}^{mk} r_{mj}^{fa} t_i^e - P(ij)\sum_{efm} l_{fe}^{mk}\left(t_{mj}^{fa} - t_m^a t_j^f\right) r_i^e\\
&\quad - \frac{1}{2}\sum_{efm} l_{ef}^{mk} r_{ij}^{ef} t_m^a - \frac{1}{2}\sum_{efm} l_{ef}^{mk}\left(t_{ij}^{ef} + P(ij) t_i^e t_j^f\right) r_m^a + \sum_{e} r_{ij}^{ae} l_e^k\\
(\Gamma_N)_{ciab} +&= P(ab)\sum_{n}\left(r_n^a l_c^n + \frac{1}{2}\sum_{em} r_{mn}^{ea} l_{ec}^{mn}\right) t_i^b + P(ab)\sum_{n}\left(t_n^a l_c^n + \frac{1}{2}\sum_{em} t_{mn}^{ea} l_{ec}^{mn}\right) r_i^b\\
&\quad + P(ab)\sum_{fmn} l_{cf}^{nm} r_{im}^{bf} t_n^a + P(ab)\sum_{fmn} l_{cf}^{nm}\left(t_{im}^{bf} - t_i^f t_m^b\right) r_n^a\\
&\quad + \frac{1}{2}\sum_{emn} r_{mn}^{ab} l_{ec}^{mn} t_i^e + \frac{1}{2}\sum_{emn}\left(t_{mn}^{ab} + P(ab) t_m^a t_n^b\right) l_{ec}^{mn} r_i^e - \sum_{m} r_{im}^{ab} l_c^m
\end{aligned}
$$

Figure C.7: Connected contributions to the two-body density matrices for excited state properties $\langle 0|\,\hat{L}(e^{-\hat{T}}\{\hat{a}_p^\dagger \hat{a}_q^\dagger \hat{a}_s \hat{a}_r\} e^{\hat{T}}\hat{R})_{\mathrm{C}}\,|0\rangle$ at the EE-EOM-CC2 and EE-EOM-CCSD levels of theory. At CC2, blue- coloured terms contribute. At CCSD purple- and blue- coloured terms contribute.

$$(\Gamma_N)_{abcd} \mathrel{+}= \frac{1}{2} \sum_{lm} \lambda_{ab}^{lm} t_{lm}^{cd}$$

$$(\Gamma_N)_{ijkl} \mathrel{+}= \frac{1}{2} \sum_{de} \lambda_{de}^{kl} t_{ij}^{de}$$

$$(\Gamma_N)_{iabj} \mathrel{+}= \sum_{ld} t_{li}^{db} \lambda_{da}^{lj}$$

$$(\Gamma_N)_{ijab} \mathrel{+}= \frac{1}{2} \sum_{efmn} t_m^a t_n^b t_{ij}^{ef} \lambda_{ef}^{mn} + \frac{1}{2} \sum_{efmn} t_{mn}^{ab} t_i^e t_j^f \lambda_{ef}^{mn} - P(ab)P(ij) \sum_{efmn} t_m^a t_i^e t_{jn}^{bf} \lambda_{ef}^{mn} - \frac{1}{2} P(ab)P(ij) \sum_{efmn} t_i^e t_j^b t_{mn}^{af} \lambda_{ef}^{mn} - \frac{1}{2} P(ij)P(ab) \sum_{efmn} t_m^a t_j^b t_{in}^{ef} \lambda_{ef}^{mn}$$

$$(\Gamma_N)_{ijka} \mathrel{+}= -\frac{1}{2} P(ij) \sum_{del} t_j^a t_{il}^{de} \lambda_{de}^{kl} - P(ij) \sum_{del} t_i^d t_{jl}^{ae} \lambda_{de}^{kl} + \frac{1}{2} \sum_{del} t_{ij}^{de} t_l^a \lambda_{de}^{kl}$$

$$(\Gamma_N)_{ciab} \mathrel{+}= +\frac{1}{2} P(ab) \sum_{dlm} t_i^b t_{lm}^{da} \lambda_{dc}^{lm} + P(ab) \sum_{dlm} t_l^a t_{im}^{bd} \lambda_{cd}^{lm} - \frac{1}{2} \sum_{dlm} t_{lm}^{ab} t_i^d \lambda_{cd}^{lm}$$

Figure C.8: Additional second-order contribution to the two-body reduced density matrices at the MP2 and CC2 levels of theory. Only needed for calculation of properties not participating in the Hamiltonian. Red-coloured terms are the only terms that contribute at the MP2 level of theory.

$$(\gamma_N)_{ab} \mathrel{+}= \sum_{m} \mathscr{c}_a^m c_m^b + \frac{1}{2} \sum_{emn} \mathscr{c}_{ae}^{mn} c_{mn}^{be}$$

$$(\gamma_N)_{ij} \mathrel{+}= -\sum_{e} \mathscr{c}_e^j c_i^e - \frac{1}{2} \sum_{efm} \mathscr{c}_{ef}^{mj} c_{mi}^{ef}$$

$$(\gamma_N)_{ia} \mathrel{+}= \mathscr{c}_0 c_i^a + \sum_{em} \mathscr{c}_m^a c_{ea}^{mi}$$

$$(\Gamma_N)_{abcd} \mathrel{+}= \frac{1}{2} \sum_{mn} \mathscr{c}_{ab}^{mn} c_{mn}^{cd}$$

$$(\Gamma_N)_{ijkl} \mathrel{+}= \frac{1}{2} \sum_{ea} \mathscr{c}_{ea}^{kl} c_{ij}^{ef}$$

$$(\Gamma_N)_{ijab} \mathrel{+}= \mathscr{c}_0 c_{ij}^{ab}$$

$$(\Gamma_N)_{iabj} \mathrel{+}= \mathscr{c}_a^j c_i^b + \sum_{em} \mathscr{c}_{ea}^{mj} c_{mi}^{eb}$$

$$(\Gamma_N)_{ijka} \mathrel{+}= -\sum_{e} \mathscr{c}_e^k c_{ij}^{ea}$$

$$(\Gamma_N)_{ciab} \mathrel{+}= \sum_{m} \mathscr{c}_c^m c_{mi}^{ab}$$

Figure C.9: One- and two-body reduced density matrices at the CIS and CISD levels of theory $\langle 0| \hat{\mathscr{C}}\{\dots\}\hat{C}\,|0\rangle$. At CIS, only the red-coloured terms contribute. Coefficients $c_{i\dots}^{a\cdots}$ regard the ket state and $\mathscr{c}_{a\dots}^{i\cdots} = (c^*)_{i\dots}^{a\cdots}$ the bra state.

term is also calculated with recycled function for the ground-state properties (fig. C.2 and C.5) and reference contributions are not needed for transition properties.

The matrices at the CC2 level do not necessarily use the same factorisation as CCSD (which is described in the equations shown here). Instead a different factorisation is used, that ensures that all N^6 steps are avoided.

For the calculation of ground-state properties that involve the two-electron reduced density when the property is not part of the Hamiltonian, the two-body reduced density matrices at the MP2 and CC2 levels of theory need additional second-order terms on top of those described in fig. C.5. These are shown in fig. C.8. In practice, the additional terms are added for calculations at the MP2 level of theory. These matrices at MP2 have the same form as the MP3 two-body reduced density matrices. For calculations at the CC2 level of theory, the functions for the ground-state two-electron reduced density matrices at the CCSD level are used and $t_2 t_2 \lambda_2$ terms are subtracted. This affects only the $ijab$ block

$$\begin{aligned}(\Gamma_N)^{\mathrm{CC2,mod}}_{ijab} =& (\Gamma_N)^{\mathrm{CCSD,mod}}_{ijab} - \frac{1}{4}\sum_{efmn} \lambda^{mn}_{ef} t^{ab}_{mn} t^{ef}_{ij} - P(ij)\sum_{efmn} \lambda^{mn}_{ef} t^{ea}_{mi} t^{bf}_{jn} \\ &+ \frac{1}{2}P(ab)\sum_{efmn} t^{eb}_{ij} t^{af}_{mn} \lambda^{mn}_{ef} + \frac{1}{2}P(ij)\sum_{efmn} t^{ab}_{mj} t^{ef}_{in} \lambda^{mn}_{ef}.\end{aligned}$$

Because of the $t_2\lambda_2$ terms, the second-order contributions to the CC2 two-body reduced density matrices necessarily scale at most as N^6.

The one- and two-body reduced density matrices at the CIS and CISD levels of theory can be seen in fig. C.9. As mentioned in sec. 5.2 the CIS matrices can be used to calculate the spin multiplicity of excited states assuming they are spin eigenstates.

In the equations seen in the following figures, the permutation operators are introduced

$$P(pq) d_{p\ldots} d'_{q\ldots} = d_{p\ldots} d'_{q\ldots} - d_{q\ldots} d'_{p\ldots}$$

The functions that handle the creation of the one- and the two-body reduced densities are found in the `DensMat1` and `DensMat2` libraries. The correctness of the implemented matrices is tested by calculating the correlation energy via eq. (2.7.16). This is done by the `testEnergyS` function of the `Prop2` library.

C.2 Orbital relaxation and solving the z-vector

For the calculation of properties as analytic derivatives, in addition to the one- and two-body matrices described in the previous section, the z-vector is needed. As explained in subsec. 2.7.3, the matrices are first symmetrized according to eq. (2.7.17). This is handled by the `groupS:symmetrize` and `group:symmetrize` functions that in turn call the `flex::symmetrize` functions.

The symmetrized matrices are in turn used to derive the occupied-occupied and virtual-virtual block eq.(2.7.24) and (2.7.24) if this is needed. In order to finally derive the occupied-virtual and virtual-occupied block, the $\mathbf{X}$ matrix is calculated. Before calling a linear solver, eq. (2.7.30) is brought in the following form

$$\begin{aligned}\mathbf{A}^{*\intercal}\mathbf{z}^* + \mathbf{B}^{\intercal}\mathbf{z} &= \mathbf{X} \\ \left[\mathbf{A}^{\intercal}_{\mathrm{Re}} - i\mathbf{A}^{\intercal}_{\mathrm{Im}}\right]\left[\mathbf{z}_{\mathrm{Re}} - i\mathbf{z}_{\mathrm{Im}}\right] + \left[\mathbf{B}^{\intercal}_{\mathrm{Re}} + i\mathbf{B}^{\intercal}_{\mathrm{Im}}\right]\left[\mathbf{z}_{\mathrm{Re}} + i\mathbf{z}_{\mathrm{Im}}\right] &= \mathbf{X}_{\mathrm{Re}} + i\mathbf{X}_{\mathrm{Im}} \\ \begin{pmatrix} \mathbf{B}^{\intercal}_{\mathrm{Re}} + \mathbf{A}^{\intercal}_{\mathrm{Re}} & -\mathbf{B}^{\intercal}_{\mathrm{Im}} - \mathbf{A}^{\intercal}_{\mathrm{Im}} \\ \mathbf{B}^{\intercal}_{\mathrm{Im}} - \mathbf{A}^{\intercal}_{\mathrm{Im}} & \mathbf{B}^{\intercal}_{\mathrm{Re}} - \mathbf{A}^{\intercal}_{\mathrm{Re}} \end{pmatrix} \begin{pmatrix} \mathbf{z}_{\mathrm{Re}} \\ \mathbf{z}_{\mathrm{Im}} \end{pmatrix} &= \begin{pmatrix} \mathbf{X}_{\mathrm{Re}} \\ \mathbf{X}_{\mathrm{Im}} \end{pmatrix},\end{aligned}$$

where the real and the imaginary parts of the complex entries are written as index. The last equation can then be used to call a linear solver (for real double precision float numbers) to derive the z-amplitudes for the occupied-virtual space. These amplitudes, substitute the occupied-virtual space of the one-body density matrices. A common practice in QCUMBRE in order to be able to calculate

both orbital-relaxed and unrelaxed properties, is to save the symmetrized $(\rho_N)_{ia}$ in `rho_ia` and the relaxed $(\rho_N)^{\text{rel}}_{ai}$ in `Z_ai`. The whole procedure is handled by the `ZvecSolvS` function.

Lastly the I_{pq} Lagrange multipliers are calculated in the `ContractionsIsymmS` function using the equations derived in subsec. 2.7.3. Both `ZvecSolvS` and `ContractionsIsymmS` are found in the `ZvecSolv` library.

As already mentioned, this tactic for the calculation of the orbital relaxation is completely independent on the exact post-HF level, and is applicable as long both the one- and the two-body density matrices are available.

The correctness of the implementation was tested against numerical gradients for electric dipole moments. Agreement was achieved up to the seventh decimal place. Because of the absence of analytic geometric gradients, the I_{pq} Lagrange multipliers are not completely tested. Their correctness is assumed, as recycled function are used in `ContractionsIsymmS`.

C.3 Multi-root Davidson procedure

The Davidson procedure in QCUMBRE has been implemented in such a way, so that in each Davidson cycle, one root of the matrix is found. The root can moreover be chosen, in the sense that in step (0) (in fig. 4.1) the CIS guess can be give that has the maximum overlap with the root wanted. Additionally, after the diagonalization of the effective matrix in step (3), the eigenvalue-eigenvector pair that takes part in the rest of the algorithm is that one, that has the most overlap with the initial guess if above a convergence criterion, or with eigenvector of the previous iteration if below a convergence, at which point the root is characterised as "locked". This tactic however excludes in many cases roots that have a predominant double-excitation character with respect to the reference, since they are not captured at the CIS level, unless other kind of initial guesses are given. In the cases of two or more multiconfigurational excited states that have a similar overlap with a given initial guess or with eachother before convergence the algorithm may fail to find all of them, or may convergence to the same state despite using different initial guesses.

The aforementioned problematic cases for this single-root Davidson algorithm can be addressed by considering multiple roots in a Davidson cycle. Such a procedure is named multi-root Davidson or generalized Davidson procedure[147] and was implemented in QCUMBRE during this work. The multi-root Davidson may offer faster convergence, since the new direction arising from one root may help with the convergence of another, allows excited states with a predominant double-excitation character to come natural as solutions in the algorithm and is guaranteed not to converge to a single state twice, since the solutions are guaranteed to be orthogonal to each other in every iteration because they arise from the diagonalization of the same effective matrix.

In the mutli-root Davidson procedure, only roots associated with the same IRREP may be considered in one Davidson cycle. Considering more IRREPs is problematic undermines the motivation of exploiting symmetry, since the base vector and solutions are no longer symmetric raising the computational cost, and the convergence is worsened because before convergence non-physical mixture between states associated with different IRREPs occurs. Ideally, states of different spin-multiplicities should not be considered together for the same reasons, but this is not so easily regulated in an unrestricted approach.

Starting from step (0), the multi-root Davidson receives as many initial guesses as the number of roots asked. In each iteration, as many new σ_I^k vectors are calculated as roots asked. If above the "lock" criterion, the eigenvalue-eigenvector pairs chosen after step (3) are those with the lowest λ value. If the roots are "locked" the overlap criterion is used. The residual and convergence is checked for each one of the eigenvectors chosen in step (5). The algorithm stops when all roots asked have reached the convergence criterion. Otherwise, a new direction is calculated for all roots (even those already converged). During the Gram-Schmidt orthogonalisation of the new directions in step (7), some of the new directions are not incorporated in the new set of base vectors, if their norm is below one millionth of the convergence criterion $\frac{\text{conv. crit.}}{1000}$.

An aspect of the algorithm not addressed so far is the size of the set of basis vector. In the single-root Davidson the maximum size is user-defined. When the size of the set is to became greater than

the maximum size, the existing base vectors are discarded and substituted by the most recent trial eigenvector solution, before orthogonalising the new direction. In the multi-root Davidson case the restart criterion does not simply checks the size of the set of base vectors, but dynamically decides on restarting the set based on the development of the convergence. If n_b^k the size of the set of base vectors and $c_{\max}^k$ the convergence of the least converged root in iteration k, then the e^k criterion is defined as

$$e^k = \frac{c_{\max}^{k-1}}{c_{\max}^k} \cdot \frac{1}{n_b^k}.$$

The algorithm restarts the set of base vectors, if their size exceeds the maximum or if $e^k < \frac{1}{\max(n_b)}$, with $\max(n_b)$ the maximum number of base vectors. This criterion takes care that the development of convergence is smooth by eliminating elements of the set of the base vectors that raise the convergence instead of lowering it.

In general, the multi-root Davidson has been proven to be less numerically stable than the single-root version. The numerical instability presents itself by the creation new base vectors associated with the trivial eigenvector solution of $r_I = 0$. In order to partially remedy this instability, the new base vector in step (7) is not the only vector that is being orthogonalised against the old vectors, by all vectors are orthogonlised a new against each other in each iteration. Since this is a rather costly choice, it can be regulated by the user with the `reorthogonalize` keyword.

Even when using the all available tricks, the multi-root Davidson may still be proven to be numerically unstable in the current implementation, especially if very strict convergence criteria are asked. In order to achieve this, the partially converged roots of the multi-root Davidson can be passed to a single-root Davidson cycle which is numerically more stable. The current implementation automatically calls the single-root Davidson procedure if the maximum number of iteration has been reached with no convergence, and passes the roots that have been "locked". This is though a trial and error procedure for the user. In an attempt to make it automatic, an break criterion has been implemented and can be used with the `auto-multi-break` keyword. If the keyword has been set to `on`, the multi-root Davidson cycle stops, if all roots asked are "locked" and half of them are converged. The unconverged roots are then passed to the single-root Davidson cycle.

The multi-root Davidson procedure is implemented in the `Generalized_DavidsonS` function.

List of acronyms

AO . . . . . Atomic Orbital

BFGS . . . . . Broyden Fletcher Goldfarb Shanno

BO . . . . . Born Oppenheimer

CC . . . . . Coupled Cluster

CI . . . . . Configuration Interaction

DCD . . . . . Double-Coset Decomposition

DCR . . . . . Double-Coset Representative

DFT . . . . . Density-Functional Theory

DIIS . . . . . Direct Inversion of the Iterative Space

EA . . . . . Electron Affinity

EE . . . . . Excitation Energy

EOM . . . . . Equation of Motion

FCI . . . . . Full Configuration Interaction

ff . . . . . Finite magnetic Field

flop . . . . . FLOating-point OPeration

GIAO . . . . . Gauge-origin Including Atomic Orbital

GUI . . . . . Graphical User Interface

HF . . . . . Hartree Fock

I/O . . . . . Input/Output

IP . . . . . Ionization Potential

IRREP . . . . . IRreducible REPresentation

LCAO . . . . . Linear Combination of Atomic Orbitals

LR . . . . . Linear Response

MBPT . . . . . Many-Body Perturbation Theory

MO . . . . . Molecular Orbital

MOM . . . . . Maximum-Overlap Method

MP . . . . . Møller Plesset

MWD . . . . . Magnetic White Dwarf

NR . . . . . Newton Raphson

PG . . . . . Point Group

RHF . . . . . Restricted Hartree Fock

RO . . . . . Restricted Open-shell

SAO . . . . . Symmetry-Adapted Orbital

SCF . . . . . Self-Consistent Field

SF . . . . . Spin Flip

UHF . . . . . Unrestricted Hartree Fock

unc . . . . . UNContracted

WD . . . . . White Dwarf

Bibliography

[1]T. S. Kuhn, *The Structure of Scientific Revolutions* (University of Chicago Press, 1962).

[2]W. Heitler and F. London, "Wechselwirkung neutraler Atome und homöopolare Bindung nach der Quantenmechanik", Zeitschrift für Phys. 1927 446 **44**, 455–472 (1927).

[3]*The Nobel Prize in Chemistry 1998 to Walter Kohn for his development of the density-functional theory and to John Pople for his development of computational methods in quantum chemistry.*

[4]P. Schmelcher, L. S. Cederbaum, P. Schmelcher, and L. S. Cederbaum, "Molecules in strong magnetic fields: Some perspectives and general aspects", Int. J. Quantum Chem. **64**, 501–511 (1997).

[5]O. Kahn, *Molecular magnetism* (Dover Publications, 1993).

[6]D. Gatteschi, R. Sessoli, and J. Villain, *Molecular Nanomagnets* (Oxford University Press, Sept. 2006), pp. 1–408.

[7]S. P. Sauer, I. Paidarová, and J. Oddershede, "Correlated and gauge origin independent calculations of magnetic properties I. Triply bonded molecules", Mol. Phys. **81**, 87–118 (1994).

[8]S. P. A. Sauer, I. Paidarová, and J. Oddershede, "Correlated and gauge origin independent calculations of magnetic properties II. Shielding constants of simple singly bonded molecules", Theor. Chim. Acta **88**, 351–361 (1994).

[9]A. Soncini and P. Fowler, "Non-linear ring currents: effect of strong magnetic fields on π-electron circulation", Chem. Phys. Lett. **400**, 213–220 (2004).

[10]A. Soncini and L. F. Chibotaru, "Mechanisms of Spin-Mixing Instabilities in Antiferromagnetic Molecular Wheels", Phys. Rev. Lett. **99**, 077204 (2007).

[11]S. Sun, D. Williams-Young, and X. Li, "An ab Initio Linear Response Method for Computing Magnetic Circular Dichroism Spectra with Nonperturbative Treatment of Magnetic Field", J. Chem. Theory Comput. **15**, 3162–3169 (2019).

[12]A. Pausch, C. Holzer, and W. Klopper, "Efficient Calculation of Magnetic Circular Dichroism Spectra Using Spin-Noncollinear Linear-Response Time-Dependent Density Functional Theory in Finite Magnetic Fields", J. Chem. Theory Comput. **18**, 3758 (2022).

[13]E. I. Tellgren, T. Helgaker, and A. Soncini, "Non-perturbative magnetic phenomena in closed-shell paramagnetic molecules", Phys. Chem. Chem. Phys. **11**, 5489 (2009).

[14]F. London, "Théorie quantique des courants interatomiques dans les combinaisons aromatiques", J. Phys. Radium **8**, 397–409 (1937).

[15]E. I. Tellgren, A. Soncini, and T. Helgaker, "Nonperturbative ab initio calculations in strong magnetic fields using London orbitals", J. Chem. Phys. **129**, 154114 (2008).

[16]P. Schmelcher and L. S. Cederbaum, "On molecules and ions in strong magnetic fields", Int. J. Quantum Chem. **40**, 371–385 (1991).

[17]J. C. Kemp, J. B. Swedlund, J. D. Landstreet, and J. R. P. Angel, "Discovery of Circularly Polarized Light from a White Dwarf", Astrophys. J. **161**, L77 (1970).

[18]K. K. Lange, E. I. Tellgren, M. R. Hoffmann, and T. Helgaker, "A Paramagnetic Bonding Mechanism for Diatomics in Strong Magnetic Fields", Science **337**, 327–331 (2012).

[19]B. Murdin, J. Li, M. Pang, E. Bowyer, K. Litvinenko, S. Clowes, H. Engelkamp, C. Pidgeon, I. Galbraith, N. Abrosimov, H. Riemann, S. Pavlov, H.-W. Hübers, and P. Murdin, "Si:P as a laboratory analogue for hydrogen on high magnetic field white dwarf stars", Nat. Commun. **4**, 1469 (2013).

[20]E. I. Tellgren, A. M. Teale, J. W. Furness, K. K. Lange, U. Ekström, and T. Helgaker, "Non-perturbative calculation of molecular magnetic properties within current-density functional theory", J. Chem. Phys. **140**, 034101 (2014).

[21]S. Stopkowicz, J. Gauss, K. K. Lange, E. I. Tellgren, and T. Helgaker, "Coupled-cluster theory for atoms and molecules in strong magnetic fields", J. Chem. Phys. **143**, 074110 (2015).

[22]F. Hampe and S. Stopkowicz, "Equation-of-motion coupled-cluster methods for atoms and molecules in strong magnetic fields", J. Chem. Phys. **146**, 154105 (2017).

[23]S. Stopkowicz, "Perspective: Coupled cluster theory for atoms and molecules in strong magnetic fields", Int. J. Quantum Chem. **118**, e25391 (2018).

[24]M. A. Hollands, S. Stopkowicz, M.-P. Kitsaras, F. Hampe, S. Blaschke, and J. J. Hermes, "A DZ white dwarf with a 30 MG magnetic field", Monthly Notices of the Royal Astronomical Society **520**, 3560–3575 (2023).

[25]D. Koester and G. Chanmugam, "Physics of white dwarf stars", Reports Prog. Phys. **53**, 837–915 (1990).

[26]R. H. Garstang, "Atoms in high magnetic fields (white dwarfs)", Reports Prog. Phys. **40**, 105–154 (1977).

[27]W. Rosner, G. Wunner, H. Herold, and H. Ruder, "Hydrogen atoms in arbitrary magnetic fields. I. Energy levels and wavefunctions", J. Phys. B At. Mol. Phys. **17**, 29–52 (1984).

[28]H. Forster, W. Strupat, W. Rosner, G. Wunner, H. Ruder, and H. Herold, "Hydrogen atoms in arbitrary magnetic fields. II. Bound-bound transitions", J. Phys. B At. Mol. Phys. **17**, 1301–1319 (1984).

[29]J. L. Greenstein, "The identification of hydrogen in GRW +70 deg 8247", Astrophys. J. **281**, L47 (1984).

[30]R. J. W. Henry and R. F. Oconnell, "On the magnetic field in the white dwarf GRW + 70.8247 deg", Astrophys. J. **282**, L97 (1984).

[31]R. J. W. Henry and R. F. Oconnell, "Hydrogen spectrum in magnetic white dwarfs - H-alpha, H-beta and H-gamma transitions", Publ. Astron. Soc. Pacific **97**, 333 (1985).

[32]J. L. Greenstein, R. J. W. Henry, and R. F. Oconnell, "Futher identifications of hydrogen in GRW +708247", Astrophys. J. **289**, L25 (1985).

[33]G. D. Schmidt, R. G. Allen, P. S. Smith, and J. Liebert, "Combined Ultraviolet-Optical Spectropolarimetry of the Magnetic White Dwarf GD 229", Astrophys. J. **463**, 320 (1996).

[34]G. D. Schmidt, R. G. Allen, P. S. Smith, and J. Liebert, "Erratum: "Combined Ultraviolet-Optical Spectropolarimetry of the Magnetic White Dwarf GD 229" (ApJ, 463, 320 [1996])", Astrophys. J. **473**, 569–569 (1996).

[35]S. Jordan, P. Schmelcher, W. Becken, and W. Schweizer, "Evidence for helium in the magnetic white dwarf gd 229", Astron. Astrophys. **336**, L33–L36 (1998).

[36]D. T. Wickramasinghe and L. Ferrario, "Magnetism in Isolated and Binary White Dwarfs", Publ. Astron. Soc. Pacific **112**, 873–924 (2000).

[37]B. Zuckerman, D. Koester, I. N. Reid, and M. Hunsch, "Metal Lines in DA White Dwarfs", Astrophys. J. **596**, 477–495 (2003).

[38]E. L. Degl'Innocenti and M. Landolfi, *Polarization in Spectral Lines* (Springer Netherlands, Dordrecht, 2004).

[39]P. Dufour, J. Liebert, G. Fontaine, and N. Behara, "White dwarf stars with carbon atmospheres", Nature **450**, 522–524 (2007).

[40]S. V. Berdyugina, A. V. Berdyugin, and V. Piirola, "Molecular Magnetic Dichroism in Spectra of White Dwarfs", Phys. Rev. Lett. **99**, 091101 (2007).

[41]S. Jordan, "Magnetic fields in White Dwarfs and their direct progenitors", Proc. Int. Astron. Union **4**, 369–378 (2008).

[42]B. Zuckerman, C. Melis, B. Klein, D. Koester, and M. Jura, "Ancient planetary systems are orbiting a large fraction of white dwarf stars", Astrophys. J. **722**, 725–736 (2010).

[43]S. Xu, M. Jura, D. Koester, B. Klein, and B. Zuckerman, "Discovery of molecular hydrogen in white dwarf atmospheres", Astrophys. J. **766**, L18 (2013).

[44]L. Ferrario, D. de Martino, and B. T. Gänsicke, "Magnetic White Dwarfs", Space Sci. Rev. **191**, 111–169 (2015).

[45]A. Kawka, S. Vennes, L. Ferrario, and E. Paunzen, "Evidence of enhanced magnetism in cool, polluted white dwarfs", Mon. Not. R. Astron. Soc. **482**, 5201–5210 (2019).

[46]J. D. Landstreet, S. Bagnulo, G. G. Valyavin, L. Fossati, S. Jordan, D. Monin, and G. A. Wade, "On the incidence of weak magnetic fields in DA white dwarfs", Astron. Astrophys. **545**, A30 (2012).

[47]S. Bagnulo and J. D. Landstreet, "Discovery of six new strongly magnetic white dwarfs in the 20 pc local population", Astron. Astrophys. **643**, A134 (2020).

[48]G. R. Burbidge and E. M. Burbidge, "The composition and spectra of white dwarfs", Publ. Astron. Soc. Pacific **66**, 308–311 (1954).

[49]V. Weidemann, "Chemical Composition and Distribution of White Dwarfs", in *Planet. nebul.* (Springer Netherlands, Dordrecht, 1968), pp. 423–424.

[50]O. Straniero, I. Dominguez, G. Imbriani, and L. Piersanti, "The Chemical Composition of White Dwarfs as a Test of Convective Efficiency during Core Helium Burning", Astrophys. J. **583**, 878–884 (2003).

[51]A. Kramida, Yu. Ralchenko, J. Reader, and NIST ASD Team, NIST Atomic Spectra Database https://physics.nist.gov/asd. National Institute of Standards and Technology, Gaithersburg, MD. 2022.

[52]*300 Tesla Single-Turn Magnet - MagLab.*

[53]D. Nakamura, A. Ikeda, H. Sawabe, Y. H. Matsuda, and S. Takeyama, "Record indoor magnetic field of 1200 T generated by electromagnetic flux-compression", Rev. Sci. Instrum. **89**, 095106 (2018).

[54]A. F. Starace, "Quasi-Landau spectrum of a hydrogen like atom in a high magnetic field", J. Phys. B At. Mol. Phys. **6**, 585–590 (1973).

[55]S. T. Chui, ""Excitonic" matter in a superstrong magnetic field", Phys. Rev. B **9**, 3438–3446 (1974).

[56]R. A. Lewis, A. Bruno-Alfonso, G. V. B. de Souza, R. E. M. Vickers, J. A. Colla, and E. Constable, "Spherical, cylindrical and tetrahedral symmetries; hydrogenic states at high magnetic field in Si:P", Sci. Rep. **3**, 3488 (2013).

[57]M. J. Pemberton, T. J. P. Irons, T. Helgaker, and A. M. Teale, "Revealing the exotic structure of molecules in strong magnetic fields", J. Chem. Phys. **156**, 204113 (2022).

[58]J. J. Dongarra, J. Du Croz, S. Hammarling, and I. S. Duff, "A set of level 3 basic linear algebra subprograms", ACM Transactions on Mathematical Software **16**, 1–17 (1990).

[59]W. Becken, P. Schmelcher, and F. K. Diakonos, "The helium atom in a strong magnetic field", J. Phys. B At. Mol. Opt. Phys. **32**, 1557–1584 (1999).

[60]L. C. de Melo, T. K. Das, R. C. Ferreira, L. C. M. Miranda, and H. S. Brandi, "The H_2^+ molecule in strong magnetic fields, studied by the method of linear combinations of orbitals", Phys. Rev. A **18**, 12–14 (1978).

[61]T. Detmer, P. Schmelcher, F. K. Diakonos, and L. S. Cederbaum, "Hydrogen molecule in magnetic fields: The ground states of the Σ manifold of the parallel configuration", Phys. Rev. A **56**, 1825–1838 (1997).

[62]T. Detmer, P. Schmelcher, and L. S. Cederbaum, "Hydrogen molecule in a magnetic field: The lowest states of the Π manifold and the global ground state of the parallel configuration", Phys. Rev. A **57**, 1767–1777 (1998).

[63]P. Schmelcher, L. S. Cederbaum, and H. D. Meyer, "Electronic and nuclear motion and their couplings in the presence of a magnetic field", Phys. Rev. A **38**, 6066–6079 (1988).

[64]P. Schmelcher, L. S. Cederbaum, and H. D. Meyer, "On the validity of the Born-Oppenheimer approximation in magnetic fields", J. Phys. B At. Mol. Phys,. **21** (1988).

[65]P. Schmelcher and L. S. Cederbaum, "Molecules in strong magnetic fields: Properties of atomic orbitals", Phys. Rev. A **37**, 672–681 (1988).

[66]O.-A. Al-Hujaj and P. Schmelcher, "Lithium in strong magnetic fields", Phys. Rev. A **70**, 033411 (2004).

[67]E. Tellgren, T. Helgaker, A. Soncini, K. K. Lange, A. M. Teale, U. Ekström, S. Stopkowicz, J. H. Austad, and S. Sen, *LONDON, a quantum-chemistry program for plane-wave/gto hybrid basis sets and finite magnetic field calculations*, londonprogram.org.

[68]*QUEST, A rapid development platform for QUantum Electronic Structure Techniques, 2017; quest.codes.*

[69]S. G. Balasubramani, G. P. Chen, S. Coriani, M. Diedenhofen, M. S. Frank, Y. J. Franzke, F. Furche, R. Grotjahn, M. E. Harding, C. Hättig, A. Hellweg, B. Helmich-Paris, C. Holzer, U. Huniar, M. Kaupp, A. Marefat Khah, S. Karbalaei Khani, T. Müller, F. Mack, B. D. Nguyen, S. M. Parker, E. Perlt, D. Rappoport, K. Reiter, S. Roy, M. Rückert, G. Schmitz, M. Sierka, E. Tapavicza, D. P. Tew, C. van Wüllen, V. K. Voora, F. Weigend, A. Wodyński, and J. M. Yu, "TURBOMOLE: Modular program suite for ab initio quantum-chemical and condensed-matter simulations", J. Chem. Phys. **152**, 184107 (2020).

[70]A. Pausch and W. Klopper, "Efficient evaluation of three-centre two-electron integrals over London orbitals", Mol. Phys. **118**, e1736675 (2020).

[71]G. Vignale and M. Rasolt, "Density-functional theory in strong magnetic fields", Phys. Rev. Lett. **59**, 2360–2363 (1987).

[72]*BAGEL, Brilliantly Advanced General Electronic-structure Library. http://www.nubakery.org under the GNU General Public License.*

[73]D. B. Williams-Young, A. Petrone, S. Sun, T. F. Stetina, P. Lestrange, C. E. Hoyer, D. R. Nascimento, L. Koulias, A. Wildman, J. Kasper, J. J. Goings, F. Ding, A. E. DePrince, E. F. Valeev, and X. Li, "The Chronus Quantum software package", WIREs Computational Molecular Science **10**, `10.1002/wcms.1436` (2020).

[74]S. Lehtola, M. Dimitrova, and D. Sundholm, "Fully numerical electronic structure calculations on diatomic molecules in weak to strong magnetic fields", Mol. Phys. **118**, e1597989 (2020).

[75]F. A. Bischoff, "Structure of the H_3 molecule in a strong homogeneous magnetic field as computed by the Hartree-Fock method using multiresolution analysis", Phys. Rev. A **101**, 053413 (2020).

[76]F. Hampe, S. Stopkowicz, N. Groß, M.-P. Kitsaras, L. Grazioli, and S. Blaschke, *QCUMBRE, quantum chemical utility enabling magnetic-field dependent investigations benefitting from rigorous electron-correlation treatment*, qcumbre.org.

[77]J. F. Stanton, J. Gauss, L. Cheng, M. E. Harding, D. A. Matthews, and P. G. Szalay, *CFOUR, Coupled-Cluster techniques for Computational Chemistry, a quantum-chemical program package*, With contributions from A.A. Auer, R.J. Bartlett, U. Benedikt, C. Berger, D.E. Bernholdt, S. Blaschke, Y. J. Bomble, S. Burger, O. Christiansen, D. Datta, F. Engel, R. Faber, J. Greiner, M. Heckert, O. Heun, M. Hilgenberg, C. Huber, T.-C. Jagau, D. Jonsson, J. Jusélius, T. Kirsch, K. Klein, G.M. Kopper, W.J. Lauderdale, F. Lipparini, T. Metzroth, L.A. Mück, D.P. O'Neill, T. Nottoli, D.R. Price, E. Prochnow, C. Puzzarini, K. Ruud, F. Schiffmann, W. Schwalbach, C. Simmons, S. Stopkowicz, A. Tajti, J. Vázquez, F. Wang, J.D. Watts and the integral packages MOLECULE (J. Almlöf and P.R. Taylor), PROPS (P.R. Taylor), ABACUS (T. Helgaker, H.J.

Aa. Jensen, P. Jørgensen, and J. Olsen), and ECP routines by A. V. Mitin and C. van Wüllen. For the current version, see http://www.cfour.de.

[78]D. A. Matthews, L. Cheng, M. E. Harding, F. Lipparini, S. Stopkowicz, T.-C. Jagau, P. G. Szalay, J. Gauss, and J. F. Stanton, "Coupled-cluster techniques for computational chemistry: The CFOUR program package", J. Chem. Phys. **152**, 214108 (2020).

[79]J. Gauss, F. Lipparini, S. Burger, S. Blaschke, M.-P. Kitsaras, T. Nottoli, J. Oswald, and S. Stopkowicz, *MINT, Mainz INTegral package*, Johannes Gutenberg-Universität Mainz, unpublished, 2015-2023.

[80]F. Hampe, N. Gross, and S. Stopkowicz, "Full triples contribution in coupled-cluster and equation-of-motion coupled-cluster methods for atoms and molecules in strong magnetic fields", Phys. Chem. Chem. Phys. **22**, 23522–23529 (2020).

[81]F. Hampe and S. Stopkowicz, "Transition-Dipole Moments for Electronic Excitations in Strong Magnetic Fields Using Equation-of-Motion and Linear Response Coupled-Cluster Theory", J. Chem. Theory Comput. **15**, 4036–4043 (2019).

[82]O. Christiansen, H. Koch, and P. Jørgensen, "The second-order approximate coupled cluster singles and doubles model CC2", Chem. Phys. Lett. **243**, 409–418 (1995).

[83]O. Christiansen, H. Koch, and P. Jørgensen, "Response functions in the CC3 iterative triple excitation model", J. Chem. Phys. **103**, 7429–7441 (1995).

[84]H. Koch, O. Christiansen, P. Jørgensen, A. M. Sanchez de Merás, and T. Helgaker, "The CC3 model: An iterative coupled cluster approach including connected triples", J. Chem. Phys. **106**, 1808–1818 (1997).

[85]D. A. Matthews and J. F. Stanton, "A new approach to approximate equation-of-motion coupled cluster with triple excitations", J. Chem. Phys. **145**, 124102 (2016).

[86]K. Raghavachari, G. W. Trucks, J. A. Pople, and M. Head-Gordon, "A fifth-order perturbation comparison of electron correlation theories", Chem. Phys. Lett. **157**, 479–483 (1989).

[87]G. D. Purvis, H. Sekino, and R. J. Bartlett, "Multiplicity of many-body wavefunctions using unrestricted Hartree-Fock reference functions", Collect. Czechoslov. Chem. Commun. **53**, 2203–2213 (1988).

[88]J. F. Stanton, "On the extent of spin contamination in open-shell coupled-cluster wave functions", J. Chem. Phys. **101**, 371–374 (1994).

[89]W. Chen and H. B. Schlegel, "Evaluation of S^2 for correlated wave functions and spin projection of unrestricted Møller–Plesset perturbation theory", J. Chem. Phys. **101**, 5957–5968 (1994).

[90]A. I. Krylov, "Spin-contamination of coupled-cluster wave functions", J. Chem. Phys. **113**, 6052–6062 (2000).

[91]S. Reine and T. Saue, eds., *European Summerschool in Quantum Chemistry Book II*, 11th edition (ESQC committee 2019, Palermo, 1999) Chap. VII Molecular Magnetic Properties.

[92]K. G. Dyall and K. Fægri, *Introduction to relativistic quantum chemistry* (Oxford University Press, 2007).

[93]J. D. Jackson, *Classical Electrodynamics* (Wiley, 1998).

[94]R. E. Moss, *Advanced Molecular Quantum Mechanics* (Springer Netherlands, 1973).

[95]D. J. Griffiths, *Introduction to Quantum Mechanics* (Pearson Prentice Hall, 2005).

[96]T. Helgaker, P. Jørgensen, and J. Olsen, *Molecular Electronic-Structure Theory* (Wiley, 2000).

[97]E. I. Tellgren, S. S. Reine, and T. Helgaker, "Analytical GIAO and hybrid-basis integral derivatives: application to geometry optimization of molecules in strong magnetic fields", Phys. Chem. Chem. Phys. **14**, 9492 (2012).

[98]T. J. P. Irons, J. Zemen, and A. M. Teale, "Efficient Calculation of Molecular Integrals over London Atomic Orbitals", J. Chem. Theory Comput. **13**, 3636–3649 (2017).

[99]T. J. P. Irons, G. David, and A. M. Teale, "Optimizing Molecular Geometries in Strong Magnetic Fields", J. Chem. Theory Comput. **17**, 2166–2185 (2021).

[100]J. J. Sakurai, *Modern quantum mechanics*, edited by S. F. Tuan (Addison-Wesley Longman, 1994).

[101]A. Szabo and N. L. Ostlund, *Modern Quantum Chemistry: Introduction to Advanced Electronic Structure Theory* (Dover Publications, 1996).

[102]T. Koopmans, "Über die Zuordnung von Wellenfunktionen und Eigenwerten zu den Einzelnen Elektronen Eines Atoms", Physica **1**, 104–113 (1934).

[103]I. Shavitt and R. J. Bartlett, *Many – Body Methods in Chemistry and Physics* (Cambridge University Press, Cambridge, 2009).

[104]C. Møller and M. S. Plesset, "Note on an Approximation Treatment for Many-Electron Systems", Phys. Rev. **46**, 618–622 (1934).

[105]T. J. Lee, A. P. Rendell, K. G. Dyall, and D. Jayatilaka, "Open-shell restricted Hartree–Fock perturbation theory: Some considerations and comparisons", J. Chem. Phys. **100**, 7400–7409 (1994).

[106]S. E. Wheeler, W. D. Allen, and H. F. Schaefer, "On the convergence of Z-averaged perturbation theory", J. Chem. Phys. **128**, 074107 (2008).

[107]T. D. Crawford, H. F. Schaefer, and T. J. Lee, "On the energy invariance of open-shell perturbation theory with respect to unitary transformations of molecular orbitals", J. Chem. Phys. **105**, 1060–1069 (1996).

[108]J. Olsen, P. Jørgensen, T. Helgaker, and O. Christiansen, "Divergence in Møller–Plesset theory: A simple explanation based on a two-state model", J. Chem. Phys. **112**, 9736–9748 (2000).

[109]J. Čížek, "On the Correlation Problem in Atomic and Molecular Systems. Calculation of Wavefunction Components in Ursell-Type Expansion Using Quantum-Field Theoretical Methods", J. Chem. Phys. **45**, 4256–4266 (1966).

[110]T. D. Crawford and H. F. Schaefer, "An Introduction to Coupled Cluster Theory for Computational Chemists", in *Reviews in computational chemistry*, Vol. 14 (John Wiley & Sons, Ltd, Jan. 2007), pp. 33–136.

[111]A. Köhn and A. Tajti, "Can coupled-cluster theory treat conical intersections?", J. Chem. Phys. **127**, 044105 (2007).

[112]S. Thomas, F. Hampe, S. Stopkowicz, and J. Gauss, "Complex ground-state and excitation energies in coupled-cluster theory", **119**, 10.1080/00268976.2021.1968056 (2021).

[113]P. Piecuch and K. Kowalski, "In search of the relationship between multiple solutions characterizing coupled-cluster theories", in *Computational chemistry: reviews of current trends* (WORLD SCIENTIFIC), pp. 1–104.

[114]H. J. Monkhorst, "Calculation of properties with the coupled-cluster method", Int. J. Quantum Chem. **12**, 421–432 (1977).

[115]S. V. Levchenko and A. I. Krylov, "Equation-of-motion spin-flip coupled-cluster model with single and double substitutions: Theory and application to cyclobutadiene", J. Chem. Phys. **120**, 175–185 (2004).

[116]J. F. Stanton and J. Gauss, "Analytic energy derivatives for ionized states described by the equation-of-motion coupled cluster method", J. Chem. Phys. **101**, 8938–8944 (1994).

[117]M. Nooijen and R. J. Bartlett, "Equation of motion coupled cluster method for electron attachment", J. Chem. Phys. **102**, 3629–3647 (1995).

[118]E. F. Kjønstad and H. Koch, "Resolving the notorious case of conical intersections for coupled cluster dynamics", J. Phys. Chem. Lett. **8**, 4801–4807 (2017).

[119]J. Gauss, "Molecular properties", in *Modern methods and algorithms of quantum chemistry*, edited by J. Grotendorst (John von Neumann Institute for Computing, Jülich, 2000) Chap. Molecular, pp. 541–592.

[120]L. Adamowicz, W. D. Laidig, and R. J. Bartlett, "Analytical gradients for the coupled-cluster method", Int. J. of Quantum Chem. **26**, 245–254 (1984).

[121]S. V. Levchenko, T. Wang, and A. I. Krylov, "Analytic gradients for the spin-conserving and spin-flipping equation-of-motion coupled-cluster models with single and double substitutions", J. Chem. Phys. **122**, 224106 (2005).

[122]J. F. Stanton and R. J. Bartlett, "The equation of motion coupled-cluster method. A systematic biorthogonal approach to molecular excitation energies, transition probabilities, and excited state properties", J. Chem. Phys. **98**, 7029–7039 (1993).

[123]J. F. Stanton, "Many-body methods for excited state potential energy surfaces. I. General theory of energy gradients for the equation-of-motion coupled-cluster method", J. Chem. Phys. **99**, 8840–8847 (1993).

[124]J. F. Stanton and J. Gauss, "Analytic energy derivatives for the equation-of-motion coupled-cluster method: Algebraic expressions, implementation and application to theS 1 state of HFCO", Theor. Chim. Acta **91**, 267–289 (1995).

[125]M. Kállay and J. Gauss, "Calculation of excited-state properties using general coupled-cluster and configuration-interaction models", J. Chem. Phys. **121**, 9257–9269 (2004).

[126]M. Caricato, G. W. Trucks, and M. J. Frisch, "On the difference between the transition properties calculated with linear response- and equation of motion-CCSD approaches", J. Chem. Phys. **131**, 174104 (2009).

[127]H. Koch and P. Jørgensen, "Coupled cluster response functions", J. Chem. Phys. **93**, 3333–3344 (1990).

[128]O. Christiansen, P. Jørgensen, and C. Hättig, "Response functions from Fourier component variational perturbation theory applied to a time-averaged quasienergy", Int. J. Quantum Chem. **68**, 1–52 (1998).

[129]E. Dalgaard and H. J. Monkhorst, "Some aspects of the time-dependent coupled-cluster approach to dynamic response functions", Phys. Rev. A **28**, 1217–1222 (1983).

[130]N. C. Handy and H. F. Schaefer III, "On the evaluation of analytic energy derivatives for correlated wave functions", J. Chem. Phys. **81**, 5031–5033 (1984).

[131]T. Helgaker and P. Jørgensen, "Configuration-interaction energy derivatives in a fully variational formulation", Theor. Chim. Acta **75**, 111–127 (1989).

[132]J. F. Stanton and J. Gauss, "Perturbative treatment of the similarity transformed Hamiltonian in equation-of-motion coupled-cluster approximations", J. Chem. Phys. **103**, 1064–1076 (1995).

[133]J. J. Eriksen, P. Jørgensen, J. Olsen, and J. Gauss, "Equation-of-motion coupled cluster perturbation theory revisited", J. Chem. Phys. **140**, 174114 (2014).

[134]S. R. Gwaltney and M. Head-Gordon, "A second-order correction to singles and doubles coupled-cluster methods based on a perturbative expansion of a similarity-transformed Hamiltonian", Chem. Phys. Lett. **323**, 21–28 (2000).

[135]S. R. Gwaltney and M. Head-Gordon, "A second-order perturbative correction to the coupled-cluster singles and doubles method: CCSD(2)", J. Chem. Phys. **115**, 2014–2021 (2001).

[136]S. Hirata, M. Nooijen, I. Grabowski, and R. J. Bartlett, "Perturbative corrections to coupled-cluster and equation-of-motion coupled-cluster energies: A determinantal analysis", J. Chem. Phys. **114**, 3919–3928 (2001).

[137]S. Hirata, P.-D. Fan, A. A. Auer, M. Nooijen, and P. Piecuch, "Combined coupled-cluster and many-body perturbation theories", J. Chem. Phys. **121**, 12197 (2004).

[138]T. Shiozaki, K. Hirao, and S. Hirata, "Second- and third-order triples and quadruples corrections to coupled-cluster singles and doubles in the ground and excited states", J. Chem. Phys. **126**, 244106 (2007).

[139]P. Pulay, "Convergence acceleration of iterative sequences. the case of SCF iteration", Chemical Physics Letters **73**, 393–398 (1980).

[140]P. Pulay, "Improved SCF convergence acceleration", J. Comput. Chem **3**, 556–560 (1982).

[141]A. C. Paul, R. H. Myhre, and H. Koch, "New and Efficient Implementation of CC3", J. Chem. Theory Comput. **17**, 117–126 (2021).

[142]M.-P. Kitsaras and S. Stopkowicz, "Spin contamination in MP2 and CC2, a surprising issue", J. Chem. Phys. **154**, 131101 (2021).

[143]I. Shavitt, C. Bender, A. Pipano, and R. Hosteny, "The iterative calculation of several of the lowest or highest eigenvalues and corresponding eigenvectors of very large symmetric matrices", J. Comput. Phys. **11**, 90–108 (1973).

[144]E. R. Davidson, "Use of double cosets in constructing integrals over symmetry orbitals", J. Chem. Phys. **62**, 400 (1975).

[145]K. Hirao and H. Nakatsuji, "A generalization of the Davidson's method to large nonsymmetric eigenvalue problems", J. Comput. Phys. **45**, 246–254 (1982).

[146]R. B. Morgan and D. S. Scott, "Generalizations of Davidson's Method for Computing Eigenvalues of Sparse Symmetric Matrices", SIAM J. Sci. Stat. Comput. **7**, 817–825 (1986).

[147]M. Crouzeix, B. Philippe, and M. Sadkane, "The Davidson Method", SIAM J. Sci. Comput. **15**, 62–76 (1994).

[148]Y. S. Lee, S. A. Kucharski, and R. J. Bartlett, "A coupled cluster approach with triple excitations", J. Chem. Phys. **81**, 5906–5912 (1984).

[149]J. F. Stanton, "Why CCSD(T) works: a different perspective", Chem. Phys. Lett. **281**, 130–134 (1997).

[150]K. Kowalski and P. Piecuch, "The method of moments of coupled-cluster equations and the renormalized CCSD[T], CCSD(T), CCSD(TQ), and CCSDT(Q) approaches", J. Chem. Phys. **113**, 18 (2000).

[151]T. D. Crawford and J. F. Stanton, "Investigation of an asymmetric triple-excitation correction for coupled-cluster energies", Int. J. Quantum Chem. **70**, 601–611 (1998).

[152]A. G. Taube and R. J. Bartlett, "Improving upon CCSD(T): ΛCCSD(T). I. Potential energy surfaces", J. Chem. Phys. **128**, 044110 (2008).

[153]J. F. Stanton and J. Gauss, "A simple correction to final state energies of doublet radicals described by equation-of-motion coupled cluster theory in the singles and doubles approximation", Theor. Chim. Acta **93**, 303 (1996).

[154]P. Fowler and E. Steiner, "Paramagnetic closed-shell molecules: the isoelectronic series CH^+ , BH and BeH^-", Mol. Phys. **74**, 1147–1158 (1991).

[155]M. Schreiber, M. R. Silva-Junior, S. P. A. Sauer, and W. Thiel, "Benchmarks for electronically excited states: CASPT2, CC2, CCSD, and CC3", J. Chem. Phys. **128**, 134110 (2008).

[156]A. I. Krylov, "The Quantum Chemistry of Open-Shell Species", in *Rev. comput. chem.* Edited by A. L. Parrill and K. B. Lipkowitz (John Wiley & Sons, Ltd, Apr. 2017), pp. 151–224.

[157]L. Reimund, "Untersuchung des CH-Radikals im starken Magnetfeld mit hochgenauen Equation-of-Motion-Coupled-Cluster-Methoden", Bachelor thesis (Johannes Gutenberg Universität Mainz, 2022).

[158]R. Al-Saadon, T. Shiozaki, and G. Knizia, "Visualizing Complex-Valued Molecular Orbitals", J. Phys. Chem. A **123**, 3223–3228 (2019).

[159]A. I. Krylov, "From orbitals to observables and back", J. Chem. Phys. **153**, 080901 (2020).

[160]R. S. Mulliken, "Electronic Structures of Polyatomic Molecules and Valence. II. General Considerations", Phys. Rev. **41**, 49–71 (1932).

[161]V. Vallet, U. Wahlgren, and I. Grenthe, "Probing the nature of chemical bonding in uranyl(VI) complexes with quantum chemical methods", J. Phys. Chem. A **116**, 12373–12380 (2012).

[162]Q. Y. Wu, J. H. Lan, C. Z. Wang, C. L. Xiao, Y. L. Zhao, Y. Z. Wei, Z. F. Chai, and W. Q. Shi, "Understanding the bonding nature of uranyl ion and functionalized graphene: A theoretical study", J. Phys. Chem. A **118**, 2149–2158 (2014).

[163]W. Su, S. Pan, X. Sun, S. Wang, L. Zhao, G. Frenking, and C. Zhu, "Double dative bond between divalent carbon(0) and uranium", Nat. Commun. **9**, 4997 (2018).

[164]H. R. Larsson, H. Zhai, C. J. Umrigar, and G. K. L. Chan, "The Chromium Dimer: Closing a Chapter of Quantum Chemistry", J. Am. Chem. Soc. **144**, 15932–15937 (2022).

[165]V. I. Minkin, "Glossary of terms used in theoretical organic chemistry", Pure Appl. Chem. **71**, 1919–1981 (1999).

[166]A. B. Sannigrahi and T. Kar, "Molecular orbital theory of bond order and valency", J. Chem. Educ. **65**, 674 (1988).

[167]R. F. W. Bader, *Atoms in Molecules: A Quantum Theory* (Clarendon Press, 1990).

[168]G. Knizia, "Intrinsic atomic orbitals: An unbiased bridge between quantum theory and chemical concepts", J. Chem. Theory Comput. **9**, 4834–4843 (2013).

[169]R. B. Woodward and R. Hoffmann, "Stereochemistry of Electrocyclic Reactions", J. Am. Chem. Soc. **87**, 395–397 (1965).

[170]J. R. Asher, "An animated visualization of orbital angular momentum and spin-orbit coupling", Int. J. Quantum Chem. **118**, e25683 (2018).

[171]G. Schaftenaar and J. Noordik, J. Comput. Aided Mol. Des. **14**, 123–134 (2000).

[172]M. D. Hanwell, D. E. Curtis, D. C. Lonie, T. Vandermeerschd, E. Zurek, and G. R. Hutchison, "Avogadro: An advanced semantic chemical editor, visualization, and analysis platform", J. Cheminform. **4**, 1–17 (2012).

[173]*IQmol Molecular Viewer*, http://iqmol.org/.

[174]*NumPy*, https://numpy.org/.

[175]*Mayavi: 3D scientific data visualization and plotting in Python — mayavi 4.8.1 documentation*, https://docs.enthought.com/mayavi/mayavi/.

[176]P. G. Szalay and J. Gauss, "Spin-restricted open-shell coupled-cluster theory for excited states", J. Chem. Phys. **112**, 4027–4036 (2000).

[177]P. G. Szalay, J. Vázquez, C. Simmons, and J. F. Stanton, "Triplet instability in doublet systems", J. Chem. Phys. **121**, 7624–7631 (2004).

[178]E. P. Wigner, *Group theory and its application to the quantum mechanics of atomic spectra* (Academic Press, New York, 1959).

[179]P. D. Dacre, "On the use of symmetry in SCF calculations", Chem. Phys. Lett. **7**, 47–48 (1970).

[180]M. Elder, "Use of molecular symmetry in SCF calculations", Int. J. Quantum Chem. **7**, 75–85 (1973).

[181]D. M. Bishop, *Group Theory and Chemistry* (Dover Publications, 1973).

[182]S. L. Altmann, *Induced representations in crystals and molecules* (Academic Press, New York, 1977).

[183]S. Reine and T. Saue, eds., *European Summerschool in Quantum Chemistry Book I*, 11th edition (ESQC committee 2019, Palermo, 1999) Chap. III Molecular Symmetry and Quantum Chemistry.

[184]S. L. Altmann and P. Herzig, *Point-group Theory Tables*, Second (Oxford University Press, 2011).

[185]J. S. Lomont, *Applications of finite groups* (Academic Press, 1959), p. 346.

[186]P. R. Taylor, "Symmetry-adapted integral derivatives", Theor. Chim. Acta **69**, 447–460 (1986).

[187]J. A. Green, *Sets and groups* (Routledge & K. Paul, 1988).

[188]A. Pausch, M. Gebele, and W. Klopper, "Molecular point groups and symmetry in external magnetic fields", J. Chem. Phys. **155**, 201101 (2021).

[189]J. F. Stanton, J. Gauss, J. D. Watts, and R. J. Bartlett, "A direct product decomposition approach for symmetry exploitation in many-body methods. I. Energy calculations", J. Chem. Phys. **94**, 4334–4345 (1991).

[190]D. Hilbert and R. Courant, *Methods of Mathematical Physics* (Wiley-Interscience, 1962).

[191]J. Gauss, J. F. Stanton, and R. J. Bartlett, "Coupled-cluster open-shell analytic gradients: Implementation of the direct product decomposition approach in energy gradient calculations", J. Chem. Phys. **95**, 2623–2638 (1991).

[192]*Cluster TCEMPIRE — Theoretische Chemie*.

[193]S. Reine and T. Saue, eds., *European Summerschool in Quantum Chemistry Book II*, 11th edition (ESQC committee 2019, Palermo, 1999) Chap. IX Geometry Optimizations for Minima and Saddle Points.

[194]E. B. Wilson, J. C. Decius, and P. C. Cross, *Molecular vibrations, the Theory of Infrared and Raman Vibrational Spectra* (Dover Publications, 1955).

[195]D.-H. Lu, M. Zhao, and D. G. Truhlar, "Projection operator method for geometry optimization with constraints", J. Comput. Chem. **12**, 376–384 (1991).

[196]J. Baker, "Geometry optimization in Cartesian coordinates: Constrained optimization", J. Comput. Chem. **13**, 240–253 (1992).

[197]J. Baker and D. Bergeron, "Constrained optimization in cartesian coordinates", J. Comput. Chem. **14**, 1339–1346 (1993).

[198]C. Eckart, "Some Studies Concerning Rotating Axes and Polyatomic Molecules", Phys. Rev. **47**, 552–558 (1935).

[199]J. Parsons, J. B. Holmes, J. M. Rojas, J. Tsai, and C. E. M. Strauss, "Practical conversion from torsion space to Cartesian space forin silico protein synthesis", J. Comput. Chem. **26**, 1063–1068 (2005).

[200]L.-P. Wang and C. Song, "Geometry optimization made simple with translation and rotation coordinates", J. Chem. Phys. **144**, 214108 (2016).

[201]E. A. Coutsias, C. Seok, and K. A. Dill, "Using quaternions to calculate RMSD", J. Comput. Chem. **25**, 1849–1857 (2004).

[202]R. Fletcher, *Practical Methods of Optimization* (John Wiley & Sons, Ltd, Chichester, West Sussex England, May 2000).

[203]C. Holzer, A. M. Teale, F. Hampe, S. Stopkowicz, T. Helgaker, and W. Klopper, "GW quasiparticle energies of atoms in strong magnetic fields", J. Chem. Phys. **150**, 214112 (2019).

[204]I. N. Reid, J. Liebert, and G. D. Schmidt, "Discovery of a Magnetic DZ White Dwarf with Zeeman-Split Lines of Heavy Elements", Astrophys. J. **550**, L61–L63 (2001).

[205]M.-P. Kitsaras, L. Grazioli, and S. Stopkowicz, "Use of the approximate Coupled-Cluster methods, CC2 and CC3, for the treatment of atoms and molecules in a finite magnetic field", in preparation, 2023.

[206]L. Monzel, A. Pausch, L. D. M. Peters, E. I. Tellgren, T. Helgaker, and W. Klopper, "Molecular dynamics of linear molecules in strong magnetic fields", J. Chem. Phys. **157**, 054106 (2022).

[207]E. I. Tellgren, T. Culpitt, L. D. M. Peters, and T. Helgaker, "Molecular vibrations in the presence of velocity-dependent forces", J. Chem. Phys. **158**, 124124 (2023).

[208]M. Wibowo, T. J. P. Irons, and A. M. Teale, "Modeling Ultrafast Electron Dynamics in Strong Magnetic Fields Using Real-Time Time-Dependent Electronic Structure Methods", J. Chem. Theory Comput. **17**, 2137–2165 (2021).

[209]J. M. Hollas, *Modern Spectroscopy* (John Wiley & Sons, 2004).

[210]R. S. Mulliken, "Electronic Population Analysis on LCAO–MO Molecular Wave Functions. I", J. Chem. Phys. **23**, 1833–1840 (1955).

[211]E. R. Davidson, "Properties and Uses of Natural Orbitals", Rev. Mod. Phys. **44**, 451–464 (1972).

[212]J. von Neumann and E. P. Wigner, "Über merkwürdige diskrete Eigenwerte", in *Collect. work. eugene paul wigner* (Springer Berlin Heidelberg, Berlin, Heidelberg, 1993), pp. 291–293.

[213]R. L. Martin, "Natural transition orbitals", J. Chem. Phys. **118**, 4775–4777 (2003).

[214]K. D. Nanda and A. I. Krylov, "Visualizing the Contributions of Virtual States to Two-Photon Absorption Cross Sections by Natural Transition Orbitals of Response Transition Density Matrices", J. Phys. Chem. Lett. **8**, 3256–3265 (2017).

[215]Y. C. Park, A. Perera, and R. J. Bartlett, "Low scaling EOM-CCSD and EOM-MBPT(2) method with natural transition orbitals", J. Chem. Phys. **149**, 10.1063/1.5045340 (2018).

[216]V. R. Saunders and I. H. Hillier, "A 'Level-Shifting' method for converging closed shell Hartree-Fock wave functions", Int. J. Quantum Chem. **7**, 699–705 (1973).

[217]A. T. B. Gilbert, N. A. Besley, and P. M. W. Gill, "Self-Consistent Field Calculations of Excited States Using the Maximum Overlap Method (MOM)", J. Phys. Chem. A **112**, 13164–13171 (2008).

[218]G. David, T. J. P. Irons, A. E. A. Fouda, J. W. Furness, and A. M. Teale, "Self-Consistent Field Methods for Excited States in Strong Magnetic Fields: a Comparison between Energy- and Variance-Based Approaches", J. Chem. Theory Comput. **17**, 5492–5508 (2021).